SHAKING TABLE MODEL TESTS ON DYNAMIC INTERACTION BETWEEN CROSS SECTION OF FLEXIBLE UNDERGROUND STRUCTURES AND LIQUEFIED SOIL

液状化地盤と埋設柔構造物断面の
動的相互作用に関する実験的研究

Yukio Tamari

溜　　幸　生

SHAKING TABLE MODEL TESTS ON DYNAMIC INTERACTION BETWEEN CROSS SECTION OF FLEXIBLE UNDERGROUND STRUCTURES AND LIQUEFIED SOIL

液状化地盤と埋設柔構造物断面の
動的相互作用に関する実験的研究

by

Yukio Tamari
溜　　幸　生

November, 2003

A dissertation submitted to the department of civil engineering, in the requirements for the degree of Doctor of Engineering at The University of Tokyo

Thesis supervisor : Professor TOWHATA, Ikuo
Department of civil engineering,
School of engineering, The University of Tokyo

Thesis committee : Professor TATSUOKA, Fumio
Professor KONAGAI, Kazuo
Professor KOSEKI, Junichi
Professor YANG, Dawen

ABSTRACT

In recent years, the importance of seismic design has been increasing continuously in such public underground structures as ducts for utility pipelines or conveyances of sewage, road tunnels, and subway stations. Furthermore, the nonlinear behavior of soils as well as structures came to be considered in seismic design procedures. In spite of this situation, however, the mechanism of the interaction between liquefied soil and the underground structure during earthquakes has not yet been fully understood. Therefore, there is a need to study more clearly the detailed mechanism of the seismic interaction considering soil liquefaction.

This dissertation deals with the dynamic interaction between liquefied soil and a cross section of a flexible underground structure during earthquakes. Study has been conducted in order to investigate experimentally the nature and mechanism of dynamic interaction of underground structure with soil subjected to liquefaction, and to propose a method to quantitatively evaluate the dynamic earth pressure which acts on the underground structure. A box-shaped culvert, which is often used in such infrastructures as those for embedded tunnels, common duct for utility pipelines, and water channels, is selected as a typical type of underground structure in this study.

A series of 1G shaking table tests was carried out on an aluminum model structure which was embedded in saturated cohesionless soil and fixed at its base. A special attempt was made to experimentally reproduce a cyclic stress-strain relationship as well as an effective stress path of soil around the embedded structure during shaking by installing such a variety of transducers as those for acceleration, displacement, pore pressure and earth pressure. Moreover, earth pressure and bending strain of the flexible wall of the embedded structure model were measured. The acceleration and the frequency of input motion, the relative density of the backfill and the tensile strength of the structure were varied in tests.

From the measurements, the stress-strain relationship and the effective stress path during shaking were reproduced quantitatively. In this process, the shear stresses were derived considering not only the inertia force of the soil mass but also the normal stress difference induced by the existence of the structure. The shear strains were reproduced taking both soil displacements and wall displacements of the structure into account. The change with time of shear modulus of soil as well as the natural frequency of the backfill was derived based on the stress-strain relationship. The decrease of the shear modulus in the process of soil liquefaction due to shaking

was observed in a quantitative manner.

The amplification and the phase difference of shaking between the top and the bottom of the cross section of structure were analyzed from recorded accelerations. It was clarified that the decrease of the shear modulus of the backfill could bring about the resonance of underground structures during earthquakes. In addition, the amount of the amplification ratio at the resonance seemed to have a relation with the damping ratio of backfill during excitation. Furthermore, it was experimentally shown that a complicated change of amplification occurs due to residual shear modulus of backfill when the dense backfill behaves in a dilative manner.

The analytical study was made based on the elastic beam theory. The curvatures and the deflections of wall were calculated by superposition of an elastic beam considering the measured earth pressures as a load. It was found that the calculated curvatures or deflections agree with the measured quantities reasonably as long as the natural frequency of the backfill became less than about half of that of the structure itself. It was suggested that the deformations of the structure at the resonance and during liquefaction could be calculated by a simple method of calculation.

In order to understand the effects of dynamic earth pressures during shaking, the phase difference between displacement and earth pressures on structure's side face were analyzed by using recorded data. It was indicated that natural frequencies of structure and backfill as well as the dilative nature of the soil significantly affect the type of soil-structure interaction. In addition, it was found that the dynamic earth pressures during soil liquefaction have strong correlation with the acceleration on the wall of structure than the normal strain of soil near the structure.

To facilitate the practical design of cross section of underground structures, an analytical method was developed to assess the dynamic pressures acting on a flexible wall during liquefaction. The amplification and the phase difference between the top and the bottom of a cross section observed in a series of shaking table tests were taken into account in the solution. A comparison was made between measured and calculated dynamic pressure for several test results in order to show that the proposed solution of dynamic pressure on flexible wall gives good results. Based on the results, a basic idea of a seismic effect on the underground structure subjected to soil liquefaction is presented.

ACKNOWLEDGEMENT

The author wishes to express his sincere gratitude to the advisor, Professor Ikuo Towhata of the University of Tokyo, from whom he has received continuous technical guidance since October 1998 in various aspects of this research. His accurate indication, constructive advises and continuous encouragement were gratefully acknowledged. The author is deeply thankful to his critical reading and careful corrections of the draft.

The author also expresses his grateful thanks to Professor F. Tatsuoka of the University of Tokyo, Professor K. Konagai of the University of Tokyo, Professor J. Koseki and Professor D. Yang of the University of Tokyo for their discussions, constructive advices and helpful suggestions. The author is deeply thankful for their serving as members of the thesis committee.

A series of tests in this research was carried out as a part of a research project in the Tokyo Electric Power Company (TEPCO), Tokyo, Japan. Special appreciation is expressed to the staff of the TEPCO. The author is grateful to Mr. T. Nishioka (now Tokyo Electric Power Services Co., Ltd), Mr. M. Harada, Mr. T. Nomoto and Mr. M. Tsuda, who provided the part of the research project for the author's academic degree. Their advise as well as technical discussions in this research project are deeply appreciated.

Thanks are extended to the corporate members in Tokyo Electric Power Services Co., Ltd who helped and supported the present research. The author is substantially thankful to his former supervisors, Mr. T. Kodama and Mr. M. Sugisawa for their continuous encouragement. The appreciation is expressed to Mr. M. Adachi, Dr. M Sato, Mr. K. Ozeki and Dr. K. Matsubara for their help and valuable advises in a series of tests. The author is particularly grateful to Dr. M. Takahashi for the skill in tests as well as helpful suggestions in the laboratory. The author would like to thank Mr. Y. Seshimo, Dr. H. Nakase and many other colleagues in the company for their useful advises and friendly cooperation. The assistance by Mr. M. Nishiyama of Seiken corporation for manufacturing and preparation of structure models used in this study is also acknowledged gratefully.

Special gratitude is also addressed to the former adviser Professor S. Sakurai of Kobe

University (now Construction Engineering Institute), and Professor N. Shimizu, who inspired the confidence at the initiation of the research. Their continuous encouragement throughout the author's career as a civil engineer is fully acknowledged.

The author would like to express his sincere thanks to the colleagues during his visit to the Geotechnical Engineering Laboratory of the University of Tokyo in 1989. He appreciates Mr. I. Seko, Dr. M. Yoshimine and Dr. R.P. Orense for their encouragement and warm friendship. The author has learned many through their dissertations.

Last but not least, I thank my parents and brother who have been a constant source of encouragement. I thank my wife, Yuka and my children. They have never complained the isolated environment that I needed to write the draft. All their patience, understanding and support have made the completion of dissertation possible.

Contents

NOTATION

A	cross sectional area of member (Chapter 2)
A	constant in soil displacement function in x-direction (Chapter 8)
A_k,B_k	finite Fourier coefficients
B	breadth of the container (Chapter 2)
B	constant in soil displacement function in y-direction (Chapter 8)
b	width of cross section of sample
D	damping ratio
EI	bending stiffness
F	resultant force of earth pressure
G	shear modulus of soil
H	depth of liquefied ground (Chapter 1)
H	height of the model ground (Chapter 2)
H	height of underground structure (Chapter 8)
K	coefficient of earth pressure (Chapter 2)
K	bulk modulus of liquefiable soil (Chapter 8)
K_0	coefficient of earth pressure at rest
K_{liq}	ratio of total pressures between horizontal and vertical direction during complete liquefaction (=1.0)
k	spring constant
k_h	coefficient of horizontal seismic acceleration
L	length of the container (Chapter 2)
M	bending moment
m	mass
N	number of time history data
n	number of cycles
P	concentrated load
p	pressure (compression as negative)
p	dynamic pressure (compression as negative, Chapter 8)
R	reaction
r_u	pore pressure ratio = $\Delta u / \sigma_v'$
T	period

t	thickness
u	displacement in the direction of x (Chapter 4)
u	deflection of wall (Chapter 6)
V	shear force
v	displacement in the direction of z (Chapter 4)
W_P	static water pressure
x, y, z	coordinate axes
Z	coordinate axes in vertical direction (height from the bottom)
α	acceleration
α , β	constants in a generalized solution of differential equation (Chapter 8)
γ	shear strain
γ_s	unit weight of saturated soil
γ_w	unit weight of water
γ '	submerged unit weight of soil
$\triangle \sigma_h$	increment of monotonic component of earth pressure
δ	displacement of wall
δ	angle of phase difference in radian (Chapter 8)
δ	friction constant between the soil and the wall (Appendix A)
ε	bending strain
ε_h	normal strain of soil in the horizontal direction
ρ	mass density of liquefiable soil
ρ_w	mass density of water
ξ	local coordinate in the horizontal direction in a soil mass (Chapter 4)
ξ , ζ	dummy integration valuable (Chapter 6)
ξ	displacement of a particle of liquefied soil in the direction of x (Chapter 8)
η	displacement of a particle of liquefied soil in the direction of y (Chapter 8)
θ	angle of phase difference in degree (Chapter 5)
θ	deflection angle
ν	natural frequency
σ , σ_x	normal stress, normal stress in the x direction
σ_{hd}	fluctuating component of earth pressure
σ_T	total pressure
σ_h'	effective horizontal pressure
$\sigma_{h,liq}$'	horizontal pressure due to completely liquefied soil (= σ_{v0}')
σ_u	tensile strength

σ_v'	effective overburden pressure
σ_{v0}'	initial effective over burden pressure
σ_Y	yield stress
τ	shear stress
τ	friction between the soil and the wall of container (Appendix A)
ϕ	curvature
ω	angular frequency

Subscripts

a	amplitude
bottom, top	bottom of the structure, top of the structure, respectively
d	dynamic
fluc.	fluctuating
g	at the base ground (Chapter 8)
i	element designation
m	mean values
mono.	monotonic
s	static
soil	in soil
struc.	at a structure
t	at the top of structure (Chapter 8)
x, y	along *x* and along *y*, respectively

Chapter 1

INTRODUCTION

1.1 GENERAL REMARKS

Soil liquefaction is generally known as a phenomenon in which soil behaves as a very soft material during earthquakes. The term of soil liquefaction is commonly used to define a condition in which a saturated cohesionless soil is transformed from solid condition to a liquefied state by static or cyclic loading. It is not disastrous in itself; however, it may cause a drastic loss of strength or stiffness that results in settlement or tilting of buildings, uplift of underground structures, lateral spreading in a wide area, or other seismic hazards. Numerous extensive studies since 1960s have unveiled the mechanism of liquefaction and the nature of soil during the phenomenon (e.g. Ishihara, 1996; PHRI, 1997; JGS, 1998).

On the other hand, large underground structures such as ducts for utility pipelines or conveyances of sewage, road tunnels, subway stations, have been constructed as important public facilities in urban area. Due to siting requirements, those underground structures were sometimes constructed not only in the stable basement layer but also in soft ground or sandy ground vulnerable to liquefaction during earthquakes. Going with the enlargement of scale of those underground structures, extensive researches on seismic design methods have been conducted since the middle of 1970s.

In seismic design of large reinforced concrete (RC) underground structures, the responses of structures are usually examined not only in the longitudinal direction but also in the cross section of transverse direction. Since it was indicated that the response of an underground structure is produced primarily by the ground deformations (Tamura et al., 1975; Hamada, 1978, Tohma et al., 1984), the seismic deformation method (or the response displacement method) was developed for practical design calculations of cross sections (e.g. Kuribayashi et al., 1977). Normally such seismic effects as deformation of ground under free-field condition, frictional shear force on the surface, and inertia forces of the structure are applied on a frame-spring model (Kawashima, 1994). The method has been commonly used for practical seismic design of underground structures (JRA,

1992).

The January 17 1995 Hyogoken-Nambu (Kobe) earthquake (M=7.2) caused severe damage to various structures in an urban area. Among these, a subway station, which was constructed in early 1960s, completely collapsed due to the earthquake (Iida et al., 1996; Samata, 1996). It became the first serious damage in large underground structures and one of the amazing events in the earthquake. Since then, the importance of seismic design has been increasing continuously for that type of underground structures. According to key concepts proposed after the earthquake by Japan Society of Civil Engineers (JSCE, 2000), strong motions has been used as a "Level 2 motion" in seismic design of civil structures. Owing to strong motions in seismic design, the consideration of the effect of soil liquefaction has become inevitable. In this regard, several design codes have been revised to require the effect of liquefaction for underground structures (e.g., JSCE, 1998; RTRI, 1999).

Many efforts have been made to clarify the interactive behavior of box-shaped cross sections of underground structures in a decade (Watanabe et al., 1991abc; Tateishi, 1992; Penzien et al., 1992; Matsuda et al., 1997; Kawama et al, 2001; Ohtomo et al., 2002), and partially embedded structures (Koga et al.,1996). One of the limitations of past studies on the interaction problem of cross sections was that the effect of liquefied soil was not studied in the most experiments, with only the non-liquefied condition attracting much attention. For that reason, the mechanism of the seismic interaction between liquefied soil and the cross section of underground structure, which is flexibly deform in a transverse direction during earthquake, has not been fully understood. Therefore, there is a need to study in detail the mechanism, and to propose a method in order to assess the problem of the determination of seismic effects.

The study presented herein is an attempt to clarify the seismic interaction between a box-shaped cross section of flexible underground structure and liquefied soil.

1.2 BRIEF REVIEW OF PREVIOUS STUDIES

1.2.1 Soil-structure interaction of large underground structures

The seismic soil-structure interaction associated with large underground structures is one of the important research topics in the field of structural dynamics and geotechnical earthquake engineering. In the past few decades, considerable research has been conducted on this topic.

In order to facilitate the practical seismic design of RC box sections of underground structures, dynamic earth pressures acting on a box section during earthquakes were examined experimentally and analytically by Watanabe et al.(1991a, 1991b). A series of shaking table model tests was performed on a two-span box section of structure in dry sand. The depth of the structure from the ground surface and the stiffness of the box section were varied in tests. The model was shaken by a sinusoidal wave with the intensity of 50gal～300gal. The numerical experiments were then conducted by means of finite element method on the buried structure model, in which the ratio between the apparent shear stiffness of the box section and that of the displaced soil element, β , was taken as a representative parameter.

It was found qualitatively that i) the shear force at the bottom of the box section, αT_L, (=2 α τ_L・a, see Fig.1.1(a)), became smaller than the shear force due to shear stress of soil at the same depth in surrounding ground, T_L, (=2 τ_L・a), when the apparent shear stiffness of box section was smaller than that of soil, ii) the difference of resultant shear force between the top and the bottom, $T_u - \alpha T_u$, resulted in the horizontal normal earth pressure P_1 at the side of structure (see Fig.1.1(b)). Namely, $2P_1$ was equal to the difference of $T_u - \alpha T_u$. iii) the inertia force of the structure also could turn into the horizontal normal earth pressure P_2 (see Fig.1.1(c)). Actually when the apparent shear stiffness of box section was smaller than that of soil, the horizontal normal dynamic earth pressure P acted as a reaction to restrain the shear deformation of the box section. In the inverse situation, the horizontal normal dynamic earth pressure P acted as a load to promote the shear deformation of the section. Based on the parametric study, a key coefficient, α , which determined the normal earth pressure P, was formulated as a function of the ratio, β . Then the approximated equation to specify the dynamic earth pressures was proposed. Finally, the equation was generalized so that it can work with random input motions (Watanabe et al., 1991c).

The practical simplified method using a frame-spring model for a cross section in the transverse direction was originally proposed by Kuribayashi et al.(1977), which was a quasi-static manner capable of seismic design calculations considering soil-structure interaction. This method is called “the seismic deformation method”. This method was then introduced into some seismic design codes. Fig.1.2 shows the seismic loads and the frame-spring model for a cross section as employed in the design code for underground parking lots (e.g. JRA, 1992). The seismic action due to the deformation of free field $p(z)$, the frictional shear forces on the surface of the structure τ_U, τ_B, τ_S, and the inertia force of the structure P_I are applied on the frame-spring model. The normal springs as well as the shear springs were attached on the surface of the structure.

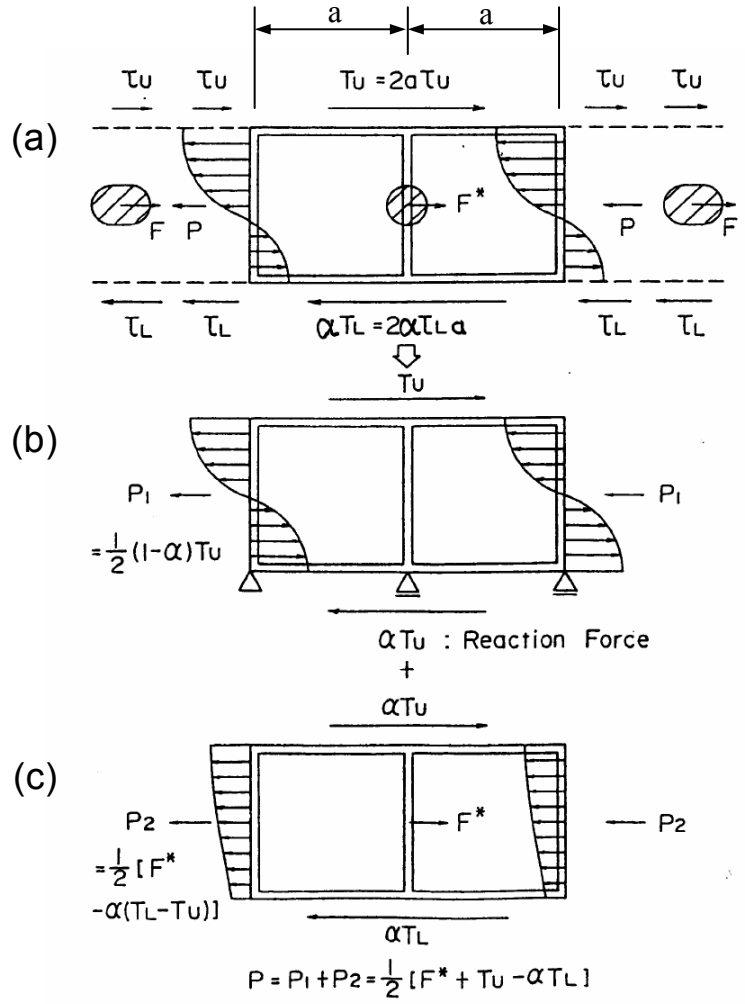

Fig.1.1: Conceptual figure concerning the generation of dynamic earth pressure (Watanabe et al., 1991b)

Tateishi (1992) verified theoretically the validity of the seismic deformation method using a frame-spring model (Fig.1.2). It was indicated that such responses as bending moment and shear force of the cross section by the seismic deformation method were reasonably equal to those by the dynamic finite element analysis at the time when the maximum relative displacement between the top and the bottom of the box section occurred. Further, it was shown that the inertia forces of the structure affected dominantly the response of sectional forces when the structure was buried at shallow portion of ground.

Other type of practical simplified methods were proposed by Katayama (1990), Penzien et al.(1992) and Tateishi (1995). Those were based on a soil-structure model of static finite element analysis instead of a frame-spring model.

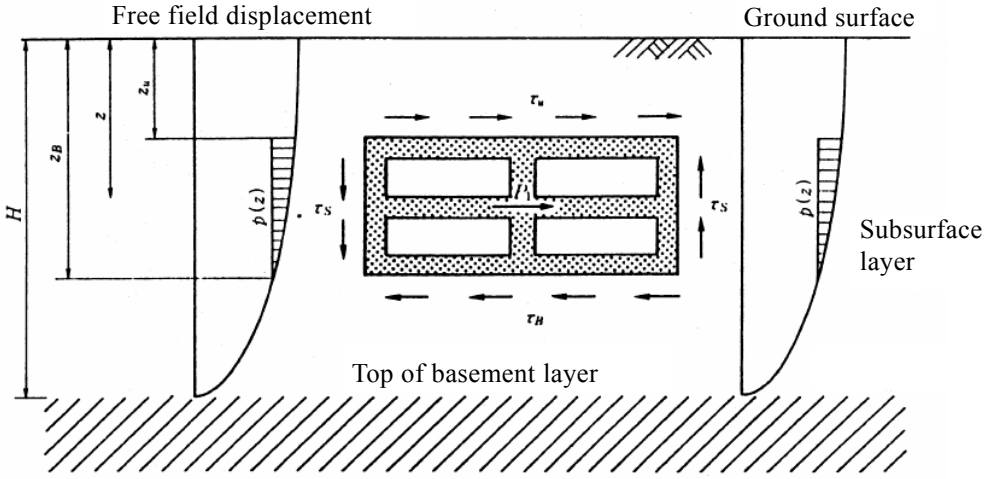

$p(z)$: Seismic earth pressure acting on the structure

τ_U, τ_B, τ_S : Seismic shear force acting on the surface of the structure

P_I : Inertia force of the structure

(a) Seismic loads accounted for seismic design of a cross section

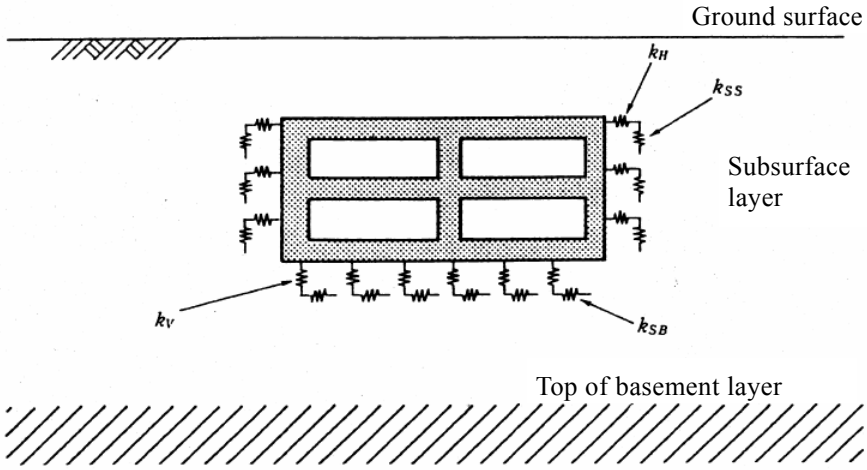

(b) Frame-spring model

Fig.1.2: A frame-spring model of underground structure for the seismic deformation method (JRA, 1992)

The effects of slipping and separation at the interface between the outer surface of a cut-and-cover tunnel and the backfill during earthquakes were examined by shaking table tests (Kawama et al, 2001). It was assumed that the structure was constructed in clayey soft ground. The aluminum structure model of two or three span's box section was installed in the model ground which was made of silicon. Subgrade reaction on the surface of the structure during shaking was measured by two directional load cells with pressure measuring plates. Teflon sheets were inserted between the silicon model ground and the structure to simulate slipping and separation. The soil-structure model was shaken by the sinusoidal wave with the maximum acceleration of 50 gal.

Fig.1.3 shows typical test results. It was shown that the slipping and separation effect affected local normal forces and shear force (see Fig.1.3(a) and (b)) but the total horizontal force was almost the same between those test results (see Fig.1.3(c)(i) and (ii)). Consequently, the relative displacement between the top and the bottom of the box section and the bending moment of the center wall become equal to each other without any effect of slipping and separation. The analytical study was then conducted on the shaking table tests by such methods as dynamic FEM and the seismic deformation method. It was found that both analytical methods give reasonably good results.

Non-linear seismic interaction as well as plastic deformation performance of RC underground structures which was seismically induced were studied by large scale shaking table tests using half scale RC structures (Ohtomo et al., 2002). The shaking table tests were conducted using a large laminar box measuring, 6.0m high, 3.0m wide and 11.6m long. The two span's model structure, of which the height and the width were 1.75m and 3.0m, respectively, was buried in dry sand as shown in Fig.1.4(a). The apparent shear stiffness of the structure was 0.2 times that of soil element displaced by the structure. The soil-structure model was shaken by observed seismic ground motions in the Hyogoken-Nambu (Kobe) earthquake (1995) with varying maximum acceleration of 100gal～1100gal. Major findings as obtained from the tests were shown as what follows. i) Horizontal frictional force at the surface of upper slab predominantly affects the shear deformation of the cross section. ii) Applying the strong input motion of 1100gal, non-linear behavior was observed both in the soil and the structure in which the maximum shear strain of the surrounding soil amounted to 3%～5%, and the shear deformation of the structure reached twelve or thirteen times as large as the yield deformation (see Fig.1.4(b)). iii) The shear deformation of the box section is primary controlled by the deformation of surrounding ground. iv) The wall of the model structure underwent flexural failure. Cracks due to bending deformation of the wall were observed

at the corner. Thus, the feature of the damage of underground RC box section due to strong earthquakes was experimentally clarified.

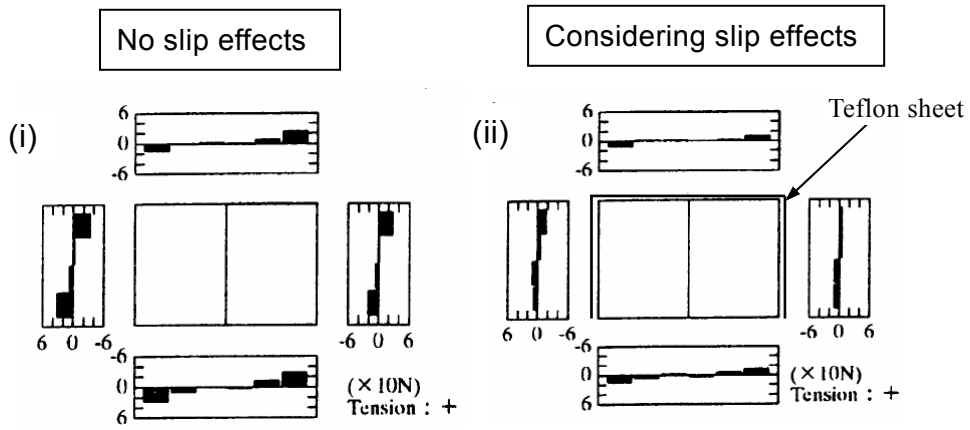

(a) Measured normal forces

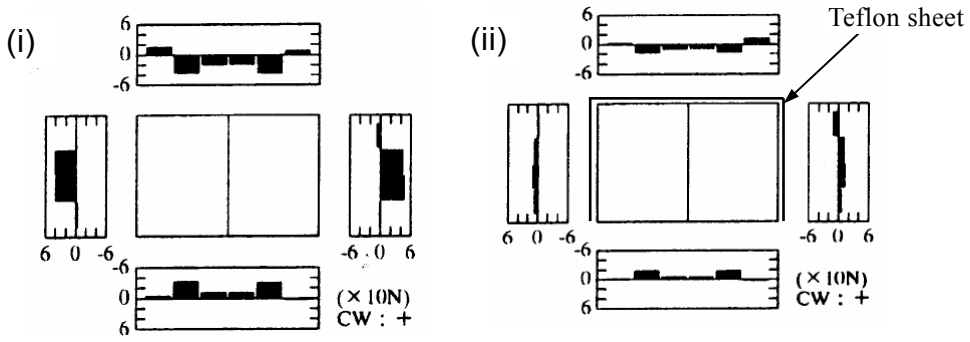

(b) Measured shear forces

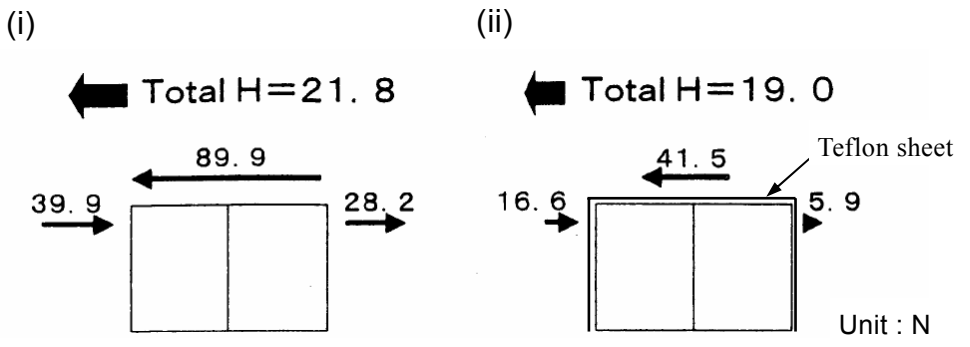

(c) Total forces

Fig.1.3: Measured local and total forces of underground structure model in shaking table test (Kawama et al., 2001)

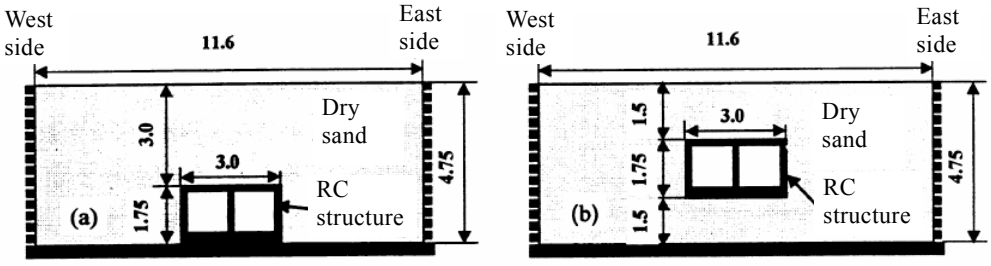

(a) Schematic figure of soil-structure model (Unit in meters)

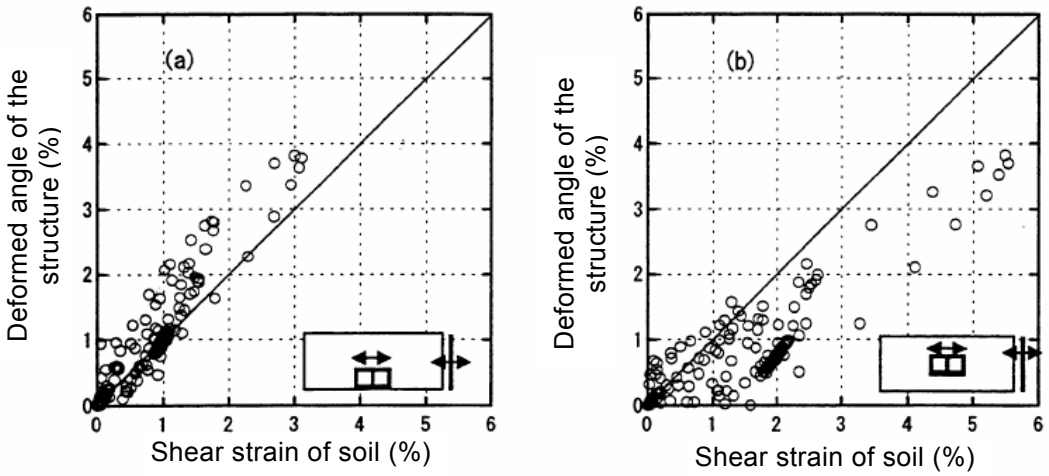

(b) Experimentally obtained relationship between the deformed angle at the structure and the shear strain of surrounding soil

Fig.1.4: Large scale shaking table tests results (Ohtomo et al., 2002)

It is noteworthy in the abovementioned studies that the discussions are limited to non-liquefied soil during earthquakes. Neither a build-up of the excess pore water pressure due to cyclic loading nor a reduction of shear modulus accompanied by pore pressure build-up in surrounding soil was not taken into account.

1.2.2 Case study on damaged large underground structures

Subway structures in Kobe city, Japan were severely damaged during the 1995 Hyogoken-Nambu earthquake, and the damaged structures were reconstructed completely within one year (Samata,

1996). It was the first serious event for large underground structures due to earthquakes. The damages were primary concentrated on the center columns at stations as well as in tunnels between stations. Many studies were carried out to understand the mechanism of damage and to develop a calculation method for future seismic design.

A detailed survey on Daikai subway station which completely collapsed during the earthquake was conducted by Iida et al.(1996). The station was a box frame structure with columns at the center, measuring 17m wide and 7.17m high in the exterior dimensions, and 120m long. A complete collapse occurred in more than half of the center columns, which resulted in the failure and collapse of the ceiling slab and subsidence of filling materials over the station by more than 2.5 m at maximum. The typical damage patterns in the transverse direction are shown in Fig.1.5. It was suggested that a strong horizontal force was imposed on the structure from the surrounding subsoils below the ground surface. The relative displacement of the surrounding soils between the ceiling level and base level during the earthquake, and inertia force of the overburden soil transferred to the ceiling slab are supposed to cause the damage. They listed such important items for future researches as i) behavior of the ground to evaluate the relative displacement between the top and the bottom of the structure, ii) soil-structure interaction between the underground structure and surrounding soil to evaluate the load acting on the structure from the surrounding soil, iii) effect of overburden soil which provides an inertia force on the underground structure.

Yamato et al.(1996) investigated the cause of damage of Daikai subway station by analytical method. Numerical calculation was conducted by two kinds of method as those for the dynamic finite element analysis with soil-structure model and the static non-linear analysis of frame models of the structure. In-situ tests and laboratory tests were carried out to obtain the material properties of both concrete and soil. Non-linearity of soil and structural member in dynamic analysis were considered by the equivalent linear method. The time when the relative displacement between the top and bottom of the structure became the maximum was selected. Then static analysis was conducted by applying nodal forces derived by the dynamic analysis on the non-linear structure model in a static manner. The results of the analysis showed clearly that the center columns collapsed before the walls and the ceiling yielded. It was inferred that the failure and collapse of the center column resulted in the breakdown of the ceiling and the subsidence of subsoil over the station after the earthquake.

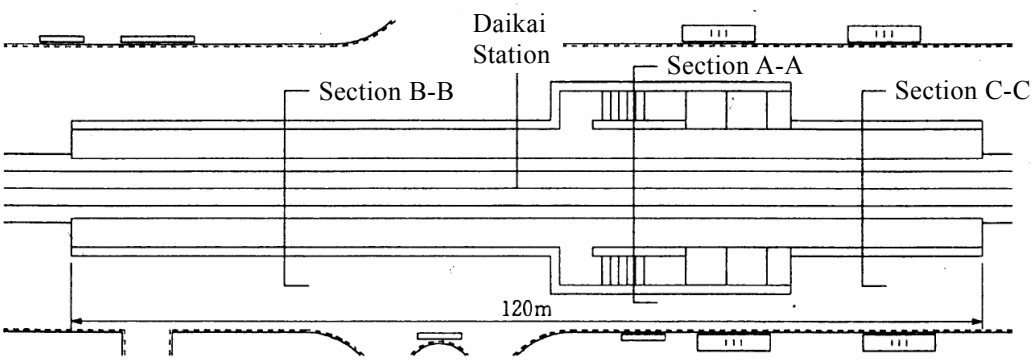

(a) Plan

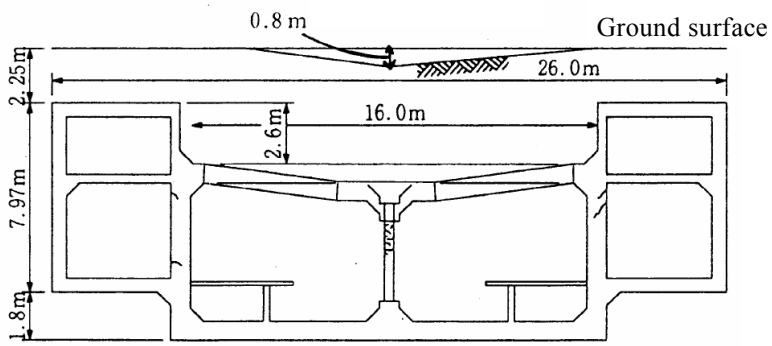

(b) Section A-A

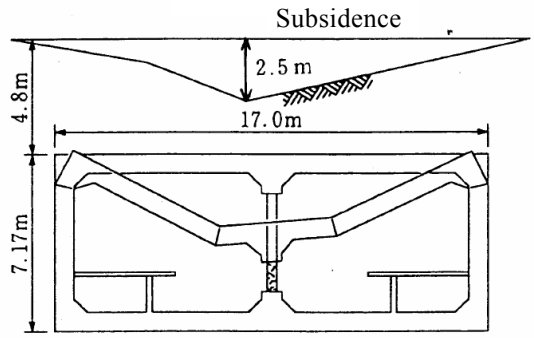

(c) Section B-B

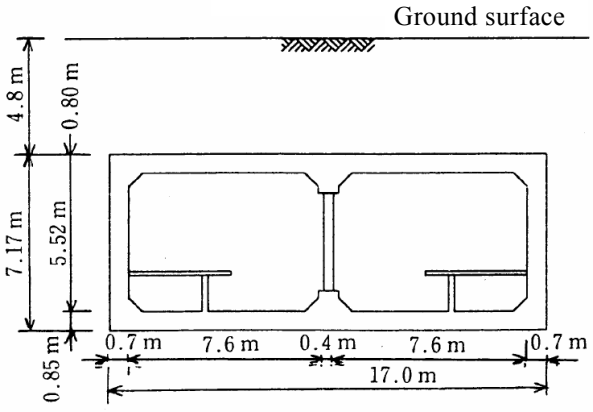

(d) Section C-C

Fig.1.5: Schematic figure showing the typical damage patterns of Daikai subway station in the transverse direction (Samata, 1996)

Tohda et al.(1996) summarized characteristic features of damage to the public sewerage systems due to the 1995 Hyogoken-Nambu (Kobe) earthquake in the Hanshin area in Japan. Among these, a damage of vertical shafts for a shield driven tunnel, which was constructed for the installation of two pressure pipelines to convey the sewage and cooling water, was reported as that due to soil liquefaction. The shield driven tunnel connected between two plants at Rokko Island and the mainland having a length of 560m, an external diameter of 2.75m, and an internal diameter of 2.4m. The damaged vertical shafts were located near revetments at the edge of reclaimed ground. The dimensions of the damaged vertical shaft at Rokko Island were 14m× 11.0m×42.04m, and at the mainland 9.4m×9.4m×32.5m. It was found after the earthquake that two vertical shafts deformed horizontally causing cracking in the walls which was accompanied by water leakage. Cracks of the inclination about 45 degrees with horizontal line were observed at both vertical shafts. Furthermore, the horizontal displacement about the maximum of 0.1m toward the sea at a construction joint was detected, in which the location of displaced joints corresponded to the boundary of soil deposit between the fill and alluvial clay. The lateral movements of the revetments near the vertical shafts were observed to be about 2m at Rokko Island and 0.7m at the mainland, causing the lateral displacement of backfill due to liquefaction. It was considered that the damage of the vertical shafts was caused by the lateral spread of liquefied backfill.

Matsuda et al.(1997) accounted for the damage of Kamisawa subway station in Kobe city by a sequence of three kinds of analysis. The station was a two or three story's RC box frame structure of 400m long with center columns. The severe damages of the center columns were concentrated at only the half of the station. The numerical analyses as those for one dimensional earthquake response analysis of surrounding ground, two dimensional finite element dynamic analysis, and three dimensional non-linear static analysis of cross sections were performed. The horizontal acceleration and the vertical acceleration were taken into account in the finite element dynamic analysis. It was found that the severely damaged section of the station coincided with the ground where the horizontal relative displacement along the depth became large during the earthquake. The result of dynamic finite element analysis of soil-structure model indicated that the maximum shear force of the center column at the damaged section exceeded the shear strength so that the collapse of the center column could occur during the earthquake. It was also shown by the three dimensional non-linear static analysis that shear force of center columns significantly increased before the stresses of slab and the wall reached the stage of yielding.

Nakamura (2000) studied two subway structures of different damage in degree, as those for Daikai station with severe damage, and Kosoku-Nagata station with moderate damage. The

distance of two stations was only about 1.3 km and the seismic motion therein was considered to be the same. Numerical calculation was conducted by the combined procedure of the dynamic analysis and the static non-linear analysis which was proposed by Yamato et al.(1996). It was found that the difference of the initial shear modulus of surrounding ground between two stations resulted in the difference of the shear deformation of the structures. It suggested that the ground condition could cause the difference of seismic damage of underground structures.

Matsuda et al.(2000) conducted dynamic analysis of Sannomiya subway station in Kobe city by two different numerical methods of the equivalent linear method and the direct integration method. The Sannomiya station was a three-story and two-span's RC structure, measuring about 15m wide, and 20.5m high in the cross section. The center columns were located at every 5m in the longitudinal direction to support the slabs. The primary damage concentrated on center columns of only the first story. The complex theories involving the constitutive model of soil and non-linearity of RC members were considered in the direct integration method. By the linear equivalent method, the significant shear collapse of RC members was predicted not only at the center columns but also at the slabs, which did not have damage during the earthquake. By the direct integration method, in contrast, the shear collapse at only the center column was reasonably predicted. It suggested that the non-liner soil-structure analysis by the direct integration method could predict the damage of RC cross section of underground structures.

It is noted that no evidence of liquefaction such as sand boiling was reported around the damaged underground structure although subway structures were located under the water table. For this reason, all the studies above were conducted without the effect of generation of excess pore water pressures.

1.2.3 Soil-structure interaction associated with soil liquefaction

The seismic interaction problems associated with the liquefied soil have been studied focusing on such variety of structures as piled foundations (e.g. Tatsuoka et al., 1978; Tokimatsu et al., 1991; Sawada et al., 1998; Nishimura et al., 1998), buried structures (e.g. Katada and Hakuno, 1981; Iwatate et al., 1982; Koga et al., 1996), quay walls of gravity type (Matsuo et al., 1960; Tsuchida, 1968; Inagaki et al., 1996; Kohama et al., 1998; Ghalandarzadeh et al., 1998), and others (Tanaka, Y. et al., 1994; Tanaka H. et al., 1994). Although the seismic behavior of these types of structures could be different from that of the box-shaped cross sections, the fundamental characteristics of

interaction are drawn by those studies.

Pile foundations

Since piled foundations are considered to play an important role to enhance a seismic stability of structures at a site susceptible to soil liquefaction, many efforts have been made on dynamic interaction problems between piled foundations and liquefied soil.

Tatsuoka et al.(1978) carried out a comprehensive series of shaking table tests to clarify the dynamic behavior of group pile foundations. It was shown that the dynamic behaviors of pile foundations were unstationary in the process of liquefaction of surrounding ground. It was due to the fact that the fundamental natural frequency of piled foundation model decreased as the soil liquefied.

Tokimatsu et al.(1991) conducted a large scale shaking table tests and an analytical study on the effect of ground displacement on the stresses of piles. Observations and analysis were carried out focusing on interactive behaviors in such various states of ground as before liquefaction, in the process of pore water pressure build-up and during complete liquefaction. Major findings as obtained from the tests were, i) a bending moments of pile before the build-up of excess pore water pressure were very similar to the values which were calculated considering inertia forces at the pile head and the subgrade reaction, ii) the pile stresses were affected not only by the acceleration at the pile head but also by ground displacements when the pore pressure build-up. It was recommended that the effect of dynamic ground displacement should be considered for calculations of pile stresses when the pile foundation was located in the ground susceptible to soil liquefaction. It was also shown that the seismic deformation method was one of the effective methods for pile stress calculations.

Sawada et al.(1998) indicated from the results of shaking table tests that pile foundations underwent resonance with the predominant frequency of an input motion as a transient response in the process of liquefaction. The considerable cause of the resonance was a reduction of the fundamental natural frequency of pile foundations. In this respect, an analytical study on calculation method for pile stresses were conducted focusing on the phenomenon of resonance of a pile foundation in such various situations of ground as in the process of liquefaction and during complete liquefaction. It was shown that complicated behaviors of pile foundations due to change of a natural frequency during liquefaction could be simulated by dynamic analysis with a simplified model, in which a single mass model was connected in parallel with non-linear stress

strain model of soil.

Nishimura et al.(1998) carried out a series of shaking table tests on dynamic interaction between pile foundations and surrounding soft ground. An applicability of the seismic deformation method, which was often used for underground structures, was examined for pile foundations constructed in soft ground. Silicon was used for the material of model ground in the experiment. The natural periods of not only pile foundations but also the surrounding ground were varied in tests. It was shown that i) the dynamic feature of soil-pile system depended on the magnitude relation of the natural period between the ground and the pile foundation, ii) stresses of piles during earthquakes were strongly affected by not only inertia forces at pile top but also ground displacements. Furthermore, it was indicated that pile stresses could be predicted reasonably by the seismic deformation method with combination of loading considering phase differences between the structure and the ground.

Quay walls of gravity type

Fundamental investigations by shaking table tests have been made on dynamic pressures due to completely liquefied soil acting on a rigid wall which translates in the horizontal direction. Tsuchida (1968) divided the total pressures acting on the wall into two components, i) the monotonic component which is exerted by the unit weight of liquefied soil, and ii) the fluctuating component which oscillates around the pressures of the monotonic component. The amplitude of pressures of fluctuating component was found to be approximately equal to the values calculated by Westergaard's formula (Westergaard, 1933) which was originally proposed for reservoir water in dams. The resulting formulas for the total pressure which consists of the monotonic and the fluctuating components are given by

$$\sigma_T = \gamma_s \cdot y \pm \frac{7}{8} \cdot k_h \cdot \gamma_s \sqrt{H \cdot y} \tag{1.1}$$

where σ_T is the total pressure on the wall due to liquefied soil, γ_s is the unit weight of saturated soil, k_h is the coefficient of the horizontal seismic acceleration expressed in fractions of the gravitational acceleration, H is the depth of liquefied soil, and y is the depth where the pressure is calculated. Fig.1.6 shows the comparison between the measured values and calculated values of earth pressures due to liquefied soil. It is seen that the agreements are very well.

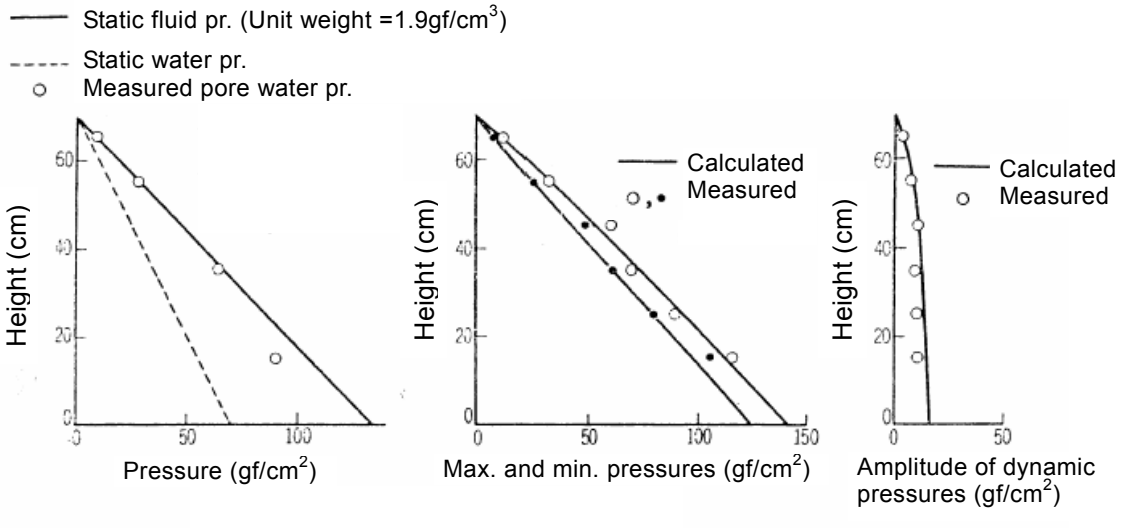

(a) Onahama sand (Intensity of acceleration : 64gal, 3Hz)

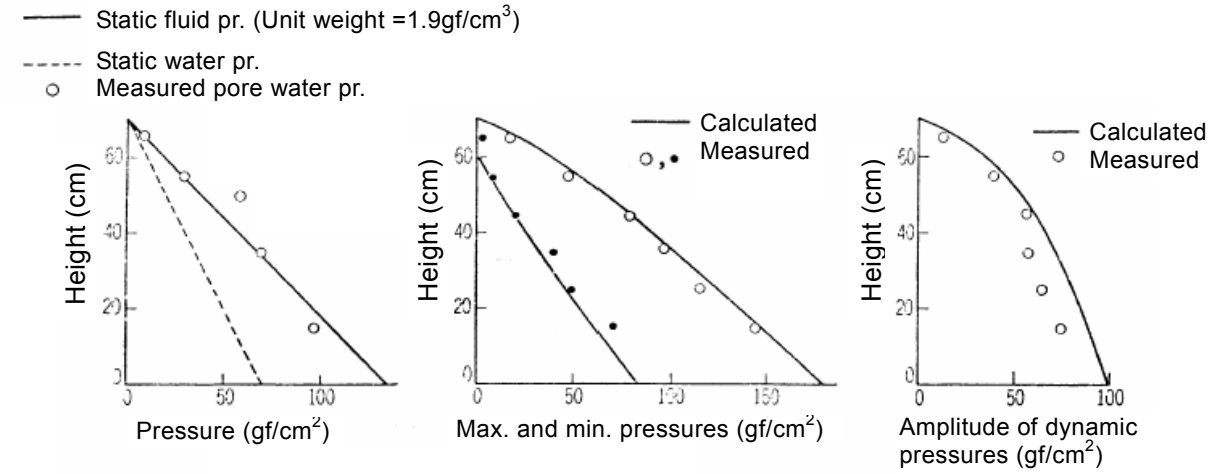

(b) Takahagi sand (Intensity of acceleration : 41gal, 3Hz)

Fig.1.6: Dynamic pressures on a rigid wall (Tsuchida, 1968)

Shaking table model tests on quay walls of gravity type have been conducted by using scaled model to clarify the mechanism of the interactive behavior as well as the damage due to past earthquakes. Ghalandarzadeh et al.(1998) detected that the dynamic earth pressure acting on the wall and the wall displacement with inertia force became in-phase. This supports the idea of seismic coefficient when the liquefaction in the foundation sand beneath the wall has occurred, inducing the lateral displacement of the wall.

Kohama et al.(1998) indicated that the interactive behavior of quay walls was quite variable depending on the occurrence of liquefaction in the backfill. Namely, the fluctuating earth pressure on the quay wall suppresses the movement of the quay wall before liquefaction, whereas the sliding of the quay wall is enhanced after liquefaction of the backfill. The amplitude of the observed fluctuating component of earth pressures on the quay wall due to liquefied soil appeared to agree reasonably with the calculation by Westergaard's formula.

Embedded structures

Katada et al.(1981) conducted a series of shaking table tests on a behavior of embedded structure varying a water content of surrounding ground in order to clarify the effect of incomplete liquefied ground on an embedded structures. It was experimentally indicated that the response of the embedded structure in unsaturated soil with low water content became larger than that of the structure embedded in saturated soil. In addition, the large response of the embedded structure in unsaturated soil continued longer when the water content was lower. It was considered that the large response in the process of liquefaction caused the resonance of ground with input motion in which the natural period of the ground became long due to liquefaction.

Iwatate et al.(1982) carried out an experimental and analytical study on seismic behaviors of embedded shafts in a liquefiable ground. A cylindrical shaft, whose natural frequency was about 4.6 times higher than the initial natural frequency of the ground, was used in shaking table tests. It was shown in experiments that i) the maximum dynamic earth pressure occurred just before complete liquefaction, ii) the amount of the pressure became 3～5 times as large as that of dynamic earth pressure during complete liquefaction, and iii) the strain of the structure also reached the maximum just before complete liquefaction, in which the ratio between the maximum strain and the strain during complete liquefaction was almost equal to that of dynamic earth pressures. It was presented by the analytical study that i) the measured dynamic pressures corresponded to the strain response of the embedded structure which behaved in an elastic manner,

ii) it was by the seismic deformation method of the deformation control to give reasonable agreements between the measured and the calculated strain before liquefaction, and iii) in contrast, it was by the calculation of the acceleration control, in which the inertia force of the structure and the dynamic pressures were applied on the structure, to calculate reasonable results during complete liquefaction. However, it was concluded that some difficulties still remained to evaluate precisely the maximum dynamic earth pressure just before complete liquefaction.

Seismic earth pressures acting on the wall of semi-buried roads were studied by Koga et al. (1996). A series of shaking table model tests in gravitational field was conducted with the input motion of 5Hz frequency. In addition, dynamic centrifugal model tests were conducted with the equivalent input motion of 1.2Hz frequency. Bending moments of the wall in the process of pore pressure build-up were investigated. The model used in the dynamic centrifugal test is shown in Fig.1.7(a). From the series of tests, a simplified equation to evaluate the fluctuating component of earth pressure with the monotonic component was proposed. The ratio of excess pore pressure was introduced as a considerable parameter.

The increment of monotonic component of earth pressure, $\Delta\sigma_h$ is expressed as

$$\Delta\sigma_h = (1 - K_0) \cdot \sigma_{v0}' \cdot r_u \tag{1.2}$$

where K_0 is the coefficient of earth pressure at rest at the initial state, σ_{vo}' is the initial vertical effective pressure, and r_u is the ratio of excess pore water pressure. It is noted that $\Delta\sigma_h$ is the increment from initial total horizontal pressure. On the other hand, The Westergaard's formula (Westergaard,1933) was extended to consider the fluctuating earth pressures in the process of liquefaction. The formula for the fluctuating component of earth pressure, σ_{hd} is given by

$$\sigma_{hd} = \pm\frac{7}{8} \cdot k_h \cdot (\gamma_w + r_u \cdot \gamma') \cdot \sqrt{H \cdot y} \tag{1.3}$$

where γ_w and γ' are the unit weight of water and effective unit weight of soil, respectively. r_u is the ratio of excess pore water pressure. Fig.1.7(b) shows the comparisons of measured and calculated bending moments by the seismic load by Eq.(1.3). It was shown that the calculated bending moments in a wall during liquefaction were conservatively consistent with the bending moments observed in dynamic centrifugal model tests.

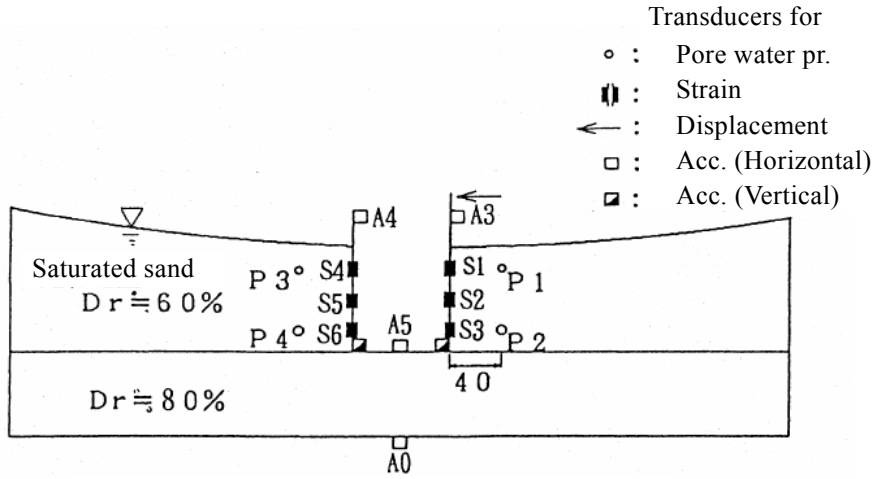

Thickness of the structure model : 1mm or 2mm

(a) Schematic figure of a semi-buried structure for dynamic centrifugal test

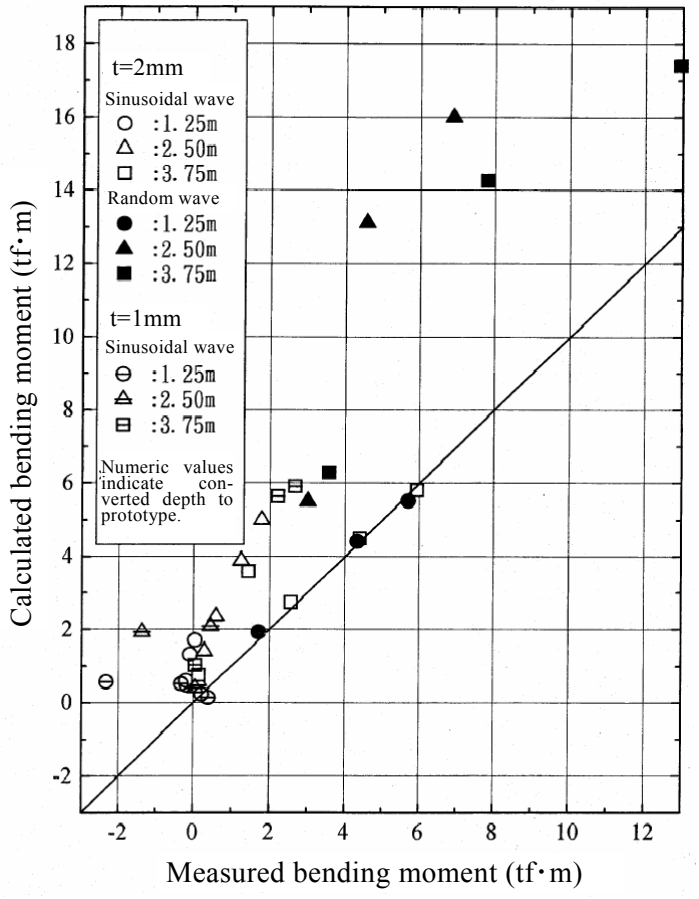

(b) Comparison between the measured values and the calculated values

Fig.1.7: Results from a series of dynamic centrifugal tests (50G) for semi-buried structure in liquefied ground (Koga et al., 1996)

Railway Technical Research Institute of Japan (RTRI) introduced the effect of liquefaction on underground structures into the seismic design code. Fig.1.8 shows the earth pressures due to liquefied soil. When the structure is located in a liquefied soil as shown Fig.1.8(a), the earth pressure due to liquefied soil, σ_T is given by

$$\sigma_T = W_P + \sigma_{h,liq}' \tag{1.4}$$

where W_p is static water pressure and $\sigma_{h,liq}$' is the horizontal pressure of completely liquefied soil.This is expressed as

$$\sigma_{h,liq}' = \gamma' \cdot h \cdot K_{liq} = \sigma_{v0}' \cdot K_{liq} \tag{1.5}$$

where γ ' is the effective unit weight of soil, h is the height and the K_{liq} is the ratio of total pressures between horizontal and vertical direction during complete liquefaction (=1.0).

When the bottom of the structure set on or in the basement layer as shown in Fig.1.8(b)(c), the earth pressure due to liquefied soil, σ_T is given by

$$\sigma_T = W_P + \sigma_{h,liq}' + \sigma_{hd} \tag{1.6}$$

where σ_{hd} is the dynamic earth pressure calculated by Eq.(1.3) (Koga, 1996). When the earth pressure, σ_T is applied on the structure, it should be noted that the effect of the ground deformation is not accounted for at the same instant.

Other type of structures

The seismic stability of a rectangular rigid block constructed by the stabilization of the Deep Mixing Method in the liquefied soil was investigated by Tanaka,Y. et al.(1994). The solution of dynamic pressures acting on a rigid block was derived by introducing the rocking motion into the Westergaard's theory (1933). The experimental fact that the rigid block in liquefied soil, which was shaken by 10Hz input motion, was stable against overturning and sliding was accounted for by using the solution.

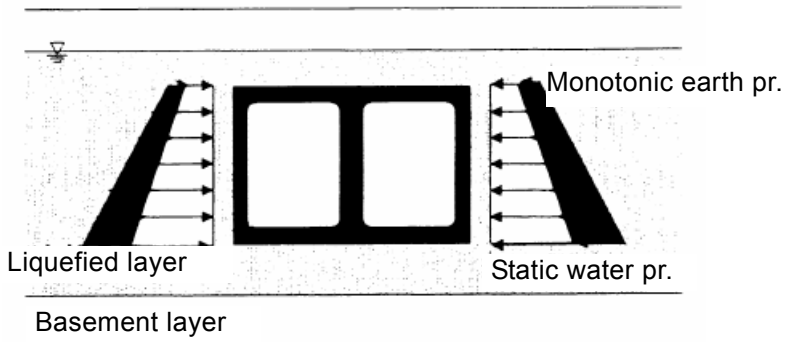

(a) Soil liquefied through the depth of surrounding ground

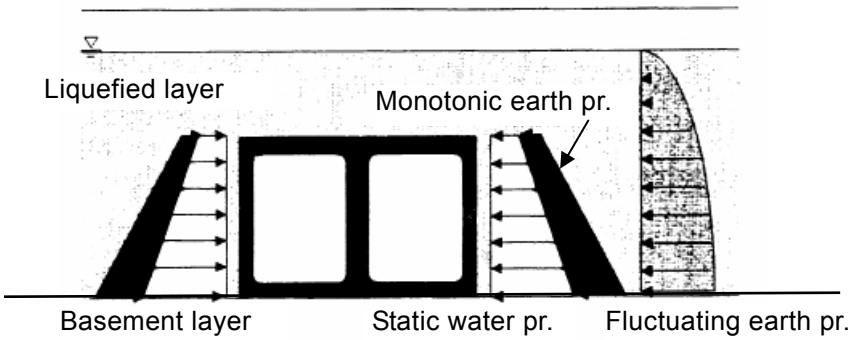

(b) Soil liquefied through the depth but the structure placed on the unliquefied basement layer

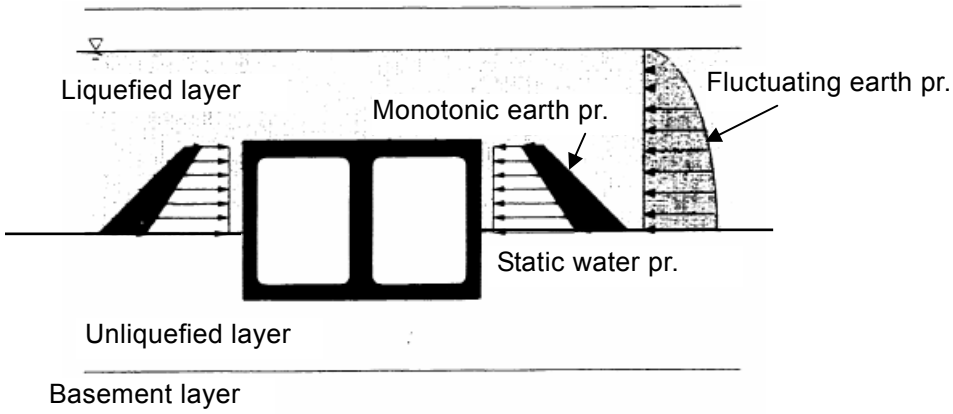

(c) Soil liquefied partially in the depth of surrounding ground

Fig.1.8: Earth pressures due to liquefied soil for seismic design (RTRI, 1999)

Tanaka, H. et al.(1994) studied dynamic earth pressures due to liquefied soil on flexible embedded walls which was used for mitigation of liquefaction-induced displacement in slopes and embankments. Shaking table tests were conducted on a loose sand deposit with a flexible wall. It was indicated that the fluctuating component of dynamic earth pressure has a strong relation with the accelerations of the flexible wall or the accelerations of ground near the wall. The measured dynamic earth pressure on the flexible wall was much smaller than the dynamic pressures calculated by the practical method assuming the flexible wall as a rigid wall (Eq.(1.3)). In addition, it was not the base acceleration but the acceleration of the flexible wall that showed better correlation with dynamic earth pressures of flexible wall when a rigid wall was assumed for the calculation.

The previous studies on the seismic interaction problems associated with liquefied soil are summarized in Table 1.1. The studies on box sections of underground structure presented in Section 1.2.1 are also included in the table.

It is seen that the assessment of dynamic earth pressure due to liquefied soil has been established focusing on chiefly such rigid structures as quay walls of gravity type, semi-buried roads and an embedded shaft both in the process of liquefaction and during liquefaction. In addition, the behaviors of pile foundations in liquefied ground as well as the mechanism of dynamic interaction have been almost clarified by extensive experimental and analytical studies. The quantitative evaluation seems possible for rigid walls and piles both in the process of liquefaction and during complete liquefaction.

In contrast with this, the effects of liquefied soil have not been focused on in the most study on box sections of underground structure. The dynamic interaction problems associated with flexible walls have not been attracted as well. It is because the severe damage of large underground structures due to earthquakes had not occurred until recent years (Iida et al., 1996), and the effect of liquefaction was not clear for damaged underground structures (Matsuda et al., 2000). Furthermore, the other reason can be considered that the assessment of uplift of structure was taken as more important problem than the dynamic interaction when surrounding ground liquefied in the past.

Table 1.1: Summary of previous studies on dynamic soil-structure interaction of underground structures

Type of structures		Contributions	Unliquefiable (or before liquefaction)	Liquefiable		Remarks
			$r_u = 0$	$0 < r_u < 1.0$	$r_u = 1.0$	
Walls	Rigid wall	Tuchida (1968)	–	○	●	Quay walls
	Rigid wall with sway and rocking motion	Kohama et al. (1998)	○	○	●	Quay walls of gravity type
		Ghalandarzadeh et al.(1998)	○	○	●	
		Tanaka,Y. et al. (1994)	–	–	● (Rocking motion)	Improved ground by deep mixing method.
	Flexible wall	Tanaka,H. et al. (1994)	–	–	○	Sheet piles
Embedded structures		Katada et al. (1981)	–	○	○	Soil with low water content
		Iwatate et al. (1982)	○	● (Before resonance)	●	Embedded shaft
		Koseki et al. (1991) Koga et al. (1996)	–	●	●	Semi-buried roads. RTRI(1999) seismic design code for embedded tunnels.
Piles		Tatsuoka et al. (1978)	○	○	○	A comprehensive series of tests
		Tokimatsu et al. (1991)	●	●	●	Considering the effect of ground displacements
		Sawada and Nishinura (1998)	●	●	●	Behavior at the resonance is clarified
Underground structures (box section)		Watanabe et al. (1991abc)	●	–	–	Box culvert
		Kawama et al. (2001)	●	–	–	Experiment on slip effects of box culvert
		Ohtomo et al. (2002)	●	–	–	Large scale test (flexible box section)
		Kuribayashi (1977) Tateishi (1992) Kawashima (1994)	◎	–	–	Seismic deformation method for box culvert. JRA(1992) seismic design code.
		Katayama (1990)	◎	–	–	Calculations based on FEM
		Penzien (1992)	◎	–	–	
		Tateishi (1995)	◎	–	–	
		The present study	○	● (Resonance)	●	Flexible structure

● : Experimental study (with quantitative evaluations of dynamic interaction)
○ : ditto (Observations of dynamic interaction)
◎ : Analytical or theoretical study – : Not focused on

1.2.4 Issues in past studies

The seismic soil-structure interaction of buried box-shaped cross sections in unliquefied ground has been clarified, and design calculation methods has been established by many previous efforts (e.g. JRA, 1992). However, it has been inevitable to take the effect of soil liquefaction including dynamic interaction into consideration in recent seismic design owing to strong design earthquakes (RTRI, 1999; JSCE, 2000).

One of the distinctive features of a box-shaped cross section is that the cross sections are subjected to shear-type deformations as a result of vertically propagating waves during earthquakes (Clough and Penzien, 1993). In most previous experimental studies on interaction between liquefied soil and structure, discussions are limited to rigid structures of which the stiffness is relatively very high in contrast with that of soil. Seismic soil-structure interaction is not clear on the cross sections with shear-type deformation of flexible walls. It is one of present issues to clarify seismic interactive behavior of such kind of underground structures and its mechanism associated with soil liquefaction.

From the viewpoint of response analysis of box-shaped cross sections, a seismic deformation method using frame-spring model has a greater capability by taking the interactive behavior into account under the control of deformation unless the backfill does not liquefy (Kawashima, 1994). However, many studies associated with liquefied soil and rigid walls have shown that the dynamic earth pressure due to liquefied soil can be evaluated by Westergaard's formula (1933) which calculates the dynamic pressures by acceleration of wall (Tsuchida, 1968; Koga et al., 1996; Ghalandarzadeh et al., 1998; Kohama et al., 1998). In addition, it is reported that the amount of dynamic earth pressures acts on a sheet pile wall, which is flexibly deform during earthquakes, has a closer relation with accelerations of the wall or ground near the wall (Tanaka. H. et al.,1994).

Although these observations suggests that the response of the cross section which flexibly deforms can be under the control of inertia force when the soil liquefies, further experimental studies associated with flexible structures are needed to make sure influential parameters for dynamic earth pressures. Furthermore, it is also important issue to develop a calculation method to evaluate the amount of dynamic earth pressures for flexible structures, which has not been proposed yet.

1.3 PURPOSE AND SCOPE OF THIS STUDY

Although many experimental and analytical studies on dynamic soil-structure interaction of underground structures has been conducted, there are still some unresolved issues on this topic as illustrated in the previous section. This study, therefore, is conducted with some of unresolved issues on dynamic interaction problems associated with a box shaped cross section, which can be flexibly deformed during earthquakes.

The primary objectives of the study are as what follows:

1. To describe the behavior of flexible box section of underground structure as a result of dynamic interaction between liquefied soil and structure. Shaking table model tests will be conducted for information on the behavior of soil as well as a structure. From the results of a series of tests, the stress-strain relationship will be reproduced during soil liquefaction and the change of property of backfill with time will be clarified.

2. To develop a new calculation method to evaluate dynamic earth pressures quantitatively. Theoretical study is also conducted considering the behavior of box section, which was observed in a series of tests.

However, it is important to mention scope of this study. It is shown as what follows:

(Scope 1). Flexible box section of which the rigidity is less than the initial rigidity of ground is considered. Actually, there are varieties of stiffness of box section in the range of 1/10 to 10 times of that of the displaced ground by a box section (Kawashima, 1994). It is supposed in this study that the natural frequency of the structure is about one half of the initial natural frequency of ground, considering extremely flexible structure in comparison with the ground.

(Scope 2). In addition, only a shear type deformation of the structure in the first order mode in the ground (e.g. JRA, 1992, see Fig.1.2(a)) is focused on. The deformation of structure with higher mode is out of scope in this study. This is because the critical stresses or relative displacements between the top and the bottom of a box section usually occurs in the first order mode deformation.

(Scope 3). The phenomenon of uplift of an underground structure, which might occur under particular condition of both the structure and the surrounding ground during earthquakes, is out of scope. It is supposed that a bottom of a box section is fixed on an unliquefied base layer (RTRI, 1999, see Fig.1.8(b)).

(Scope 4). Dynamic earth pressures only in the following states are assessed in this study on a flexible box section, i) when the dynamic earth pressure becomes the maximum in the process of liquefaction and ii) when the soil completely liquefies. Dynamic earth pressures before the maximum in the process of liquefaction with low pore pressure ratio are out of scope for the assessment. It is because the dynamic earth pressures before the maximum cannot be critical for underground structure.

(Scope 5). The effect of overburden soil is not considered in this study. In real situations of box sections of underground structure, it is often the case that overburden soil exists on its top. It is desirable to take the effect of dynamic interaction due to soil not only at its side but also at its top into consideration in order to apply to a wide range of real problems. However, it is definitely very difficult to solve both problems of dynamic effects all at once unless one of those is clarified. In this respect, only the effect of backfill at the side of the structure is taken into account in this study. The dynamic effect due to overburden soil is considered as a future topic after this study is accomplished.

The situation of this study is illustrated at the bottom line of Table 1.1 as well.

1.4 ORGANIZATION OF THIS THESIS

This chapter presents background information on this study concerning dynamic soil-structure interaction during earthquakes. A brief review of previous contributions has also been described to illustrate the recent developments in this topic. This presentation provides the framework of this study.

In Chapter 2, the methodology of shaking table model tests is presented precisely. The model specifications, properties of material, and procedure of measurements are described. Also performance of earth pressure transducers in saturated soil is illustrated in order to ensure the special attempt to reproduce shear stresses of soil near the structure.

In Chapter 3, the results of measurements in a series of shaking table test are presented. Not only results of dynamic measurements but also initial measurements of earth pressure and bending strain of structure are illustrated to ensure consistency of those quantities. Then typical dynamic behavior of structure in the liquefied soil is presented. The test results are arranged with respect to the intensity of input motion, density of backfill, and tensile strength of material of structure.

In Chapter 4, the procedure of reproduction for stress-strain relationship as well as effective stress path of soil is presented. From the reproduced stress-strain relationship, the shear modulus is calculated at each cycle of hysteresis loop. Then, the change of shear modulus with time is arranged as a representative material change due to liquefaction. The nature of backfill soil during shaking is discussed based on the results.

In Chapter 5, response characteristics of the structure are focused on. The change of amplifications as well as phase difference of acceleration between the top and bottom of the structure is analyzed with time. The influence of the property change of backfill on the response of a structure is discussed.

In Chapter 6, the earth pressures and the bending strains (or curvature) of the structure are examined. Monotonic component as well as fluctuating component of those quantities is separately analyzed. The consistency between earth pressure and bending strain during shaking is illustrated as well. In addition, mathematical formulation to solve the deformation of wall of box section is presented considering the earth pressure as an input parameter. The measured and calculated deflection from earth pressure is compared to discuss the validity of presented calculation procedure.

In Chapter 7, dynamic effects of lateral earth pressures on structure are studied. The feature of dynamic interaction with liquefied soil is shown in various aspects. The correlation between the dynamic earth pressure and acceleration together with normal strain of surrounding soil is examined.

Chapter 8 deals with the analytical work on the dynamic earth pressure acting on the flexible wall of a structure. The analytical solution of dynamic earth pressure is derived based on the control of inertia force. Comparisons between the calculated and measured dynamic earth pressures are presented in order to show that the proposed solution gives reasonably good results.

Finally, developments gained from this study are concluded in Chapter 9. Basic idea of a seismic load on underground structure in seismic design is presented. The issues for future in the problem are stated as well.

Chapter 2

METHODOLOGY OF MODEL TESTS

2.1 GENERAL REMARKS

A series of 1G shaking table tests has been conducted to investigate the dynamic interaction between liquefied soil and underground structure. A scaled underground structure made with aluminum was installed in the container. The material properties of aluminum and the structure are investigated by such mechanical tests as the tensile test and the loading test. A special attempt was made in the measurements to build the stress-strain relationship of backfill soil by using the earth pressure transducers. Performance of earth pressure transducer in saturated soil by another series of shaking table tests will be described

In this chapter, details of scaled model for shaking table, installation of transducers, the methodology of tests, and the results of examination for performance of earth pressure transducers are described.

2.2 EQUIPMENT

The experimental apparatus consists of three parts: the shaking table, the container (sand box), and the instrumentation together with data acquisition system.

2.2.1 Shaking Table

The shaking table consists of such several units as those for the control unit, the oil pressure unit, the actuator, and the shaking table. The dimension of shaking table is 2.0m in length, and 2.0m in width. The maximum loading weight on the table is 29.4 kN (3.0 tf). Fig.2.1 shows the performance of the shaking table. The capacities of the shaking table are as follows: the maximum

acceleration = 1.0 G (with frequency range of 3Hz to 50Hz), the maximum amplitude of vibration = 50mm, and the maximum velocity = 0.5m/sec. The shaking table apparatus was constructed at the Power Engineering Research and Development Center of the Tokyo Electric Power Company.

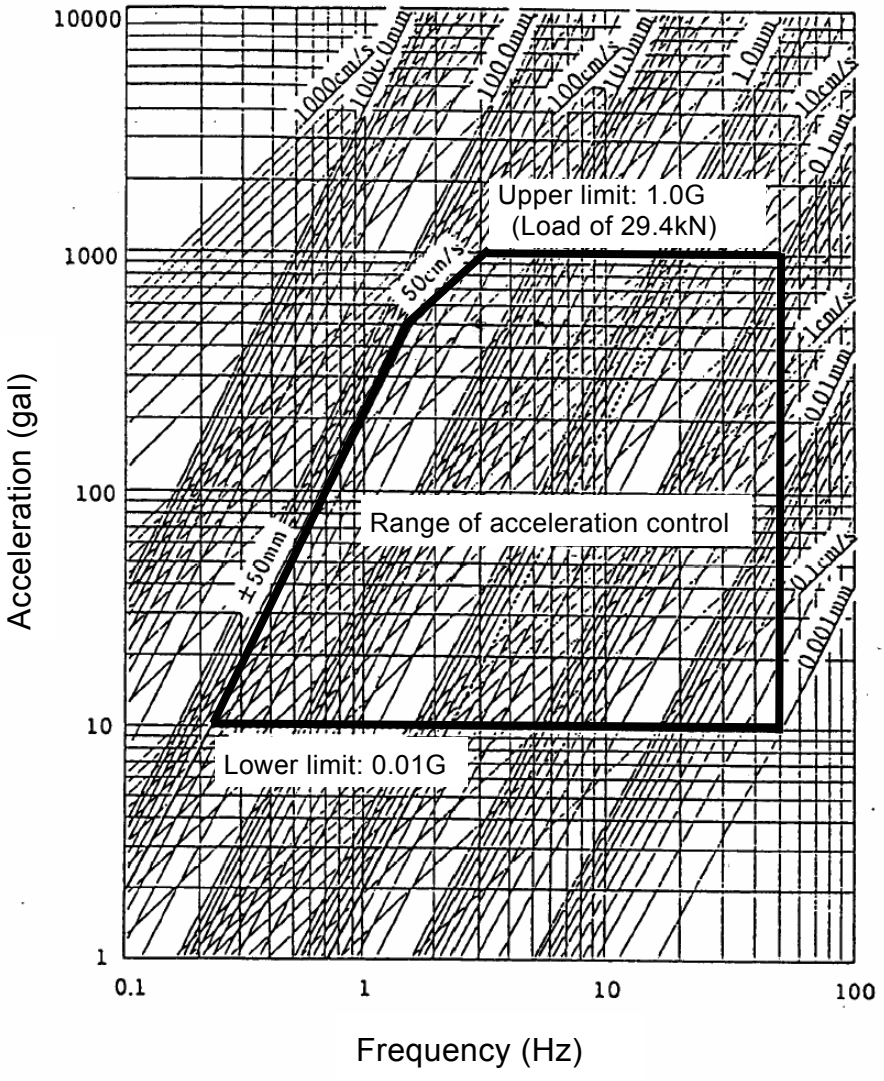

Fig.2.1: Performance of the shaking table equipment (Sinusoidal wave input)

2.2.2 Container

The container used in the experiment was a laminar box, which was originally developed by Kokusho et al.(1979). The internal dimensions of the laminar box are 1200 mm in length, 800mm in width, and 1000 mm in height. Its configuration is shown in Fig.2.2. The container consisted of eighteen laminar frames of which the height was 0.05m. The bottom laminar frame was fixed to the base plate of the container. Other laminar frames were supported by roller bearings as illustrated in Fig.2.3, and allowed to move only in the longitudinal horizontal direction. The weight of each laminar frame was approximately 106N. A physical gap of 5mm was maintained between the frames to allow for the independence in movement. A rubber membrane was placed on the side wall of the container with waterproofing at its bottom. An outer frame was equipped with vertical bars with roller bearings which support the weight of laminar frames. Photo.2.1 indicates the overview of the container.

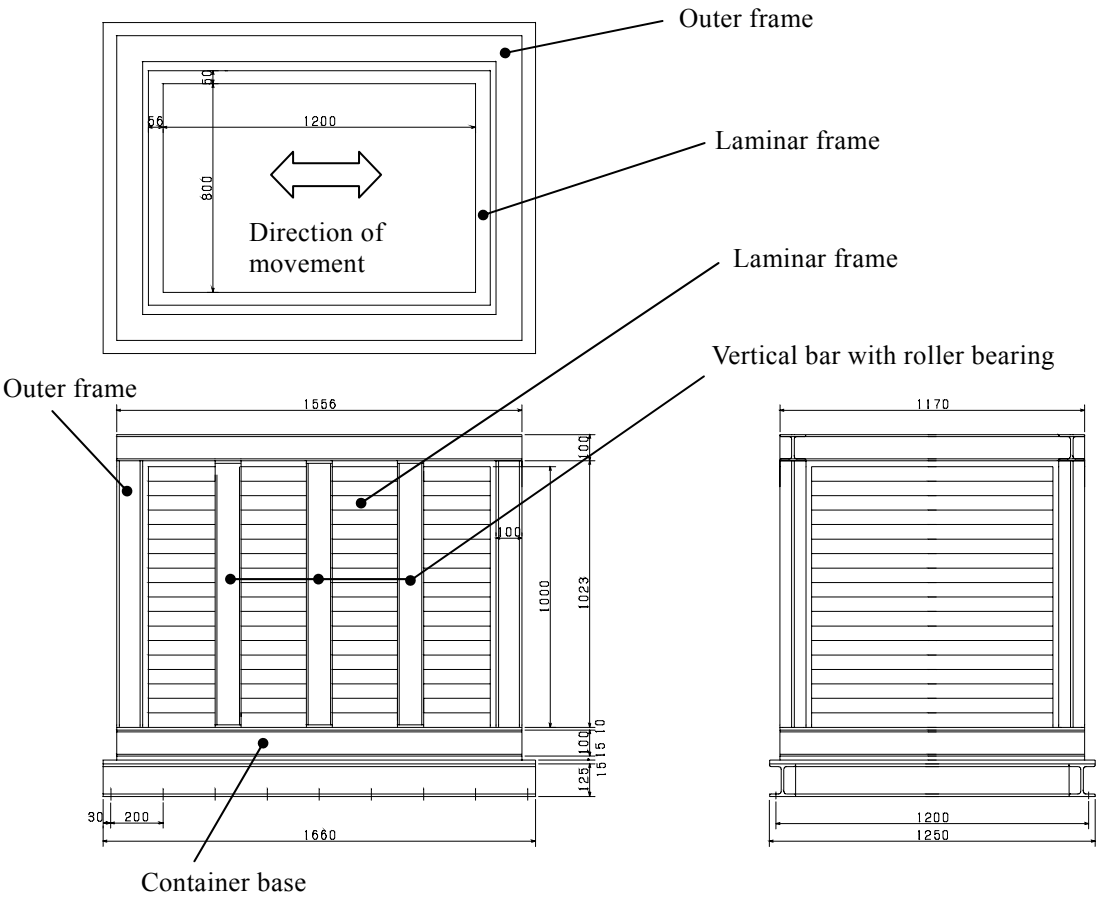

Dimensions are in millimeters

Fig.2.2: Container used in the experiment

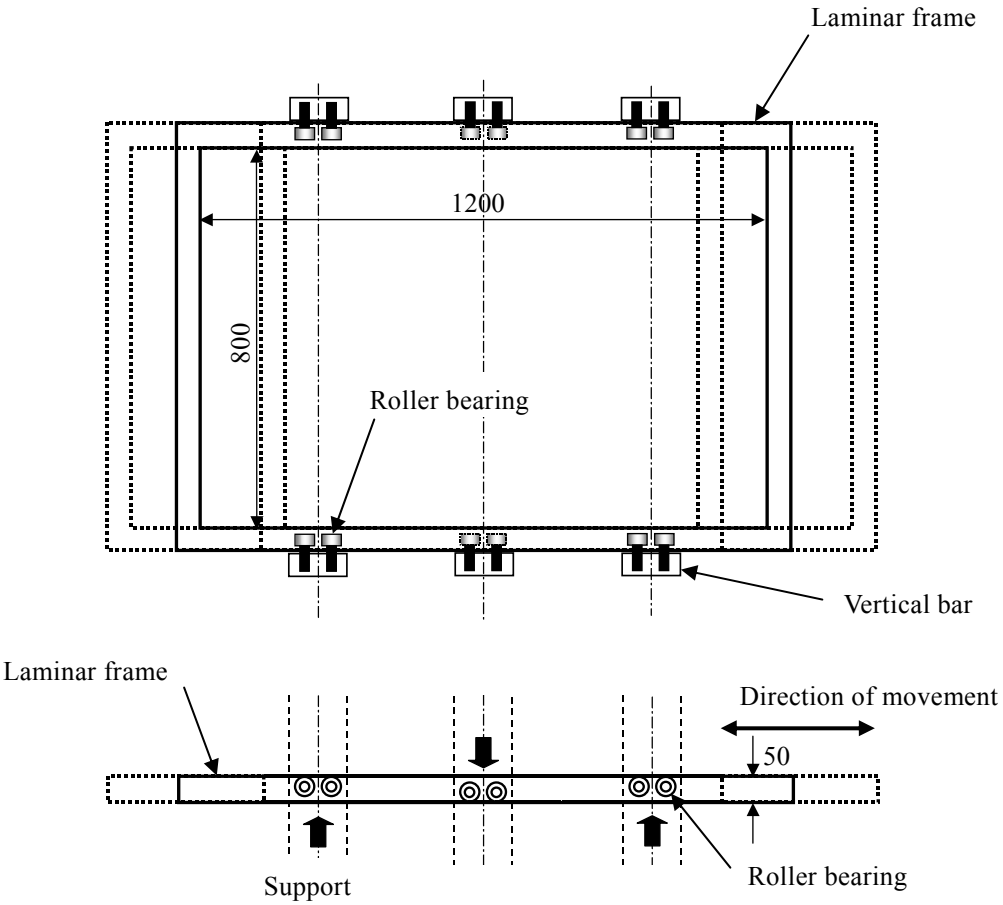

Fig.2.3: Schematic figure of movement of a laminar frame

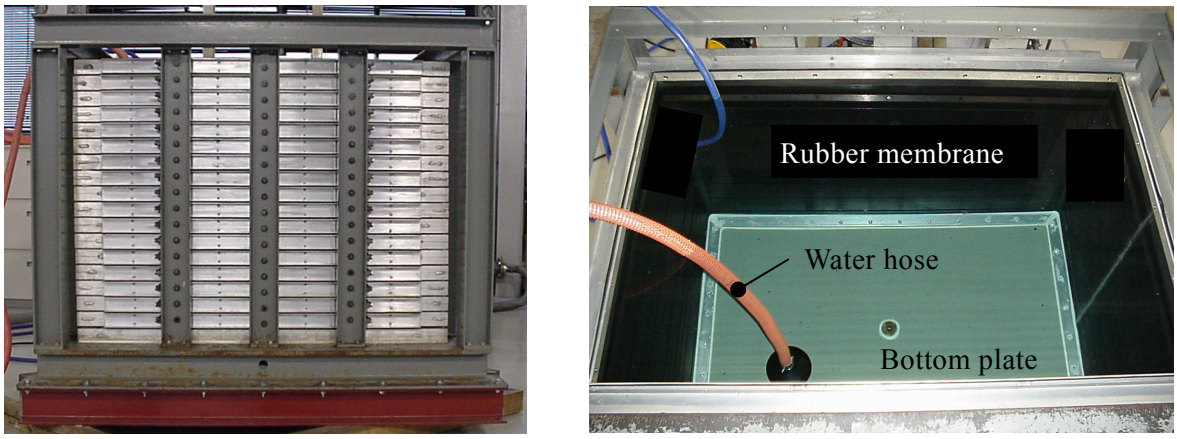

(a) Side view (b) Inside of the container (water is filled)

Photo.2.1: Overview of the container used in tests

2.2.3 Data acquisition system

Total number of transducers amounted to 48 for measurements in the experiment. The data acquisition system with 32 channels and the other data acquisition system with 16 channels were used jointly. All the transducers were connected to strain amplifiers, and the data were recorded automatically in hard disks through digital recorders.

2.3 SHAKING TABLE MODEL CONFIGURATION

2.3.1 Model configuration and material

Basic conditions for the model

The basic conditions of a structure model for shaking table tests are established considering the scope of this study presented in Section 1.3 as what follows.

1. A box shape is modeled for a cross section of an underground structure. The backfill is considered at both sides of structure as well.
2. Since actual underground structures with box sections keep space inside in a longitudinal direction for its use, the space filled with air in a longitudinal direction is kept for the structure model.
3. The bottom of a structure model is fixed rigidly on a bottom of a container, supposing a fixed base on an unliquefied base layer in an actual box section. Neither uplift nor rocking motions occurs in the structure model during shaking in tests.
4. Since a generation of excess pore water and following complete liquefaction of soil is considered in the backfill, saturated sand is used for the model ground.
5. A flexible box section of underground structure of which the rigidity is lower than the initial rigidity of ground is supposed. For the structure model in shaking table tests, the stiffness of the structure is made much less than that of backfill (about 1/50) for clear observations.
6. Overburden soil is not made in the soil-structure model, since only the effect of backfill at the side of the structure is focused on in this study.

Structure model

A structure model of a box-shaped culvert was designed to satisfy the aforementioned conditions. The cross section of structure model consists of three parts: the base plate, the side wall and the top plate (ceiling plate). It is usual that actual underground structures are made of reinforced concrete. However, owing to difficulties in preparing reinforced concrete models, aluminum (or aluminum alloy) was used for the material of the model.

It is required for the model structure to keep empty, filled with air, in the longitudinal direction. To comply with this, the structure model was set in a row in the container as illustrated in Fig.2.4(a). The side walls and the top plate of model structure was divided into three parts in the longitudinal direction (see Fig.2.4, part of (i)～(iii)). The physical gap between the structures was maintained to minimize the effects of movements of laminar frames on the structure. A physical gap of 5mm was maintained between the ends of the side walls (A in Fig.2.4), while 10mm between the model structure ends and the side walls of the container (B in Fig.2.4). The measurement was conducted at the middle part of structure that was not in contact with the side walls of the container.

The side walls of the model were bolted to the base made of a thick aluminum mass, which was fixed to the bottom plate of the container (see Fig.2.4(b)). Neither translation nor rotation was allowed at the bottom of the wall, while no rotation at its top. No uplift would be occurred when the backfill liquefied.

The depth of model ground was set as 850mm, being 85% of the height of the container. Next, the dimension of cross section was determined as large as possible within the inner size of the container. It was determined that the height of the structure was 850mm including the height of the base, and the width was 280mm (inner side of the structure), which was about one forth of the width of the container. A configuration of a modeled underground structure is depicted in Fig.2.4. The bending stiffness of the top plate was relatively high as compared with that of the walls. The walls, the top and base plates of the model were made of A5083P alloyed aluminum (Japanese Industrial Standard H4000, purity is 98.3%). A1070P aluminum plates (purity is 99.7%) were also used for side walls in a limited number of experiments. Material properties of aluminum are summarized in Table 2.1.

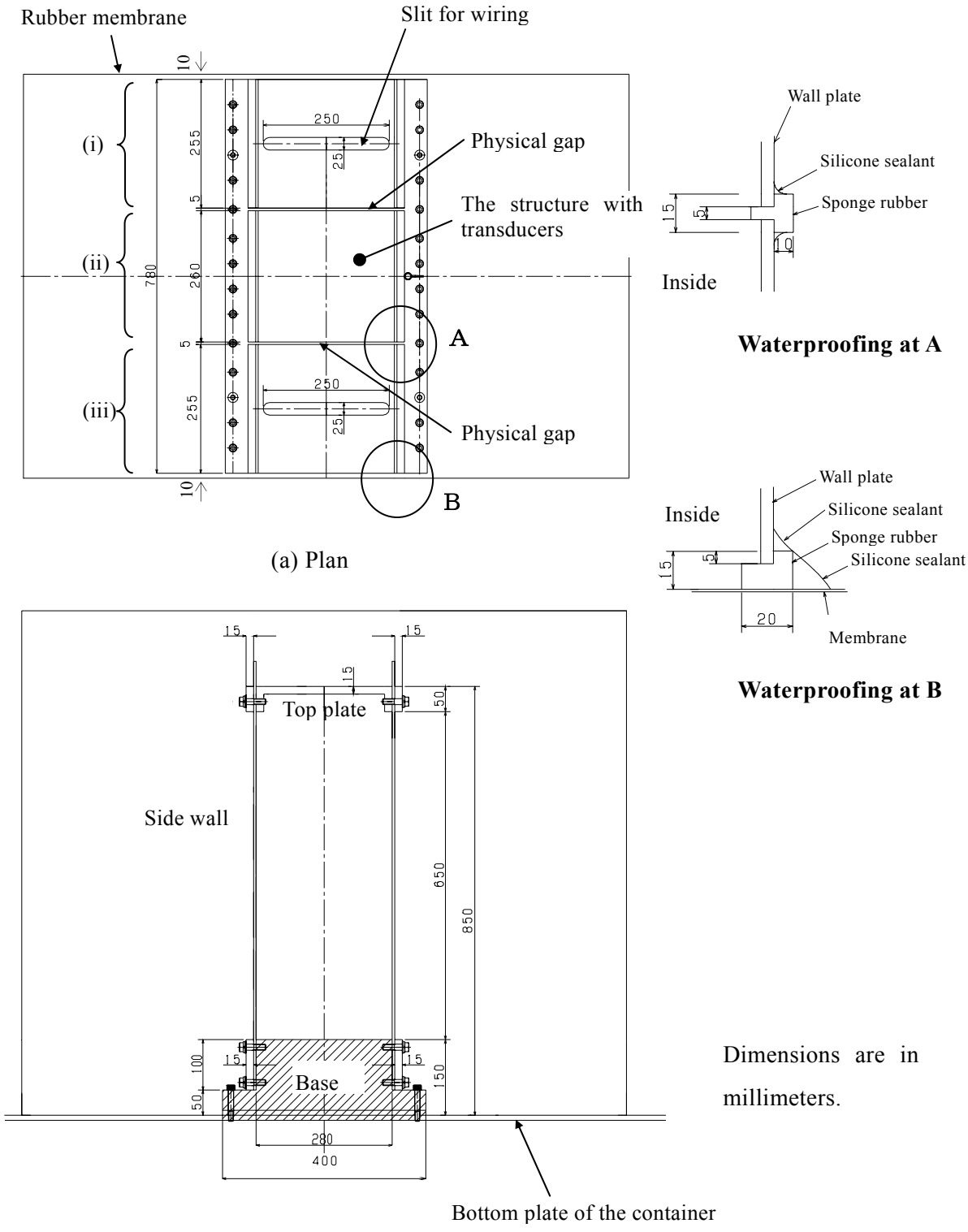

Fig.2.4: Model structure dimensions

Table 2.1. Material properties of aluminum

Designation	Young's modulus (GPa)	Poisson's ratio	Tensile strength (MPa)	Remarks
A5083P	75	0.32	146	Structure-A
A1070P	69	0.32	86	Structure-B1,B2

The thickness of the side wall was determined i) to make the natural frequency of the structure low than the initial natural frequency of backfill, ii) as thin as possible so that the amount of the shear-type deformation of the cross section during shaking may become larger, iii) in order that the yielding of aluminum may not occur before shaking. Calculations were made on the various thickness of wall of 3mm, 5mm, 10mm, applying the static water pressure and the horizontal effective earth pressure at rest. The yield stress of aluminum was conservatively estimated as 86MPa (A1070P) for a criterion. As a result, the wall of 5mm thickness was selected to satisfy the requirement.

The thickness of the top plate was determined as 15mm in order that the bending stiffness becomes relatively high as compared with that of the walls. The top plate is 3 times thicker than the side wall. In this respect, 27 times stiffer than the side wall in terms of the bending stiffness. The slit was made at the top plate for the wiring of transducers which were attached on the structure.

Model sizes and properties of members are shown in Table 2.2. The thickness of the wall shown in the table is the measured value of walls (nominal thickness of 5mm) by using a slide caliper with the accuracy of 1/20mm. The natural frequency of the structure itself was 7.8Hz for Structure-A, and 7.3Hz for Structure-B1 and B2 according to the evaluation based on the after-mentioned free vibration test. The space inside the model was kept empty throughout the tests. The natural frequency of loose backfill at the relative density of 34% with the depth of 0.85m becomes about 20Hz according to the after-mentioned weak excitation test (see Fig.3.13).

Table 2.2. Model sizes and properties

	Thickness	Moment of inertia	Bending stiffness
Wall (Structure-A)	4.97 mm	1.02×10^{-8} m^4/m	765 Nm^2/m
Wall (Structure-B1,B2)	4.87 mm	9.63×10^{-9} m^4/m	664 Nm^2/m
Top plate	15mm	2.81×10^{-7} m^4/m	20960 Nm^2/m

Backfill

Toyoura sand was employed as the backfill material. It is classified as uniform fine sand consisting of mostly subrounded to subangular particles with mostly quarts composition. The physical properties of Toyoura sand are given in Table 2.3. The backfill was made by pouring sand into deaired water in the box to achieve the initial relative density of approximately Dr = 35%. The structure model with backfill of saturated Toyoura sand is illustrated in Photo.2.4(b) in the next section.

As stated previously in the basic condition for the model, the overburden soil was not taken into account in this study. The backfill was not made on the top plate of the structure model.

Table 2.3. Properties of Toyoura sand

Specific gravity, G_s	2.65
Maximum Void Ratio, e_{max}	0.966
Minimum Void Ratio, e_{min}	0.642
Mean diameter, D_{50} (mm)	0.2

Installation of the structure model in the container

The whole structure model that consisted of wall plates and the top plate was assembled on the base plate by using bolts outside of the container. The side view of assembled structure model is presented in Photo.2.2(a). The assembled structure was then installed into the container.

A physical gap of 5mm was maintained between the ends of the side walls (A in Fig.2.4), while 10mm was maintained between the structure model ends and the side walls of the container (B in Fig.2.4). The complete waterproof works were conducted at the physical gaps between the structures to prevent leakage both soil and water. Sponge rubber was stuffed to each gap and sealed the corner by silicone sealant as illustrated at the inset of Fig.2.4. The measurement was conducted at the middle part of structure that was not in contact with the side walls of the container. The overview of assembled structure model installed in the container is presented in Photo.2.2(b).

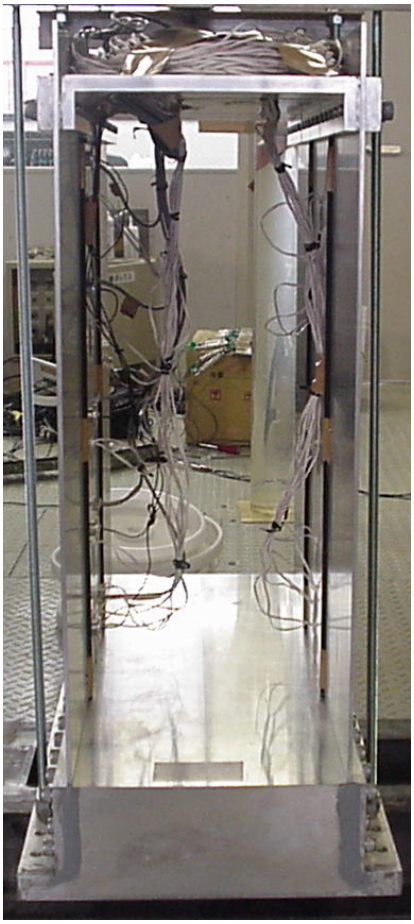

(a) Section view

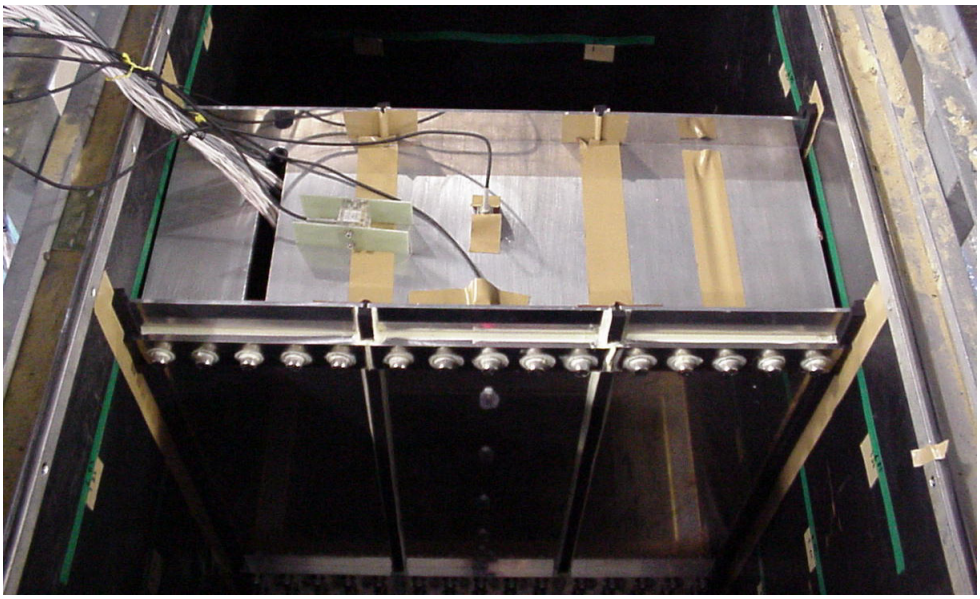

(b) Top surface (after installation in the container)

Photo.2.2: Overview of the structure model

2.3.2 Instrumentation

The major purpose of the instrumentation was to experimentally reproduce a stress-strain relationship as well as an effective stress path in the backfill soil during shaking around a structure, and to clarify the earth pressure and the deformation of the structure during liquefaction. To attain this goal, it was necessary to determine the shear stresses, shear strains, effective vertical pressures in the ground, and earth pressures, bending strains and displacement at the structure by measurements.

Shear stresses are calculated by integrating the shear stress difference at each depth with respect to the depth. A schematic figure of shear stress difference, inertia force of soil mass and normal stress difference is illustrated in Fig.2.5. The shear stress difference at each depth can be derived to measure both the acceleration in saturated soil α_x and the difference of lateral earth pressure of soil mass $\Delta\sigma_x (= \partial\sigma_x / \partial x \cdot \Delta x)$. Therefore, the accelerations and lateral earth pressures on the structure and in the soil have to be measured along the depth.

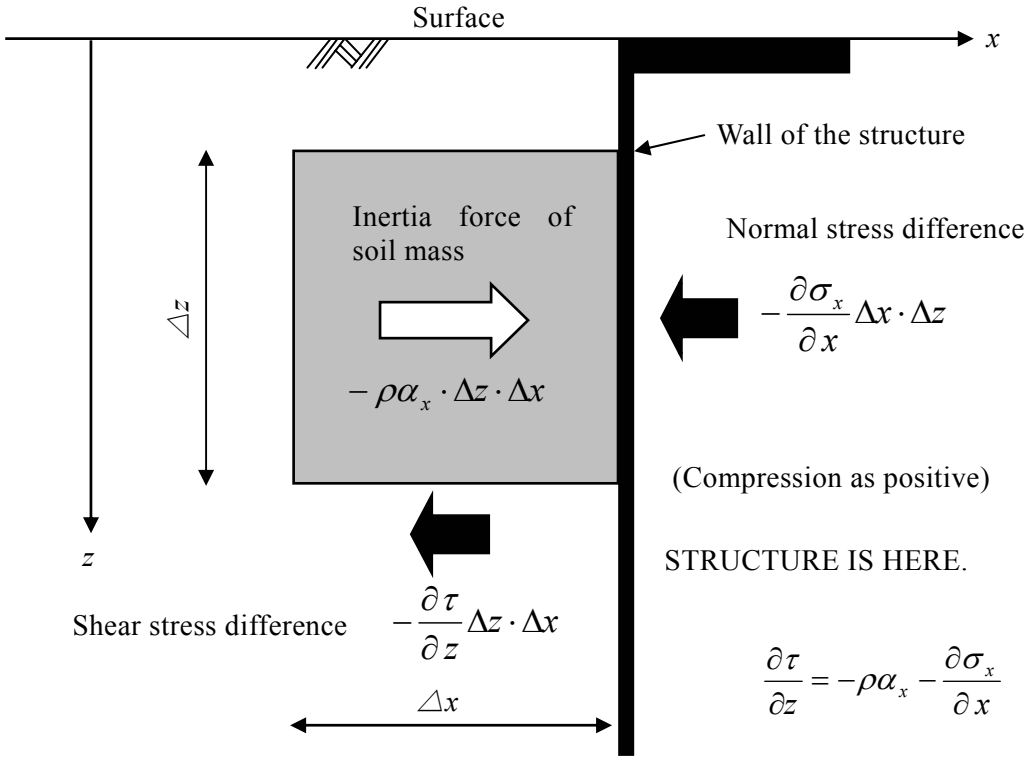

Fig.2.5: Shear stress difference and normal stress difference

Shear strains are obtained by dividing the displacements of soil by the elevation of difference. The displacements in the soil and on the wall of the structure have to be evaluated. These quantities can be calculated from accelerations and bending strains by integration. Therefore, the displacement at the top of the structure, accelerations in the soil, and bending strains of the wall have to be measured along the depth. Effective vertical stresses can be calculated by the measurement of excess pore water pressures in saturated soil. The pore water pressures in saturated soil have to be measured.

The earth pressures act on the structure are obtained to directly measure the earth pressure by using earth pressure transducers. The deflection of wall of the structure can be calculated from bending strain of wall by integration along the depth. It is desirable that the distance between the strain transducers is as short as possible.

Consequently, such a variety of transducers as those for acceleration, displacement, pore pressure and earth pressure were installed in the model ground. In addition, earth pressure and strain transducers were attached to the flexible wall of a structure model as was shown in Fig.2.6.

Accelerations on the structure and in the soil were measured using accelerometers (ASW-2A, KYOWA electronic instruments company Ltd, Japan). Displacements of structure, ground surface and laminar frames of the container were measured using laser displacement sensors (LB01, capacity =±40mm, KEYENCE CORPORATION, Japan). Bending strains of side walls of the structure were measured using strain gauges (manufactured by KYOWA electronic instruments company Ltd, Japan, type KFW-5-120-C1-23L5M3R, with a nominal resistance of 120 ohms, strain limit = 2.8%). Earth pressure transducers were used to measure static and dynamic lateral earth pressures on the wall, and measure dynamic pressures in saturated sand. Earth pressure transducers (P350SV, P350S, P325SV, capacity = 40kPa, SSK CORPORATION, Japan) were used of which the diameter of the sensing membrane was 50mm and 25mm. Pore pressure transducers (P310A, P310AV, capacity = 20kPa, SSK CORPORATION, Japan) were used to measure excess pore pressures in saturated sand and on the wall. The direction of the arrows for accelerometers and laser displacement sensors in Fig.2.6 indicate the positive directions of the measured signals.

The detailed locations of transducers on side walls are shown in Fig.2.7. The side view of structure model is shown in Photo.2.3. Earth pressure transducers, pore pressure transducers and strain gauges are attached on the left side wall. Only strain gauges are attached on the right side wall. All the cables of transducers were put inside the structure through small holes drilled on the walls. Accelerometers were attached at the top of the structure by using adhesives.

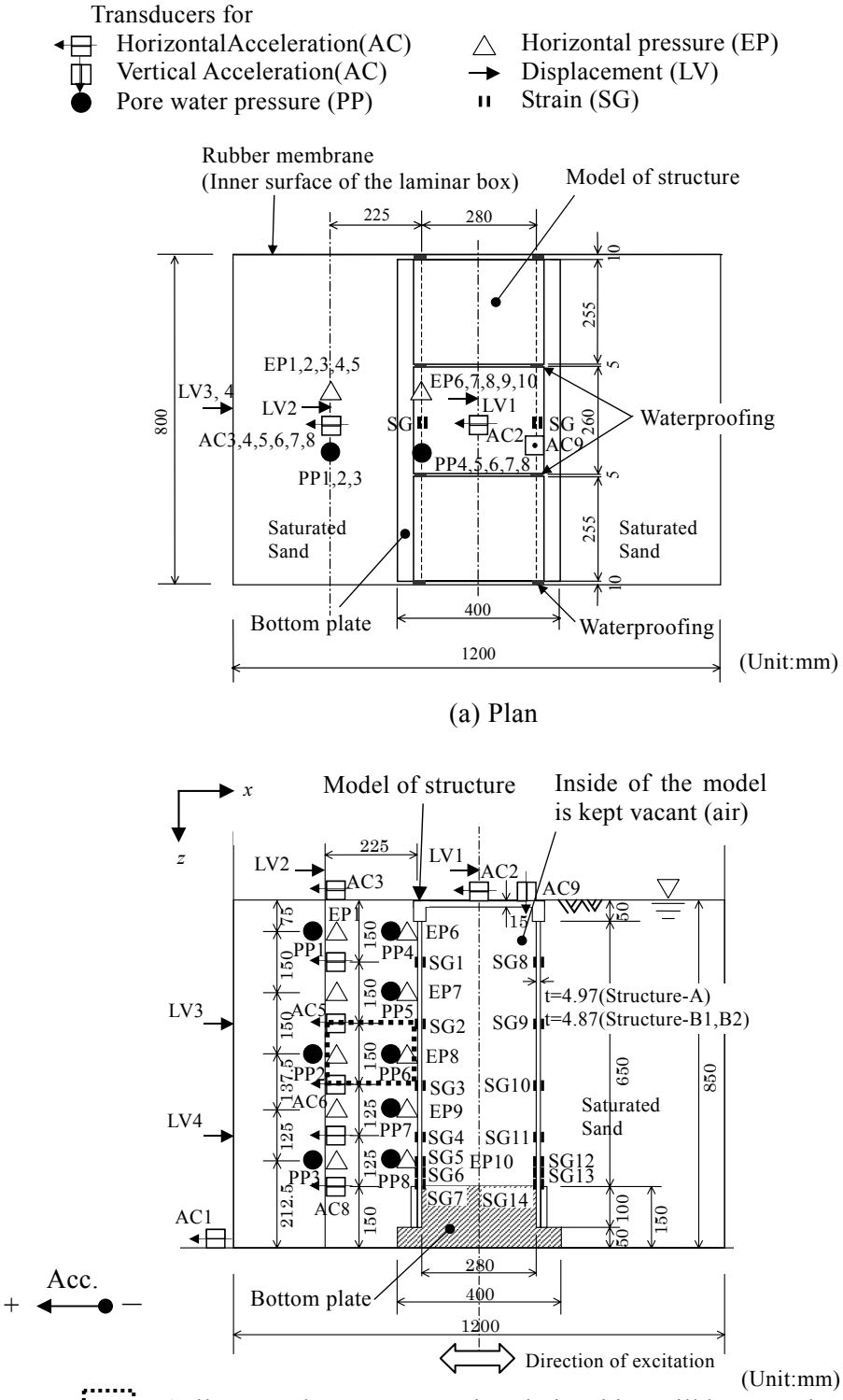

(b) Elevation

Fig.2.6: Soil-structure model and installation of transducers

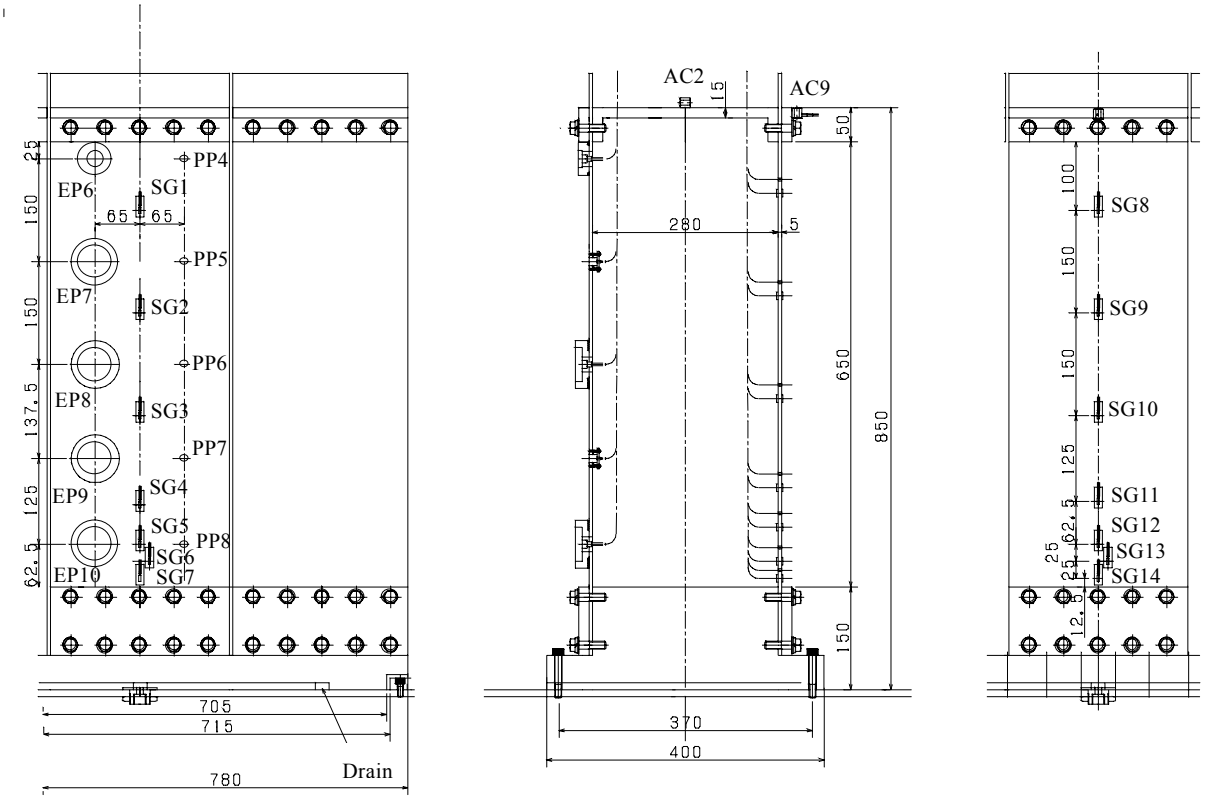

LEFT SIDE WALL **ELEVATION** **RIGHT SIDE WALL**

Size in millimeters

Fig.2.7: Location of transducers

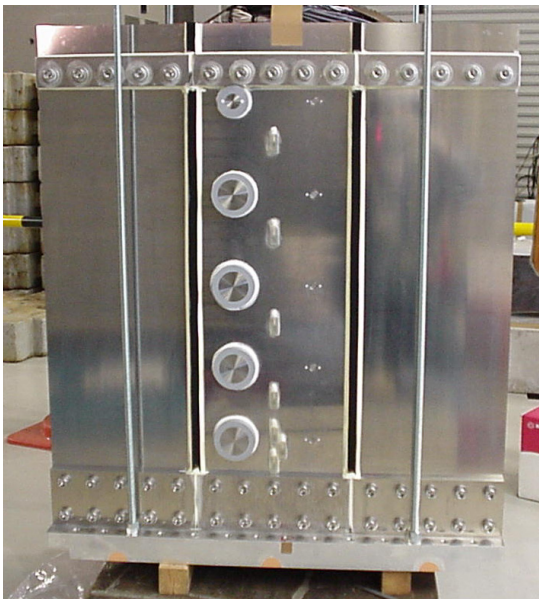

Photo.2.3: Transducers at the side of the structure model

Earth pressure transducers were mounted on the surface of the wall and fixed at two points by screws. Waterproofing was made between the back surface of transducer and the face of wall in order to prevent leakage water and sand. Pore pressure transducers were flushed and attached on the surface of wall by screws with waterproofing. There were 14 pairs of strain gauges in a half bridge configuration along the height of walls. The fixation of laser displacement sensors is illustrated in Fig.2.8. The laser displacement sensors at the top of the container were fixed at the tip of the arm plates that were bolted on the crossbeam. The crossbeam was clamped tightly at the top of the container frame. The laser displacement sensors at the side of the container were fixed on the frame in the same manner. A marker was prepared at the surface of the backfill in order to focus the laser beam on (see Photo.2.4).

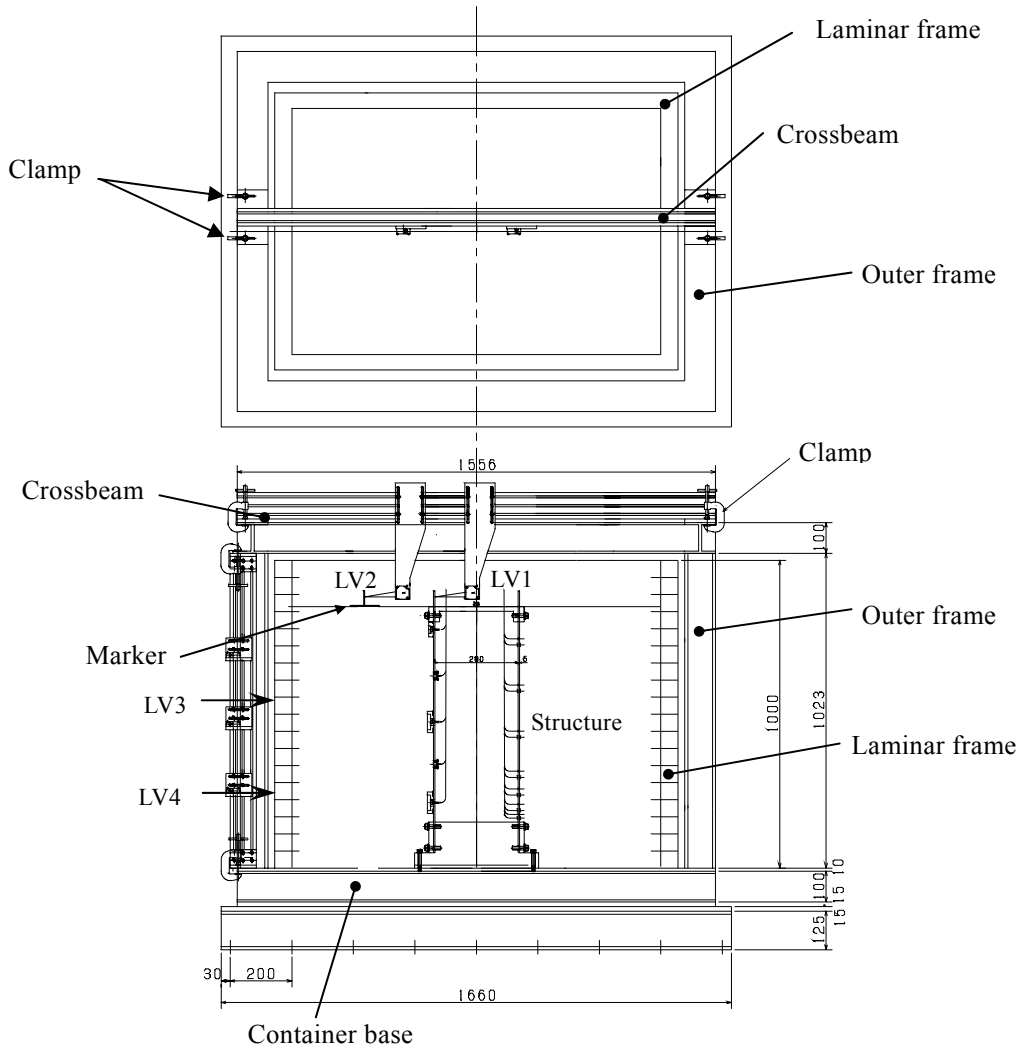

Size in millimeters

Fig.2.8: Fixiation of Laser displacement sensors

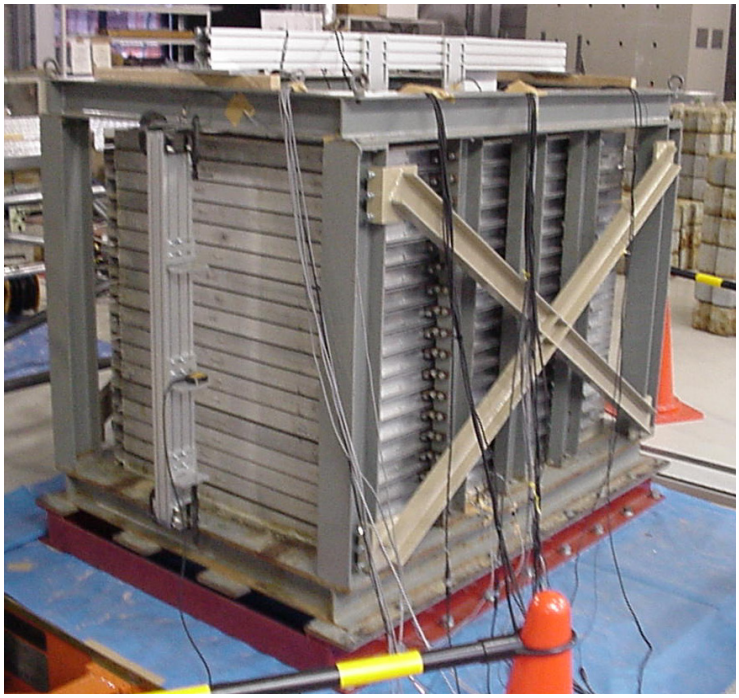

(a) Cross beam and laser displacement sensors at the side

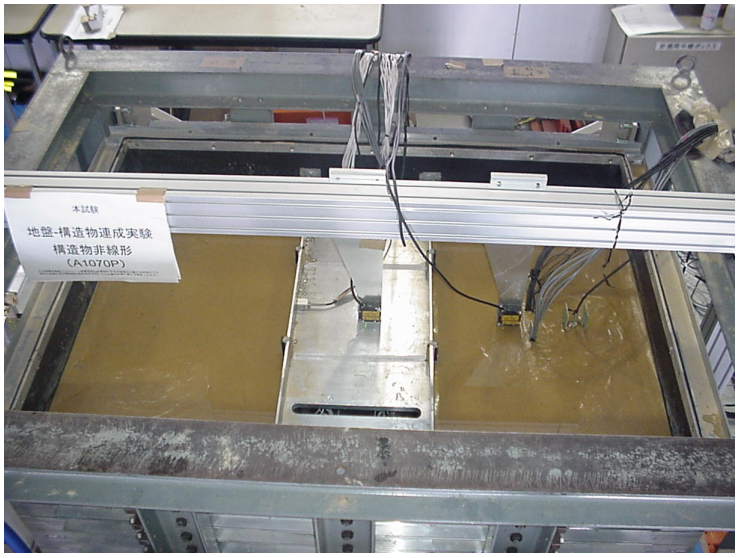

(b) Cross beam and laser displacement sensors at the top of the model

Photo.2.4: Overview of the model and installation of laser beam transducers

A special care was taken of the earth pressure transducers and the accelerometers that were placed in liquefiable saturated sand. Those transducers were fixed on thin plates as illustrated in Fig.2.9 in order to reduce as much as possible the rotation after liquefaction. The densities of accelerometers and earth pressure transducers were adjusted to the density of saturated sand (Specific gravity = 1.8) by attaching them the lightweight materials to minimize the effect of dynamic interaction between the transducers and saturated sand. Lightweight materials such as vinyl chloride plastic and acrylic plastic were used for the density adjustment. The dimensions of lightweight materials with transducers are shown at the inset of Fig.2.9.

Manufacturer's calibrations were used for all transducers. Performance of earth pressure transducers placed in saturated sand was investigated as described below because it is one of the key measurements in this study;

(a) The transducers were immersed in a cylindrical vessel filled with water. Pressure was applied in increments to the transducer by changing the depth of water. The corresponding voltage changes were recorded for the calibrations.

(b) A model ground instrumented with earth pressure transducers in saturated soil was tested by another series of shaking table test excited in the vertical direction. The dynamic pressures recorded by earth pressure transducers were compared with the dynamic pressures by the inertia force of soil mass.

Results of the second investigation will be presented in the section 2.5. Details of the series of tests are illustrated in Appendix A.

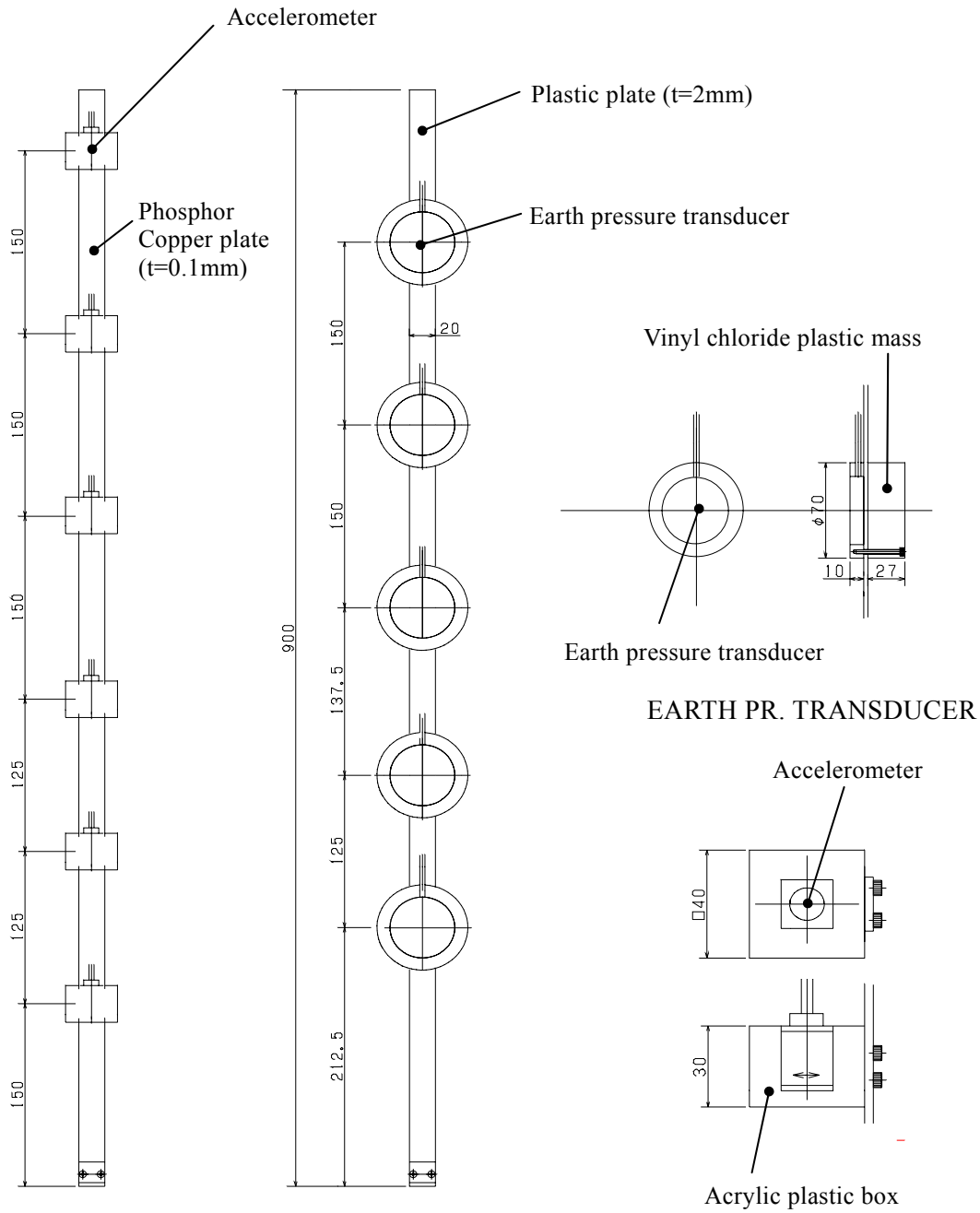

Fig.2.9: Density adjustment of accelerometers and earth pressure transducers in the saturated soil

2.4 PROPERTIES OF MATERIAL AND STRUCTURE

2.4.1 The tensile test

The standard tensile test was conducted to derive material properties of the structure model. Material samples were prepared following JIS Z2201 (Japanese Industrial Standard). The configuration of a material sample is depicted in Fig.2.10. The nominal thickness of the sample was 5mm. Two elements cross strain gauges (manufactured by KYOWA Electronic Instruments Company Ltd, Japan, type KFG-5-120-11L3M3S, with a nominal resistance of 120 ohms) were attached at the middle of both sides of a sample to measure the axial and the lateral strains. The mark points, in which the initial distance between them was 100mm, were put on the sample to measure the ultimate elongation.

The measured cross section of each sample was used to convert loads to stresses. It is shown in Table 2.4. Each area was calculated by averaging the three areas in the middle part of the sample. A slide caliper with the accuracy of 1/20mm was used for the measurement of the width and the thickness.

The stress-strain curves of the employed aluminum are shown in Fig.2.11. Fig.2.11(a) illustrates the stress-strain curves for two samples of aluminum alloy (A5083P). These curves are almost identical. Fig.2.11(b) shows the results of three samples of aluminum (A1070P). Although the result of No.1 sample is slightly different from others, all the stress-strain curves look identical on the whole.

The results of the series of the tensile tests are summarized in Table 2.5. The yield point of the A1070P material is taken as the stress which caused 0.2% parallel offset (JIS-Z2241), because a clear yield point did not occur. The tensile strength of the A5083P samples were not determined due to the technical problem in the tensile test. The manufacturer's test results are shown in the table instead. In both designations of the aluminum, the Poisson's ratio ν of the samples was derived as 0.32 in the elastic region. The Young's modulus was derived based on the initial inclination of each stress-strain curve. The ultimate strains were calculated by dividing the elongation measured between the marked points by the initial distance.

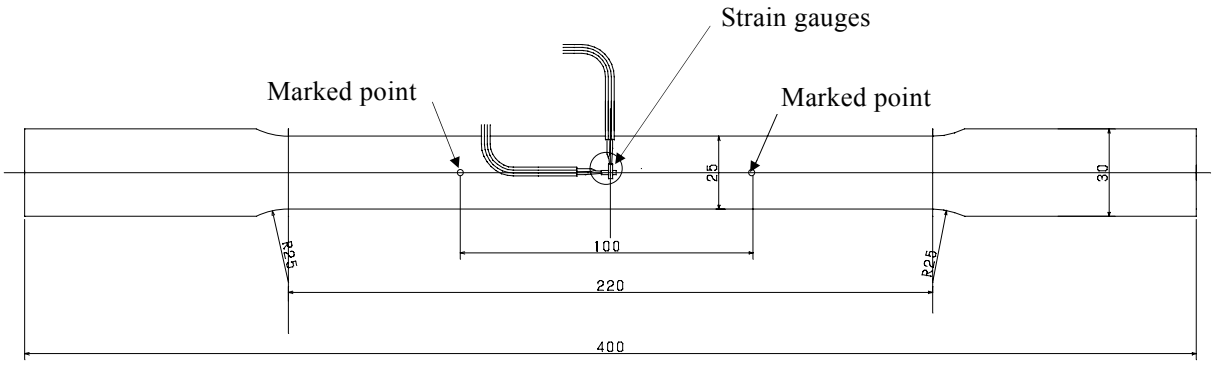

Dimensions are in millimeters

Fig.2.10: Configuration of sample (JIS Z2201)

Table 2.4. Measured area of samples

Designation	Sample No.	Initial distance between the marks (mm)	Cross section (cm^2)
A5083P	No.1	100.55	1.208
	No.2	100.55	1.207
A1070P	No.1	100.50	1.175
	No.2	100.70	1.143
	No.3	101.00	1.137

Table 2.5. Results of the tensile tests

Designation	Sample No.	Yield stress σ_Y (MPa)	Tensile strength σ_u (MPa)	Ultimate strain %	Yield stress ratio σ_Y/σ_u	Young's modulus (GPa)
A5083P	No.1	146.0	309*	28.0*	0.472	74.5
	No.2	145.5			0.471	74.5
A1070P	No.1	83.3**	97.4	36.5	0.855	68.6
	No.2	86.2**	98.5	39.9	0.875	68.6
	No.3	86.2**	98.5	33.8	0.875	68.6

*Manufacturer's test results **0.2% parallel offset

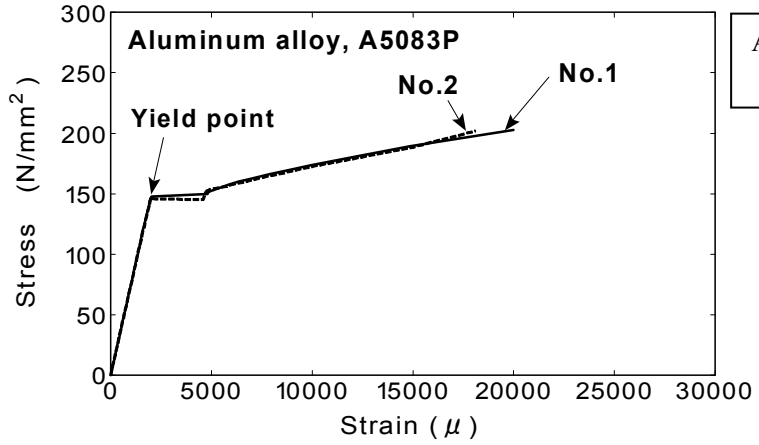

(a) Aluminum alloy (A5083P)

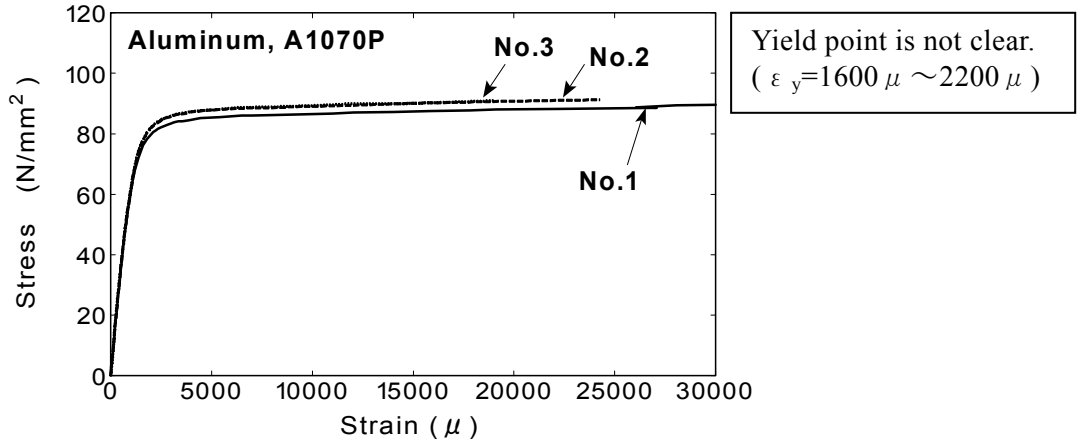

(b) Aluminum (A1070P)

Fig.2.11 Stress-strain curves of aluminum

2.4.2 The bending test

The configuration of the sample for the bending test is illustrated in Fig.2.12. The length of the sample is 550mm. The measured width and the thickness of the section are summarized in Table 2.6. The breadth *b* is calculated by averaging measurements at three points. The thickness *t* is the average thickness including the samples for the tensile test. The breadth was assumed to be 30mm for the calculation of the moment of inertia.

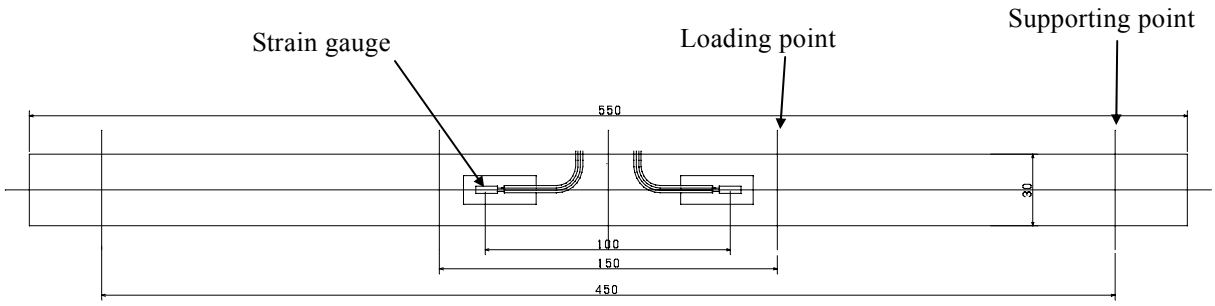

Dimensions are in millimeters

Fig.2.12: Configuration of sample

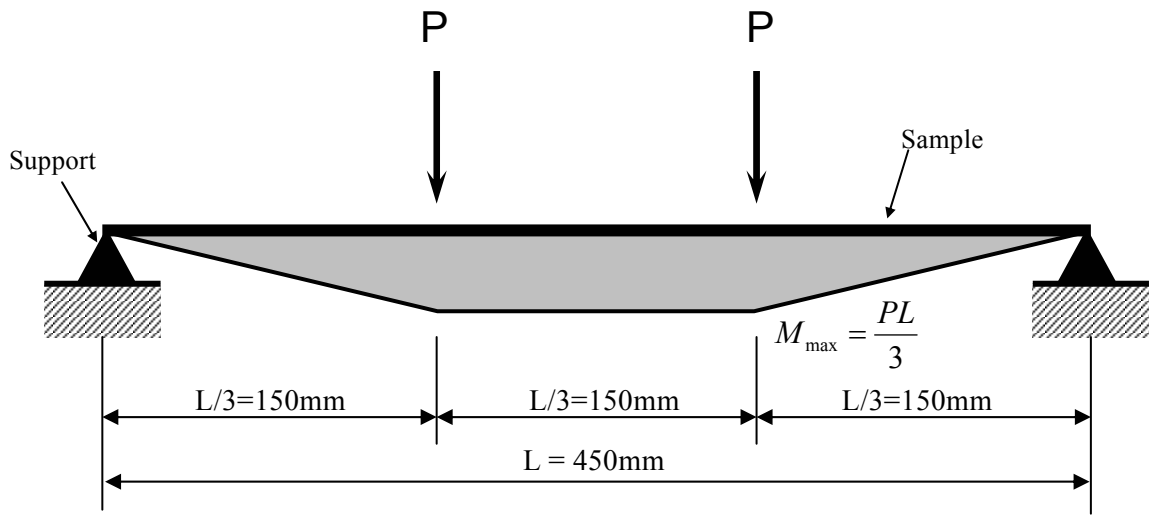

Fig.2.13: Bending moment diagram of the sample

Table 2.6 Dimensions of samples

Cross Section	Designation	Sample No.	b (mm)	t (mm)	Moment of inertia I (mm^4)
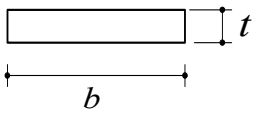	A5083P	No.1	29.98	4.95	303
	A1070P	No.1	30.00	4.74	266
		No.2	30.00		
		No.3	30.10		

Concentrated load was applied at two points as illustrated in Fig.2.13, and the bending strains were measured between the loading points where the bending moment was constant in the horizontal direction. The bending strain was measured by using the same type of the strain gauges as attached on the model structure (manufactured by KYOWA electronic instruments company Ltd, Japan, type KFW-5-120-C1-23L5M3R, with a nominal resistance of 120 ohms, strain limit = 2.8%). There are two pairs of strain gauges in a half bridge configuration. The applied load was measured by using a load cell (Tokyo Sokki Kenkyujo Company Ltd of Japan, type TCLZ-1kNA, capacity = 1kN). Photo.2.5 indicates the overview of bending test.

The experimentally obtained relationships between bending moment and curvature of each sample are shown in Fig.2.14. Bending strains corresponding to the curvatures are indicated on the axis of abscissa for which the thickness of the sample was assumed as 5mm.

Fig.2.14(a) shows the results of the aluminum alloy (A5083P). The shape of the curve is linear in the range of bending strain less than about 4000 μ, and the non-linear relationship is observed after that. As illustrated in Fig.2.11(a) of the result of the tensile test, the strain at the yield point of aluminum alloy (A5083P) is approximately 1970 μ. The end of proportionality in the relation between bending moment and curvature occurred at the bending strain of 3940 μ. The observed proportionality limit agrees with the strain at the yield point.

Fig.2.14(b) depicts the test results of the aluminum (A1070P). As the aluminum (A1070P) does not have a well-defined yield point, the proportionality limit is not clear.

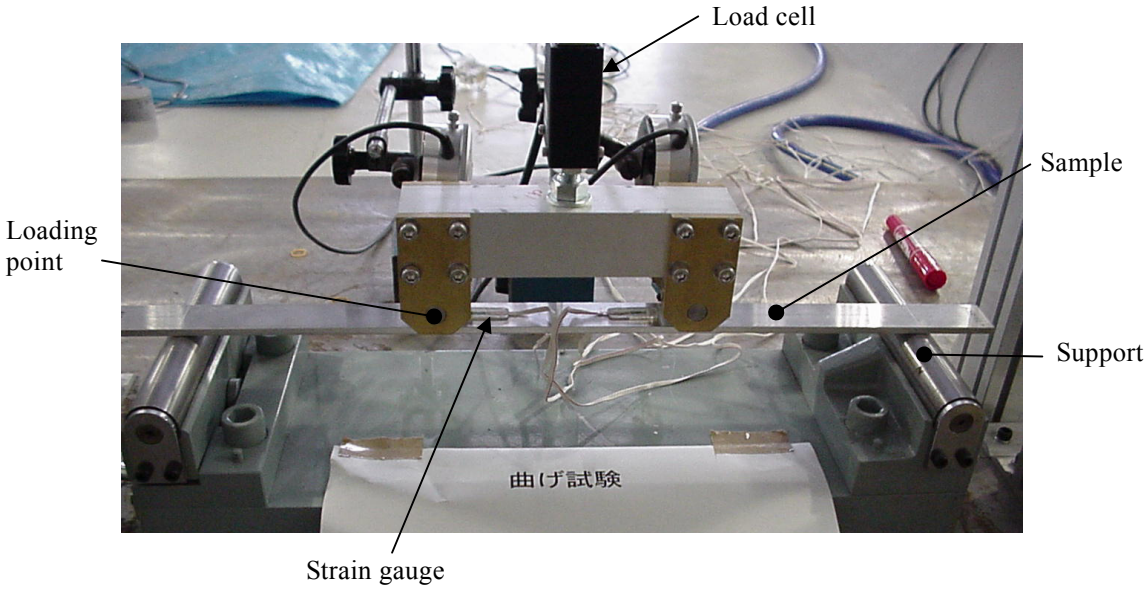

Photo.2.5: Apparatus of bending test and a sample

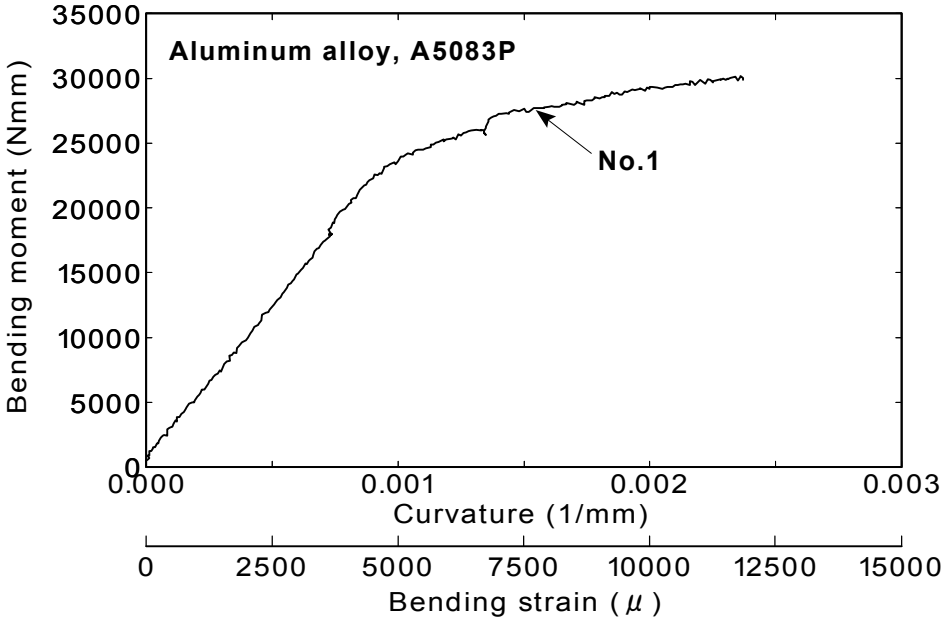

(a) Aluminum alloy (A5083P)

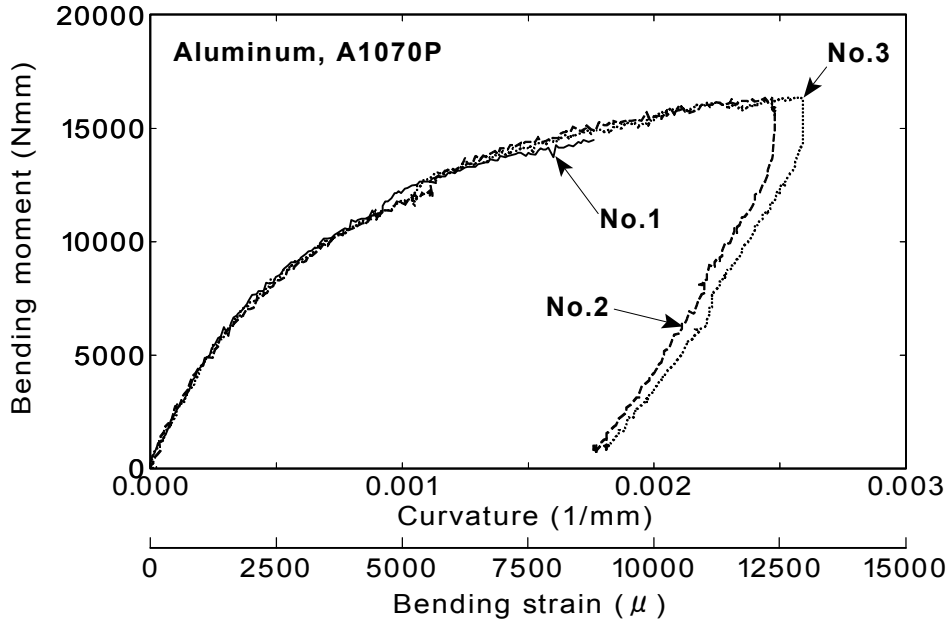

(b) Aluminum (A1070P)

Fig.2.14: The bending test results (Moment-curvature relationship)

2.4.3 Static loading on structure model

Loading with small deformation

The loading test with small deformation was conducted after fixing the structure in the container in order to examine the performance of strain gauges attached on both walls of the structure. The loading apparatus is depicted in Fig.2.15. Its photograph is presented in Photo.2.6. The test was conducted within an elastic behavior of the structure.

A hand jack was connected to the crossbeam that was clamped tightly to the outer frame of the container. The displacement was applied statically at the top of the structure by the hand jack up to about 10 mm. The load *P* at the top of the structure was measured by using the load cell (Tokyo Sokki Kenkyujo Company Ltd of Japan, type TCLZ-1kNA, capacity = 1kN). The strains on the wall were measured by strain gauges already attached the structure.

Fig.2.16 illustrates the distribution of the bending moments of the wall. The measured bending moment was plotted by ● and ○ in the figure. These were calculated by dividing the measured bending strains by the thickness of the wall. On the other hand, the bending moment was calculated from measured load *P* assuming the wall of the structure as a beam with a built-in end at its bottom, fixed end against rotation at its top.

The agreement between the measured and the calculated bending moment is good indicating that the performance of strain gauges attached on the structure is fine.

Loading with large deformation

The loading test with large deformation was performed in order to investigate the performance of a structure after yielding of material. Since a soil-structure model using Structure-B made of A1070P aluminum plate at its wall is expected to undergo a yield of material in shaking table test, only the Structure-B was tested. The test specimen for the large deformation static loading was prepared in addition to the structure for shaking table tests. The loading apparatus is illustrated in Fig.2.17. Its overview is presented in Photo.2.7. The breadth of the specimen was determined as 260 mm which was of the same breadth as the center part of structure model (see Photo.2.6).

The displacement was forced to apply statically at the top of the structure model (specimen), which was tightly connected on the rigid base, by pulling the specimen using hand jack. The load cell (Tokyo Sokki Kenkyujo Company Ltd of Japan, type TCLZ-1kNA, capacity = 1kN) was

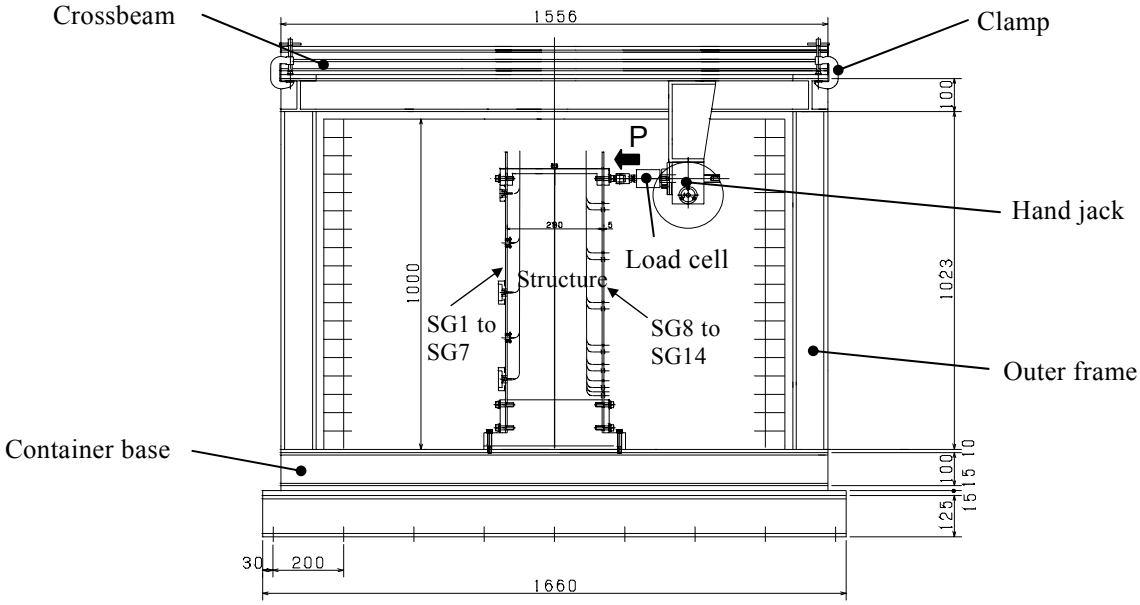

Fig.2.15: Loading apparatus for the test (for small deformation)

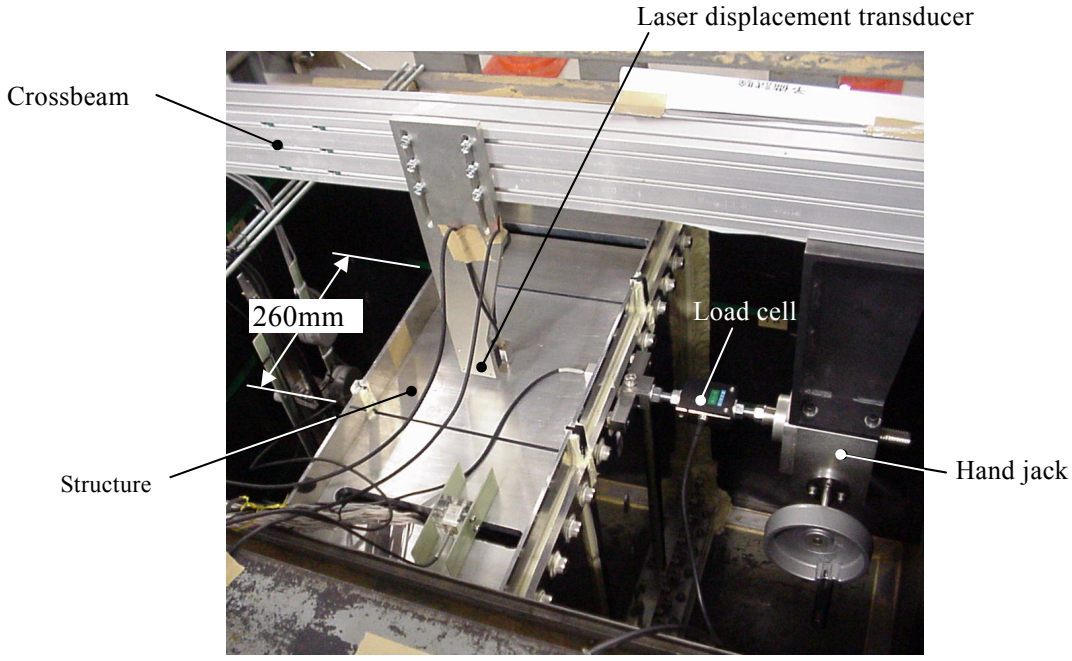

Photo.2.6: Loading apparatus and the structure model

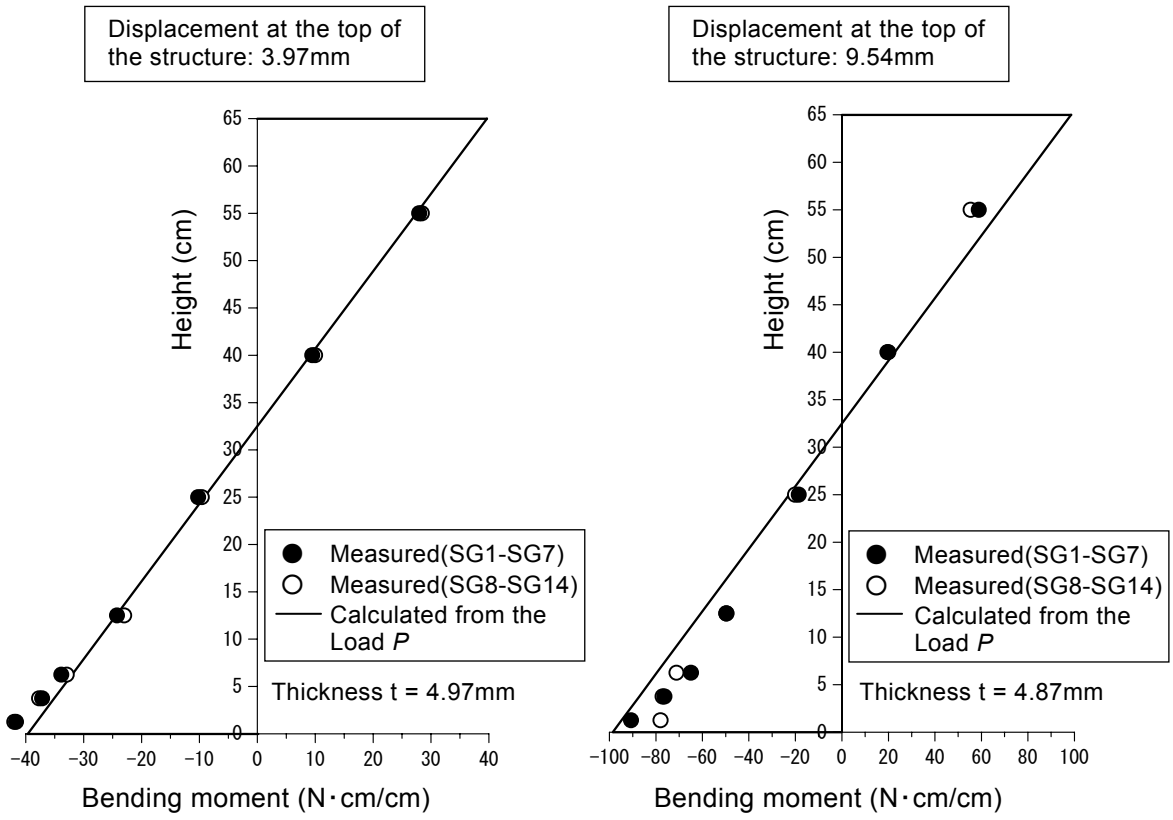

(a) Structure-A (A5083P) (b) Structure-B1 (A1070P)

Fig.2.16: Distribution of bending moment

attached in a rod between the specimen and the hand jack to measure loads. The tensile load is defined as positive in this test. To prevent the occurrence of bending stress in a load cell, ball joints were attached at its both sides. The displacement was measured at the other side of the specimen by using displacement transducer (DTH-A-100, capacity = 100mm, KYOWA electronic instruments company Ltd, Japan). The positive displacement is illustrated in Fig.2.17. Since the capacity of the displacement transducer is limited within 100m, the transducer was relocated when unload was finished. When the load was applied in the opposite direction, the specimen was turned 180 degrees on the rigid base.

The experimentally obtained relationship between the load and displacement is presented in Fig.2.18. Non-linearity is seen significantly after the displacement at the top of the specimen exceeds 50 mm. It is interesting that the gradient at the unloading is almost same as that at loading. Photo.2.8 shows the deformed structure with the maximum displacement at its top (138.94 mm). Shear type deformation is clearly seen at the large deformation of the specimen of structure model. Apparent shear modulus is calculated as about 160 kPa.

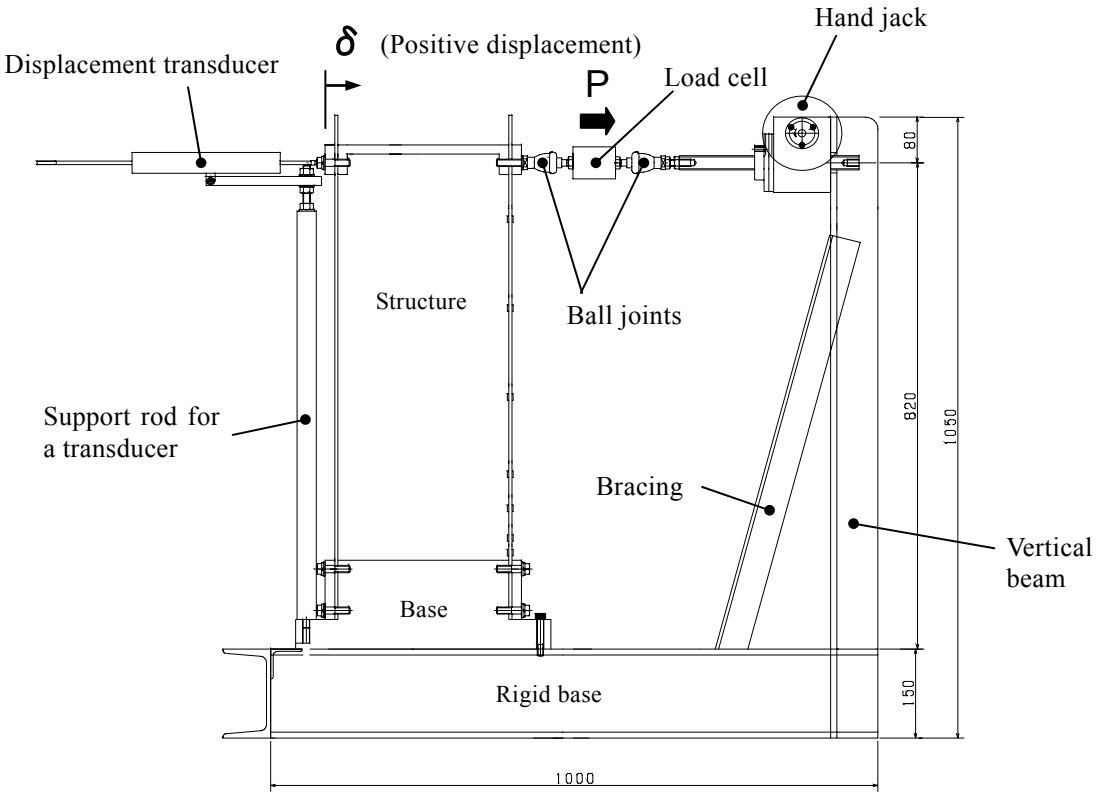

Fig.2.17: Loading apparatus for the test (for large deformation)

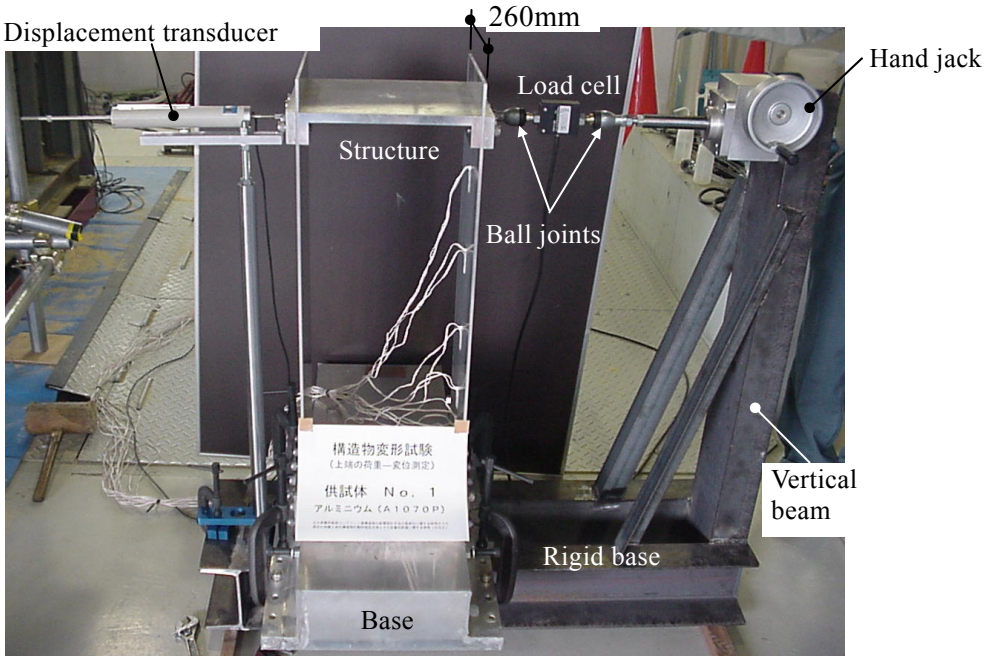

Photo.2.7: Overview of loading apparatus and the structure model

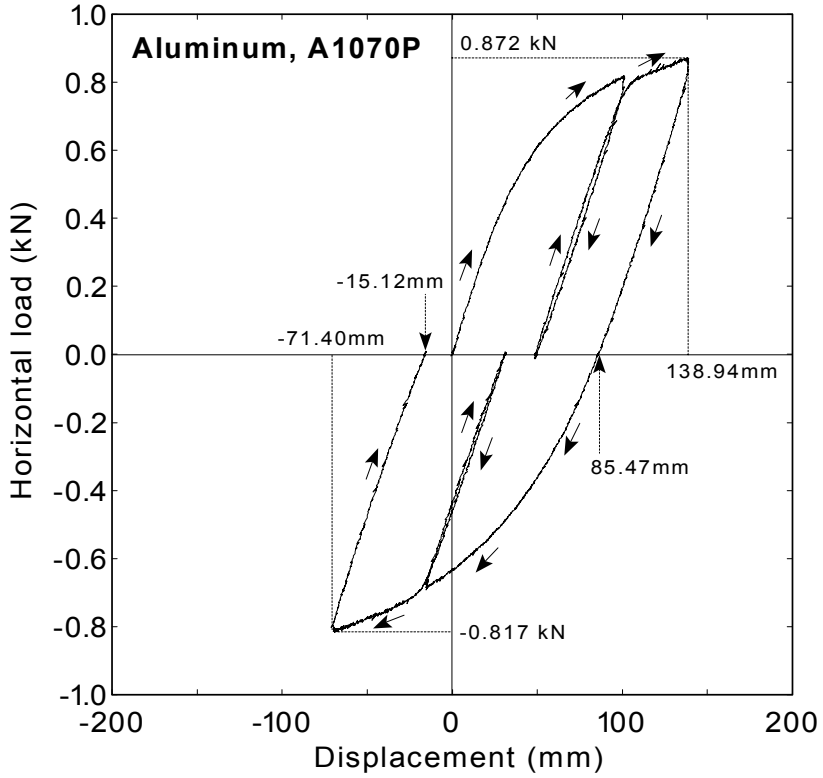

Approximate stiffness

k=0.872/(0.138-0.085)
= 16.3 kN/m
Height: 0.7m
Width :0.28m
Bredth:0.26m

Apparent shear stress

τ = 0.872/(0.26×0.28)
＝12.0 kPa

Apparent shear strain

γ = (0.138-0.085)/0.7
= 0.0757

Apparent shear modulus

G = τ / γ

= 12.0/0.0757

= 160 kPa

Fig.2.18: Experimental relationship between horizontal load and horizontal displacement of a structure

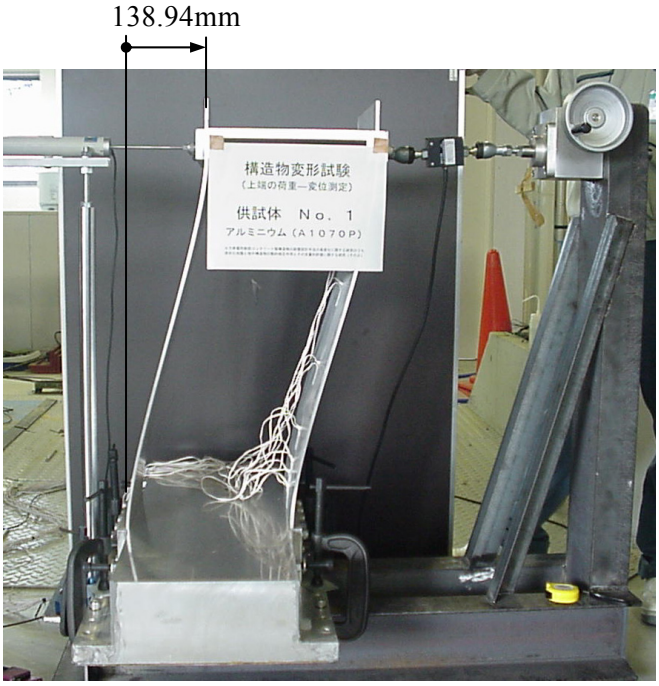

Photo.2.8: Structure model with the maximum displacement (Structure-B, A1070P)

2.4.4 The free vibration test

The free vibration test was carried out to determine the natural frequency and the damping ratio of the structure itself. Fig.2.19 shows the time history of acceleration at the top when the structure was undergoing free vibration in air. The free vibration in air was exerted by releasing the deformation of the structure instantaneously after the displacement was applied at the top. Fig.2.19(a) illustrates the whole time history during self vibration, and (b) an enlarged time history with respect to the time. The values of the acceleration and the time are written in the figure.

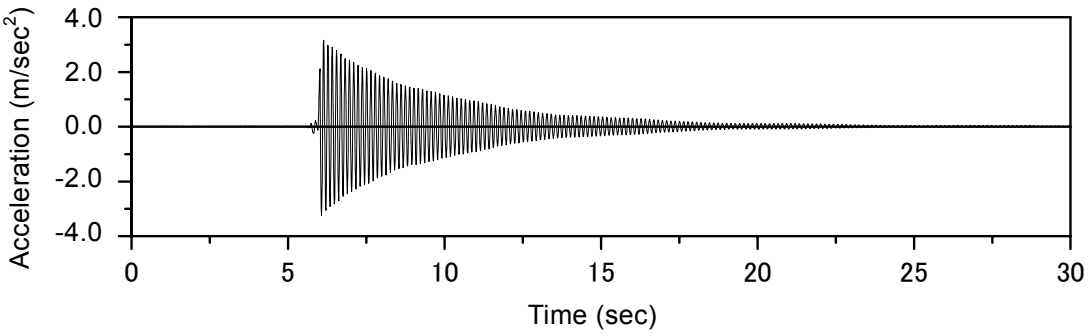

(a) Time history of acceleration at the top of the structure

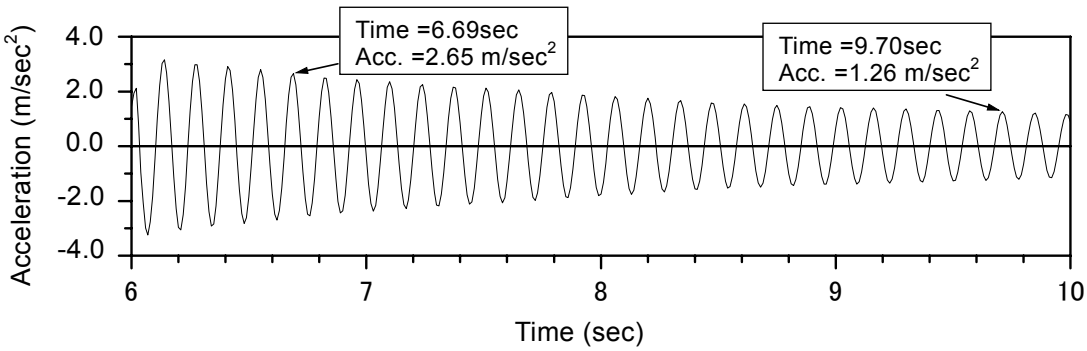

(b) The time history between the 6 seconds and 10 seconds

Fig.2.19: Result of the free vibration test of the structure (Aluminum, A1070P)

The natural frequency *f* is calculated by dividing the number of cycles by the elapsed time as;

$$f = \frac{n}{t} \tag{2.1}$$

where *n* is the number of cycles, and *t* is the elapsed time.

Damping ratio is expressed by the change of the amplitudes as what follows by using the idea of logarithmic decay;

$$\frac{1}{n}\ln\frac{x_1}{x_{1+n}} = 2\pi h \tag{2.2}$$

where x_1 is the amplitude in the initial cycle, x_{1+n} is the amplitude in the *n*th cycle after the initial cycle, and *h* is the damping ratio.

Regarding the structure as a spring-lumped mass model with a mass *m* and spring constant *k*, the natural frequency is expressed as;

$$f = 2\pi\sqrt{\frac{k}{m}} \tag{2.3}$$

On the other hand, by assuming the wall of the structure as a beam whose bottom end is built in, top end is fixed against rotation but free in translation, the spring constant *k* becomes

$$k = \frac{12EI}{H^3} \tag{2.4}$$

where EI is the bending stiffness of the walls, and *H* is the height of the wall. Substituting Eq.(2.4) into Eq.(2.3), the ratio of the natural frequency between the model of A1070P and A5083P is reduced as follows considering the mass *m* and the height of walls *H* are identical between the models;

$$\frac{f_{A5083P}}{f_{A1070P}} = \sqrt{\frac{(EI)_{A5083P}}{(EI)_{A1070P}}} \tag{2.5}$$

The natural frequency and the damping ratio of each model are summarized in Table 2.7. The natural frequency of the A5083P model was calculated by using Eq.(2.5) in which the ratio of bending stiffness of 1.15 (see Table 2.2) is considered.

Table 2.7 The Natural frequency and the damping ratio

Designation	Natural frequency (Hz)	Damping ratio (%)	Ratio of bending stiffness
A5083P (Structure-A)	7.8*	—	1.15
A1070P (Structure-B1,B2)	7.3	0.54	1.00

* calculated by Eq.(2.5).

Considering that the two models were fixed in the same manner, it is reasonable to infer that the dissipation of energy due to vibration to the base, the air resistance against the model, and the friction in the molecular structure of aluminum are identical in two models. Consequently, it can be started that the damping ratios are identical between the structures of both designations.

In this study, the natural frequency and the damping ratio of the structures are regarded as what follows on the whole;

Natural frequency : $f = 7.5$Hz
Damping ratio : $h = 0.5\%$

2.5 PERFORMANCE OF EARTH PRESSURE TRANSDUCERS IN SATURATED SOIL

One of the key measurements in this study was made of the dynamic earth pressure in saturated soil by using “earth pressure transducers”. Although there were some meaningful achievements in the use of earth pressure transducers attached on the wall tightly (M.M. Dewoolkar et al.,2000), no reliable data was obtained from earth pressure transducers embedded in saturated soil (EP1 to EP 5 shown in Fig.2.6).

The performance of earth pressure transducers in saturated soil was examined by different series of shaking table tests in which only a uniform saturated soil deposit in a soil container was shaken in the vertical direction to exert the dynamic earth pressure in the saturated soil (see

Appendix A). In this test, the dynamic earth pressures were evaluated by two different procedures; i) measured directly by earth pressure transducers which were buried in the soil, ii) calculated by integrating the inertia forces of soil mass with respect to the depth in which the inertia forces were evaluated by the measured accelerations.

It was therein supposed that the dynamic earth pressures obtained from the accelerations was correct since the acceleration measurements were more reliable. Fig.2.20 shows the ratio of amplitude between those earth pressures. It is seen that the values of the ratio are almost 1.0 under a variety of conditions such as the intensity of input motion, the frequency of input motion, the relative density of soil, and the ratio of excess pore water pressures. It suggests that the earth pressure transducers give reasonable dynamic earth pressures when the transducer is buried in saturated soil.

The detail of the test and the analysis are shown in Appendix A at the end of this thesis.

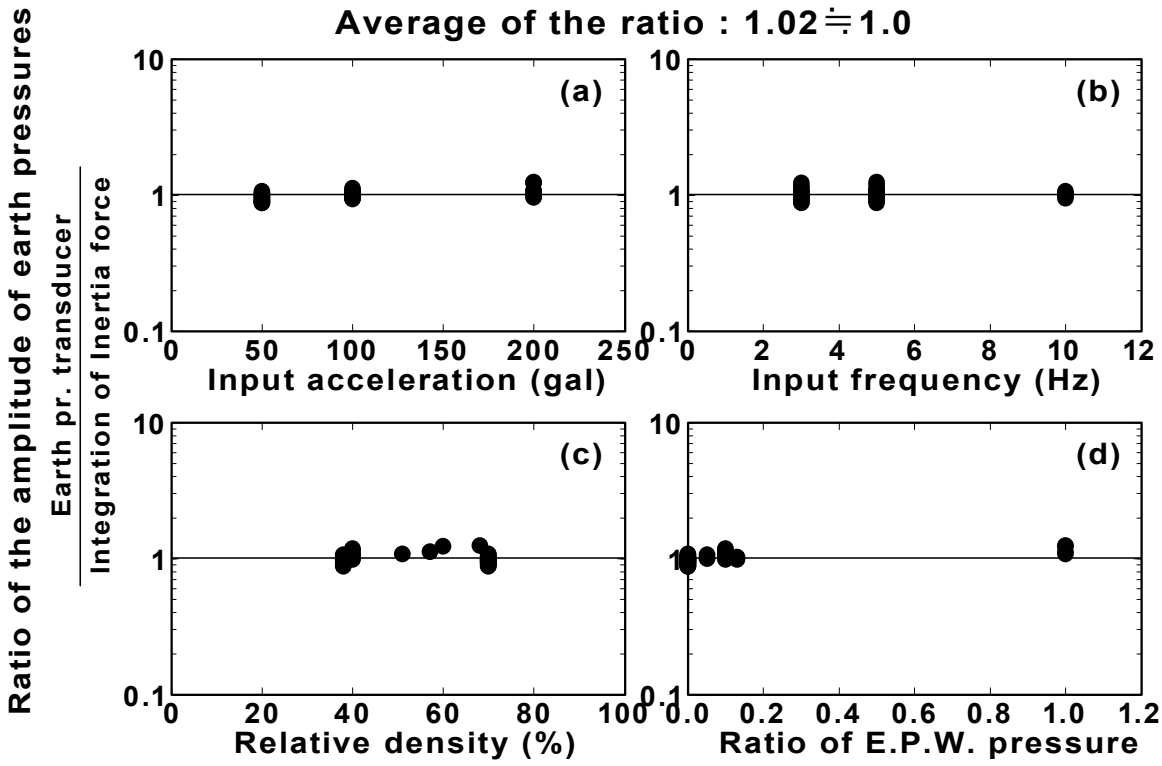

Fig.2.20: The results of calibration for the earth pressure transducers

2.6 TESTING PROCEDURE

2.6.1 Preparation of model

The shaking table model consists of a structure and backfill. The model was prepared by the following procedures.

Structure

The structure that consists of the base, the side walls and the top plate was assembled outside the container using screws. The earth pressure and pore pressure transducers as well as strain gauges were attached on the wall in advance. Waterproofing was made between the side walls after assembling the structure. The structure with transducers was brought into the container by an overhead traveling crane. The base of the structure was completely fixed on the bottom of the container by screws. The waterproofing was then made between the end of the side walls and the wall of the container (rubber membrane).

The base of the structure and the top plate were used repeatedly in other models as the behavior of the material was within the elastic manner in any shaking table tests.

Backfill

The backfill was made by pouring sand into deaired water in the container to achieve the initial relative density of 35%.

In a series of tests using Model-1(see Table 2.8), a model was shaken in several stages. Each stage of shaking was followed by a stationary period to allow for dissipation of developed excess pore water pressure as well as the measurement of settlement at the ground surface. The average relative density just before each test was calculated from the volume change due to settlement after shaking.

The tests using Model-2 and Model-3 were shaken only once after the backfill was made in a loose condition. In the test using Model-4 involving denser backfill, the model ground was subjected to a high frequency shaking (approximately 2.0 m/sec^2 acceleration at 30Hz frequency) until the required density was achieved.

2.6.2 Experimental program

Measurements before shaking

Four models in total were prepared for the tests. The initial bending strain and earth pressure generated from saturated, cohesionless soil backfills were measured for all models. The program of measurements before shaking is shown in Table 2.8. The Model-1 consists of the structure-A, which is made of A5083P aluminum plate, with the backfill of 35% relative density. The Model-2 consists of the structure-A with the backfill of 32% relative density in which the structure is the same as that used in Model-1. The Model-3 consists of the Structure-B1, which is made of A1070P aluminum plate, with backfill of 36% relative density. The Model-4 consists of Structure-B2 with backfill of 78% relative density, in which the initial relative density was 31%. Table 2.1 is referred to for material properties of the aluminum.

Table 2.8: Experimental programs for measurements before shaking (initial bending strain and earth pressure)

Case No.	Backfill	Structure		
	Relative density (%)	Structure No.	Designation	Thickness of wall (mm)
Model-1	35	Structure-A	A5083P	4.97
Model-2	32	Structure-A	A5083P	4.97
Model-3	36	Structure-B1	A1070P	4.87
Model-4	78 (31*)	Structure-B2	A1070P	4.87

*Initial relative density

Weak excitation test

Before shaking of each model, weak excitation test was conducted to determine the natural frequency of the soil-structure model. The testing program of weak excitation test is shown in Table 2.9. The test was conducted not only on the soil-structure model but also on the model of soil deposit without structure for comparison. The nominal amplitude of input acceleration was 0.05m/sec^2 and the frequency was changed in the range of 0.5Hz to 30Hz with the interval of frequency of 0.5Hz. The input motion is depicted in Fig.2.22.

Table 2.9: Experimental programs for weak excitation test

Case No	Freq. (Hz)	Acc. (m/sec^2)	Density of backfill (%)	Structure No.	Remarks
AD35	0.5～30	0.05	35	Structure-A	Model-1
AD32	0.5～30	0.05	32	Structure-A	Model-2
BD36	0.5～30	0.05	36	Structure-B1	Model-3
BD78	0.5～30	0.05	78	Structure-B2	Model-4
D34	0.5～30	0.05	34	—	Soil deposit
D69	0.5～30	0.05	69		
D90	0.5～30	0.05	90		

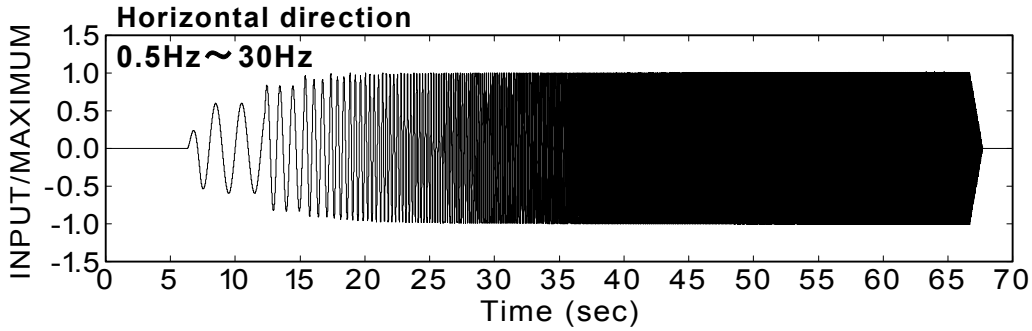

Fig.2.21: Input motion for weak excitation test (amplitude of acc.: $0.05m/sec^2$)

Strong excitation test (shaking table test)

The intensity of input motion and the density of backfill were changed in testing program. Two kinds of material for the wall of structure were used.

Input wave profile

In order to make clear the behavior of dynamic interaction between the flexible underground structure and liquefied soil, and for convenience of analysis of tests, a sinusoidal wave was used for the input motion. An example of input motion of 3Hz frequency is shown in Fig.2.22. In order to avoid a quick raise of excess pore water pressure, the input acceleration gradually increased to

the predetermined maximum value in ten cycles. Then the amplitude was maintained constant for ten cycles. Finally, the acceleration gradually decreased to zero in ten cycles. The number of cycles for constant amplitude was increased to twenty only in BD78F3A500 test to make shear strain of dense backfill large.

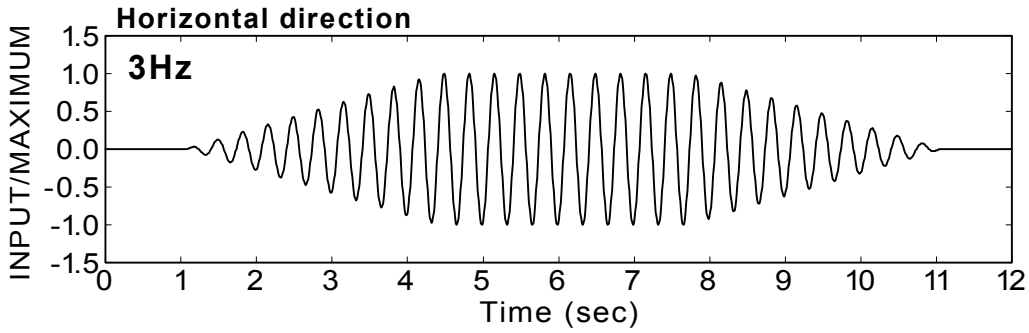

Fig.2.22: Input motion for strong excitation test (0.5m/sec^2, 2.0m/sec^2, 5.0m/sec^2)

Input acceleration

Analysis of test results has to be made not only during complete liquefaction but also in the process of pore water pressure generation. It is needed to obtain dynamic measurements from the process of pore water pressure generation in the backfill as clear as possible. In this respect, three levels of intensity of the input motion were employed. The state of the process of pore water pressure generation will continue longer in the smaller level of excitation. In contrast, the state of complete liquefaction will last long in an intense input motion. In the present study, the sinusoidal horizontal accelerations of 0.5m/sec^2, 2.0m/sec^2 and 5.0m/sec^2 were selected as the input shaking force.

Input frequency

As illustrated in Table 2.7, the natural frequency of the structure itself is about 7.5Hz. On the other hand, the initial natural frequency of backfill is approximately 20Hz in case of a loose backfill (see Fig.3.13, in Chapter 3). Since a shear type deformation only in the first order mode of the structure is focused on in this study, it was needed to give the soil-structure model a shear type deformation in the first order mode in shaking table tests. Therefore, input frequency of input motion should be lower than the natural frequency of both the liquefiable backfill and the structure. In this respect, the frequency of 3Hz was selected. The frequency of 5Hz was also selected for a variation.

Testing program

The testing program for the strong excitation test (shaking table test) is shown in Table 2.10. As stated before, the Model-1 was shaken in several stages, and The Model-2 and 3 were shaken only once. The Model-4 was subjected to high frequency shaking to achieve denser backfill of 78%, and then tested.

Table 2.10: Experimental programs for strong excitation test

Case No	Freq. (Hz)	Acc. (m/sec^2)	Backfill	Structure		Remarks
			Density (%)	No.	Thickness of wall (mm)	
AD35F3A50	3	0.5	35	Structure-A	4.97	A5083P (Moel-1)
AD39F5A50	5	0.5	39		4.97	
AD41F3A200	3	2.0	41		4.97	
AD61F3A200	3	2.0	61		4.97	
AD67F3A500	3	5.0	67		4.97	
AD32F3A500	3	5.0	32	Structure-A	4.97	A5083P (Model-2)
BD36F3A500	3	5.0	36	Structure-B1	4.87	A1070P (Model-3)
BD78F3A500	3	5.0	78	Structure-B2	4.87	A1070P (Model-4)

It should be noted that there are some limitations of this experimental program as is stated in Section 1.3. For instance, the soil-structure model is not for scaled model of a prototype underground structure. The configuration of the model is exaggerated in vertical direction to occur easily the deformation of structure for observations of dynamic interaction. In addition, frequency of input motion is not suitable in a view of similitude. Since only the effect of backfill at the side is focused on in the present study, test cases with the existence of soil on the top plate are not taken into account in the testing program.

Chapter 3

SHAKING TABLE MODEL TESTS

3.1 GENERAL REMARKS

A series of 1G shaking table tests is conducted on an aluminum structure model which is embedded in saturated cohesionless soil and fixed at the base. Such a variety of transducers as those for acceleration, displacement, pore pressure and earth pressure are installed. Earth pressure and bending strain attached on the flexible wall of the structure model are measured not only during shaking but also during preparation of model ground to obtain the initial values before shaking. The results of initial static measurements, weak excitation tests, and dynamic measurements are going to be presented in this chapter.

3.2 RESULTS OF STATIC MEASUREMENTS

3.2.1 Measurements for initial earth pressure and bending strain

Before shaking, bending strains are induced initially in the wall by lateral earth pressures. To investigate the initial values of earth pressure and bending strain, static measurements were conducted during preparation of the model ground.

Earth pressure transducers of EP6～EP10 and strain transducers attached on the left wall of SG1～SG7 were used in the static measurements. The location of used transducers is illustrated in Fig.3.1. The transducers were initialized before preparation of model ground. Then the earth pressures on the wall and bending strains on the left side wall were continuously measured until the preparation of backfill, which took several hours, was finished.

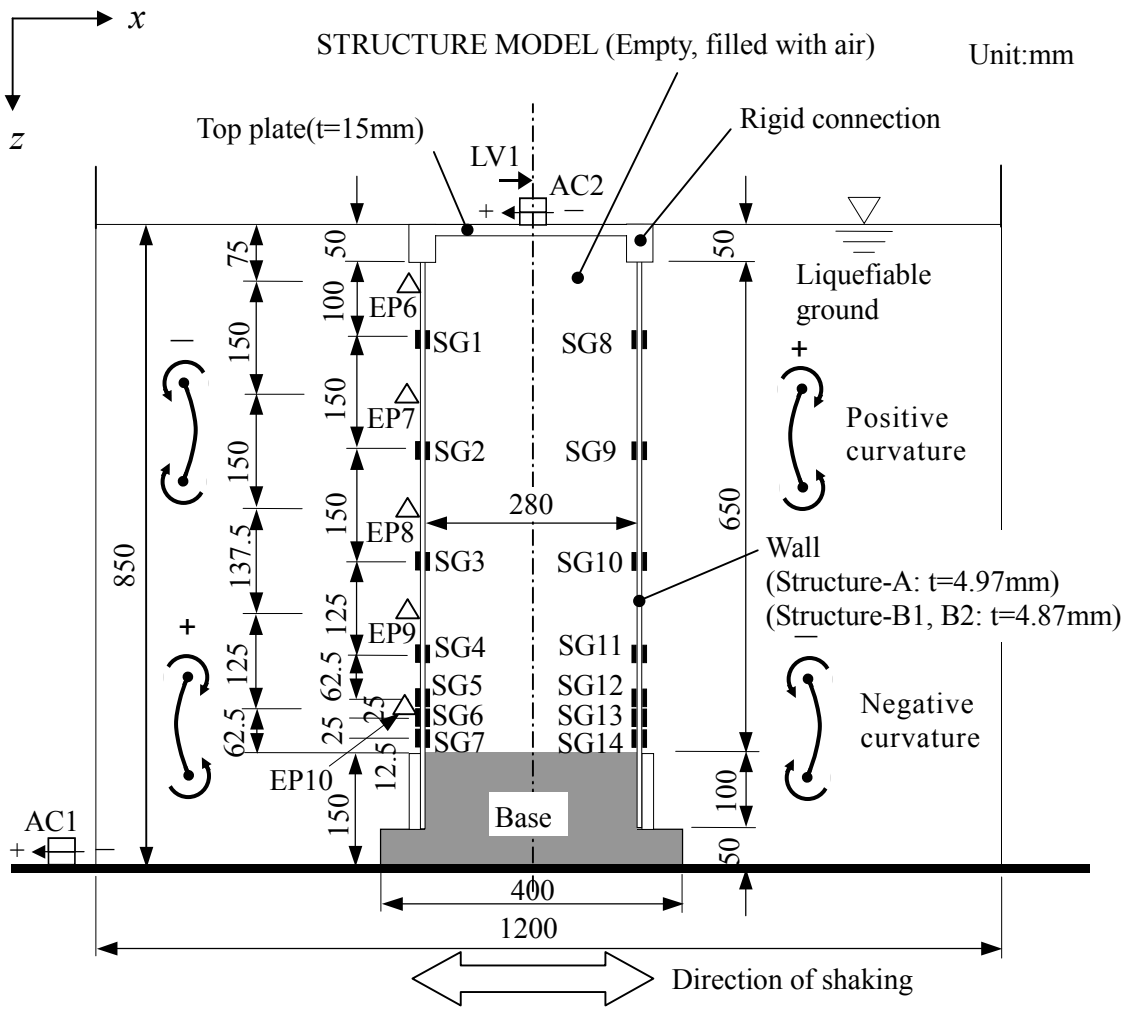

Fig.3.1: Location of earth pressure transducers and strain gauges used in static measurement (EP6～EP10, SG1～SG7)

The earth pressures and the bending strains of structure when the construction of Model-1 (relative density of 35%, Structure-A, see Table.2.8(a)) was achieved are shown in Table 3.1. In this series of tests, Compressive earth pressure is defined as positive. Note that the earth pressure shown in Table 3.1 contains static water pressure. The definition of sign of bending strain is illustrated in Fig.3.1. The distributions of measured values with respect to the depth are illustrated in Fig.3.2. The bending strains in the figure are translated to the curvature by dividing bending strain by the thickness of the wall (t=4.97mm, Structure-A).

It was seen that the earth pressure was increasing approximately proportional to the depth. The shape of the distribution of earth pressure became slightly depressed at the middle depth of the structure (GL-0.375m). The same feature was observed in the results of Model-2 and

Model-3 which will be shown later in Fig.3.4 and Fig.3.5. It was imagined that the depression of initial earth pressure was due to the static interaction between the wall and the backfill when the wall deformed slightly toward inside of the structure.

Table 3.1: Results of static measurements (Model-1, Dr=35%, Structure-A, Initial values for AD35F3A50 test)

Transducers	Location	Measured values	Remarks
EP6	GL-0.075m	0.771	
EP7	GL-0.225m	3.023	Unit:kPa
EP8	GL-0.375m	3.841	Compression
EP9	GL-0.513m	5.996	as positive
EP10	GL-0.638m	7.875	
SG1	GL-0.150m	180	
SG2	GL-0.300m	-406	
SG3	GL-0.450m	-500	
SG4	GL-0.575m	-41	Unit: μ
SG5	GL-0.6375m	448	
SG6	GL-0.6625m	695	
SG7	GL-0.6875m	915	

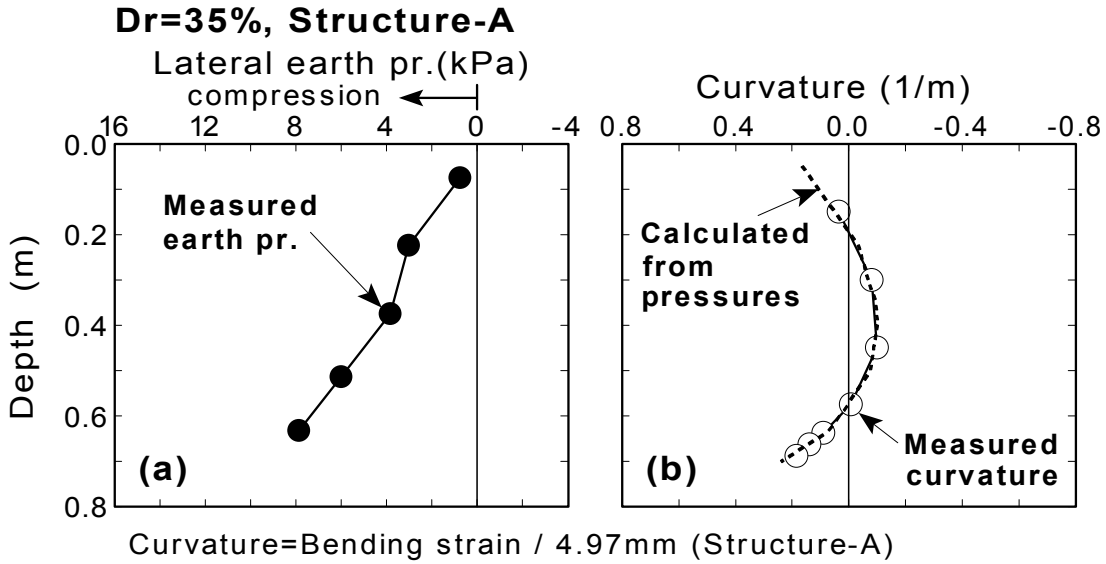

Fig.3.2: Distribution of initial values (Model-1, Dr=35%, Structure-A)

To make clear the internal consistency between the earth pressure and the curvature (the bending strain) of the wall, the calculation was conducted on an elastic beam. The model of the beam for the calculation is depicted in Fig.3.3. The curvature of the wall subjected to lateral earth pressure was calculated by dividing the bending moment of the beam by the bending stiffness *EI* of the wall. The bending moment of the wall was calculated by superposing the moments due to lateral earth pressure at each depth. Making the problem simple, lateral earth pressure is regarded as concentrated load.

Fig.3.3(a) illustrates the example of the superposition for bending moments due to three concentrated loads. The load P_i illustrated in Fig.3.3(b) is expressed as

$$P_i = p_i \cdot h_i \tag{3.1}$$

where p_i is the measured initial earth pressure at *i-th* earth pressure transducer from the surface, h_i is the length of *i-th* section. The height h_i and the distance a_i, b_i used in the calculation is summarized in Table 3.2. The height of a beam H was determined as H=0.65m for the calculation because a rigid part of 0.05m due to connection was located at the top of the wall.

The bending stiffness (EI) of elastic beam was specified as 765 Nm^2/m for Structure-A, and 664 Nm^2/m for Structure-B1 and B2 as shown in Table 2.2. The bending moments M_{1i} in the upper region and M_{2i} in the below region from the point, where a load P_i is applied, are calculated as

$$M_{1i} = P_i H \left(\frac{a_i}{H}\right)\left(\frac{b_i}{H}\right)^2 \left(\frac{3a_i + b_i}{a_i} \cdot \frac{z}{H} - 1\right) \qquad (0 \le z \le a_i) \tag{3.2}$$

$$M_{2i} = P_i H \left(\frac{a_i}{H}\right)^2 \left(\frac{b_i}{H}\right)\left(\frac{a_i + 3b_i}{b_i} \cdot \frac{H - z}{H} - 1\right) \qquad (a_i < z \le H) \tag{3.3}$$

And the bending moment at any depth z is derived by superposition of moment M_i due to a load P_i as

$$M = \sum_{i=1}^{n} M_i \tag{3.4}$$

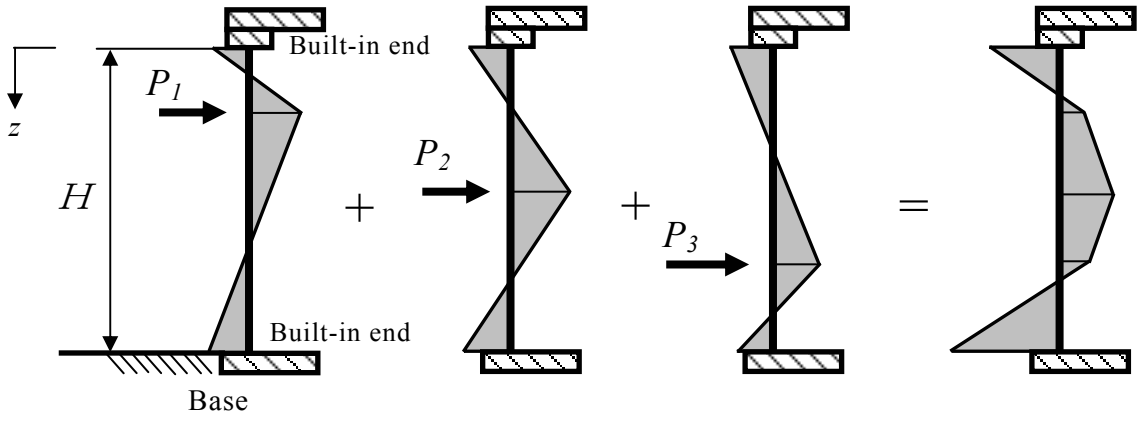

(a) Superposition of bending moments in an elastic beam

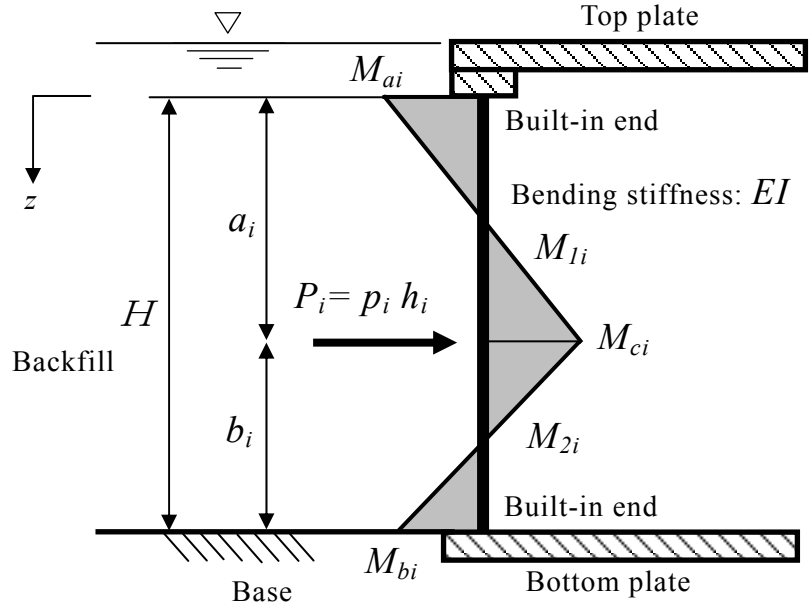

(b) Moment diagram by a load P_i

Fig.3.3: Model of wall of the structure for calculating initial curvature

Table 3.2: Height and length used for the calculation

i	Transducer	h_i (m)	a_i (m)	b_i (m)
1	EP6	0.100	0.050	0.600
2	EP7	0.150	0.175	0.475
3	EP8	0.150	0.325	0.325
4	EP9	0.125	0.463	0.187
5	EP10	0.125	0.588	0.062

$H = \Sigma\, h_i = 0.65$m

Consequently, the curvature ϕ is calculated by the following equation.

$$\phi = \frac{M}{EI} \tag{3.5}$$

Note that the behavior of the beam is in an elastic region.

The result of calculation of curvatures in Model-1 is illustrated by dashed line in Fig.3.2(b). As was seen, the calculated curvatures from the measured earth pressure agreed with the measured curvature very well. The measured initial values for Model-2 and its distributions with respect to a depth are presented in Table 3.3 and Fig.3.4, and for Model-3 Table 3.4 and Fig.3.5, respectively. The calculated curvatures from the measured earth pressures by Eq. (3.2) to Eq.(3.5) are also plotted in the figures. A good agreement between measured and calculated initial curvatures was observed in those tests. It suggests that the initial quantities measured on the wall such as lateral earth pressures and bending strains are internally consistent.

The result of static measurements of earth pressure and bending strain for Model-4 is shown in Table 3.5. The initial relative density of the backfill was 31%. After preparation, the backfill of the model was made dense by shaking and finally the relative density of 78% was attained. The earth pressure and the bending strain of the structure at each stage of the shaking will be presented in the following section.

Table 3.3: Results of static measurements (Model-2, Dr=32%, Structure-A, Initial values for AD32F3A500 test)

Transducers	Location	Measured values	Remarks
EP6	GL-0.075m	0.791	
EP7	GL-0.225m	3.042	Unit:kPa
EP8	GL-0.375m	3.838	Compression
EP9	GL-0.513m	5.994	as positive
EP10	GL-0.638m	7.868	
SG1	GL-0.150m	178	
SG2	GL-0.300m	-408	
SG3	GL-0.450m	-506	
SG4	GL-0.575m	-47	Unit: μ
SG5	GL-0.6375m	440	
SG6	GL-0.6625m	686	
SG7	GL-0.6875m	905	

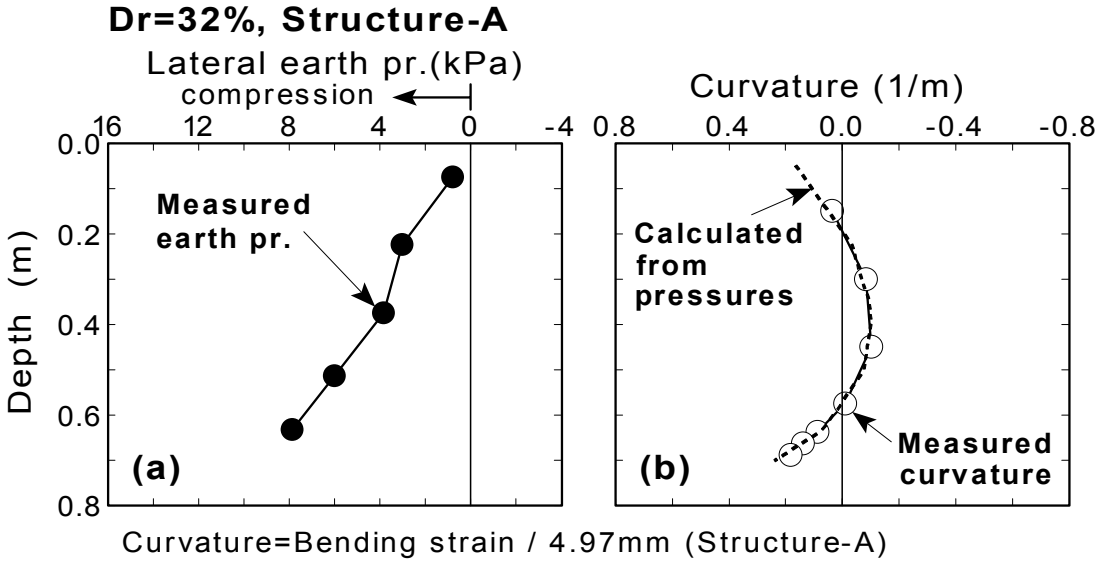

Fig.3.4: Distribution of initial values (Model-2, Dr=32%, Structure-A)

Table 3.4: Results of static measurements (Model-3, Dr=36%, Structure-B1, Initial values for BD36F3A500 test)

Transducers	Location	Measured values	Remarks
EP6	GL-0.075m	0.771	
EP7	GL-0.225m	3.190	Unit:kPa
EP8	GL-0.375m	4.414	Compression
EP9	GL-0.513m	6.575	as positive
EP10	GL-0.638m	8.016	
SG1	GL-0.150m	256	
SG2	GL-0.300m	-450	
SG3	GL-0.450m	-567	
SG4	GL-0.575m	-33	Unit: μ
SG5	GL-0.6375m	534	
SG6	GL-0.6625m	865	
SG7	GL-0.6875m	1251	

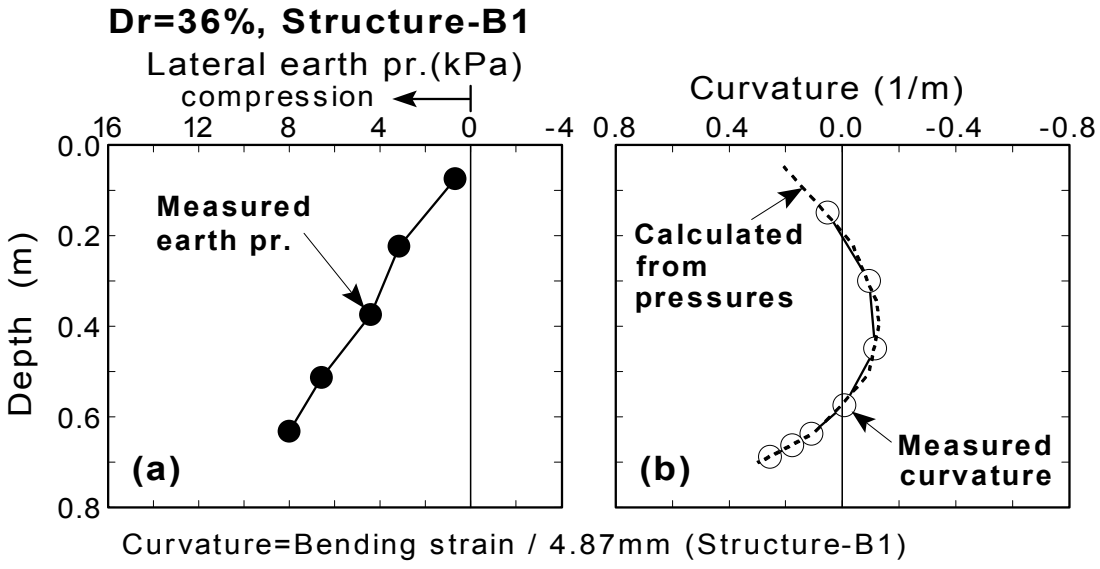

Fig.3.5: Distribution of initial values (Model-3, Dr=36%, Structure-B1)

Table 3.5: Results of static measurements (Model-4, Dr=31%, Structure-B2)

Transducers	Location	Measured values	Remarks
EP6	GL-0.075m	0.426	
EP7	GL-0.225m	1.599	Unit:kPa
EP8	GL-0.375m	2.805	Compression
EP9	GL-0.513m	4.188	as positive
EP10	GL-0.638m	5.136	
SG1	GL-0.150m	147	
SG2	GL-0.300m	-323	
SG3	GL-0.450m	-385	
SG4	GL-0.575m	2	Unit: μ
SG5	GL-0.6375m	405	
SG6	GL-0.6625m	347	
SG7	GL-0.6875m	866	

3.2.2 Initial earth pressure and bending strain at each stage of test

In a series of shaking table tests, the Model-1 and Model-4 were shaken more than 10 times after the loose backfill was prepared initially. The history of shaking for Model-1 and Model-4 is summarized in Table 3.6 and Table 3.7, respectively. Five tests were conducted in twelve stages of shaking in Model-1. Only one test was conducted after achieving the relative density of 78% in Model-4.

As is known very well, liquefaction due to seismic excitation causes a volume change of soil. Hence, a settlement of ground surface and change of density occur after liquefaction. Table 3.8 and Table 3.9 show the height of the ground surface and the measured settlement of ground after each stage of shaking. Settlements of 0.003m to 0.013m were observed after shaking depending on the intensity of input motion. Unit weights of backfill shown in the table were calculated considering the volumetric contraction.

After a stage of shaking, initial earth pressures on the structure and initial bending strains of wall could be changed due to liquefaction and reconsolidation. Then, initial values at the next stage were calculated referring to the residual values of the dynamic measurements at previous stage.

Table 3.6: History of shaking for Model-1 (Structure-A)

No.	Initial relative density (%)	Frequency (Hz)	Acceleration (m/sec^2)	Duration time (sec)	Relative density attained (%)	Remarks
1	35	3	0.5	10	39	AD35F3A50
2	39	5	0.5	6	41	AD39F5A50
3	41	3	2.0	10	46	AD41F3A200
4	46	5	2.0	6	50	
5	50	5	5.0	6	54	
6	54	3	5.0	10	59	
7*	59	5	0.5	6	59	Not liquefied
8	59	3	0.5	10	59	Not liquefied
9	59	5	2.0	6	61	
10	61	3	2.0	10	63	AD61F3A200
11	63	5	5.0	6	67	
12	67	3	5.0	10	72	AD67F3A500

*Soil added in the container to adjust the height of the surface to 0.85m

Table 3.7: History of shaking for Model-4 (Structure-B2)

No.	Initial relative density (%)	Frequency (Hz)	Acceleration (m/sec^2)	Duration time (sec)	Relative density attained (%)	Remarks
1	31	30	1.0	10	35	
2	35	30	1.0	30	38	
3	38	30	1.0	60	45	
4	45	30	1.0	60	48	
5	48	30	1.0	60	48	
6	48	30	2.0	60	51	
7	51	30	3.0	60	58	
8	58	30	3.0	60	65	
9	65	30	3.0	60	74	
10*	70	3	5.0	10	75	
11	75	3	5.0	10	78	
12	78	3	5.0	13	82	BD78F3A500

*Soil added in the container to adjust the height of the surface to 0.85m

Table 3.8: Height of the ground surface at each stage (Model-1)

No.	Initial relative density (%)	Initial average height (m)	Unit weight (kN/m^3)	Settlement (m)	Relative density attained (%)
1	35	0.848	18.67	0.005	39
2	39	0.843	18.73	0.004	41
3	41	0.839	18.76	0.007	46
4	46	0.832	18.85	0.006	50
5	50	0.826	18.91	0.006	54
6	54	0.820	18.98	0.008	59
7	59	0.856	19.07	0.000	59
8	59	0.856	19.07	0.000	59
9	59	0.856	19.07	0.003	61
10	61	0.853	19.11	0.002	63
11	63	0.851	19.14	0.005	67
12	67	0.846	19.22	0.005	72

Specific gravity of soil particle (S.G.)=2.677, e_{min}=0.635,e_{max}=0.972

Table 3.9: Height of the ground surface at each stage (Model-4)

No.	Initial relative density (%)	Average height (m)	Unit weight (kN/m^3)	Settlement (m)	Relative density attained (%)
1	31	0.851	18.48	0.006	35
2	35	0.845	18.54	0.006	38
3	38	0.839	18.59	0.010	45
4	45	0.829	18.70	0.005	48
5	48	0.824	18.75	0.000	48
6	48	0.824	18.75	0.004	51
7	51	0.820	18.79	0.010	58
8	58	0.810	18.91	0.011	65
9	65	0.799	19.03	0.013	74
10	70	0.854	19.11	0.007	75
11	75	0.847	19.20	0.005	78
12	78	0.842	19.25	0.008	82

Specific gravity of soil particle (S.G.)=2.653, e_{min}=0.642,e_{max}=0.966

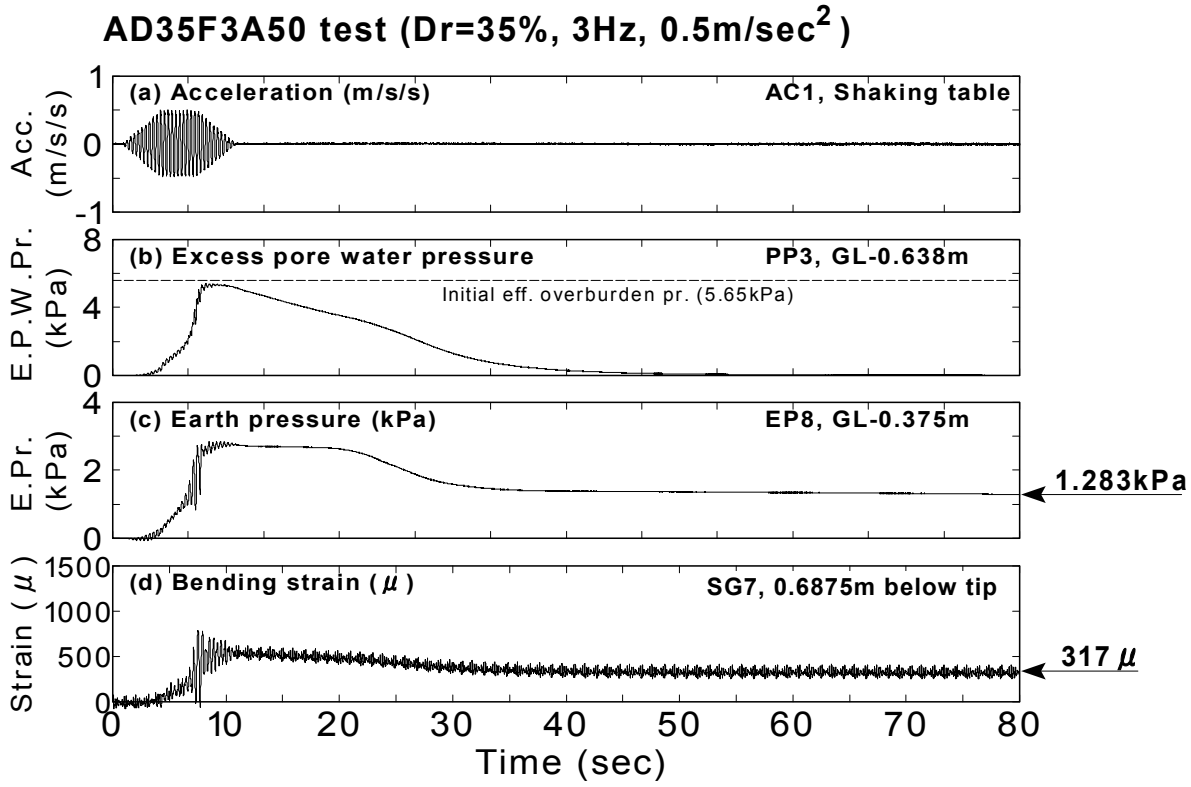

Fig.3.6: Examples of residual values of earth pressure and bending strain after dissipation of excess pore water pressure (Model-1, AD35F3A50 test, Δt=0.005sec)

The dynamic measurement at each stage of shaking was continued until the excess pore water pressure dissipated completely. Fig.3.6 illustrates the example of time histories for acceleration at shaking table (AC1), excess pore water pressure in the backfill (PP3, GL-0.638m), earth pressure on the wall (EP8, GL-0.375m), and bending strain of the wall (SG7, 0.6875m below tip) from the AD35F3A50 test.

It was seen that the excess pore water pressure built up to about the level of initial effective overburden pressure due to excitation, started to dissipate at about 12 second when the excitation ceased, and completely dissipated at 80 seconds. The lateral earth pressure and the bending strain were increasing accompanied by the excess pore water pressure, and gradually decreasing after excitation. The residual values for lateral earth pressure and the bending strain at 80 seconds were 1.283kPa and 317μ, respectively. Since the model was kept stationary during the period before next shaking, it was appropriate to assume that the residual values were kept constant until the next shaking. Hence, the initial values at the next stage was defined the sum of the initial values and the residual values at that stage.

Table 3.10: Example of accumulation of residual values

Stage	Initial values			Residual values after pore water pressure dissipation			Remarks
	Relative density (%)	EP8 (kPa)	SG7 (μ)	Density attained (%)	Δ EP8 (kPa)	Δ SG7 (μ)	
0	—	0	0	35	3.841	915	Preparation of a model
1	35	3.841	915	39	1.283	317	Input acc.=0.5m/sec^2
2	39	5.124	1232	41	—	—	Input acc.=0.5m/sec^2

Table 3.10 shows the example of calculation of residual values at transducer EP8 and SG7. Stage-0 in the table means the preparation of the model backfill. Since neither water nor soil existed in the container when the transducers were initiated, the initial values at stage-0 were zero. The residual values of stage-0 shown in the table are the result of the static measurement during the preparation of backfill. It becomes the initial values of Stage-1. The sum of the initial value and the residual value became the initial values of the next stage. Then, the sum of the initial values and the residual values at stage-1, indicated in Fig.3.6, became the initial values of stage-2. The same procedure was repeated for following stages.

The time histories for lateral earth pressures (EP6～EP10), bending strains (SG1～SG14) and excess pore water pressures on the wall (PP4～PP8) at all stages of shaking (see Table 3.6 and Table 3.7) are presented in Fig.3.35～Fig.3.60 at the end of this chapter. Those residual values as well as the initial values of all earth pressures and bending strains are shown in Table 3.18～Table 3.23 following the figures.

The initial values derived for shaking table tests are summarized in Table 3.11～Table 3.15. Since the bending strains by the transducer SG3 were not obtained correctly in the test using Model-1, residual values of the bending strain on the opposite wall of SG10 were used in place of SG3 by correcting the sign.

The maximum value of initial bending strain through the tests was 2455 μ at the BD78 F3A500 test as shown in Table 3.15. The bending strain of 2455 μ corresponds to the tensile strain of 1228 μ. The yield strain of the material (A1070P) was approximately 1600 μ ～ 2200 μ according to the tensile test (See Fig.2.11). This indicated that the initial wall behavior was in the elastic manner in all the tests. Therefore, the elastic beam was assumed

when the curvatures were calculated from the initial lateral earth pressures.

The distribution of lateral earth pressure and bending strain before shaking with respect to the depth are illustrated in Fig.3.7～Fig.3.11. The calculated curvatures from earth pressures are drawn by dashed line in the figures as well.

Table 3.11: Initial values of earth pressure and bending strain (Model-1, Dr=39%, Structure-A, Initial values for AD39F5A50 test)

Transducers	Location	Initial values (Accumulated values)	Remarks
EP6	GL-0.075m	0.480	
EP7	GL-0.225m	3.495	Unit: kPa
EP8	GL-0.375m	5.124	Compression
EP9	GL-0.513m	9.399	as positive
EP10	GL-0.638m	9.746	
SG1	GL-0.150m	266	Unit: μ
SG2	GL-0.300m	-552	
SG3	GL-0.450m	(-666)	SG10
SG4	GL-0.575m	-69	
SG5	GL-0.6375m	640	
SG6	GL-0.6625m	947	
SG7	GL-0.6875m	1232	

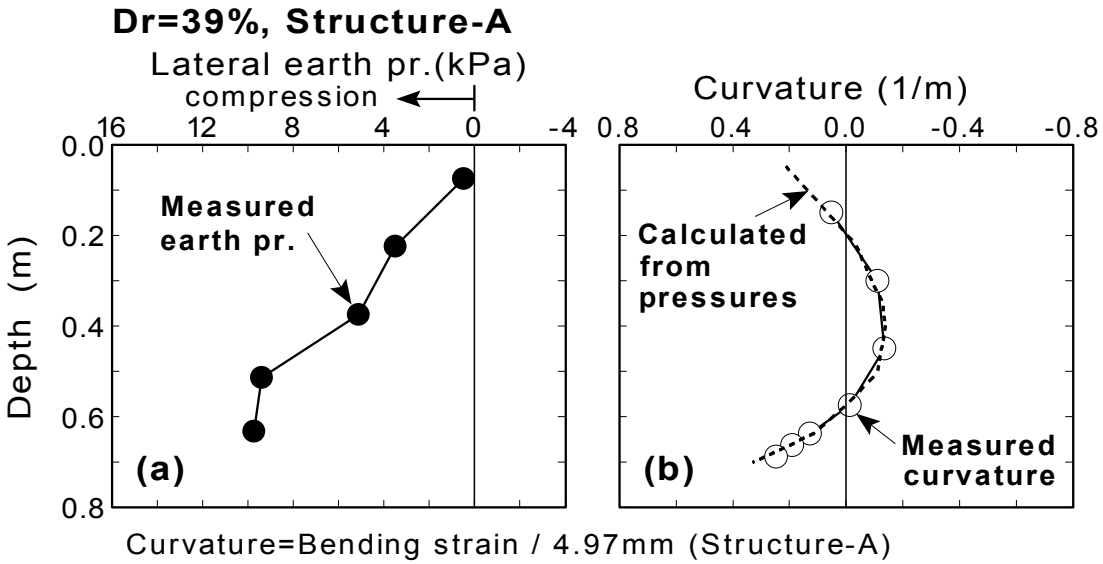

Fig.3.7: Distribution of accumulated initial values (Model-1, Dr=39%, Structure-A, AD39F5A50 test)

Table 3.12: Initial values of earth pressure and bending strain (Model-1, Dr=41%, Structure-A, Initial values for AD41F3A200 test)

Transducers	Location	Initial values (Accumulated values)	Remarks
EP6	GL-0.075m	0.487	
EP7	GL-0.225m	3.957	Unit: kPa
EP8	GL-0.375m	6.528	Compression
EP9	GL-0.513m	12.377	as positive
EP10	GL-0.638m	9.513	
SG1	GL-0.150m	261	Unit: μ
SG2	GL-0.300m	-578	
SG3	GL-0.450m	(-700)	(SG10)
SG4	GL-0.575m	-79	
SG5	GL-0.6375m	686	
SG6	GL-0.6625m	1029	
SG7	GL-0.6875m	1326	

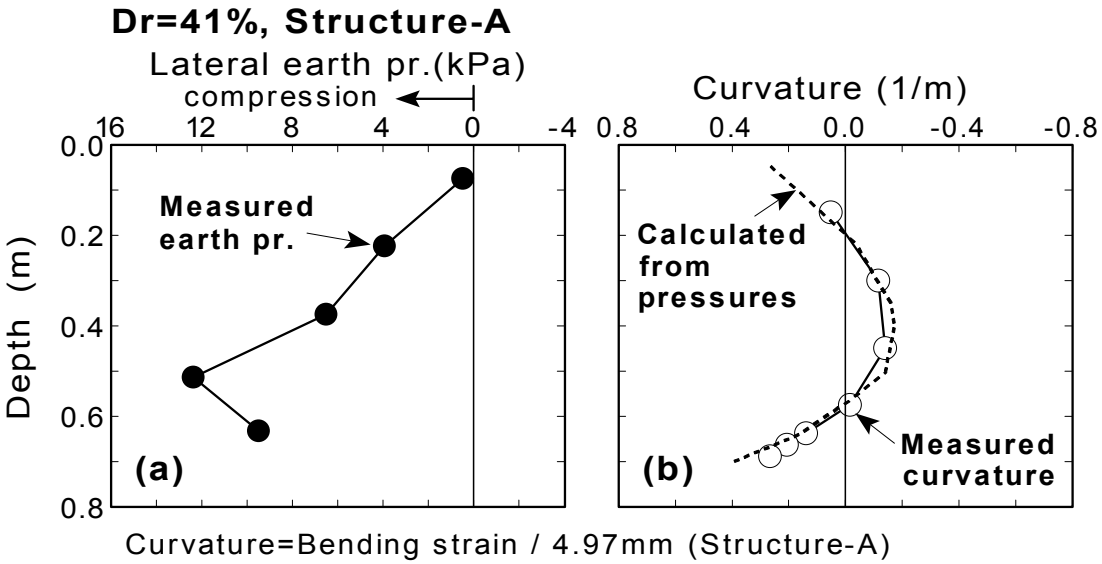

Fig.3.8: Distribution of accumulated initial values (Model-1, Dr=41%, Structure-A , AD41F3A200 test)

Table 3.13: Initial values of earth pressure and bending strain (Model-1, Dr=61%, Structure-A, Initial values for AD61F3A200 test)

Transducers	Location	Initial values (Accumulated values)	Remarks
EP6	GL-0.075m	0.203	
EP7	GL-0.225m	6.229	Unit:kPa
EP8	GL-0.375m	10.198	Compression
EP9	GL-0.513m	13.201	as positive
EP10	GL-0.638m	11.320	
SG1	GL-0.150m	349	Unit: μ
SG2	GL-0.300m	-787	
SG3	GL-0.450m	(-883)	(SG10)
SG4	GL-0.575m	-105	
SG5	GL-0.6375m	859	
SG6	GL-0.6625m	1267	
SG7	GL-0.6875m	1662	

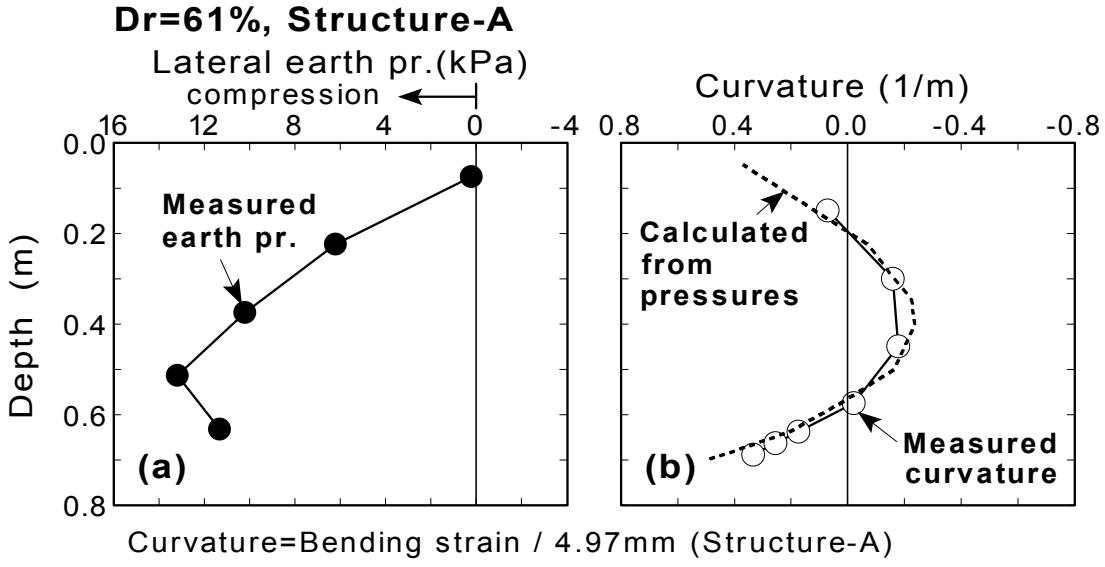

Fig.3.9: Distribution of accumulated initial values (Model-1, Dr=61%, Structure-A, AD61F3A200 test)

Table 3.14: Initial values of earth pressure and bending strain (Model-1, Dr=67%, Structure-A, Initial values for AD67F3A500 test)

Transducers	Location	Initial values (Accumulated values)	Remarks
EP6	GL-0.075m	0.075	
EP7	GL-0.225m	6.262	Unit:kPa
EP8	GL-0.375m	9.516	Compression
EP9	GL-0.513m	13.175	as positive
EP10	GL-0.638m	11.473	
SG1	GL-0.150m	326	Unit: μ
SG2	GL-0.300m	-794	
SG3	GL-0.450m	(-896)	SG10
SG4	GL-0.575m	-102	
SG5	GL-0.6375m	840	
SG6	GL-0.6625m	1310	
SG7	GL-0.6875m	1710	

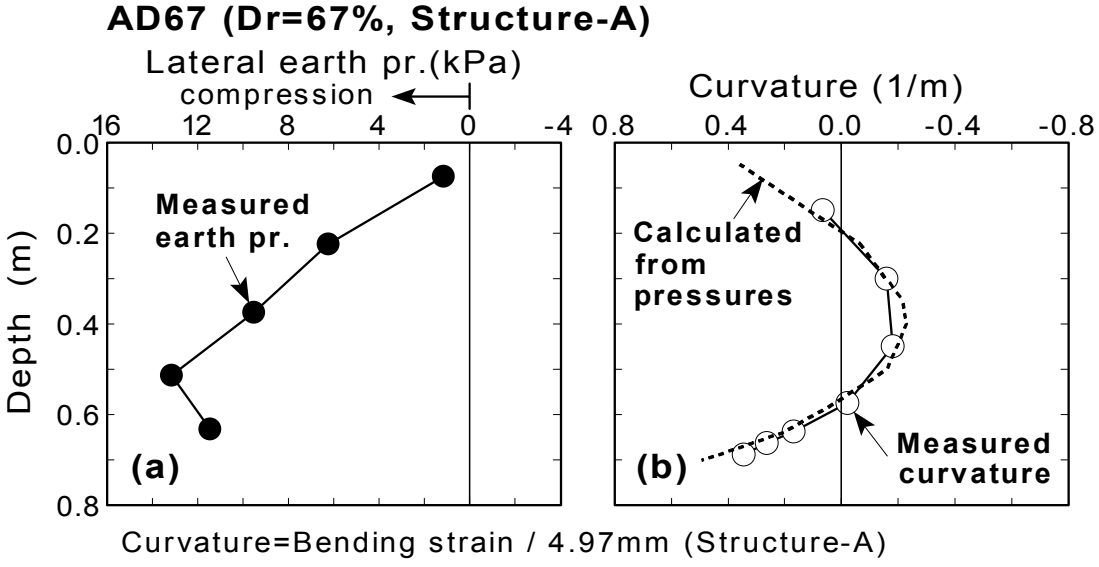

Fig.3.10: Distribution of accumulated initial values (Model-1, Dr=67%, Structure-A, AD67F3A500 test)

Table 3.15: Initial values of earth pressure and bending strain (Model-4, Dr=78%, Structure-B2, Initial values for BD78F3A500 test)

Transducers	Location	Initial values (Accumulated values)	Remarks
EP6	GL-0.075m	-	
EP7	GL-0.225m	3.739	Unit:kPa
EP8	GL-0.375m	8.704	Compression
EP9	GL-0.513m	11.204	as positive
EP10	GL-0.638m	10.806	
SG1	GL-0.150m	21	
SG2	GL-0.300m	-859	
SG3	GL-0.450m	-949	
SG4	GL-0.575m	-73	Unit: μ
SG5	GL-0.6375m	828	
SG6	GL-0.6625m	1188	
SG7	GL-0.6875m	2455	

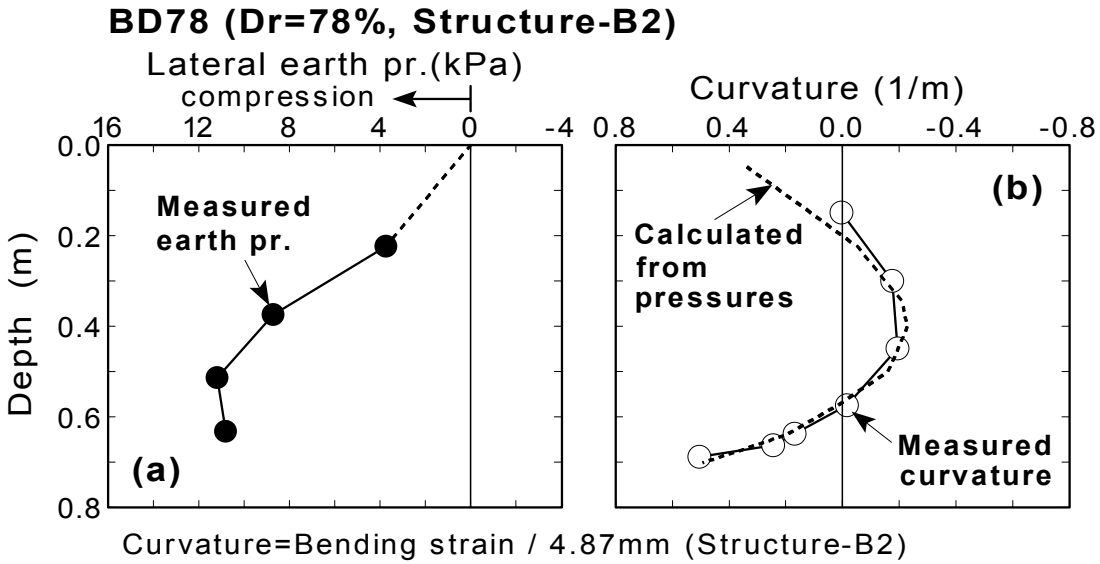

Fig.3.11: Distribution of accumulated initial values (Model-4, Dr=78%, Structure-B2, BD78F3A500 test)

It was observed that the lateral earth pressure increased in proportion to the depth, and the earth pressure at the second station from the bottom (GL-0.513m) grew more than the earth pressure at the bottom (GL-0.638m). Considering the fact that the calculated curvature at the bottom from earth pressures was slightly larger than the measured curvature, observed large earth pressure at GL-0.513m could be a local phenomenon around the earth pressure transducer. In any case, the calculated curvatures showed fairly good agreements with the measured curvatures. It suggested that the initial quantities measured on the wall such as lateral earth pressures and bending strains were internally consistent at each stage of shaking.

3.3 WEAK EXCITATION TESTS

Weak excitation tests were conducted to examine the initial natural frequency of the soil-structure model. For a comparison with the soil-structure model, the models without structure were also tested. The amplitude of input acceleration was selected as 0.05m/sec^2 not to make the backfill liquefy.

The time histories for acceleration at the shaking table (AC1) and at the top of the structure (AC2) from the AD35 test (Dr=35%、Structure-A) are illustrated in Fig.3.12(a). Fig.3.1 is referred for the location of those transducers. It was seen that the amplitude of acceleration on the shaking table (AC1) became about 0.03m/sec^2 which was smaller than the nominal amplitude of 0.05m/sec^2 at a period of 50sec～55sec. This was due to the performance of the shaking table, because the input acceleration of 0.05m/sec^2 was lower than the lower limit of acceleration control (0.1 m/sec^2; see Fig.2.1). However, no significant effects of such a slight change of input magnitude on the frequency domain was observed in the resonance curve shown in Fig.3.12(b). Therefore, all models were shaken in the same manner with amplitude of 0.05m/sec^2. It was seen in the resonance curve that the amplification became maximum of 4.0 at the frequency of 19.5Hz, and the phase difference coincided with –90 degrees at the frequency. The natural frequency of the model AD35 was regarded as 19.5Hz in this test.

The time histories of acceleration and resonance curve for all tests (AD32, BD36, BD78, D34, D69, D90) are presented in Fig.3.61～Fig.3.66 at the end of this chapter. The experimental program of Table 2.8(b) is referred to for the condition of test cases.

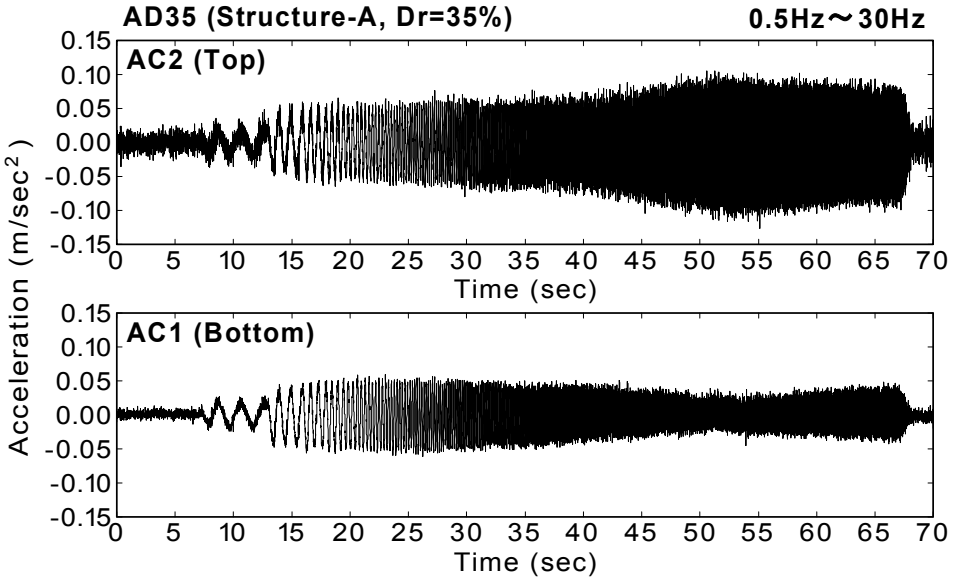

(a) Time histories of acceleration

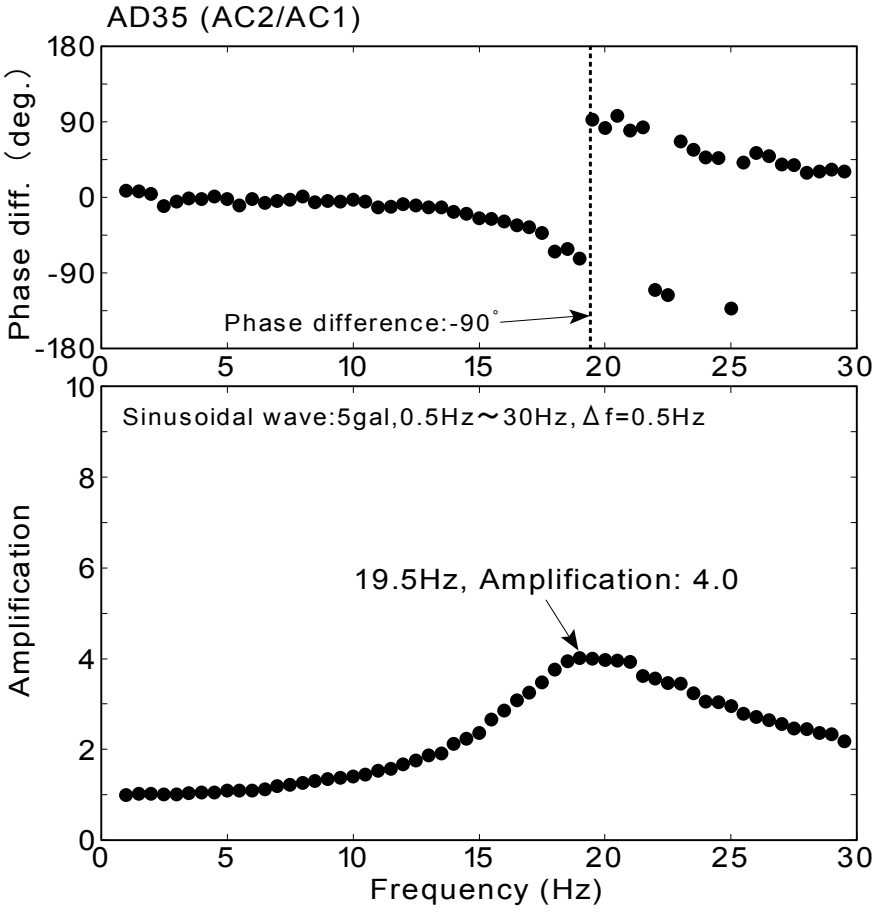

(b) Resonance curve

Fig.3.12: Result of sweep test (AD35)

Table 3.16: Summary of test results

Case No	Backfill	Structure		Natural frequency (Hz)	Amplification
	Density (%)	Designation	Natural freq. (Hz)		
AD35	35	A5083P	7.8	19.5	4.0
AD32	32	A5083P	7.8	19.5	4.4
BD36	36	A1070P	7.3	18.5	5.0
BD78	78	A1070P	7.3	21.5	7.9
D34	34	—	—	19.5	6.2
D69	69			22.0	7.4
D90	90			23.5	15.7

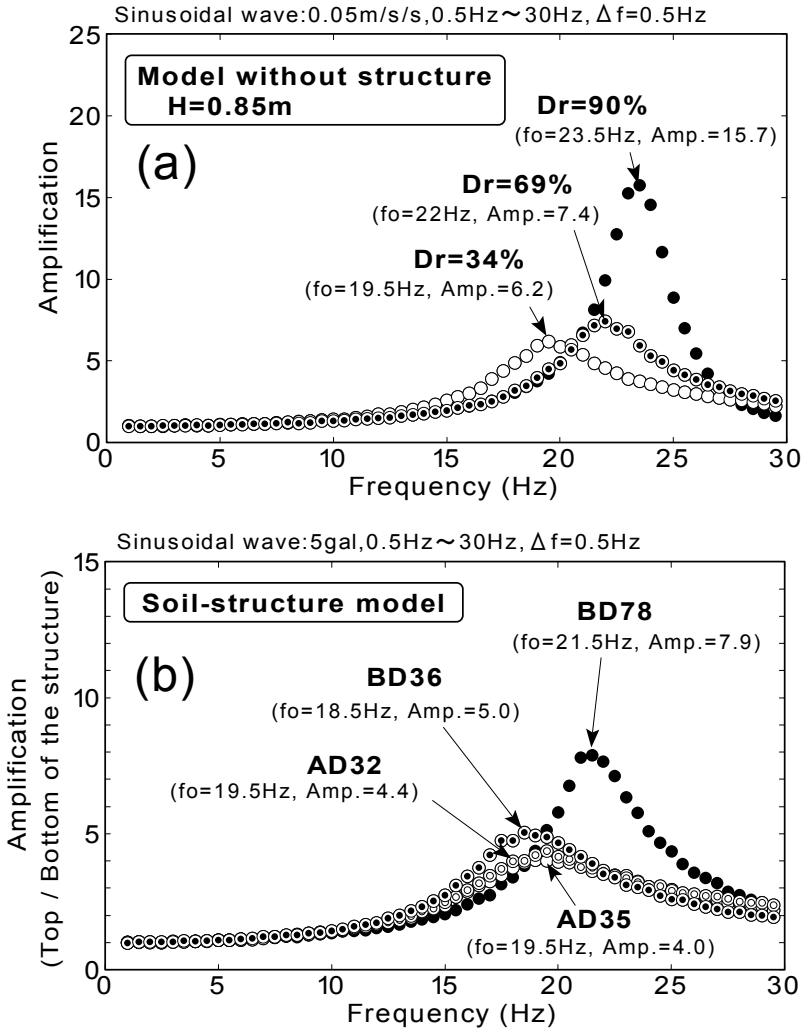

Fig.3.13: Resonance curves for the model

The natural frequencies and amplifications at each test are summarized in Table 3.16. All resonance curves for the soil-structure model, and the model without structure are depicted in Fig.3.13(a) and (b), respectively.

It was observed that the natural frequency of soil deposit became high and the amplification at the resonance went up as the backfill was denser. The almost same feature was observed at the resonance curve for the soil-structure model as shown in Fig.3.13(b). Note that no resonance was seen at the natural frequency for the structure itself of about 7.5 Hz. It suggested that the natural frequency of backfill was more dominant than the natural frequency of structure itself in this type of underground structure.

3.4 RESULTS OF DYNAMIC MEASUREMENTS

The results of dynamic measurements of the model during shaking are going to be presented. The initial height of the ground surface and the unit weight of the backfill at each test are summarized in Table 3.17. Time histories of earth pressure, and bending strain/curvature in this section are including the initial values which were calculated in the previous section. The initial values for pore water pressure were calculated by multiplying unit weight of water (assumed as 9.8kN/m^3) by each depth of pore water transducer. The locations of transducers for pore water pressure, acceleration, displacement, and earth pressure are shown in Fig.3.14. In addition, Fig.3.1 is referred for locations of strain transducers.

Table 3.17: Height of the ground surface and unit weight of soil at each test

No.	Initial relative density (%)	Initial height (m)	Unit weight (kN/m^3)	Settlement (m)	Soil property
AD35F3A50	35	0.848	18.67	0.005	Toyoura sand S.G.=2.677, e_{min}=0.635, e_{max}=0.972
AD39F5A50	39	0.843	18.73	0.004	
AD41F3A200	41	0.839	18.76	0.007	
AD61F3A200	61	0.853	19.11	0.002	
AD67F3A500	67	0.846	19.22	0.005	
AD32F3A500	32	0.850	18.50	0.016	Toyoura sand S.G.=2.653, e_{min}=0.642, e_{max}=0.966
BD36F3A500	36	0.847	18.56	0.018	
BD78F3A500	78	0.842	19.25	0.008	

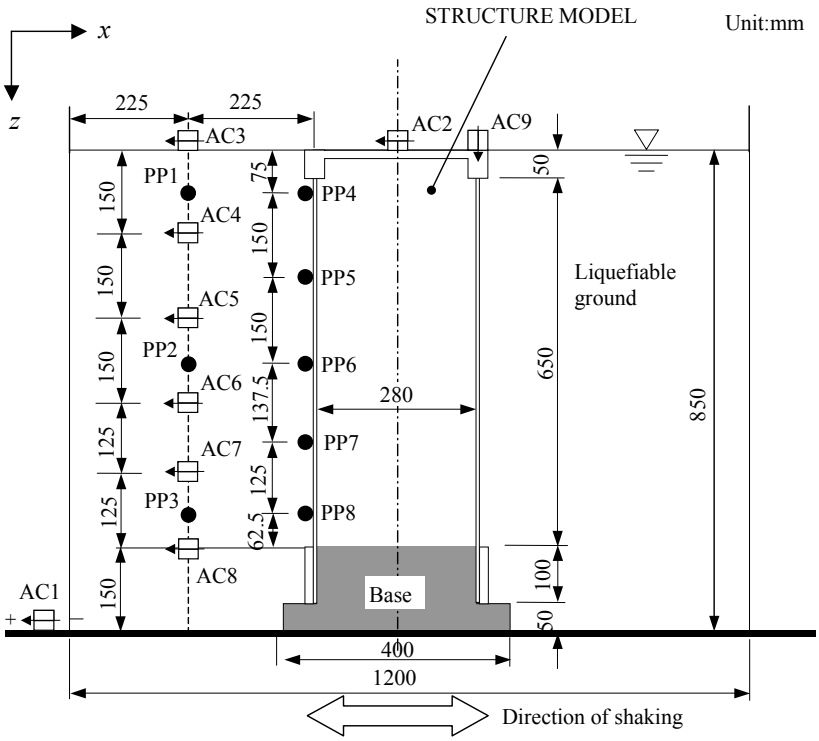

(a) Pore pressure and acceleration transducers (PP1～PP8, AC1～AC9)

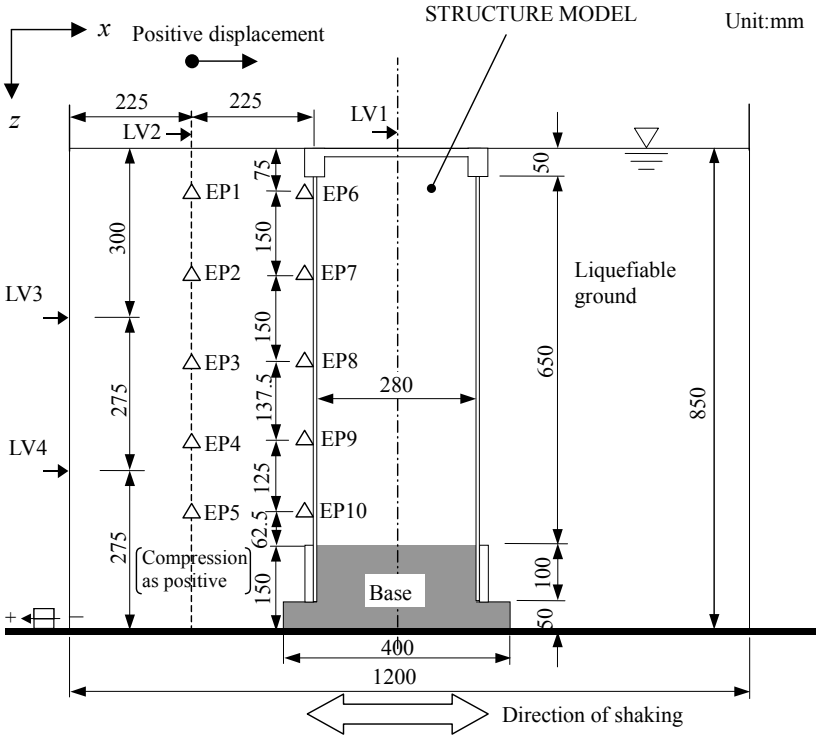

(b) Earth pressure and displacement transducers (EP1～EP10, LV1～LV4)

Fig.3.14: Location of transducers used in dynamic measurements

3.4.1 Typical measurements (Dr=35%, 0.5m/sec^2, Structure-A)

A typical behavior of the backfill and the structure during excitation is presented selecting the dynamic measurements from AD35F3A50 test. Structure-A, in which the material of wall was aluminum alloy with the tensile strength of 146MPa, was used with backfill of 35% relative density. The model was shaken horizontally by the peak acceleration of 0.5 m/sec^2.

Pore water pressure

The time histories of pore pressure are illustrated in Fig.3.15. The transducers of PP1～PP3 were located in the backfill and PP4～PP8 were attached on the wall of the structure. As mentioned at the head of this section, the static water pressures at each level of transducer were added to the measured excess pore water pressures. The horizontal portion of each time history indicates the static pressure before shaking. Therefore, the pore water pressure becomes equal to the initial total overburden pressure when the backfill liquefies completely.

It was seen that the pore water pressures built up due to shaking and reached the initial total overburden pressure at around 8 seconds indicating that the backfill liquefied due to this intensity of shaking. It is not clear why only the pore pressure PP4 at 0.075m below the upper tip of the structure did not reach the initial total overburden pressure in spite of liquefaction in most part of the backfill. The oscillation of the pore pressure PP4 seems to be once in a cycle after 8 seconds. It was imagined that the longitudinal wave was produced by means of the dynamic interaction with the structure, and propagated into the liquefied backfill.

Acceleration

The time histories of acceleration are shown in Fig.3.16. The time history of acceleration on the shaking table AC1 consisted of thirty sinusoidal waves as shown at the bottom of figures.

In the response accelerations at the top of the structure AC2, the intensity of motion at around 7.5 to 8.0 seconds was larger than the rest of time. Referring to the time histories of pore water pressure as shown in Fig.3.15, it was seen that this time period was just before the complete liquefaction of the backfill. The amplification of acceleration between 7.5 to 8.0 seconds was not seen at the deep portion of the backfill.

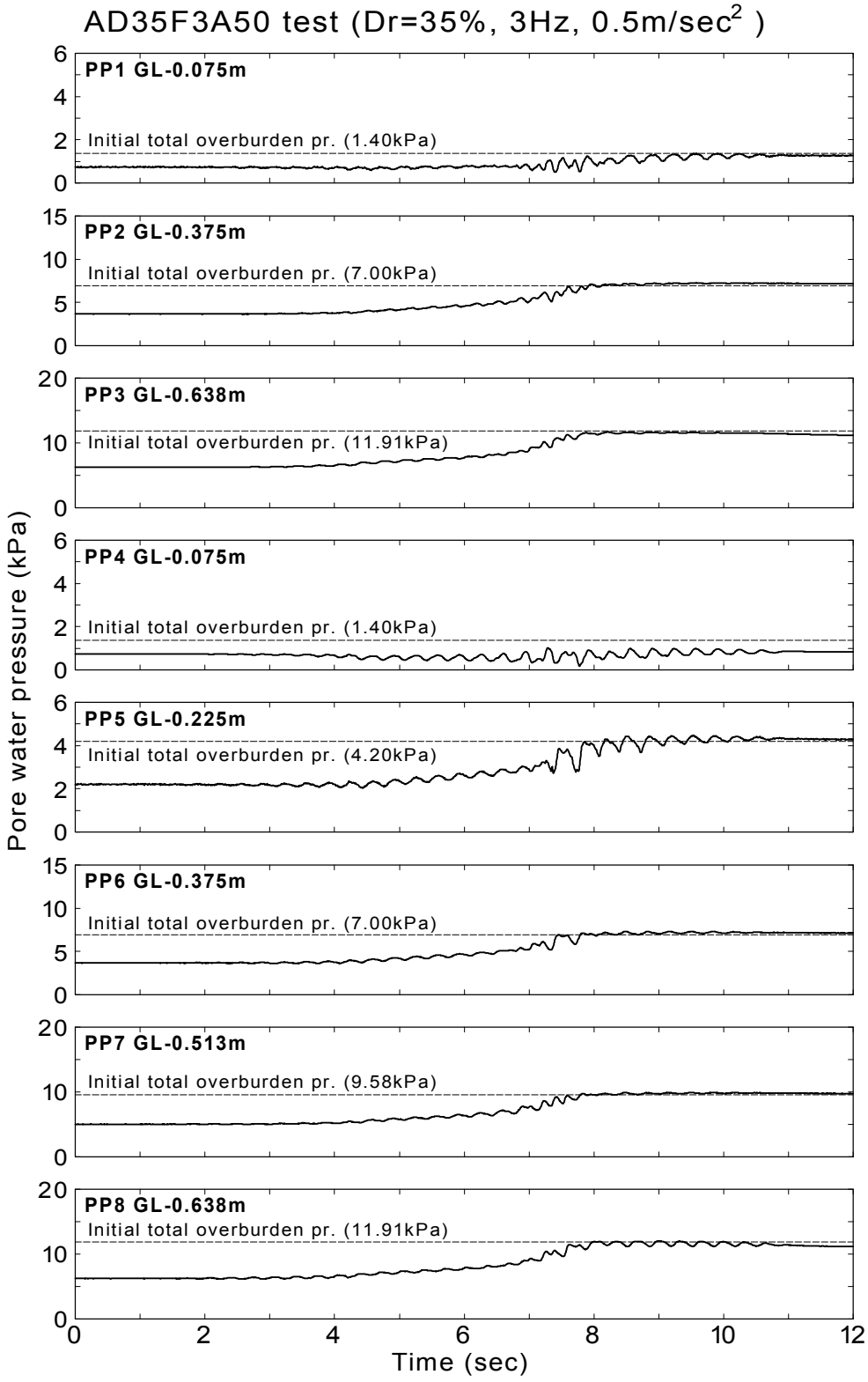

Fig.3.15: Time histories of pore water pressure for AD35F3A50 test

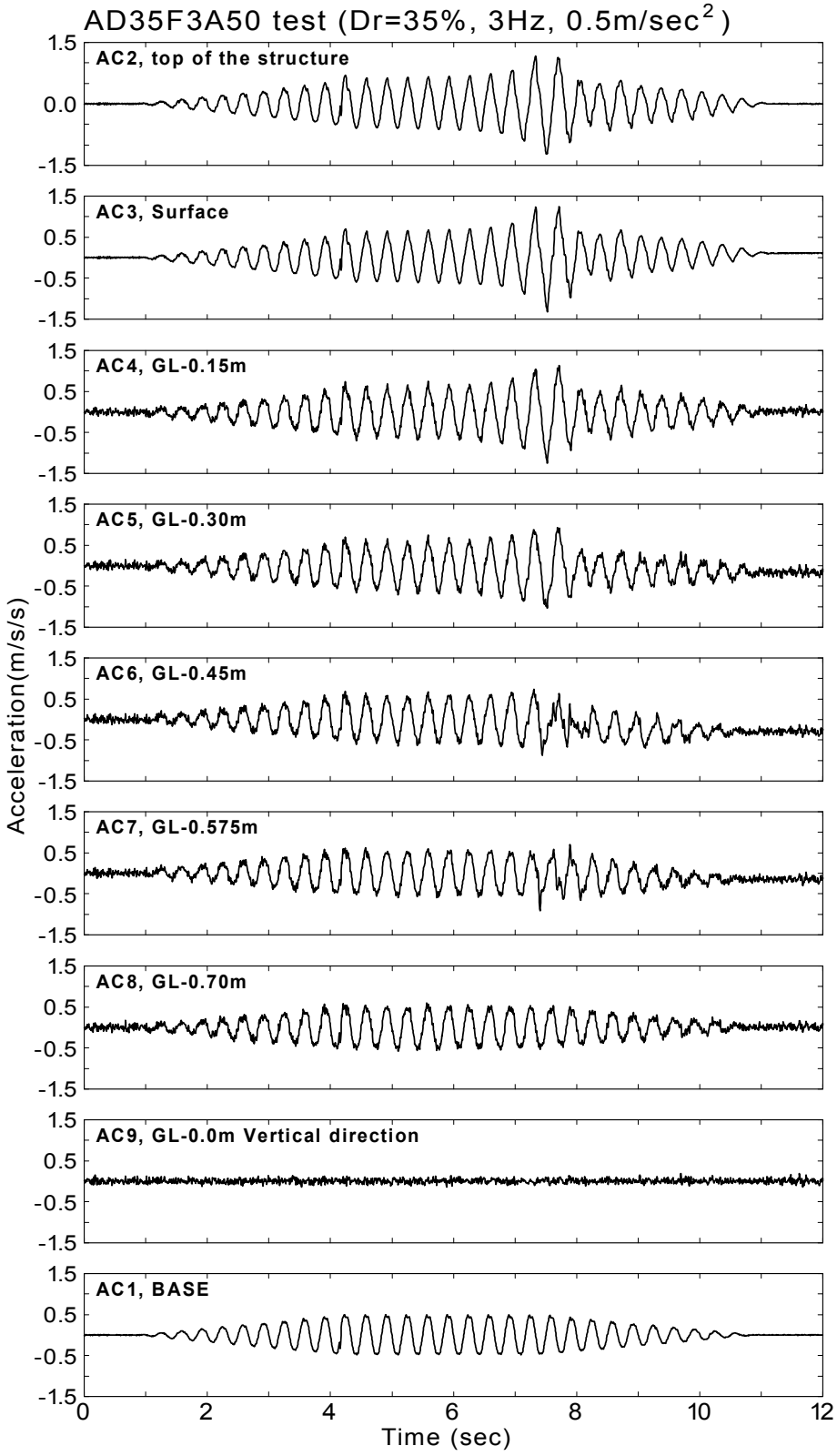

Fig.3.16: Time histories of acceleration for AD35F3A50 test

The shape of time history of acceleration at the surface of the backfill AC3 was very similar to that of AC2. The amplitude of acceleration AC3 did not reduce after the complete liquefaction of backfill whose behavior is probably similar to that of liquid. The amplitude of vertical acceleration AC9 at the top of the structure was much smaller than that of any horizontal acceleration. It shows that the horizontal response was dominant in this shaking table model tests.

Earth pressure

The time histories of lateral earth pressures during shaking are presented in Fig.3.17. The earth pressures in the backfill for EP1～EP5 are illustrated by dashed lines as a comparison with the earth pressure on the wall. The measured initial earth pressures for EP6～EP10 shown in Table 3.1 were already added on the monitored time histories both on the wall and in the backfill.

It was observed that the lateral earth pressures continued to increase during shaking accompanied by the build-up of pore water pressure (see Fig.3.15). Theoretically, the lateral earth pressure in a horizontal soil deposit becomes equal to the initial total overburden pressure when the soil liquefies completely. In the experiment, the earth pressures at GL-0.513m and GL-0.638m reached the initial total overburden pressure and the others were less or more than the initial total over burden pressure when the backfill liquefied at about 8.0 seconds.

It is seen that the earth pressures oscillates more or less as shaking goes on. Significant oscillations are observed at 7 to 8 seconds in earth pressures on the wall of EP6～EP8. In contrast with this, the amplitude of earth pressure in the soil, especially EP2, seems smaller than that of earth pressure on the wall from 7 to 8 seconds. As was shown in Fig.3.16, the acceleration of the structure was significantly amplified also at this time period of 7 to 8 seconds. It is inferred that the amplitude of earth pressures on the wall are affected by the acceleration of the structure.

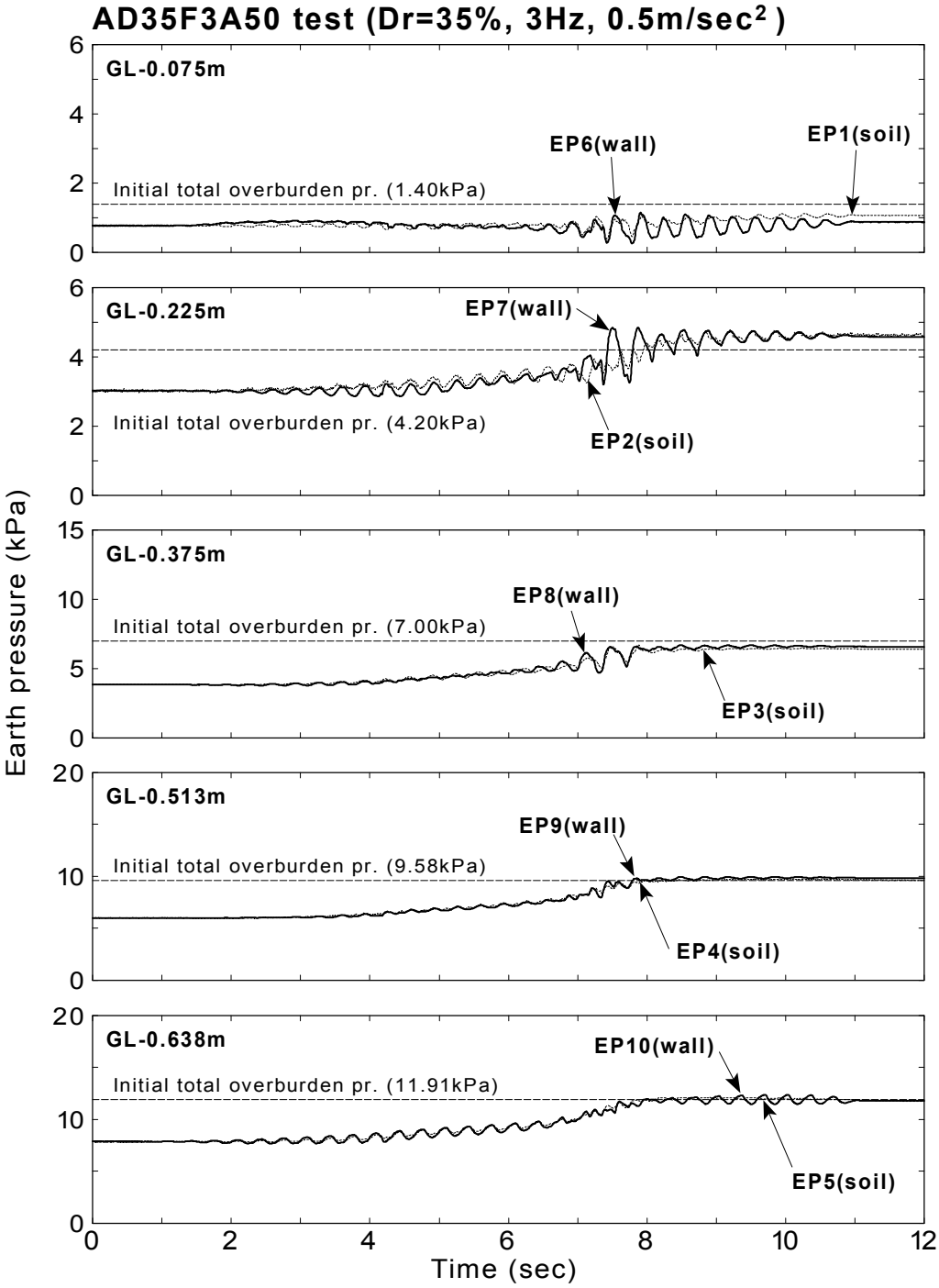

Fig.3.17: Time histories of earth pressure for AD35F3A50 test

Displacement and curvature

Fig.3.18 shows the displacement and the curvature of the structure and displacement at the surface of backfill monitored during shaking. The displacement was the relative displacement from the bottom of the container. The time history of curvature was calculated by dividing the each measured bending strain by the thickness of the wall of 4.97mm (Structure-A). The initial horizontal portion of curvature time histories indicated the accumulated static quantities shown in Table 3.1. The time history of mean value of SG2 and SG4 was presented since the bending strain SG3 could not be recorded correctly. The positive relative displacement and the positive curvature are shown in Fig.3.14(b) and Fig.3.1, respectively.

It was seen that the displacement at the top of the structure LV1 significantly increased at 7 to 8 seconds when the acceleration AC2 was amplified (see Fig.3.16). The amplitude of the displacement decreased to about half of the maximum during liquefaction of backfill after 8 seconds. The residual displacement of 2mm was read from the time history of LV2 at the ground surface. The measurement of displacement using transducer of LV3 and LV4 were not conducted in this test using Model-1.

The curvatures of both walls at 0.15m and 0.30m below tip (SG1, SG2, SG8, SG9) were oscillated in the positive direction as the top of the structure translated to the left which was defined as a negative direction of displacement. Inversely, the curvatures more than 0.575m below tip (SG4～SG7,SG11～SG14) oscillated in the negative direction at the same time instance. This indicated that the wall behaved dynamically like a beam with a built-in end at its bottom and a fixed end against rotation but free in the horizontal translation at its top. Detail analysis of wall deformation will be conducted in Chapter 6.

On the left wall, the curvatures at the top and bottom portion (SG1 and SG5～SG7) continued to increase, and those for middle portion (SG2 and SG3) continued to decrease during shaking accompanied by the increasing of lateral earth pressure (see Fig.3.17). On the right wall, the feature of gradual change of the curvature was contrary to the left wall. The absolute residual curvatures in the left wall at 12 seconds seemed to be equal to those in the right wall from the reading of time histories. It suggests that the magnitude of the lateral thrust due to liquefied backfill was equal on both sides of the structure.

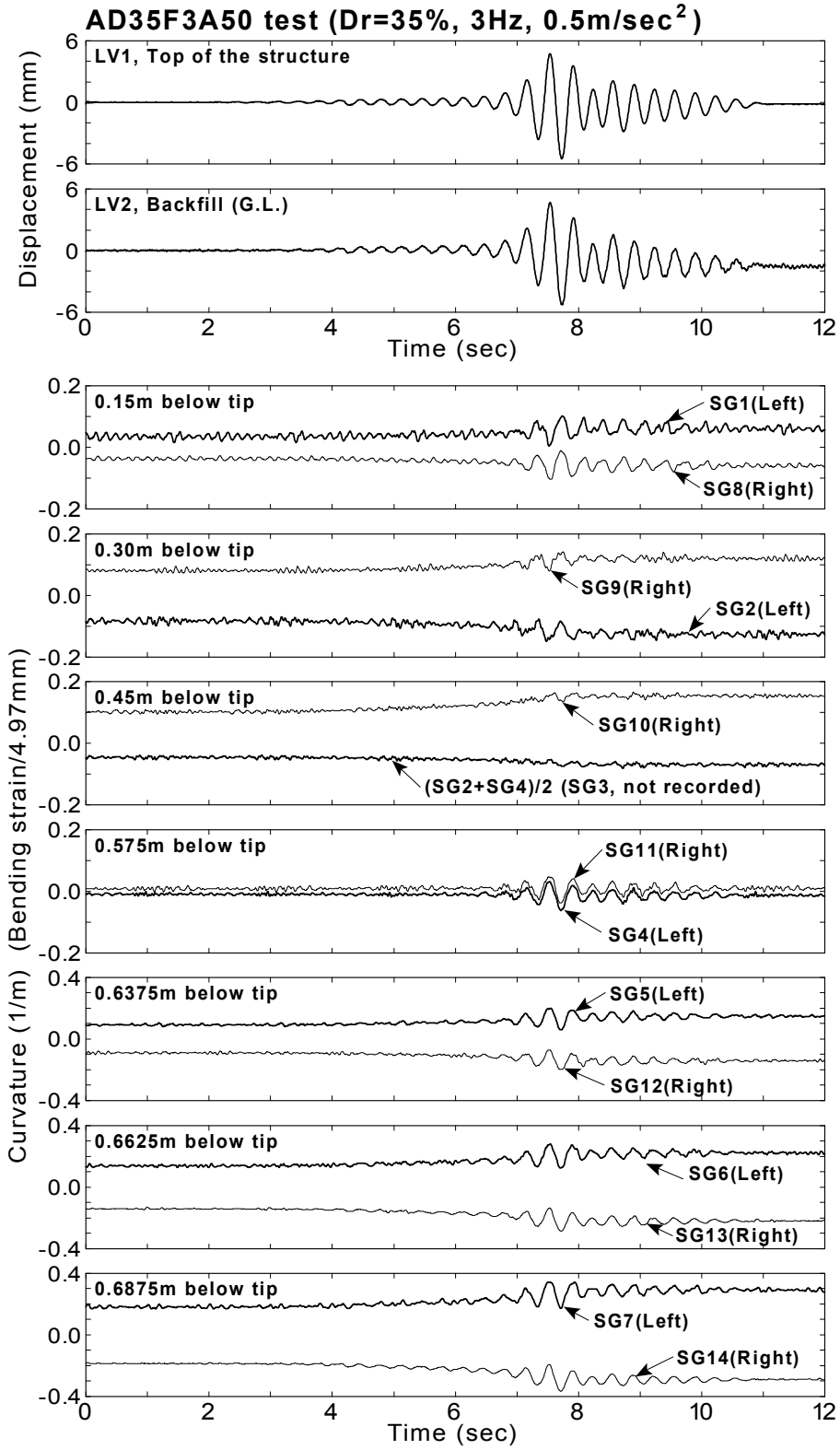

Fig.3.18: Time histories of displacement and curvature for AD35F3A50 test

3.4.2 The measurements with intense input motion (Dr=32%, 5.0m/sec^2, Structure-A)

A typical dynamic behavior of the model under the harmonic excitation of 5.0 m/sec^2 is described by presenting the measurement from AD32F3A500 test. The Structure-A is used with loose backfill of 32% relative density in this test.

Pore water pressure

The pore water pressure developments at each portion are illustrated in Fig.3.19. It was seen that the pore water pressure rapidly built up and reached the initial total overburden pressure at 2 seconds by the intense excitation. It was noted that the amplitude of input acceleration up to 2 seconds was less than the peak acceleration of 5.0 m/sec^2. As is presented in time history of acceleration on the shaking table AC1 in Fig.3.20, total of three cycles had been input to the model before 2 seconds when the backfill liquefied. The amplitudes were 0.5m/sec^2 for the first cycle, 1.0m/sec^2 for the second cycle, 1.5m/sec^2 for the third cycle.

The significant oscillation of pore water pressure around the initial total overburden pressure after 2 seconds was observed at PP6～PP8. This oscillation occurred due to translation of the wall in the liquefied backfill. The similar oscillation of pore water pressure was seen at PP2 and PP3 in the backfill. It seems that the effect of the translation of wall propagated into the liquefied soil.

The pore pressure PP1 was not recorded by accident. The pore water transducer for PP2 was placed at GL-0.45m instead of GL-0.375m only in this test.

Acceleration

Fig.3.20 depicts the records of the accelerations during the shaking. As mentioned previously, the acceleration on the shaking table (AC1) is shown at the bottom of figures.

The shape of time histories at the top of the structure (AC2), and in the backfill (AC5～AC8) was similar to a sinusoidal motion on the shaking table (AC1) through the duration. In contrast, the shapes of time histories near the surface of the backfill (AC3, AC4) were very complicated. For instance, the spiky accelerations were observed at the surface during liquefaction. Those were significant in the negative direction. It was considered that a

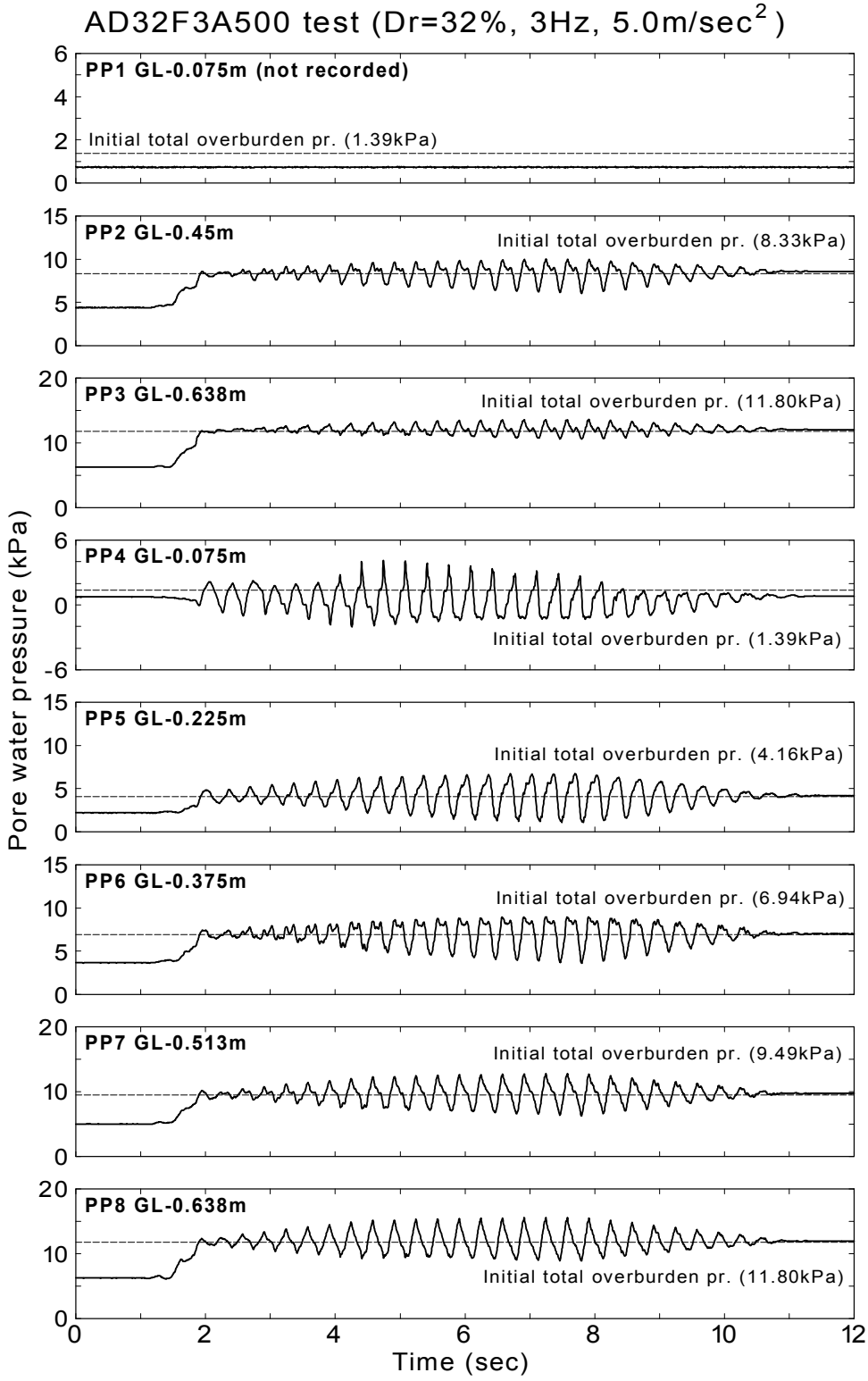

Fig.3.19: Time histories of pore water pressure for AD32F3A500 test

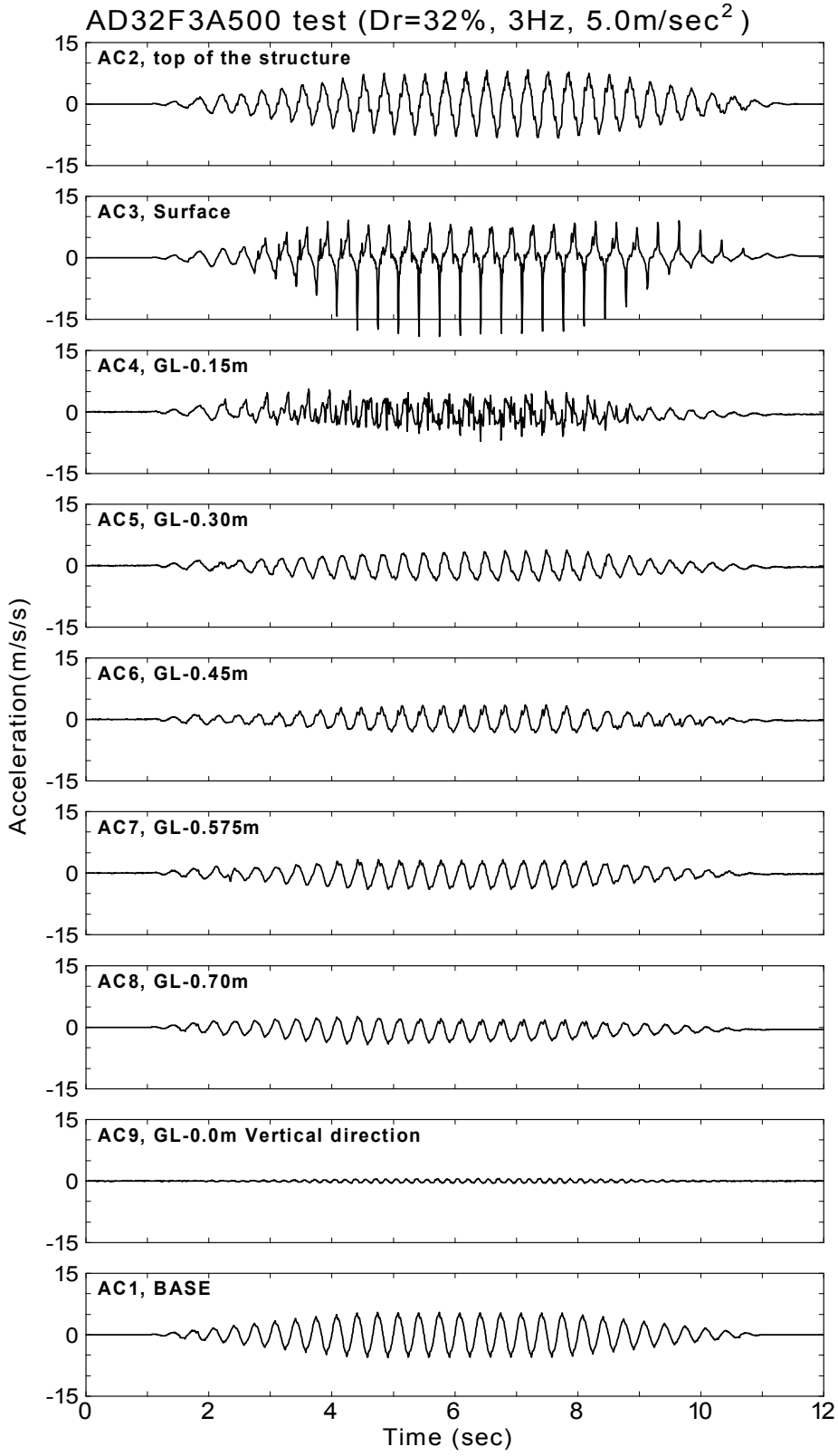

Fig.3.20: Time histories of acceleration for AD32F3A500 test

dilative behavior of liquefied soil appeared near the surface. Note that this phenomenon was repeatedly observed in BD36F3A500 in which the conditions of the backfill and input motion were identical to AD32F3A500 test (see Fig.3.29).

The time history at the second from the bottom (AC9) is the acceleration in the vertical direction at the top of the structure. The vertical acceleration was about 7% of the horizontal acceleration at the top of the structure (AC2) in terms of the magnitude. It shows that the horizontal response is much dominant comparing to the vertical response in this test. The frequency of the vertical acceleration was read as 6Hz from the time history. This was due to the large horizontal deformation of the structure; that is, the top plate translated up and down in the vertical direction when the structure deformed largely in the horizontal direction.

The results of analysis for the amplification and the phase difference of acceleration will be presented in Chapter 5. Characteristics of those phenomena will be discussed there.

Earth pressure

The time histories of lateral earth pressures are illustrated in Fig.3.21. The initial lateral pressures as shown in Table 3.3 were included in those time histories in the same manner as AD35F3A50 test.

The lateral earth pressures rapidly increased together with the pore water pressure (see Fig.3.19), and reached the initial total overburden pressure at 2 seconds except for the earth pressures at the middle depth of structure (EP3 and EP8). It was seen that the lateral earth pressures when the backfill liquefied oscillated 3Hz as well until the excitation ceased. The amplitude of the oscillation on the wall (EP6～EP10) seemed larger than those in the soil (EP1～EP5). The collision between the liquefied soil and the wall caused those oscillations of earth pressures. This kind of fluctuating earth pressures will be concerned as the dynamic interaction problems in the following chapters. The fluctuating earth pressure will be separated to the monotonically increasing earth pressure in the later discussion.

Displacement and curvature

The time histories of monitored displacements and curvatures of wall during shaking are presented in Fig.3.22. It should be noted that the displacement readings obtained between 5

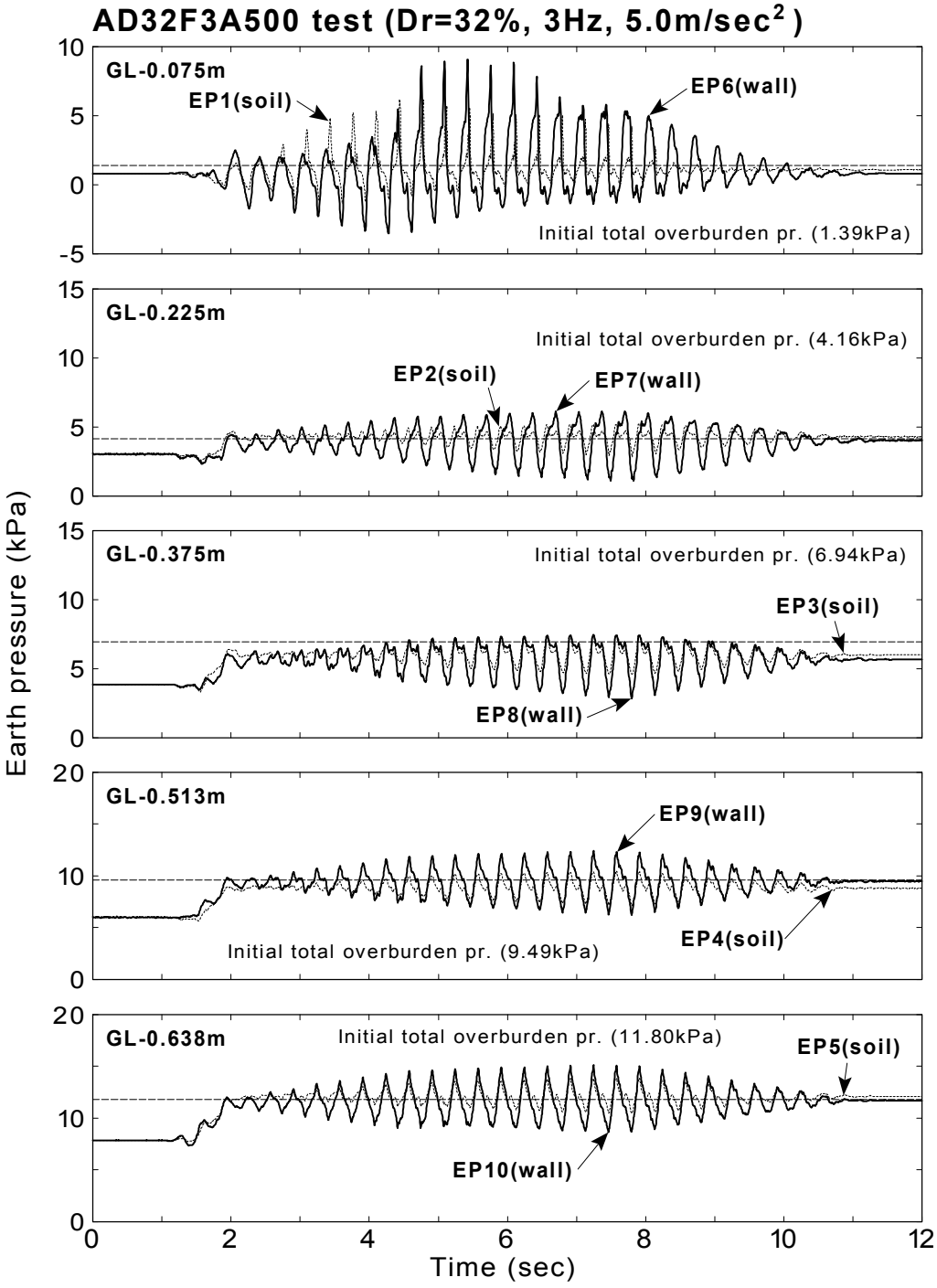

Fig.3.21: Time histories of earth pressure for AD32F3A500 test

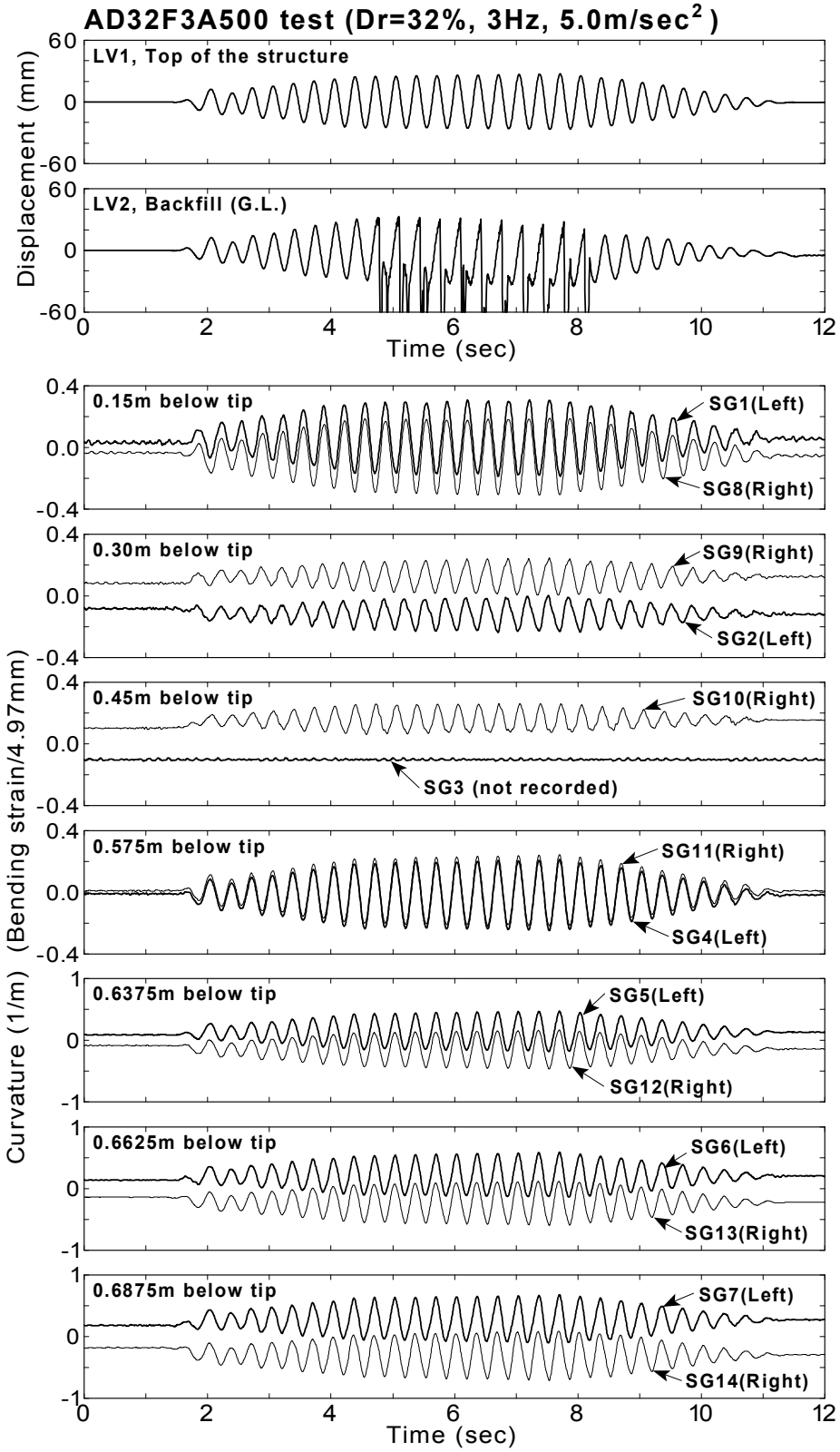

Fig.3.22: Time histories of displacement and curvature for AD32F3A500 test

to 8 seconds at the surface of the backfill (LV2) were spurious since the laser displacement transducer missed the marker during liquefaction which was placed on the backfill.

It was seen that the amplitude of displacement both on the structure (LV1) and the backfill (LV2) at around 2 seconds was slightly amplified than the following cycle. As was seen in AD35F3A50 test (see Fig.3.18), it was just before the complete liquefaction of the backfill. It suggests that the amplified response of the structure caused a resonance of the structure in liquefied backfill. The analysis focused on the phenomenon will be conducted in Chapter 5. The displacements at the side of container (LV3 and LV4) were also recorded. Those are presented in Fig.3.70 at the end of this chapter.

The maximum absolute curvature in this test occurred at the bottom of right wall (SG14) to be 0.701(1/m). This curvature was corresponded to the bending strain of 3480 μ, considering the thickness of the wall of 4.97mm (Structure-A). In this test, the wall behaved in an elastic manner throughout the shaking since the maximum value was below the yielding curvature of 0.793 (1/m), or the yielding bending strain of 3940 μ (It is twice as much as the yield strain of 1970 μ, see Fig.2.11). The curvatures of wall significantly oscillated during shaking in contrast to the previous test results in Fig.3.18. It was seen that the amplitude of both sides of curvatures at the same height was in the same magnitude, for example SG4 and SG11.

3.4.3 The measurements with dense backfill (Dr=67%, 5.0m/sec^2, Structure-A)

The typical dynamic behavior of the model with dense backfill at the relative density of 67% is described by presenting the measurement from AD67F3A500 test. The same structure (Structure-A) as used in AD32F3A500 test was used. The model was shaken at the peak acceleration of 5.0 m/sec^2.

Pore water pressure

The time histories of pore water pressure during shaking are presented in Fig.3.23. In this dense backfill, all of the pore water pressures reached the initial total overburden pressure around 2.5～3.0 seconds. The significant oscillation of pore water pressure was observed 6

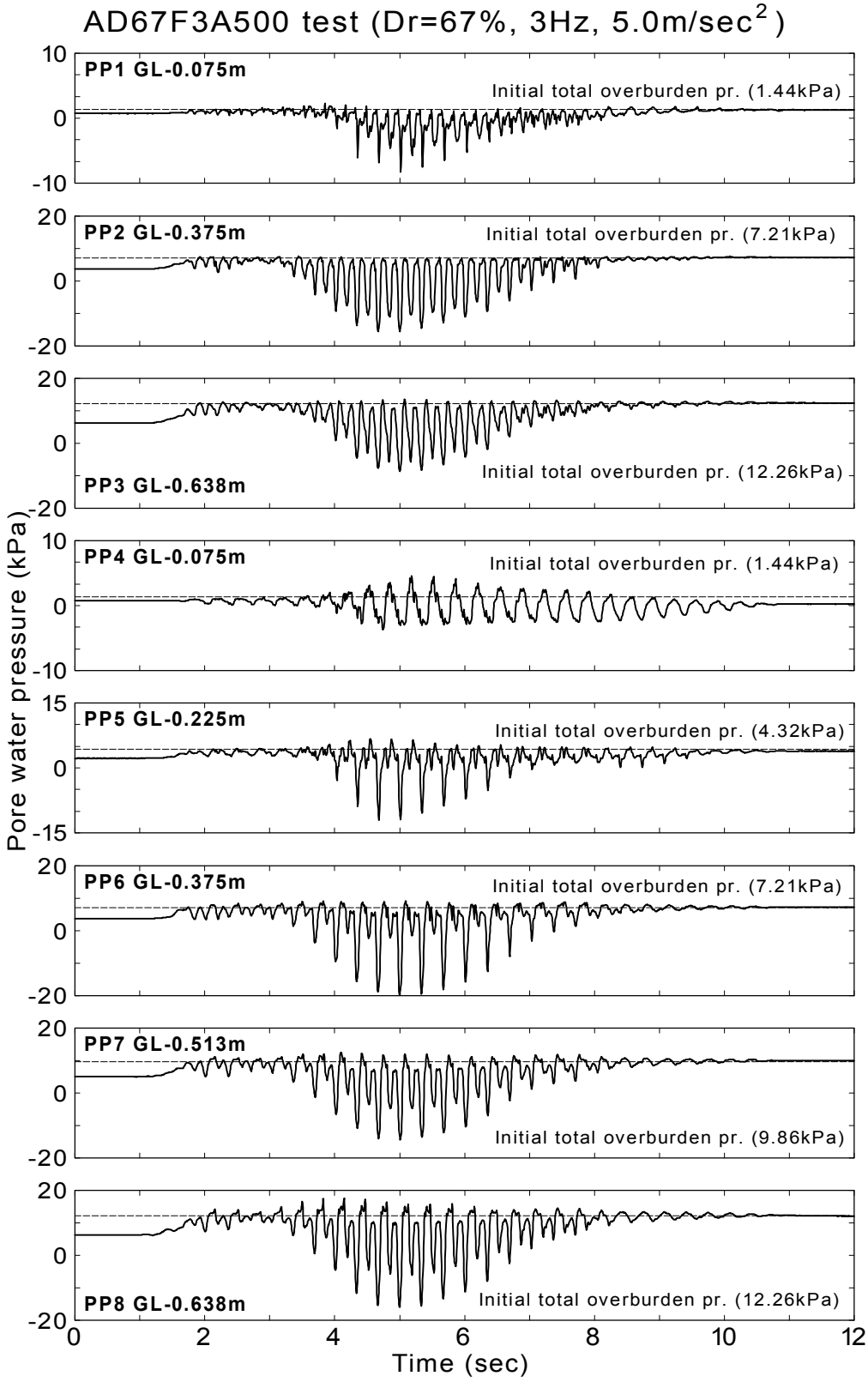

Fig.3.23: Time histories of pore water pressure for AD67F3A500 test

times in one second, which was twice in a cycle, in the backfill (PP2 and PP3). This phenomenon was characteristic of the dilative behavior of dense soil. The drop of the pore water pressures attained as much as in the negative value. It should be due to the particular condition of 1G shaking table test under which the model ground with low confining stress was shaken by extremely intense excitation.

The characteristic pore pressure behavior due to dilatancy of soil was not seen at the 0.075m below tip of the wall (PP4). It was considered that the soil near the structure was confined by existence of the wall and consequently the shear strain did not reach the level that induced the dilative behavior of soil.

The effect of the dilative behavior on the dynamic interaction, which is characteristic to the dense backfill, will be discussed in Chapter 7.

Acceleration

Fig.3.24 is the measurement of acceleration during shaking. Spiky accelerations due to dilative behavior of the backfill were seen in the time histories. The maximum values amounted to more than 20 m/sec^2 at the top of the structure and 60 m/sec^2 at the surface of backfill.

The magnitude of the vertical acceleration at the top of the structure was less than 7% of the horizontal acceleration at the same location. The horizontal motion was also dominant in this case.

Earth pressure

The time histories of lateral earth pressure are shown in Fig.3.25. It was noted that the initial earth pressures, which was consistent with the initial bending strain of the wall, exceeded the initial total overburden pressure at GL-0.225m, 0.375m, 0.513m. The shape of time histories was very complicated in contrast to those in the test with loose backfill (AD32F3A500 test, see Fig.3.21). More discussions with respect to the earth pressure in dense backfill will be made in chapter 7.

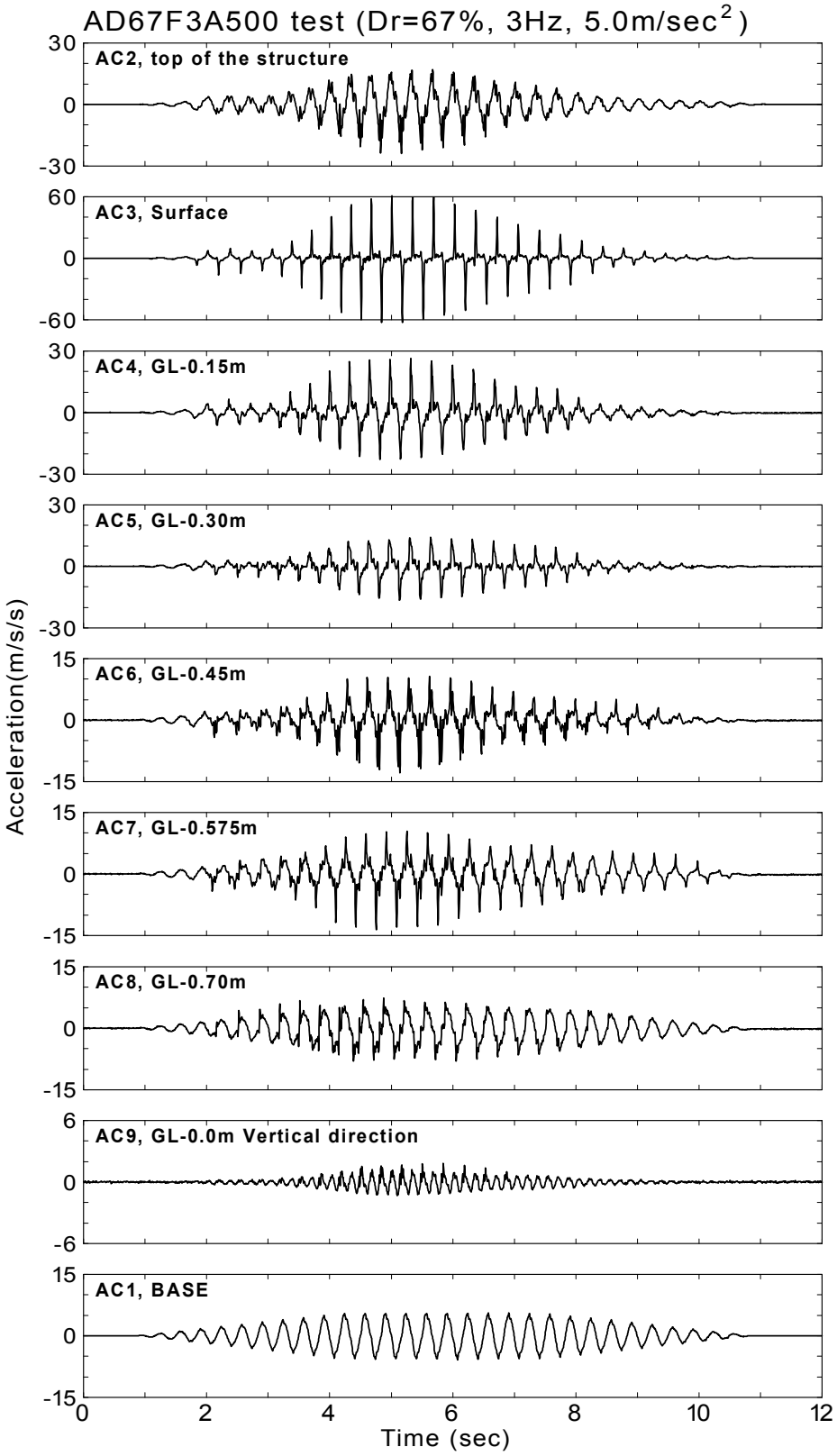

Fig.3.24: Time histories of acceleration for AD67F3A500 test

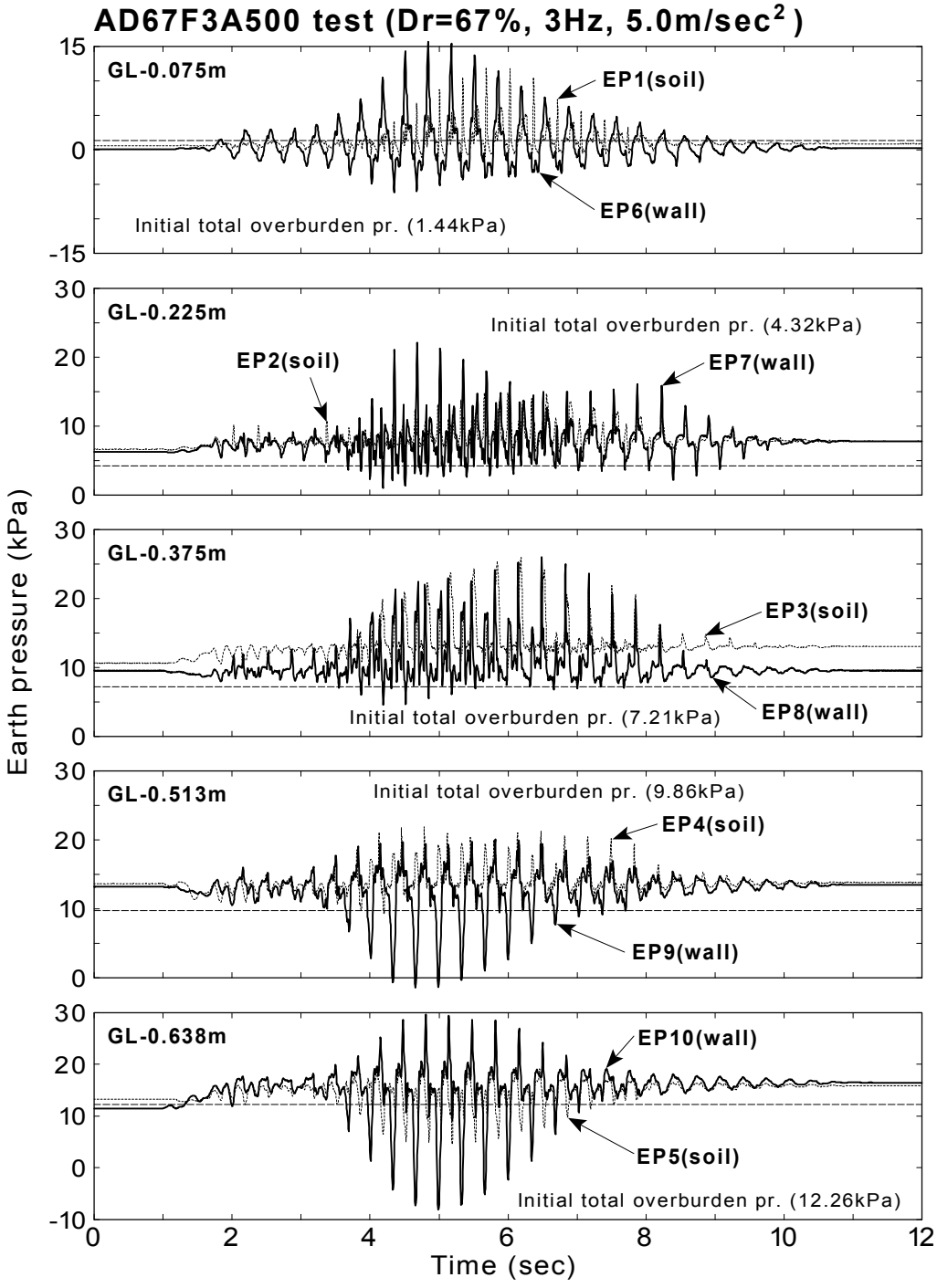

Fig.3.25: Time histories of earth pressure for AD67F3A500 test

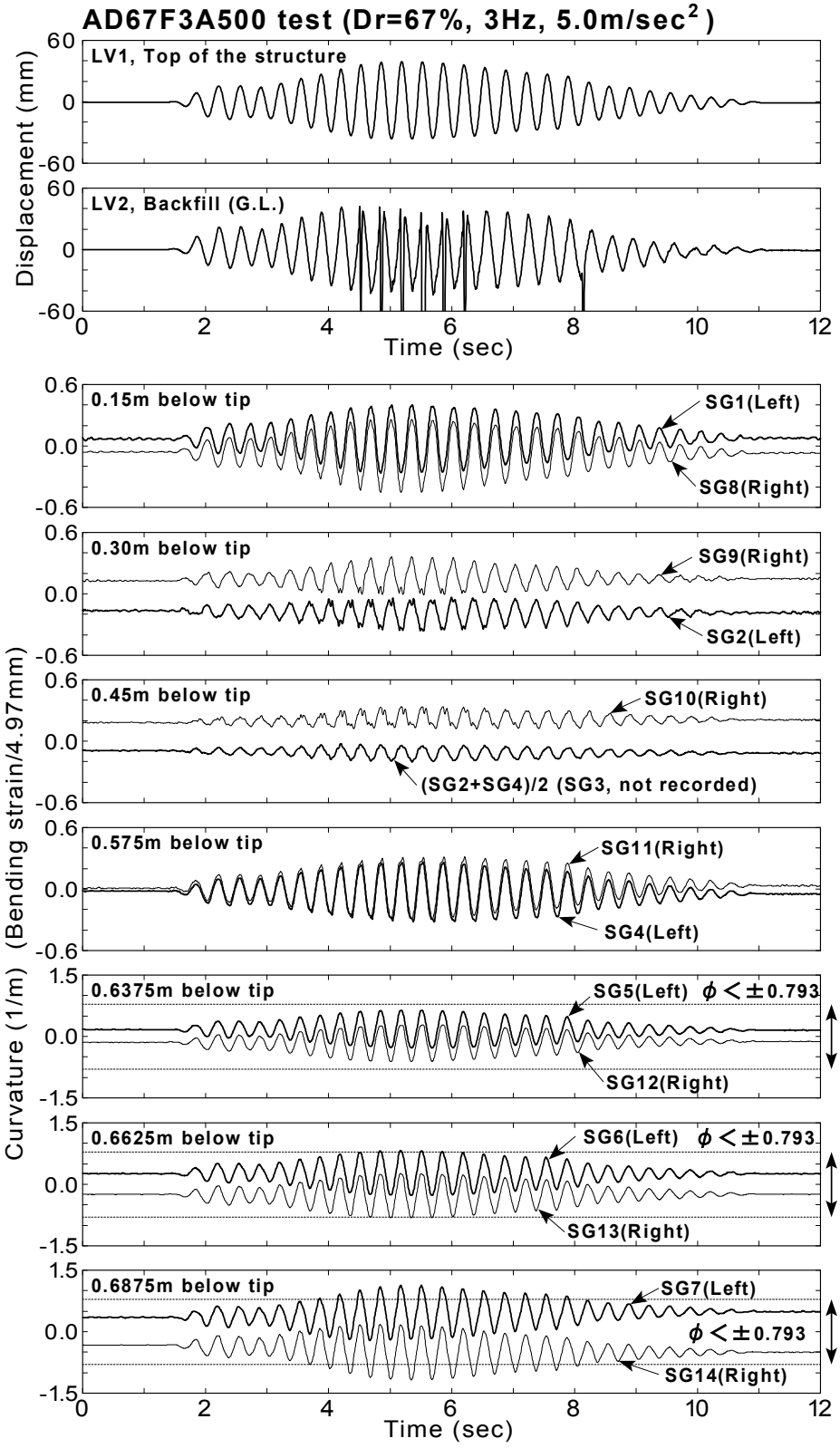

Fig.3.26: Time histories of displacement and curvature for AD67F3A500 test

Displacement and curvature

The time histories of monitored displacements and curvatures of wall during shaking are presented in Fig.3.26. It should be noted again that the displacement readings obtained between 4 to 9 seconds at the surface of the backfill (LV2) were spurious since the laser displacement transducer missed the marker by means of the intense shaking.

At the middle height of the structure of 0.3m and 0.45m below tip, it seems that the time history of the curvature contains high frequency response at about 4 to 6 seconds. It was considered that cyclic change of shear modulus of backfill due to dilative behavior caused the response of high frequency.

The measured maximum bending strain of 5870 μ exceeded the yielding bending strain of 3940 μ during shaking. Those bending strain levels are added in the experimentally obtained relationship between the bending moment and the curvature/bending strain in Fig.3.27. It is recognized that the behavior of wall in AD67F3A500 test is in a non-linear region, while AD32F3A500 test is in linear region. Only difference between the two tests is a density of backfill. It suggests that the density of soil affects the response of underground structure.

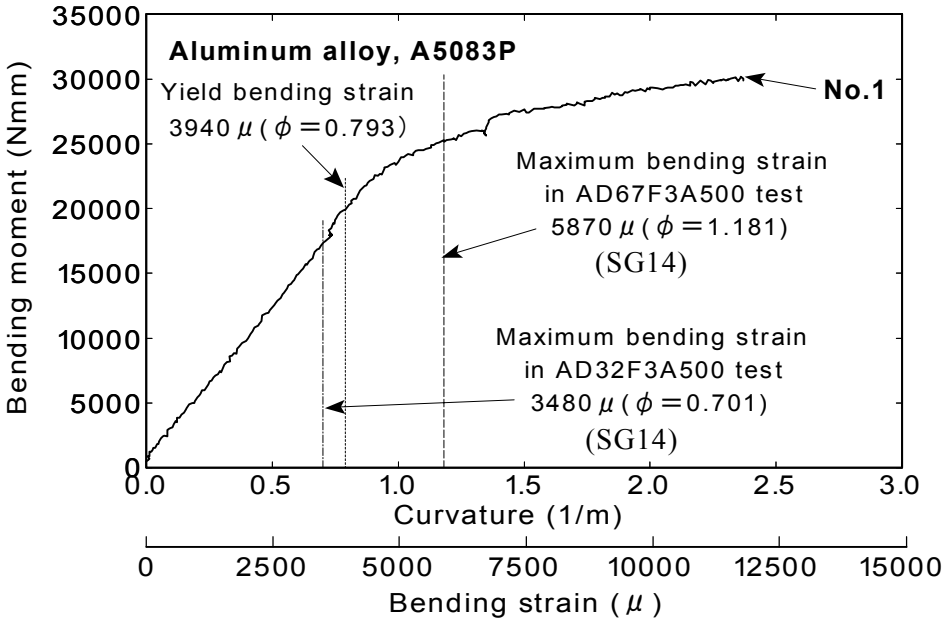

Fig.3.27: Time histories of displacement and curvature for AD67F3A500 test

3.4.4 The measurements with yielding of material (Structure-B, Dr=36%, 5.0m/sec^2)

The measurements from BD36F3A500 test will be presented. The tensile strength of material of structure (Structure-B: 86Mpa, see Table.2.1) is lower than that used in the previous tests (Structure-A: 146Mpa).

Pore water pressure

The time histories of pore water pressure at each portion are presented in Fig.3.28. It was seen that the pore water pressure rapidly built up and reached the initial total overburden pressure at 2 seconds by the excitation. The significant oscillation of pore water pressure around the initial total overburden pressure was observed at the pore water pressure on the wall of PP4～PP8 after 2 seconds. As was stated in previously, this oscillation occurred due to translation of the wall. The similar oscillation of pore water pressure in the backfill was seen at PP2 and PP3. The number of cycle in the pore pressure PP1 was observed to be six per one second between 6 to 8 seconds. It was considered that the dilative behavior was occurred near the surface of backfill.

The behavior of excess pore water pressure in this test seems very similar to that of AD32F3A500 test, in which the condition of input motion and density of backfill is almost identical (see Fig.3.19).

Acceleration

Fig.3.29 illustrates the records of the accelerations during shaking. The shape of time histories at the top of the structure (AC2), and in the backfill (AC5～AC8) was similar to a sinusoidal input motion (AC1) through the duration. In contrast, those near the surface of the backfill (AC3, AC4) were very complicated. Spiky accelerations were observed in those time histories, and those were significant in the negative direction. It is considered that the dilative behavior due to large shear strain of backfill caused the spiky response of acceleration. It is interesting to note that the same feature was observed in AD32F3A500 test in which the conditions of the backfill and input motion were identical to this test (see Fig.3.20).

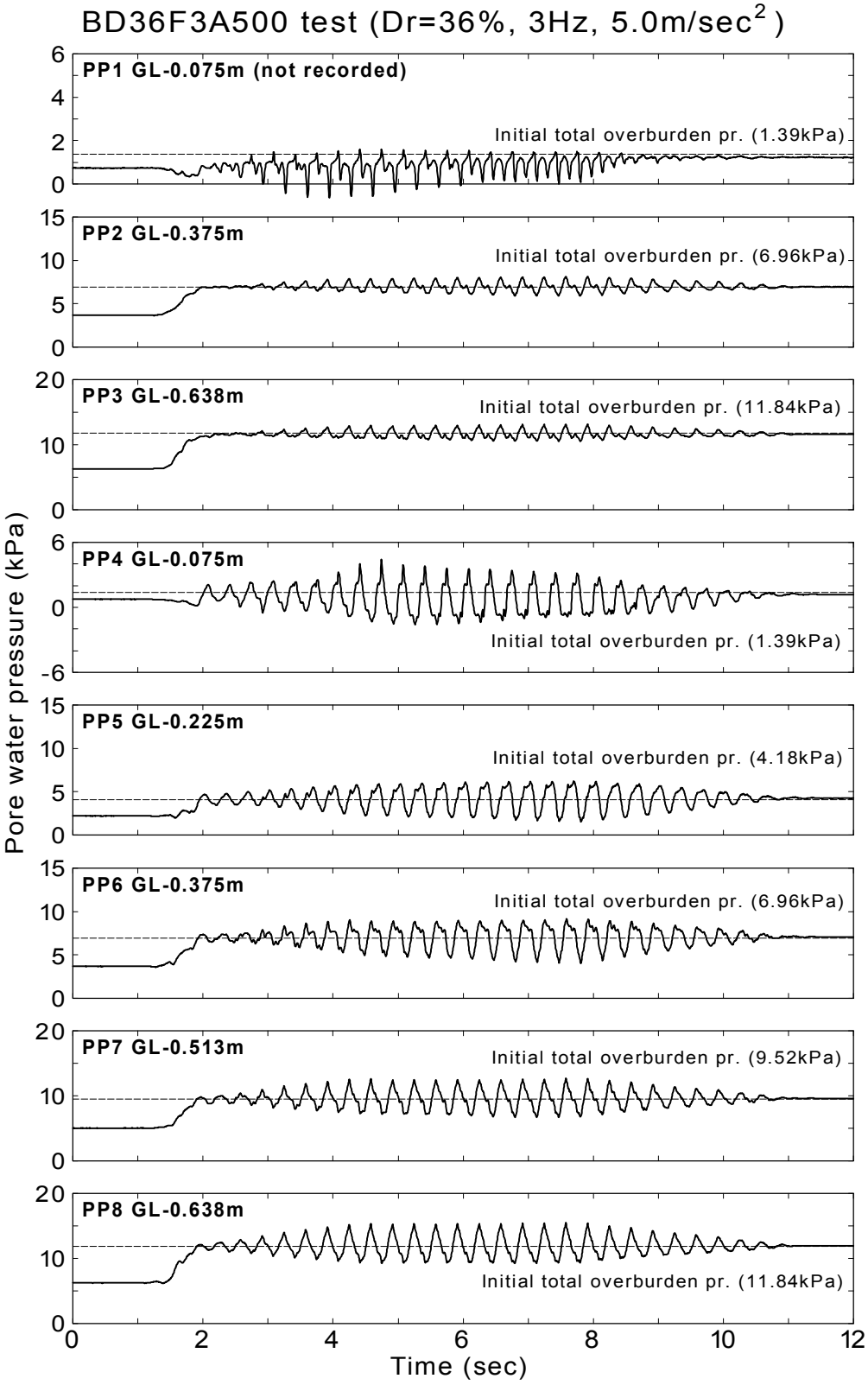

Fig.3.28: Time histories of pore water pressure for BD36F3A500 test

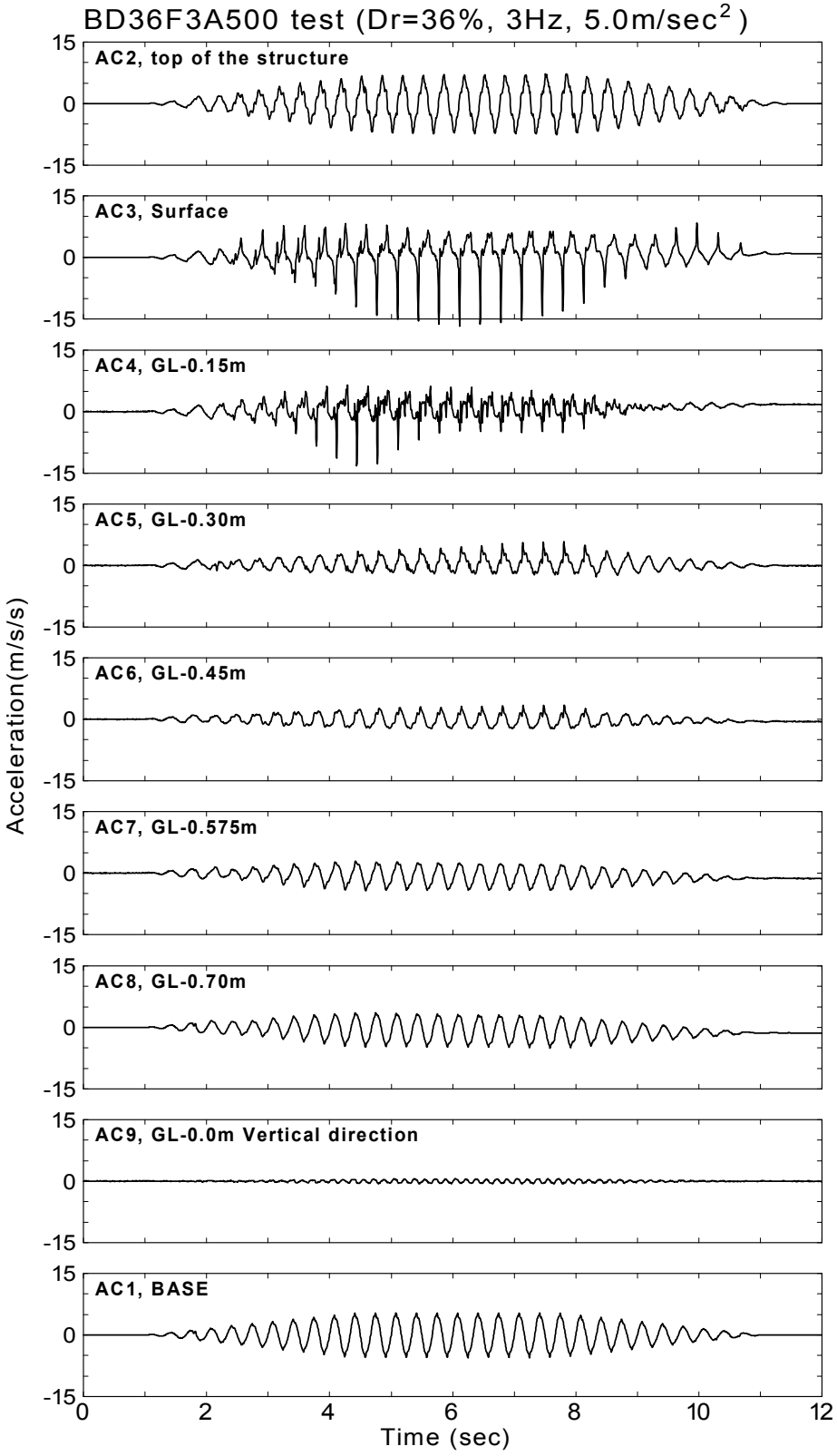

Fig.3.29: Time histories of acceleration for BD36F3A500 test

The response of the vertical acceleration (AC9) is very small comparing to that of horizontal acceleration at the top. The vertical acceleration was less than about 10% of the horizontal acceleration. As was shown in the other test results, the horizontal response was much dominant comparing to the vertical response.

Earth pressure

The time histories of lateral earth pressures are described in Fig.3.30. The initial lateral pressures were already considered in those time histories.

The lateral earth pressures rapidly increased together with the pore water pressure, and reached the initial total overburden pressure at 2 seconds except for the earth pressures at the middle depth of wall (EP8). Since this feature was observed in the other tests, for instance in AD32F3A500 test, the monotonically increasing earth pressure was affected by the deformation of flexible wall. The amplitude of the oscillation on the wall (EP6～EP10) seemed larger than those in the soil (EP1～EP5). The responses of earth pressure seem to very similar to those of AD32F3A500 test (see Fig.3.21).

Displacement and curvature

The time histories of monitored displacements and curvatures of wall during shaking are shown in Fig.3.31. The maximum amplitude of displacement at the top of the structure was measured to be 26.844mm. The displacements up to the maximum value of 26.844mm are plotted in the experimental relationship between load and displacement by a static loading in Fig.3.32. It is seen that the behavior of shear deformation of the structure is slightly non-linear around the maximum displacement of 26.844mm. It is noted that the level of maximum amplitude of displacement in this test (BD36F3A500) is almost same as that in the previous test of 27.161mm using loose backfill (AD32 F3A500).

Curvatures at the bottom of wall (SG7, SG14) are increasing monotonically with fluctuation exceeding the yield curvature of 0.657(1/m). The maximum absolute curvature at bottom of right wall (SG14) amounted to 1.506(1/m). The curvature at the end of shaking was about 1.0(1/m) being still larger than the yield curvature of 0.657(1/m). The maximum curvature was corresponded to the bending strain of 7334μ, taking the thickness of the wall of 4.87mm (Structure-B) into account. It seems that amplitude of fluctuating curvature is not

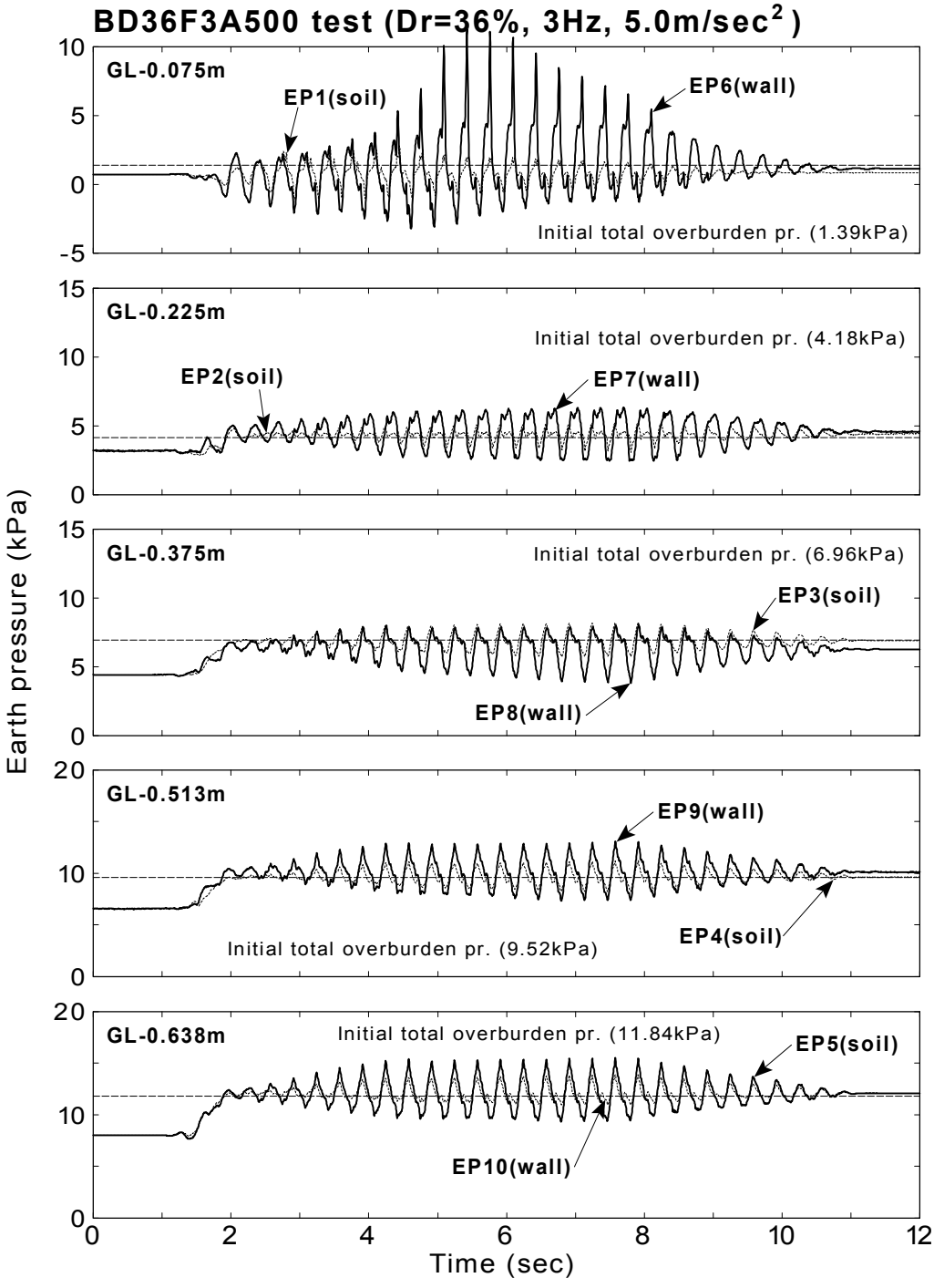

Fig.3.30: Time histories of earth pressure for BD36F3A500 test

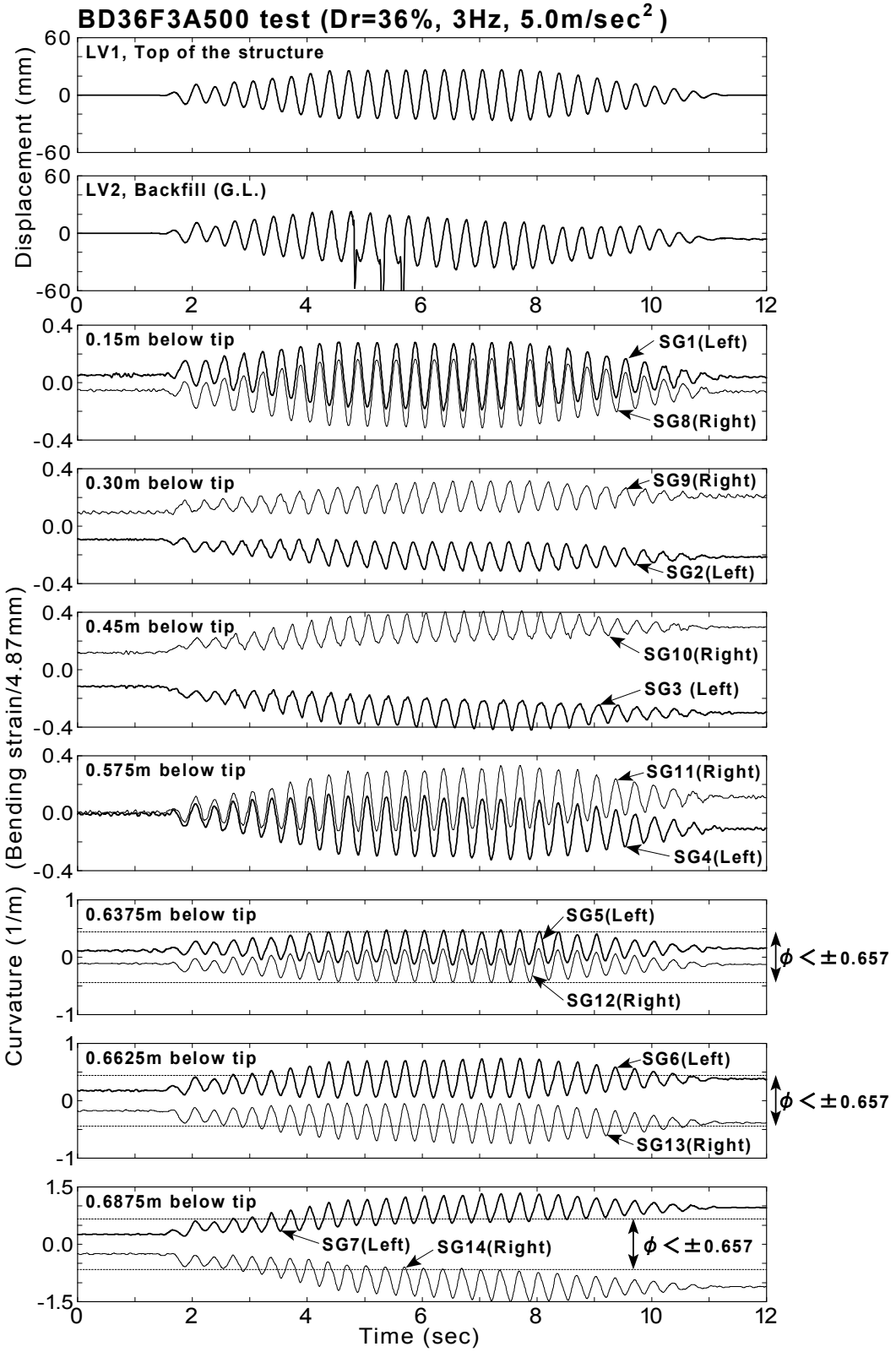

Fig.3.31: Time histories of displacement and curvature for BD36F3A500 test

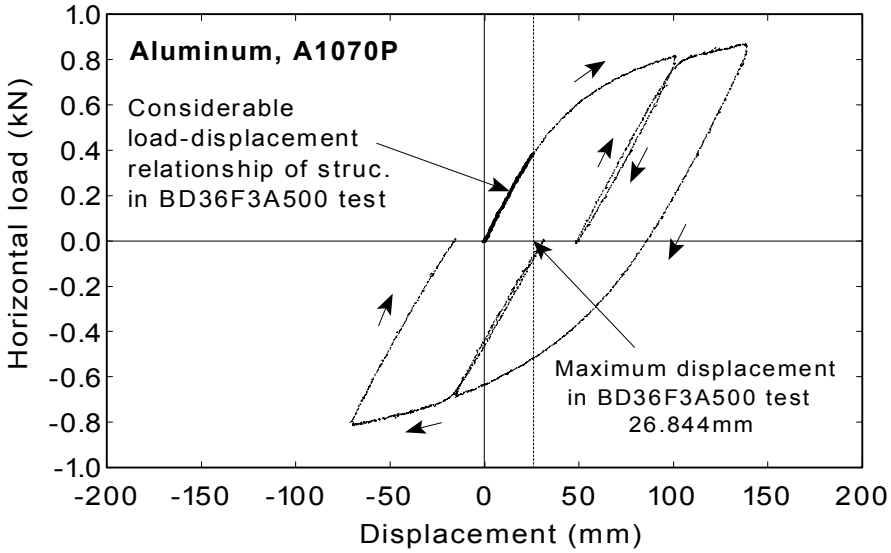

Fig.3.32: Maximum horizontal displacement in BD36F3A500 test

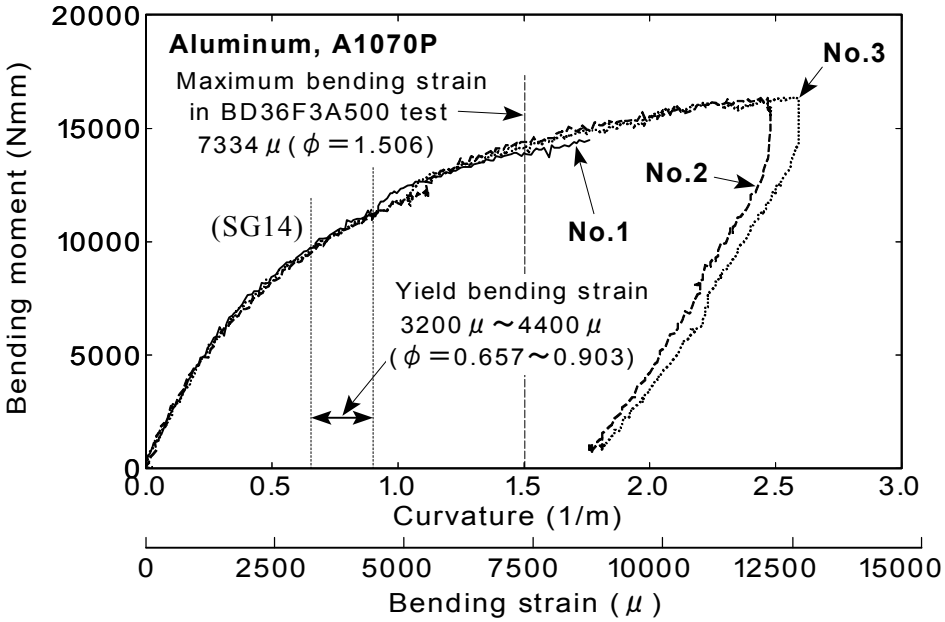

Fig.3.33: Maximum bending strain in BD36F3A500 test

so large comparing with the monotonically increased curvature. The measured curvature is compared with the yield curvature in the experimentally obtained relationship between the bending moment and the curvature/bending strain in Fig.3.33. The maximum measured bending strain was twice as large as the yield bending strain of 3200 μ ～4400 μ .

Fig.3.34 shows the distribution of residual values after shaking (figure (a)) and amplitude of curvature at 15th cycle with respect to the depth (figure (b)). The results from BD36F3A500 test and AD32F3A500 test are compared in the figure. It was observed that the

residual curvatures from BD36F3A500 test were much larger than those from AD32F3A500 test, especially at the bottom of walls. This was due to the smaller tensile strength and yield of the material of structure in BD36F3A500 test.

As was seen in the distribution of amplitude of curvature, the amplitude at the middle

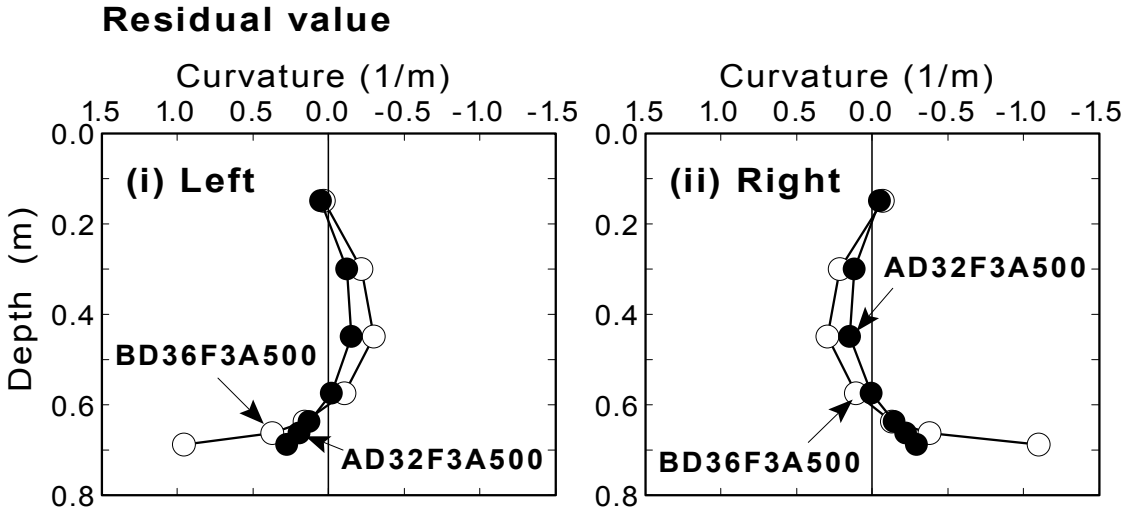

(a) Residual curvature at 12 second

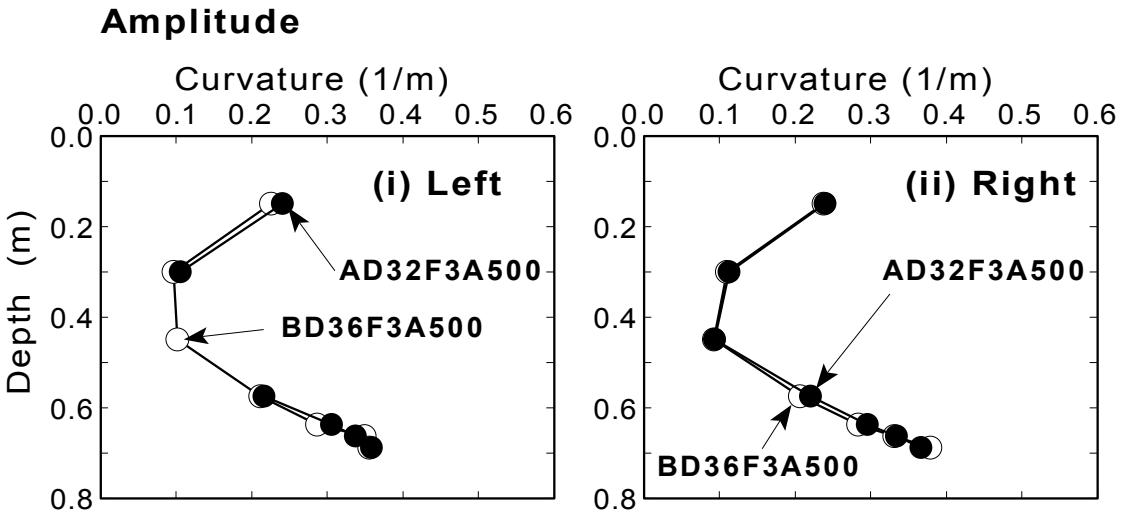

(b) Amplitude of curvature at 15th cycle

Fig.3.34: Comparison between BD36F3A500 test and AD32F3A500 test

part of the structure was smaller than those at the top and bottom of structure. The boundary condition of wall could make the bending moment small at the middle part of wall. It was remarkable that no significant differences were observed between AD32F3A500 test and BD36F3A500 test in spite of different behavior of the material. It suggests that the monotonic increasing of curvature due to yielding of material does not affect fluctuating responses significantly.

All the results of dynamic measurement during shaking are presented in Fig.3.67～Fig.3.74 at the end of this chapter. For the description of these tests (input acceleration, frequency, density of backfill, and type of structure), readers are referred to Table 2.8(c).

3.5 CONCLUDING REMARKS

A series of 1G shaking table tests using an aluminum structure model which was embedded in saturated soil was conducted in order to investigate the soil-structure dynamic interaction. The results of initial static measurements indicated that the measured initial earth pressures were internally consistent with the measured initial bending strains before each shaking. The results of weak excitation tests showed that the natural frequencies of tested soil-structure model were in the range of 18.5Hz～21.5Hz. They were closer to the natural frequencies of the backfill itself (19.5Hz～23.5Hz) than the natural frequency of the structure itself (7.3Hz ～7.8Hz).

In the results of dynamic measurements, it was observed that the earth pressure acting on the structure increased gradually accompanied by the generation of excess pore water pressure due to shaking, and its intensity of oscillation became significant just before complete liquefaction. It was also seen that the curvature of the wall, which was corresponded to the bending strain, increased and oscillated together with the earth pressure. The dilative behavior of soil was evident in the response of acceleration and earth pressure and bending strain of model with dense backfill. No significant effect of the monotonic increasing of curvature due to the yielding of material was observed on such fluctuating responses as pore water pressures, accelerations, earth pressures, and displacements at the top of the structure.

The results of measurements obtained herein will be analyzed in detail in the following chapter.

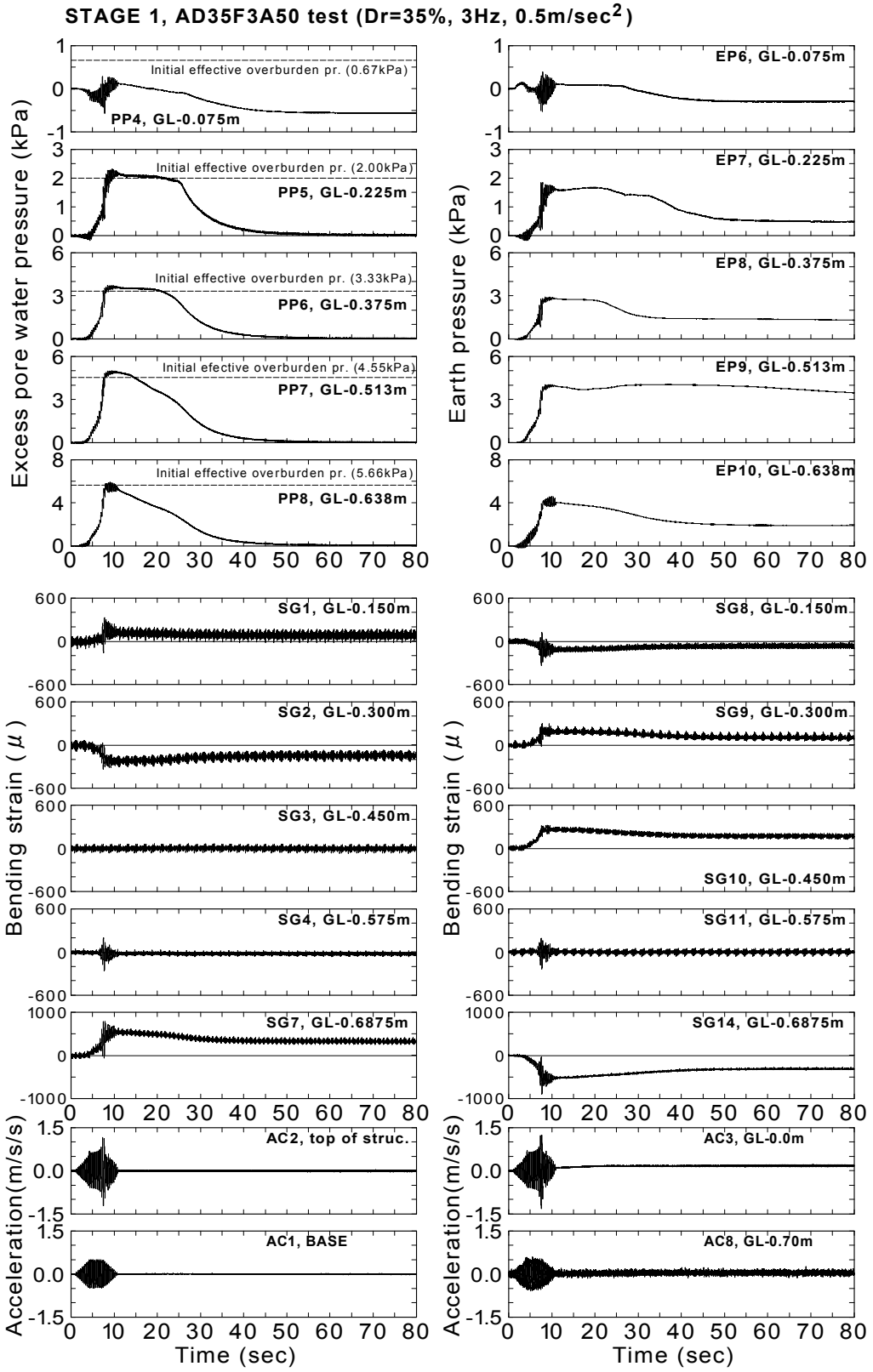

Fig. 3.35: Time histories for Stage 1 of Model No.1 (AD35F3A50 test)

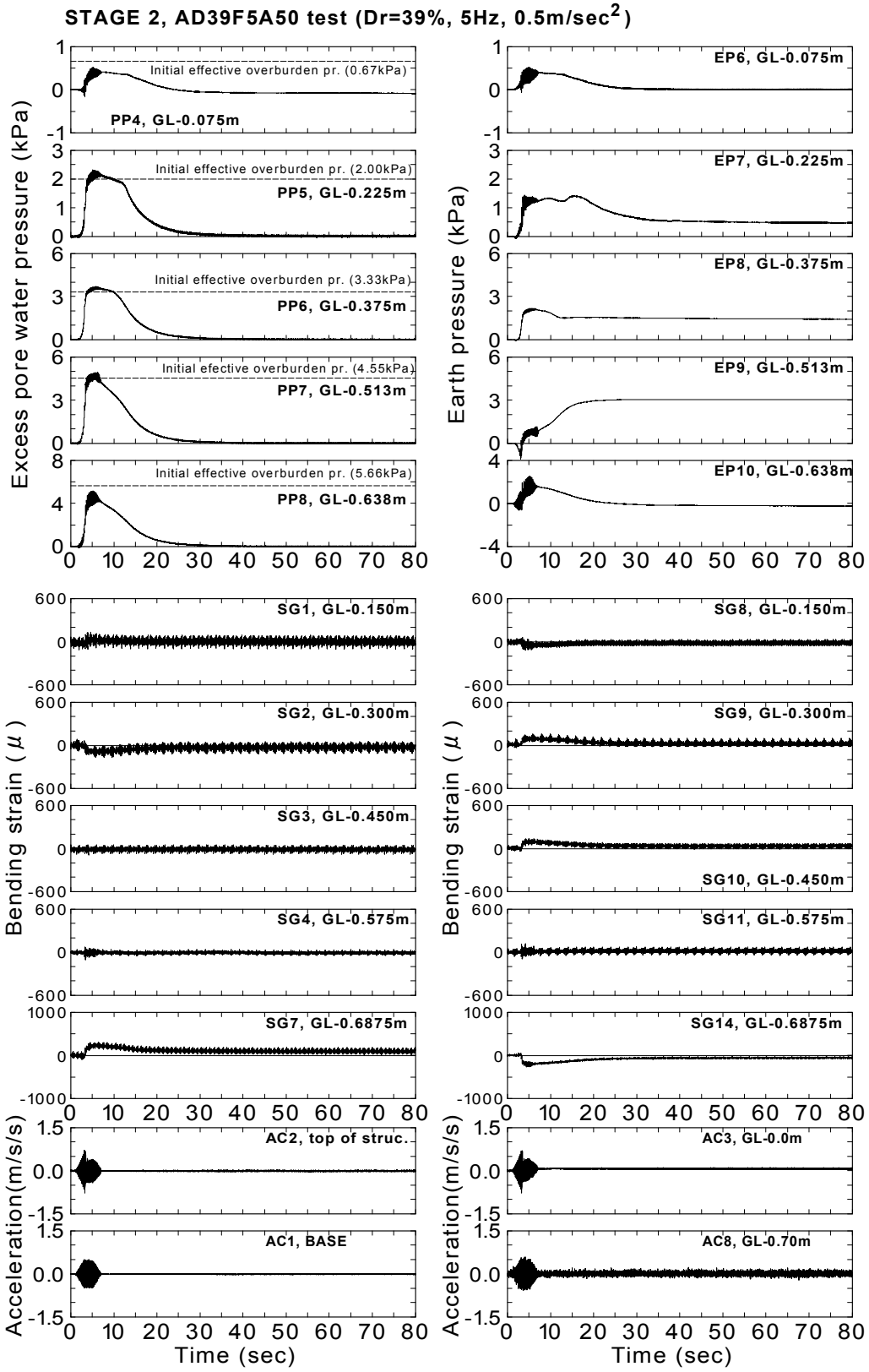

Fig. 3.36: Time histories for Stage 2 of Model No.1 (AD39F5A50 test)

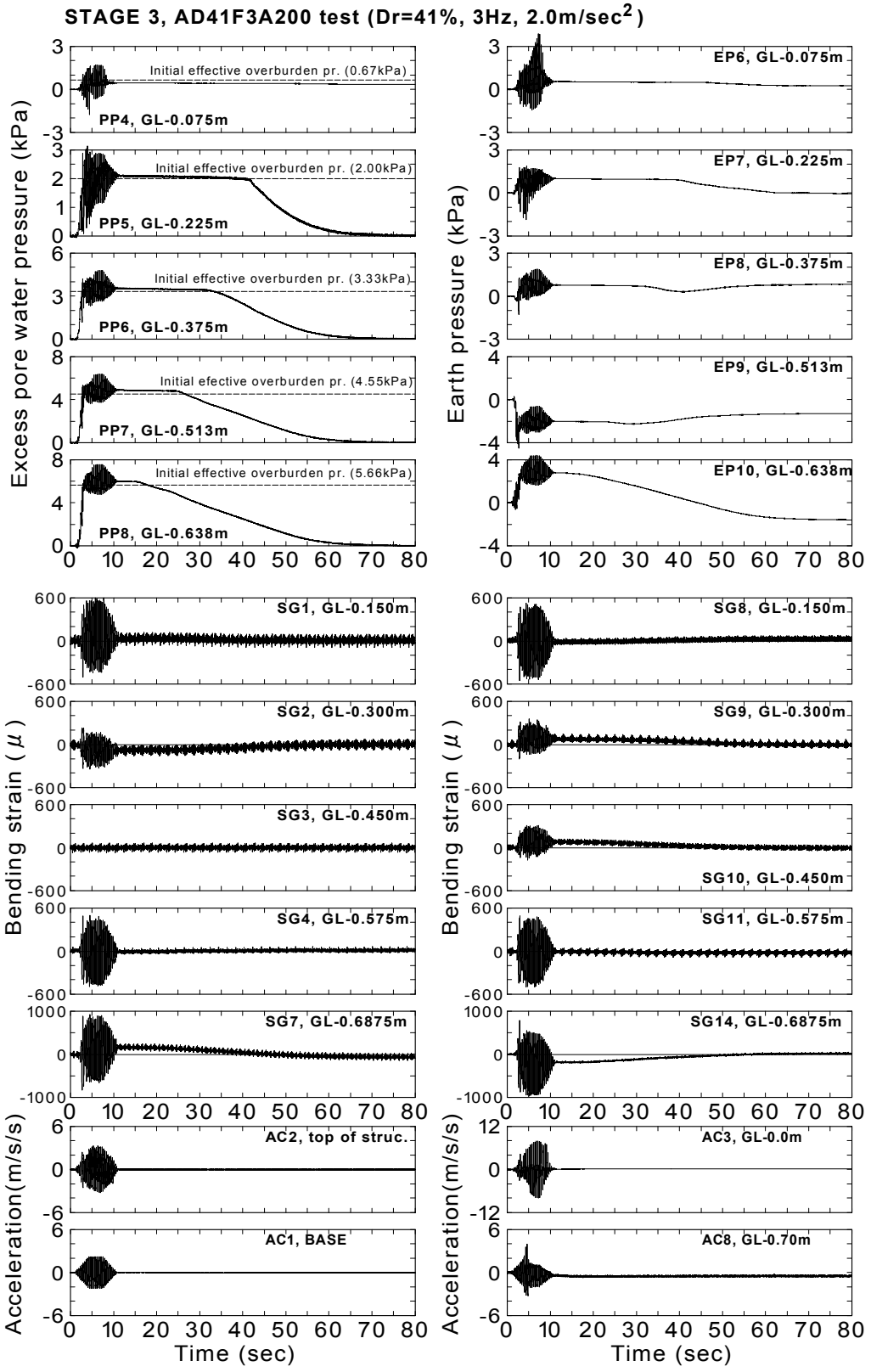

Fig. 3.37: Time histories for Stage 3 of Model No.1 (AD41F3A200 test)

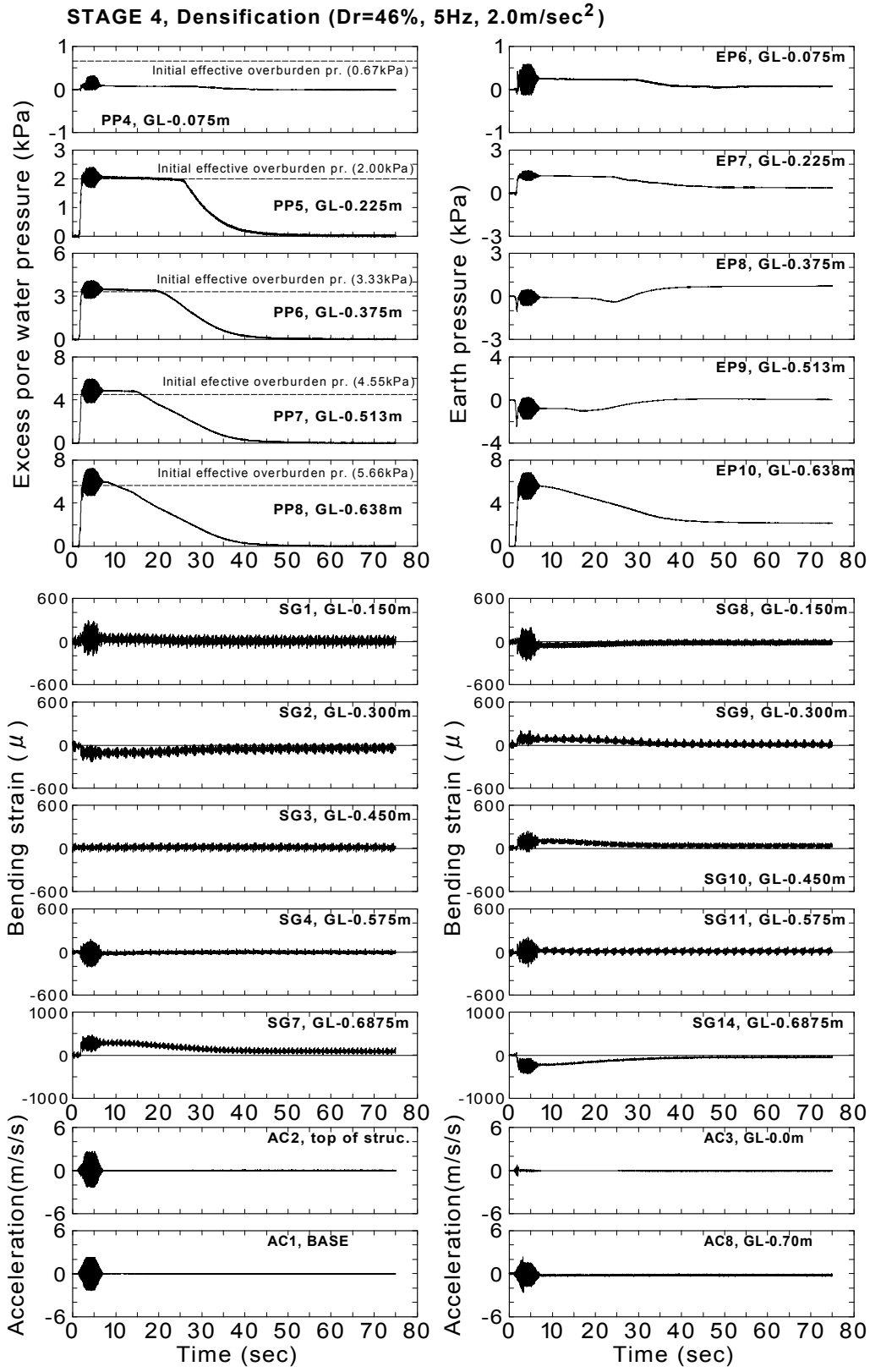

Fig. 3.38: Time histories for Stage 4 of Model No.1 (Densification)

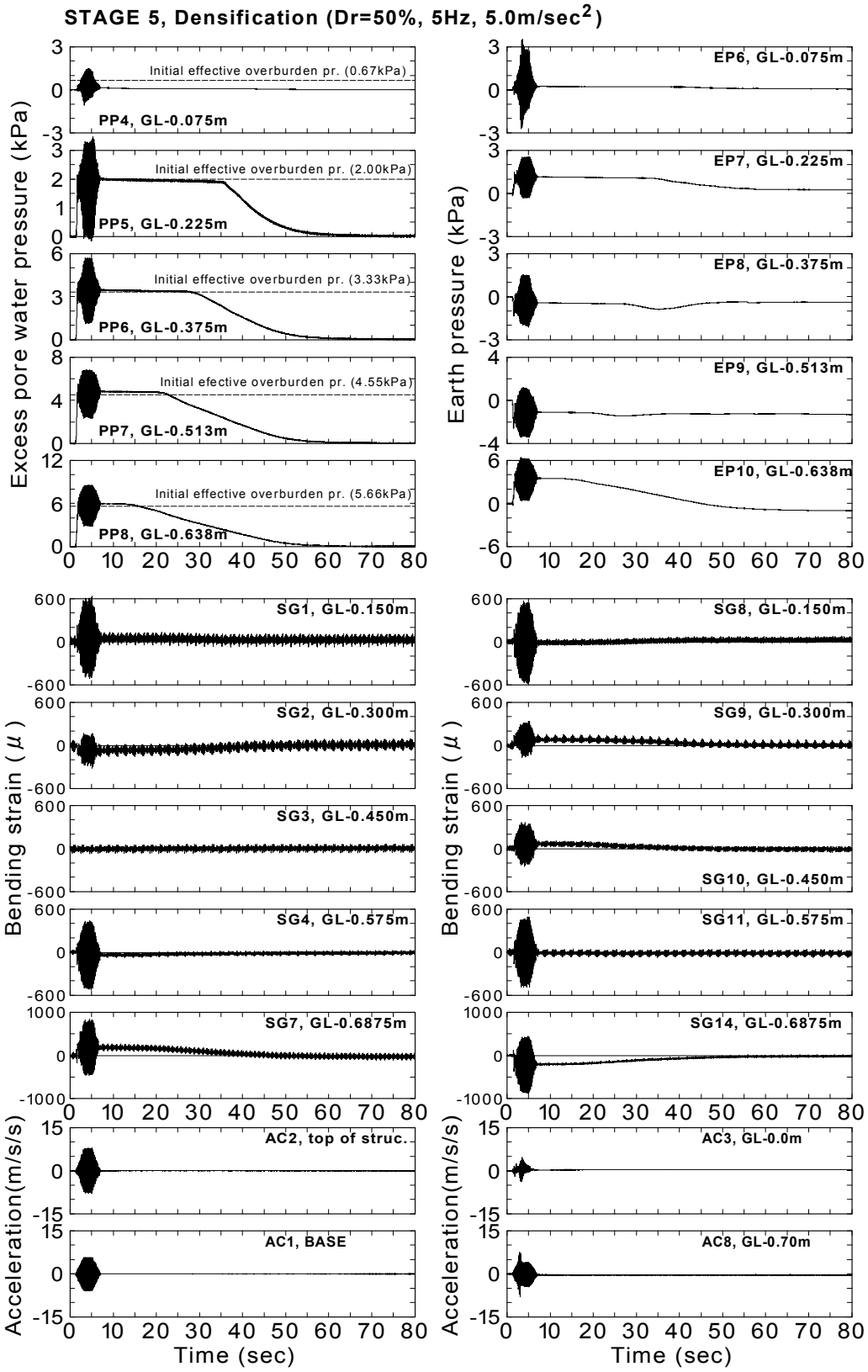

Fig. 3.39: Time histories for Stage 5 of Model No.1 (Densification)

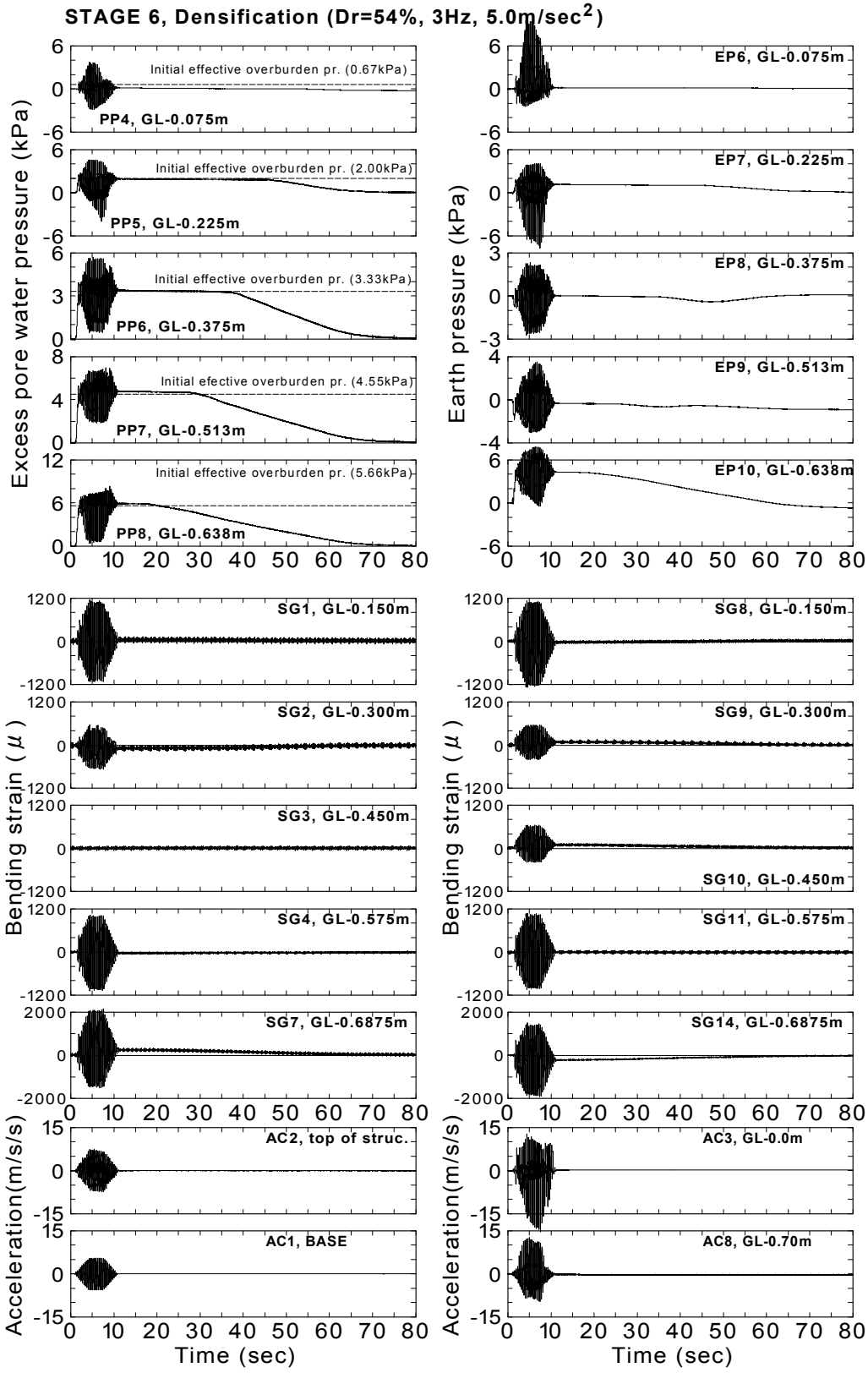

Fig. 3.40: Time histories for Stage 6 of Model No.1 (Densification)

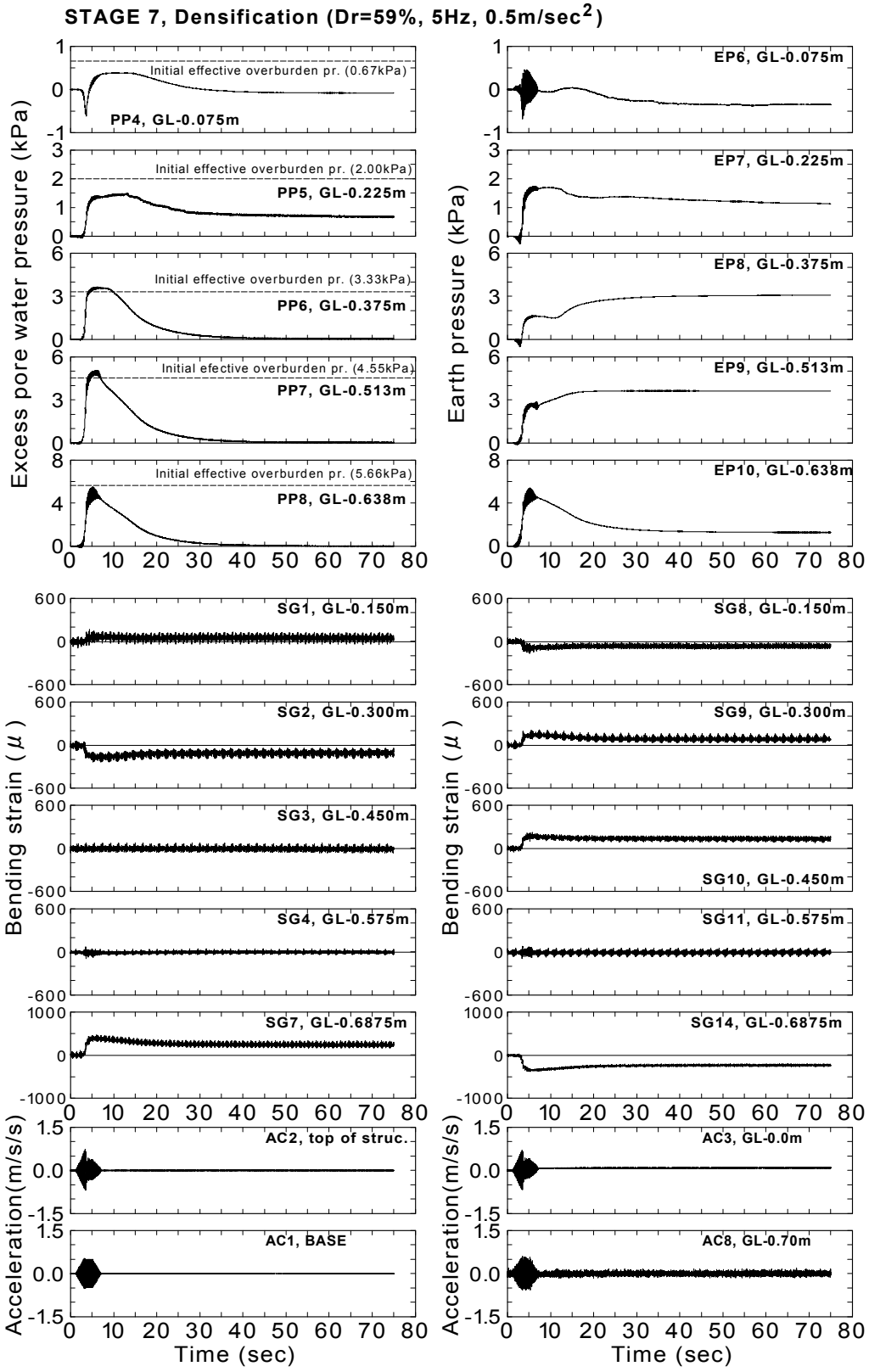

Fig. 3.41: Time histories for Stage 7 of Model No.1 (Densification)

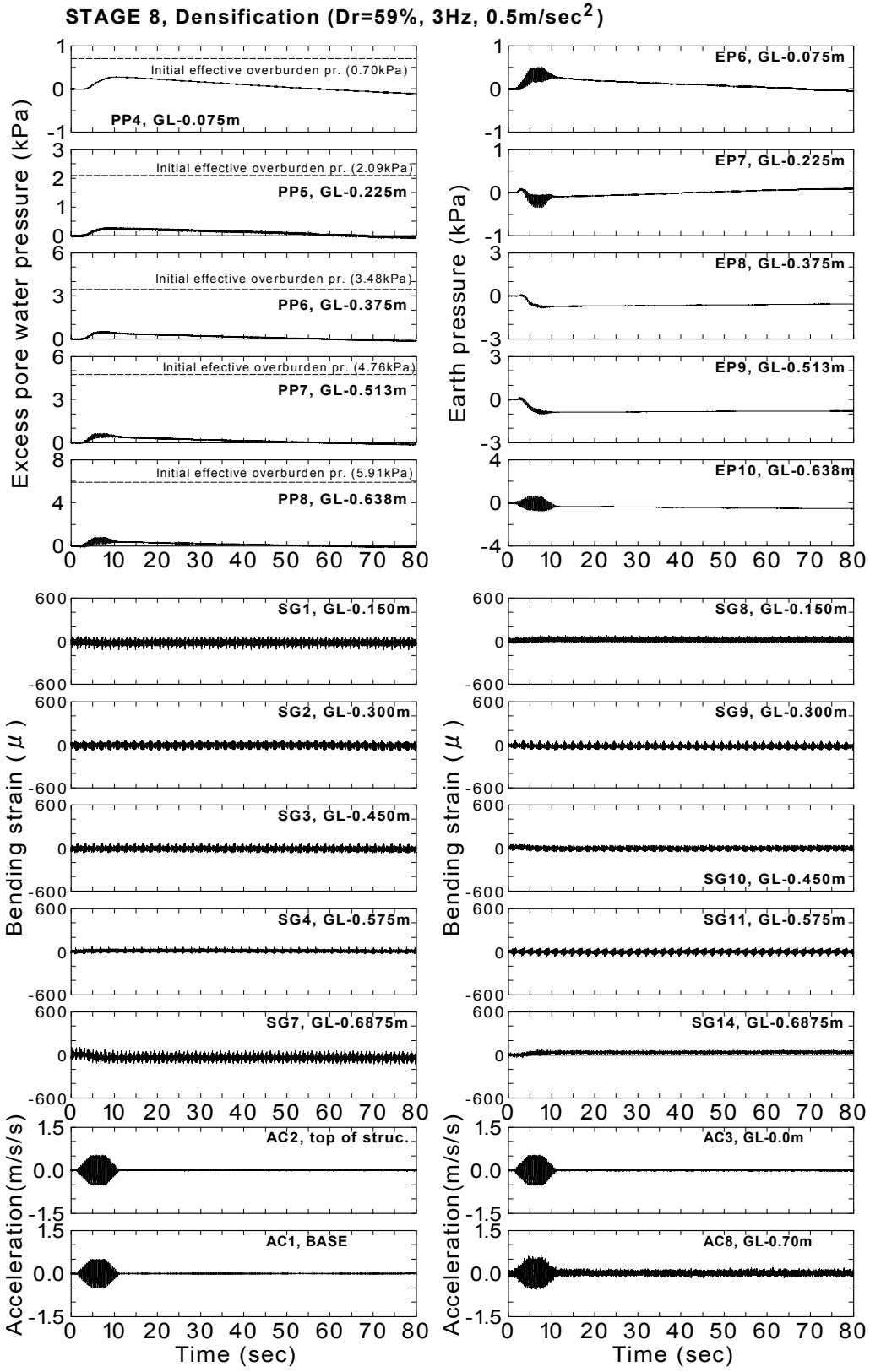

Fig. 3.42: Time histories for Stage 8 of Model No.1 (Densification)

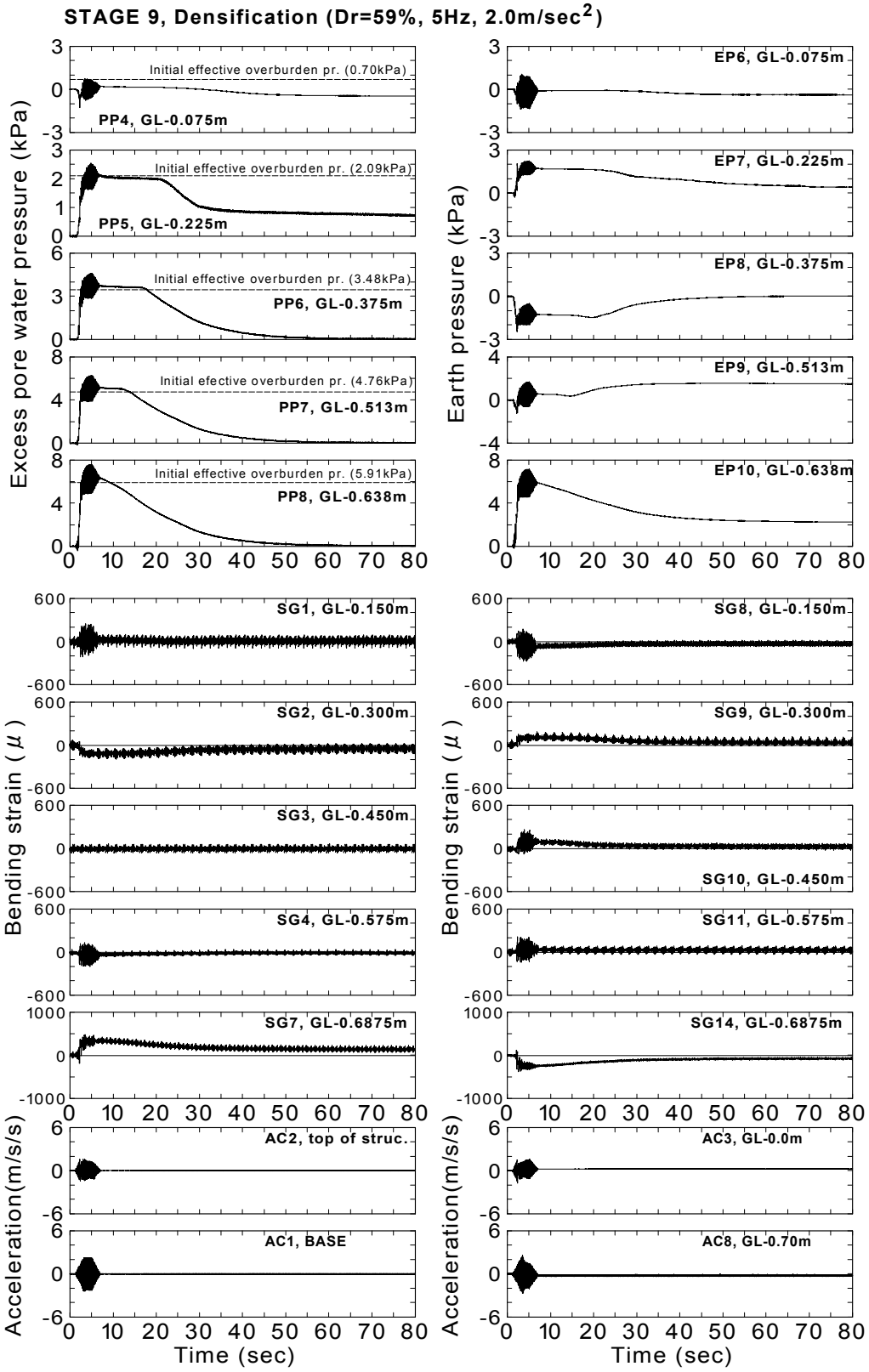

Fig. 3.43: Time histories for Stage 9 of Model No.1 (Densification)

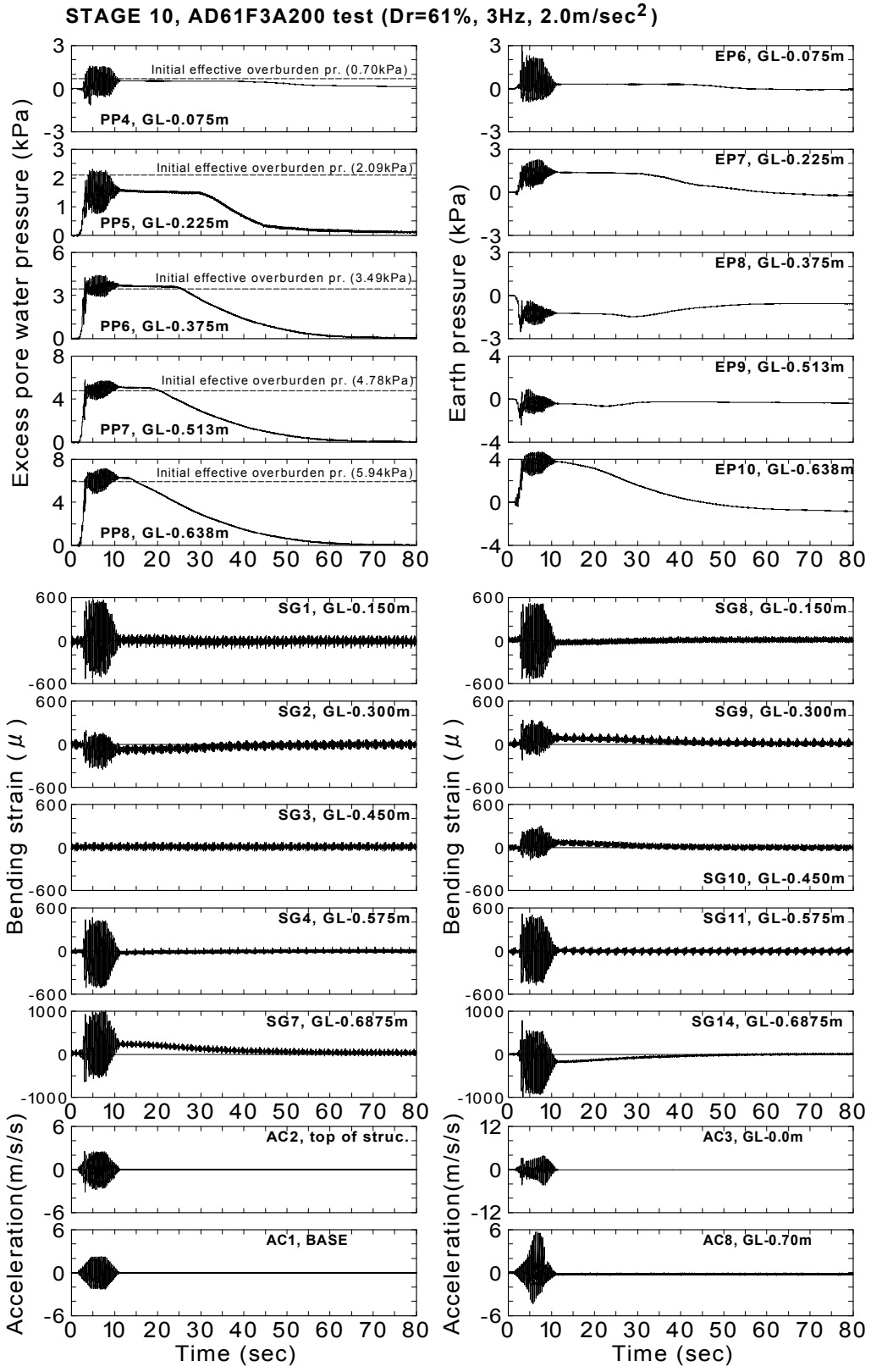

Fig. 3.44: Time histories for Stage 10 of Model No.1 (AD61F3A200 test)

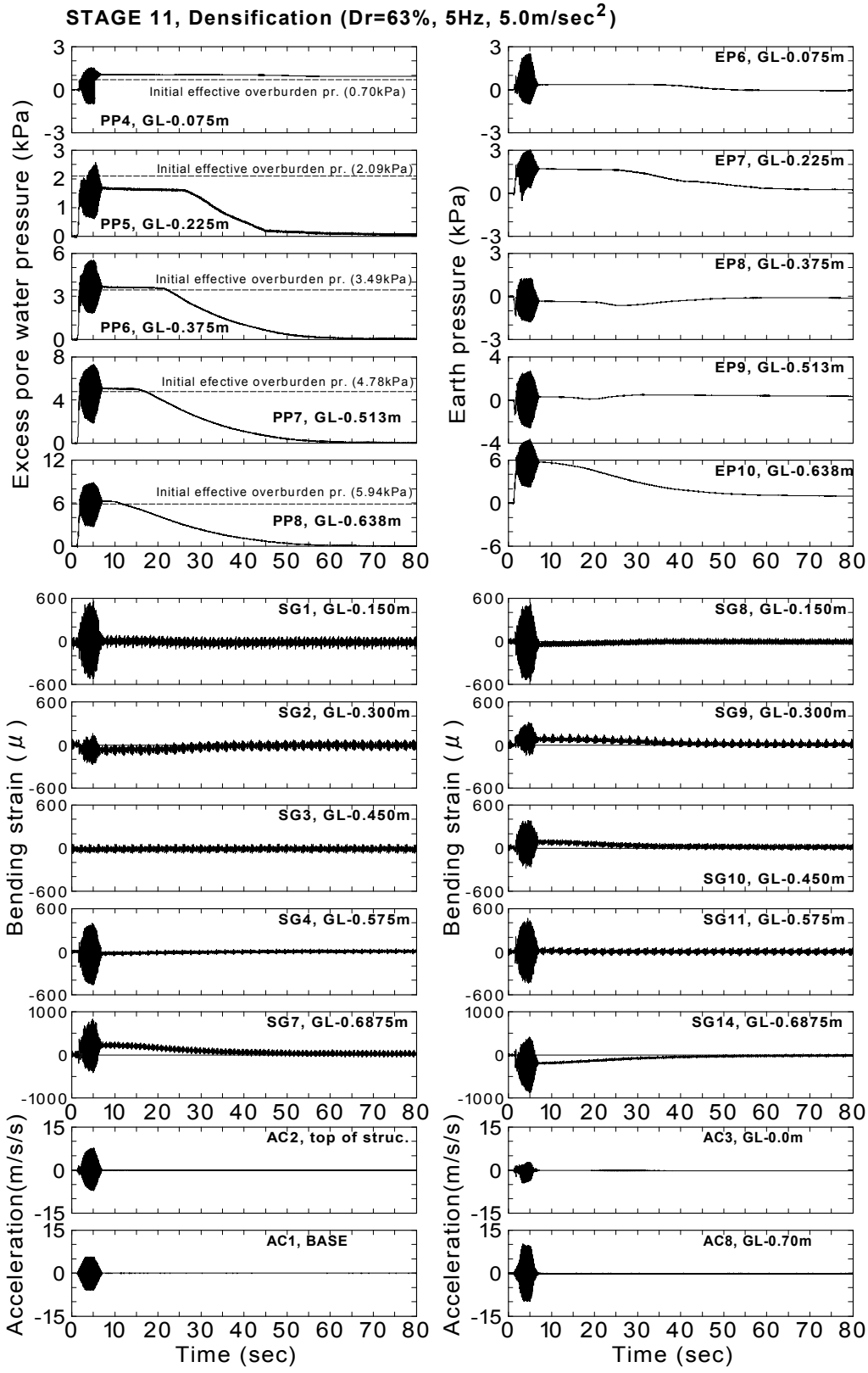

Fig. 3.45: Time histories for Stage 11 of Model No.1 (Densification)

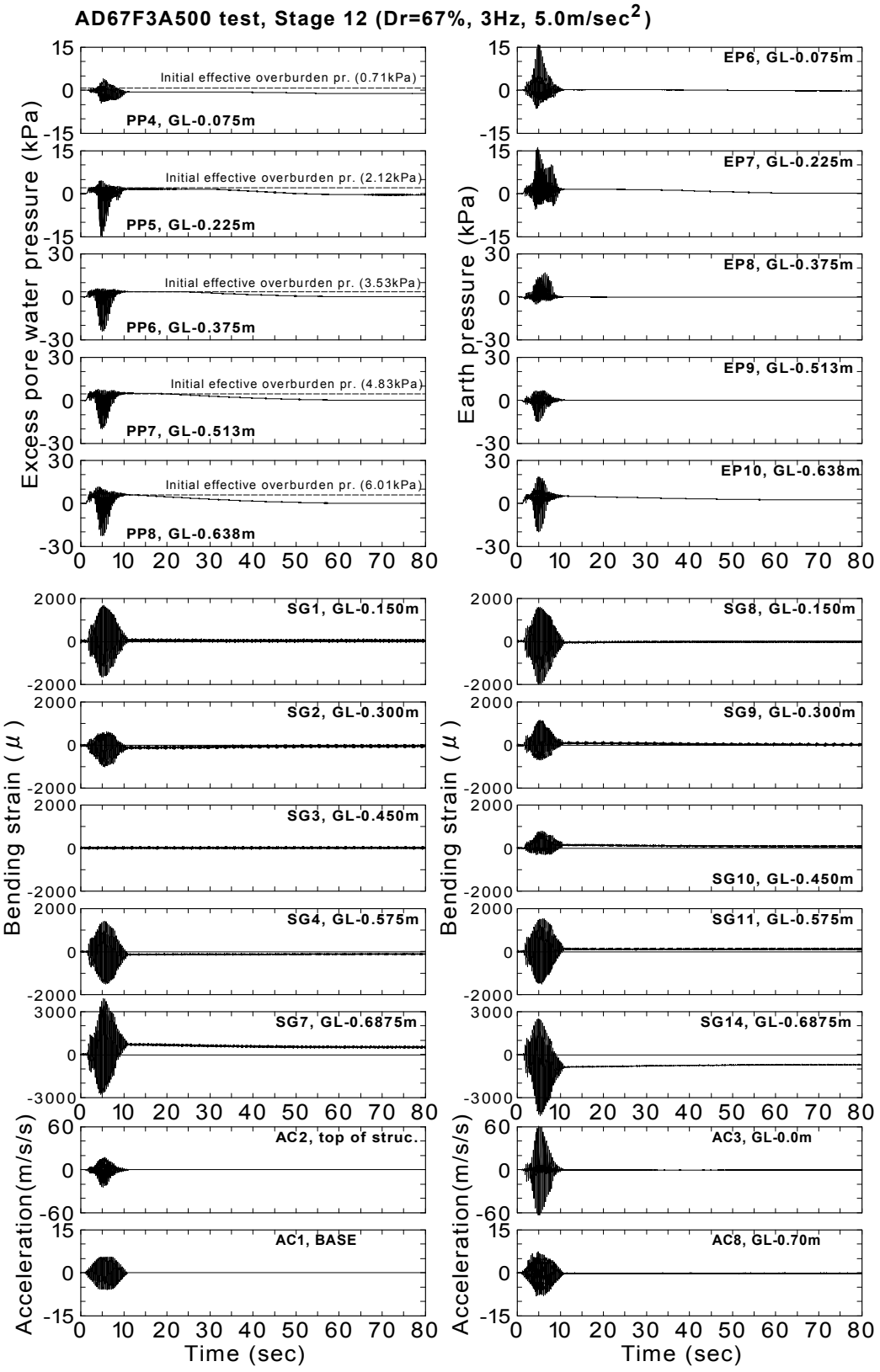

Fig. 3.46: Time histories for Stage 12 of Model No.1 (AD67F3A500 test)

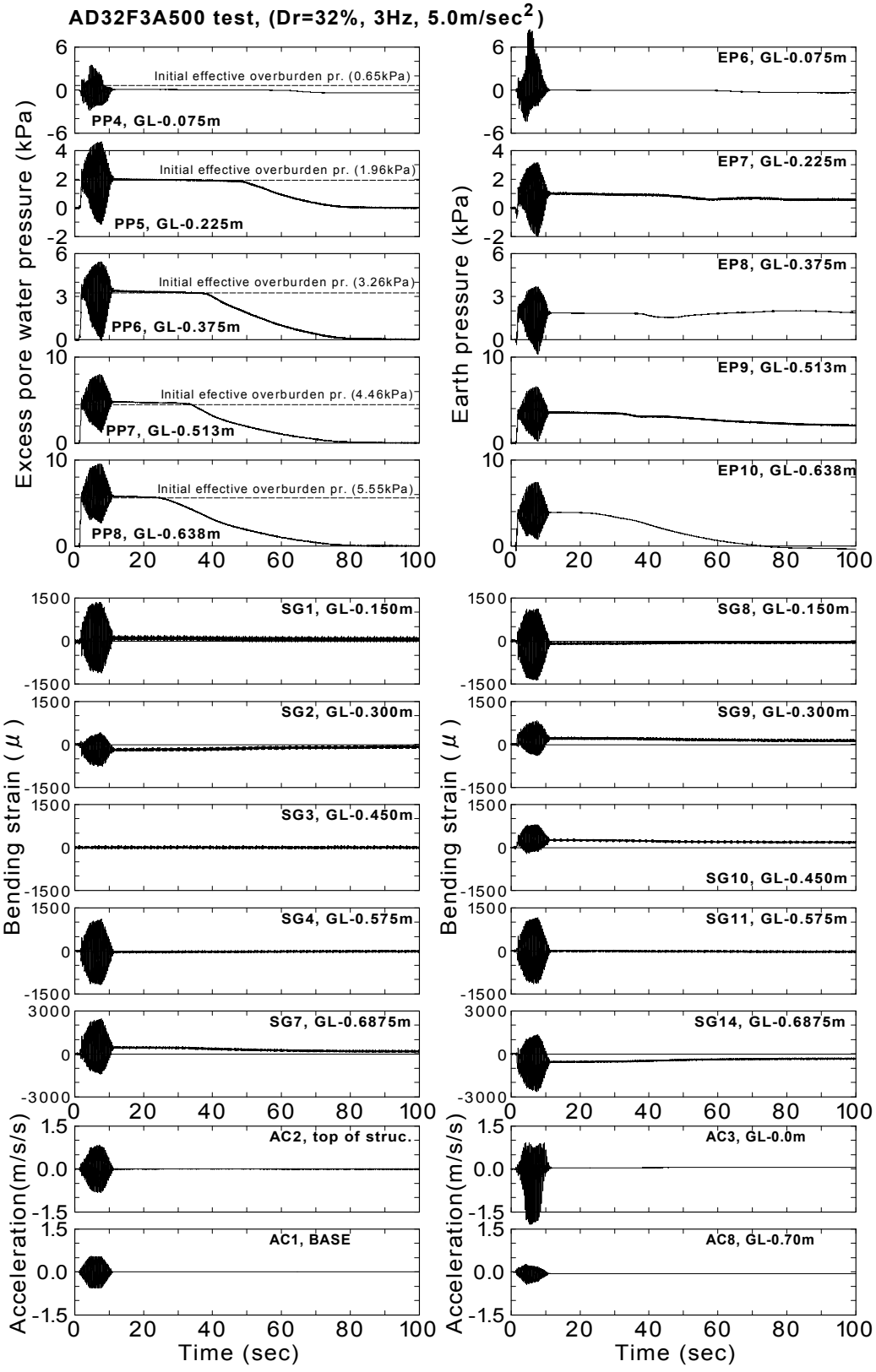

Fig. 3.47: Time histories for AD32F3A500 test (Model-2)

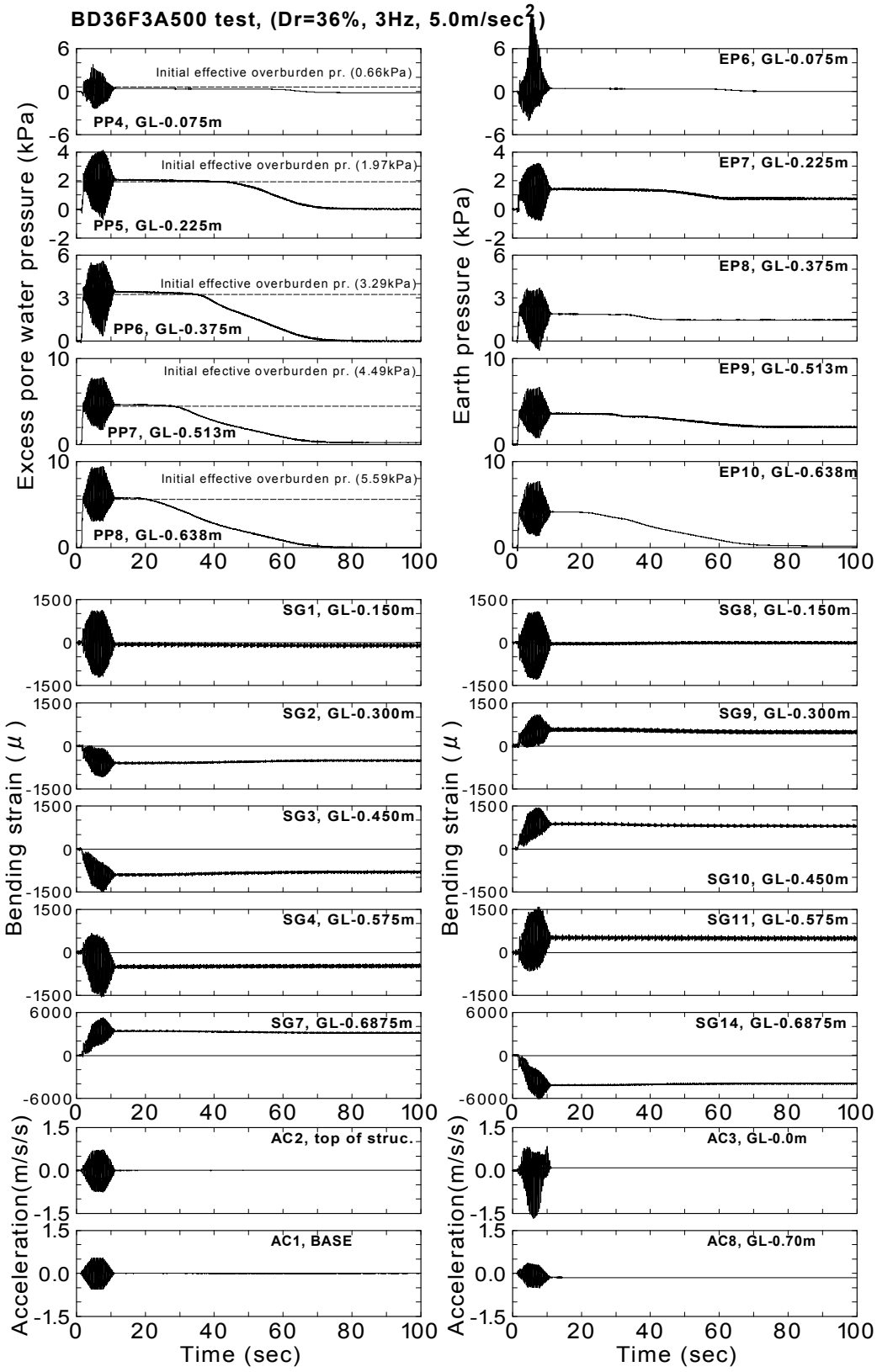

Fig. 3.48: Time histories for BD36F3A500 test (Model-3)

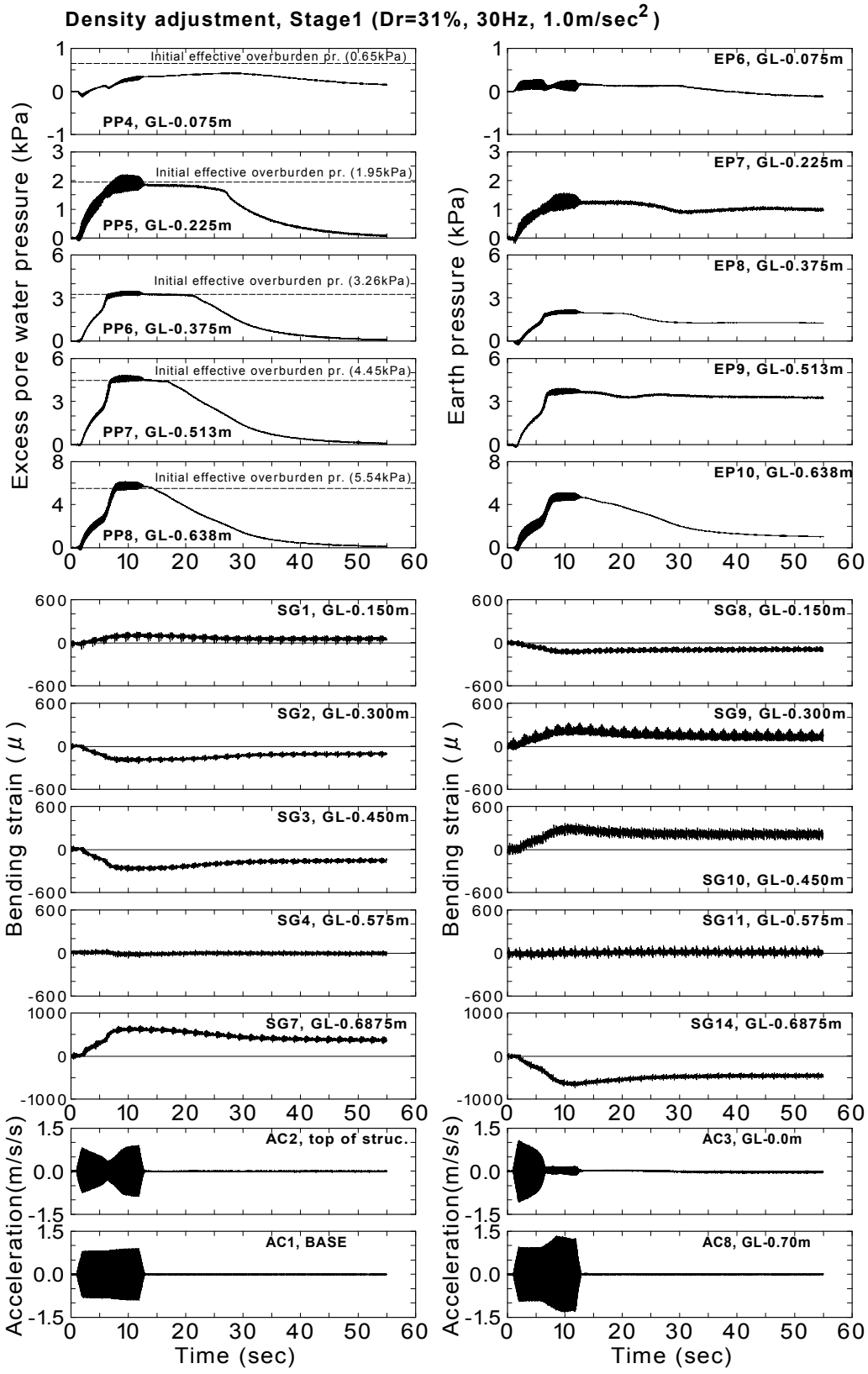

Fig. 3.49: Time histories for Stage 1 excitation (Model-4)

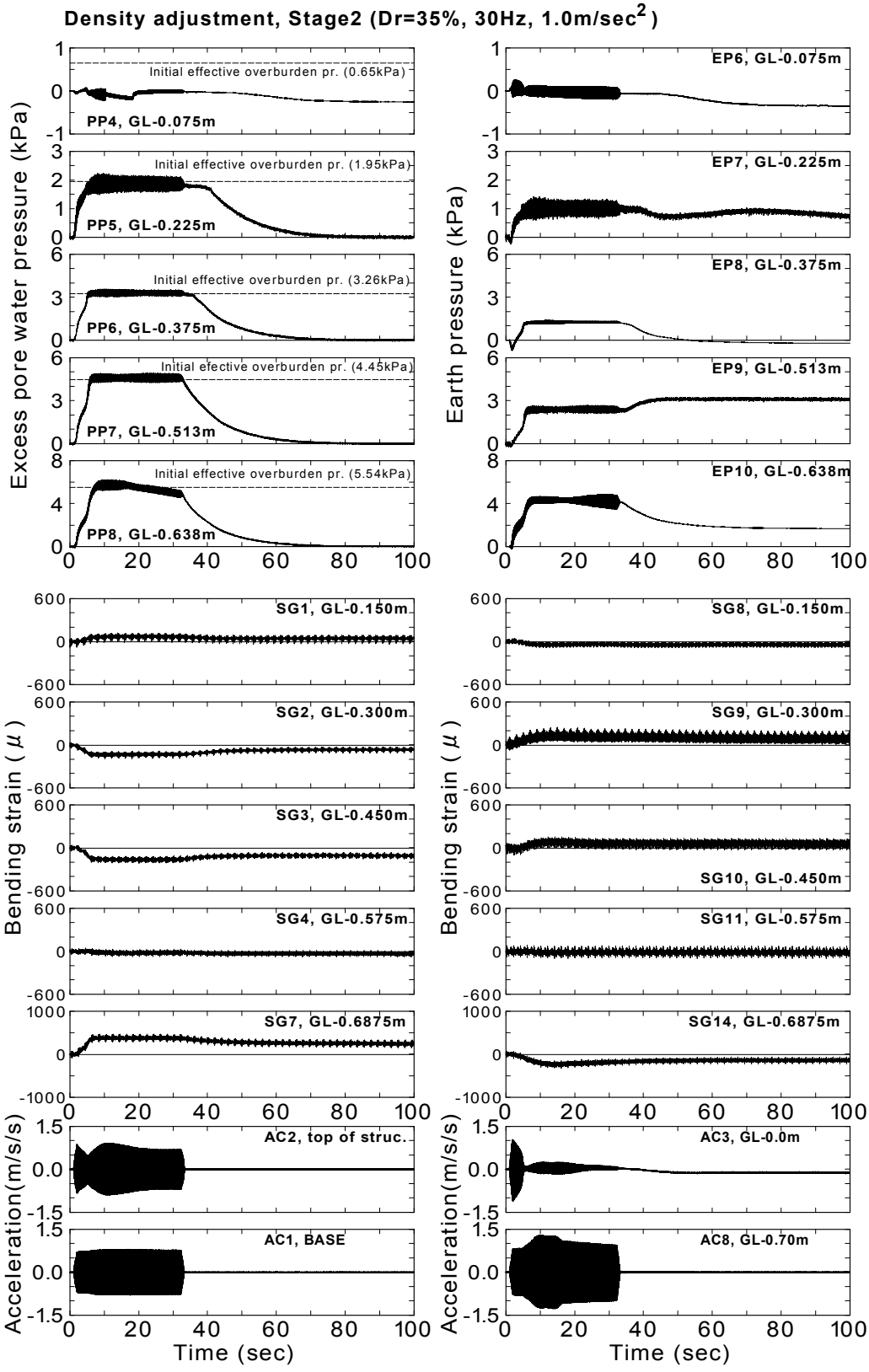

Fig. 3.50: Time histories for Stage 2 excitation (Model-4)

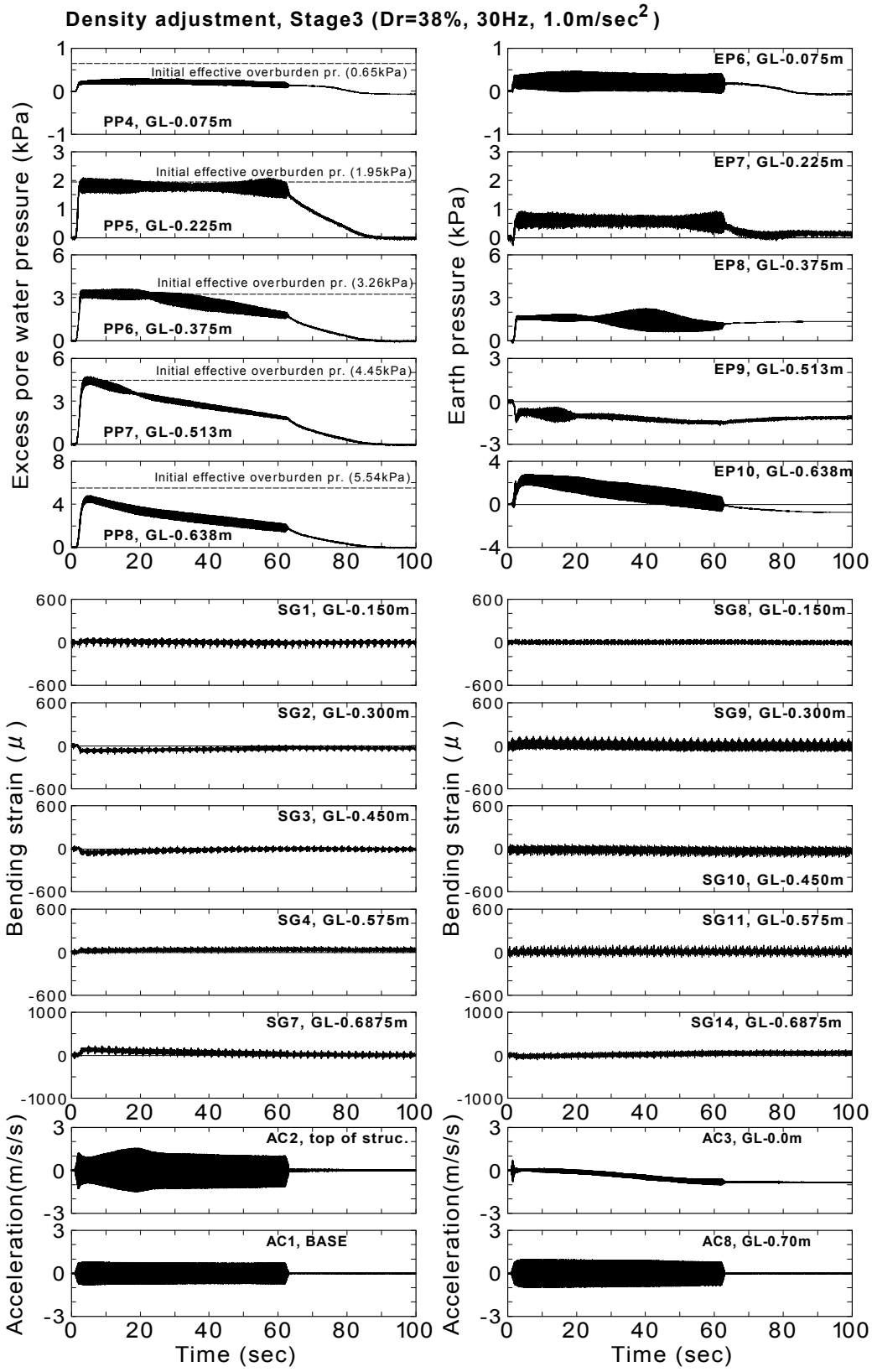

Fig. 3.51: Time histories for Stage 3 excitation (Model-4)

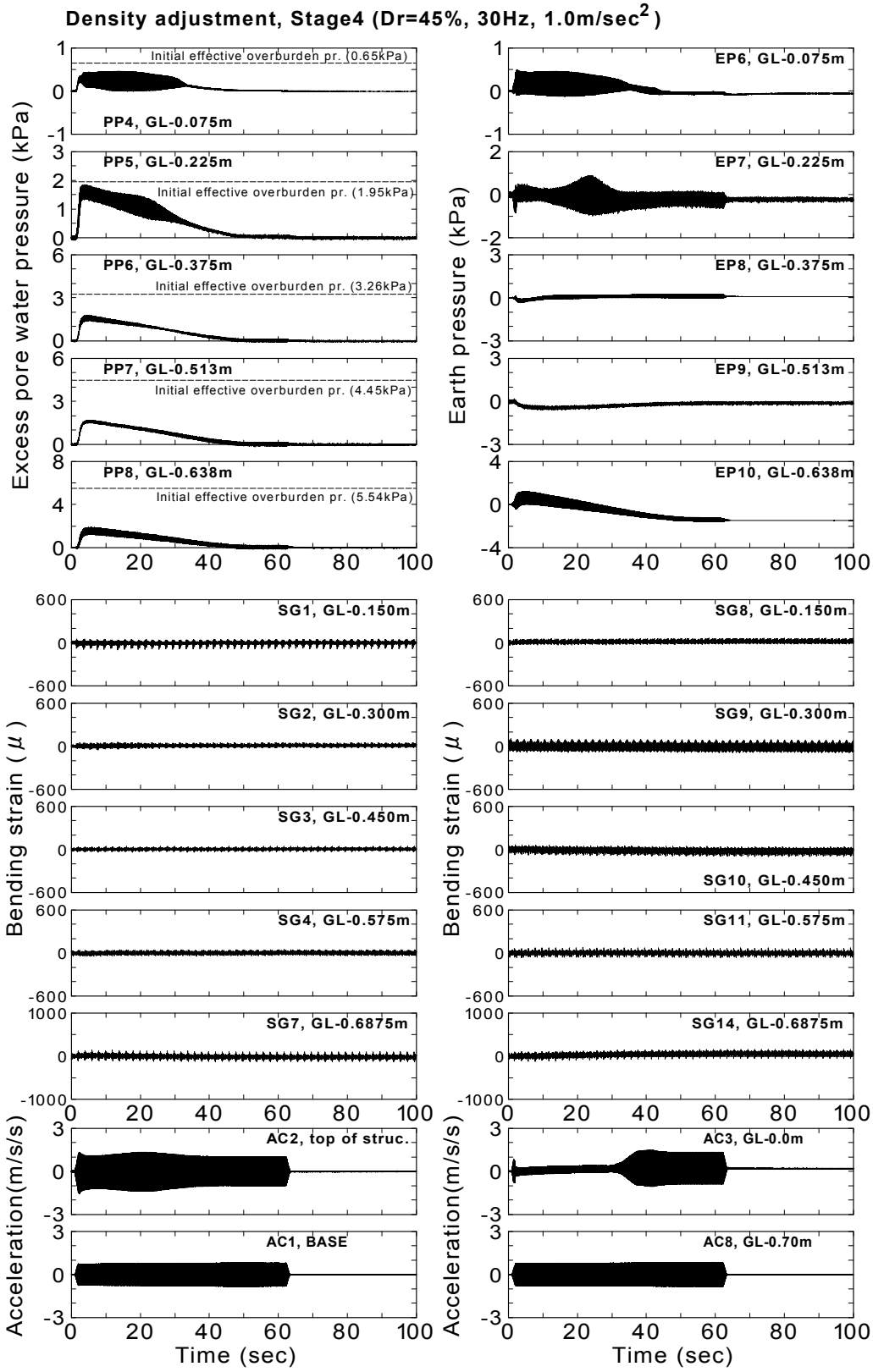

Fig. 3.52: Time histories for Stage 4 excitation (Model-4)

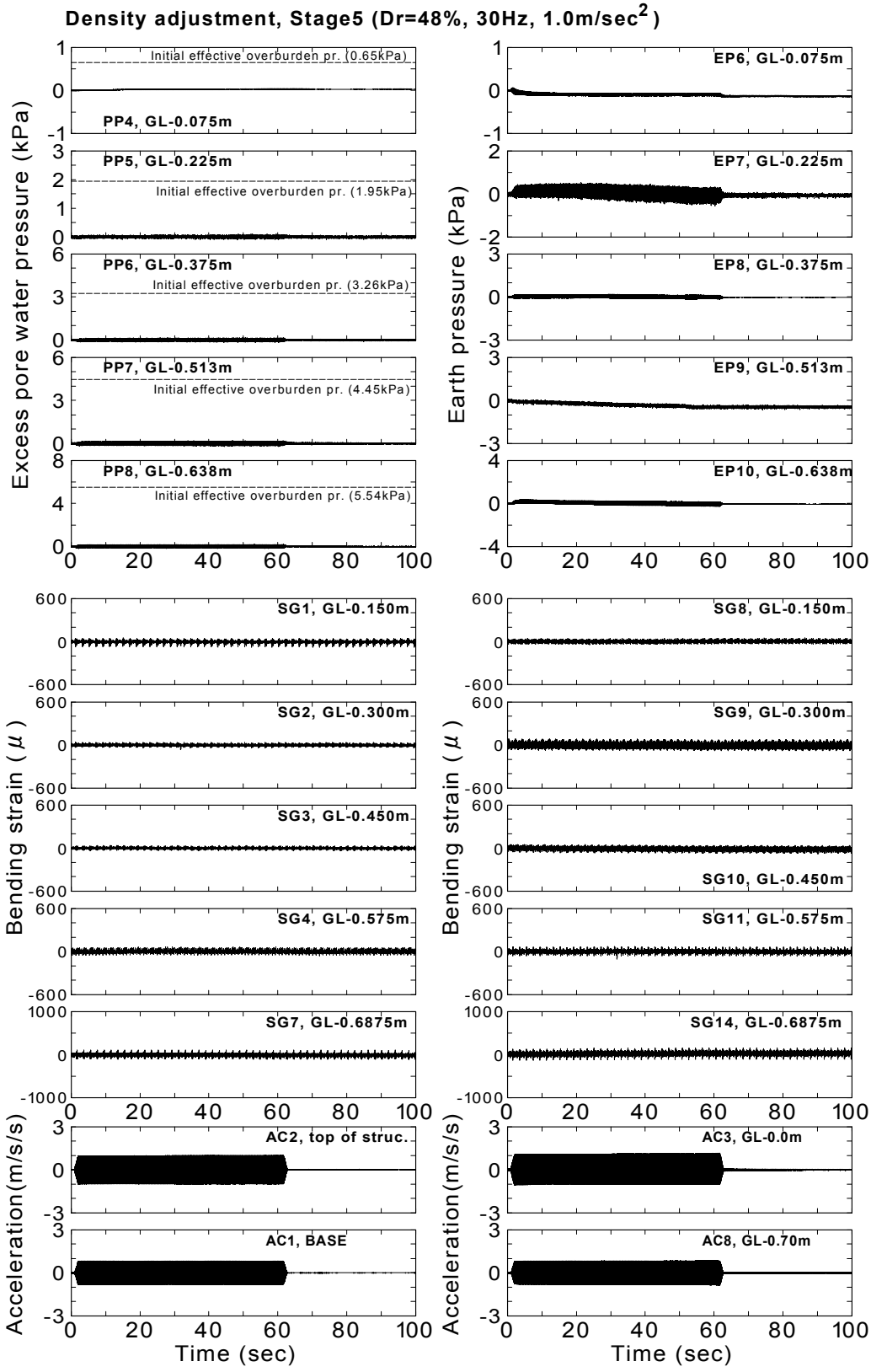

Fig. 3.53: Time histories for Stage 5 excitation (Model-4)

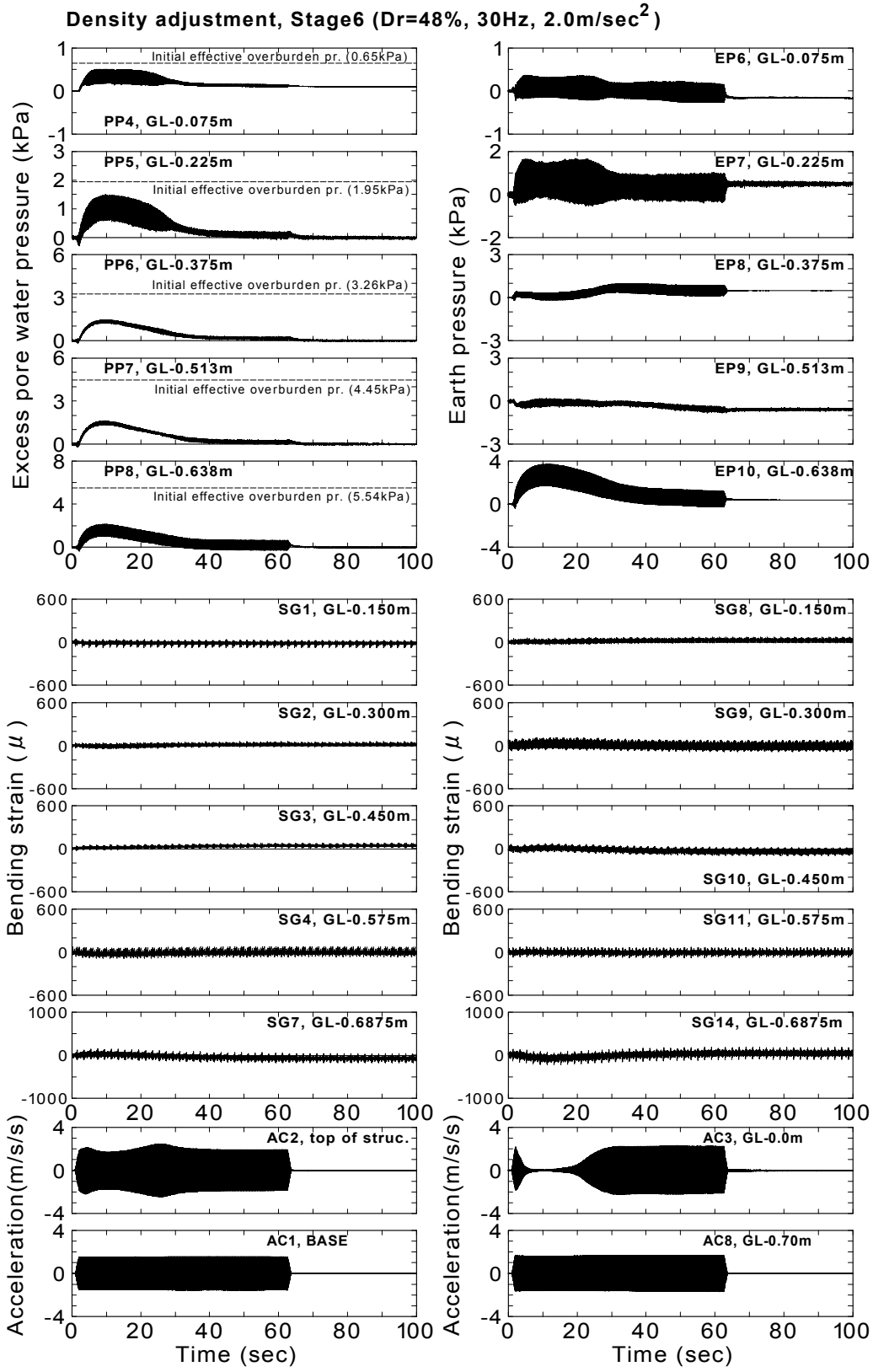

Fig. 3.54: Time histories for Stage 6 excitation (Model-4)

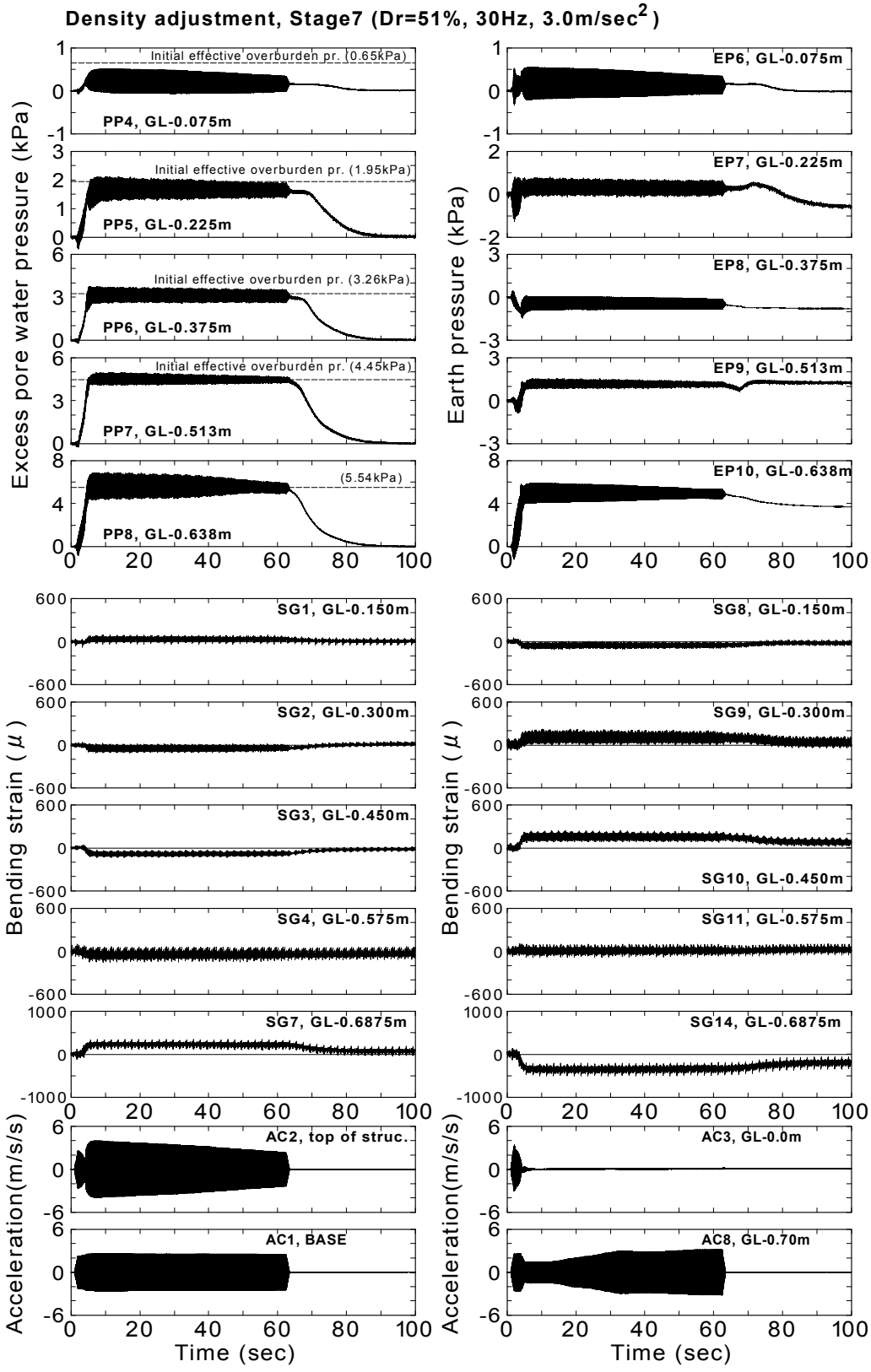

Fig. 3.55: Time histories for Stage 7 excitation (Model-4)

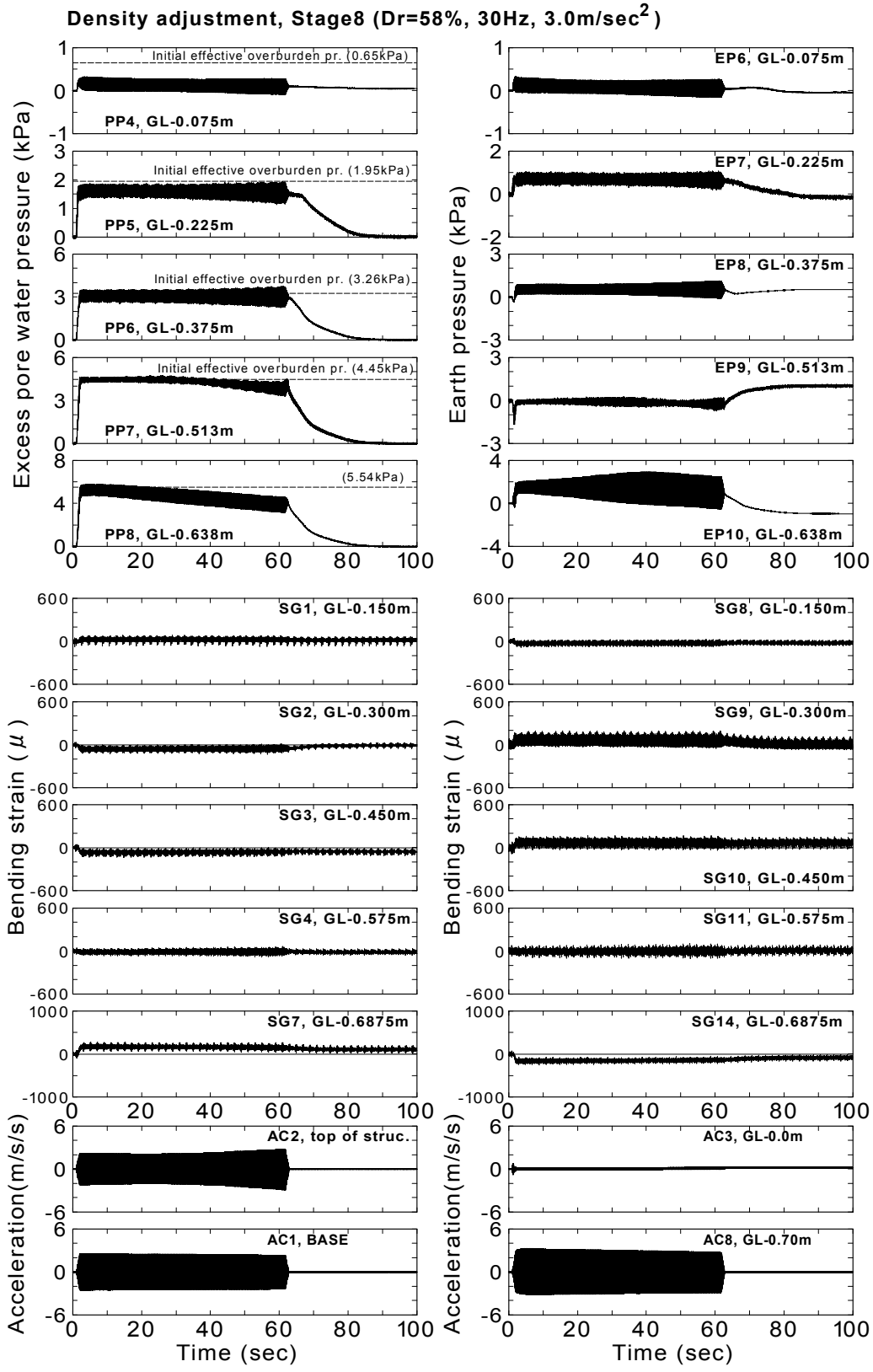

Fig. 3.56: Time histories for Stage 8 excitation (Model-4)

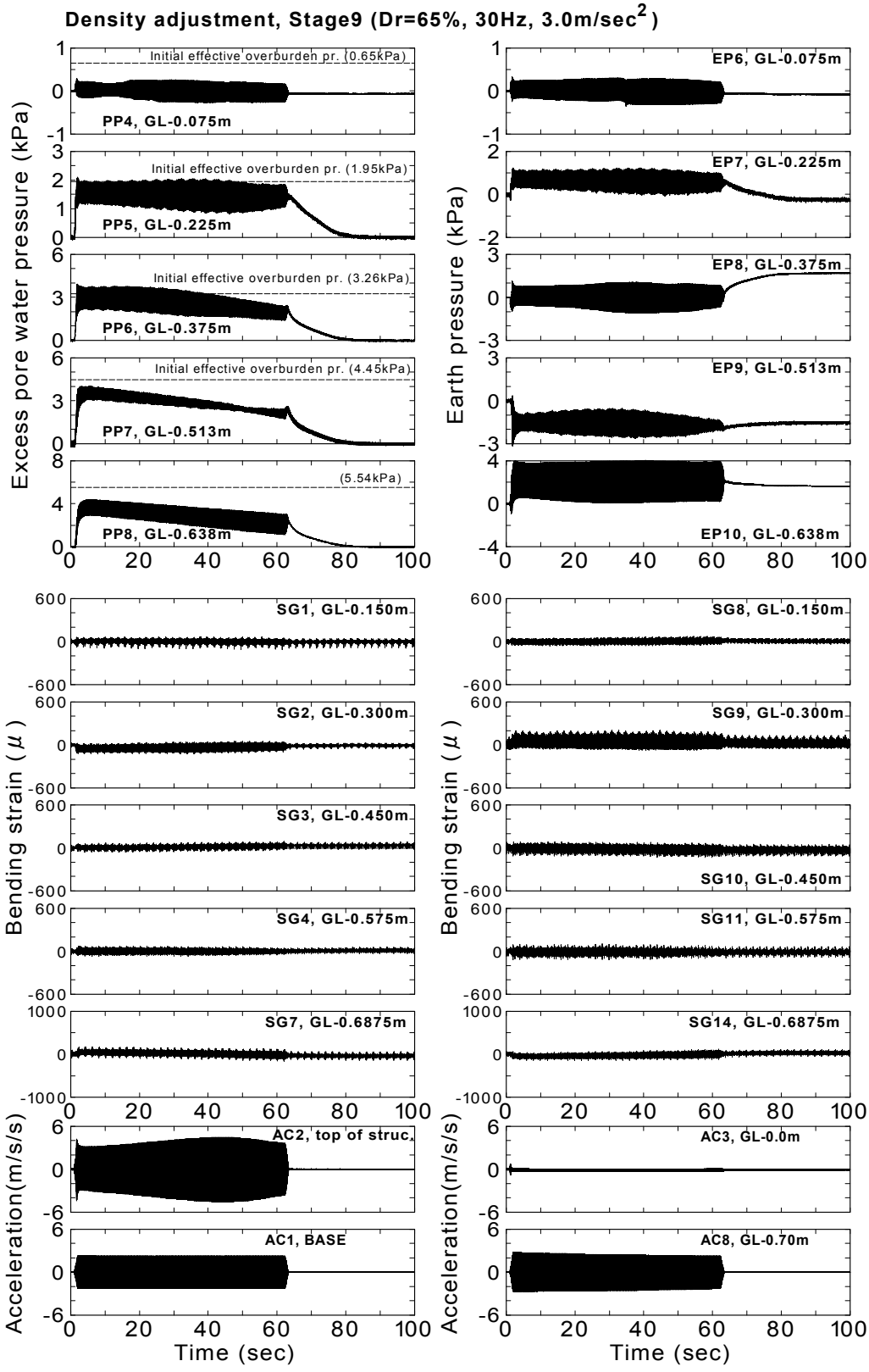

Fig. 3.57: Time histories for Stage 9 excitation (Model-4)

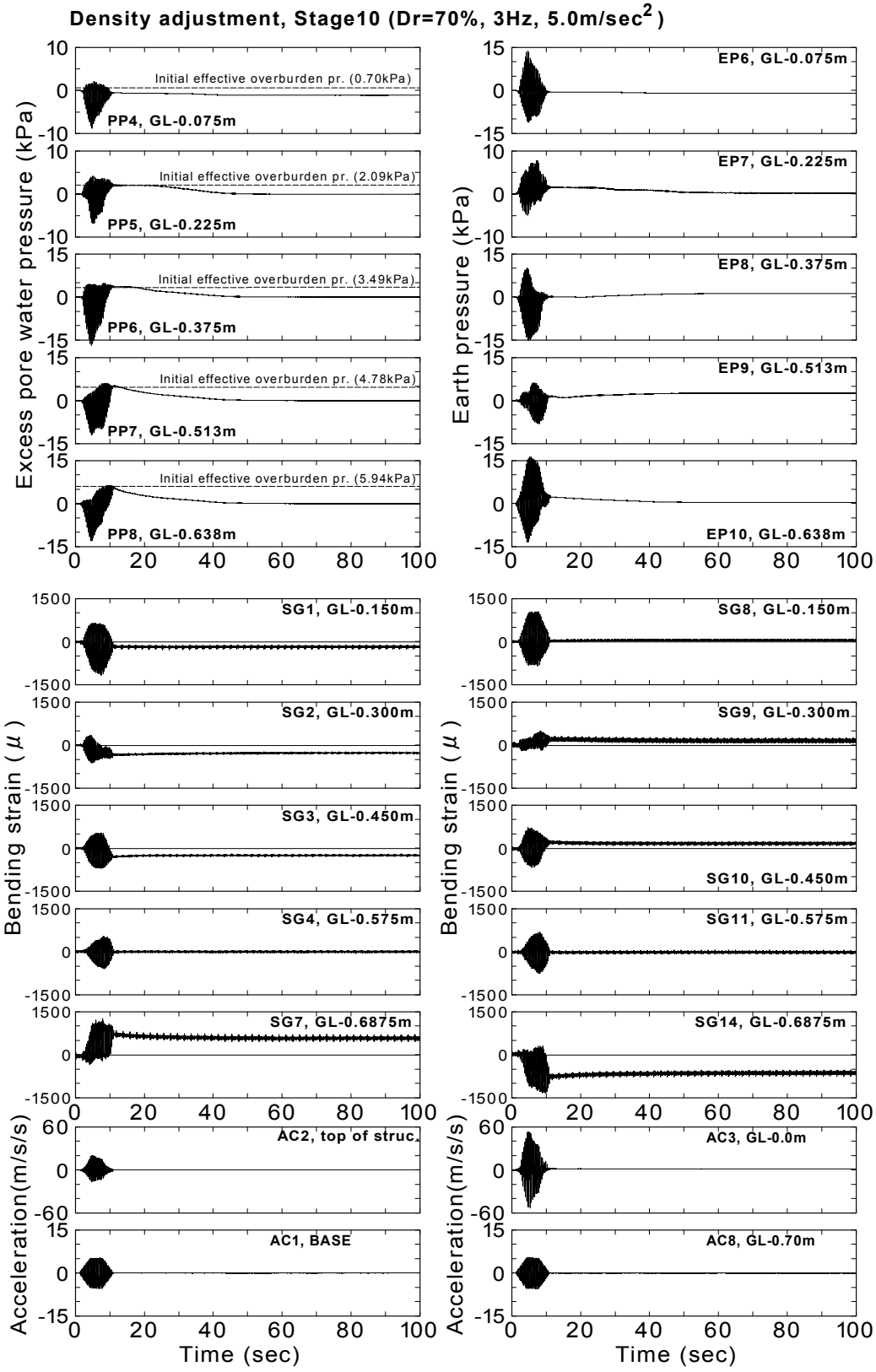

Fig. 3.58: Time histories for Stage 10 excitation (Model-4)

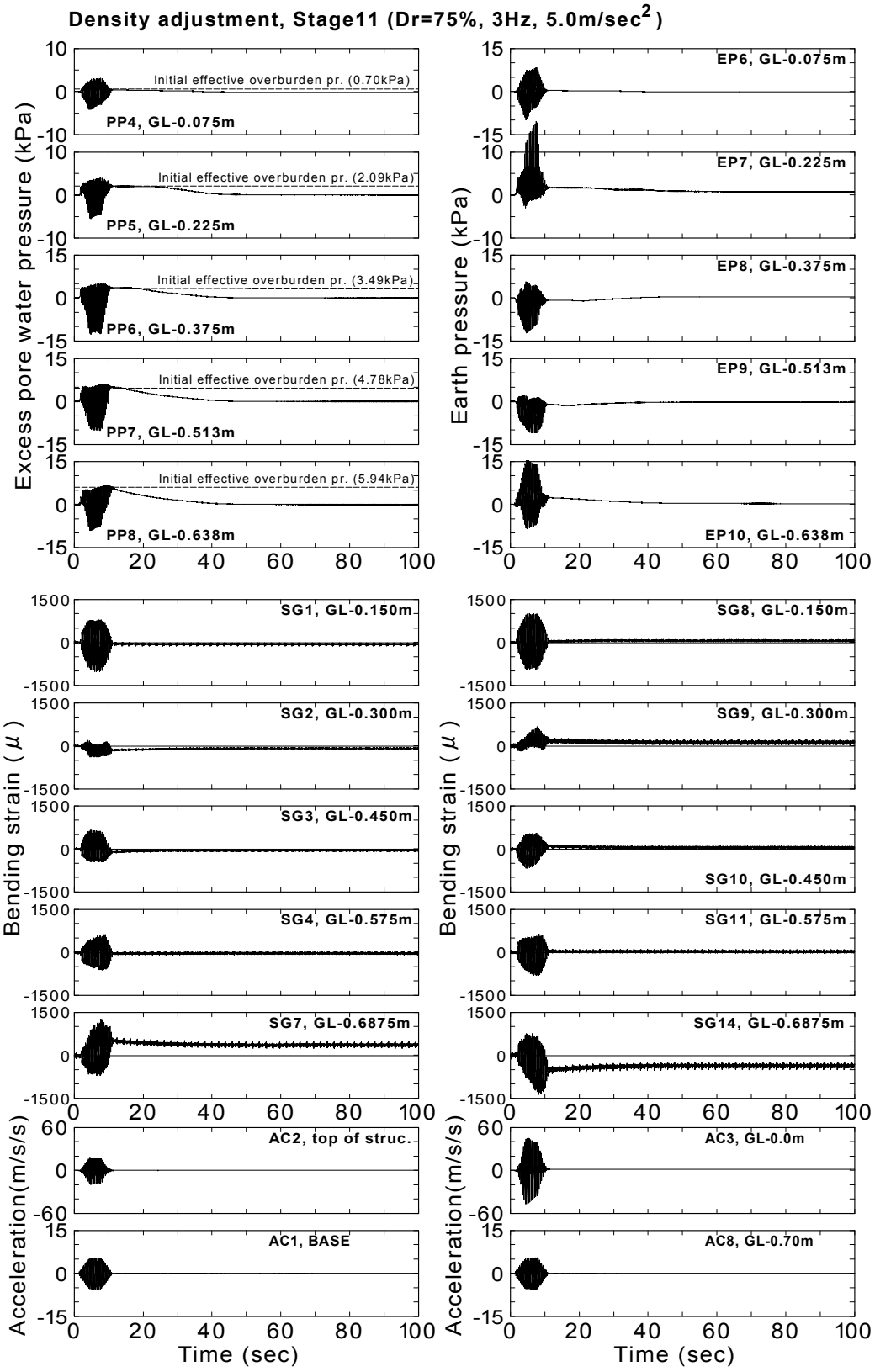

Fig. 3.59: Time histories for Stage 11 excitation (Model-4)

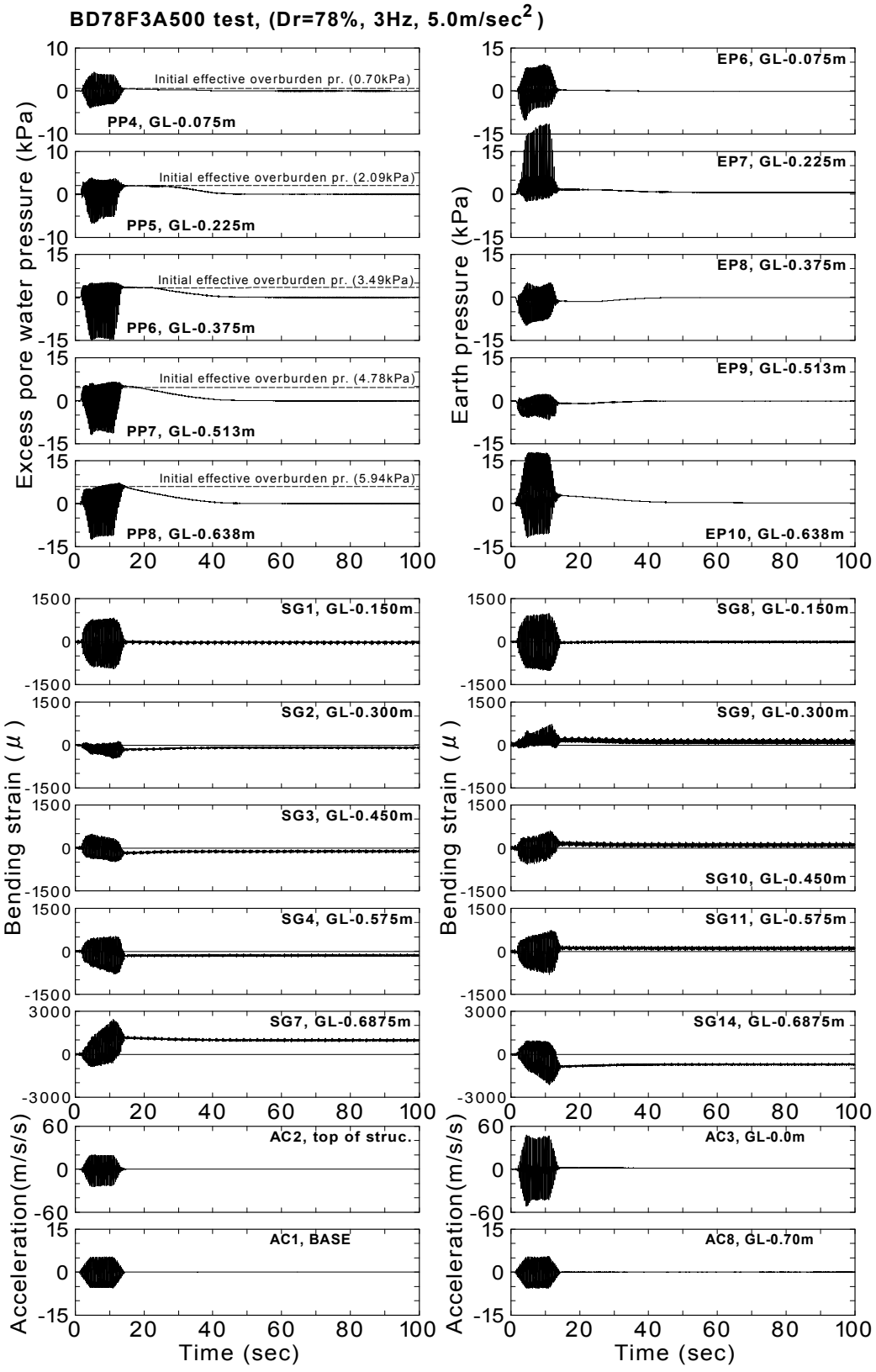

Fig. 3.60: Time histories for BD78F3A500 test (Model-4, Stage 12)

Table 3.18: Earth pressures at each stage of excitation (Model-1, Structure-A)

(a) EP6 (GL-0.075m) and EP7 (GL-0.225m)

No.	Initial values			Residual values after dissipation		
	Relative density (%)	EP6	EP7	Density attained (%)	Δ EP6	Δ EP7
1	35	0.771	3.023	39	-0.291	0.472
2	39	0.480	3.495	41	0.007	0.462
3	41	0.487	3.957	46	0.255	-0.048
4	46	0.742	3.909	50	0.065	0.363
5	50	0.807	4.272	54	0.079	0.244
6	54	0.886	4.516	59	0.091	0.107
7	59	0.977	4.623	59	-0.344	1.109
8	59	0.633	5.732	59	-0.046	0.095
9	59	0.587	5.827	61	-0.384	0.402
10	61	0.203	6.229	63	-0.068	-0.205
11	63	0.135	6.024	67	-0.060	0.238

(b) EP8 (GL-0.375m) and EP9 (GL-0.513m)

No.	Initial values			Residual values after dissipation		
	Relative density (%)	EP8	EP9	Density attained (%)	Δ EP8	Δ EP9
1	35	3.841	5.996	39	1.283	3.403
2	39	5.124	9.399	41	1.404	2.978
3	41	6.528	12.377	46	0.802	-1.266
4	46	7.330	11.111	50	0.692	0.035
5	50	8.022	11.146	54	-0.383	-1.287
6	54	7.639	9.859	59	0.088	-0.897
7	59	7.727	8.962	59	3.017	3.546
8	59	10.744	12.508	59	-0.552	-0.765
9	59	10.192	11.743	61	0.006	1.458
10	61	10.198	13.201	63	-0.564	-0.368
11	63	9.634	12.833	67	-0.118	0.342

(c) EP10 (GL-0.638m)

No.	Initial values		Residual values after dissipation	
	Relative density (%)	EP10	Density attained (%)	Δ EP10
1	35	7.875	39	1.871
2	39	9.746	41	-0.233
3	41	9.513	46	-1.562
4	46	7.951	50	2.113
5	50	10.064	54	-1.004
6	54	9.060	59	-0.676
7	59	8.384	59	1.258
8	59	9.642	59	-0.526
9	59	9.116	61	2.204
10	61	11.320	63	-0.813
11	63	10.507	67	0.966

Table 3.19: Earth pressures at each stage of excitation (Model-1, Soil)

(a) EP1 (GL-0.075m) and EP2 (GL-0.225m)

No.	Initial values			Residual values after dissipation		
	Relative density (%)	EP1 (EP6)	EP2 (EP7)	Density attained (%)	Δ EP1	Δ EP2
1	35	(0.771)	(3.023)	39	-0.058	1.998
2	39	0.713	5.021	41	0.063	-0.069
3	41	0.776	4.952	46	-0.035	-1.028
4	46	0.741	3.924	50	0.019	-0.090
5	50	0.760	3.834	54	-0.001	-0.041
6	54	0.759	3.793	59	-0.036	0.680
7	59	0.723	4.473	59	0.112	2.207
8	59	0.835	6.680	59	-0.013	0.274
9	59	0.822	6.954	61	-0.175	-0.850
10	61	0.647	6.104	63	-0.084	-0.070
11	63	0.563	6.034	67	0.032	0.606

(b) EP3 (GL-0.375m) and EP4 (GL-0.513m)

No.	Initial values			Residual values after dissipation		
	Relative density (%)	EP3 (EP8)	EP4 (EP9)	Density attained (%)	Δ EP3	Δ EP4
1	35	(3.841)	(5.996)	39	1.793	1.213
2	39	5.634	7.209	41	0.411	0.918
3	41	6.045	8.127	46	1.985	-0.141
4	46	8.030	7.986	50	0.213	0.833
5	50	8.243	8.819	54	-1.484	1.067
6	54	6.759	9.886	59	-1.630	0.174
7	59	5.129	10.060	59	3.136	3.258
8	59	8.265	13.318	59	0.449	0.184
9	59	8.714	13.502	61	0.198	1.161
10	61	8.912	14.663	63	0.896	-0.163
11	63	9.808	14.500	67	0.815	-0.865

(c) EP5 (GL-0.638m)

No.	Initial values		Residual values after dissipation	
	Relative density (%)	EP5 (EP10)	Density attained (%)	Δ EP5
1	35	(7.875)	39	1.822
2	39	9.697	41	0.616
3	41	10.313	46	-1.810
4	46	8.503	50	0.167
5	50	8.670	54	3.284
6	54	11.954	59	-1.102
7	59	10.852	59	1.971
8	59	12.823	59	-0.526
9	59	12.297	61	1.257
10	61	13.554	63	-0.132
11	63	13.422	67	-0.148

Table 3.20: Bending strains at each stage of excitation (Model-1, Structure-A)

(a) SG1 (GL-0.150m) and SG2 (GL-0.300m)

No.	Initial values			Residual values after dissipation		
	Relative density (%)	SG1	SG2	Density attained (%)	Δ SG1	Δ SG2
1	35	180	-406	39	86	-146
2	39	266	-552	41	-5	-26
3	41	261	-578	46	10	8
4	46	271	-570	50	5	-41
5	50	276	-611	54	24	14
6	54	300	-597	59	14	-11
7	59	314	-608	59	46	-112
8	59	360	-720	59	-21	-16
9	59	339	-736	61	10	-51
10	61	349	-787	63	-8	-5
11	63	341	-792	67	-15	-2

(b) SG3 (GL-0.450m) and SG4 (GL-0.575m)

No.	Initial values			Residual values after dissipation		
	Relative density (%)	SG3 (SG10)	SG4	Density attained (%)	Δ SG3 (Δ SG10)	Δ SG4
1	35	-500	-41	39	(-166)	-28
2	39	(-666)	-69	41	(-34)	-10
3	41	(-700)	-79	46	(5)	11
4	46	(-695)	-68	50	(-35)	-5
5	50	(-730)	-73	54	(12)	-6
6	54	(-718)	-79	59	(-16)	-9
7	59	(-734)	-88	59	(-127)	-5
8	59	(-861)	-93	59	(2)	3
9	59	(-859)	-90	61	(-24)	-15
10	61	(-883)	-105	63	(1)	-3
11	63	(-882)	-108	67	(-14)	6

(c) SG5 (GL-0.6375m) and SG6 (GL-0.6625m)

No.	Initial values			Residual values after dissipation		
	Relative density (%)	SG5	SG6	Density attained (%)	Δ SG5	Δ SG6
1	35	448	695	39	192	252
2	39	640	947	41	46	82
3	41	686	1029	46	-29	-54
4	46	657	975	50	58	69
5	50	715	1044	54	-18	-27
6	54	697	1017	59	7	9
7	59	704	1026	59	122	185
8	59	826	1211	59	-29	-38
9	59	797	1173	61	62	94
10	61	859	1267	63	-12	17
11	63	847	1284	67	-7	26

Table 3.20: Continued

(d) SG7 (GL-0.6875m)

No.	Initial values		Residual values after dissipation	
	Relative density (%)	SG7	Density attained (%)	Δ SG7
1	35	915	39	317
2	39	1232	41	94
3	41	1326	46	-66
4	46	1260	50	88
5	50	1348	54	-34
6	54	1314	59	27
7	59	1341	59	238
8	59	1579	59	-48
9	59	1531	61	131
10	61	1662	63	30
11	63	1692	67	18

(e) SG8 (GL-0.150m) and SG9 (GL-0.300m)

No.	Initial values			Residual values after dissipation		
	Relative density (%)	SG8 (SG1)	SG9 (SG2)	Density attained (%)	Δ SG8	Δ SG9
1	35	(-180)	(406)	39	-71	101
2	39	-251	507	41	-18	22
3	41	-269	529	46	27	-4
4	46	-242	525	50	-17	7
5	50	-259	532	54	26	0
6	54	-233	532	59	16	2
7	59	-217	534	59	-69	82
8	59	-286	616	59	18	-23
9	59	-268	593	61	-35	36
10	61	-303	629	63	8	10
11	63	-295	639	67	-8	4

(f) SG10 (GL-0.450m) and SG11 (GL-0.575m)

No.	Initial values			Residual values after dissipation		
	Relative density (%)	SG10 (SG3)	SG11 (SG4)	Density attained (%)	Δ SG10	Δ SG11
1	35	(500)	(41)	39	166	0
2	39	666	41	41	34	17
3	41	700	58	46	-5	-25
4	46	695	33	50	35	11
5	50	730	44	54	-12	-21
6	54	718	23	59	16	-9
7	59	734	14	59	127	-4
8	59	861	10	59	-2	-2
9	59	859	8	61	24	30
10	61	883	38	63	-1	1
11	63	882	39	67	14	1

Table 3.20: Continued

(g) SG12 (GL-0.6375m) and SG13 (GL-0.6625m)

No.	Initial values			Residual values after dissipation		
	Relative density (%)	SG12 (SG5)	SG13 (SG6)	Density attained (%)	Δ SG12	Δ SG13
1	35	(-448)	(-695)	39	-165	-247
2	39	-613	-942	41	-14	-39
3	41	-627	-981	46	10	13
4	46	-617	-968	50	-2	-27
5	50	-619	-995	54	-13	-13
6	54	-632	-1008	59	3	3
7	59	-629	-1005	59	-121	-188
8	59	-750	-1193	59	23	32
9	59	-727	-1161	61	-23	-54
10	61	-750	-1215	63	19	-1
11	63	-731	-1216	67	5	-6

(h) SG14 (GL-0.6875m)

No.	Initial values		Residual values after dissipation	
	Relative density (%)	SG14 (SG7)	Density attained (%)	Δ SG14
1	35	(-915)	39	-313
2	39	-1228	41	-53
3	41	-1281	46	19
4	46	-1262	50	-43
5	50	-1305	54	-19
6	54	-1324	59	-24
7	59	-1348	59	-236
8	59	-1584	59	37
9	59	-1547	61	-76
10	61	-1623	63	5
11	63	-1618	67	-15

Table 3.21: Earth pressures at each stage of excitation (Model-4, Structure-B2)

(a) EP6 (GL-0.075m) and EP7 (GL-0.225m)

No.	Initial values			Residual values after dissipation		
	Relative density (%)	EP6	EP7	Density attained (%)	Δ EP6	Δ EP7
1	31	0.426	1.599	35	-0.112	0.970
2	35	0.314	2.569	38	-0.344	0.718
3	38	-0.030	3.287	45	-0.070	0.140
4	45	-0.100	3.427	48	-0.059	-0.203
5	48	-0.159	3.224	48	-0.131	-0.056
6	48	-0.290	3.168	51	-0.163	0.497
7	51	-0.453	3.665	58	-0.015	-0.546
8	58	-0.468	3.119	65	-0.043	-0.137
9	65	-0.511	2.982	70	-0.079	-0.234
10	70	-0.590	2.748	75	-0.976	0.231
11	75	-1.566	2.979	78	-0.095	0.760

(b) EP8 (GL-0.375m) and EP9 (GL-0.513m)

No.	Initial values			Residual values after dissipation		
	Relative density (%)	EP8	EP9	Density attained (%)	Δ EP8	Δ EP9
1	31	2.805	4.188	35	1.235	3.207
2	35	4.040	7.395	38	-0.207	3.037
3	38	3.833	10.432	45	1.324	-1.118
4	45	5.157	9.314	48	0.083	-0.111
5	48	5.240	9.203	48	-0.029	-0.434
6	48	5.211	8.769	51	0.473	-0.553
7	51	5.684	8.216	58	-0.773	1.232
8	58	4.911	9.448	65	0.514	1.010
9	65	5.425	10.458	70	1.648	-1.504
10	70	7.073	8.954	75	1.191	2.463
11	75	8.264	11.417	78	0.440	-0.213

(c) EP10 (GL-0.638m)

No.	Initial values		Residual values after dissipation	
	Relative density (%)	EP10	Density attained (%)	Δ EP10
1	31	5.136	35	1.007
2	35	6.143	38	1.636
3	38	7.779	45	-0.735
4	45	7.044	48	-1.456
5	48	5.588	48	-0.055
6	48	5.533	51	0.372
7	51	5.905	58	3.639
8	58	9.544	65	-0.948
9	65	8.596	70	1.600
10	70	10.196	75	0.328
11	75	10.524	78	0.282

Table 3.22: Earth pressures at each stage of excitation (Model-4, Soil)

(a) EP1 (GL-0.075m) and EP2 (GL-0.225m)

No.	Initial values			Residual values after dissipation		
	Relative density (%)	EP1 (EP6)	EP2 (EP7)	Density attained (%)	Δ EP1	Δ EP2
1	31	(0.426)	(1.599)	35	-0.034	0.715
2	35	0.392	2.314	38	-0.415	1.309
3	38	-0.023	3.623	45	-0.139	-0.129
4	45	-0.162	3.494	48	-0.144	0.052
5	48	-0.306	3.546	48	-0.076	0.195
6	48	-0.382	3.741	51	-0.278	-0.334
7	51	-0.660	3.407	58	-0.099	-0.178
8	58	-0.759	3.229	65	0.012	0.235
9	65	-0.747	3.464	70	-0.155	-0.985
10	70	-0.902	2.479	75	-0.519	-0.274
11	75	-1.421	2.205	78	-0.168	0.533

(b) EP3 (GL-0.375m) and EP4 (GL-0.513m)

No.	Initial values			Residual values after dissipation		
	Relative density (%)	EP3 (EP8)	EP4 (EP9)	Density attained (%)	Δ EP3	Δ EP4
1	31	(2.805)	(4.188)	35	1.760	2.798
2	35	4.565	6.986	38	1.426	1.714
3	38	5.991	8.700	45	0.846	-1.301
4	45	6.837	7.399	48	0.230	-0.541
5	48	7.067	6.858	48	0.235	-0.251
6	48	7.302	6.607	51	0.233	-0.431
7	51	7.535	6.176	58	0.894	2.188
8	58	8.429	8.364	65	-0.266	-0.520
9	65	8.163	7.844	70	-0.477	0.099
10	70	7.686	7.943	75	0.727	0.098
11	75	8.413	8.041	78	1.887	0.068

(c) EP5 (GL-0.638m)

No.	Initial values		Residual values after dissipation	
	Relative density (%)	EP5 (EP10)	Density attained (%)	Δ EP5
1	31	(5.136)	35	1.685
2	35	6.821	38	0.788
3	38	7.609	45	-1.522
4	45	6.087	48	-0.517
5	48	5.570	48	0.194
6	48	5.764	51	0.060
7	51	5.824	58	0.758
8	58	6.582	65	2.173
9	65	8.755	70	-0.285
10	70	8.470	75	0.421
11	75	8.891	78	-0.212

Table 3.23: Bending strains at each stage of excitation (Model-4, Structure-B2)

(a) SG1 (GL-0.150m) and SG2 (GL-0.300m)

No.	Initial values			Residual values after dissipation		
	Relative density (%)	SG1	SG2	Density attained (%)	Δ SG1	Δ SG2
1	31	147	-323	35	54	-105
2	35	201	-428	38	47	-62
3	38	248	-490	45	2	-37
4	45	250	-527	48	1	16
5	48	251	-511	48	-4	-3
6	48	247	-514	51	-17	21
7	51	230	-493	58	6	12
8	58	236	-481	65	20	-10
9	65	256	-491	70	0	-11
10	70	256	-502	75	-177	-273
11	75	79	-775	78	-58	-84

(b) SG3 (GL-0.450m) and SG4 (GL-0.575m)

No.	Initial values			Residual values after dissipation		
	Relative density (%)	SG3	SG4	Density attained (%)	Δ SG3	Δ SG4
1	31	-385	2	35	-155	-8
2	35	-540	-6	38	-106	-35
3	38	-646	-41	45	-8	37
4	45	-654	-4	48	5	0
5	48	-649	-4	48	-2	2
6	48	-651	-2	51	43	1
7	51	-608	-1	58	-17	-32
8	58	-625	-33	65	-58	-11
9	65	-683	-44	70	37	9
10	70	-646	-35	75	-248	1
11	75	-894	-34	78	-55	-39

(c) SG5 (GL-0.6375m) and SG6 (GL-0.6625m)

No.	Initial values			Residual values after dissipation		
	Relative density (%)	SG5	SG6	Density attained (%)	Δ SG5	Δ SG6
1	31	405	347	35	134	233
2	35	539	580	38	106	186
3	38	645	766	45	20	17
4	45	665	783	48	-7	-11
5	48	658	772	48	-10	-11
6	48	648	761	51	-48	-52
7	51	600	709	58	-8	28
8	58	592	737	65	56	84
9	65	648	821	70	-31	-43
10	70	617	778	75	192	312
11	75	809	1090	78	19	98

Table 3.23: Continued

(d) SG7 (GL-0.6875m)

No.	Initial values		Residual values after dissipation	
	Relative density (%)	SG7	Density attained (%)	Δ SG7
1	31	866	35	367
2	35	1233	38	240
3	38	1473	45	2
4	45	1475	48	-15
5	48	1460	48	-13
6	48	1447	51	-68
7	51	1379	58	75
8	58	1454	65	101
9	65	1555	70	-44
10	70	1511	75	580
11	75	2091	78	364

(e) SG8 (GL-0.150m) and SG9 (GL-0.300m)

No.	Initial values			Residual values after dissipation		
	Relative density (%)	SG8 (SG1)	SG9 (SG2)	Density attained (%)	Δ SG8	Δ SG9
1	31	(-147)	(323)	35	-92	133
2	35	-239	456	38	-39	83
3	38	-278	539	45	-5	-10
4	45	-283	529	48	25	-19
5	48	-258	510	48	4	-9
6	48	-254	501	51	28	-10
7	51	-226	491	58	-17	34
8	58	-243	525	65	-22	0
9	65	-265	525	70	9	24
10	70	-256	549	75	51	146
11	75	-205	695	78	65	111

(f) SG10 (GL-0.450m) and SG11 (GL-0.575m)

No.	Initial values			Residual values after dissipation		
	Relative density (%)	SG10 (SG3)	SG11 (SG4)	Density attained (%)	Δ SG10	Δ SG11
1	31	(385)	(-2)	35	207	9
2	35	592	7	38	54	-13
3	38	646	-6	45	-32	10
4	45	614	4	48	-17	-4
5	48	597	0	48	-15	3
6	48	582	3	51	-41	-1
7	51	541	2	58	79	25
8	58	620	27	65	68	9
9	65	688	36	70	-34	-8
10	70	654	28	75	169	-19
11	75	823	9	78	51	28

Table 3.23: Continued

(g) SG12 (GL-0.6375m) and SG13 (GL-0.6625m)

No.	Initial values			Residual values after dissipation		
	Relative density (%)	SG12 (SG5)	SG13 (SG6)	Density attained (%)	Δ SG12	Δ SG13
1	31	(-405)	(-347)	35	-160	-274
2	35	-565	-621	38	-78	-115
3	38	-643	-736	45	41	42
4	45	-602	-694	48	24	36
5	48	-578	-658	48	10	8
6	48	-568	-650	51	34	46
7	51	-534	-604	58	-83	-153
8	58	-617	-757	65	-53	-66
9	65	-670	-823	70	17	28
10	70	-653	-795	75	-193	-357
11	75	-846	-1152	78	-22	-125

(h) SG14 (GL-0.6875m)

No.	Initial values		Residual values after dissipation	
	Relative density (%)	SG14 (SG7)	Density attained (%)	Δ SG14
1	31	(-866)	35	-459
2	35	-1325	38	-139
3	38	-1464	45	55
4	45	-1409	48	50
5	48	-1359	48	22
6	48	-1337	51	46
7	51	-1291	58	-200
8	58	-1491	65	-86
9	65	-1577	70	29
10	70	-1548	75	-633
11	75	-2181	78	-367

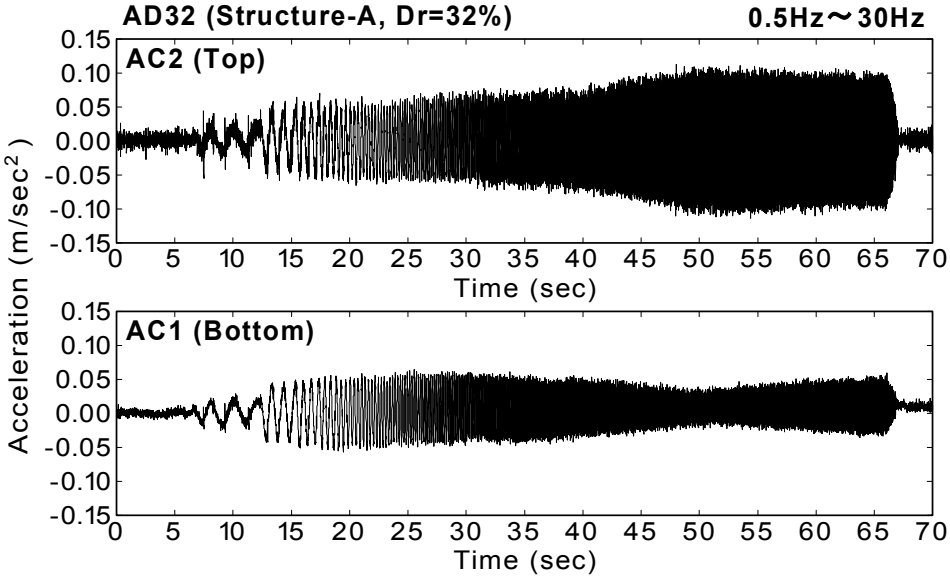

(a) Time histories of acceleration

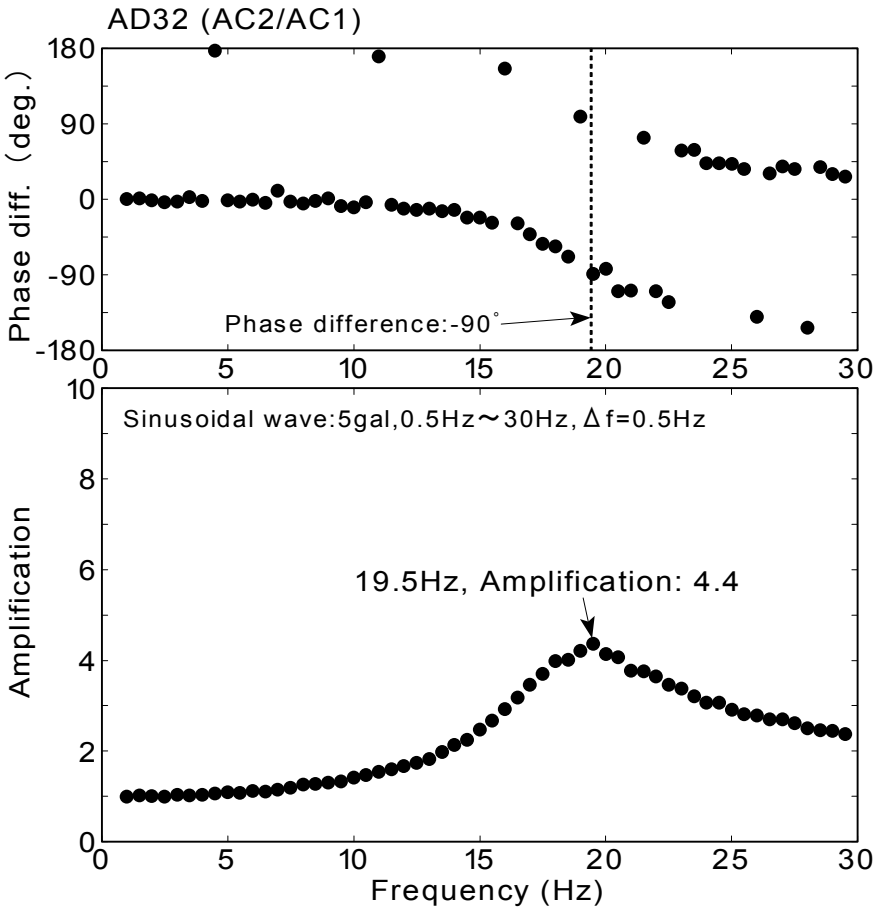

(b) Resonance curve

Fig.3.61: Result of sweep test (AD32)

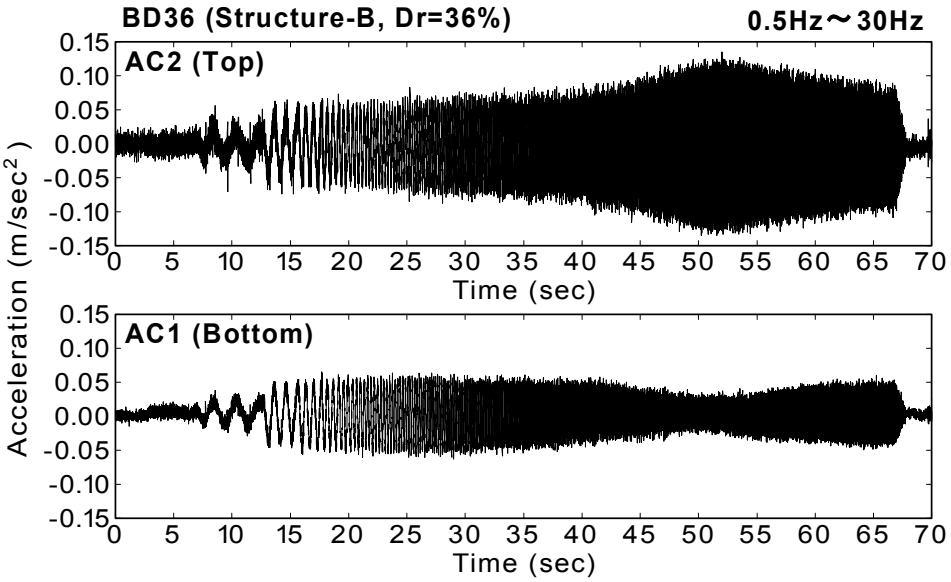

(a) Time histories of acceleration

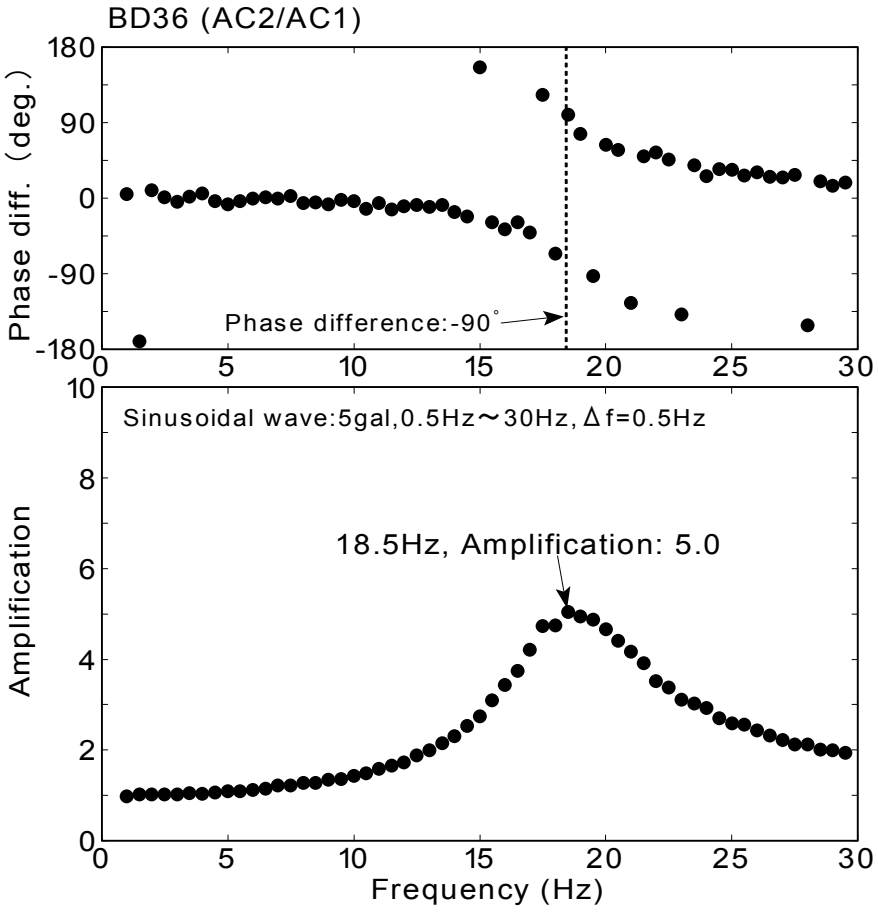

(b) Resonance curve

Fig.3.62: Result of sweep test (BD36)

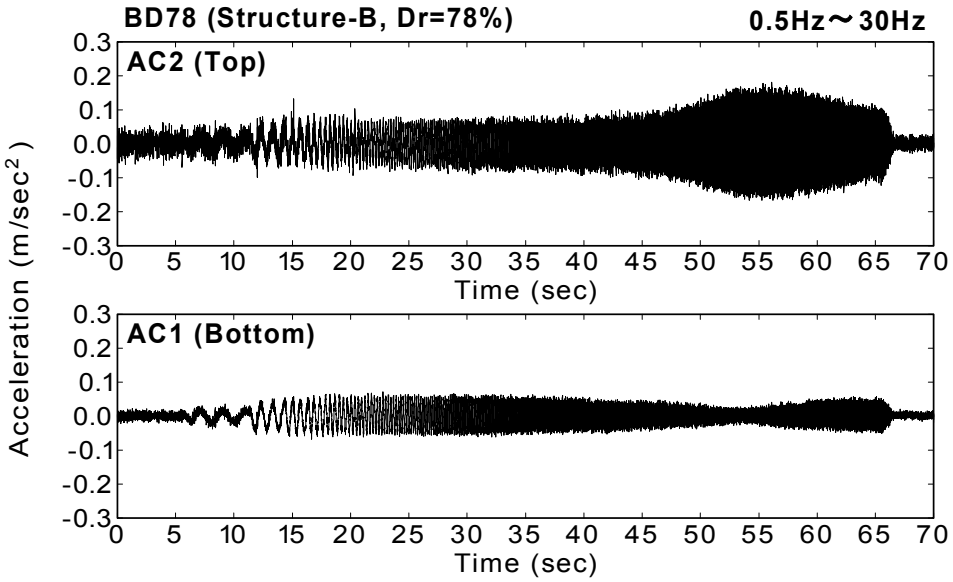

(a) Time histories of acceleration

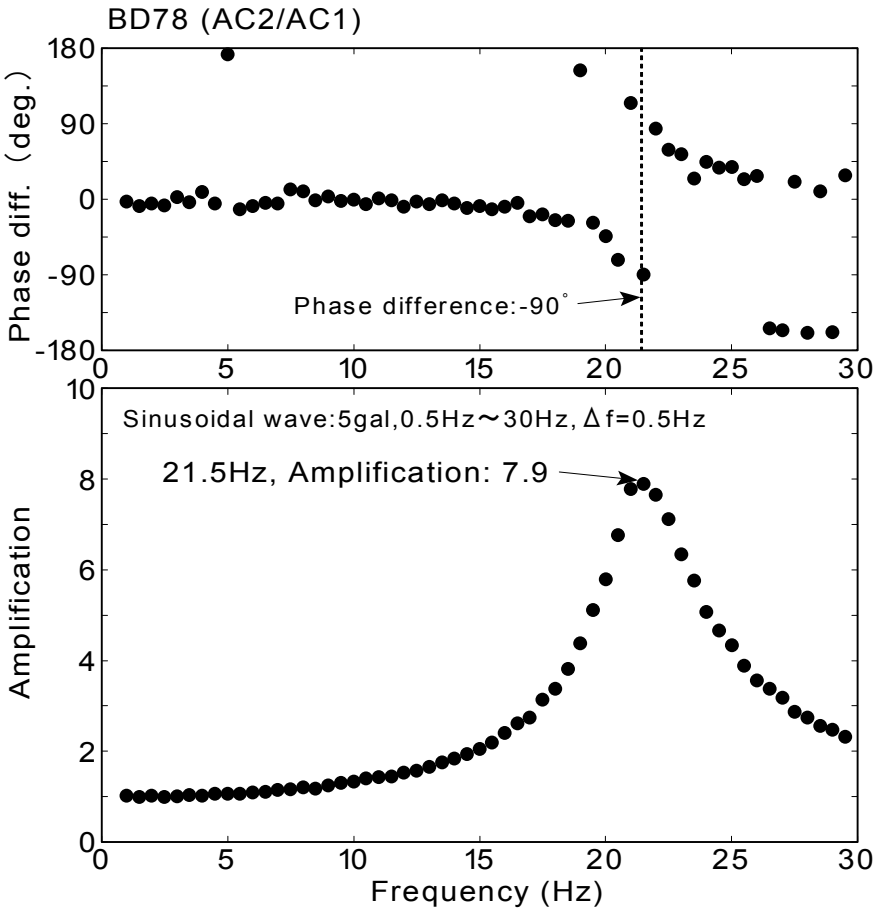

(b) Resonance curve

Fig.3.63: Result of sweep test (BD78)

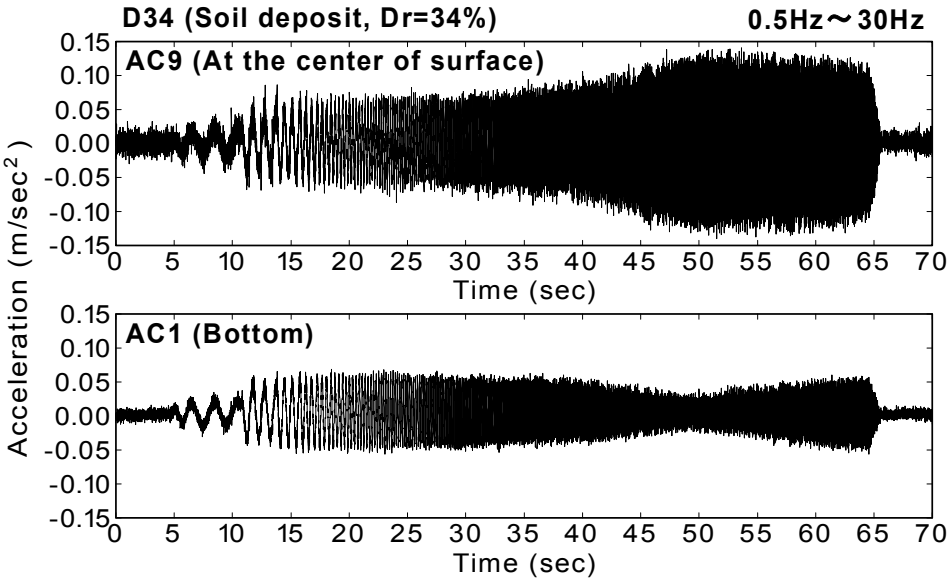

(a) Time histories of acceleration

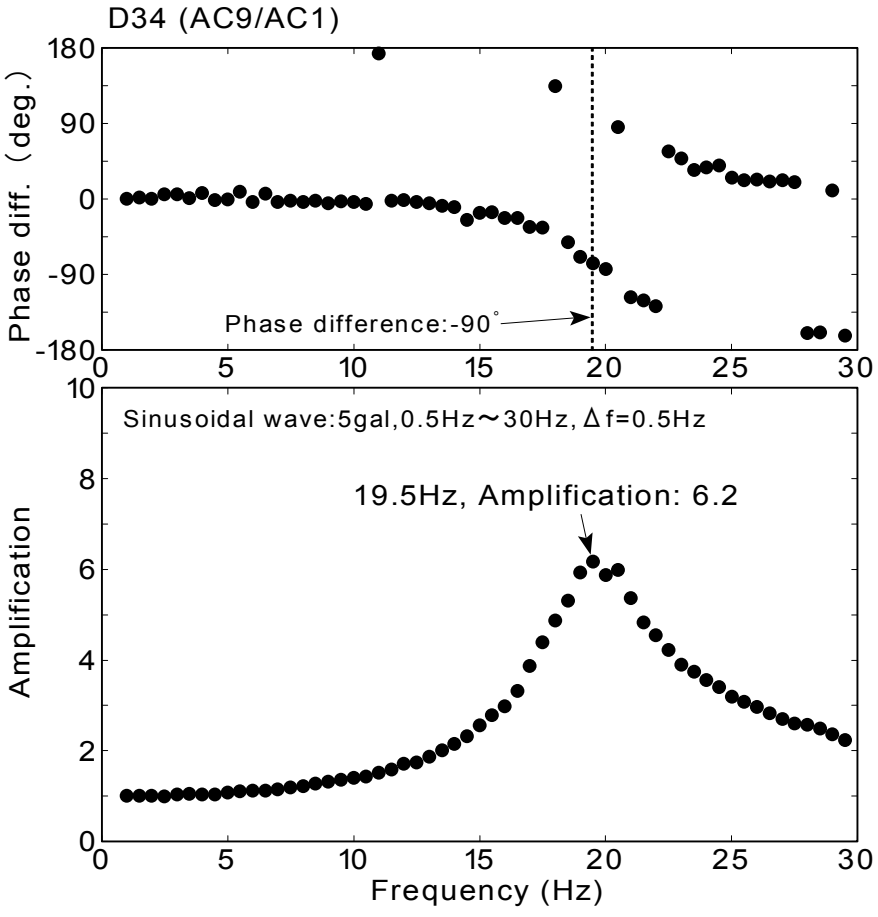

(b) Resonance curve

Fig.3.64: Result of sweep test (D34)

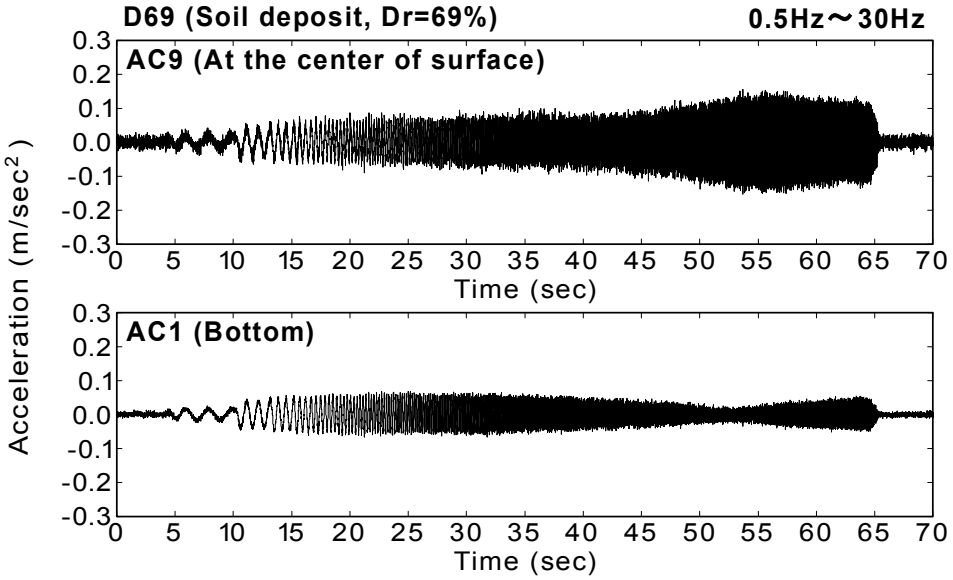

(a) Time histories of acceleration

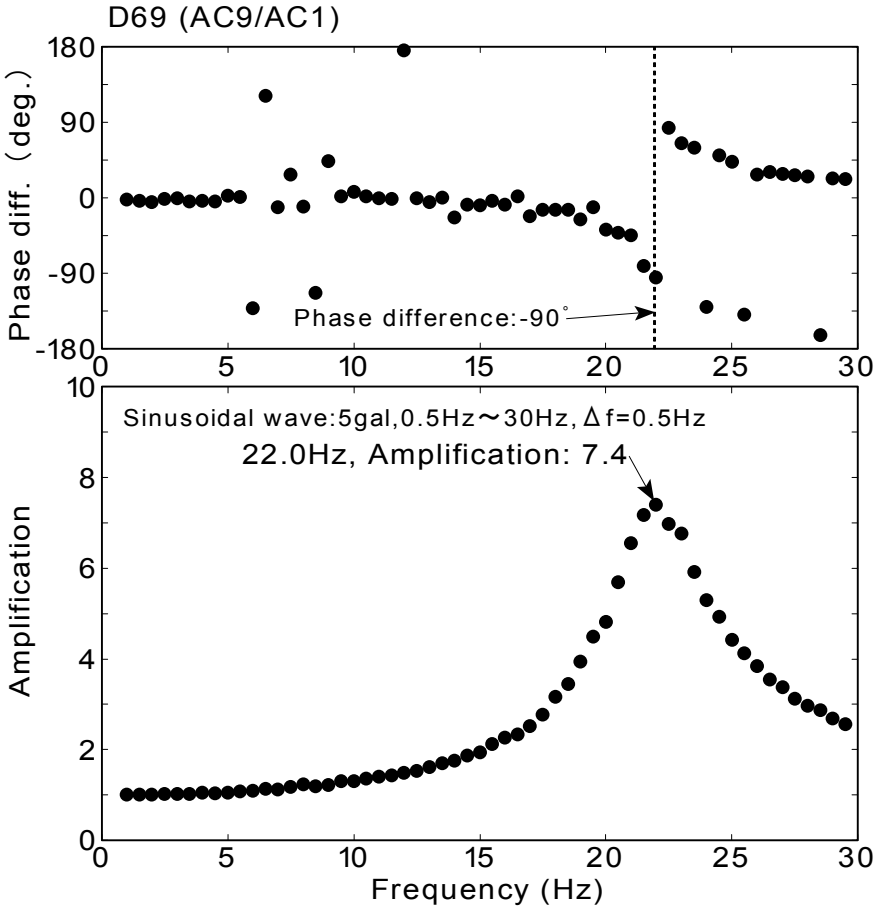

(b) Resonance curve

Fig.3.65: Result of sweep test (D69)

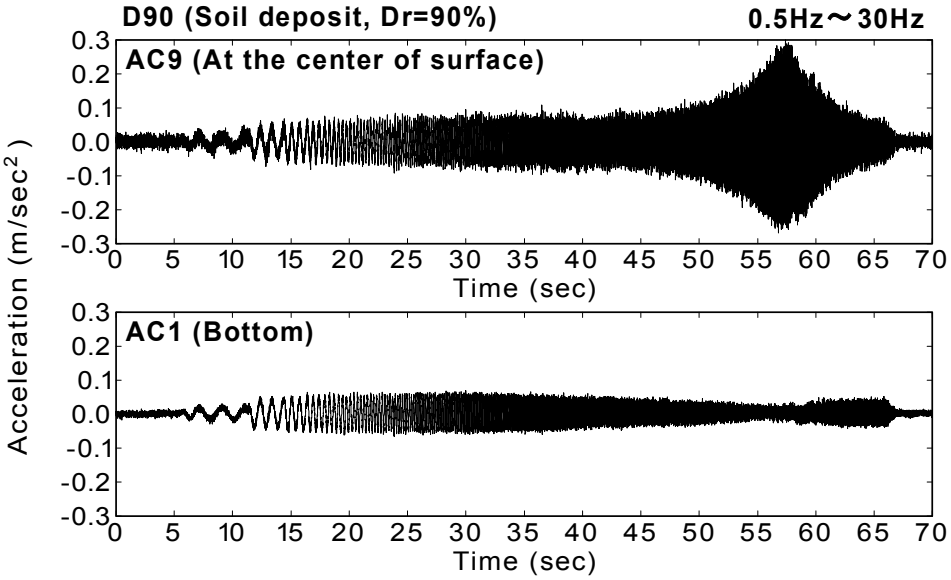

(a) Time histories of acceleration

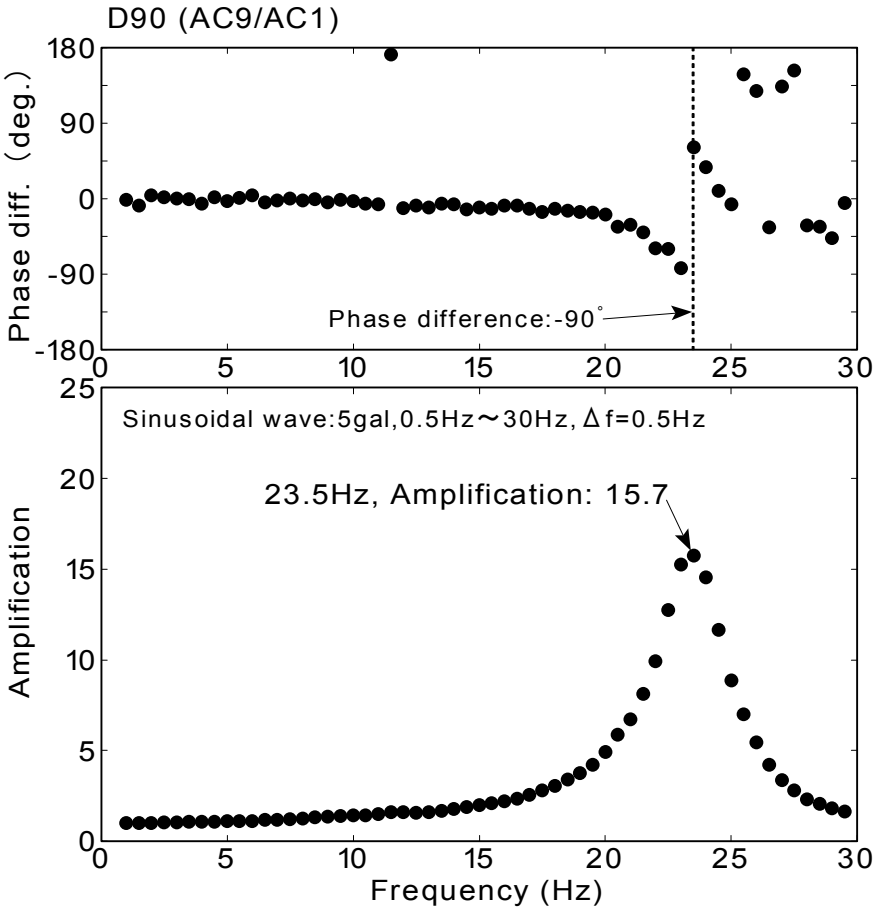

(b) Resonance curve

Fig.3.66: Result of sweep test (D90)

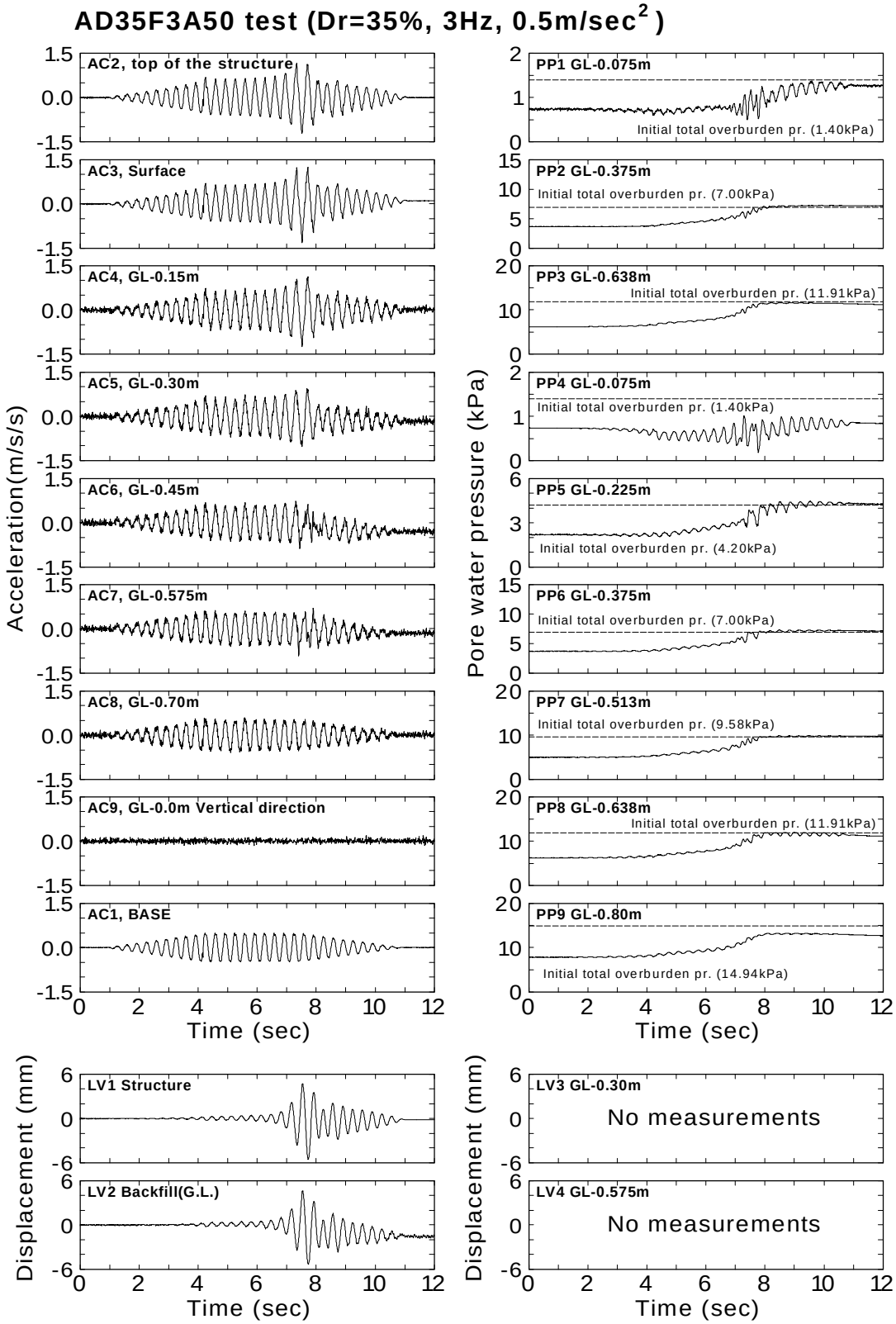

Fig.3.67: Time histories for AD35F3A50 test

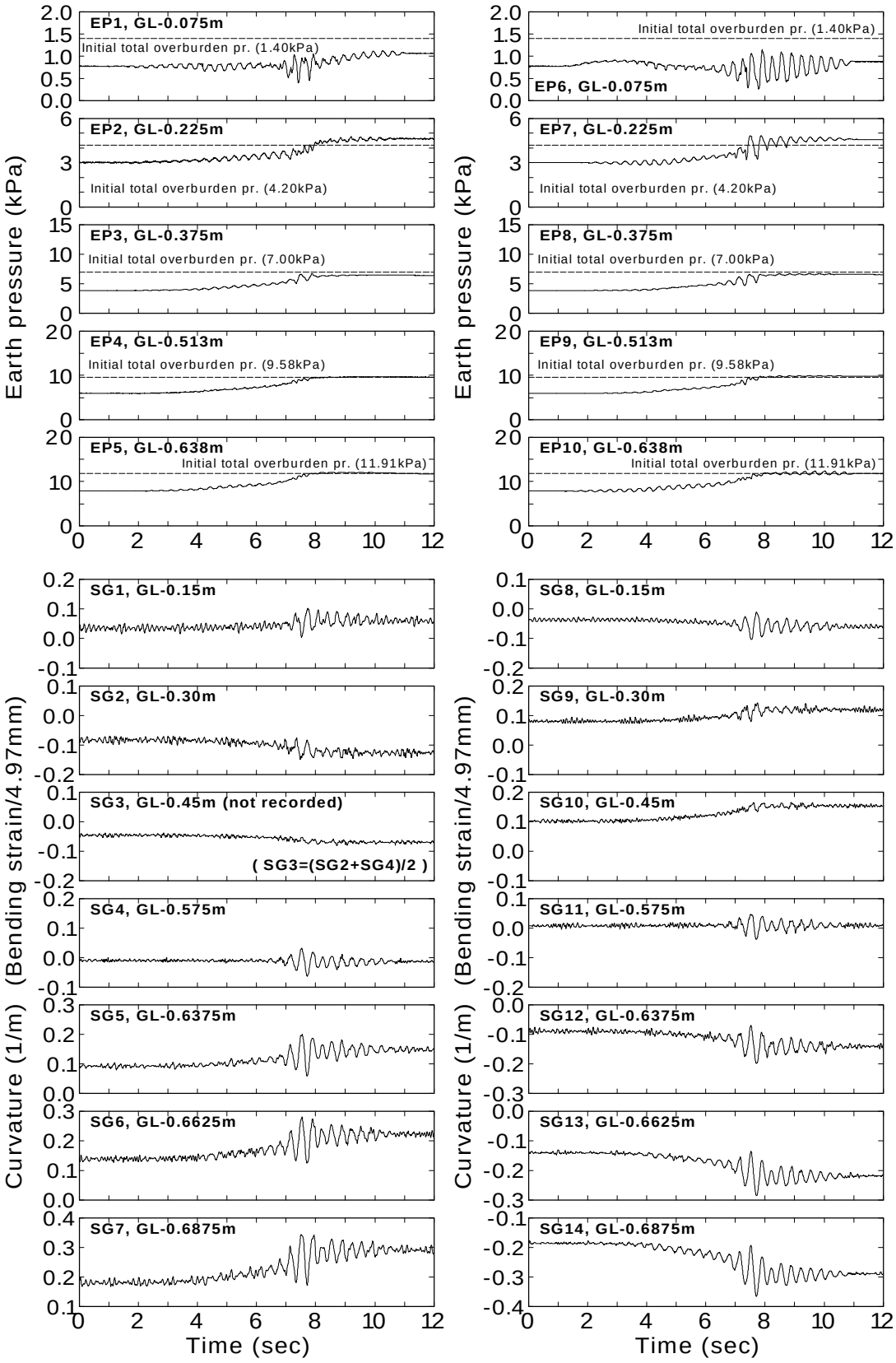

Fig.3.67: Time histories for AD35F3A50 test (Continued)

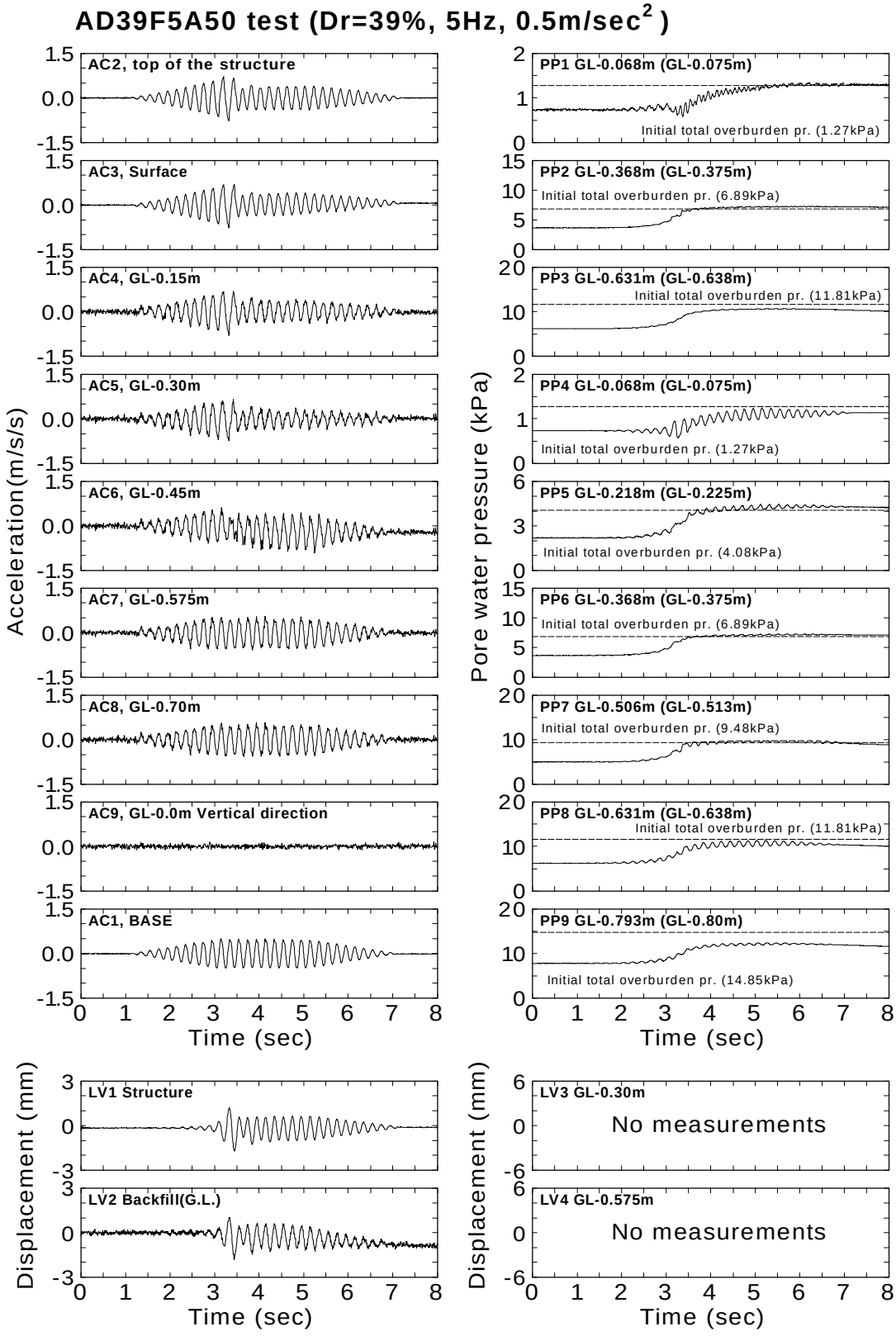

Fig.3.68: Time histories for AD39F5A50 test

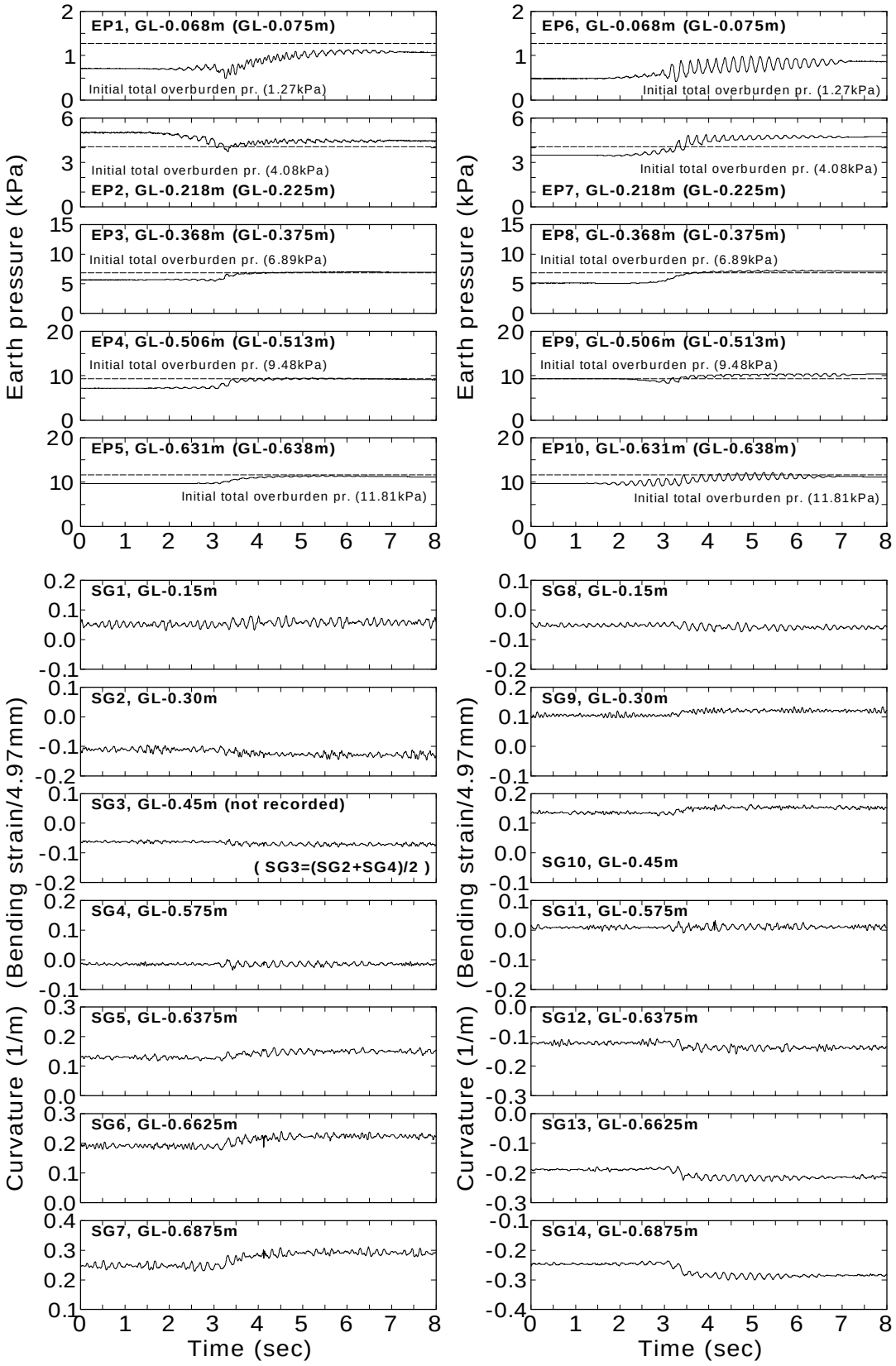

Fig.3.68: Time histories for AD39F5A50 test (Continued)

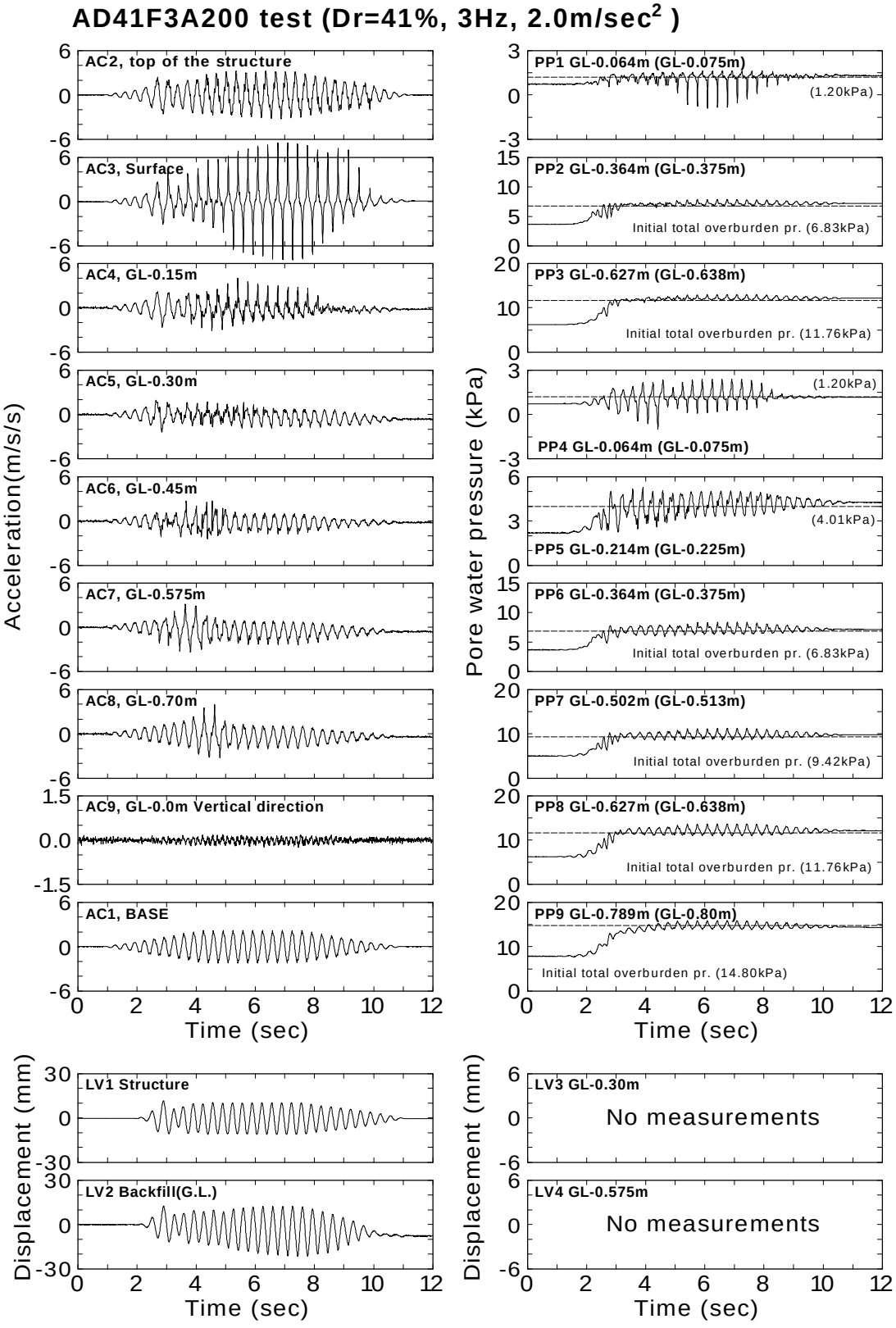

Fig.3.69: Time histories for AD41F3A200 test

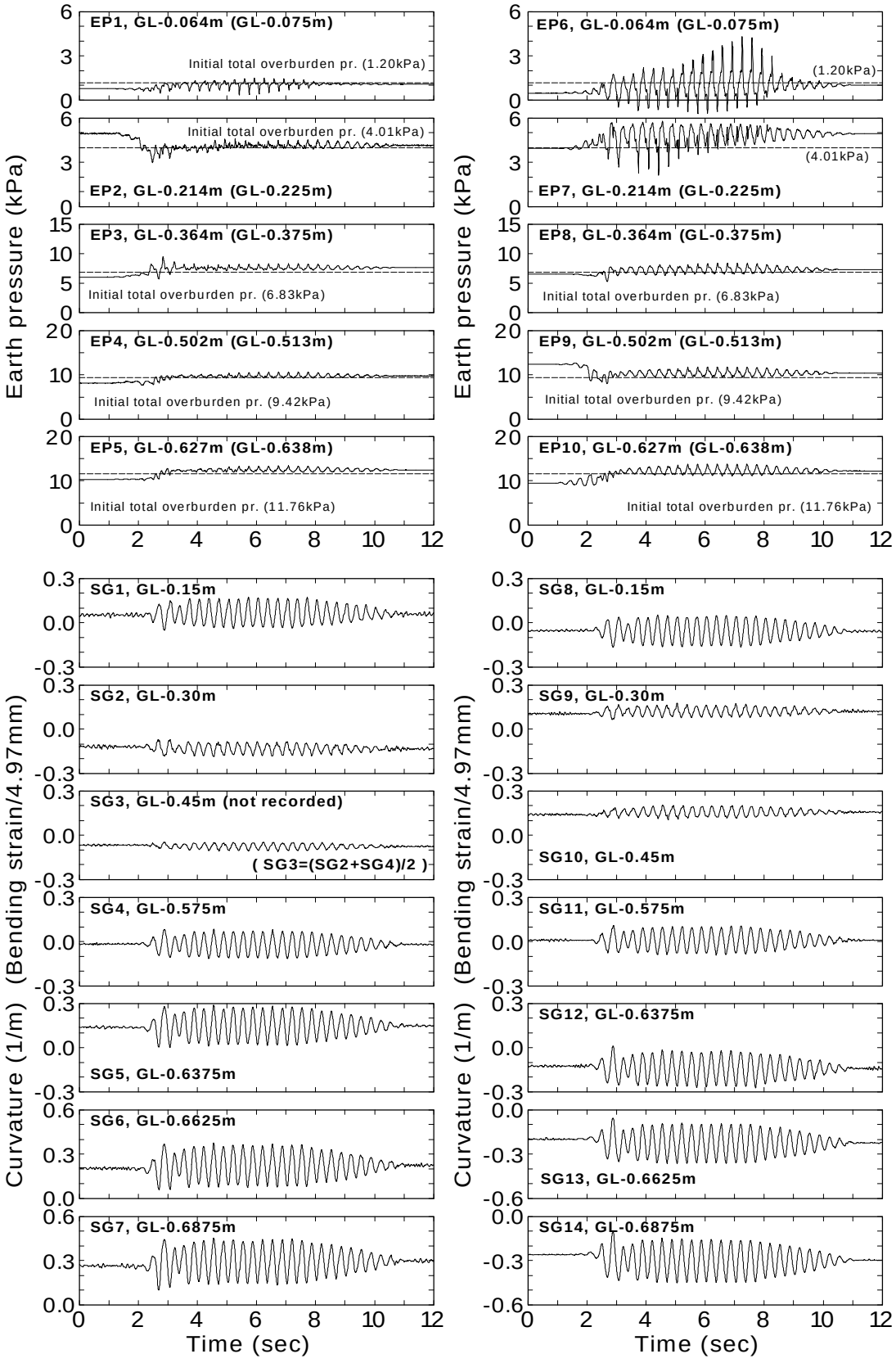

Fig.3.69: Time histories for AD41F3A200 test (Continued)

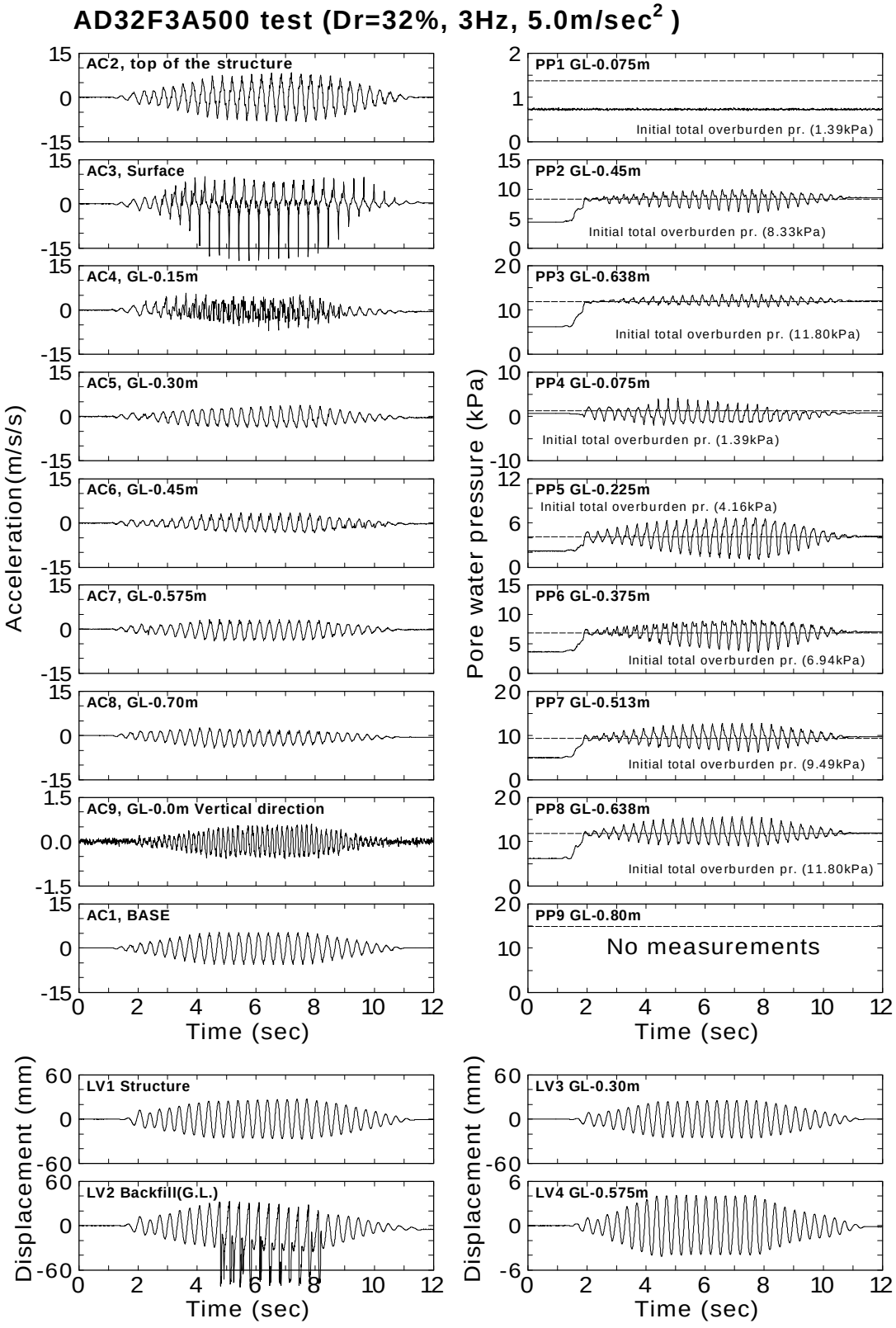

Fig.3.70: Time histories for AD32F3A500 test

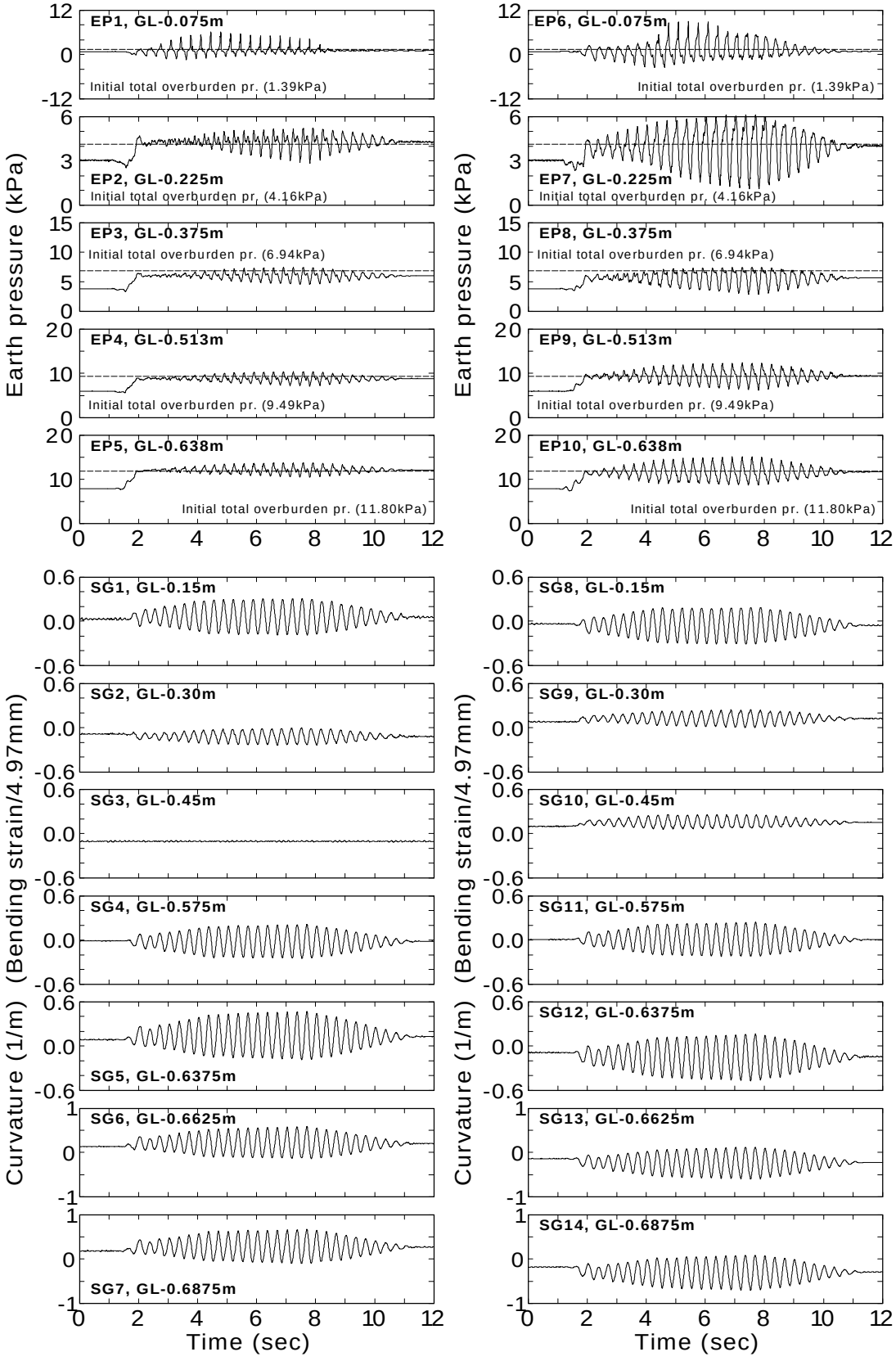

Fig.3.70: Time histories for AD32F3A500 test (Continued)

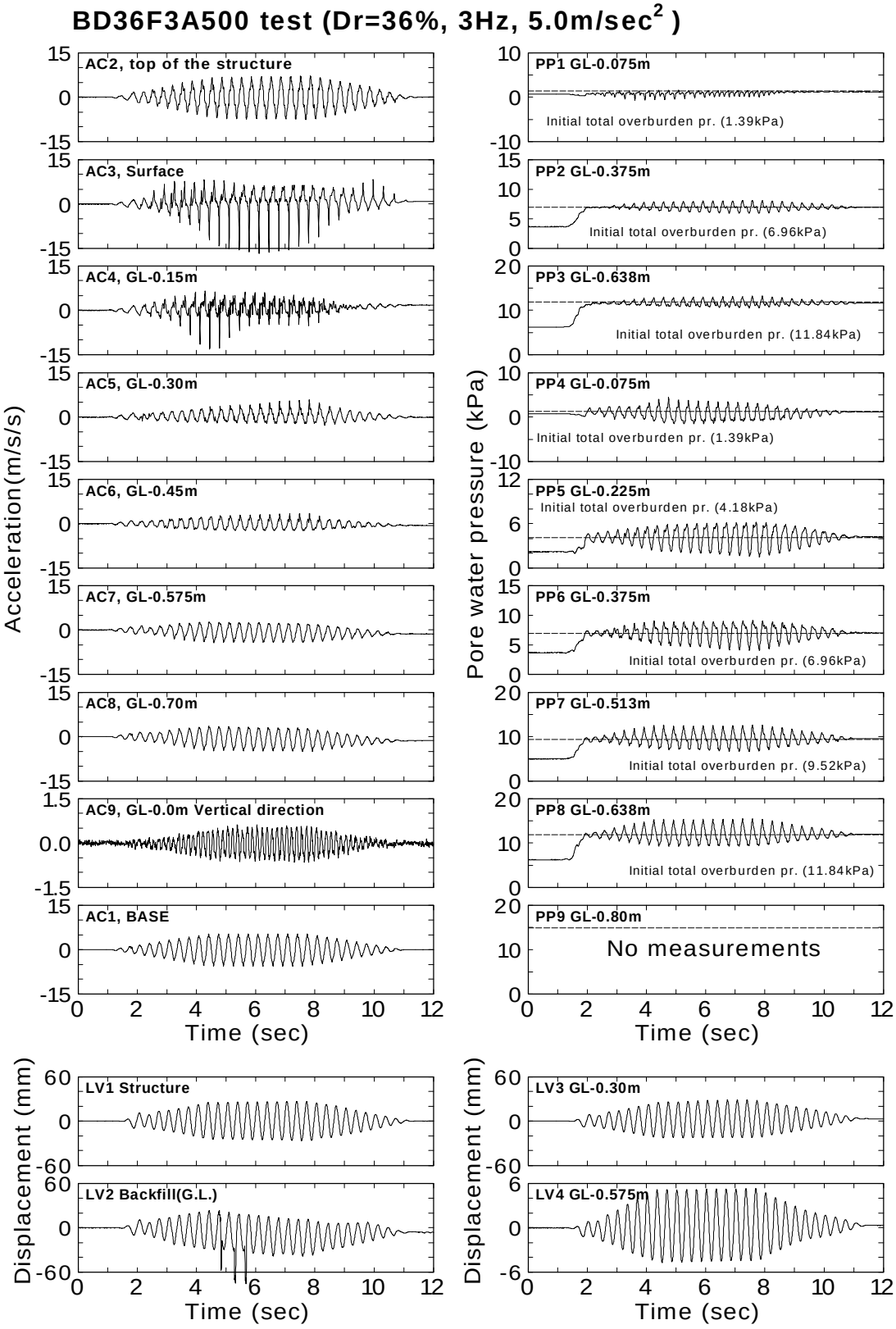

Fig.3.71: Time histories for BD36F3A500 test

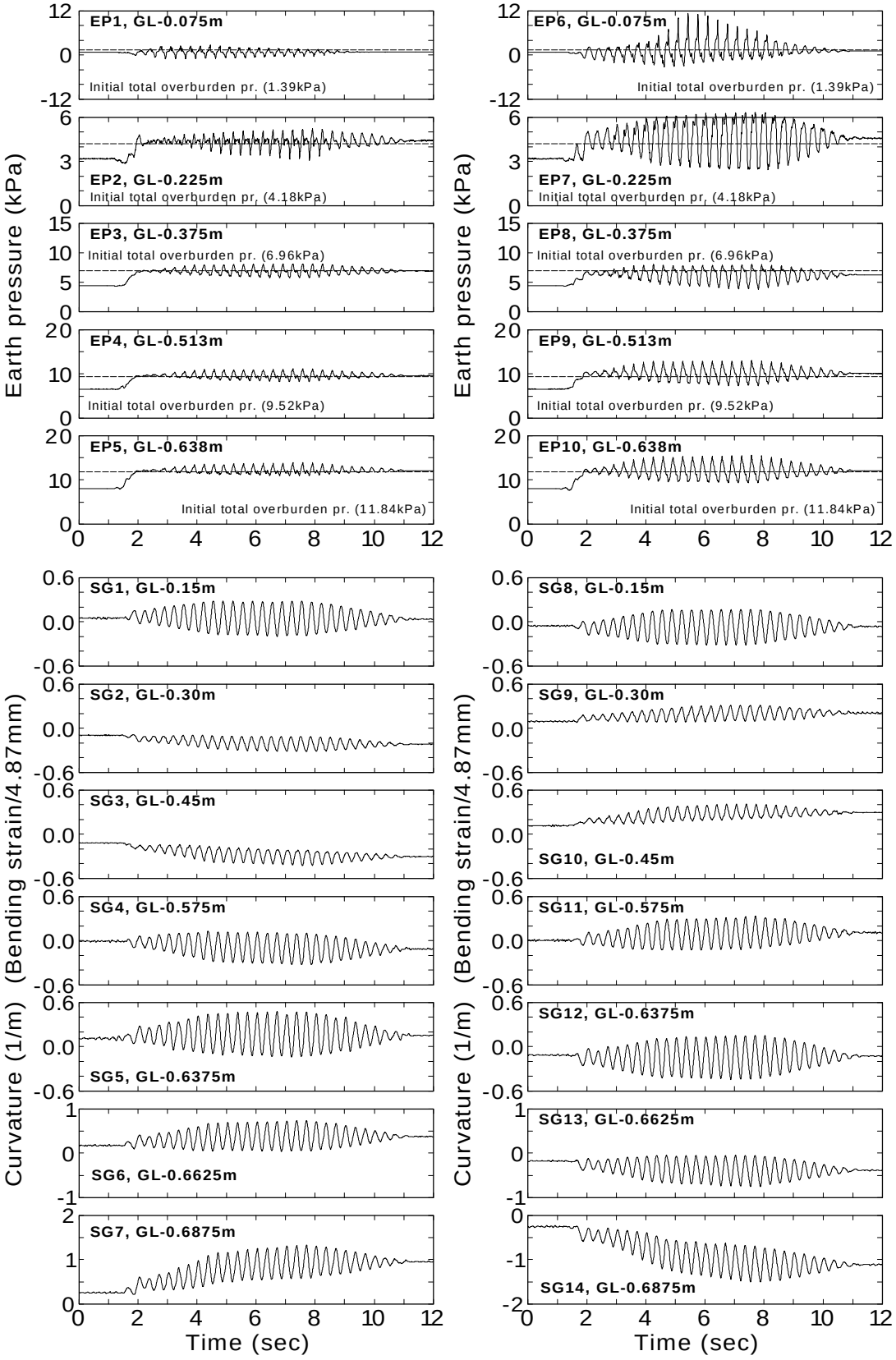

Fig.3.71: Time histories for BD36F3A500 test (Continued)

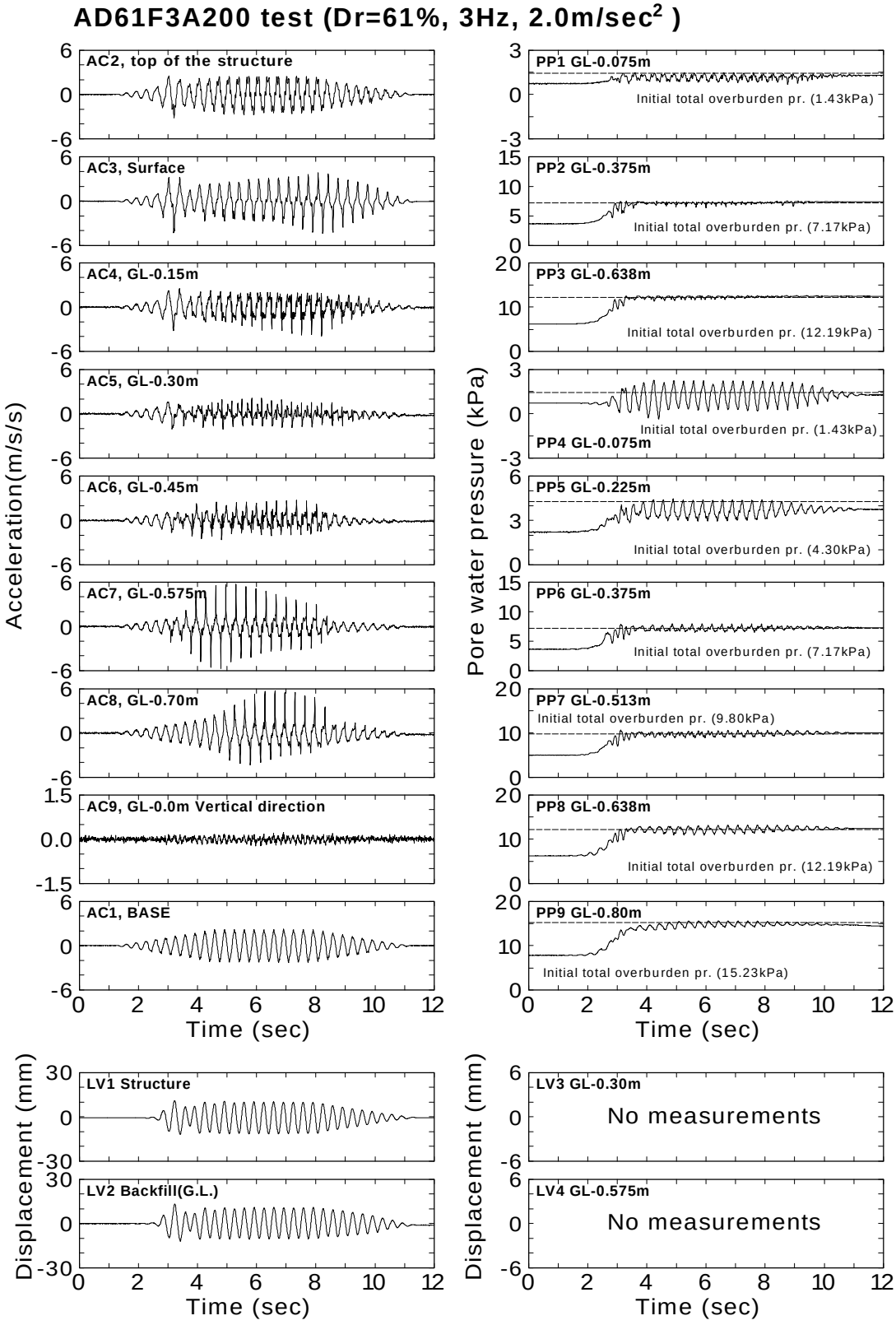

Fig.3.72: Time histories for AD61F3A200 test

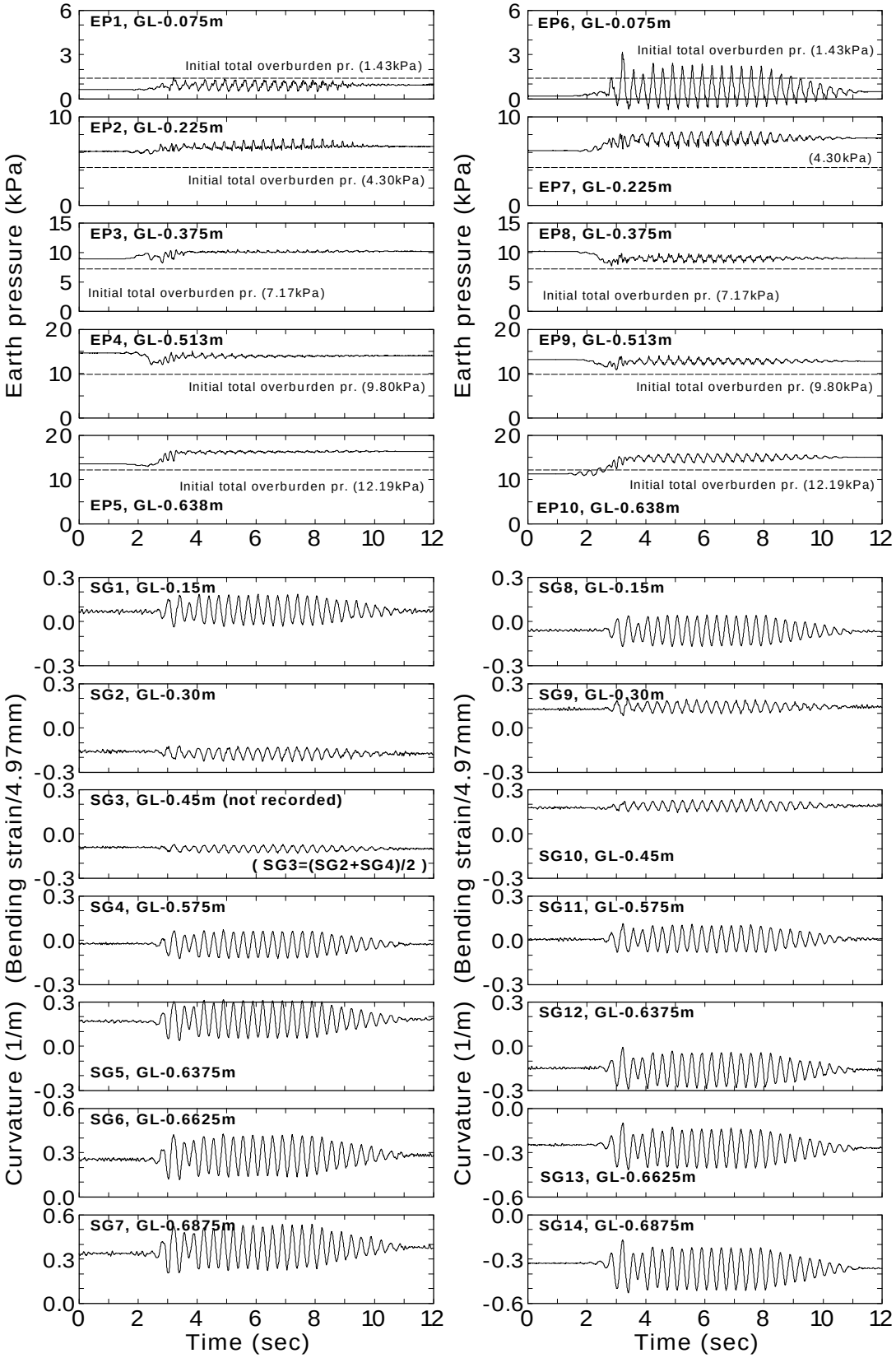

Fig.3.72: Time histories for AD61F3A200 test (Continued)

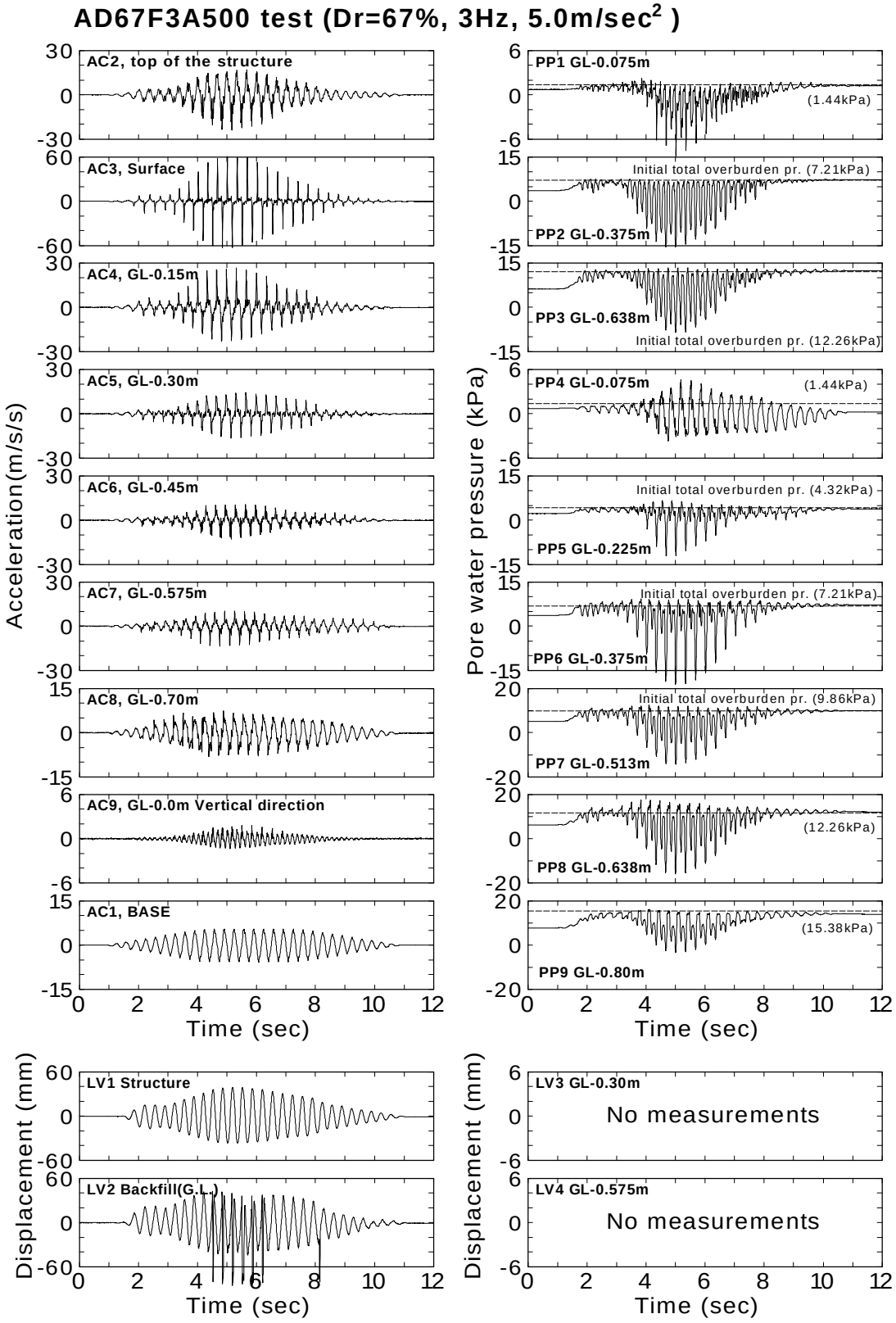

Fig.3.73: Time histories for AD67F3A500 test

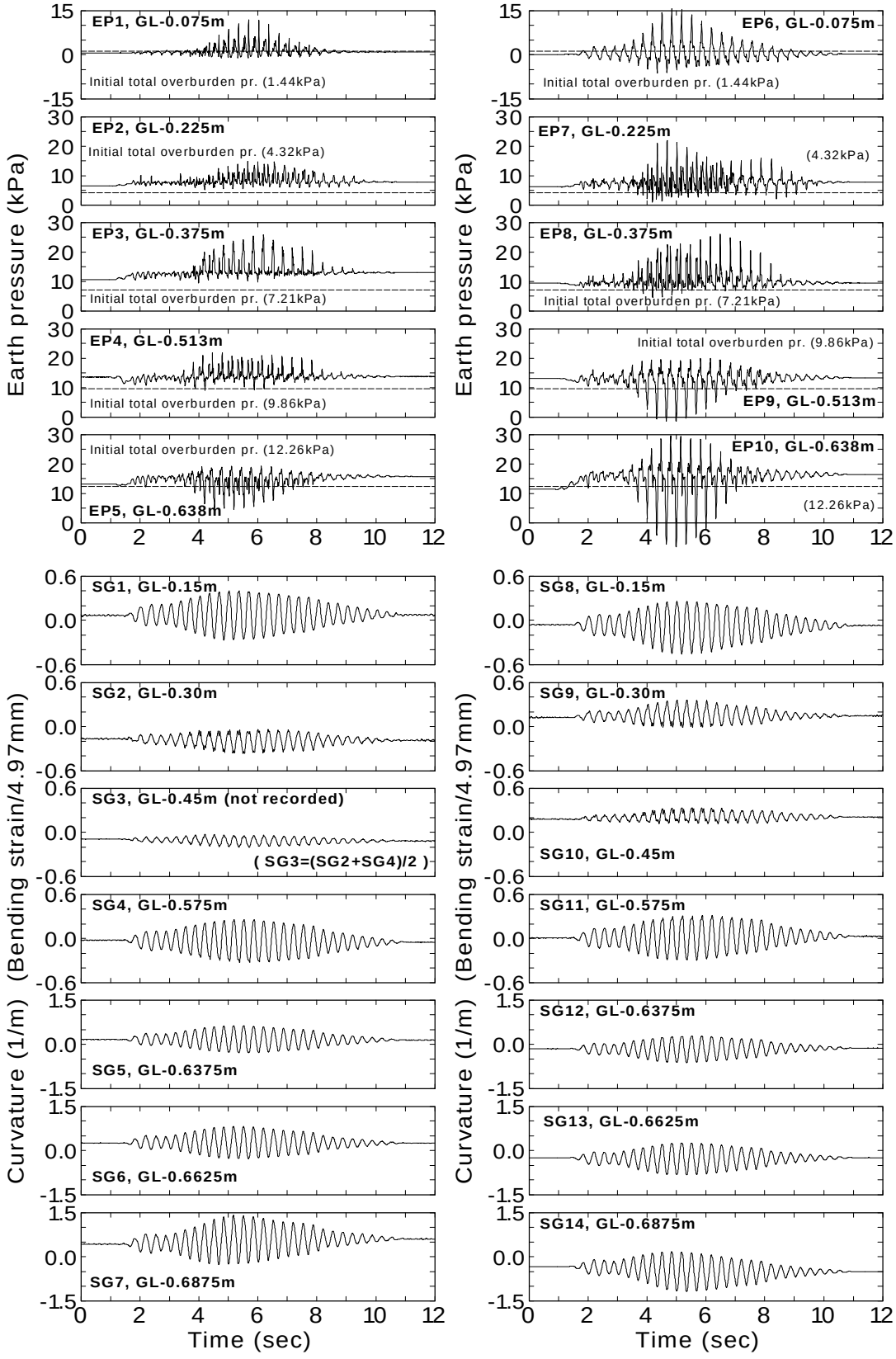

Fig.3.73: Time histories for AD67F3A500 test (Continued)

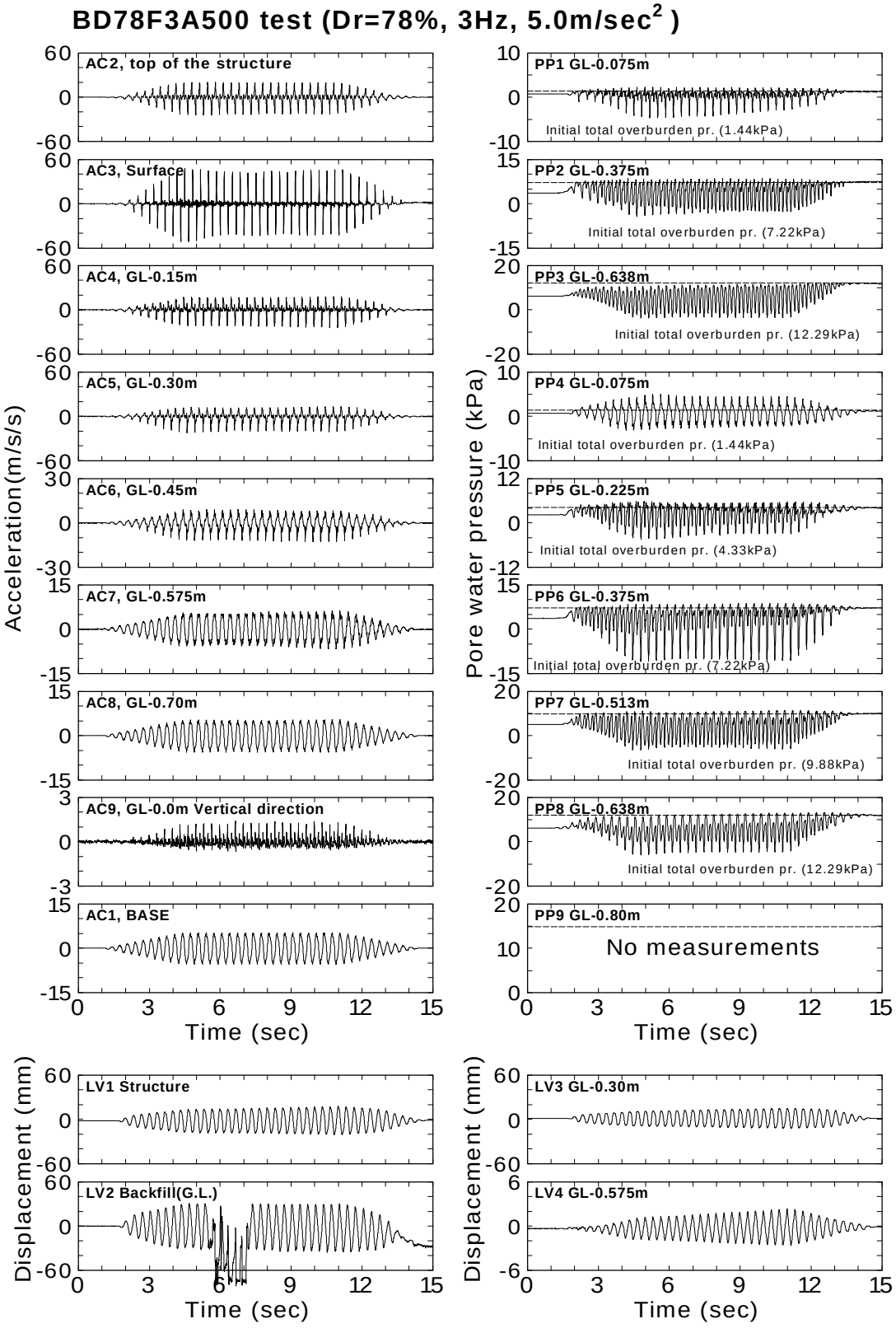

Fig.3.74: Time histories for BD78F3A500 test

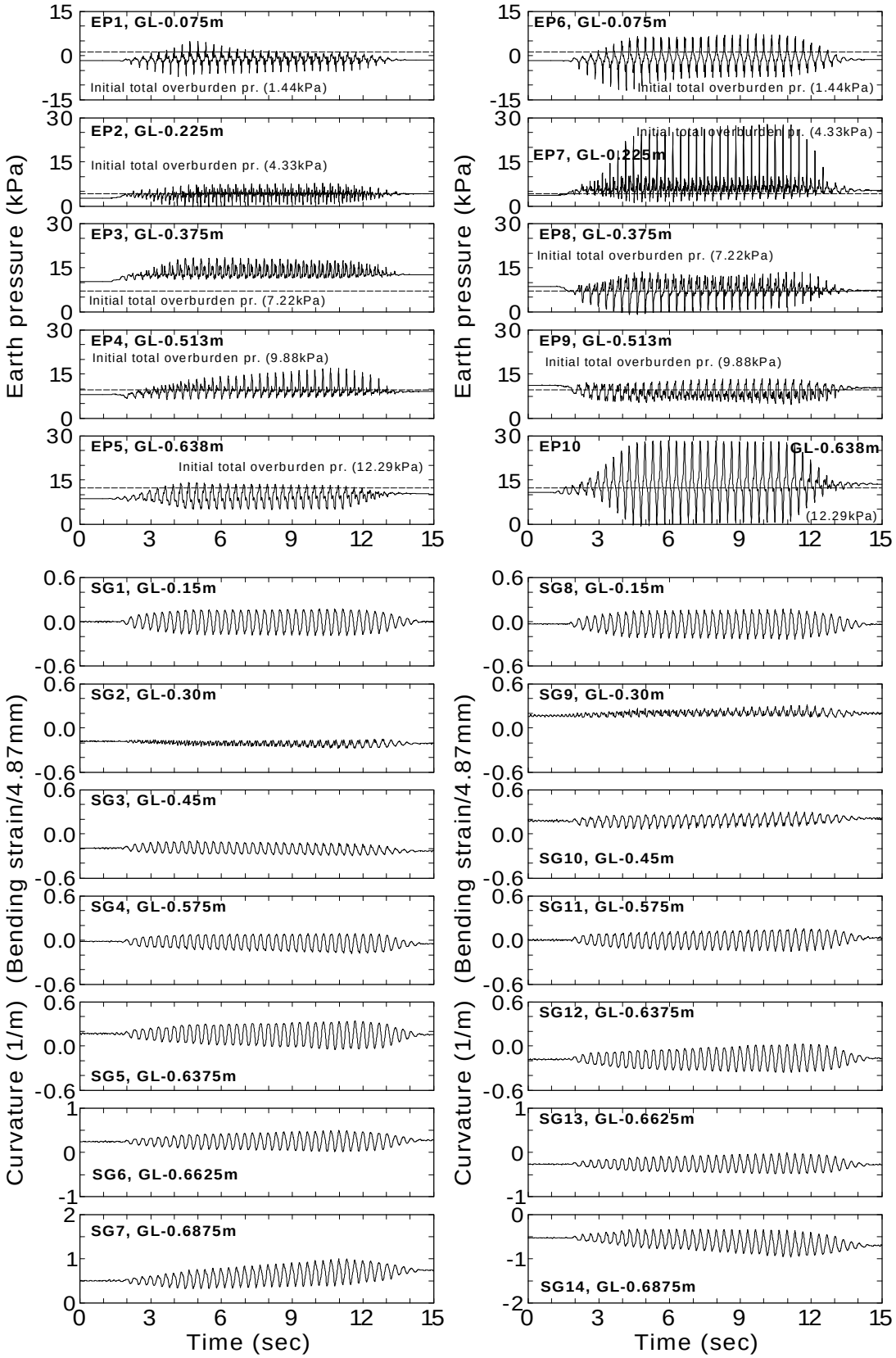

Fig.3.74: Time histories for BD78F3A500 test (Continued)

Chapter 4

STRESS-STRAIN RELATIONSHIP OF SOIL DURING SHAKING

4.1 GENERAL REMARKS

One of the key investigations in this study is to reproduce the stress-strain relationship and the effective stress path of backfill soil near the structure. The stress-strain relationship will be the most useful information to understand the dynamic soil-structure interaction of the embedded structure particularly in liquefied backfill.

The reproduced stress-strain relationship of backfill during shaking as well as the mathematical formulation and the calculation procedure are going to be described. The effect of the structure is taken into account to reproduce the shear stresses and the shear strains. The change of shear modulus of backfill with respect to time, which will be calculated from the stress-strain relationship, will also be presented in this chapter. The results will be referred to as the fundamental information to examine the mechanism of dynamic soil-structure interaction after the following chapter.

4.2 MATHEMATICAL FORMULATION

This kind of attempts has ever been made focusing on the foundation ground of such structures as embankments (Koga and Matsuo, 1990) and a quay wall of gravity type (Ghalandarzadeh et al., 1998). In the previous studies, shear stress generated on a horizontal plane at a depth was estimated using several measurements. From the test results in this study presented in Chapter 3, it is observed that the horizontal responses are much predominant comparing to the vertical responses (e.g. see, Fig.3.16, AC9). Since the vertical response is relatively insignificant, the force

equilibrium only in the horizontal direction is taken into account herein. The shear stress generated on a horizontal plane is reproduced considering the effect of the vertical wall of the structure.

4.2.1 Shear stress

Formulation

A free-body diagram of the simplified problem of saturated soil mass is shown in Fig.4.1. Considering the force equilibrium in the horizontal direction, it can be shown that

$$-\rho\alpha_x \cdot dx \cdot dz + \left\{\sigma_x - \left(\sigma_x + \frac{\partial \sigma_x}{\partial x} dx\right)\right\} \cdot dz + \left\{\tau - \left(\tau + \frac{\partial \tau}{\partial z} dz\right)\right\} \cdot dx = 0 \tag{4.1}$$

This equation is reduced to be;

$$-\rho\alpha_x = \frac{\partial \sigma_x}{\partial x} + \frac{\partial \tau}{\partial z} \tag{4.2}$$

where ρ is the mass density of saturated soil. Transposing the first term of the right-hand side, the shear stress difference is expressed as

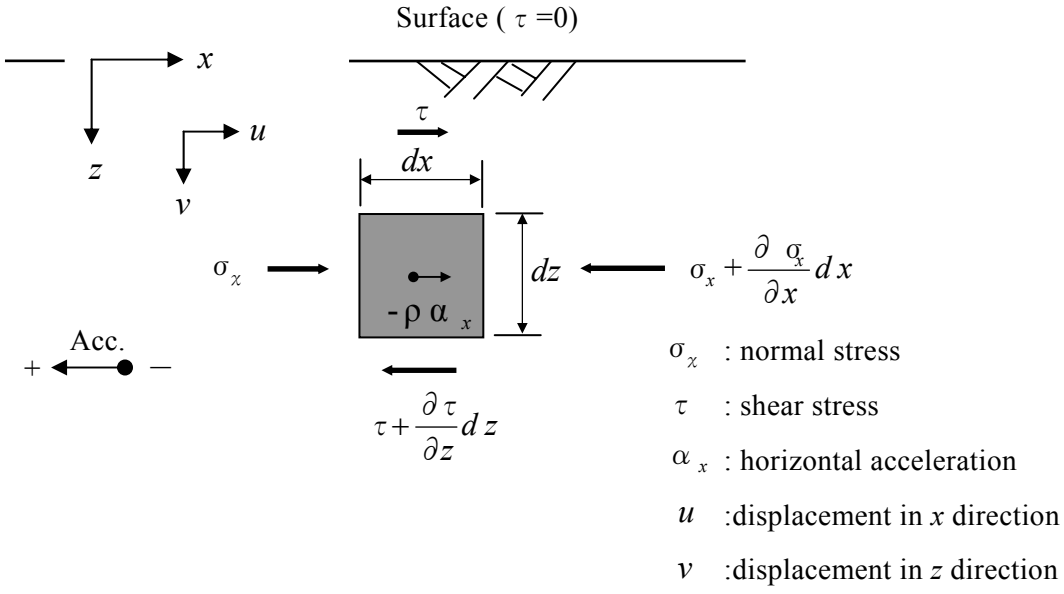

Fig.4.1: Free-body diagram of soil mass in the horizontal direction

$$\frac{\partial}{\partial z}\tau(x,z,t) = -\rho \cdot \alpha_x(x,z,t) - \frac{\partial}{\partial x}\sigma_x(x,z,t) \tag{4.3}$$

Eq.(4.3) is subject to the boundary condition:

$$\tau(x,0,t) = 0 \quad (at\ the\ ground\ surface) \tag{4.4}$$

Integrating Eq.(4.3) once with respect to z and considering the boundary condition of (4.4), the shear stress at any depth and a particular time instance t at particular horizontal coordinate x is calculated as

$$\tau(x,z,t) = \int_0^z \{-\rho \cdot \alpha_x(x,\xi,t) - \frac{\partial}{\partial x}\sigma_x(x,\xi,t)\}\ d\xi \tag{4.5}$$

where ξ is a dummy integration valuable.

Acceleration of soil mass

Acceleration $\alpha_x(x, \xi, t)$ in Eq.(4.5) can be evaluated by interpolating the accelerations at the corner of each soil mass. Fig.4.2 illustrates the soil mass located on the left side of the structure. Considering that the shape of the soil mass is rectangular, the acceleration $\alpha_{xi,i+1}$ at the center of the i-th soil mass from the surface is calculated as

$$\alpha_{xi,i+1}(t) = \frac{\{\alpha_{x,i}(t) + \alpha_{x,i+1}(t)\} + \{\alpha^{struc}{}_{x,i}(t) + \alpha^{struc}{}_{x,i+1}(t)\}}{4} \tag{4.6}$$

where α_{xi} and α_{xi+1} are the measured accelerations in the backfill, and $\alpha^{struc}{}_{x,i}$ and $\alpha^{struc.}{}_{x,i+1}$ are the calculated accelerations from the bending strain at the wall. The calculation procedures of wall acceleration from bending strains will be described in the following section 4.3. In case that the calculation of the wall acceleration from the measured bending strain is difficult due to a problem of measurements (for example, AD39F5A50 test; see Table 4.3), the wall acceleration can be regarded approximately equal to the acceleration in the backfill, that is,

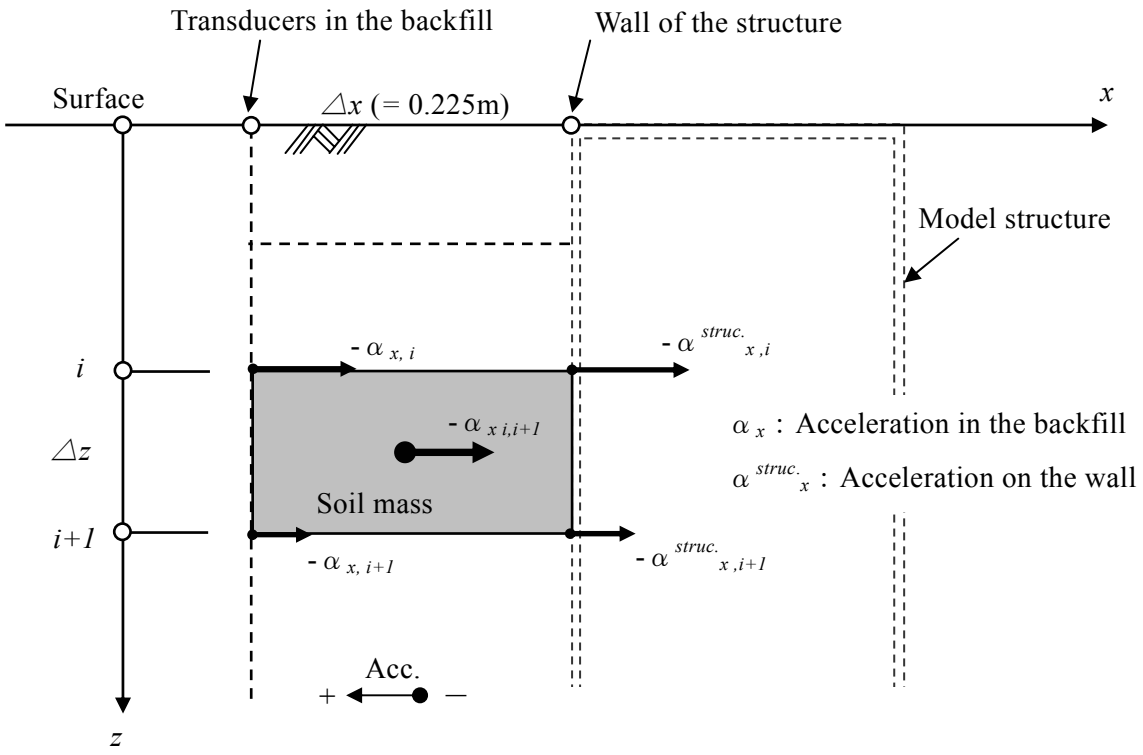

Fig.4.2: Horizontal acceleration at a soil mass

$$\left.\begin{aligned} \alpha_{x,i}(t) &\cong \alpha^{struc.}{}_{x,i}(t) \\ \alpha_{x,i+1}(t) &\cong \alpha^{struc.}{}_{x,i+1}(t) \end{aligned}\right\} \tag{4.7}$$

In this case, Eq.(4.6) results in

$$\alpha_{x\,i,i+1}(t) \cong \frac{\alpha_{x\,i}(t) + \alpha_{x\,i+1}(t)}{2} \tag{4.8}$$

Normal stress difference

Normal stress difference $\partial\sigma_x / \partial x$ can be specified as

$$\frac{\partial}{\partial x}\sigma_x(x,\xi,t) = \Delta\ \sigma_x(x,\xi,t) / \Delta\ x \tag{4.9}$$

where $\Delta\sigma_x(x, \xi, t)$ is a difference of the measured lateral earth pressures both on the wall and in the soil, while Δx is the width of the soil mass (Δx = 0.225m).

Fig.4.3 shows the assumed distribution of lateral earth pressures. The measured lateral earth pressures are interpolated by a piece-wise linear function and assumed to be zero at the surface at each time step. The normal stress difference at *i*-th soil mass $(\partial\sigma_x/\partial x)_{i,i+1}$ is expressed as

$$\left(\frac{\partial}{\partial x}\sigma_x(x,\xi,t)\right)_{i,i+1} = \frac{\Delta\sigma_{x(i,i+1)}(t)}{\Delta x} = \frac{\sigma_{x(i,i+1),struc.}(t) - \sigma_{x(i,i+1),soil}(t)}{\Delta x} \tag{4.10}$$

where, $\sigma_{x(i,i+1),soil.}$ and $\sigma_{x(i,i+1),struc.}$ are the normal stresses on both sides of a soil mass. The former is in the soil and the latter on the wall of the structure, respectively. The normal stress in the soil is calculated considering the distribution of earth pressure by a piece-wise linear function as

$$\sigma_{x(i,i+1),soil.}(t) = \frac{EP_i(t) + 2EP_{i,i+1}(t) + EP_{i+1}(t)}{4} \tag{4.11}$$

where $EP_{i,i+1}(t)$ is the measured earth pressure from *i*-th transducer from the surface and $EP_i(t)$, $EP_{i+1}(t)$ are interpolated earth pressures at the middle depth of transducers as shown in Fig.4.3. They are calculated as what follows;

$$EP_i(t) = EP_{i-1,i}(t)\cdot\left(\frac{\Delta z_{i,i+1}}{\Delta z_{i-1,i} + \Delta z_{i,i+1}}\right) + EP_{i,i+1}(t)\cdot\left(\frac{\Delta z_{i-1,i}}{\Delta z_{i-1,i} + \Delta z_{i,i+1}}\right) \tag{4.12}$$

$$EP_{i+1}(t) = EP_{i,i+1}(t)\cdot\left(\frac{\Delta z_{i+1,i+2}}{\Delta z_{i,i+1} + \Delta z_{i+1,i+2}}\right) + EP_{i+1,i+2}(t)\cdot\left(\frac{\Delta z_{i,i+1}}{\Delta z_{i,i+1} + \Delta z_{i+1,i+2}}\right) \tag{4.13}$$

The normal stress on the wall of the structure $\sigma_{x(i,i+1),struc.}(t)$ is calculated in the same manner.

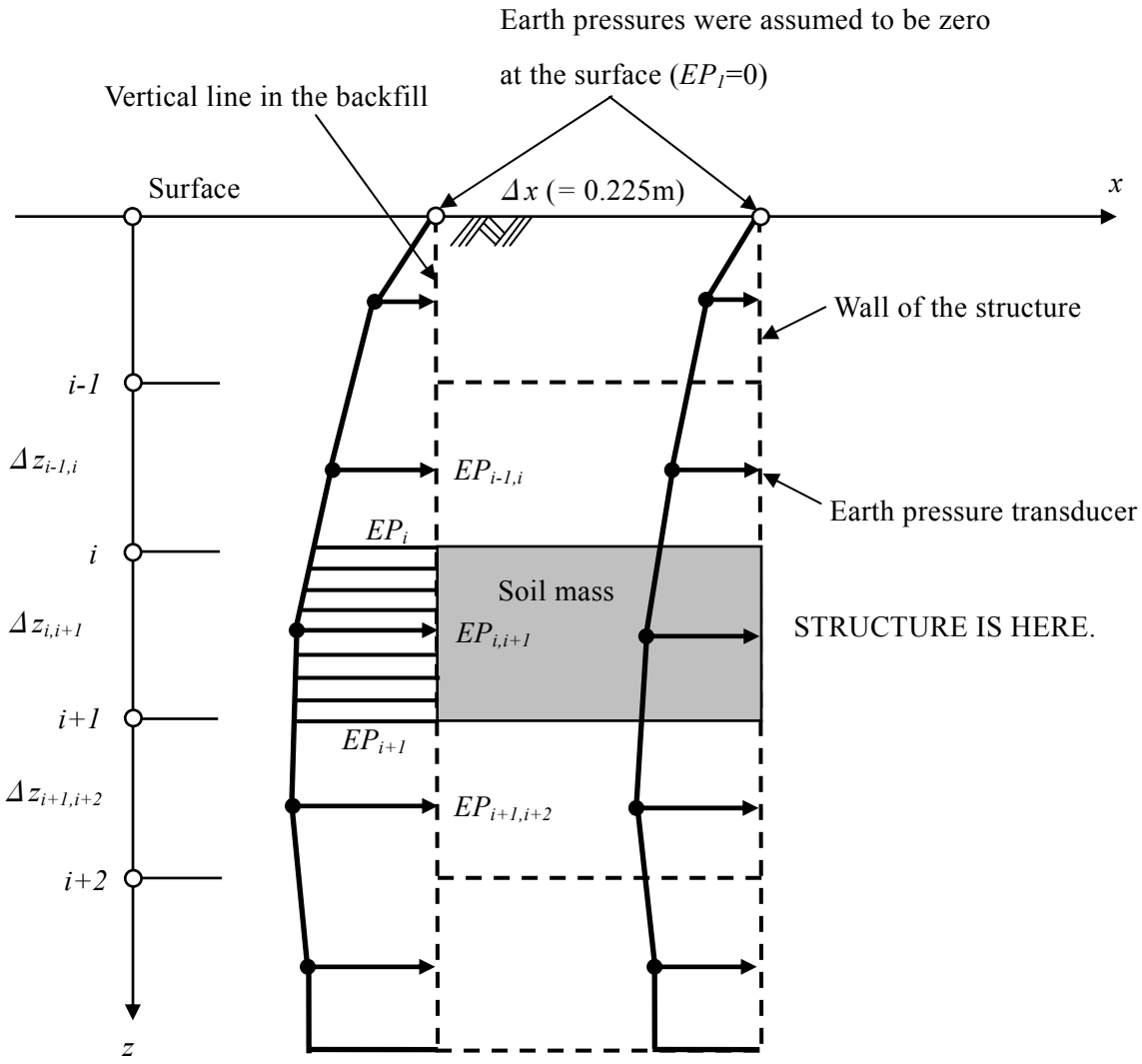

Fig.4.3: Earth pressure distributions approximated by piece-wise linear function

Shear stress at a particular depth

The shear stress at the bottom of the third soil mass from the surface (see Fig.2.6(b)) is calculated by summing the shear stress difference as

$$\tau_{3,4}(t) = \sum_{i=1}^{3}\left(\frac{\partial \tau}{\partial z}\Delta z\right)_{,i} = \sum_{i=1}^{3}\left\{-\rho\alpha_{x(i,i+1)}(t) - \frac{\sigma_{x(i,i+1),struc.}(t) - \sigma_{x(i,i+1),soil}(t)}{\Delta x}\right\}\cdot\Delta z_{i,i+1} \quad (4.14)$$

where Δz is the height of each soil mass. Transducers referred to for calculation of shear stresses by Eq.(4.14) and the height of each soil mass Δz are shown in Table 4.1. Thus, at each time step, the shear stress at a particular depth in saturated soil can be obtained. Combining calculated shear stress at all time steps, complete time histories of shear stress can be obtained.

Table 4.1: Transducers referred to for calculation for shear stresses by Eq.(4.14)

i	Earth pressure		Acceleration (bending strain)				$\Delta z_{i,i+1}$ (m)
	$EP_{i,i+1}$ (backfill)	$EP_{i,i+1}$ (wall)	α_{xi}	α_{xi+1}	$\alpha^{s}_{x\,i}$	$\alpha^{s}_{x\,i+1}$	
1	EP1	EP6	AC3	AC4	AC2	SG1	0.150
2	EP2	EP7	AC4	AC5	SG1	SG2	0.150
3	EP3	EP8	AC5	AC6	SG2	SG3	0.150
4	EP4	EP9	AC6	AC7	SG3	SG4	0.125
5	EP5	EP10	AC7	AC8	SG4	AC1	0.125

Δx = 0.225m

4.2.2 Shear strain

Formulation

The shear strain of a soil mass is expressed in the plane strain condition as

$$\gamma = \frac{\partial u}{\partial z} + \frac{\partial v}{\partial x} \quad (4.15)$$

where u and v are displacements in the horizontal and vertical directions, respectively. The positive direction is shown in Fig.4.1. In this experimental study, the shaking was exerted only in the horizontal direction. In this respect, it was found in the previous chapter that the vertical response

was less than one tenth of horizontal response. Hence, it is appropriate that the vertical displacement of a soil mass is ignored. This implies,

$$\frac{\partial v}{\partial x} \cong 0 \tag{4.16}$$

Consequently, the shear strain of a soil mass is expressed as what follows.

$$\gamma = \frac{\partial u}{\partial z} \tag{4.17}$$

Shear strain at a particular soil element

The shear strains of the soil element adjacent to the wall (see Fig.2.4) were calculated from displacements of soil u and displacements of wall $u^{struc.}$ at the corner of the soil element. Fig.4.4 illustrates the deformation of i-th soil element from the surface and the displacements at the corner.

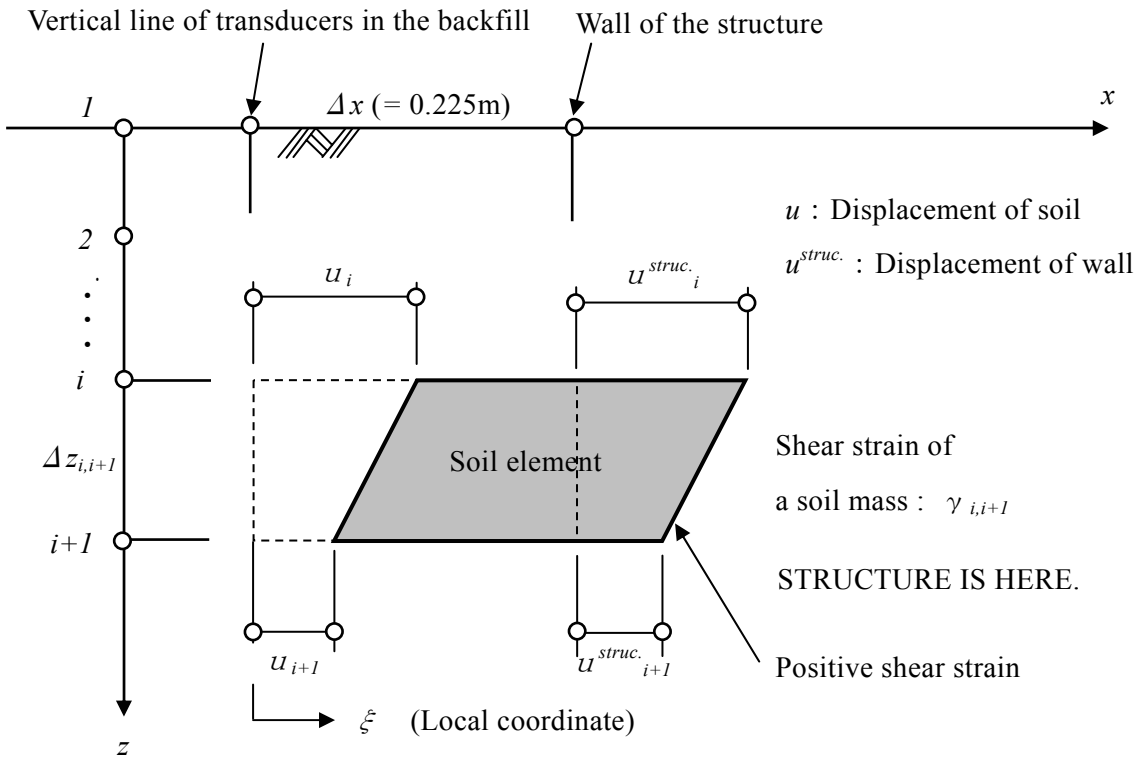

Fig.4.4: Shear deformation of a soil element

The vertical displacements were neglected since the vertical responses were found to be very small comparing to the horizontal responses. The shear strain of the soil element $\gamma_{i,i+1}$ is calculated assuming a constant strain in the vertical direction and a linear interpolation in the horizontal direction as

$$\gamma_{i,i+1}(\xi,t) = \gamma^{soil}{}_{i,i+1}\left(1-\frac{\xi}{\Delta x}\right)+\gamma^{struc.}{}_{i,i+1}\frac{\xi}{\Delta x} \qquad (0 \le \xi \le \Delta x) \tag{4.18}$$

where

$$\gamma^{soil}{}_{i,i+1} = \frac{u_i - u_{i+1}}{\Delta\ z_{i,i+1}} \tag{4.19}$$

$$\gamma^{struc.}{}_{i,i+1} = \frac{u^{struc.}{}_i - u^{struc.}{}_{i+1}}{\Delta\ z_{i,i+1}} \tag{4.20}$$

The shear strain at the center of a soil element is derived substituting $\xi = \Delta x/2$ in Eq.(4.18).

The soil displacements were calculated by integrating twice the measured accelerations with respect to time. The wall displacements were calculated by integrating twice the measured wall curvatures with respect to depth. Details of numerical integration will be presented in the section 4.3. Transducers referred to for calculation of shear strains by Eq.(4.18) and the height of each soil element Δz are shown in Table 4.2.

Table 4.2: Transducers referred to for calculation of shear strains by Eq.(4.18)

i	Displacement				$\Delta z_{i,i+1}$ (m)
	u_i	u_{i+1}	$u^{struc.}{}_i$	$u^{struc.}{}_{i+1}$	
1	AC3	AC4	AC2	SG1	0.150
2	AC4	AC5	SG1	SG2	0.150
3	AC5	AC6	SG2	SG3	0.150
4	AC6	AC7	SG3	SG4	0.125
5	AC7	AC8	SG4	AC1	0.125

Δx = 0.225m

Average shear strain of whole backfill

The average shear strain of whole backfill near the structure can be calculated by dividing the displacement at the top (LV1) by the height of the structure (H = 0.7m) as

$$\gamma(t) = u_{z=0}(t) / H \tag{4.21}$$

In this case, shear strain becomes constant in the vertical direction.

4.2.3 Effective vertical stress

The effective vertical stress σ_v' is calculated from measured excess pore water pressures as

$$\sigma_v' = \sigma_{v0}' - \Delta u \tag{4.22}$$

where σ_{v0}' is the initial effective vertical stress and Δu is the excess pore water pressure. The initial vertical stress is calculated by multiplying the effective unit weight of soil γ' by depth z as

$$\sigma_{v0}' = \gamma' \cdot z \tag{4.23}$$

The effective unit weight was assumed constant in the vertical direction. Pore water pressure transducer in the backfill was referred to for the excess pore water pressure, Δu, in Eq.(4.22).

4.3 NUMERICAL INTEGRATION AND DIFFERENTIATION

A procedure of data analysis to reproduce shear stress and shear strain is summarized in Fig.4.5. Numerical integration will be conducted to calculate displacements in the backfill and on the wall. Differentiation will be made to derive accelerations on the wall where the displacements are derived by numerical integration. The calculation procedures for numerical integration and differentiation, and example of calculation will be presented in this section.

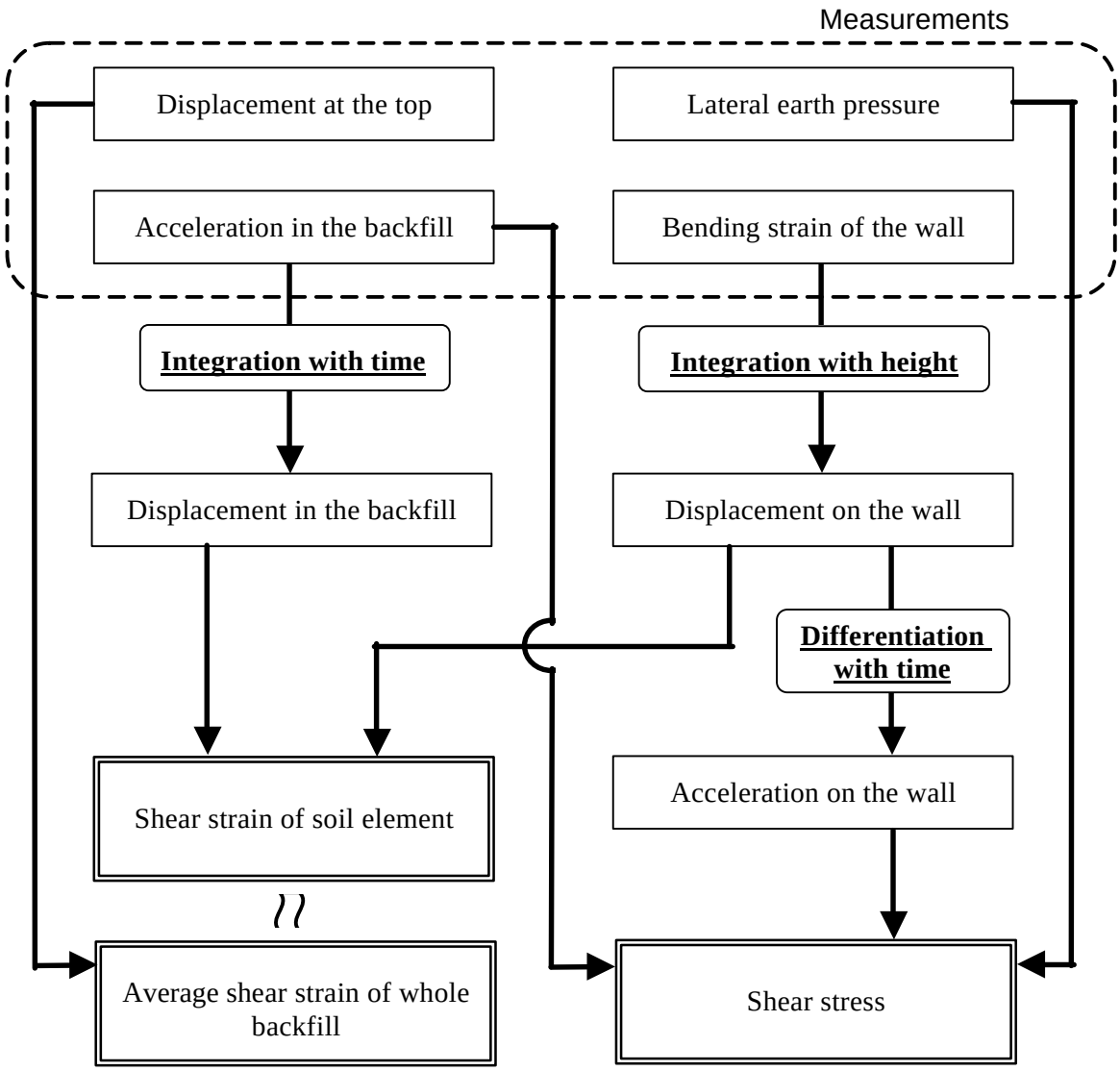

Fig.4.5: A flow of data analysis to reproduce shear stress and shear strain

4.3.1 Numerical integration of acceleration for displacements

The displacement in the backfill at each depth was calculated by integrating the acceleration (AC3～AC8) twice with respect to time. Fig.4.6 shows the procedure of calculation. Before the numerical integration, the long-period components more than 1 second of acceleration time history were removed by a digital filtering procedure using FFT (Fast Fourier Transform). Then, the acceleration time history was integrated once assuming a linear variation in each time interval Δt as shown in Fig.4.7.

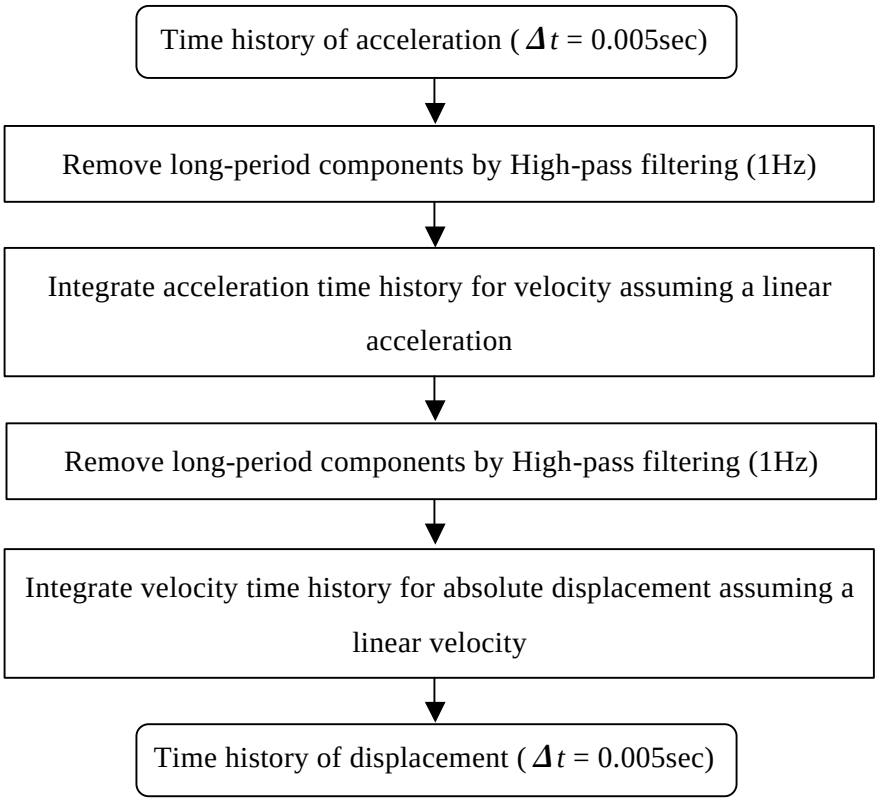

Fig.4.6: Procedure of the numerical integration of acceleration for displacement

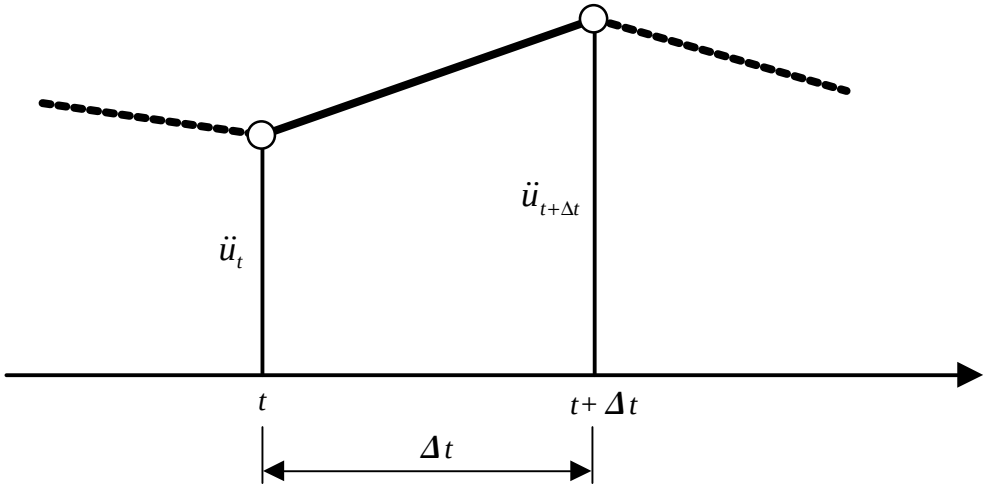

Fig.4.7: Assumption of a linear variation of acceleration

The velocity $\dot{u}_{t+\Delta t}$ at the time of $t+\Delta t$ is expressed by the following equation referring to the velocity $\dot{u}_t$ at the time of t as

$$\dot{u}_{t+\Delta t} = \dot{u}_t + (\Delta t)\ddot{u}_t + \frac{1}{2}(\Delta t)(\ddot{u}_{t+\Delta t} - \ddot{u}_t) \tag{4.24}$$

where $\ddot{u}_t$ and $\ddot{u}_{t+\Delta t}$ are accelerations given. The initial acceleration at t=0 was assumed to be zero. Thus, the time history of velocity is calculated step by step. The same procedure of the digital high-pass filtering and integration of velocity time history was conducted. The displacement at the time of $t+\Delta t$ is given by

$$u_{t+\Delta t} = u_t + (\Delta t)\dot{u}_t + \frac{1}{2}(\Delta t)(\dot{u}_{t+\Delta t} - \dot{u}_t) \tag{4.25}$$

Note that the displacement derived by integration of acceleration is the absolute displacement. The absolute displacement was converted to the displacement relative to the bottom of the container by subtracting the absolute displacement at the base (AC1) from the calculated absolute displacement at each point (AC3～AC8).

Time histories of displacement calculated from acceleration at the top of the structure (AC2) are shown in Fig.4.8 together with the time histories of displacement (LV1) measured by the laser displacement transducer. Measured time history is illustrated by solid line and calculated time history by dashed line. Fig.4.8(a) is the result from AD35F3A50 test. It was seen that both time histories were almost identical except for the residual value. The residual displacement of about 0.2mm was observed at 12 seconds in the measured displacement. On the other hand, no residual displacements were calculated in the displacement due to numerical integration. It was because of the high-pass filtering of 1Hz before the integration.

Fig.4.8(b) shows the result of AD39F5A50 test which was shaken by 5Hz harmonic excitation. Fig.4.8(c) and (d) illustrate the time histories from AD32F3A500 test and AD67F3A500 test, which were shaken by intense excitation with the peak acceleration of 5.0 m/sec^2. It was noted that spiky acceleration with high frequency components was observed in AD67F3A500 test (see, Fig.3.23). It was observed that the calculated time history agreed with the measured time history in all the tests in spite of different conditions of input motion. It suggests that the procedure of numerical integration by Fig.4.6 gives good results.

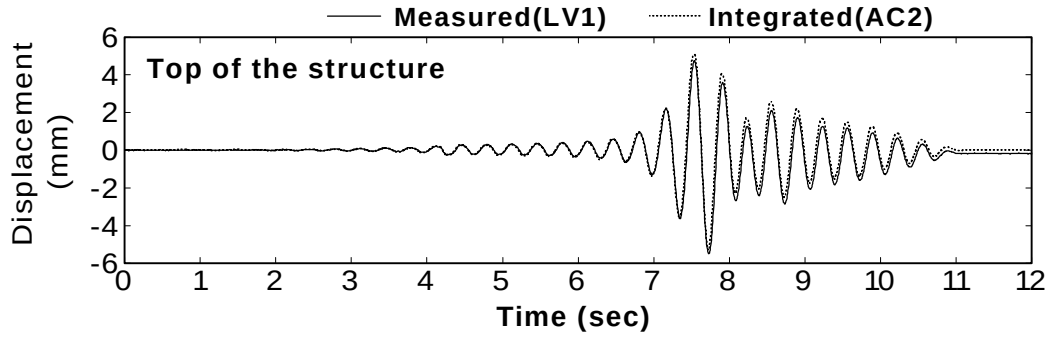

(a) AD35F3A50 test

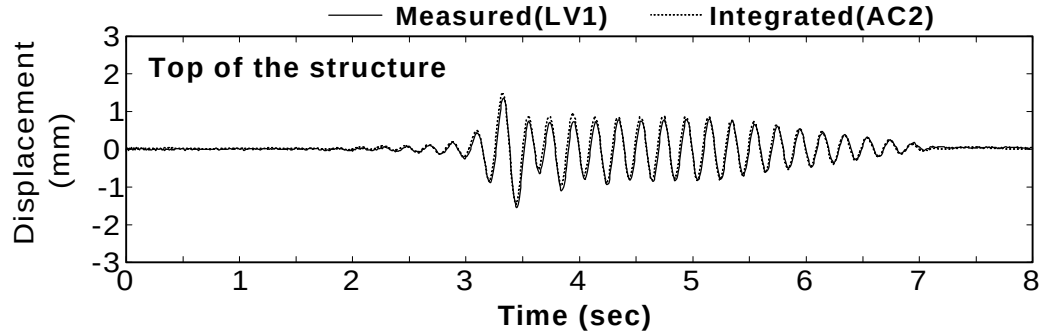

(b) AD39F5A50 test

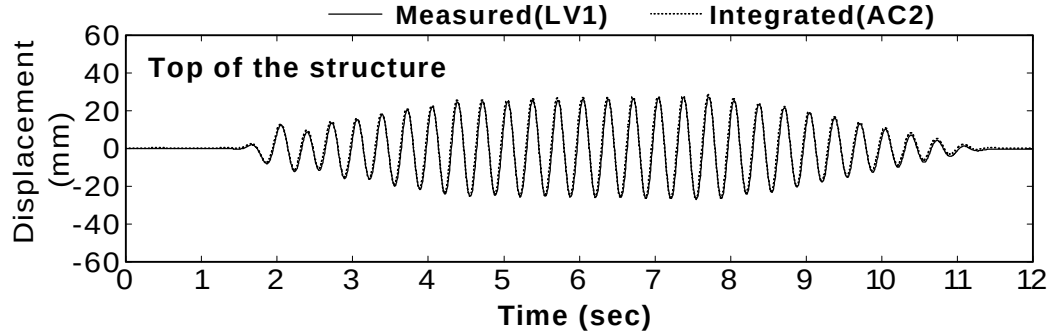

(c) AD32F3A500 test

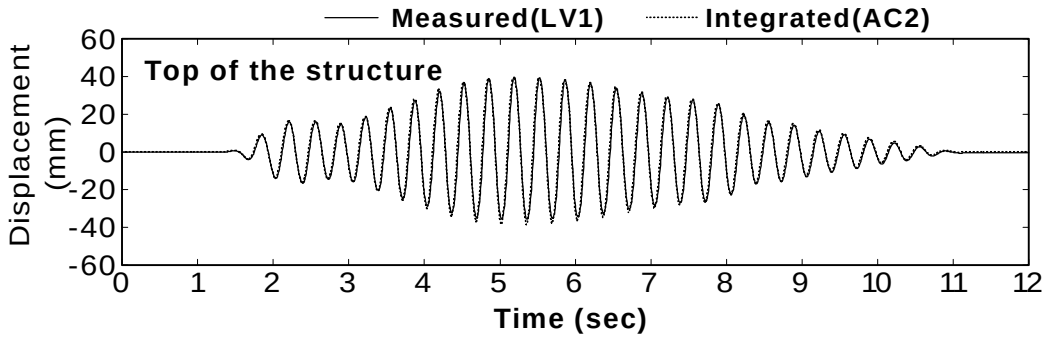

(d) AD67F3A500 test

Fig.4.8: Displacements derived by numerical integration of acceleration

4.3.2 Numerical integration of curvature for deflections

The deflection in the wall of the structure at each depth was calculated by integrating the curvature twice with respect to height. Fig.4.9 shows the procedure of the calculation. The measured bending strain was converted to curvature, and integration was conducted in all time steps. Fig.4.10 illustrates the definition of coordinate for the analysis. u is the deflection of the wall, and Z is a coordinate in the vertical direction from the bottom of the wall ($Z = H - z$). The curvature was assumed constant in a small piece of the wall ΔZ. The suffix i means the quantity at the height Z_i.

The deflection u_{i+1} at the height Z_{i+1} is expressed as follows depending on the Taylor expansion,

$$u_{i+1} = u_i + (\Delta Z)\frac{du_i}{dZ} + \frac{1}{2}(\Delta Z)^2\frac{d^2u_i}{dZ^2} + \frac{1}{6}(\Delta Z)^3\frac{d^3u_i}{dZ^3} + \cdots \tag{4.26}$$

where

$$\frac{du_i}{dZ} = q_i \tag{4.27}$$

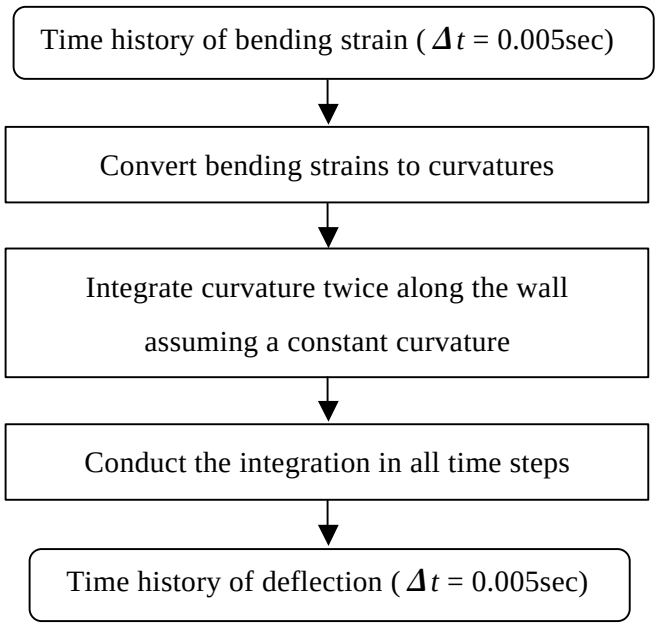

Fig.4.9: Procedure of the numerical integration of acceleration for deflection

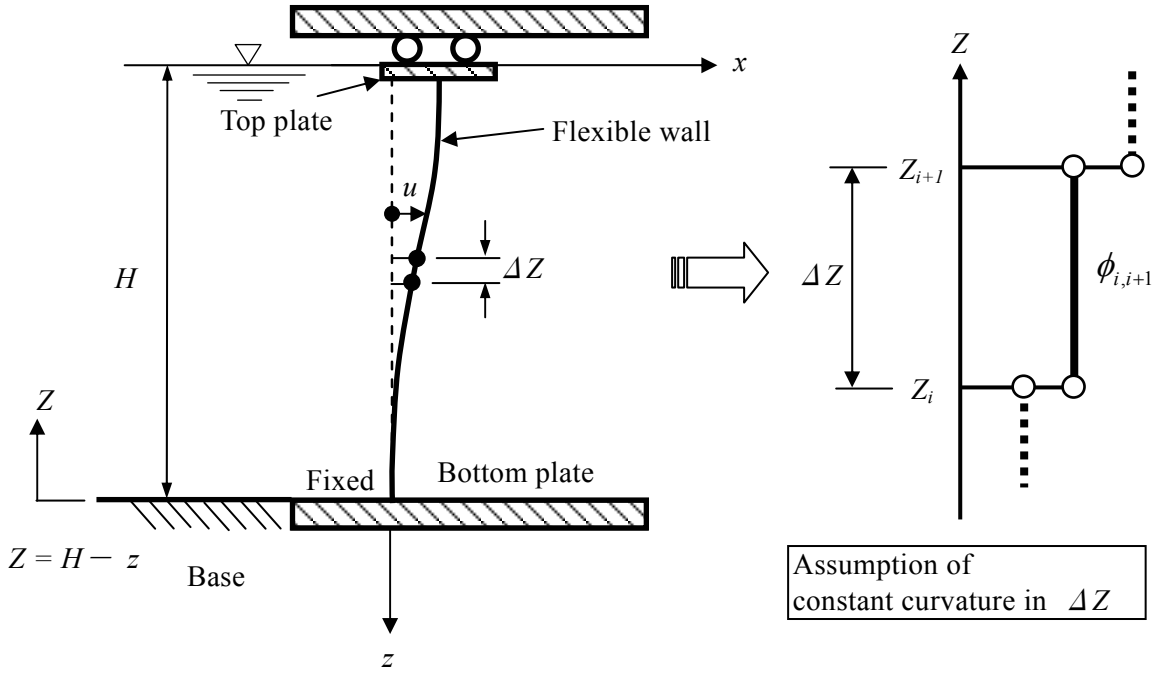

Fig.4.10: Definition of a coordinate and a constant curvature

and

$$\frac{d^2u_i}{dZ^2} = \frac{d\theta_i}{dZ} = \phi_{i,i+1} \quad (const.) \tag{4.28}$$

Considering that differential coefficients higher than the second order become zero, Eq.(4.26) is rewritten as

$$u_{i+1} = u_i + (\Delta Z)\cdot\theta_i + \frac{1}{2}(\Delta Z)^2\cdot\phi_{i,i+1} \tag{4.29}$$

where the slope θ_i is calculated as

$$\theta_i = \phi_{i-1,i}\cdot(\Delta Z) + \theta_{i-1} \tag{4.30}$$

The schematic figure of the deflection u_{i+1} is depicted in Fig.4.11. It is seen that the deflection u_{i+1} is calculated by summing u_i, $\theta_i\Delta Z$ and $(\Delta Z)^2\cdot\phi_{i,i+1}/2$. The deflection at each height is calculated step by step by Eq.(4.29) with the boundary condition of

$$u_1=0 \text{ and } \theta_1 = 0 \quad \text{at } Z=0 \tag{4.31}$$

It should be noted that the calculated deflections by Eq.(4.29) with boundary condition of (4.32) will be relative values with respect to the bottom of the structure.

Fig.4.12 shows the assumed distribution of the curvature at each time step for the numerical integration. The curvatures between the transducers were interpolated by a linear function and those at the edge of the wall were extrapolated linearly. ΔZ was specified as 1mm in the calculation. The measured bending strain was converted to the curvature by dividing the bending strain by the thickness of the wall of 4.97mm for Structure-A, and 4.87mm for Structure-B1, B2.

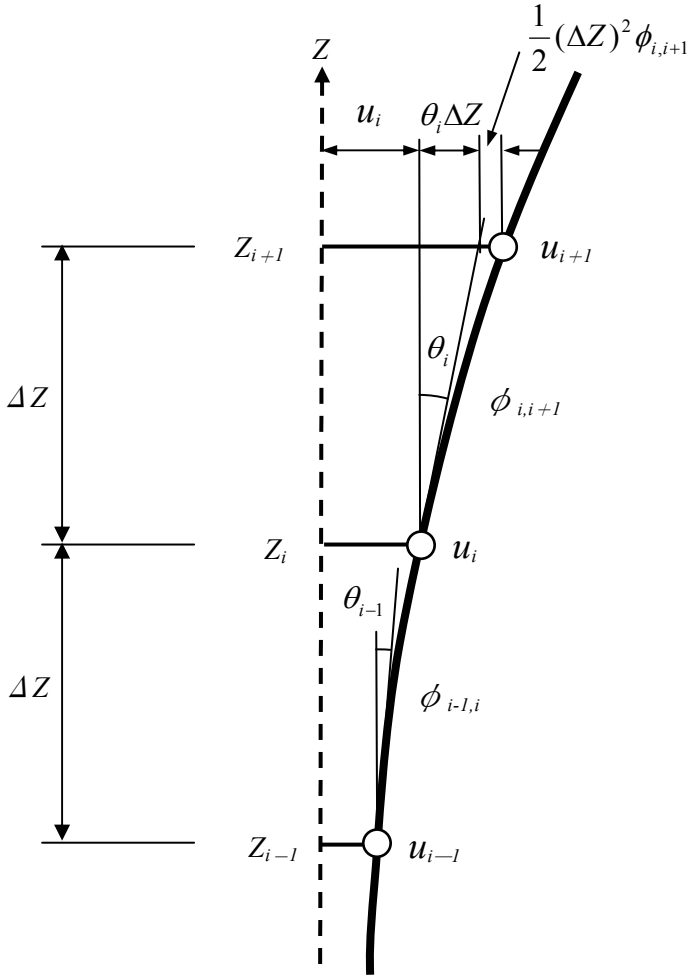

Fig.4.11: Deflection of a beam at a node *i+1*

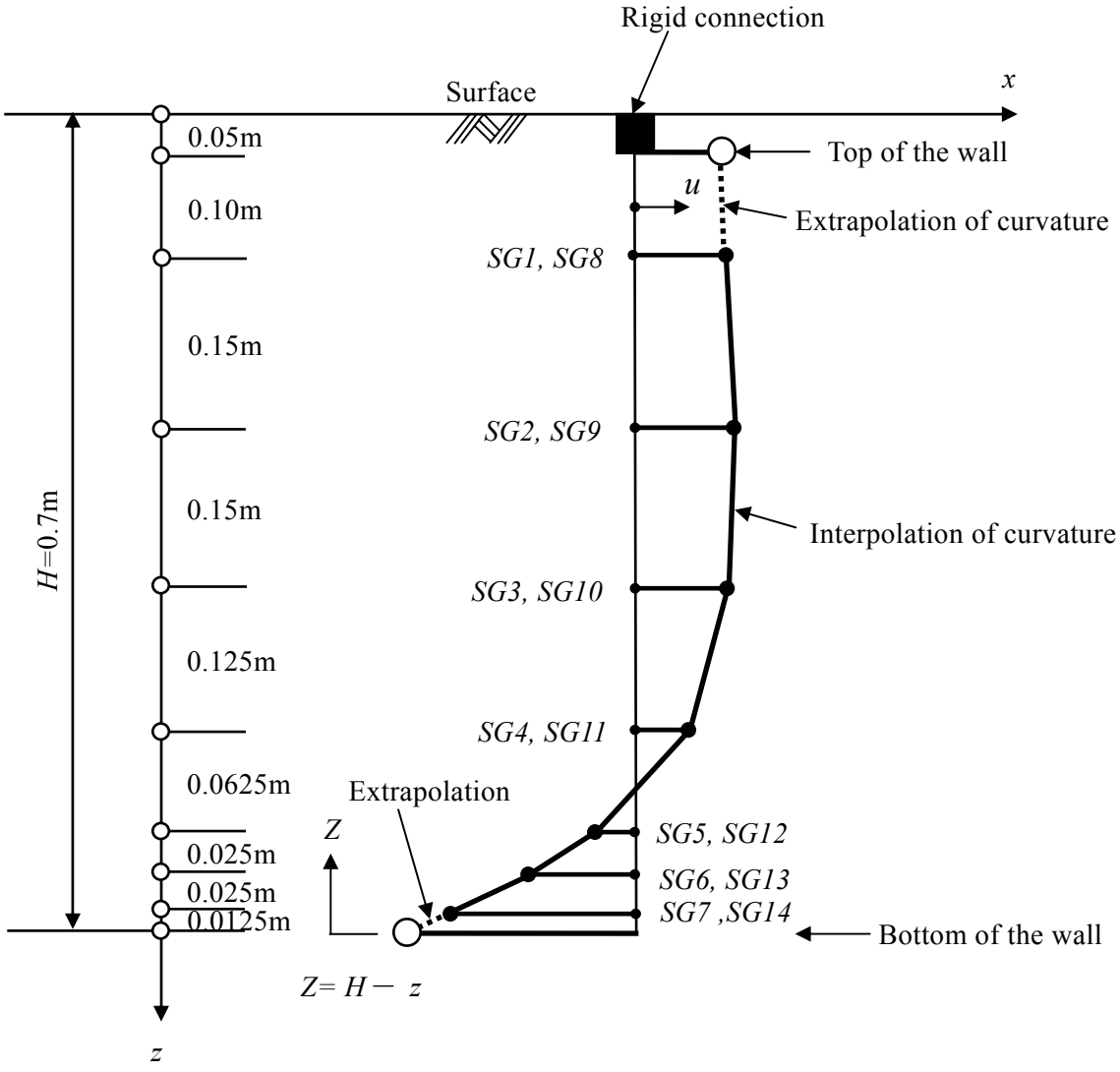

Fig.4.12: Assumed distribution of curvature for the numerical integration

The time histories of displacement at the top of structure derived by numerical integration are compared with the measured displacements in Fig.4.13. It is noted that the measured displacement (LV1) is a relative displacement between the top and the bottom of structure. The curvatures of right wall (SG8～SG14) were used for this calculation.

Fig.4.13(a) shows the time histories of displacement from AD35F3A50 test. It was seen that the calculated displacement due to integration agreed with measured displacement satisfactory from 7 to 10 seconds when the displacement was amplified to about 5mm. The irregular amplitude and periods were observed, however, in calculated displacement in the time period of 0 to 6 seconds and 10.5 to 12.0seconds. The amplitude of measured displacement was relatively small during those time periods. It was remarkable that amplitude of about 1mm was calculated before shaking when the displacement of that level could not occur. It is due to the noises contained in the bending strain time histories as seen in Fig.3.18.

Fig.4.13(b) illustrates the time histories of displacement from AD39F5A50 test. In this test, the amplitude of displacement was less than 2mm throughout the excitation. It was seen that the calculated displacement contained irregular amplitudes of about 1mm, and the agreement was not so good with the measured displacement before liquefaction of 1 second～4.5 seconds.

Fig.4.13(c) and (d) show the results from AD32F3A500 test and AD67F3A500 test, respectively. The amplitude of measured displacement exceeded 20mm in both tests. In both cases, the time history of calculated displacement by integration of curvature was consistent with the measured displacement. It was considered that the noises in the measured curvature (see, Fig.3.22 and Fig.3.26) did not affect the displacement since the level of noise amplitude became relatively smaller than the level of amplitude due to excitation.

It was suggested that the procedure of numerical integration shown in this section is appropriate to calculate the deflection at any height of the wall. It should be noted that the calculated deflection less than 1mm is not meaningful.

4.3.3 Numerical differentiation of wall displacement for accelerations

The accelerations on the wall of the structure at each depth were calculated by differentiating the displacement of the wall, which was derived by integrating the measured curvature twice with respect to height. Fig.4.14 shows the procedure of the calculation. Numerical differentiation was conducted in the frequency domain. A measure by appropriate digital filtering was taken to remove noises of high frequency components. Then, the appropriate frequencies will be determined.

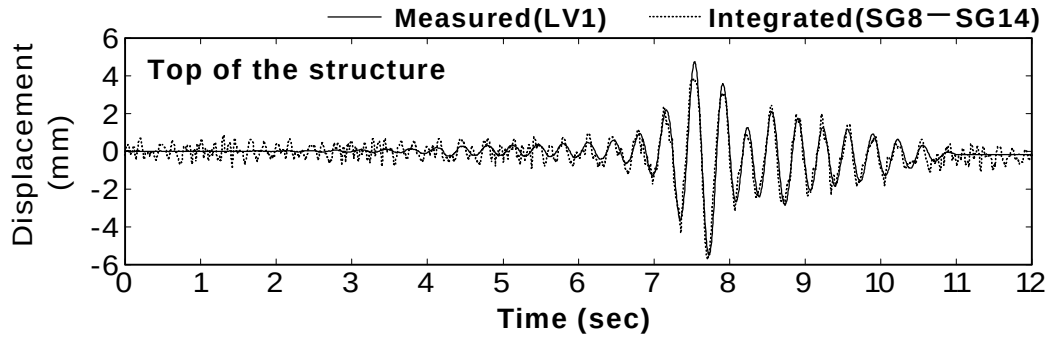

(a) AD35F3A50 test

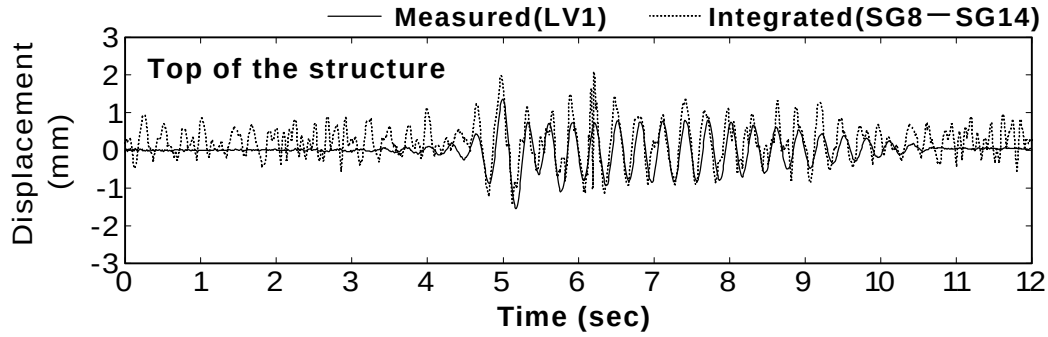

(b) AD39F5A50 test

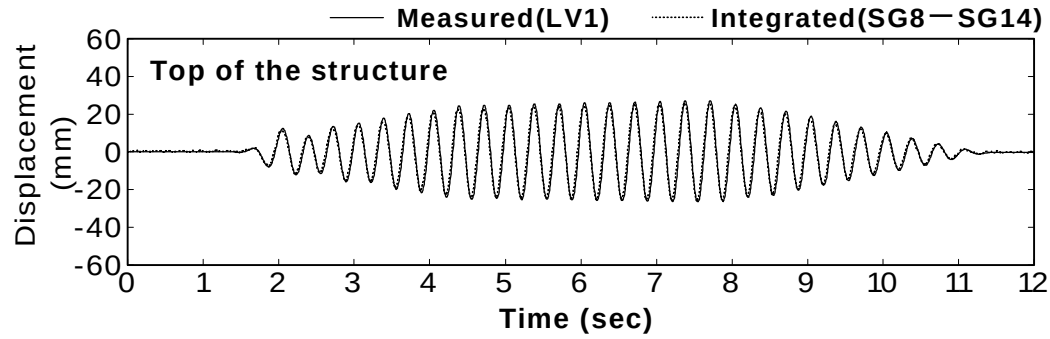

(c) AD32F3A500 test

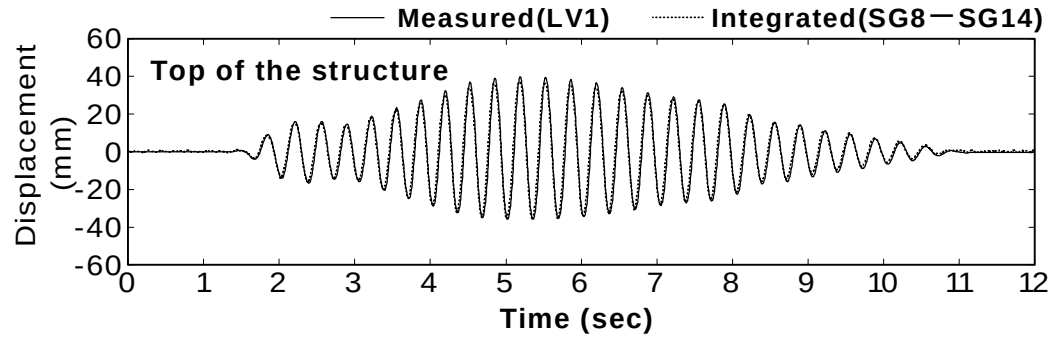

(d) AD67F3A500 test

Fig.4.13: Displacements derived by numerical integration of curvature

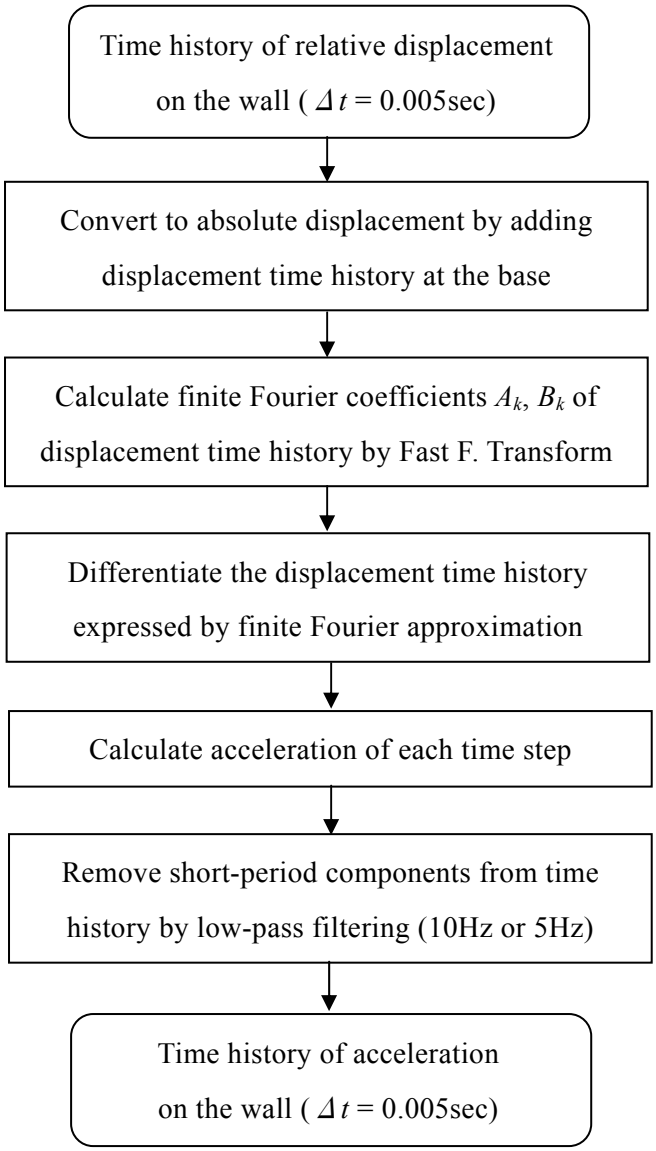

Fig.4.14: Procedure of the numerical differentiation of wall displacement for acceleration

Mathematical formulation of numerical differentiation

The time history of displacement is expressed in the manner of finite Fourier approximation as

$$\tilde{u}(t) = \frac{A_0}{2} + \sum_{k=1}^{N/2-1} \{A_k \cos 2\pi f_k t + B_k \sin 2\pi f_k t\} + \frac{A_{N/2}}{2} \cos 2\pi f_{N/2} t \tag{4.32}$$

where N is number of time history data, Δt is a time interval, and A_k, B_k are finite Fourier coefficients, and

$$f_k = k/(N\Delta t) \tag{4.33}$$

The finite Fourier coefficients A_k, B_k are calculated by using the FFT (Fast Fourier Transform) technique. The time history of velocity is calculated as what follows by differentiating Eq.(4.32) once with respect to time,

$$\begin{aligned} \frac{\partial \tilde{u}}{\partial t}(t) = & \sum_{k=1}^{N/2-1} \{- A_k (2\pi f_k) \sin 2\pi f_k t + B_k (2\pi f_k) \cos 2\pi f_k t\} \\ & - \frac{A_{N/2}}{2} (2\pi f_k) \sin 2\pi f_{N/2} t \end{aligned} \tag{4.34}$$

The time history of acceleration is derived by differentiating Eq.(4.34) once as

$$\begin{aligned} \frac{\partial^2 \tilde{u}}{\partial t^2}(t) = & \sum_{k=1}^{N/2-1} \{- A_k (2\pi f_k)^2 \cos 2\pi f_k t - B_k (2\pi f_k)^2 \sin 2\pi f_k t\} \\ & - \frac{A_{N/2}}{2} (2\pi f_k)^2 \cos 2\pi f_{N/2} t \end{aligned} \tag{4.35}$$

Acceleration at each time step is calculated by Eq.(4.35). Thus, the time history of acceleration on the wall is derived.

Verification of procedure of numerical differentiation

To verify the calculation procedure aforementioned, the measured time history of displacement at the top of the structure (LV1) was differentiated. The calculated acceleration was compared with the measured acceleration at the top of the structure (AC2).

Calculated accelerations with various low-pass filtering frequencies are compared with the measured accelerations from AD35F3A50 test in Fig.4.15. The calculated acceleration without low-pass filtering is illustrated in Fig.4.15(b). It is seen that many high frequency components appeared in the calculated time history. It is apparently inconsistent with the measured

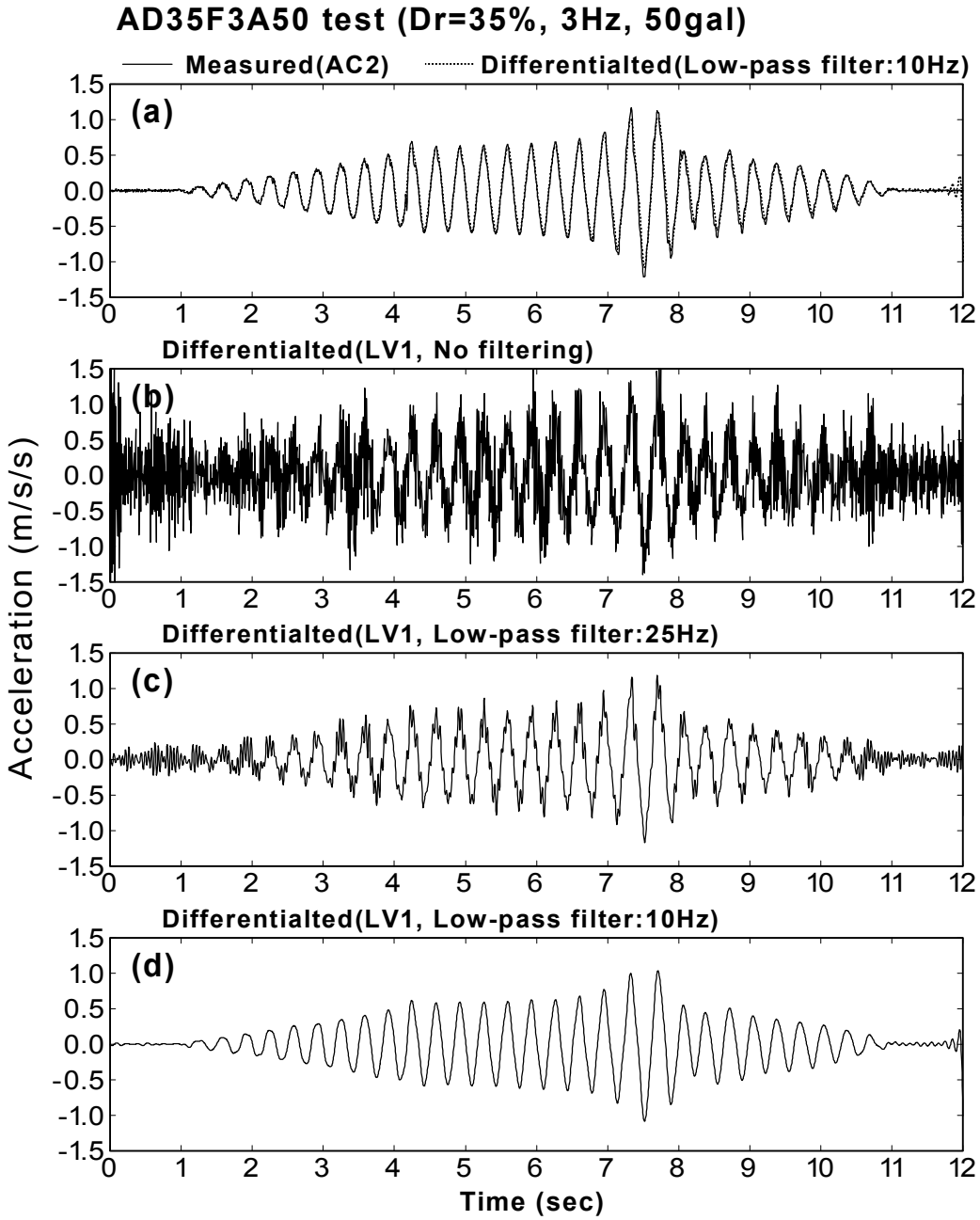

Fig.4.15: Accelerations derived by numerical differentiation of measured displacement (AD35F3A50 test)

acceleration which is illustrated by solid line in Fig.4.15(a). Then, the digital filtering was introduced to remove the high frequency components from the time history of Fig.4.15(b). Fig.4.15(c) is the result of the low-pass filtering with cut-off frequency of 25Hz. It was seen that the shape of the time history became closer to the measured time history than before. Fig.4.15(d)

shows the result of low-pass filtering with the cut-off frequency of 10Hz. This time history is compared with the measured time history in Fig.4.15(a). The agreement is satisfactory with this cut-off frequency of 10 Hz.

The results of calculation from AD67F3A500 test are illustrated in Fig.4.16. Fig.4.16(b) shows the calculated acceleration through the excitation, and (c) is the time history from 5 to 6 seconds enlarged in terms of the time axis. It was seen that the acceleration derived by the numerical differentiation is almost identical with the measured acceleration without any low-pass filtering. It shows that the procedure of the numerical differentiation shown in this section is effectual, and it should be noted that the appropriate low-pass filtering is preferable depending on displacement time history which will be differentiated.

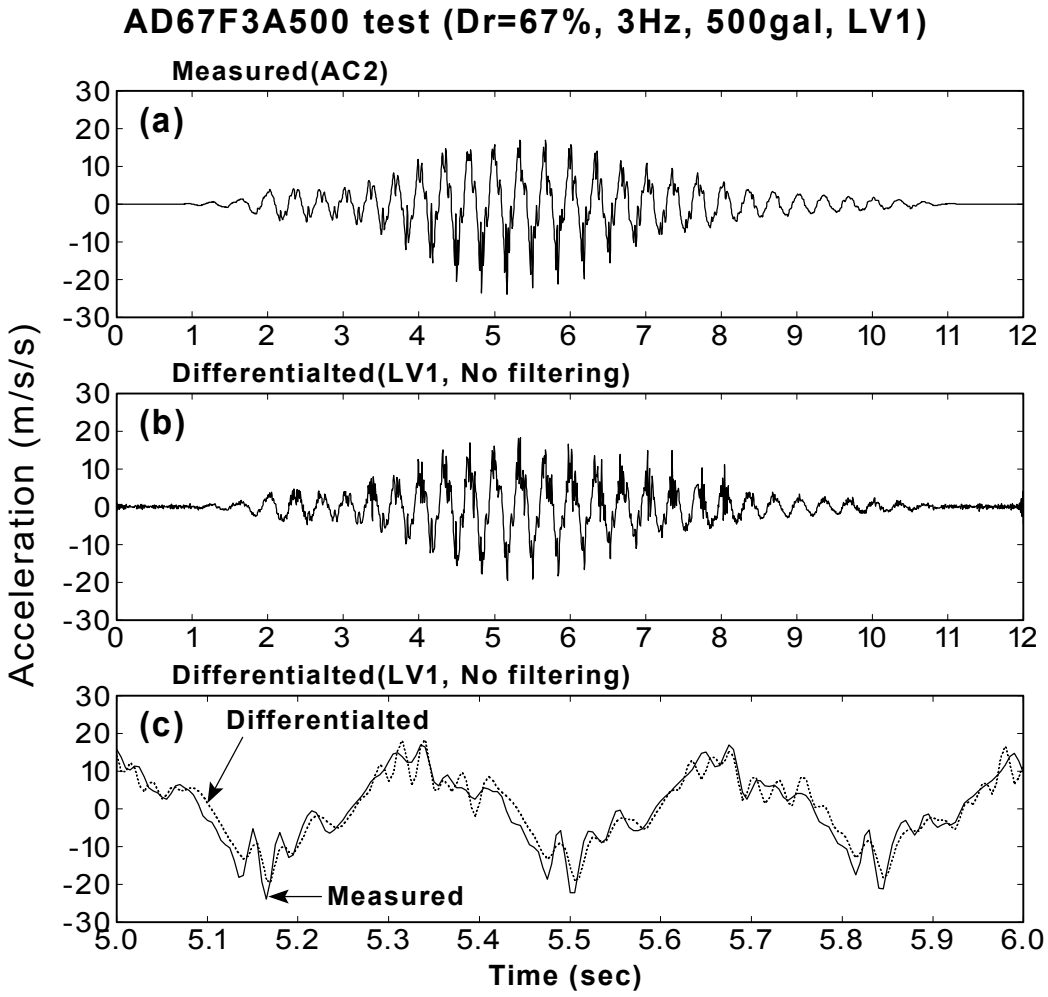

Fig.4.16: Accelerations derived by numerical differentiation of measured displacement (AD67F3A500 test)

Determination of filtering frequencies for acceleration on the wall

To determine the appropriate cut-off frequency for low-pass filtering, the wall acceleration which is derived by numerical differentiation was filtered by various cut-off frequencies. The displacement at the top derived by the integration of curvature is denoted by SGLV1 here. It is not exactly same as the displacement LV1 which was measured by the laser displacement transducer.

Fig.4.17 shows the results from AD35F3A50 test. The measured acceleration at the top of the structure is illustrated in Fig.4.17(a) by a solid line for the comparison. Fig.4.17(b) is the result without any filtering procedure. It was seen that many high frequency components were contained in the time history, and the maximum amplitude reached about a level of 10m/sec^2. Fig.4.17(c) and (d) are the results of filtering frequencies of 10Hz and 5Hz, respectively. The latter is closer to the measured acceleration than the former. The calculated acceleration of 5Hz filtering is compared with the measured acceleration in Fig.4.17(a). The agreement was satisfactory during excitation of 1sec～11sec. The filtering frequency of 5Hz seems to the appropriate cut-off frequency for this test.

Fig.4.18 illustrates the results from AD39F5A50 test. Fig.4.18(a) compares the measured acceleration with the acceleration with filtering frequency of 6Hz. It was seen that the amplitude of acceleration changed irregularly during excitation. The appropriate acceleration on the wall could not be reproduced by the differentiation in this test. Fig.4.19 depicts the results from AD41F3A200 test. By comparing the results which is shown in Fig.4.19(b)～(d), a frequency of 5Hz seemed to give the best result for this test. Fig.4.20 illustrates the results from AD67F3A500 test. As shown in Fig.4.20(d) and (f), the result with a cut-off frequency of 10Hz agrees well with the measured acceleration. The frequency of 10Hz seems to be the appropriate cut-off frequency for the test.

The cut-off frequencies for low-pass filtering are summarized in Table 4.3. 5Hz was selected for tests shaken by the peak acceleration of 0.5m/sec^2 and 2.0m/sec^2. And 10Hz were selected for the tests with the peak acceleration of 5.0m/sec^2.

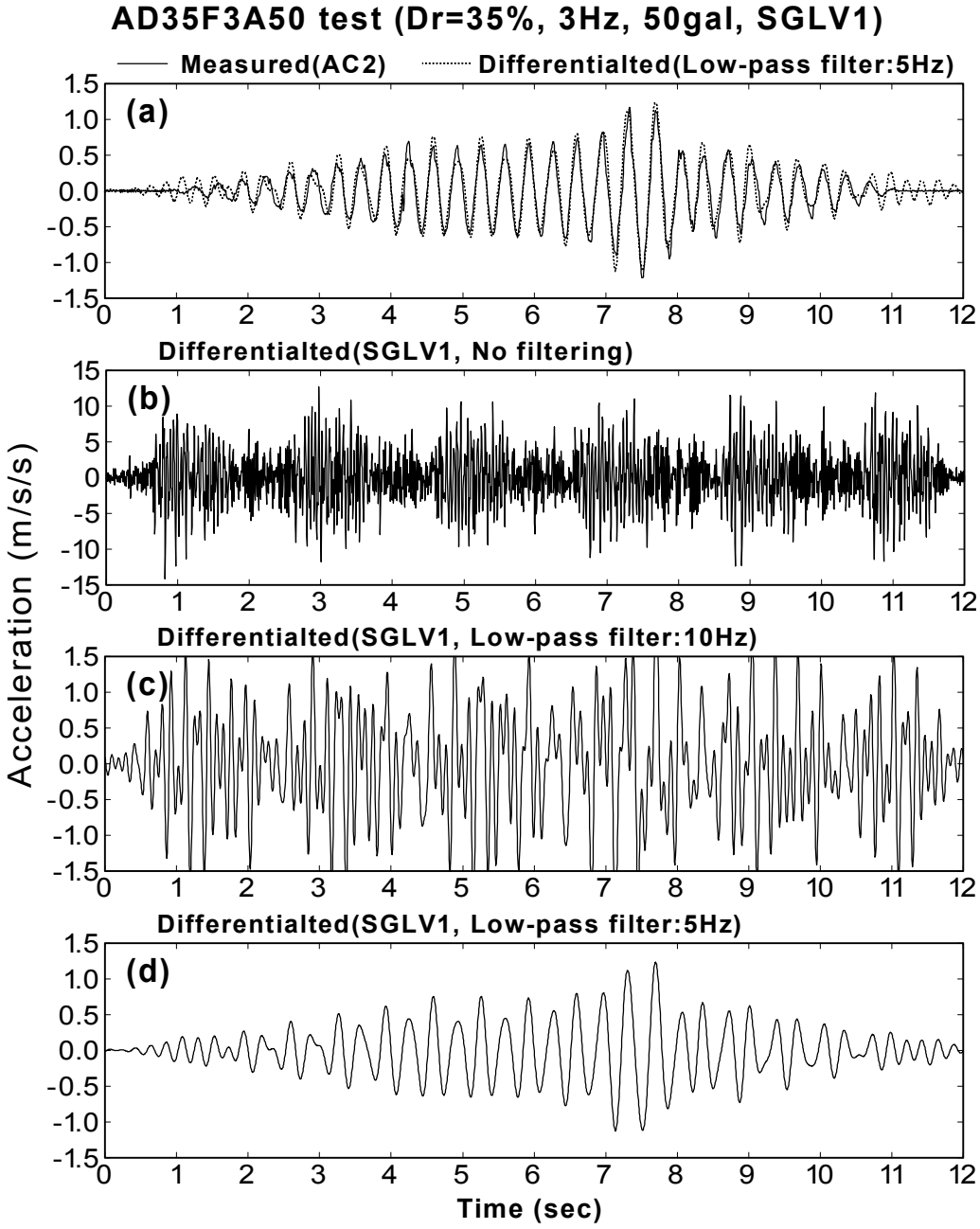

Fig.4.17: Accelerations derived by numerical differentiation of calculated displacement (AD35F3A50 test)

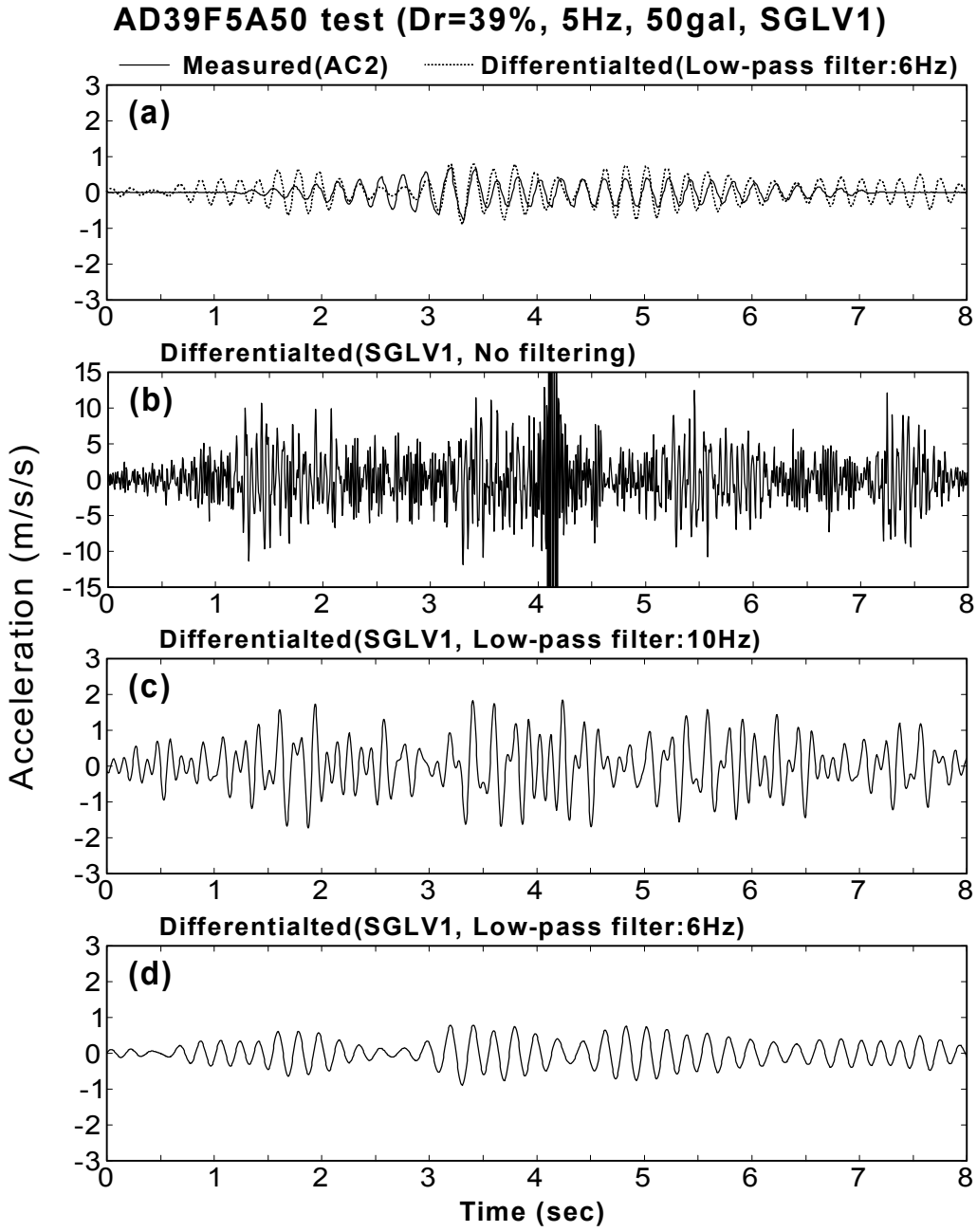

Fig.4.18: Accelerations derived by numerical differentiation of calculated displacement (AD39F5A50 test)

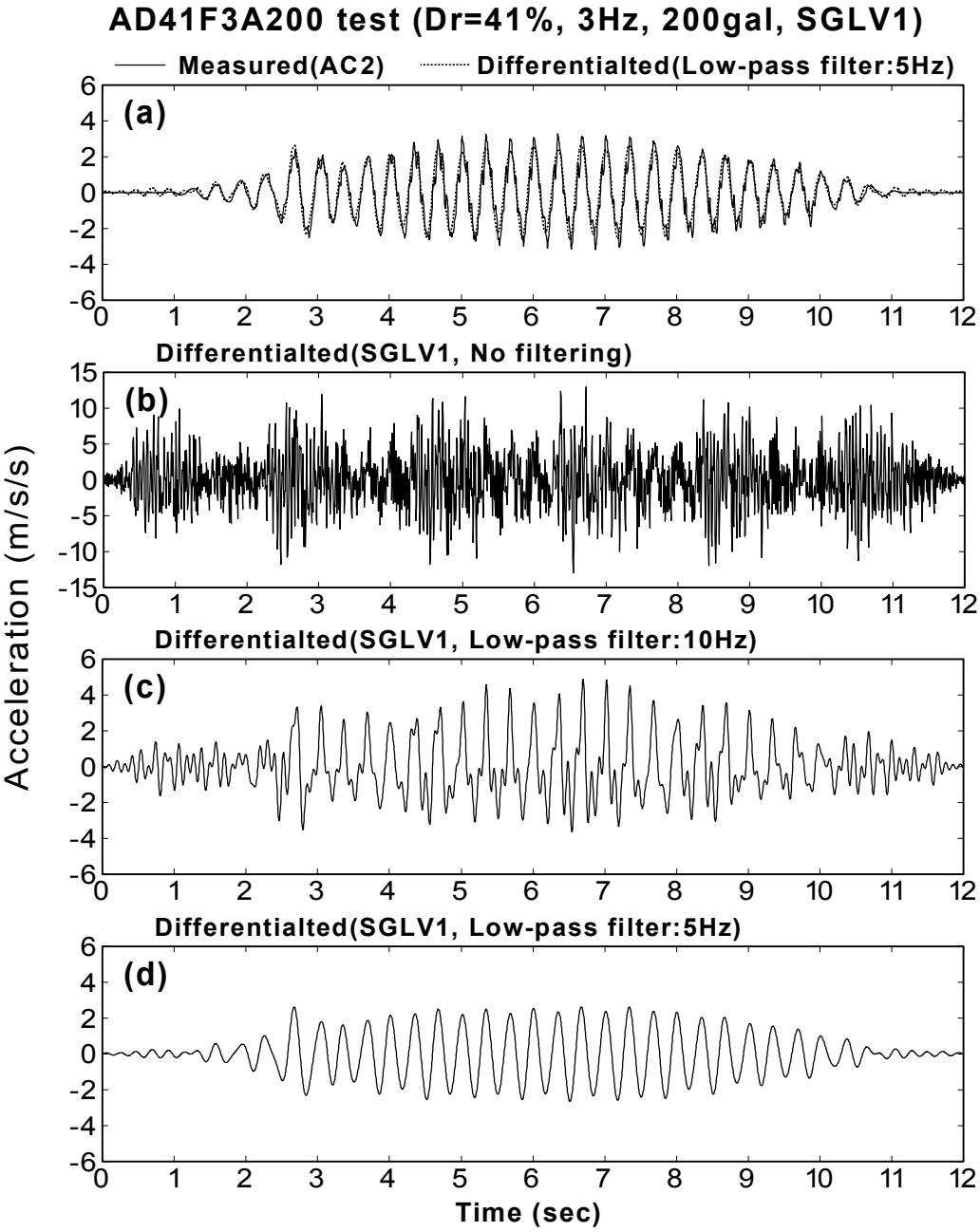

Fig.4.19: Accelerations derived by numerical differentiation of calculated displacement (AD41F3A200 test)

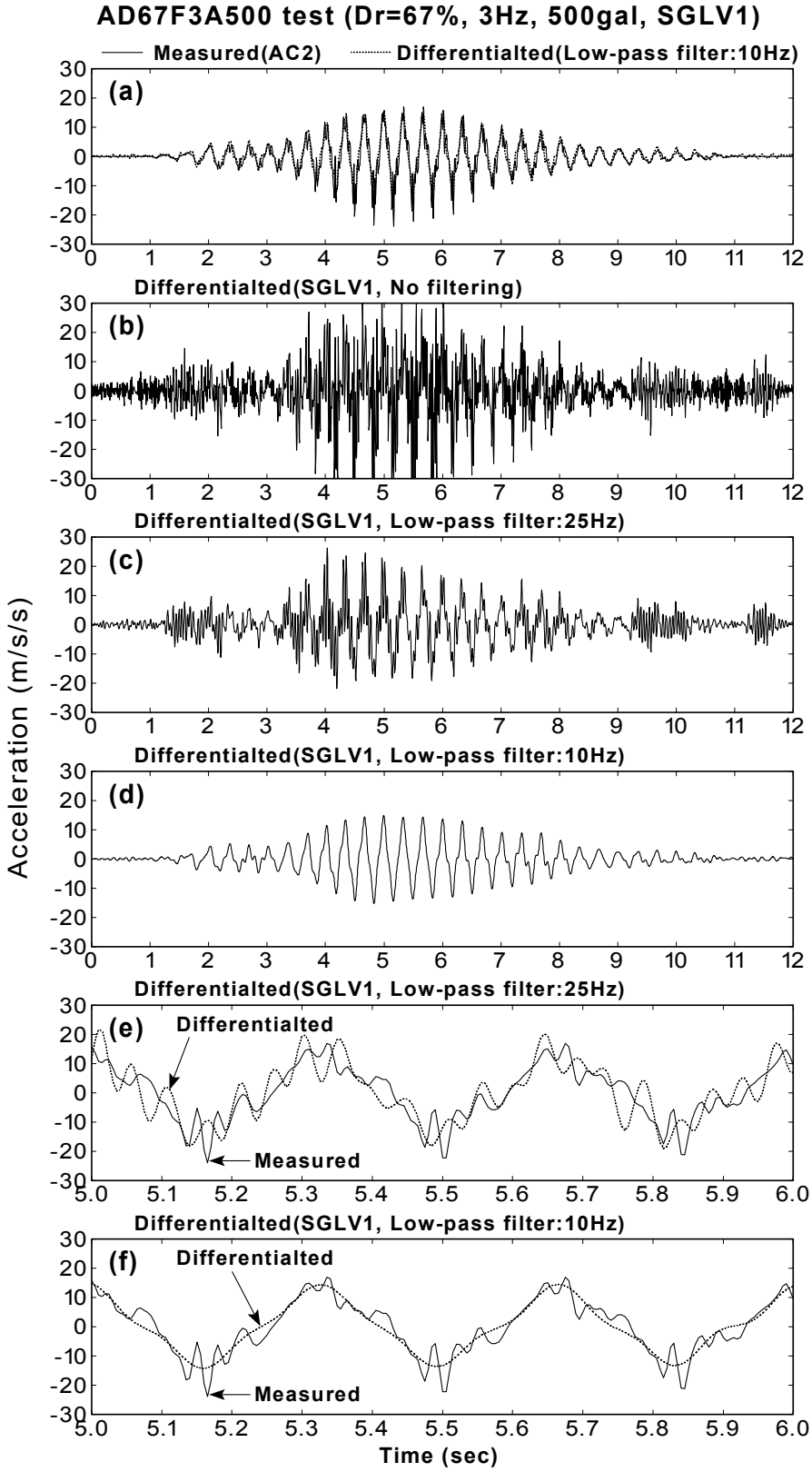

Fig.4.20: Accelerations derived by numerical differentiation of calculated displacement (AD67F3A500 test)

Table 4.3: Cut-off frequency of low-pass filtering for the acceleration on the wall

Case No	Freq. (Hz)	Acc. (m/sec^2)	Cut-off frequency (Hz)	Remarks
AD35F3A50	3	0.5	5	Could not be reproduced
AD39F5A50	5	0.5	—	
AD41F3A200	3	2.0	5	
AD61F3A200	3	2.0	5	
AD67F3A500	3	5.0	10	
AD32F3A500	3	5.0	10	
BD36F3A500	3	5.0	10	
BD78F3A500	3	5.0	10	

Since the wall acceleration could not be calculated correctly only in AD39F5A50 test by the numerical differentiation (see, Fig.4.18), the alternative equation of Eq.(4.8) is selected to calculate the inertia force of soil mass, in which only the acceleration in the backfill is taken into account.

4.4 STRESS-STRAIN RELATIONSHIP

A soil mass in the backfill at the middle depth of the structure (GL-0.30m～GL-0.45m) will be focused on to reproduce stress-strain relationship and effective stress path. Shear stress as well as inertia forces of soil mass and normal stress differences will be presented in the process of calculation.

4.4.1 Inertia force and stress difference

Typical results (AD35F3A50 test)

The time histories of inertia force, normal stress difference of each soil mass and pore pressure in the backfill from AD35F3A50 test are illustrated in Fig.4.21. Eqs.(4.6) and (4.10) were employed for the calculation of acceleration and normal stress difference, respectively. The height of the soil mass Δz was multiplied to those quantities. Long-period components in these time histories were

removed by the high-pass digital filtering of 1Hz.

It was seen in Fig.4.21(a) that the inertia force of a soil mass, $-\rho \cdot \alpha_x \cdot \Delta z$, near the surface amplified just before the liquefaction at about 7.5 seconds. It was similar to the shape of the time history of acceleration at the surface (see.Fig.3.16). The amplitude of the normal stress difference, $\partial \sigma_x / \partial x \cdot \Delta z$, was smaller than that of inertia force in 2～3 seconds (see arrows in Fig.4.21(c)) when the pore pressure did not build up yet. It became the same level of amplitude during liquefaction at around 9～10 seconds.

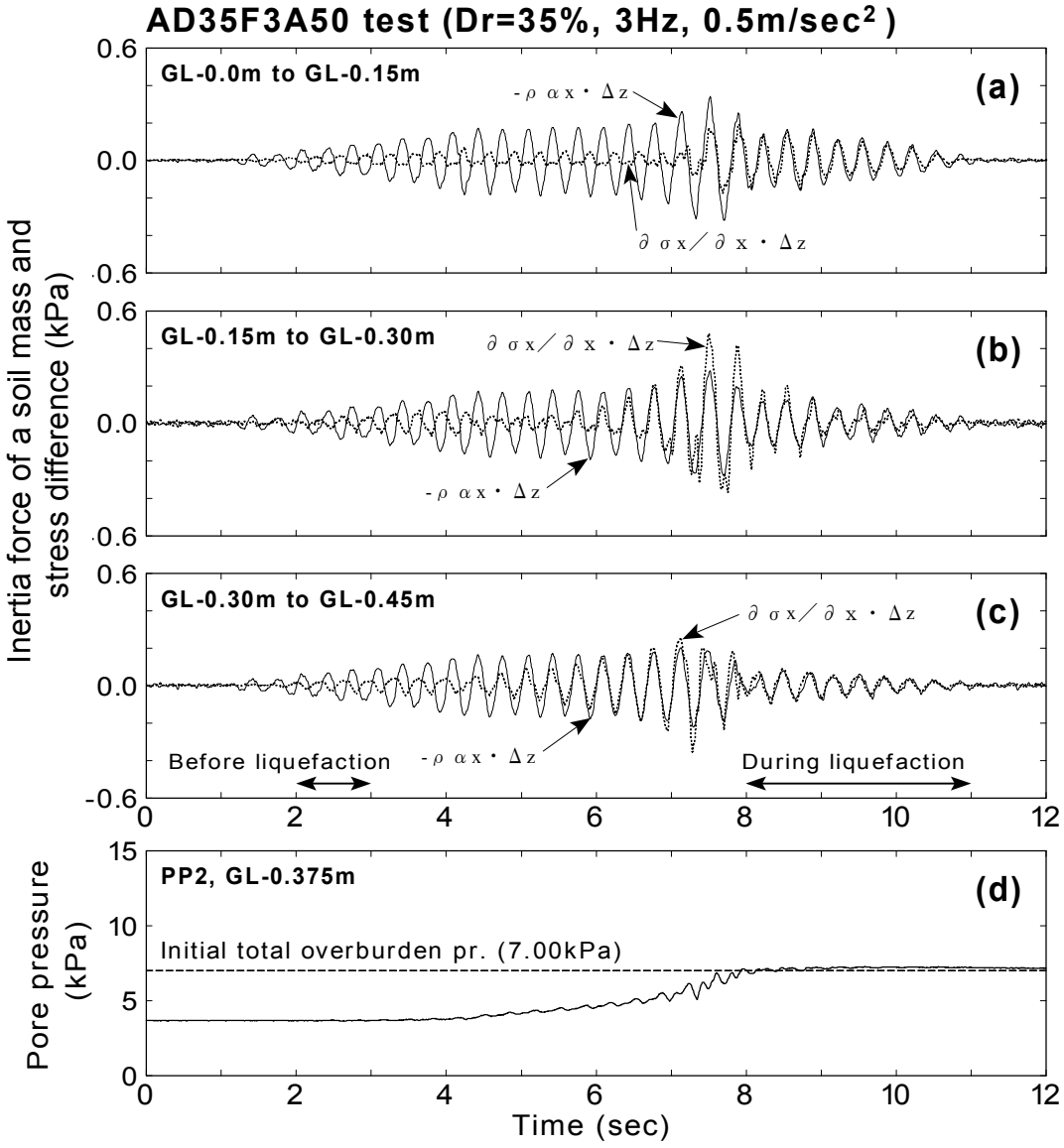

Fig.4.21: Inertia force of a soil mass and normal stress difference (AD35F3A50 test, GL-0.0m～GL-0.45m)

Time histories of inertia force and normal stress difference before liquefaction (2～3 seconds) and during liquefaction (9～10 seconds) are shown in Fig.4.22. It was observed that time histories before liquefaction were out-of-phase, whereas they changed into in-phase during liquefaction. It was imagined that the shear stress difference was produced in a soil mass before liquefaction (2～3 seconds), causing out-of-phase between inertia force and normal stress difference. According to the force equilibrium in a soil mass expressed by Eq.(4.2), the equality of inertia force to normal stress difference means null shear stress difference in a soil mass. When inertia force and normal stress difference was in-phase (9～10 seconds), provably the shear stress itself was very small by means of liquefaction.

The time histories of the calculated shear stress difference at each soil mass is shown in Fig.4.23. They were calculated as the difference of the inertia force and the normal stress difference shown in Fig.4.21. The amplitude of the shear stress difference at any depth became small after 7～8 seconds when the backfill liquefied. The shear stress will be calculated as the sum of these shear stress differences as expressed by Eq.(4.14).

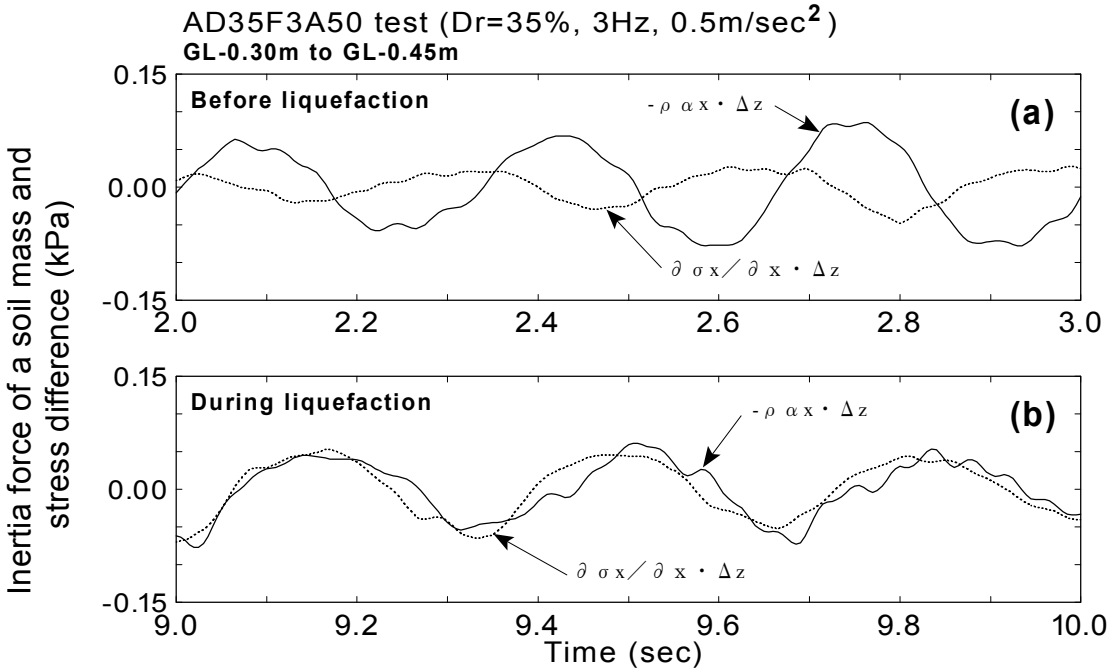

Fig.4.22: Inertia force of a soil mass and normal stress difference before and during liquefaction (AD35F3A50 test, GL-0.30m～GL-0.45m)

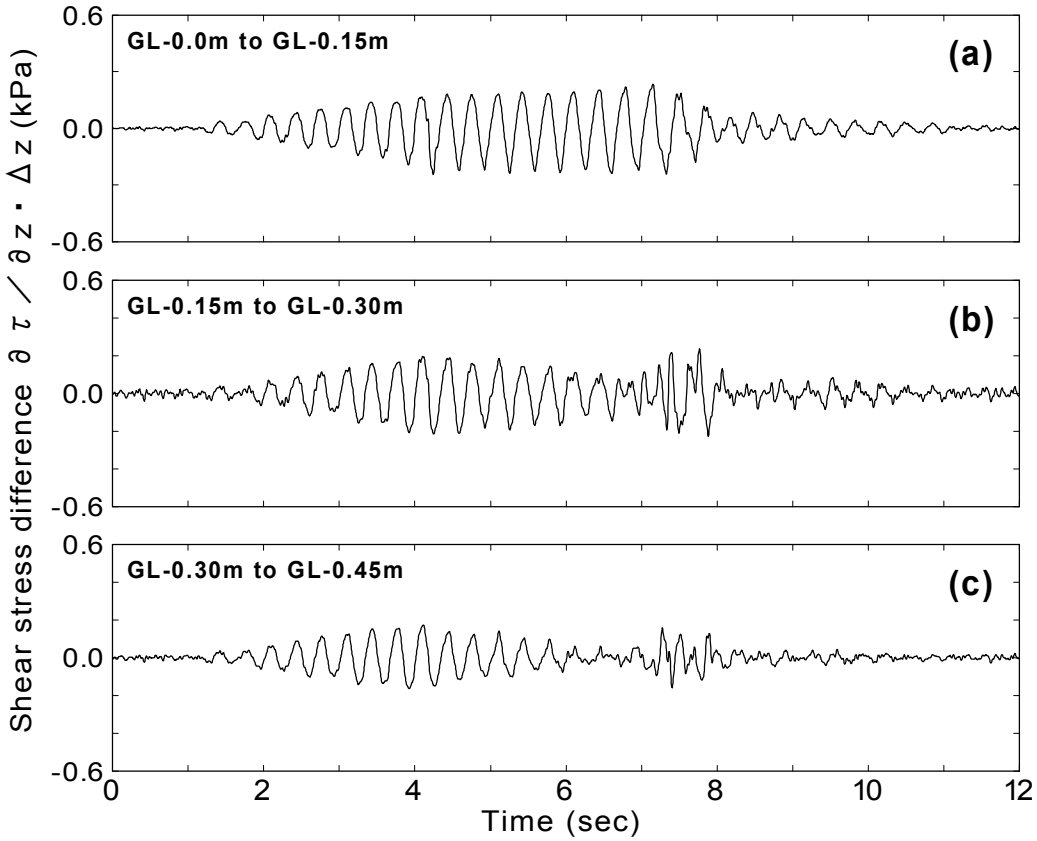

Fig.4.23: Time histories of shear stress difference at each soil mass (AD35F3A50 test, GL-0.0m～GL-0.45m)

The time histories of inertia force, normal stress difference and shear stress difference of a soil mass at GL-0.45m to GL-0.70m are presented in Fig.4.24. The pore water pressure time history at GL-0.638m (PP3) is illustrated in the figure. Change of amplitude with time of the inertia force and normal stress difference at GL-0.45m to GL-0.575m seems similar to that at GL-0.30m to GL-0.45m, which is illustrated in Fig.4.21(c). In contrast, it is observed that amplitude of normal stress difference becomes much larger than that of inertia force of a soil mass after 8 seconds. As a result of this, shear stress difference increases during the time period as observed in Fig.4.24(d). Referencing to the pore water pressure time history in Fig.4.24(e), the pore water pressure does not reach the initial overburden pressure after 8 seconds. It means that the soil at around GL-0.638m does not liquefy completely. It is considered that the unliquefied soil has still some rigidity and the shear stress difference occurs in the soil mass.

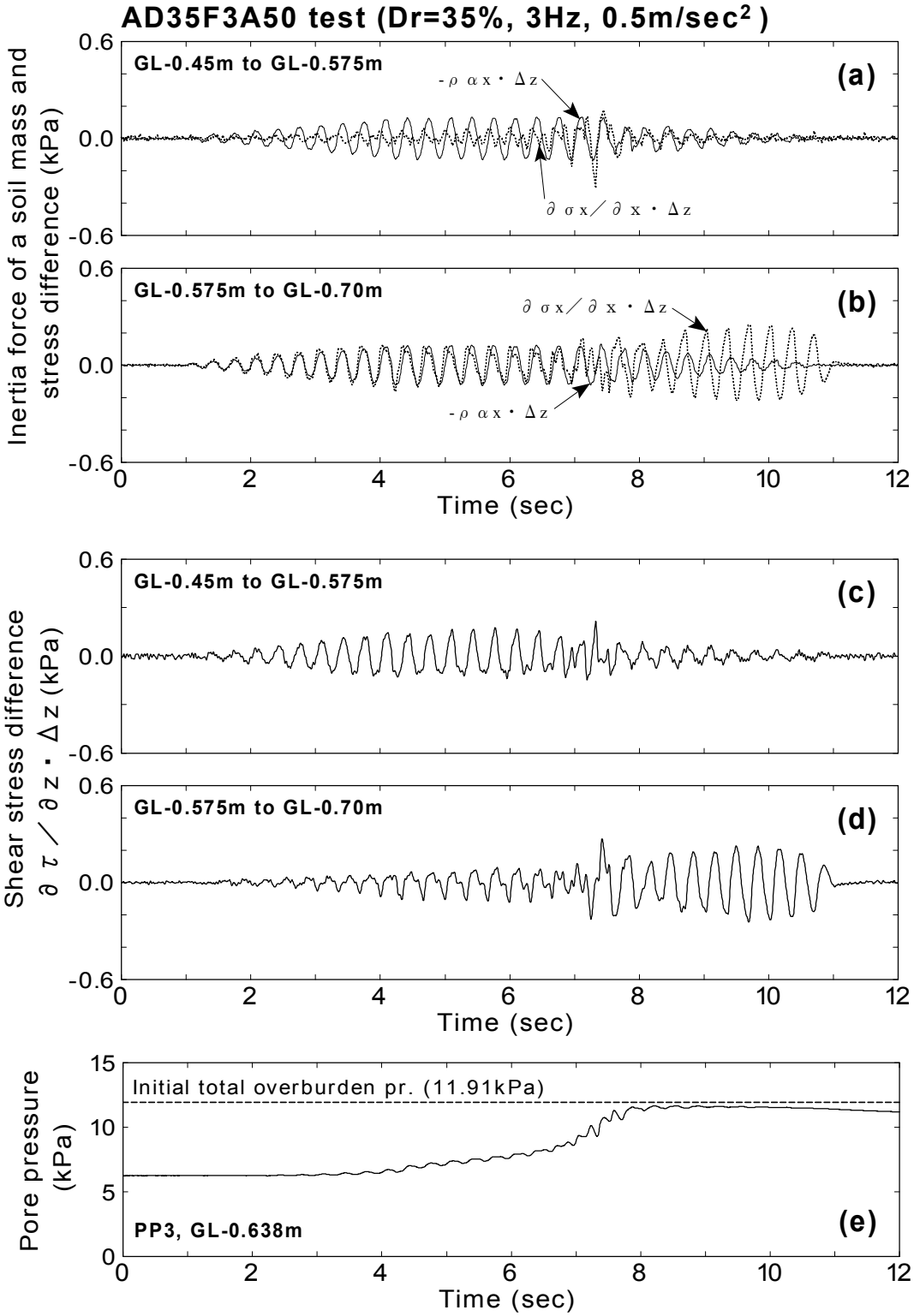

Fig.4.24: Inertia force and stress differences at each soil mass (AD35F3A50 test, GL-0.45m～GL-0.70m)

Results of the test with intense input motion (AD32F3A500 test)

The time histories of inertia force, normal stress difference of each soil mass and pore pressure from AD32F3A500 test are shown in Fig.4.25. The high-pass digital filtering of 1Hz was conducted in these time histories in order to remove long-period components. The pore water pressure built up rapidly and reached the initial total overburden pressure in a second in consequence of the intense input motion of 5.0m/sec^2.

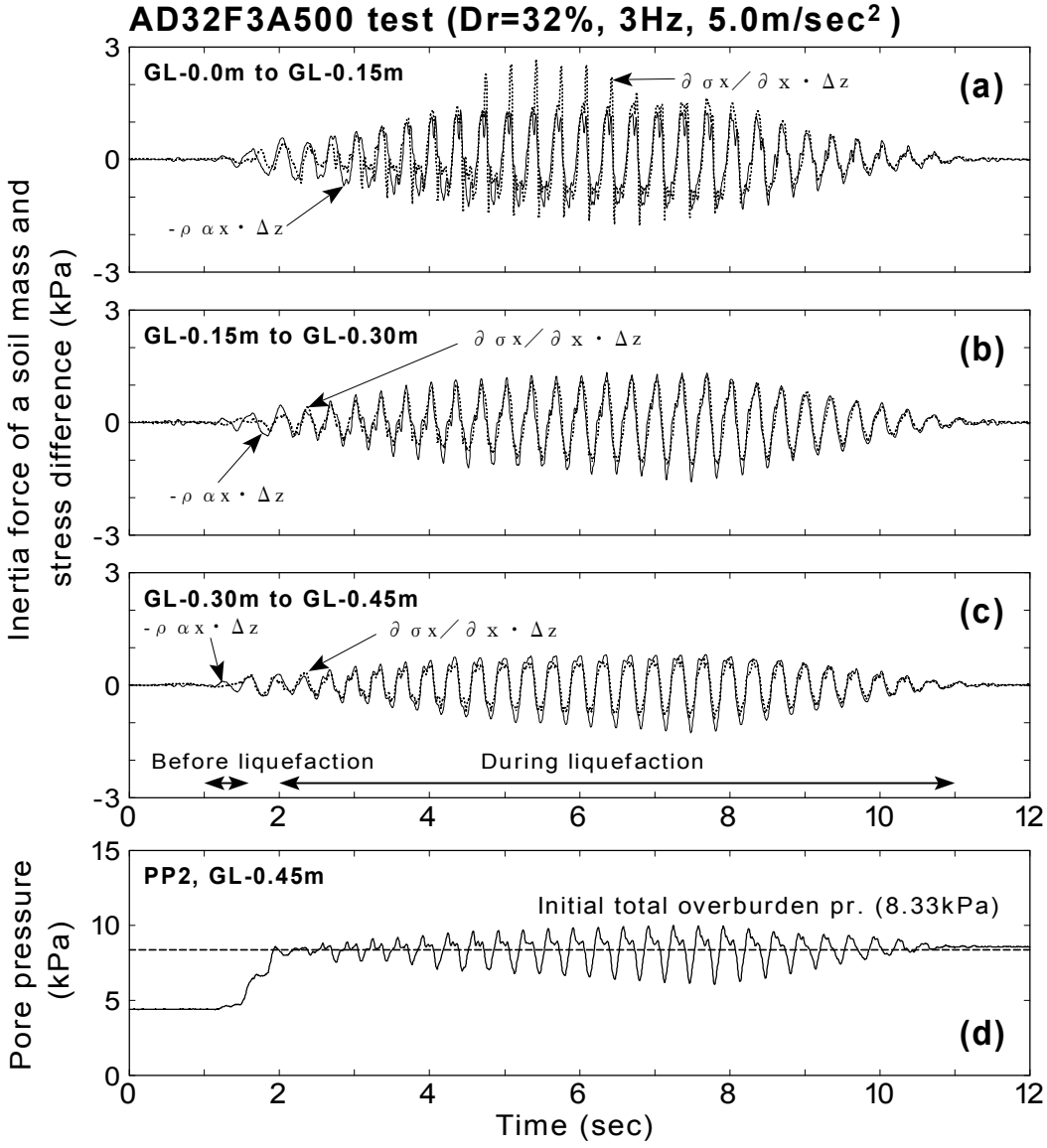

Fig.4.25: Inertia force of a soil mass and normal stress difference (intense input motion, AD32F3A500 test, GL-0.0m～GL-0.45m)

The amplitude of the normal stress difference near the surface (GL-0.0m – GL-0.15m) became larger from 5 to 7 seconds. It was because that the earth pressure measured on the wall (EP6) became much larger than the earth pressure in the backfill (EP1) during the time (see Fig.3.21). In the soil mass located underground, the normal stress difference was almost identical to the inertia force after 2 seconds when the soil liquefied.

Time histories of inertia force and normal stress difference before liquefaction of 1.0～1.6 seconds (see arrows in Fig.4.25(c)) and 9～10 seconds when the soil liquefied completely are shown in Fig.4.26. It is seen that the normal stress difference and the inertia force were out-of-phase at 1.0～1.6 seconds before liquefaction and in-phase 9.0～10 seconds. It suggests that shear stress difference is produced in a soil mass before liquefaction and it becomes nearly zero during liquefaction. The time histories of shear stress differences which were calculated from the inertia force and the normal stress difference shown in Fig.4.25 are illustrated in Fig.4.27. It was observed that the amplitude of shear stress difference did not amplify during the intense shaking.

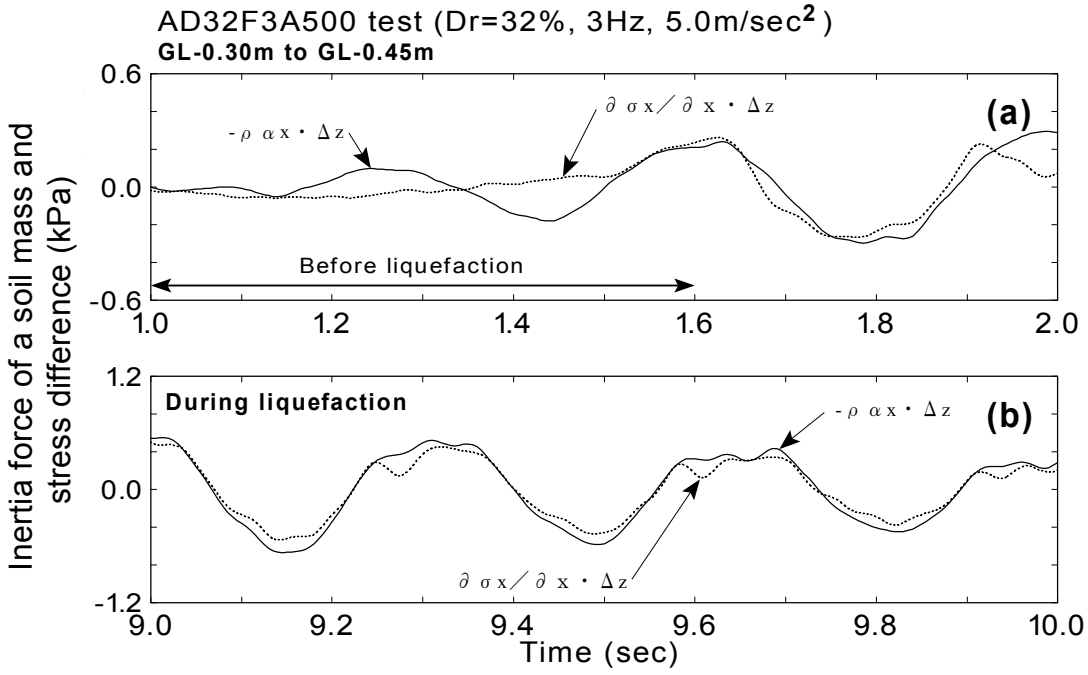

Fig.4.26: Inertia force of a soil mass and normal stress difference before and during liquefaction (intense input motion, AD32F3A500 test, GL-0.30m～GL-0.45m)

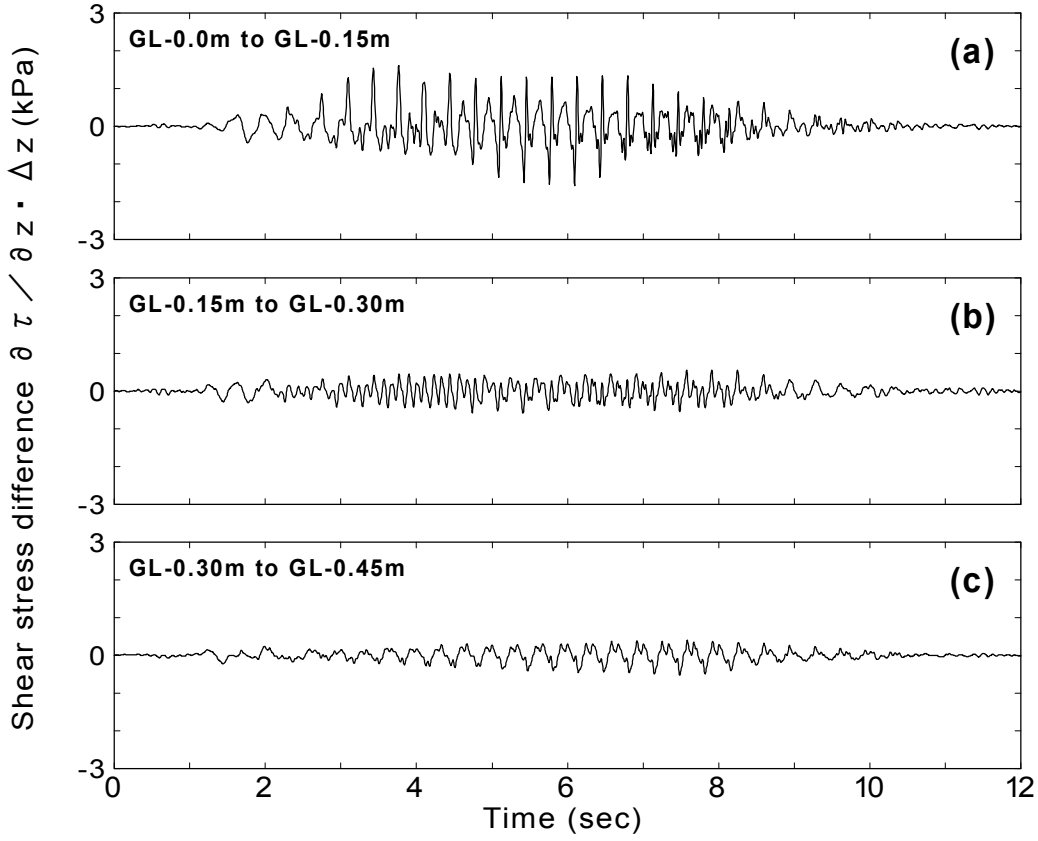

Fig.4.27: Time histories of shear stress difference at each soil mass (intense input motion, AD32F3A500 test, GL-0.0m～GL-0.45m)

The time histories of inertia force, normal stress difference and shear stress difference of a soil mass at GL-0.45m to GL-0.70m are depicted in Fig.4.28 with the pore water pressure time history at GL-0.638m (PP3). The time history of inertia force and that of normal stress difference seems identical after 2 seconds. It is seen in Fig.4.28(e) that the pore water pressure reaches the initial overburden pressure after 2 seconds, indicating complete liquefaction of backfill. It is considered that the liquefied soil loses its stiffness and the shear stress difference does not occur in the soil mass. As a result of this, the inertia force becomes equal to the normal stress difference.

The amplitude of shear stress difference after 2 seconds seems about a level of 0.3kPa. Comparing with the amplitude of shear stress difference in AD35F3A50 test illustrated in Fig.4.24(d), the amplitude of 0.3kPa is of the same level. It suggests that the complete liquefied soil does not produce shear stress difference so much even though the soil is shaken by intense motion.

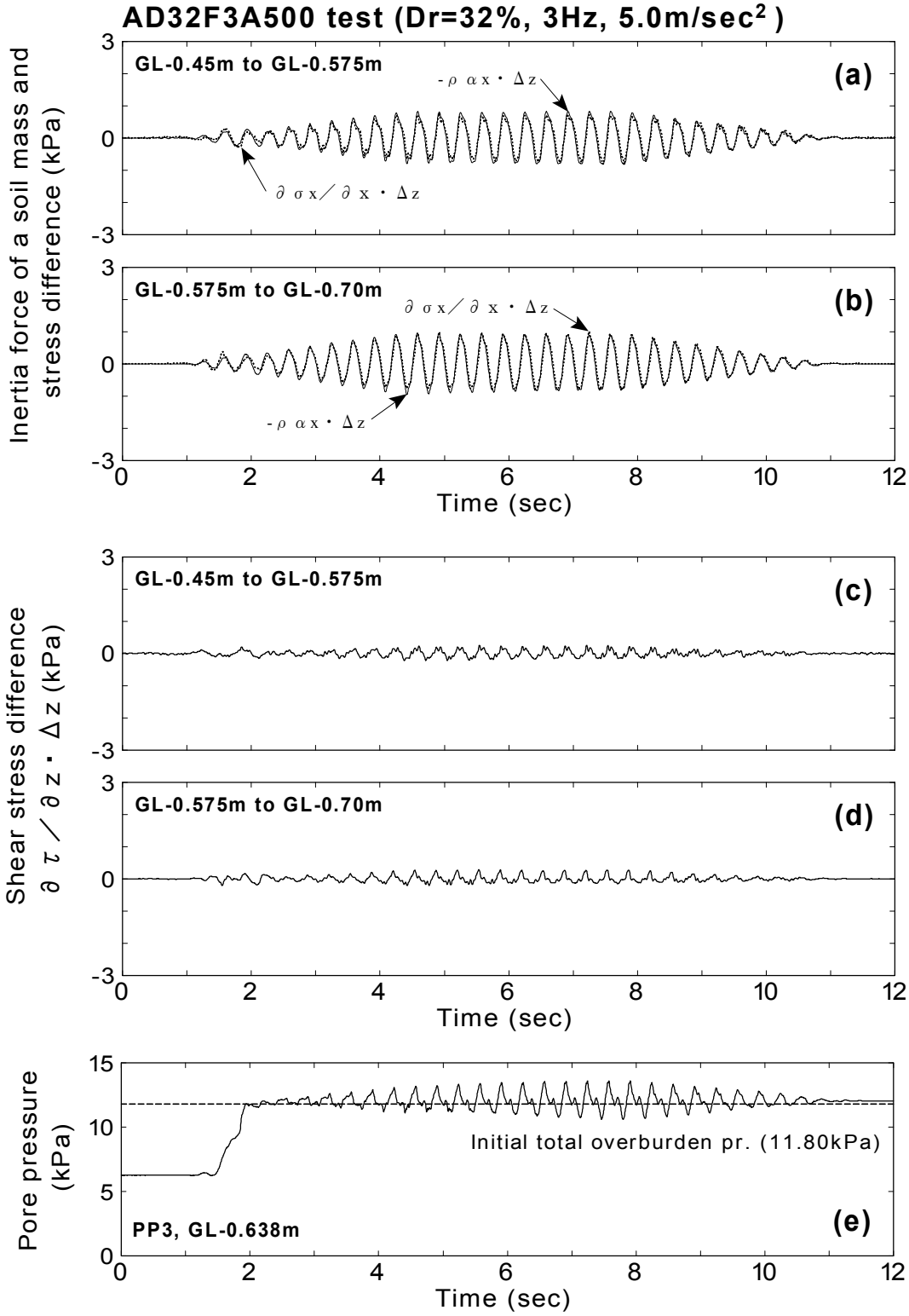

Fig.4.28: Inertia force and stress differences at each soil mass (intense input motion, AD32F3A500 test, GL-0.45m～GL-0.70m)

Results of the test with dense backfill (AD67F3A500 test)

The time histories of inertia force, normal stress difference of each soil mass from AD67F3A500 test are shown in Fig.4.29. The high-pass digital filtering of 1Hz was conducted in these time histories. The dense backfill at the relative density of 67% was employed in this test. The pore water pressure reached the initial total overburden pressure at about 2 seconds, and the oscillation of 6Hz, which was twice as that of input frequency of 3Hz, was observed significantly during 3～8 seconds. It seems to be caused by the dilative behavior of soil.

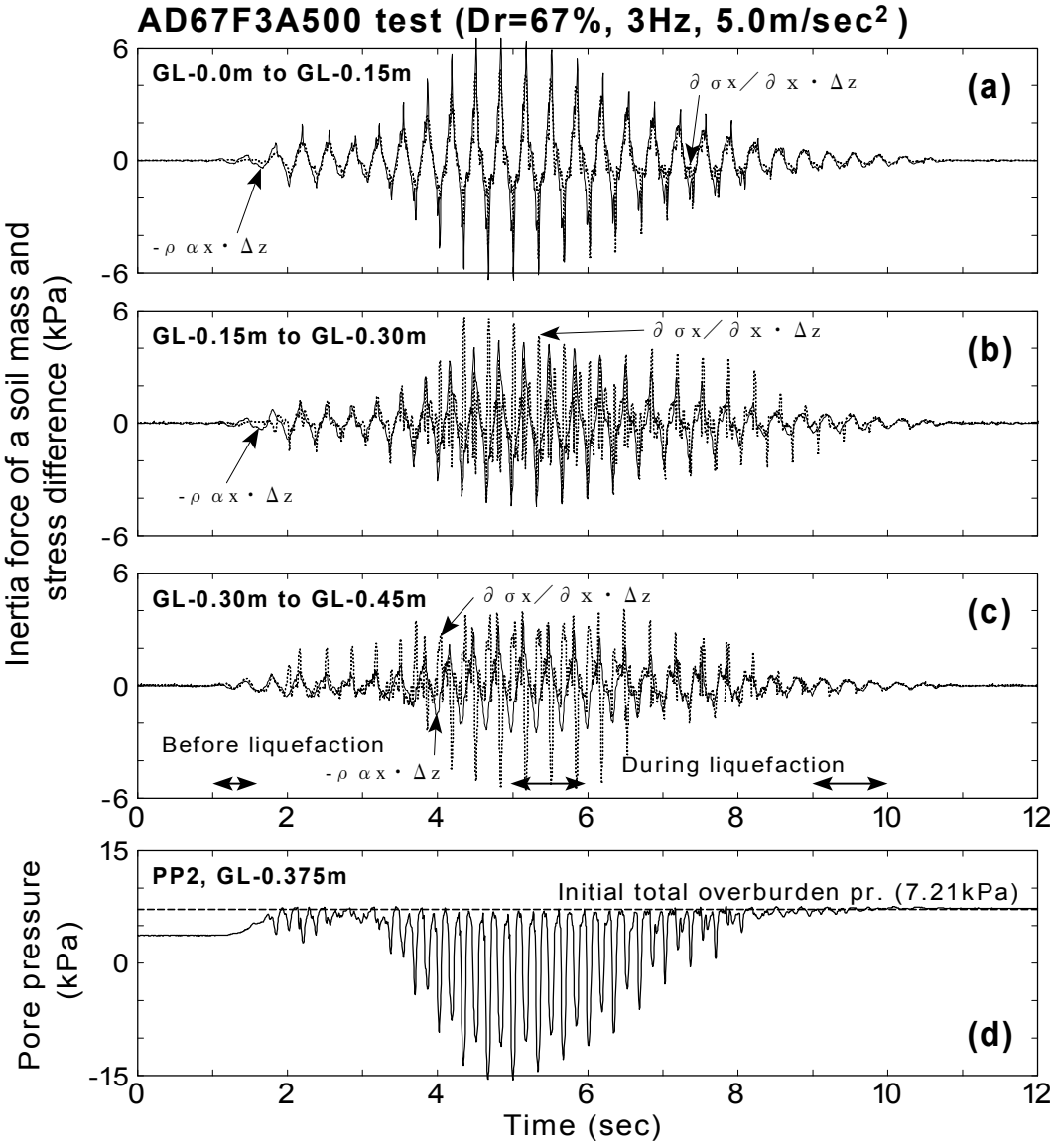

Fig.4.29: Inertia force of a soil mass and normal stress difference (dense backfill, AD67F3A500 test, GL-0.0m～GL-0.45m)

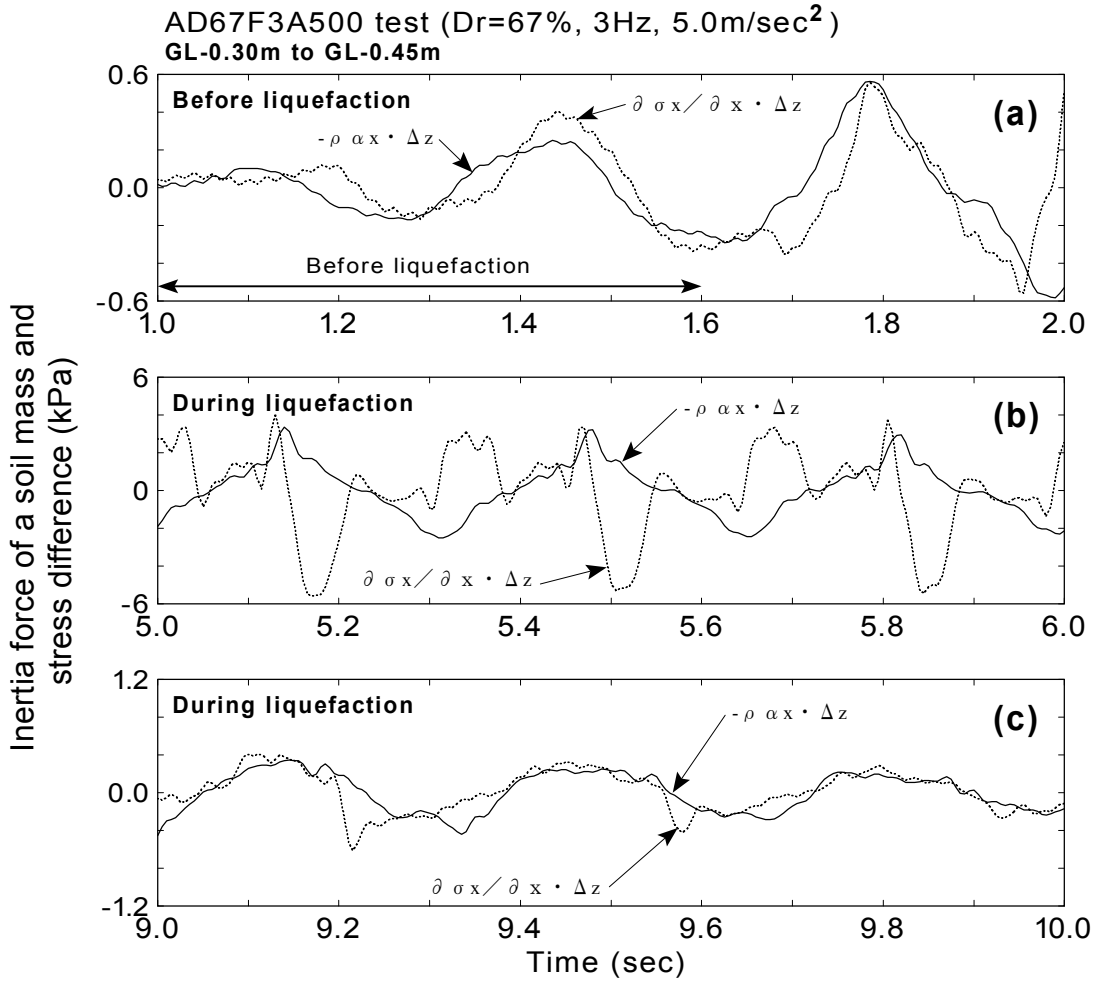

Fig.4.30: Inertia force of a soil mass and normal stress difference before and during liquefaction (dense backfill, AD67F3A500 test, GL-0.30m～GL-0.45m)

Time histories before liquefaction (1.0～1.6 seconds, see Fig.4.29(c)), the period when the oscillation of 6Hz was observed (5.0～6.0 and), and during liquefaction (9.0～10.0 seconds) are shown in Fig.4.30. The shape of time history of inertia forces was recognized as a sinusoidal wave of 3Hz. In contrast, that of the normal stress difference was very complicated. It was also seen in this test that the normal stress difference and the inertia force were out-of-phase before liquefaction, and almost in-phase from 9 to 10 seconds when the soil liquefied.

The feature was observed to be different at 5.0～6.0 seconds. The time history of the normal stress difference partially coincided with that of the inertia force, but rapidly depart from the level of the inertia force cyclically. The enlarged time history of normal stress difference from 5 to

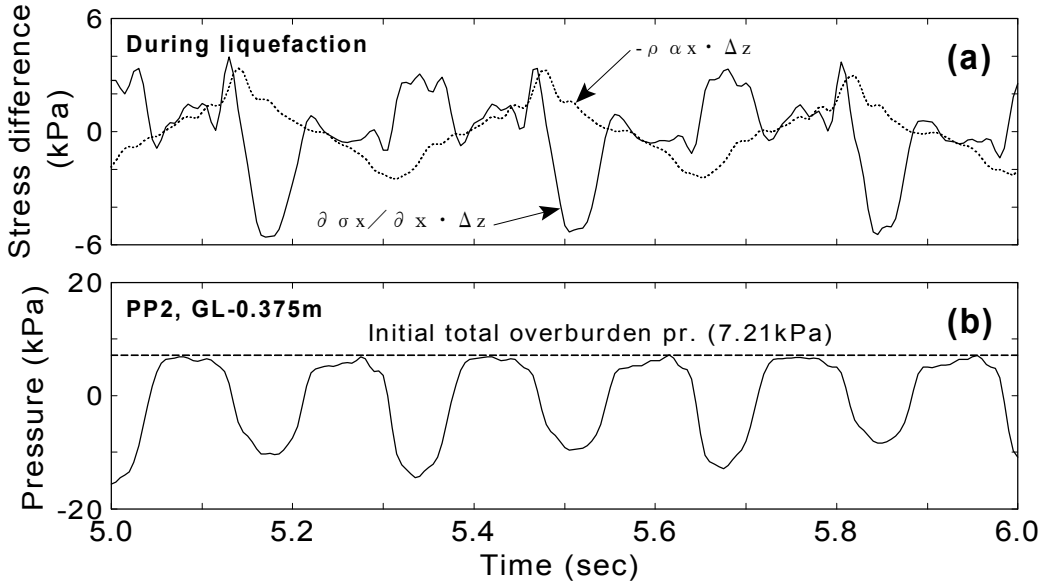

Fig.4.31: Time histories of shear stress difference at each soil mass (dense backfill, AD67F3A500 test)

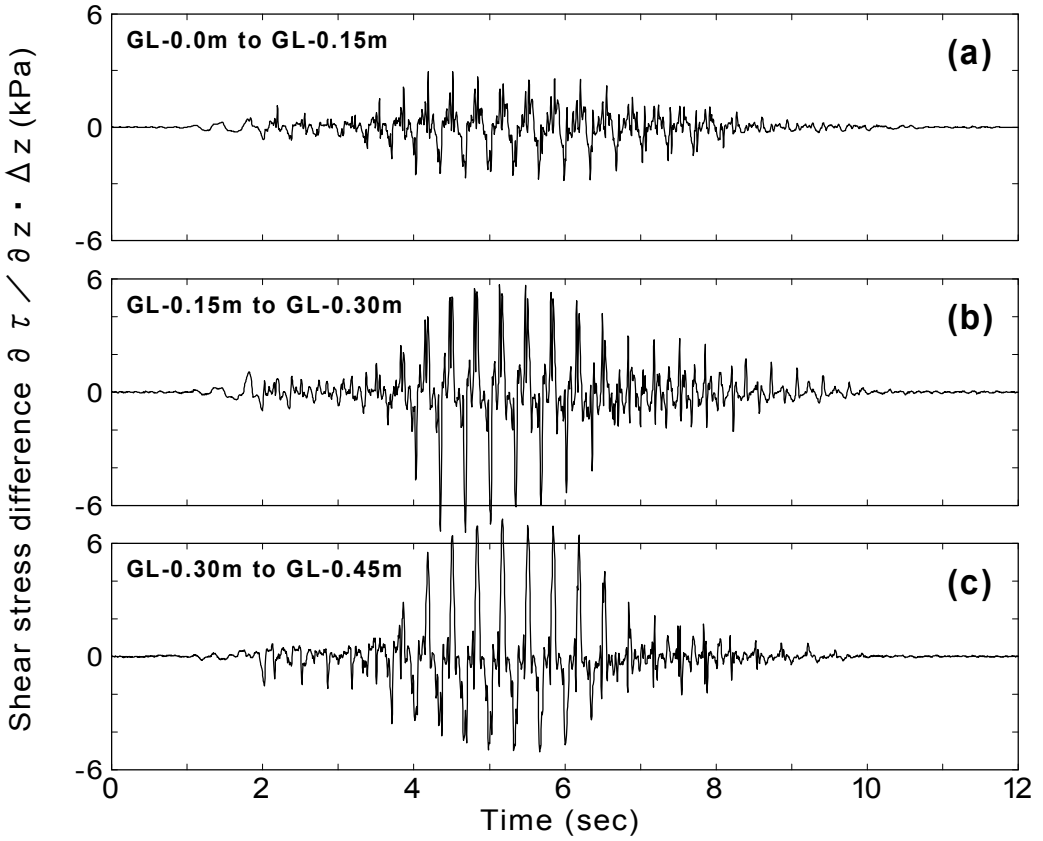

Fig.4.32: Time histories of shear stress difference at each soil mass (dense backfill, AD67F3A500 test, GL-0.0m～GL-0.45m)

6 seconds is shown in Fig.4.31 with the pore water pressure. The time when the normal stress difference departed from the inertia force coincided with the time when the pore water pressure decreased due to the dilative manner of soil. It seems that the normal stress difference during excitation in a dense backfill was influenced by the dilative behavior of soil. The time histories of the shear stress differences at each soil mass are illustrated in Fig.4.32. It was seen that the amplitude was significantly increased from 4 to 8 seconds when the soil behaved in the dilative manner.

The time histories of inertia force, normal stress difference and shear stress difference of a soil mass at GL-0.45m to GL-0.70m are illustrated in Fig.4.33 with the pore water pressure time history at GL-0.638m (PP3). As was seen previously, the time history of inertia force is very different from that of normal stress difference in this portion of backfill. Significant spiky response of normal stress difference is seen during 4 to 8 seconds. From the time history of pore water pressure in Fig.4.33(e), it coincides with time period when significant decrease of pore water pressure appears. The normal stress difference is influenced by the dilative behavior of backfill through the depth.

Results of the other tests

The time histories of the normal stress difference and the inertia force from the AD39F5A50 test (shaking of 5Hz in frequency), AD41F3A200 test, AD61F3A200 test, BD36F3A500 test (yielding of material of the structure), and BD78F3A500 test (dense backfill) will be illustrated in Fig.4.79 ～Fig.4.88 at the end of this chapter.

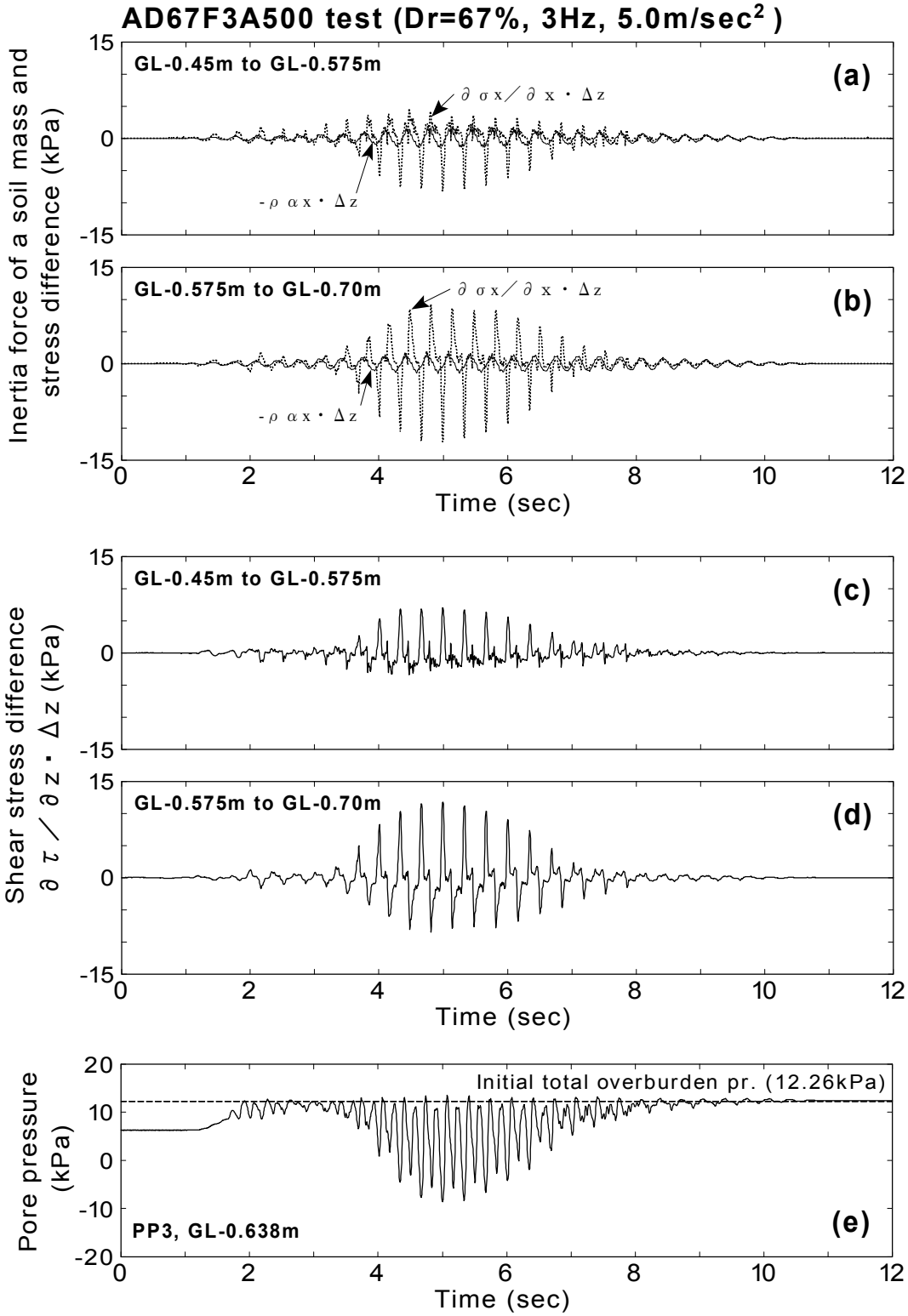

Fig.4.33: Inertia force and stress differences at each soil mass (dense backfill, AD67F3A500 test, GL-0.45m～GL-0.70m)

4.4.2 Time histories of shear stress and effective vertical stress

The time histories of the reproduced shear stress and the effective vertical stress at the middle of backfill (GL-0.30m～GL-0.45m) are shown in Fig.4.34～Fig.4.37.

Typical results (AD35F3A50 test)

Fig.4.34 presents the results of AD35F3A50 test. The model was shaken by the peak acceleration of 0.5m/sec^2. It was observed that the amplitude of the shear stress, which was about the level of 0.5kPa at about 4 seconds, was decreased gradually accompanied by as the decrease of effective vertical stress. The amplitude of shear stress decreased less than 0.3kPa after the effective vertical stress reached zero. It indicates that the backfill lost its stiffness due to soil liquefaction.

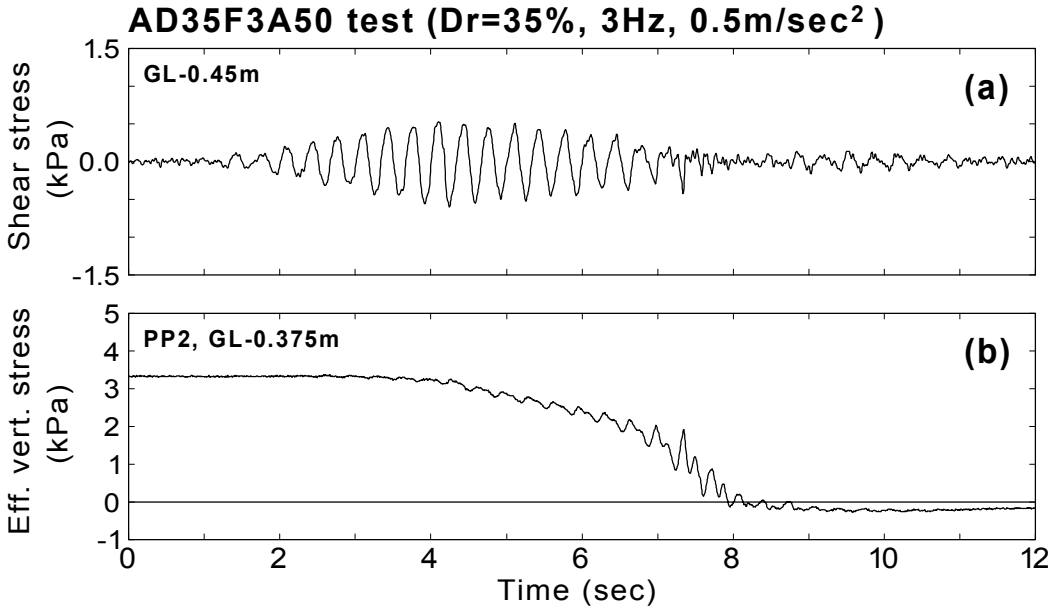

Fig.4.34: Shear stress and effective vertical stress (AD35F3A50 test)

Results of the test with intense input motion (AD32F3A500 test)

The time histories from AD32F3A500 test are depicted in Fig.4.35. The model was shaken by a peak acceleration of 5.0m/sec^2 in amplitude. The effective vertical stress decreased to zero in two or three cycles. The amplitude of the shear stress was less than the level of 2.0kPa after that. High frequency components were observed during intense excitation of 4～8 seconds in the time history of shear stress. It is because of the spiky response of shear stress which was observed near the surface (see Fig.4.27(a)).

Results of the test with dense backfill (AD67F3A500 and BD78F3A500 test)

Fig.4.36 shows the results from AD67F3A500 test in which the dense backfill of relative density of 67% is used. The model was also shaken by a peak acceleration of 5.0m/sec^2. The significant oscillation of effective vertical stress is seen during excitation. This is characteristic of the tests involving a dense backfill. The amplitude of the shear stress amounted to 10～15kPa, being much larger than that observed in the tests with loose backfill.

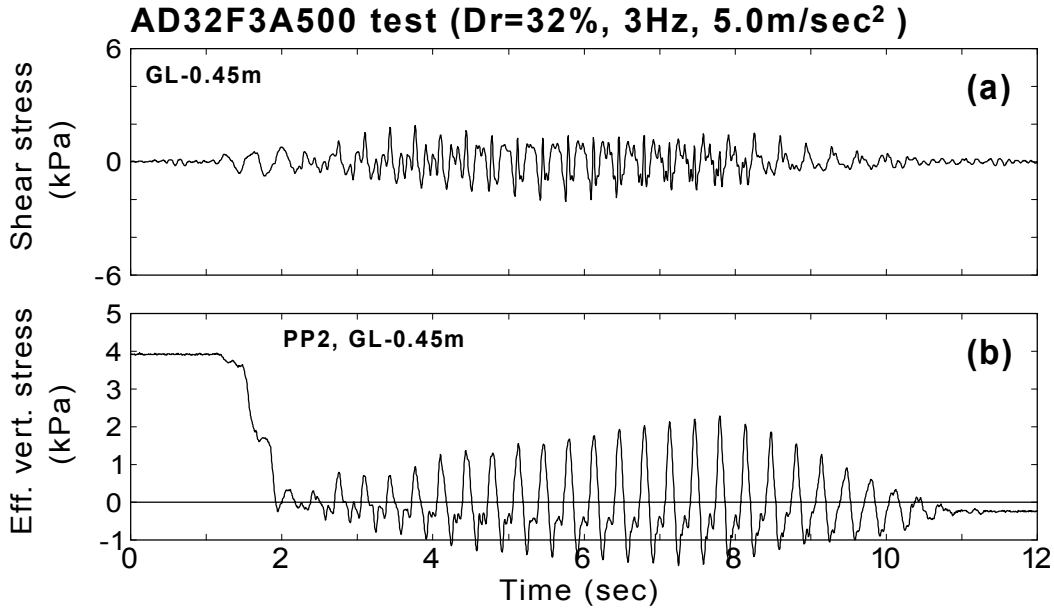

Fig.4.35: Shear stress and effective vertical stress (intense input motion, AD32F3A500 test)

Fig.4.37 illustrates the results from BD78F3A500 test with the dense backfill. The relative density of backfill in this test is 78%, being higher than the backfill in AD67F3A500 test. The fluctuation of the effective vertical stress is seen from 2 to 13 seconds. The amplitude of the shear stress amounted to about 18kPa, indicating the dense backfill induces the large amplitude of shear stress than the loose backfill.

The enlarged time histories of the shear stress and effective vertical stress from 5 to 6 seconds from both tests are shown in Fig.4.38. It was seen that the effective vertical stress increased cyclically as much as about 20kPa in AD67F3A500 test and about 10kPa in BD78F3A500 test. It was also observed that the time when the peak of shear stress appeared in the positive or negative direction coincided with the time when the effective vertical stress increased. It was inferred that the high rigidity was induced in a soil mass due to high effective stresses, consequently, large shear stress amplitudes were produced in a dense backfill. The more precise observation of the behavior of dense backfill will be made in the Chapter 7.

Results from the other tests

The results from the other tests of AD39F5A50 (shaking of 5Hz in frequency), AD41F3A200, AD61F3A200 and BD36F3A500 tests (yielding of material of the structure) are presented in Fig.4.39～Fig.4.42 in the same manner.

The reproduced time histories of shear stress at the other depth of backfill (GL-0.0m to GL-0.30m and GL-0.45m to GL-0.70m), and the effective vertical stress (GL-0.075m and GL-0.638m) are shown in Fig.4.89～Fig.4.96 at the end of this chapter.

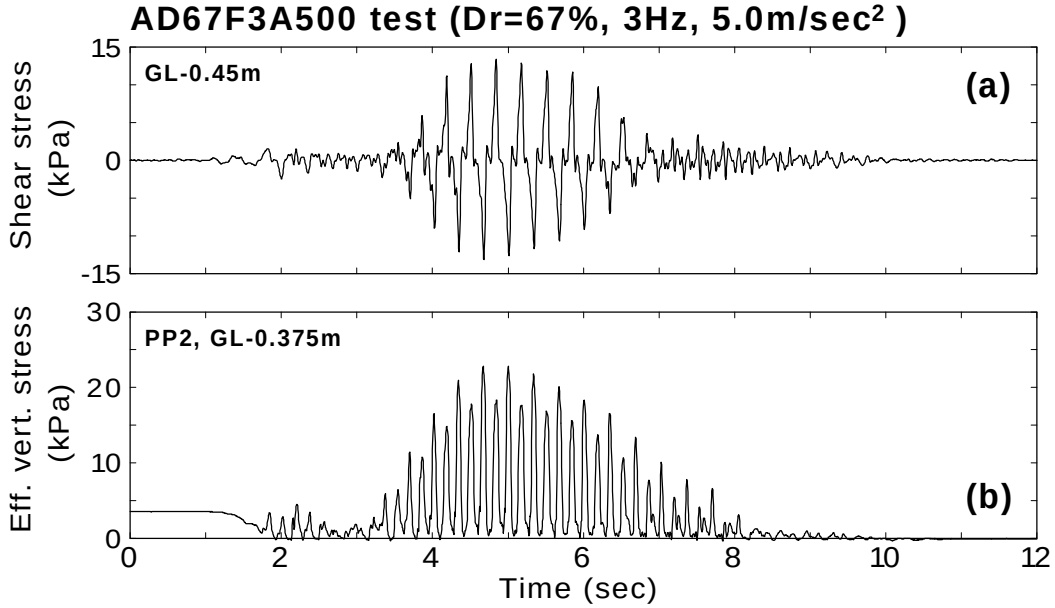

Fig.4.36: Shear stress and effective vertical stress (dense backfill, AD67F3A500 test)

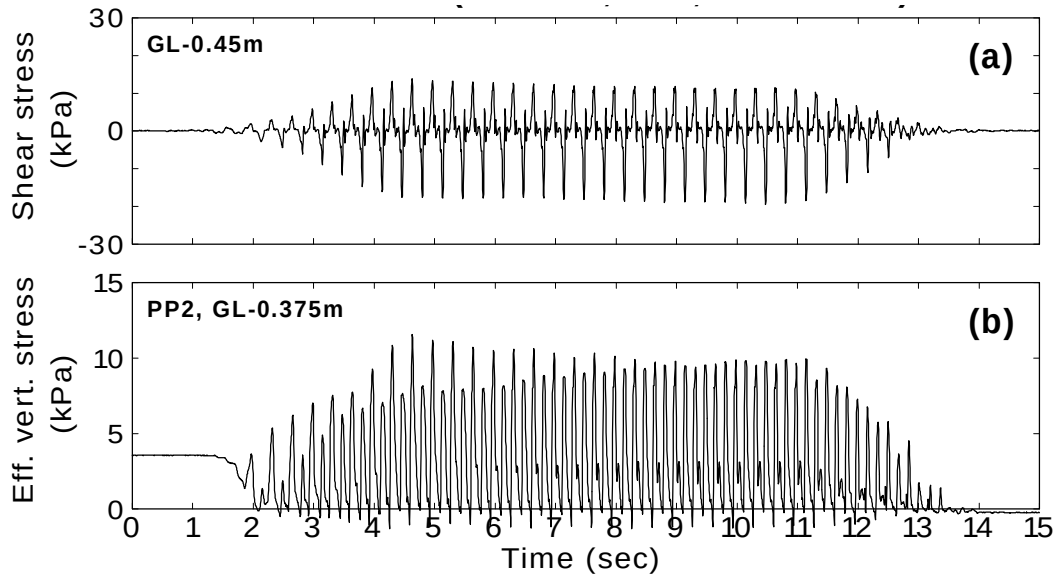

Fig.4.37: Shear stress and effective vertical stress (dense backfill, BD78F3A500 test)

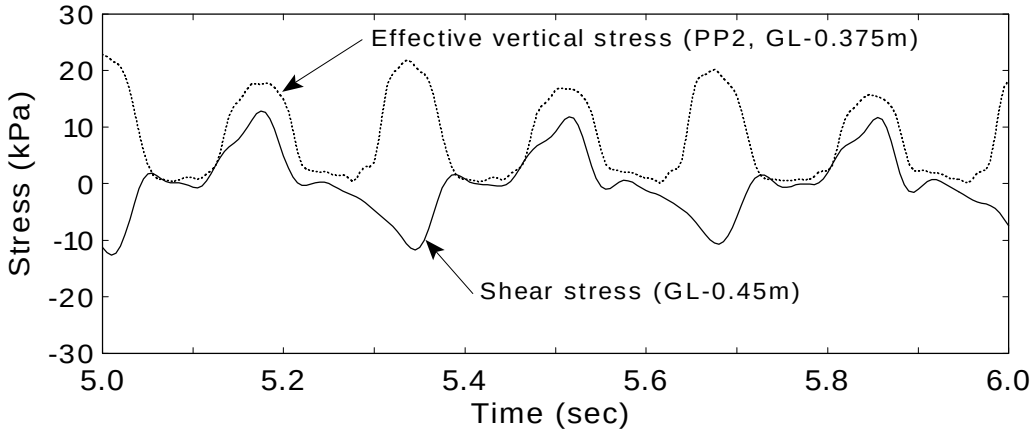

(a)AD67F3A500 test

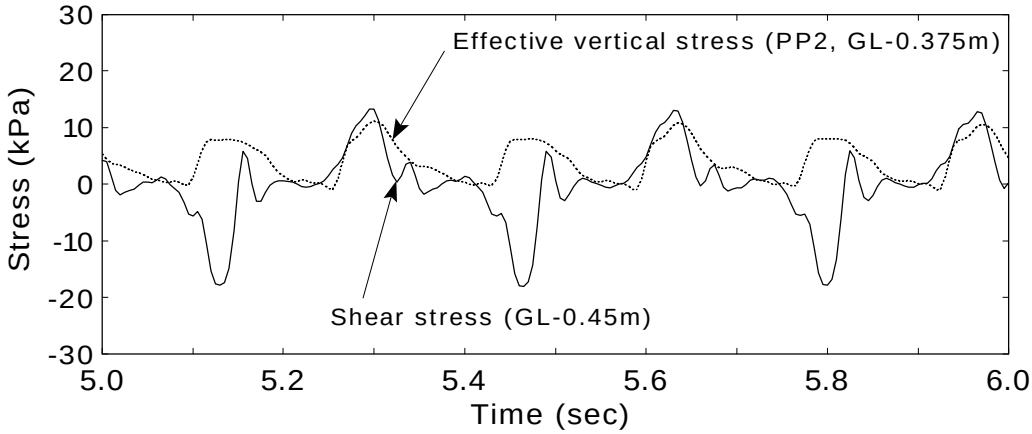

(b)BD78F3A500 test

Fig.4.38: Shear stress and effective vertical pressure in the dense backfill

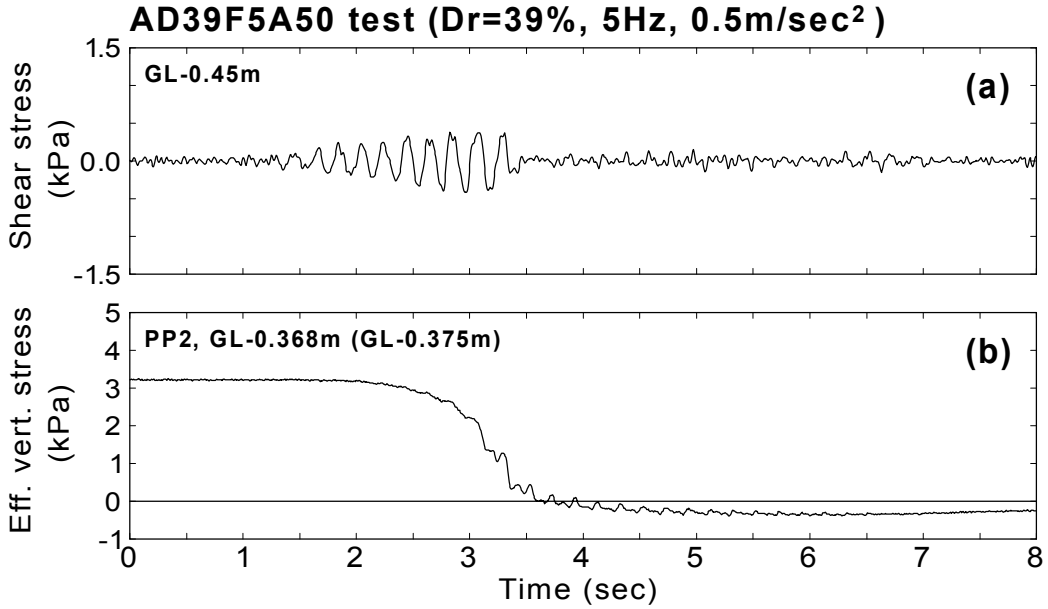

Fig.4.39: Shear stress and effective vertical stress (shaking of 5Hz in frequency, AD39F5A50 test)

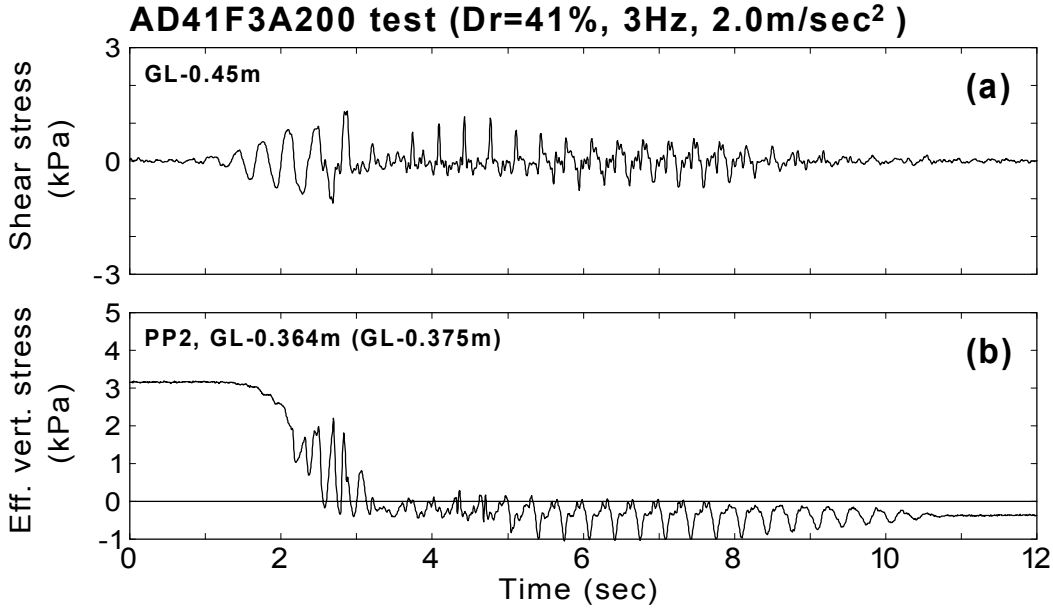

Fig.4.40: Shear stress and effective vertical stress (AD41F3A200 test)

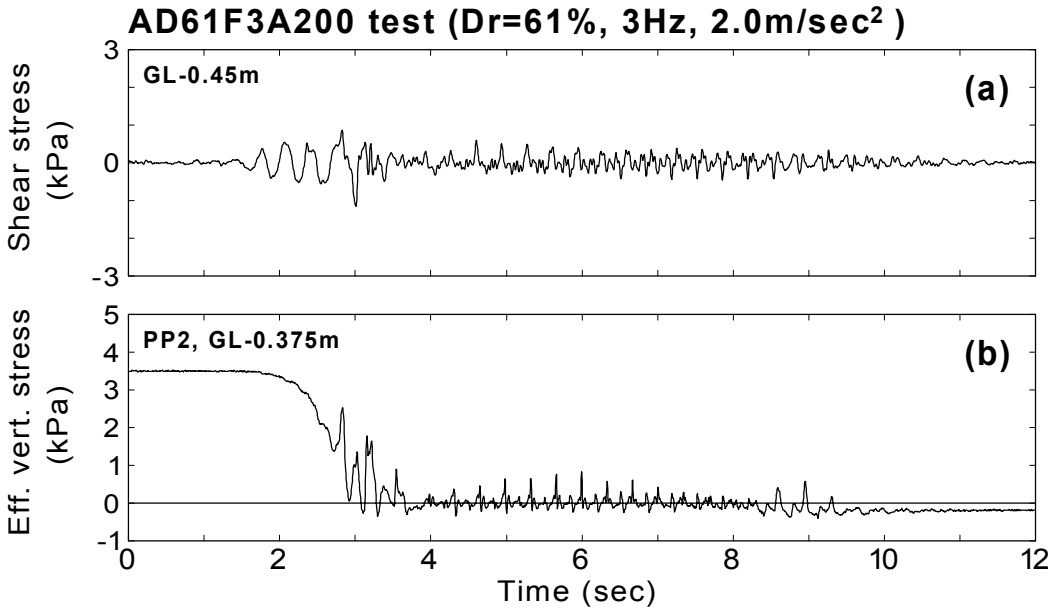

Fig.4.41: Shear stress and effective vertical stress (AD61F3A200 test)

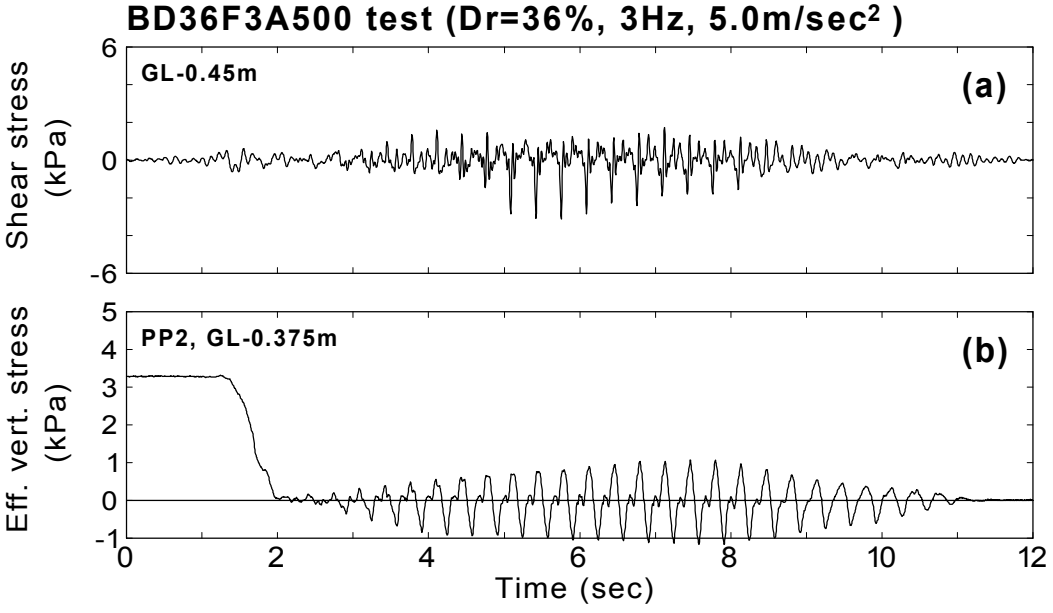

Fig.4.42: Shear stress and effective vertical stress (yielding of material of the structure, BD36F3A600 test)

4.4.3 Time histories of shear strain

The time histories of the shear strains at the middle depth of the backfill (GL-0.30m～GL-0.45m) are shown in Fig.4.43～Fig.4.46. The figure (a) shows the calculated shear strain of a soil element as well as the average shear strain of whole backfill. The former was calculated based on Eq.(4.18), and the latter Eq.(4.21). The figure (b) illustrates the time history of pore water pressure (PP2). The figure (c) shows the enlarged time histories of shear strains in a small level, and (d) depicts the combined reproduced shear strain of a soil element.

Typical results (AD35F3A50 test)

The time histories of shear strain from AD35F3A50 test is shown in Fig.4.43. It was seen that the shear strain amplified to 1.0 % just before the complete liquefaction of about 7.5 seconds. The shear strain of a soil element, which was of the same magnitude as the average shear strain initially, became about twice greater than the average shear strain of whole backfill when the backfill liquefied. It shows that the shear strain in the backfill (GL-0.3m～GL-0.45m) grew significantly during liquefaction. The residual shear strain of 0.2% was calculated at 12 seconds in the soil element (see Fig.4.43(a)). It is considered to be the residual shear strain due to the deflection of the wall during liquefaction.

Fig.4.43(c) shows the enlarged time histories of shear strain from 1 to 7 seconds. The backfill had not liquefied completely yet during this time period. It was observed in the result of shear strain of a soil element that an irregular time history curve with amplitude of about 0.1% appeared significantly from 1 to 6 seconds. As was shown in Fig.4.13(a)(b), it was confirmed that the displacement derived by the integration of measured curvature contained some noise responses. Since the shear strain in a soil element is calculated from the wall displacement (see Eq.(4.18)) which contains this kind of noise responses, it is considered that calculated shear strain also contains noise responses. Therefore, the irregular time history with amplitude of about 0.1% between 0 to about 5 seconds (see dotted line) is considered to be noise responses. In contrast, no noise responses are seen in the average shear strain of whole backfill in Fig.4.43(c) (see solid line). It causes the accurate direct measurement of displacement at the top of the structure. It is considered that the average shear strain of whole backfill is more reliable in a small range of shear strain than the calculated shear strain of soil element.

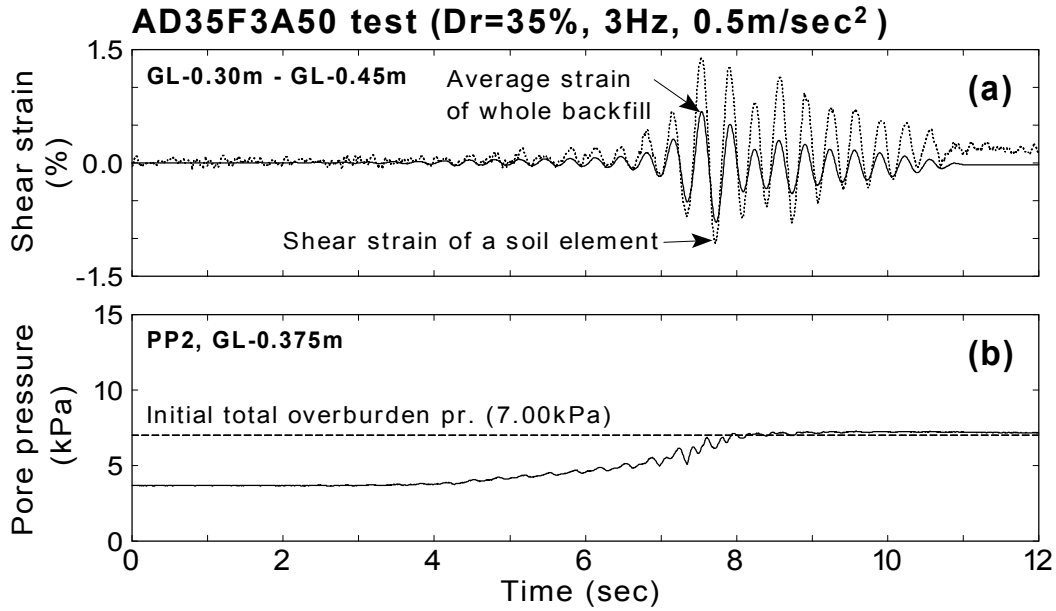

Time histories of (a) shear strains, and (b) pore water pressure

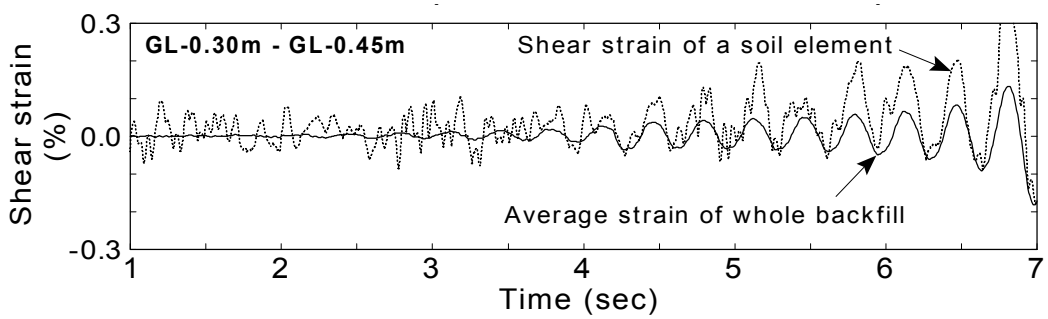

(c) Shear strain of a soil element and average shear strain of whole backfill in a small strain level

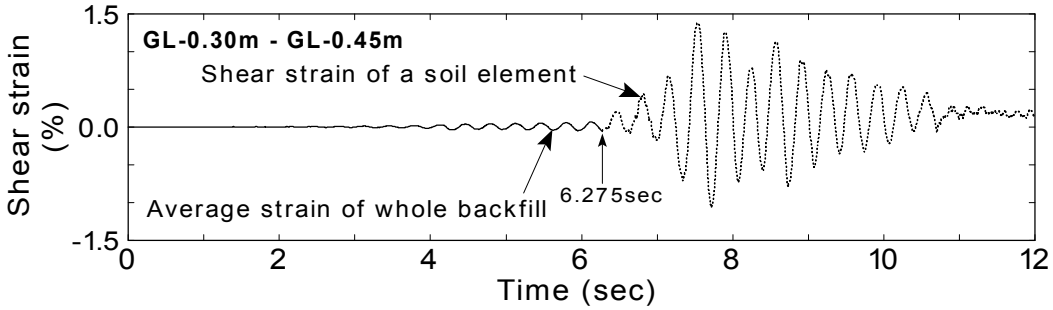

(d) Reproduced time history of shear strain

Fig.4.43: Time histories of shear strains (AD35F3A50 test)

Hence, the shear strains of soil element (dotted lines) less than the level of about 0.1% were replaced by the average shear strain of whole backfill (solid line), which is more reliable in a small level of shear strain. The time history of the reproduced shear strain is illustrated in Fig.4.43(d). In this test, the shear strain before 6.275 seconds were replaced by the average shear strain.

Results of the test with intense input motion (AD32F3A500 test)

The results from AD32F3A500 test are presented in Fig.4.44. The model is shaken by intense acceleration of 5.0 m/sec^2, which is ten times as intense as that of the typical test of AD35F3A50. It is seen that the shear strain of soil element increased rapidly from 1.5 seconds, being the maximum at about 6 seconds. The maximum shear strain is amounted to 5%. The shear strain of whole backfill is used before 1.60 seconds.

Results of the test with dense backfill (AD67F3A500 and BD78F3A500 test)

Fig.4.45 shows the results with dense backfill from AD67F3A500 test. It is seen in Fig.4.45(a) that the amplitude of the shear strain, which increases during the time period from 1.5 seconds to 2.5 seconds, is decreasing once after 2.5 seconds. It increases again from 4 seconds, being the maximum through the duration at about 6 seconds. The maximum amplitude of shear strain is about 7%, being apparently larger than the shear strain in the loose backfill of AD32F3A500 test in spite of the same input condition. It is because the resonance of the soil-structure system occurred in this test. The further discussion will be made about the resonance in the Chapter 5.

The time histories of shear strain from BD78F3A500 test, in which the dense backfill is also used, are shown in Fig.4.46. It is observed that the shear strain of soil mass increases gradually as the shaking goes on, being the maximum of 4～5% at about 11 seconds. It is smaller than the maximum shear strain of 7% observed in AD67F3A500 test. It is considered that the denser backfill prevented the occurrence of a large shear strain.

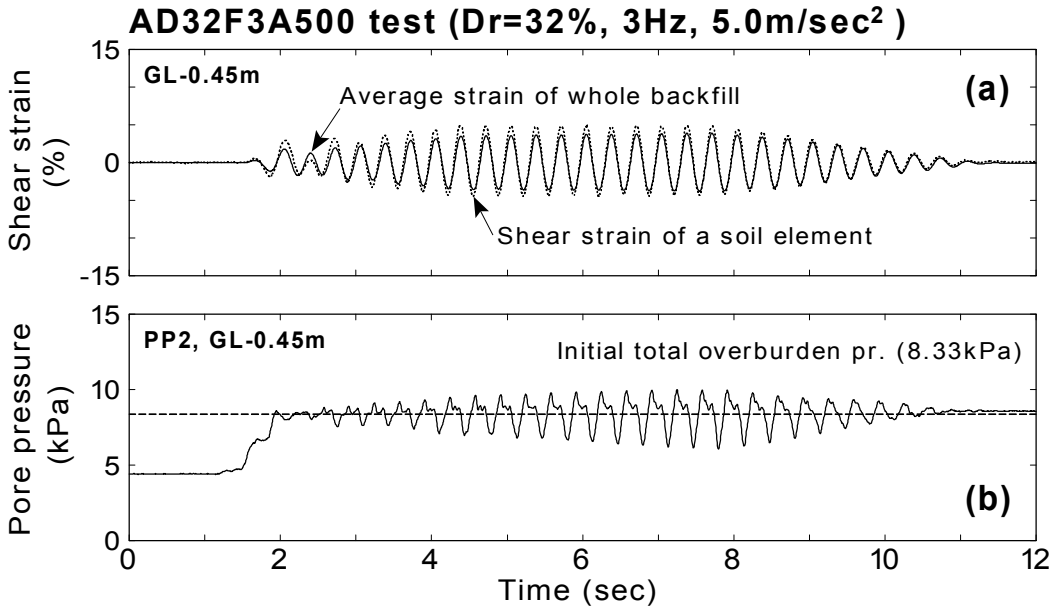

Time histories of (a) shear strains, and (b) pore water pressure

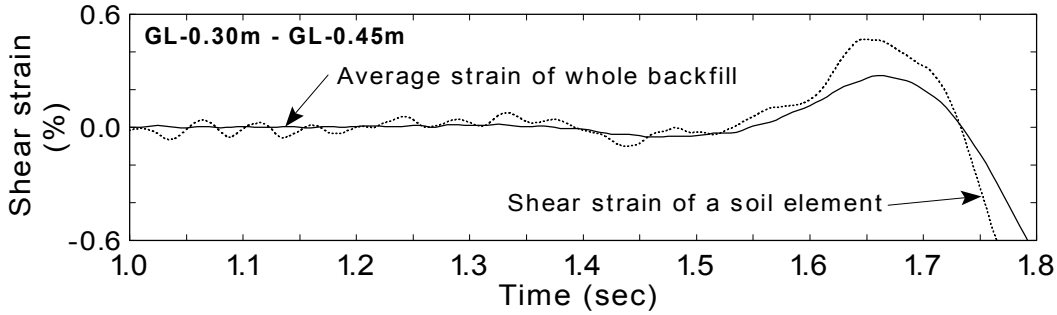

(c) Shear strain of a soil element and average shear strain of whole backfill in a small strain level

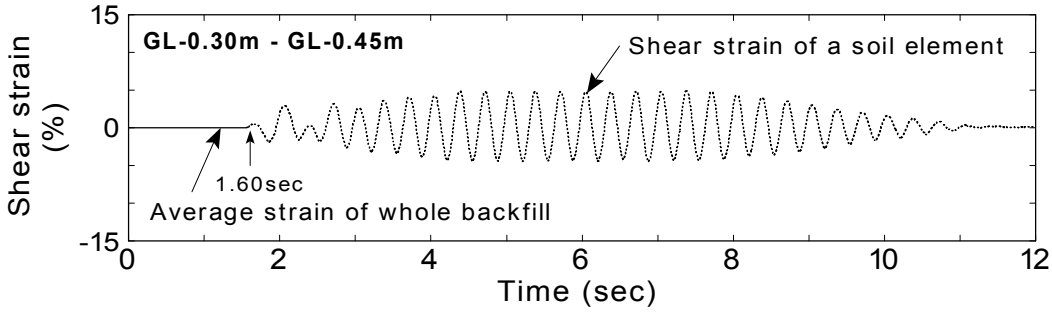

(d) Reproduced time history of shear strain

Fig.4.44: Time histories of shear strains (intense input motion, AD32F3A500 test)

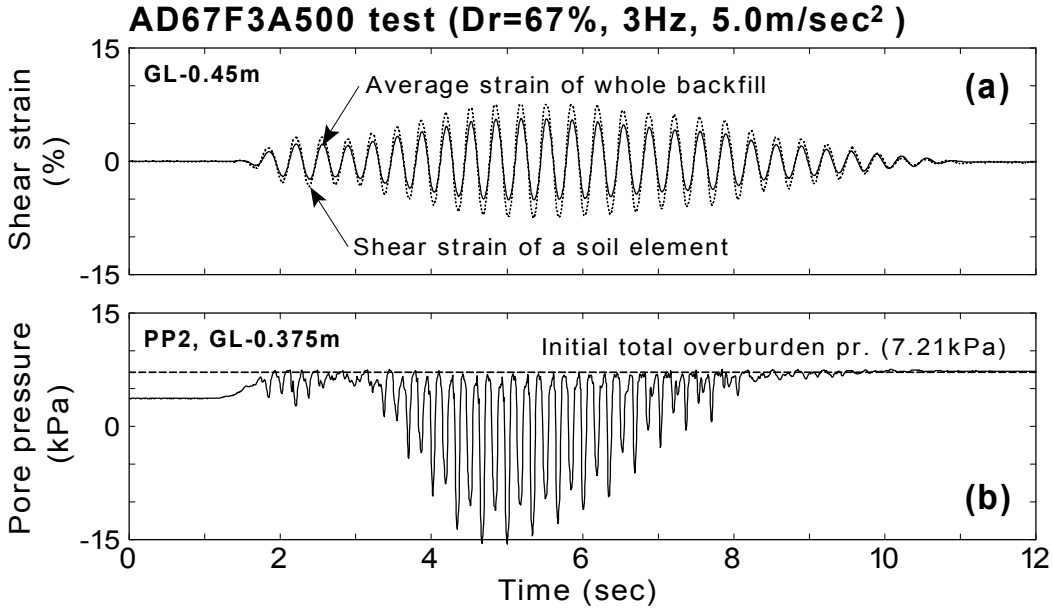

Time histories of (a) shear strains, and (b) pore water pressure

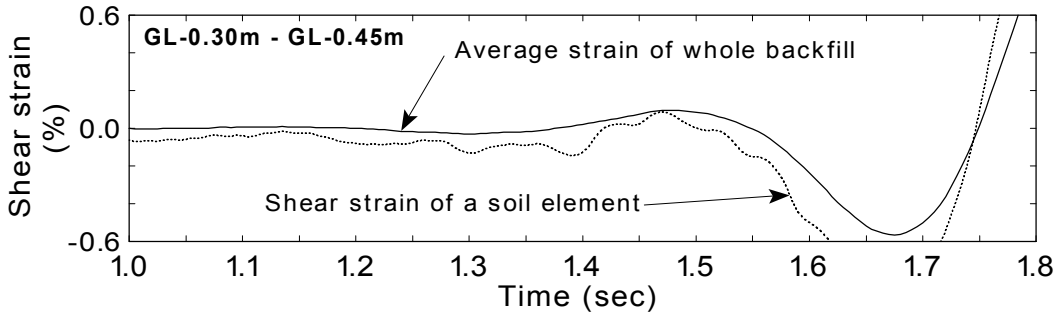

(c) Shear strain of a soil element and average shear strain of whole backfill in a small level

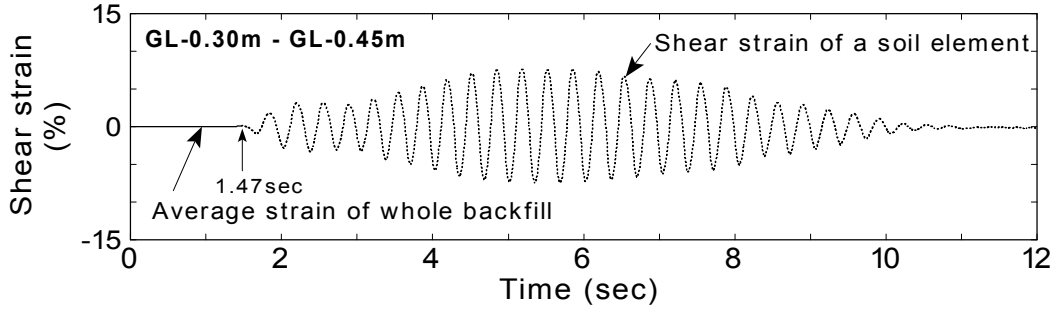

(d) Reproduced time history of shear strain

Fig.4.45: Time histories of shear strains (dense backfill, AD67F3A500 test)

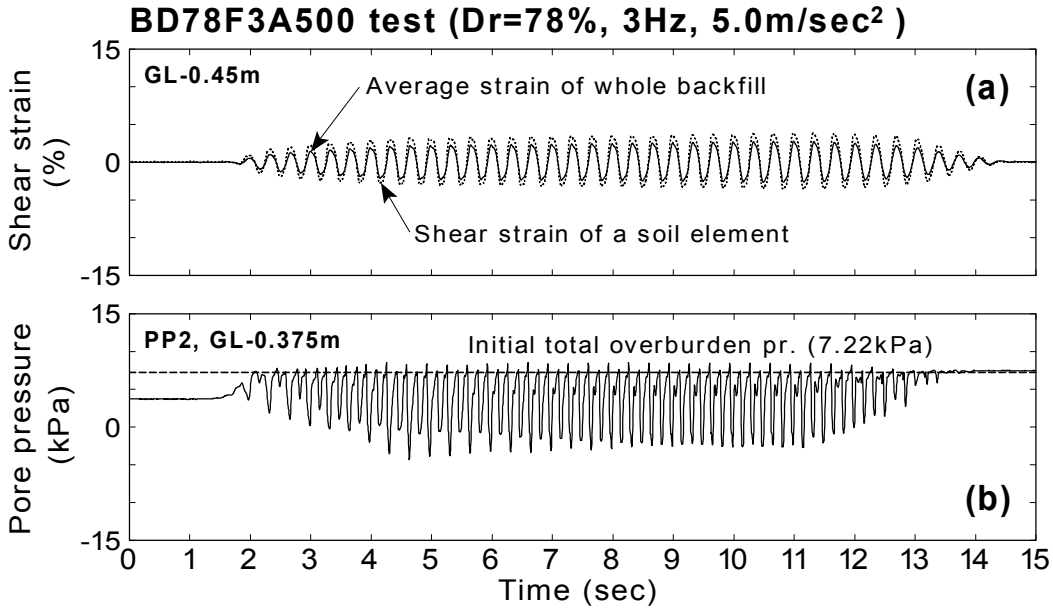

Time histories of (a) shear strains, and (b) pore water pressure

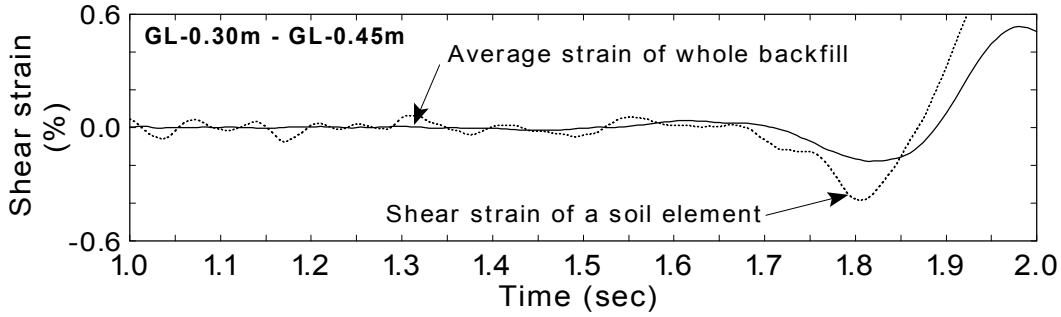

(c) Shear strain of a soil element and average shear strain of whole backfill in a small level

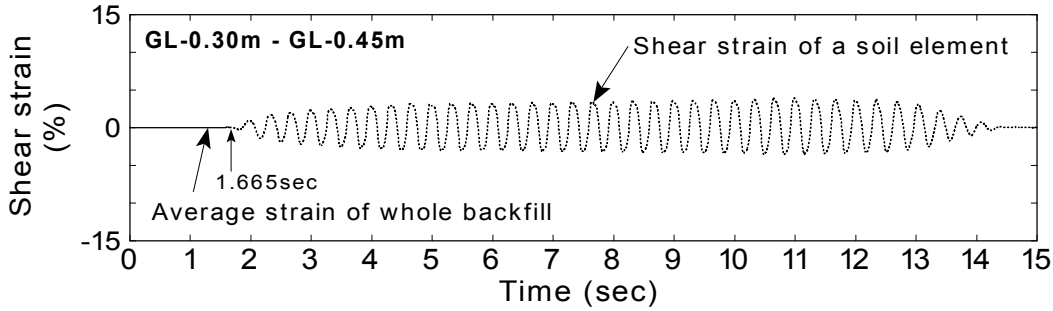

(d) Reproduced time history of shear strain

Fig.4.46: Time histories of shear strains (dense backfill, BD78F3A500 test)

Results from the other tests

Fig.4.47 demonstrates the shear strains from AD39F5A50 test. The shear strain, maintaining the small level of less than 0.1% before 3.02 seconds, amplified up to the level of 0.4% after 3.3 seconds when the pore water pressure built up. Noise responses are seen in the shear strain of the soil element before 3 seconds in Fig.4.47(c). Time history of shear strain of a soil element before 3.02 seconds is replaced by the time history of shear strain of whole backfill, which contains less noise responses. Reproduced shear strain is shown in Fig.4.47(d).

The time histories of shear strain from AD41F3A200 test are illustrated in Fig.4.48. The model was shaken by the input acceleration of 2.0m/sec^2 in this test. Since the peak acceleration is larger than that of previously presented test (AD35F3A50 test), the shear strain is increasing at about 2 seconds and becomes maximum at 2.5 to 3 seconds as observed in Fig.4.48(a). The maximum amplitude of shear strain seems about 2.5%. The shear strain of a soil element became approximately identical to the average shear strain of whole backfill after 6 seconds. The average shear strain of whole backfill was used before 2.065 seconds.

Fig.4.49 illustrate the shear strains from AD61F3A200 test. High frequency noise responses are recognized in the shear strain of soil element before about 2 seconds as shown in figures (c). The average shear strain of whole backfill was used before 2.74 seconds.

Fig.4.50 demonstrates the shear strains from BD36F3A500 tests. As previously indicated, the material of the structure yielded and the curvature of wall increased monotonically in the direction in which the wall deforms toward inside of the structure (see Fig.3.31). It is seen in Fig.4.50(a) that the maximum shear strain of soil element is about 4%, being the same level as observed in AD32F3A500 test of 5% (see Fig.4.44). It was considered that the shear strain of soil element was not influenced significantly by the monotonically increased curvature, that is, the deformation of wall.

The time histories of the shear strains at the other depth of backfill (GL-0.0m to GL-0.30m and GL-0.45m to GL-0.70m) are illustrated in Fig.4.97～Fig.4.104 at the end of this chapter.

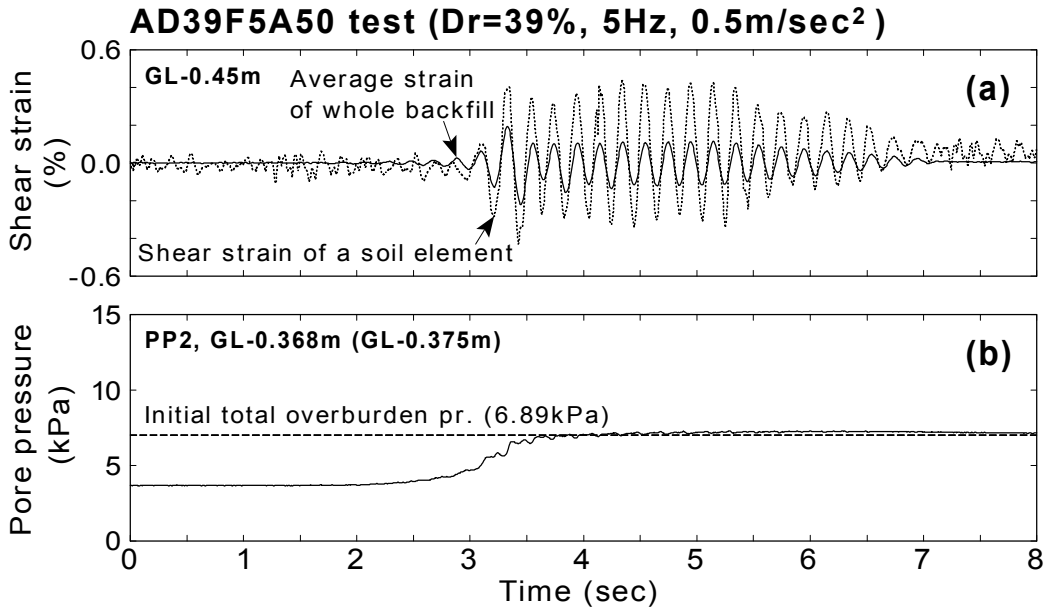

Time histories of (a) shear strains, and (b) pore water pressure

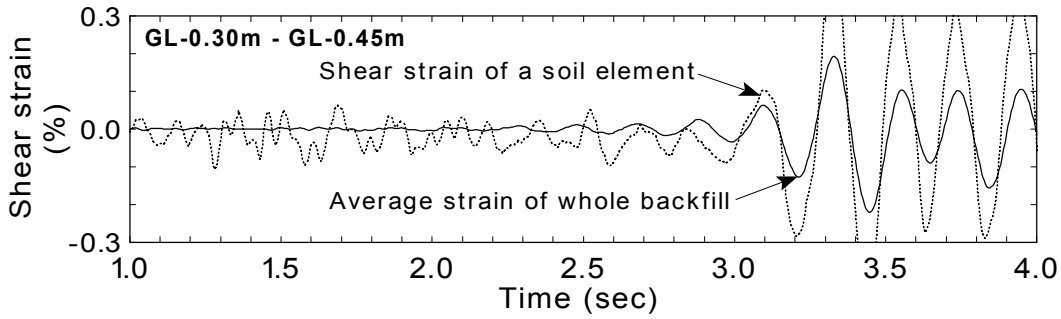

(c) Shear strain of a soil element and average shear strain of whole backfill in a small strain level

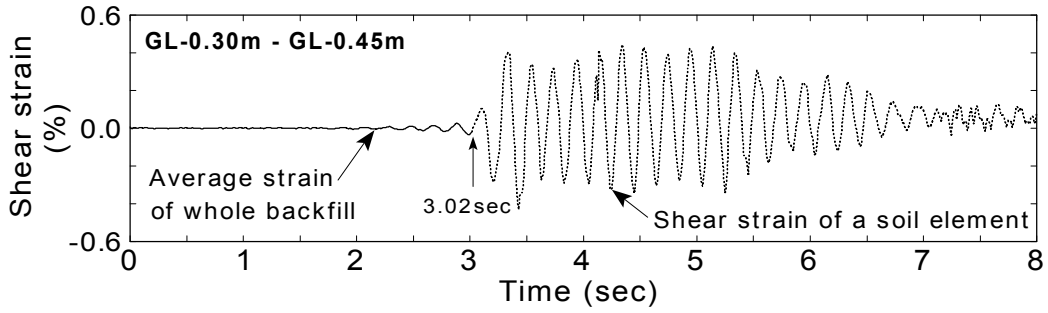

(d) Reproduced time history of shear strain

Fig.4.47: Time histories of shear strains (AD39F5A50 test)

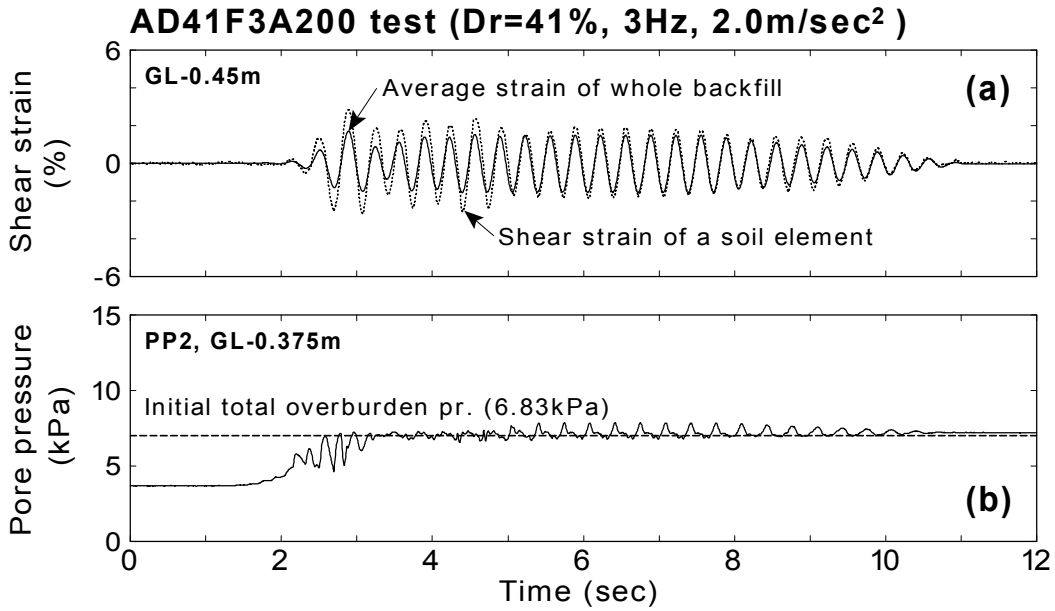

Time histories of (a) shear strains, and (b) pore water pressure

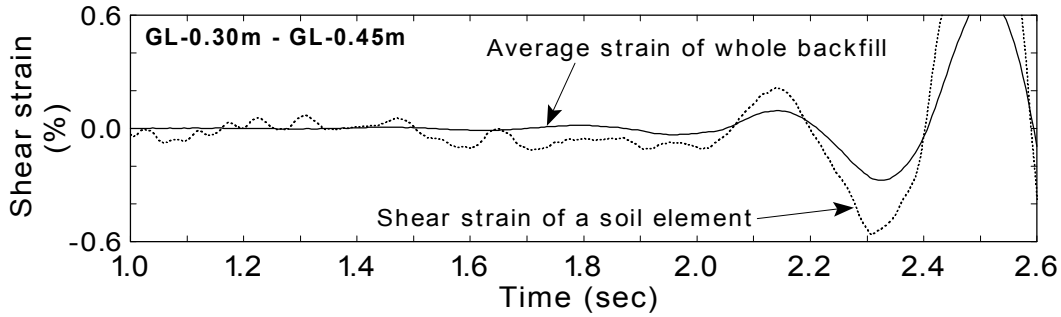

(c) Shear strain of a soil element and average shear strain of whole backfill in a small strain level

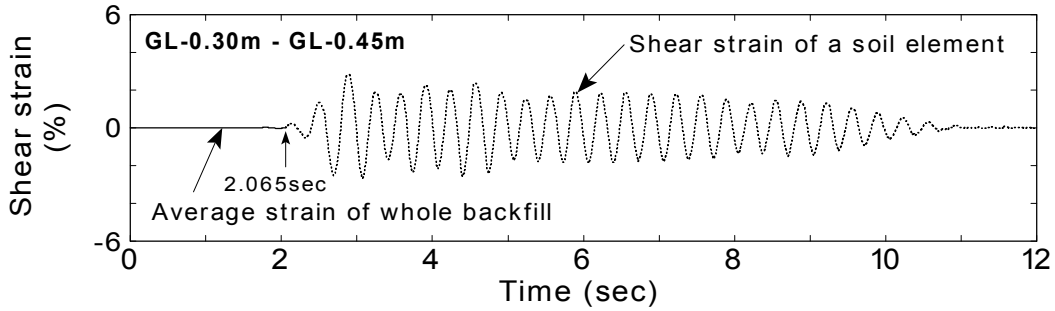

(d) Reproduced time history of shear strain

Fig.4.48: Time histories of shear strains (AD41F3A200 test)

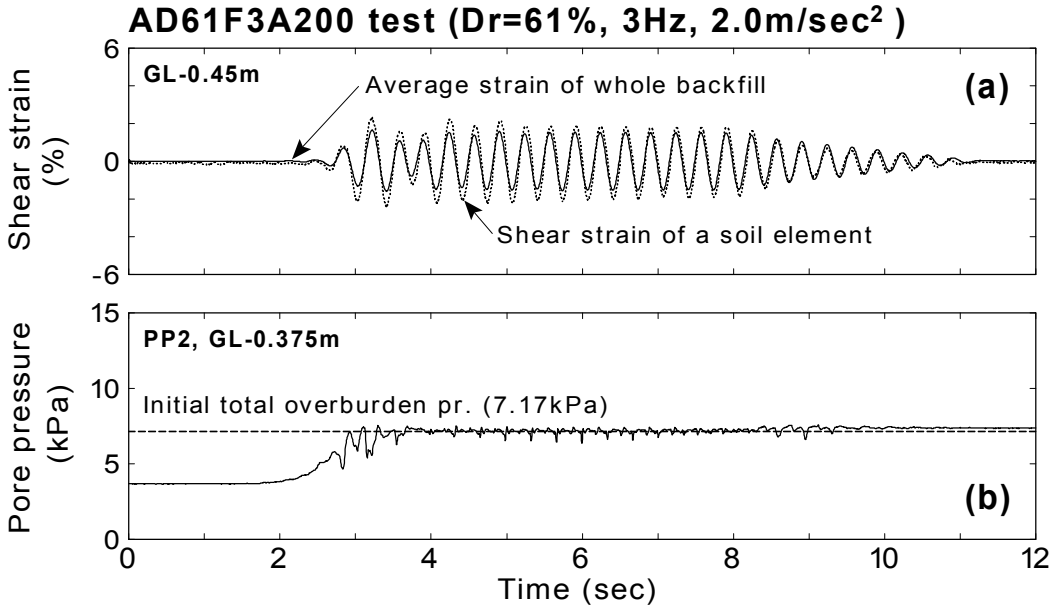

Time histories of (a) shear strains, and (b) pore water pressure

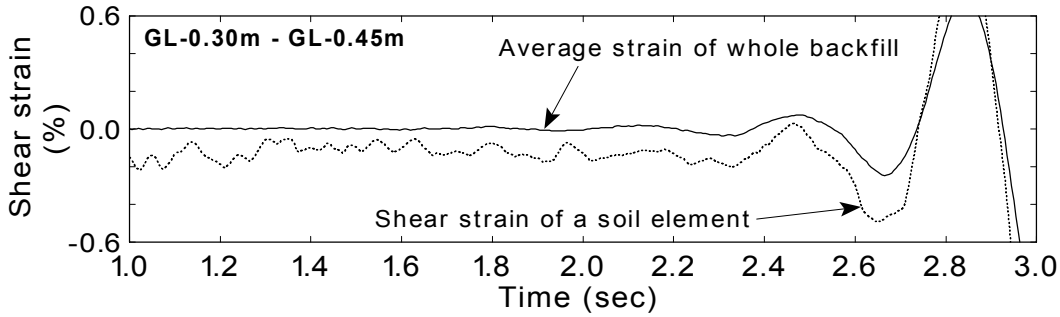

(c) Shear strain of a soil element and average shear strain of whole backfill in a small strain level

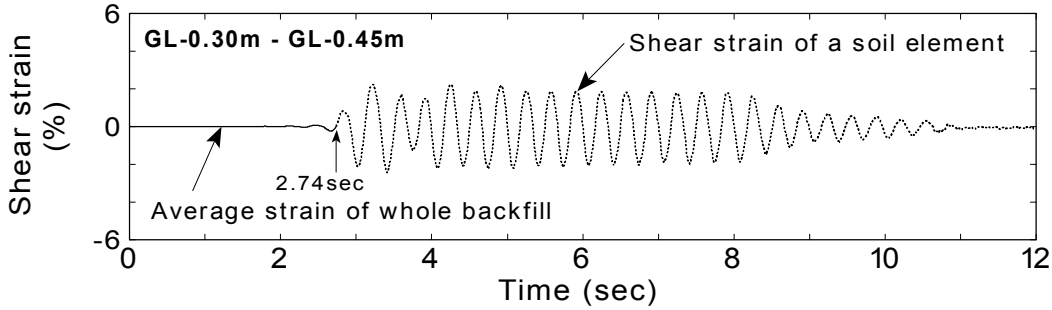

(d) Reproduced time history of shear strain

Fig.4.49: Time histories of shear strains (AD61F3A200 test)

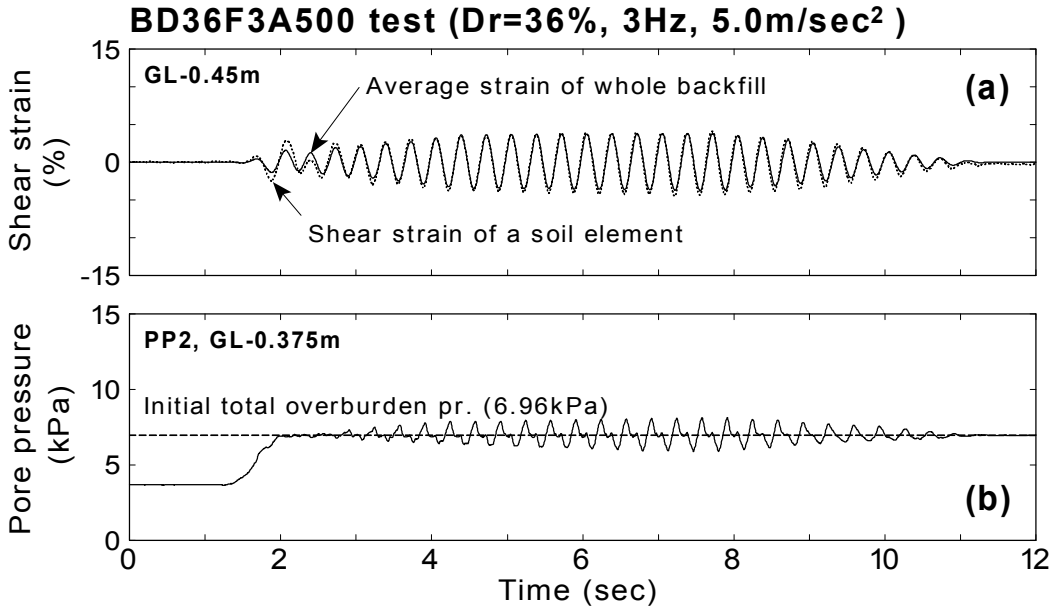

Time histories of (a) shear strains, and (b) pore water pressure

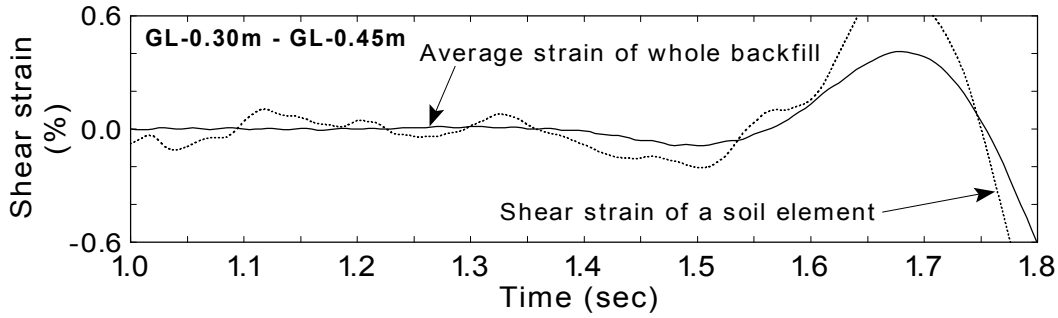

(c) Shear strain of a soil element and average shear strain of whole backfill in a small strain level

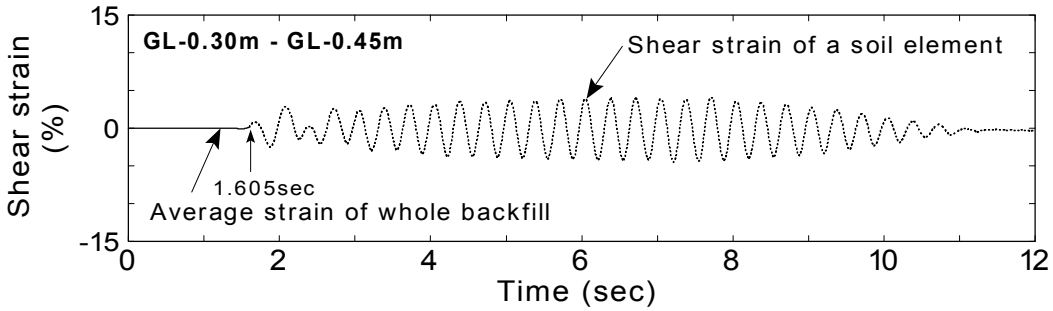

(d) Reproduced time history of shear strain

Fig.4.50: Time histories of shear strains (BD36F3A500 test)

4.4.4 Stress-strain relationship and effective stress path

Stress strain relationship at the middle depth of backfill

The stress-strain relationship and the effective stress path at the middle depth (GL-0.3m～GL-0.45m) are depicted in Fig.4.51～Fig.4.54.

Typical results (AD35F3A50 test)

Fig.4.51(a) shows the results from AD35F3A50 test shaken by the peak acceleration of 0.5m/sec^2. It was initially close to a linear elasticity as shown in the central part of the figure, and gradually changed into a behavior of liquefaction; i.e. the shear strain grew rapidly in the amplitude. The pore water build-up and the consequent onset of liquefaction were observed in the stress path shown in Fig.4.51(a)(ii).

For the comparison, the stress strain relationship and the stress path in which the effect of the normal stress difference, $\partial\sigma_x / \partial x \cdot dx$, is not taken into account in the calculation of shear stresses (Koga et al., 1996) is presented in Fig.4.51(b). The approximate shear modulus during complete liquefaction is shown in the stress strain relationship, and the assumed failure line of 45 degrees is illustrated in the stress path.

It is seen in Fig.4.51(b)(i) that the shear modulus during complete liquefaction is about 30kPa, suggesting the effects of the stiffness of the structure. Furthermore, the stress path at zero effective vertical stress moves beyond the failure line in Fig.4.51(b)(ii), where theoretically the stress path never comes. It suggests that the calculated shear stress without the effect of the normal stress difference is somewhat inconsistent with theoretical behavior of soil. Therefore, it can be said that the consideration of the effect of the normal stress difference, $\partial\sigma_x / \partial x \cdot dx$, is very important to calculate shear stresses of soil near a structure.

Results of the test with intense input motion (AD32F3A500 test)

Fig.4.52 shows the results from AD32F3A500 test shaken by 5.0m/sec^2 of intensity. The behavior of linear elasticity in the central part of the stress-strain relationship was not seen clearly due to the hysteresis loop during liquefaction. When the shear strain reached the level of about 4%, the shear

stress amplitude was only 2 or 3 kPa. The effective vertical stress, which was initially about 3kPa, was reduced to zero in one or two cycles of motion.

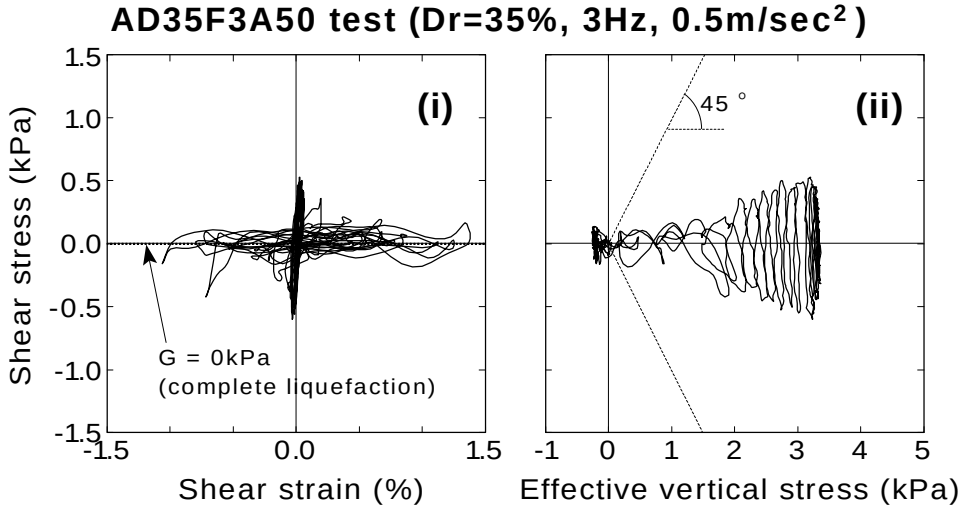

(a) The effect of normal stress difference, $\partial s_x / \partial x \cdot dx$, is considered

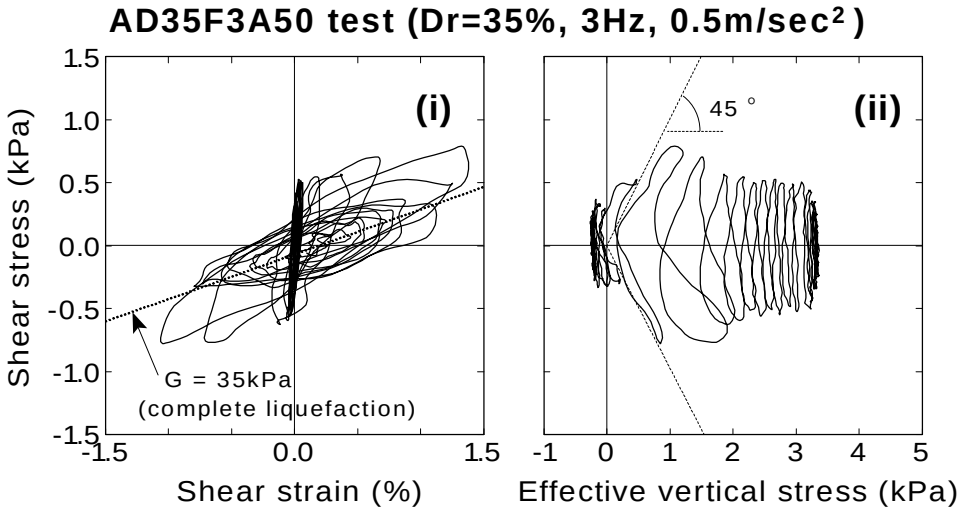

(b) The effect of normal stress difference, $\partial s_x / \partial x \cdot dx$, is neglected

Fig.4.51: Reproduced stress-strain relationship and stress path (AD35F3A50 test, loose backfill, GL-0.3m～GL-0.45m)

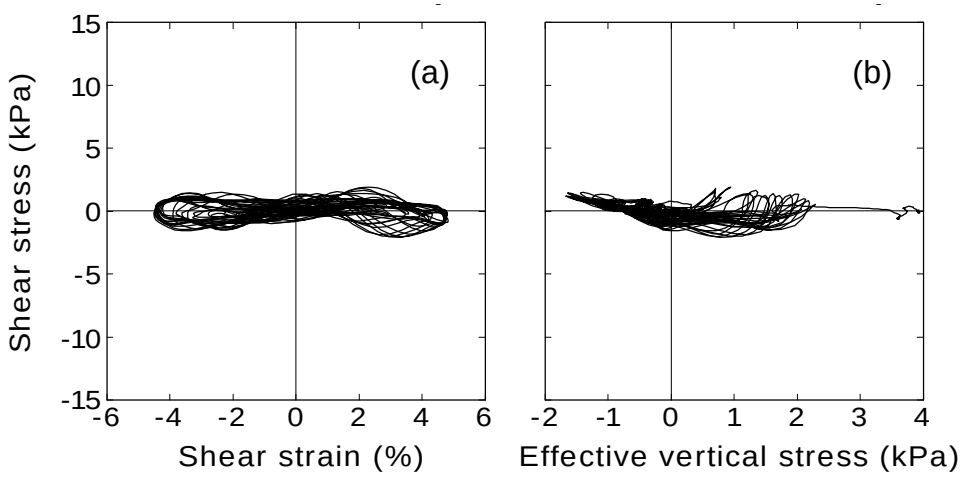

Fig.4.52: Reproduced stress-strain relationship and stress path (intense input motion, AD32F3A500 test, loose backfill, GL-0.3m～GL-0.45m)

Results of the test with dense backfill (AD67F3A500 and BD78F3A500 test)

In the case of the same structure and intensity of motion, the feature of stress-strain relationship and stress path for AD67F3A500 test shown in Fig.4.53(a) is different from AD32F3A500 test with the backfill at 32% relative density. The shear stress at about 4% shear strain reached about 14kPa at *A* in Fig.4.53(a)(i). The effective vertical stress shown in Fig.4.53(a)(ii) reached about 18kPa at *B* in spite of the initial effective vertical stress of about 3kPa. Fig.4.53(b) shows the result from BD78F3A500 test. The feature observed in AD67F3A500 test looked more pronounced due to denser relative density of 78%.

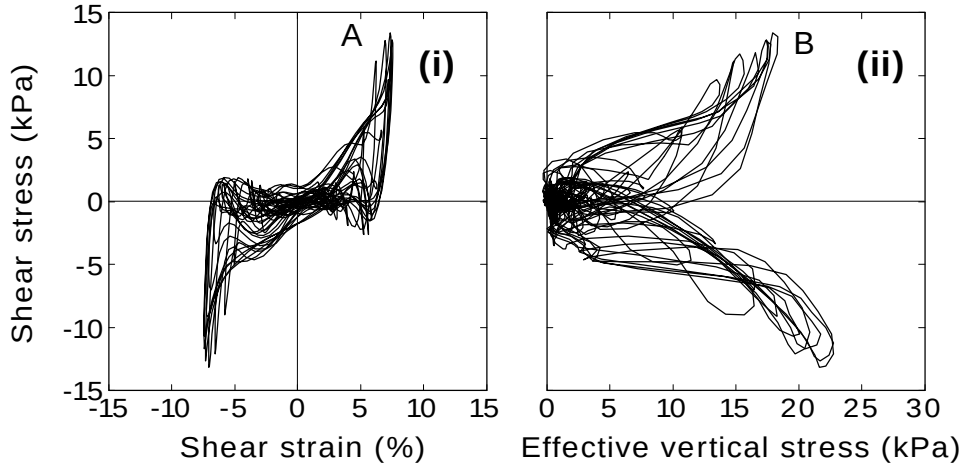

(a) AD67F3A500 test

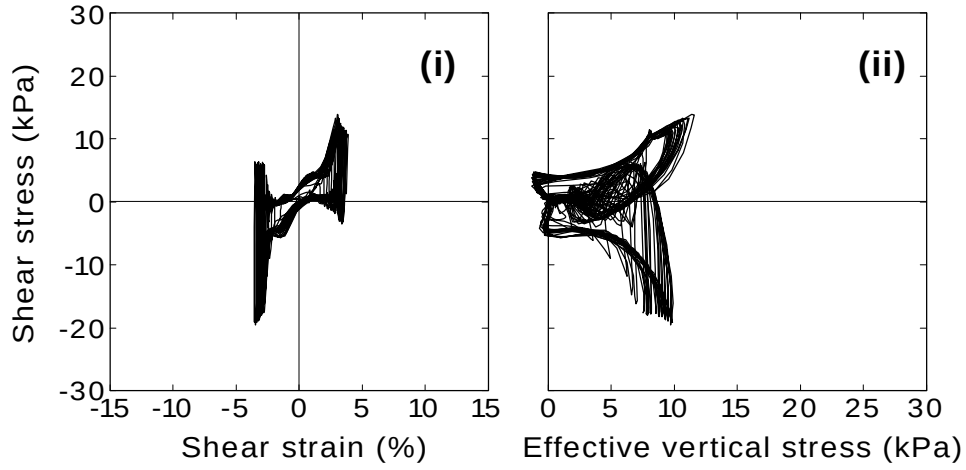

(b) BD78F3A500 test

Fig.4.53: Reproduced stress-strain relationship and stress path (dense backfill)

Results from the other tests

Fig.4.54(a) illustrates the results from AD39F5A50 test, which was shaken by 5Hz excitation with the peak acceleration of 0.5m/sec^2. The amplitude of shear strain was observed less than 0.5%. This is smaller than that of shear strain observed in AD35F3A50 test. The smaller shear strain was caused by the higher input frequency of 5Hz.

The stress-strain relationship and effective stress path from AD41F3A200 test are shown in Fig.4.54(b). In this test, the peak acceleration of input motion was 2.0m/sec^2 and relative density of

the backfill was 41%. The amplitude of shear strain reached the level of about 2.5% in this case. The effective vertical stress, being initially about 3kPa in the stress path as shown in Fig.4.54(b)(ii), was reduced to zero after several cycles of the motion.

Fig.4.54(c) depicts the stress-strain relationship from AD61F3A200 test. It was observed that the amplitude of shear stress and shear strain was about the level of 1.2kPa and 2.5%, respectively, which was of the same level as that of AD41F3A200 test.

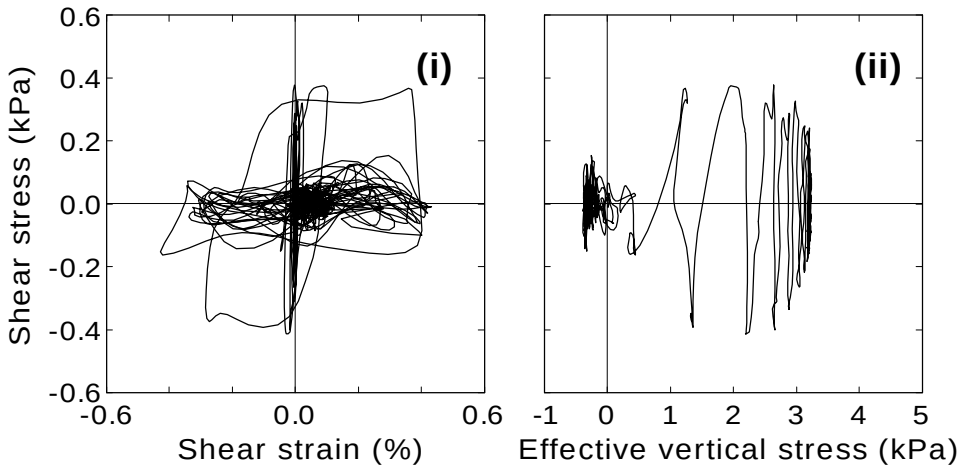

(a) AD39F5A50 test

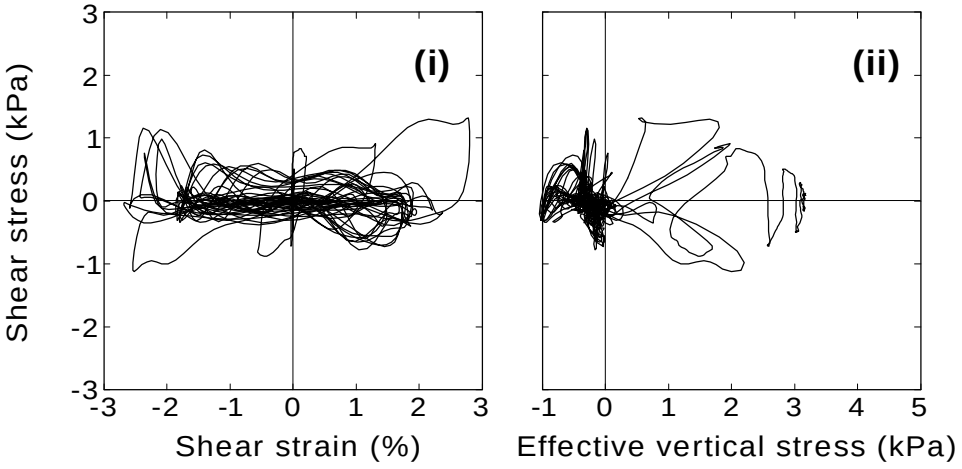

(b) AD41F3A200 test

Fig.4.54: Reproduced stress-strain relationship and stress path (Other test results, GL-0.3m～GL-0.45m)

Fig.4.54(d) shows the results of BD36F3A500 test with 36% relative density of sand shaken by 5.0m/sec^2 of intensity. In this case, the wall yielded just before the liquefaction (see Fig.3.32). In spite of the yielding of the wall, the same feature was seen in the stress-strain relationship, and corresponding stress path.

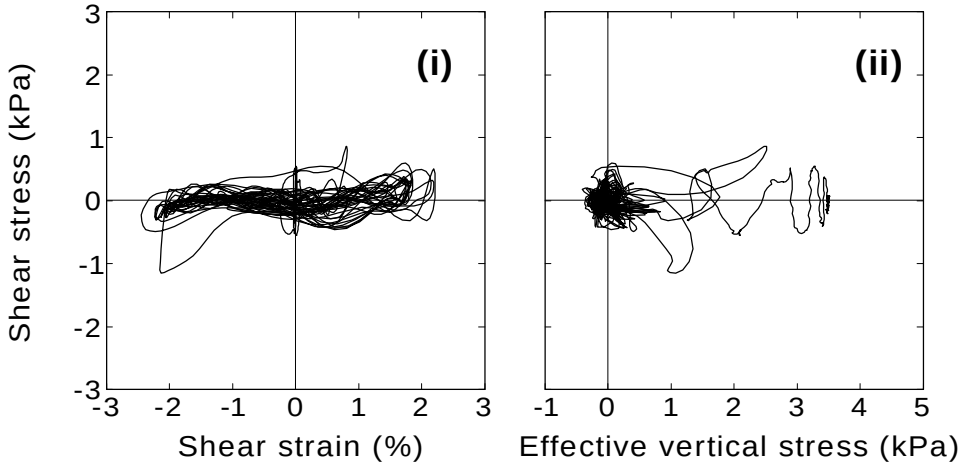

(c) AD61F3A200 test

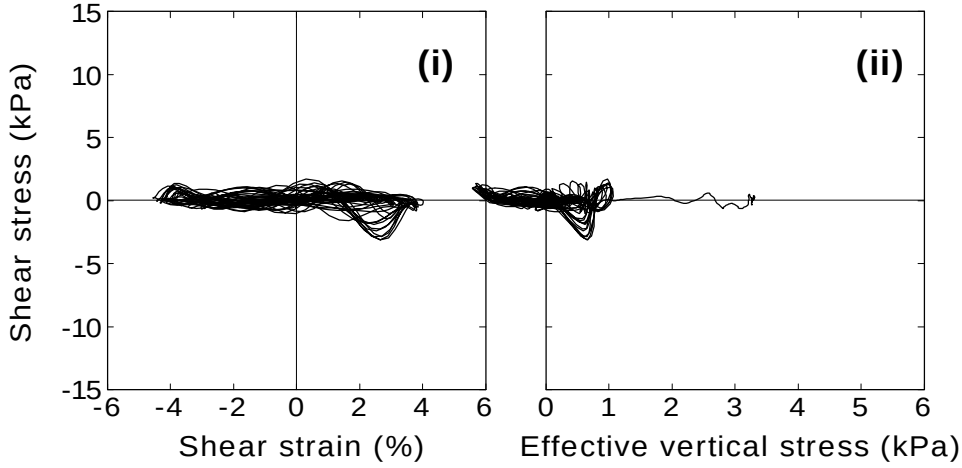

(d) BD36F3A500 test

Fig.4.54: Continued

Typical difference of stress strain relationship

The acceleration response at the top of structure (AC2) from AD32F3A500 test was shown in Fig.3.20. In this test with backfill of 32% relative density, the response acceleration was about 7 m/sec^2. The higher response acceleration for dense sand deposit from AD67F3A500 test was produced as shown in Fig.3.24 by the dilative behavior of sand which allowed the greater

magnitude of shear stress. It suggests that the soil around the embedded structure behaves in a dilative manner during seismic shaking when the backfill soil is dense.

Fig.4.55(a) shows the typical change of the stress-strain relationship before and during liquefaction. The shape of the stress-strain relationship, being initially (8^{th} cycle) close to a linear elasticity, was changing to be flat as the effective stress path moved to the origin.

Fig.4.55(b) illustrates the typical difference of the shape of the stress-strain relationship between the loose and the dense backfill. The shape was flat in the loose backfill. In contrast, the amplitude of the shear stress was larger in the dense backfill than the loose backfill. It is noted that

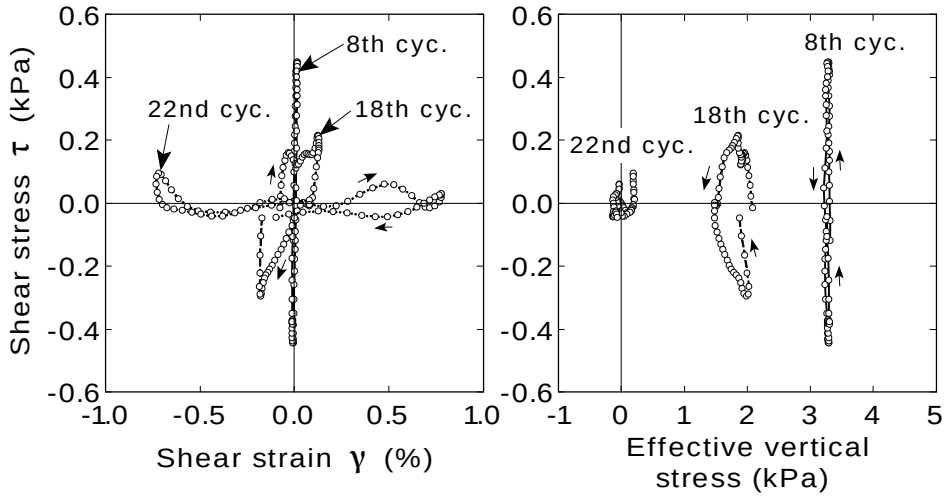

(a) Before and during liquefaction

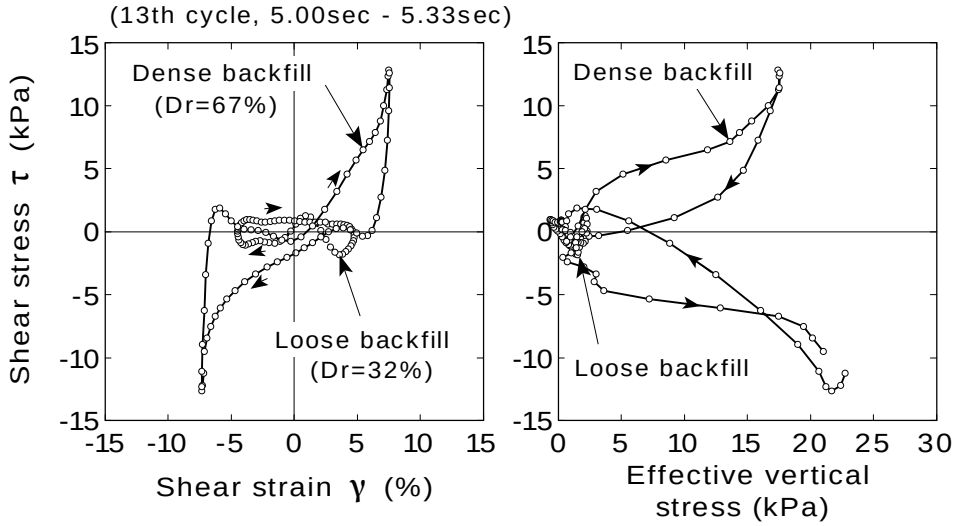

(b) Loose and dense backfill

Fig.4.55: Typical difference of stress-strain relationship and stress path

the effective vertical stress was significantly increased in the dense backfill.

Stress strain relationship at the whole depth of backfill

The stress-strain relationship and the effective stress path at each depth of the backfill are illustrated in Fig.4.56～Fig.4.59. The stress path is reproduced at three depth where the excess pore water pressures (PP1～PP3) are measured. The results at the middle depth of backfill (GL-0.30m to GL-0.45m), which were previously presented, are included.

Typical results (AD35F3A50 test)

The results from AD35F3A50 test are presented in Fig.4.56. The amplitude of shear strain at GL-0.3m～GL-0.575m becomes about the level of 1.5% at the maximum (see figures (d) and (f)). In contrast, the shear strain of soil mass at shallow portion (GL-0.0m to GL-0.15m) and deep portion (GL-0.575m to GL-0.70m) is less than 0.5%, being smaller than the middle portion of backfill. Considering that the wall of box section is connected rigidly with the top and bottom plate as illustrated in Chapter 2 (see Fig.2.4), The deflection angle at the middle of wall should become larger than that at the bottom or top of wall. It is inferred that the dynamically fluctuated deflection angle affects the shear strain of soil mass which is adjacent to the wall. The detail of dynamic deflection of wall will be presented in Chapter 6.

It is seen that shear strain at the deep part of backfill is shifted in the positive direction (see figures (f) and (g). The positive shear strain is illustrated in Fig.4.4). This behavior of shear strain seems the effect of deflection of wall due to monotonically increased lateral earth pressure by liquefaction (see Fig.3.17). The detail of wall deflection due to monotonically increased earth pressure will be described also in Chapter 6.

It is typically observed in Fig.4.56(e) and (h) that the stress path reach the origin as shaking goes on, showing onset of soil liquefaction. The stress path at the soil mass of the surface (GL-0.0m～GL-0.15m, figure (b)) shows the complicated behavior.

Results of the test with intense input motion (AD32F3A500 test)

The stress-strain relationships from AD32F3A500 test are illustrated in Fig.4.57. The feature of

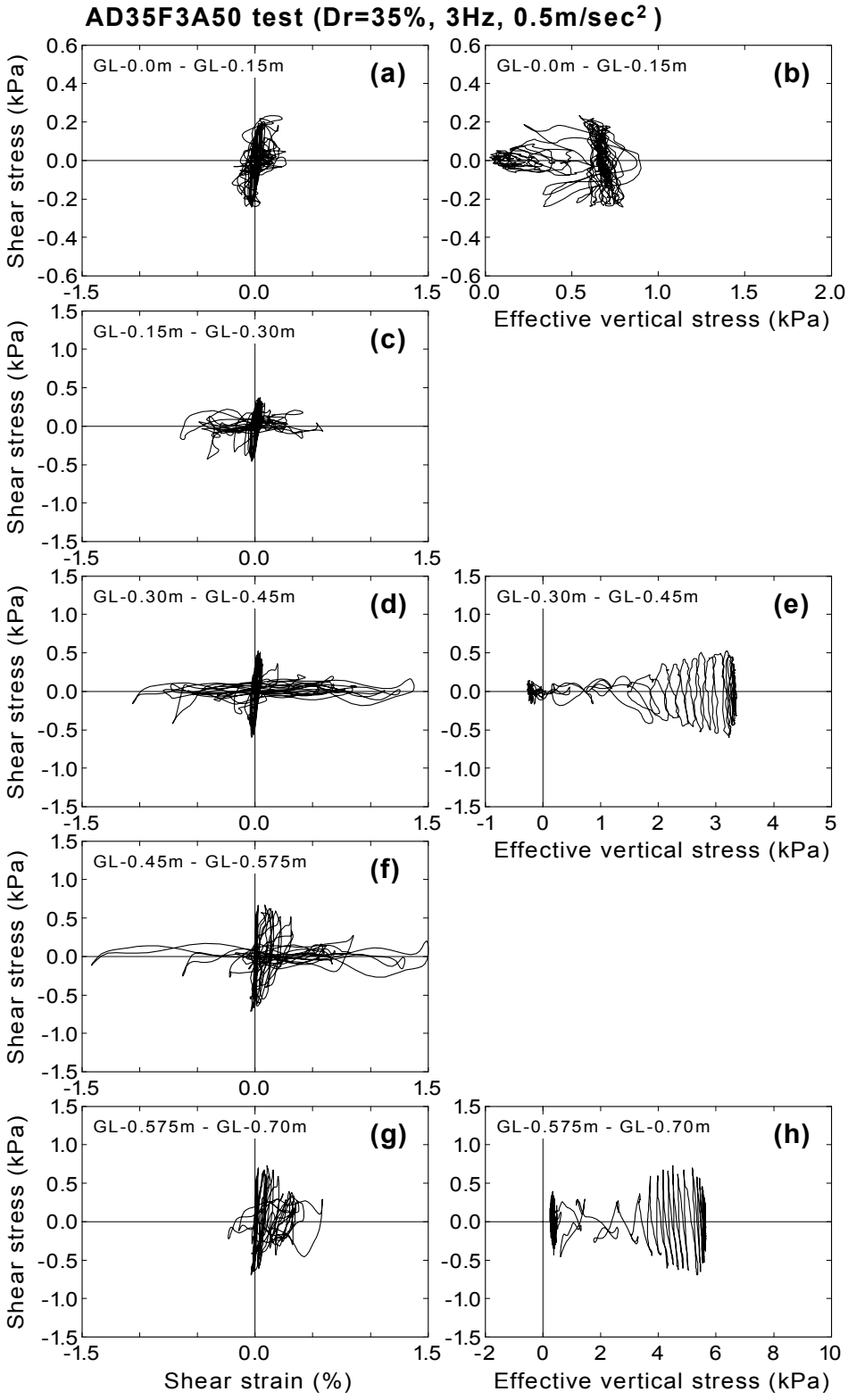

Fig.4.56: Reproduced stress-strain relationship at each soil element (AD35F3A50 test)

stress-strain relationship of complete liquefaction, being flat in shape (see Fig.4.52(a)) is seen through the depth of the backfill. Note that the stress path in figure (b) is incorrect since the excess pore water pressure in the backfill (PP1) was not recorded correctly.

Results of the test with dense backfill (AD67F3A500 and BD78F3A500 test)

The results from AD67F3A500 test are presented in Fig.4.58. As previously described referring to Fig.4.53(b)(i), the stress-strain relationship and effective stress path at the soil mass of GL-0.30m to GL-0.45m shows the dilative behavior of soil. This feature of stress-strain relationship is observed in the soil mass at the top to bottom of backfill. The dilative behavior was considered to occur in the whole depth of backfill in this test. The amplitude of shear strain becomes about 7.5% at the middle depth of backfill (GL-0.30m～GL-0.45m), being the maximum through the depth.

The stress-strain relationships from BD78F3A500 test in which dense backfill is used is illustrated in Fig.4.59. The typical shape of stress-strain relationship when the dilative behavior occurs in dense backfill is observed through the depth. It seems that a complete loss of stiffness of soil did not occur. The amount of shear strain amplitude is approximately 2.5% at the deepest soil mass (see figure (g)), about 4% at the middle (see figure (d)), and 6% at near the surface (see figure (a)), indicating a feature decreasing with depth. It is considered that the amount of shear strain amplitude in unliquefied backfill is affected by the shear modulus of soil, which becomes large with depth in uniform backfill.

Results from the other tests

The stress-strain relationship and the stress path from AD39F5A50 test are illustrated in Fig.4.60. Note that the shear strain time history used in the stress-strain relationship of both (a) and (c) is the average shear strain of whole backfill (see, Fig.4.98(a) and (b)). The amplitude of shear strain at the middle depth of backfill (GL-0.30m to GL-0.45m) grows up to about 0.4% (see figure (d)), indicating the maximum shear strain through the depth. The shear strain amplitude at the deep part or shallow part is seen to be about 0.2%. This is about the half of the shear strain amplitude at the middle depth. It is also observed that the shear strain is increasing in the positive direction at the deep part of the backfill (see figure (f) and (g)). Those features were observed previously in

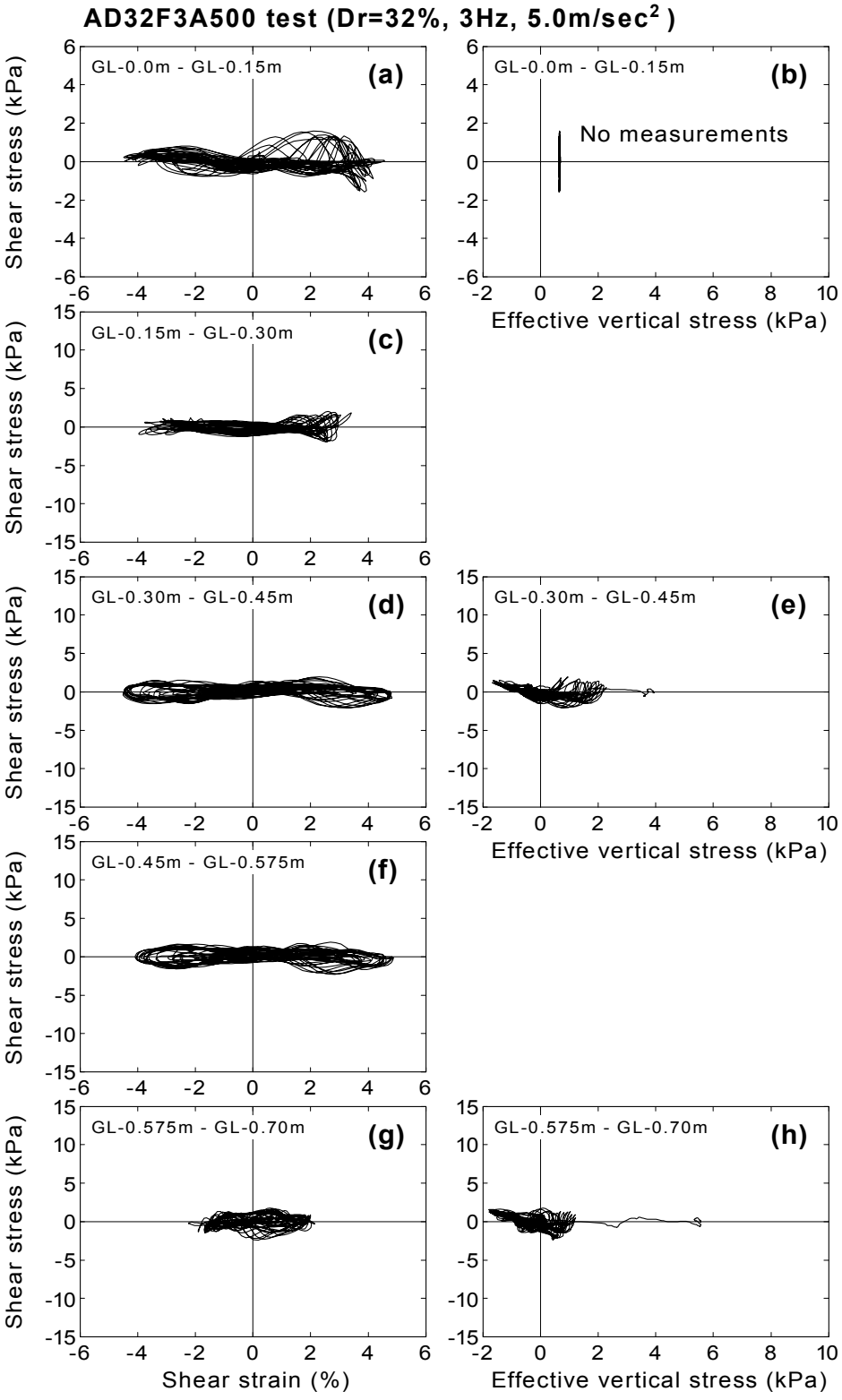

Fig.4.57: Reproduced stress-strain relationship at each soil element (AD32F3A500 test)

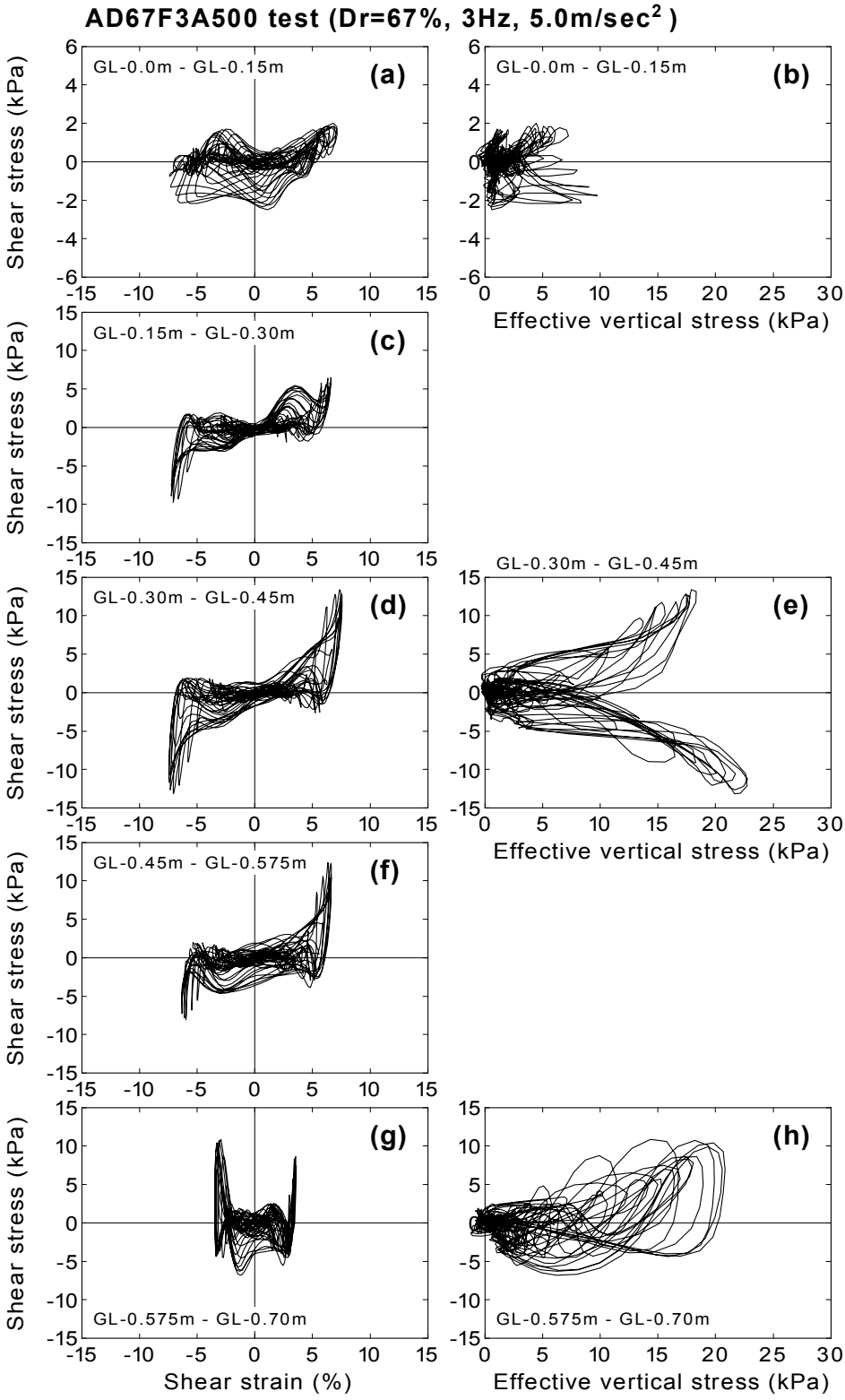

Fig.4.58: Reproduced stress-strain relationship at each soil element (AD67F3A500 test)

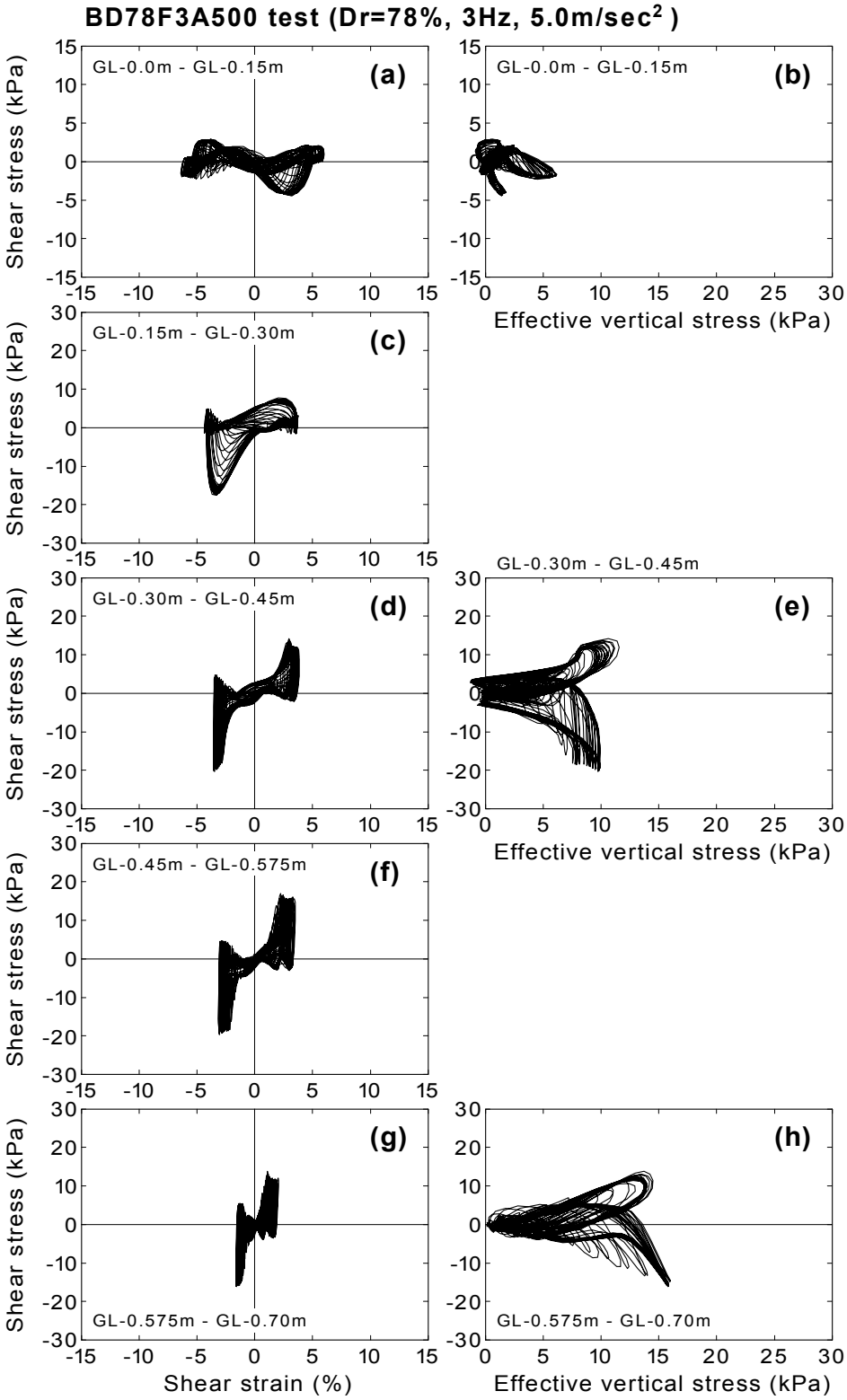

Fig.4.59: Reproduced stress-strain relationship at each soil element (BD78F3A500 test)

AD35F3A50 test, causing the effect of deformation of wall which is increased monotonically due to lateral earth pressure during liquefaction. In the stress path at the deepest soil mass (GL-0.575m ～GL-0.70m) shown in figure (h), the path does not reach at the origin of the stress space. It indicates that the soil did not liquefy completely at the deep part of the backfill in this test.

The results from AD41F3A200 test are shown in Fig.4.61. The amplitude of shear strains reach approximately 2.5% not only the middle depth of GL-0.3m to GL-0.45m (see figure (d)) but also the other depth (see figures (a) and (g)). The time histories of shear strain corresponding to these stress-strain relationships are illustrated in figure (iii) of Fig.4.99 at the end of this chapter. Referencing to those time histories in Fig.4.99, it is observed that the time when the shear strain increases is depending on the depth. In this test, the effective vertical stress becomes zero at whole depth at around 3 seconds (see Fig.4.91). The shear strain at the depth of GL-0.0m to GL-0.15m increases at the last half of shaking of 8 seconds. In contrast, the shear strain at the depth of GL-0.575m to GL-0.70m amplifies at the initial of shaking of around 4 seconds. One reason considered is that the density of backfill was slightly different between the depths of backfill due to repeated shaking of structure model. It is inferred that the soil becomes denser at the shallow part of backfill than the deep part by repeated shaking of 0.5 m/sec^2 in the past (AD35F3A50 and AD39F3A50 tests), causing initial softening of soil at the deep part.

The stress-strain relationship derived by AD61F3A200 test is depicted in Fig.4.62. The maximum amplitude of shear strain about 2.5% appears at the middle depth of backfill (GL-0.30m ～GL-0.45m, see figure (d)). The same feature was observed previously in AD35F3A50 test and AD39F5A50 test. It is considered that the dynamic deflection of wall affects the shear strain amplitude in the backfill.

The results from BD36F3A500 test are depicted in Fig.4.63. From the shape of stress-strain relationship, it is recognized that the loss of shear modulus due to liquefaction occurred through the depth. It is noteworthy that the shear strain at upper part of backfill is shifted in the negative direction (see figures (a)(c), refer to Fig.4.4 for the positive shear strain), in contrast, at the bottom part in the positive direction (see figures (f)(g)). It is seen that the material of wall yielded at its bottom at about 2 seconds and the deflection of the wall amounted about 10mm in the maximum after shaking. The amount of deflection in this test is twice as much as the shear strain in AD32F3A500 test. The shift of shear strain either in the positive or negative direction causes the large deflection of wall. The detail of deflection will be described in Chapter 6 (see Figs.6.29 and 6.30).

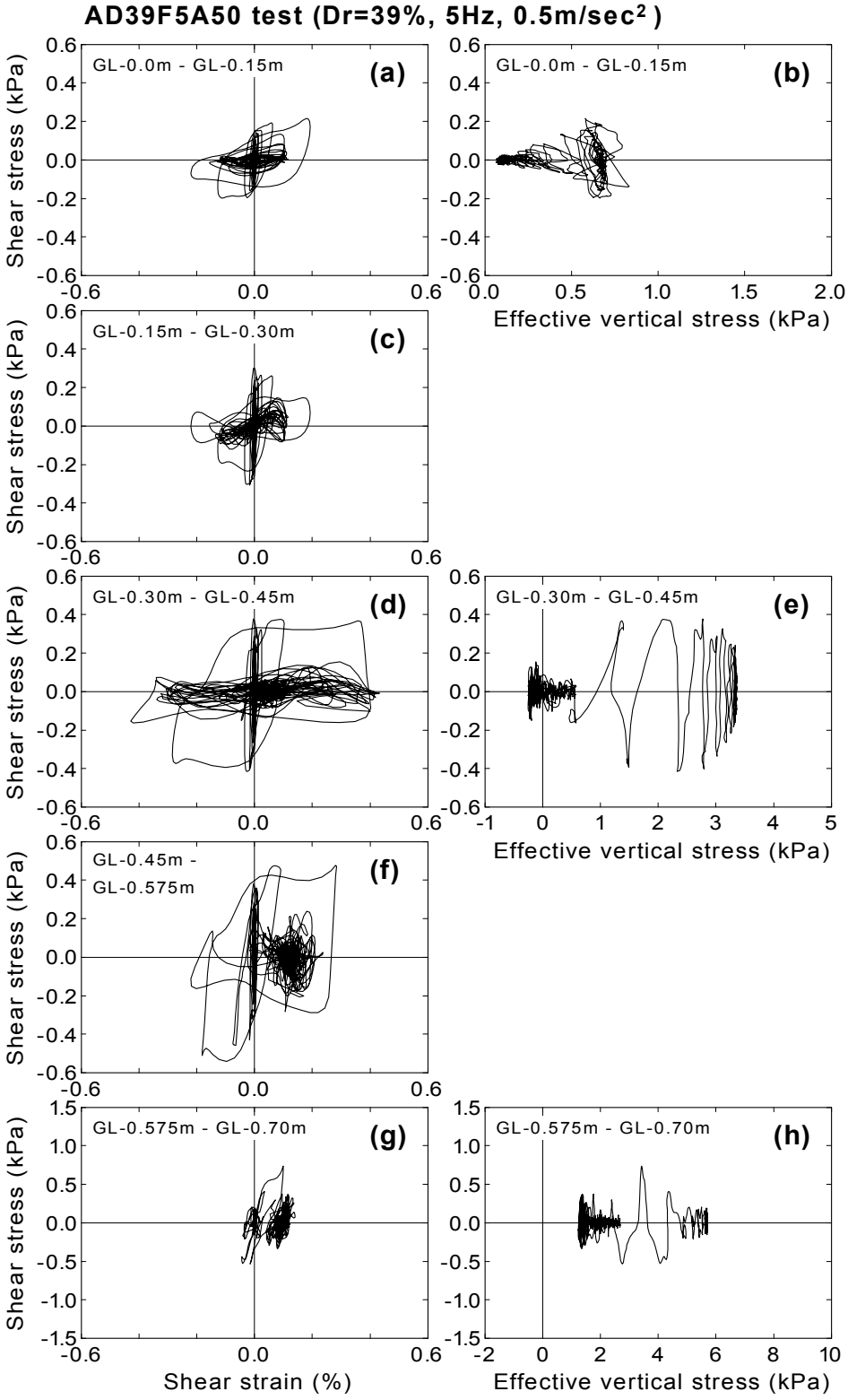

Fig.4.60: Reproduced stress-strain relationship at each soil element (AD39F5A50 test)

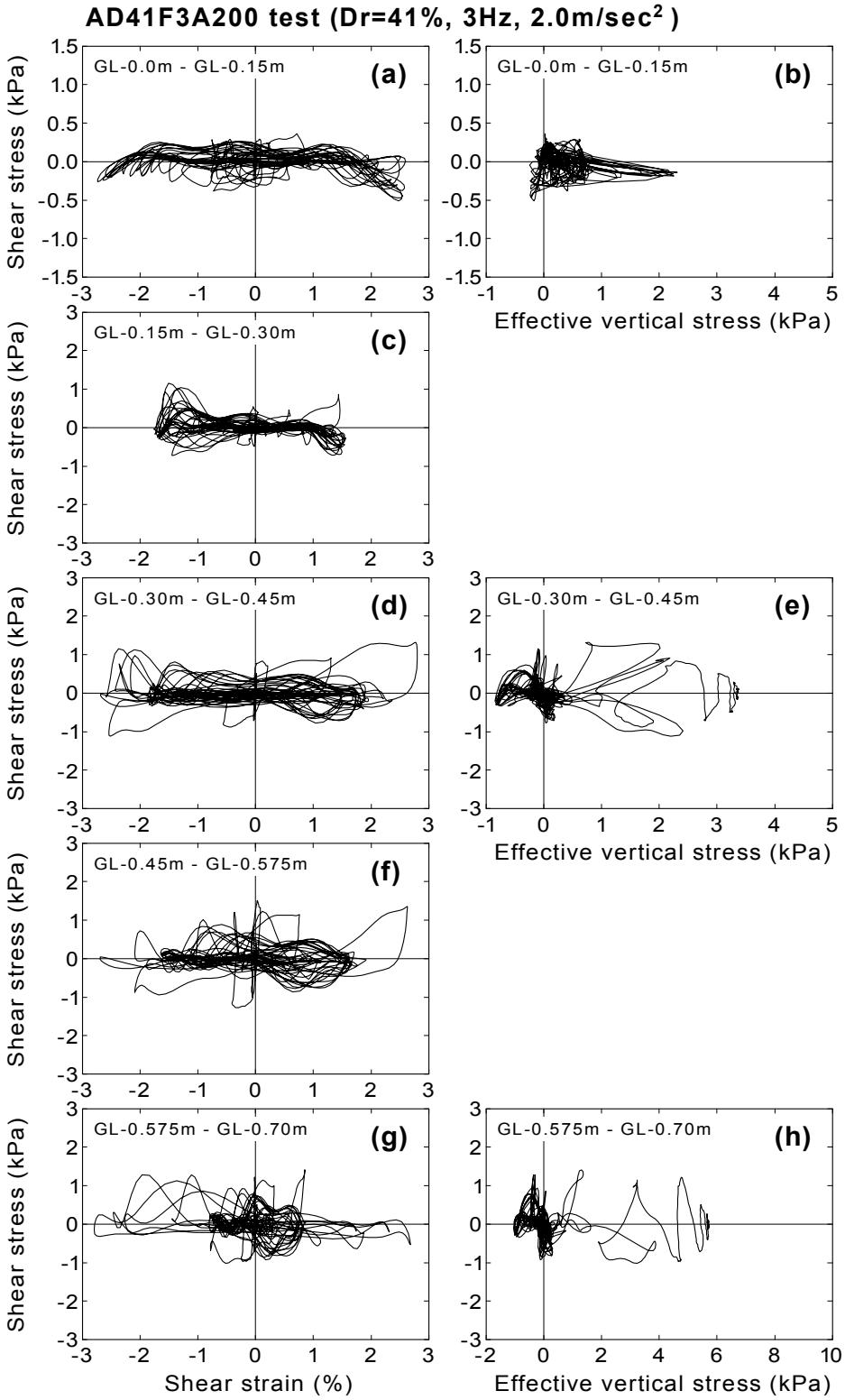

Fig.4.61: Reproduced stress-strain relationship at each soil element (AD41F3A200 test)

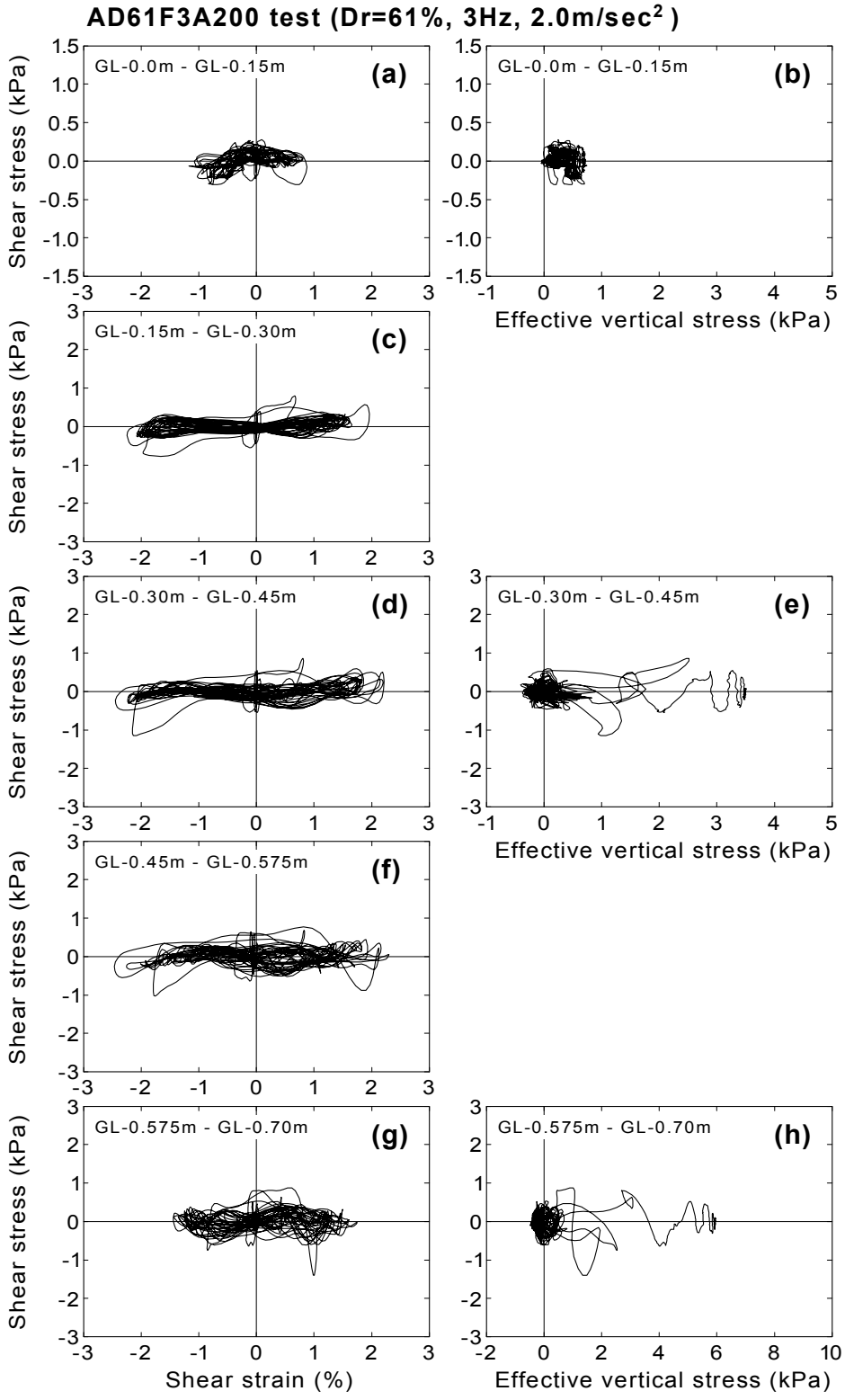

Fig.4.62: Reproduced stress-strain relationship at each soil element (AD61F3A200 test)

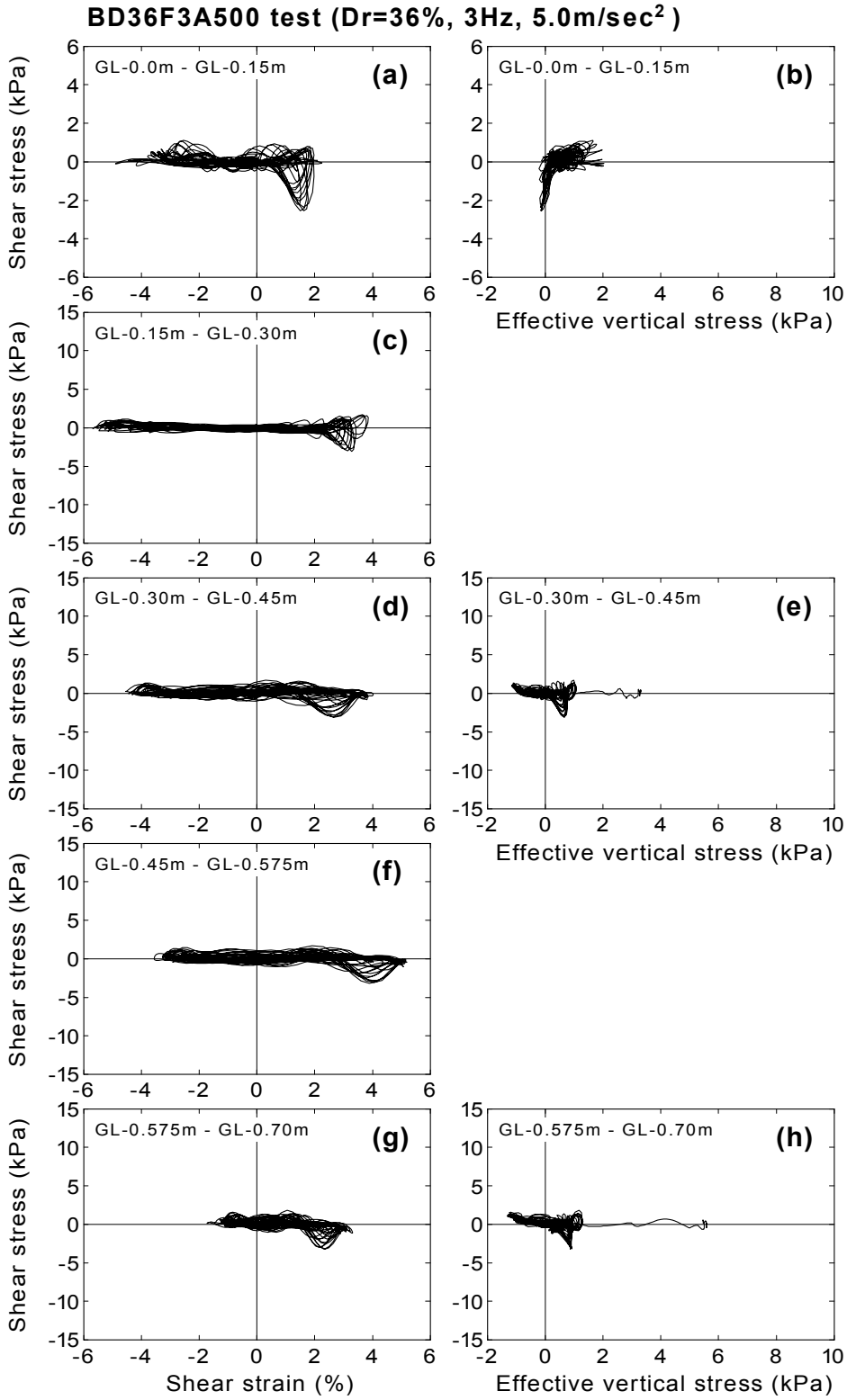

Fig.4.63: Reproduced stress-strain relationship at each soil element (BD36F3A500 test)

4.5 CHANGE OF NATURAL FREQUENCY OF BACKFILL DURING SHAKING

4.5.1 Calculation procedure of shear modulus and damping ratio of soil

Shear modulus

Let a sinusoidally reciprocating shear stress τ be applied to a soil mass exhibiting viscoelastic response as

$$\tau = \tau_a \sin \omega t \tag{4.36}$$

where τ_a is the amplitude, t is the time, and ω stands for the angular frequency. As a result of the shear stress application, shear strain with the same frequency will be produced accompanied by a time delay as

$$\gamma = \gamma_a \sin(\omega t - \delta) \tag{4.37}$$

where γ_a is the amplitude in strain and δ stands for the angle of phase difference indicating the time lag in strain response to the application of the stress. By eliminating the parameter ωt between Eqs.(4.36) and (4.37), a single relation as follows is obtained (Ishihara, 1996),

$$\tau = G\gamma \pm G'\sqrt{{\gamma_a}^2 - \gamma^2} \tag{4.38}$$

where

$$G = \frac{\tau_a}{\gamma_a}\cos\delta, \qquad G' = \frac{\tau_a}{\gamma_a}\sin\delta \tag{4.39}$$

This is an alternative expression of the stress-strain relationship derived from the pair of Eqs.(4.36) and (4.37). An alternative expression is obtained by decomposing the right-hand side of Eq.(4.38) into two parts,

$$\tau = \tau_1 + \tau_2 \tag{4.40}$$

where

$$\tau_1 = G \cdot \gamma \qquad \text{and} \tag{4.41}$$

$$\left(\frac{\tau_2}{G'\gamma_a}\right)^2+\left(\frac{\gamma}{\gamma_a}\right)^2=1 \tag{4.42}$$

The relation expressed by Eq.(4.41) is depicted in Fig.4.64(a) as a straight line with slope *G*. In addition, the relation by Eq.(4.42), which indicates an ellipse in the plot of the τ_2 versus γ, is also illustrated in Fig.4.64(a). The stress-strain relationship expressed by Eq.(4.40) becomes an ellipse with an inclined axis as illustrated in Fig.4.64(b).

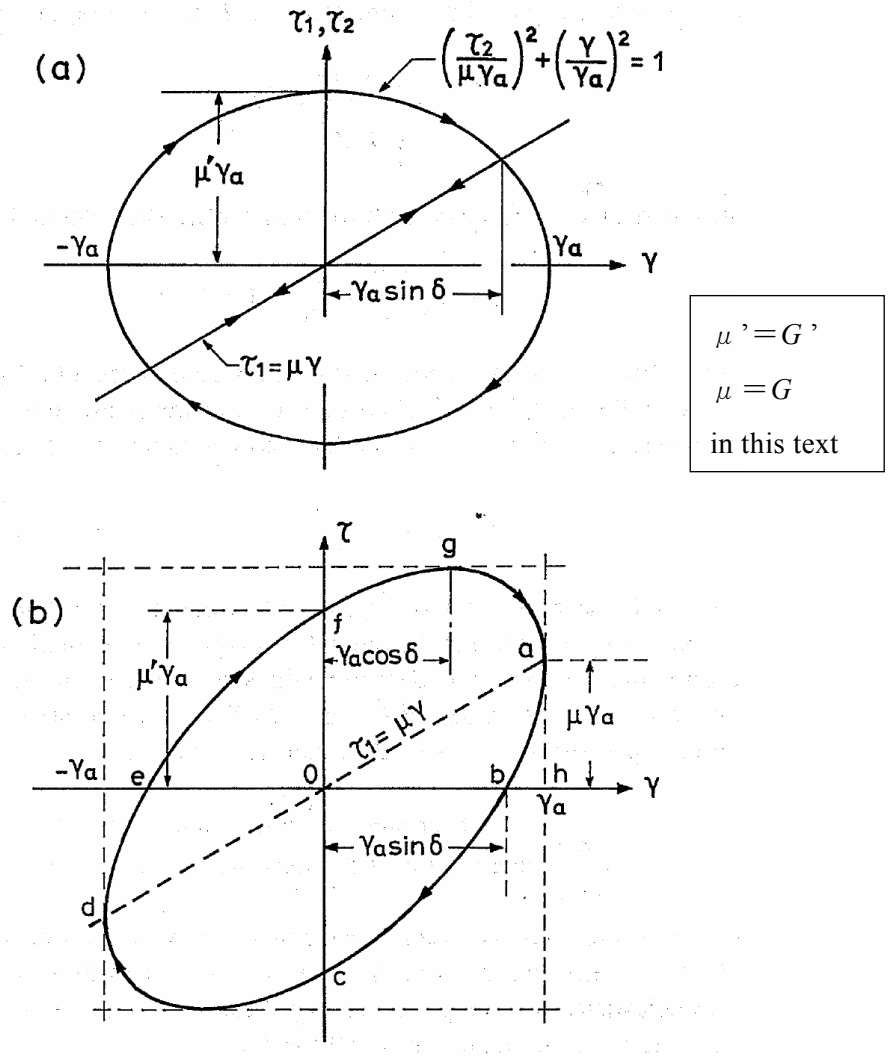

Fig.4.64: Decomposition of the viscoelastic stress-strain model into elastic and viscous components (after Ishihara, 1996)

Substituting Eqs.(4.36) and (4.37) into Eq.(4.38), the stress-strain relationship is expressed with a parameter ωt as

$$\begin{aligned}\tau &= G\cdot\gamma_a \sin(\omega t-\delta) \pm G'\cdot\gamma_a\sqrt{1-\sin^2(\omega t-\delta)} \\ &= G\cdot\gamma_a \sin(\omega t-\delta) \pm G'\cdot\gamma_a \cos(\omega t-\delta)\end{aligned} \tag{4.43}$$

Multiplying the shear strain γ to both sides of Eq.(4.43), the following equation is obtained,

$$\begin{aligned}\tau\cdot\gamma &= G\cdot{\gamma_a}^2 \sin^2(\omega t-\delta) \pm G'\cdot{\gamma_a}^2 \cos(\omega t-\delta)\cdot\sin(\omega t-\delta) \\ &= G\cdot{\gamma_a}^2 \sin^2(\omega t-\delta) \pm \frac{1}{2}G'\cdot{\gamma_a}^2 \sin\{2(\omega t-\delta)\}\end{aligned} \tag{4.44}$$

Integrating both sides of Eq.(4.44) with respect to the parameter ωt from δ to $2\pi+\delta$, G' in the second term in the right-hand side is eliminated as

$$\begin{aligned}\int_{\delta}^{2\pi+\delta}\tau\cdot\gamma\, d(\omega t) &= G\int_{\delta}^{\pi+\delta}{\gamma_a}^2\sin^2(\omega t-\delta)\,d(\omega t) + G'\int_{\delta}^{\pi+\delta}\frac{1}{2}{\gamma_a}^2\sin\{2(\omega t-\delta)\}d(\omega t) \\ &\quad + G\int_{\pi+\delta}^{2\pi+\delta}{\gamma_a}^2\sin^2(\omega t-\delta)d(\omega t) - G'\int_{\pi+\delta}^{2\pi+\delta}\frac{1}{2}{\gamma_a}^2\sin\{2(\omega t-\delta)\}d(\omega t) \\ &= G\int_{\delta}^{2\pi+\delta}\gamma^2\,d(\omega t)\end{aligned} \tag{4.45}$$

The shear modulus G in one cycle is derived from the shear stress and the shear strain as

$$G = \frac{\oint\tau\cdot\gamma\, d(\omega t)}{\oint\gamma^2 d(\omega t)} \tag{4.46}$$

Eq.(4.46) can be expressed in the other way as

$$G = \frac{\sum_{i=1}^{n}(\tau_i-\tau_m)(\gamma_i-\gamma_m)}{\sum_{i=1}^{n}(\gamma_i-\gamma_m)^2} \tag{4.47}$$

where γ_m and τ_m are the mean values of strain and stress, and n is the number of data in a cycle. Thus, the shear modulus G can be calculated from the shear stresses and the shear strains obtained

by tests.

Damping ratio

The energy dissipation per cycle is represented by the area enclosed by the hysteresis loop ΔW as illustrated in Fig.4.65. The damping ratio, D is defined as

$$D = \frac{\eta}{2} = \frac{1}{4\pi}\frac{\Delta W}{W} \tag{4.48}$$

where η is the loss coefficient and W is the maximum stored energy. This is calculated as

$$W = \frac{1}{2} G \cdot \gamma_a \tag{4.49}$$

where G is the shear modulus and γ_a is the strain amplitude in a cycle.

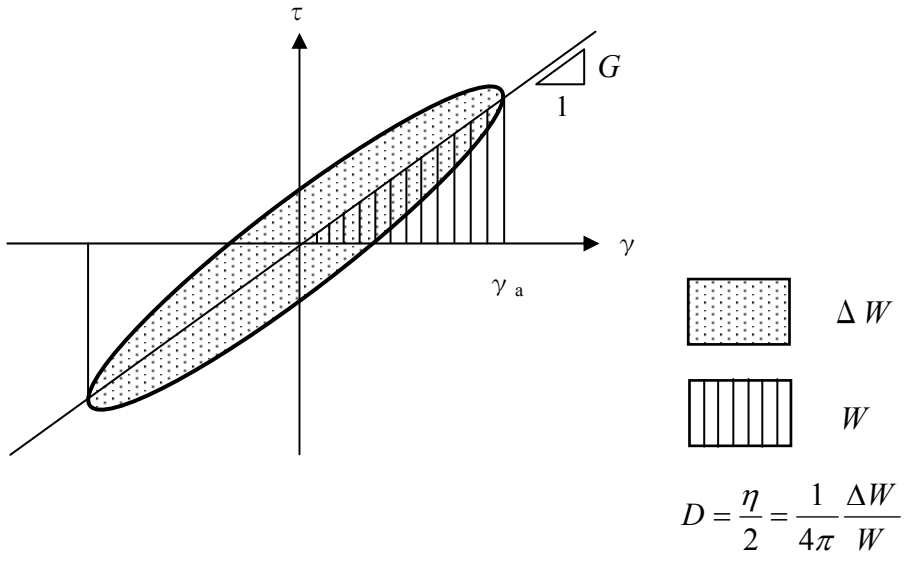

Fig.4.65: Definition of damping ratio (after Ishihara, 1996)

The area enclosed by the hysteresis loop ΔW is calculated using reproduced shear stress τ_i and shear strain γ_i at each time step as

$$\Delta W = \int \tau \, d\gamma = \sum_{i=1}^{n} \frac{(\tau_i + \tau_{i+1})}{2} \cdot (\gamma_{i+1} - \gamma_i) \tag{4.50}$$

where n is the number of data in a cycle.

4.5.2 Change of shear modulus and damping ratio with time

The share modulus and the damping ratio during shaking will be calculated referring to reproduced stress-strain relationships at the depth of GL-0.30m to GL-0.45m.

Typical results (AD35F3A50 test)

An example of the reproduced stress-strain relationship from AD35F3A50 test is illustrated in Fig.4.66. This is the hysteresis loop from 5.67 to 6.00 seconds which is the 15th cycle of 3Hz input motion. The direction of rotation was observed to be clockwise. A loop consists of 67 data of

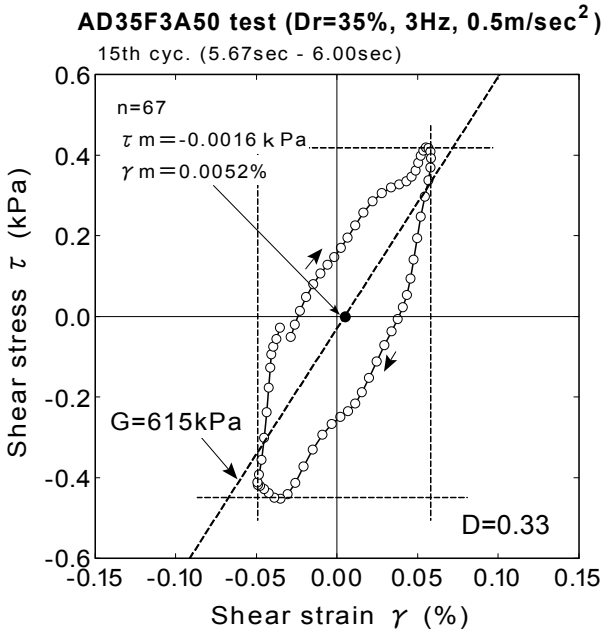

Fig.4.66: Example of stress-strain relationship in one cycle (AD35F3A50 test)

stresses and strains since the sampling frequency was 200Hz. Based on the Eq.(4.47), shear modulus *G* of the loop illustrated in Fig.4.66 was calculated to be 615 kPa. The straight line with the slope of 615 kPa is drawn in the figure. Damping ratio by Eq.(4.50) was calculated to be 0.33. It is seen that the physical relationship between the htsteresis loop and the straight line of G=615 kPa is qualitatively similar to that of ideal stress-strain relationship illustrated in Fig.4.64.

In order to examine the change of shear modulus and damping ratio of the backfill during shaking, those values were calculated by Eq.(4.47) and (4.50), respectively. The calculation was conducted in each cycle of the hysteresis loop with the time interval of a half cycle (0.165sec. for 3Hz shaking, 0.10sec. for 5Hz shaking). Fig.4.67 shows the hysteresis loop at the depth of GL-0.30m to GL-0.45m of each cycle from AD35F3A50 test. The calculated values of the shear modulus *G* and the damping ratio *D*, and the straight line with the slope of *G* from each cycle are described in each figure. In case that the shear modulus was calculated as negative with small absolute values, the shear modulus was regarded as zero.

It was observed that the hysteresis loops during 5^{th} to 15^{th} cycles (2.33sec to 6.00 sec) were in the shape of ellipse rotating clockwise. The shape was very complicated during 1^{st} to 4^{th} cycle (1.00sec to 2.33sec) when the amplitude of shear strain was less than the level of 0.01%. The shear modulus of 458kPa at 16^{th} cycle (6.00 sec to 6.33sec) was reduced to zero at 21^{st} cycle (7.67sec to 8.00sec). Zero shear modulus was maintained from 21^{st} cycle to 25^{th} cycle (7.67sec to 9.33sec). It was imagined that the backfill behaved as liquid during this period.

The change of the shear modulus and damping ratio at each cycle as well as the time history of the ratio of excess pore water pressure, shear stress and shear strain are illustrated in Fig.4.68. The time instance at the center of a cycle was selected for the data plot on Fig.4.68 except for time history (c) (e.g. 2.165 seconds was of a representative time in a cycle between 2.00 seconds and 2.33 seconds). The amplitude of shear stress and shear strain were defined as a half of difference between the maximum and the minimum values in a cycle. The time period when the soil liquefied completely is indicated in the figure.

The shear stress amplitude in Fig.4.68(a) is observed to increase linearly from 1.0 second to 4.2 seconds. This is due to the input motion whose acceleration amplitude increases gradually (see Fig.3.16). It is seen that the shear stress during liquefaction becomes about one sixth of its maximum amplitude. This is because the reduction of response due to softening of backfill.

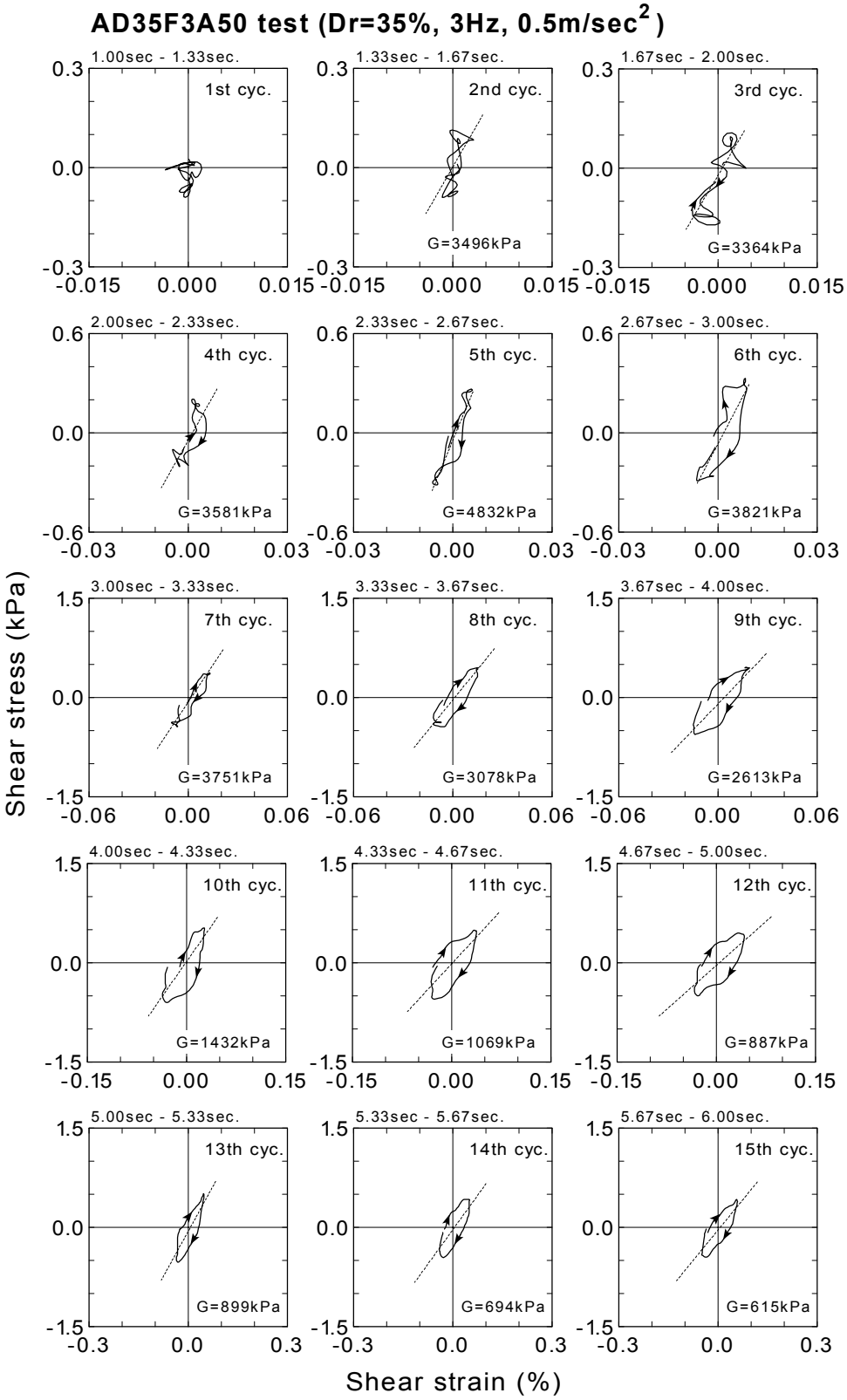

Fig.4.67: Stress-strain relationship of each cycle and calculated shear modulus (AD35F3A50 test, 1～15 cycles)

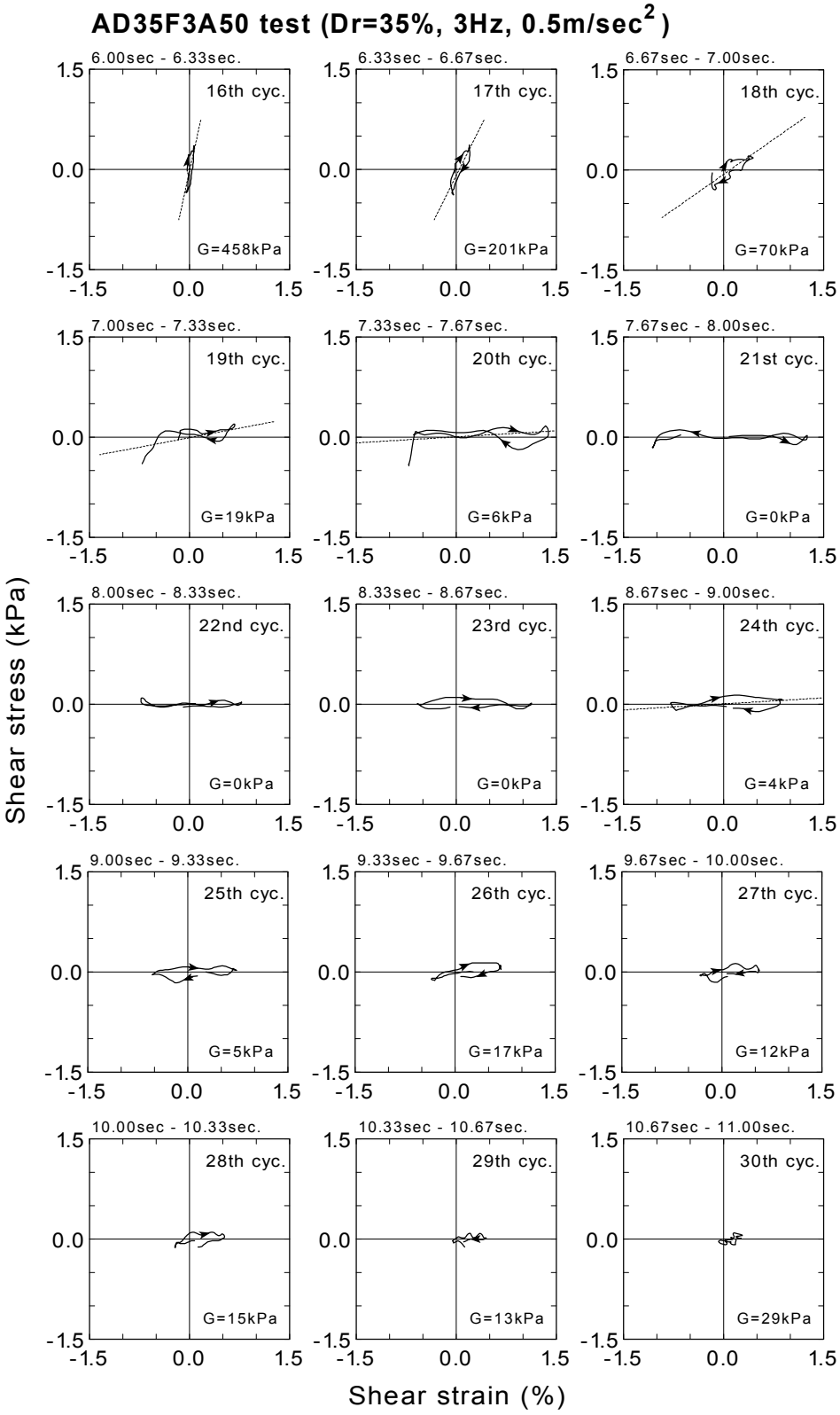

Fig.4.67: Continued (AD35F3A50 test, 16～30 cycles)

It was seen in Fig.4.68(d) that the shear modulus of initially about 5000kPa decreased to zero, as the shear strain and the ratio of excess pore water pressure was increased by the shaking. The shear strain reached the level of 1 % just before 8 seconds when the backfill liquefied completely. The reduction of shear modulus is seen during 2.5 seconds to 3.5 seconds when the excess pore water pressure has not built up yet. This is due to increase of shear strain amplitude. From 1.5 to 2.5 seconds, the value of shear modulus increased from about 3000kPa to 5000kPa in spite of the growing of the shear strain. It was imagined that the reproduced stress and strain was not accurate enough to detect the shear modulus of backfill in the small strain level of less than 0.01%. It is observed that shear strain continue to increase up to 8.0 seconds, and maintains large strain amplitude of a level of 1.0% during liquefaction. The damping ratio being initially approximately 0.1 is observed to increase up to about 0.4 as the shear strain amplitude increases. Slight decrease of damping ratio is seen from 5 seconds to 7 seconds when excess pore water pressure builds up rapidly. The shear modulus and shear stress decrease in this time period, but the reason of reduction of damping ratio is not clear. The damping ratios during complete liquefaction were not calculated correctly due to irregular shape of hysteresis loop.

Results of the test with intense input motion (AD32F3A500 test)

Fig.4.69 shows the results from AD32F3A500 test. The shear modulus, damping ratio and the amplitude of shear strain at each cycle, and the ratio of excess pore water pressure time histories under the input motion of 5.0m/sec^2 are illustrated in the same fashion. It was seen that the reduction of shear modulus become rapid as intensity of input motion was larger as compared with AD35F3A50 test, in which the large amplitude of shear strain and the more rapid build-up of pore water pressure did not occur. In case of 5.0 m/sec^2 shaking, the excess pore water pressures changed cyclically during liquefaction in the range of about 0.5 to 1.3. This is considered to be the effect of longitudinal wave (*P* wave) due to existence of the structure. The damping ratio seems to be incorrectly calculated between 2 seconds and 10 seconds.

It is seen in Fig.4.69 that the shear stress amplitude during complete liquefaction of about 2.5 kPa is larger than that of before liquefaction of 0.8 kPa. Theoretically, shear stress during liquefaction must be smaller than that of before liquefaction. The same feature is observed in BD36F3A500 test in which loose backfill was used and shaken by intense input motion of 5.0 m/sec^2 (see Fig.4.115(a)). One reason is that the acceleration amplitude before liquefaction in those

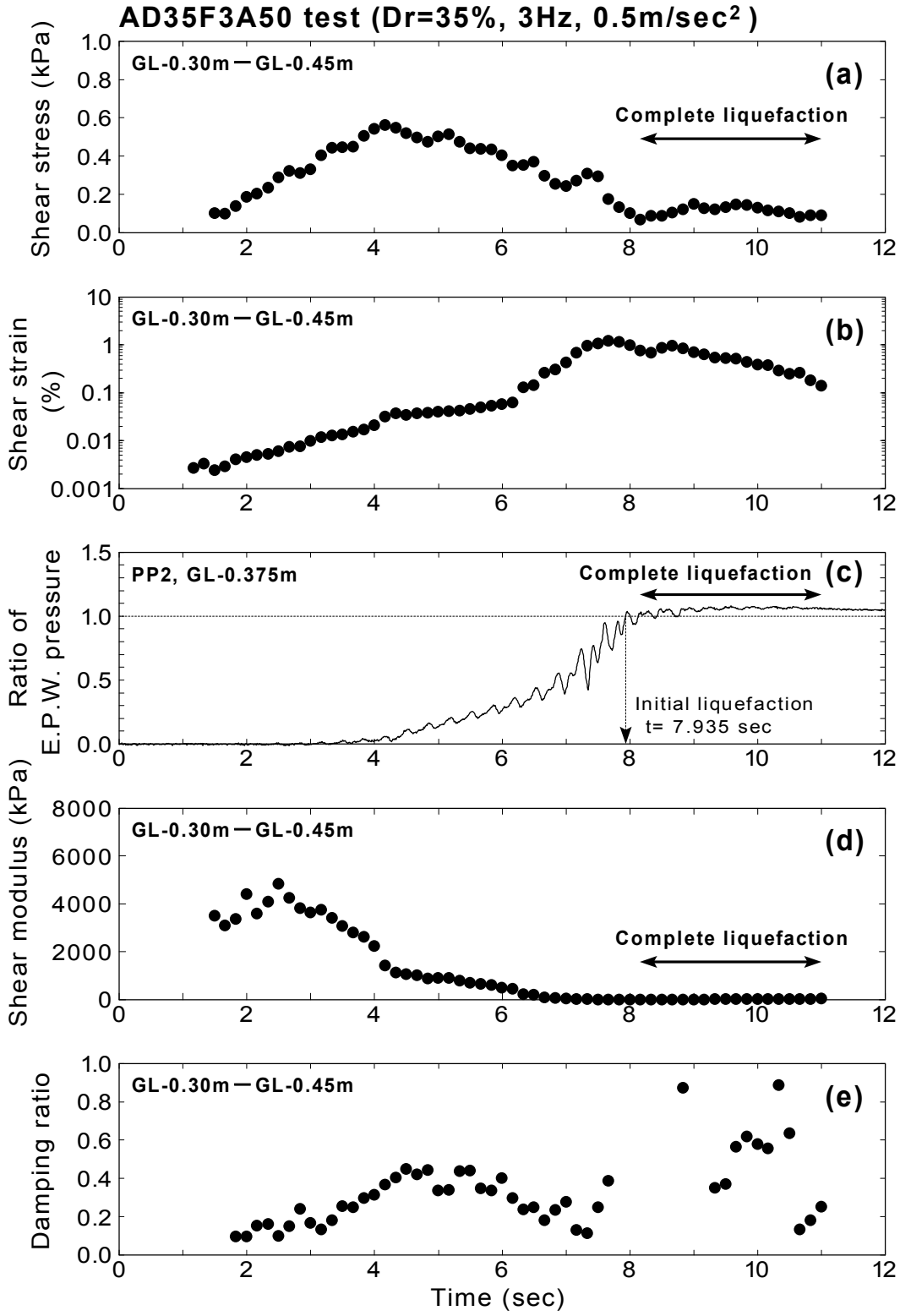

Fig.4.68: Change of shear modulus and damping ratio with respect to time (AD35F3A50 test)

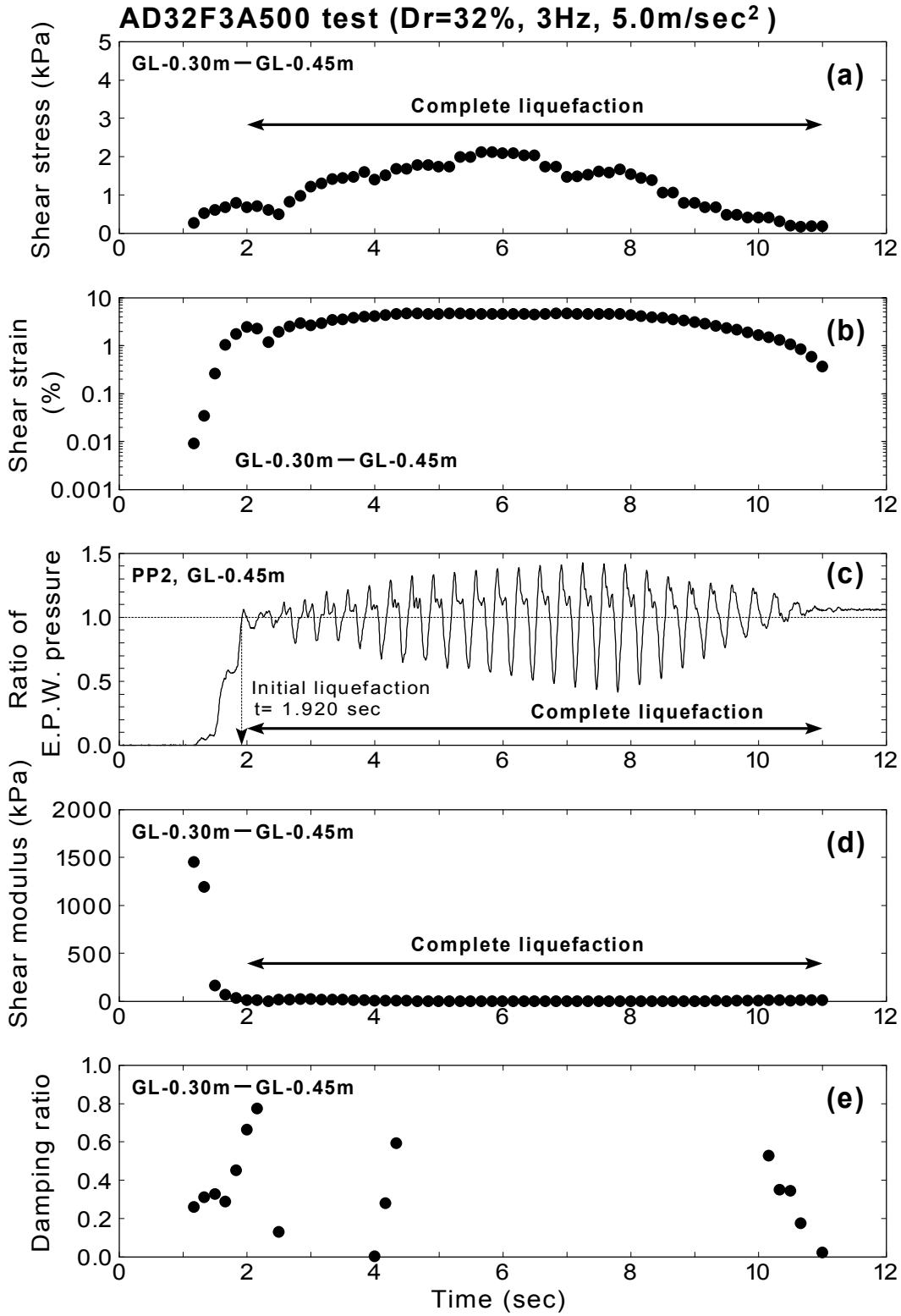

Fig.4.69: Change of shear modulus and damping ratio with respect to time (AD32F3A500 test)

tests, which is approximately 1.5～2.0 m/sec^2, is smaller than that during liquefaction of 5.0 m/sec^2. It is considered that accurate reproduction of shear stress in liquefied soil is difficult when input motion is intense.

Results of the test with dense backfill (AD67F3A500 test)

The results from AD67F3A500 test in which the dense backfill was used are depicted in Fig.4.70. As is seen in the time history of ratio of excess pore water pressure (see figure(c)), the reduction of pore pressure ratio is cyclically observed between 3.0 seconds to 8.0 seconds, indicating the dilative behavior of backfill. In addition, the shear stress amplitude during the time period is amplified. It was seen that the shear modulus of backfill, which was once reduced to zero at about 3 seconds, had a small value of about 100 kPa at 4.0 to 7.0 seconds when the ratio of excess pore pressure significantly oscillated. It suggests that the increase of shear modulus due to dilative behavior of soil caused the amplification of shear stress. It is peculiar that the damping ratio around 6 seconds is slightly smaller than that of initial damping ratio before 2 seconds.

Results of the other tests

All the other stress-strain relationship at the depth of GL-0.30m to GL-0.45m and calculated shear modulus of each cycle are shown in Fig.4.105～Fig.4.111 at the end of this chapter. The change of shear modulus and shear strain as well as the time history of the ratio of excess pore water pressure from AD39F5A50, AD41F3A200, AD61F3A200, BD36F3A500 and BD78F3A500 test are shown in Fig.4.112～Fig.4.116.

Average shear modulus during liquefaction

The average shear modulus during liquefaction in each test is summarized in Table 4.3. Approximate initial shear modulus was calculated from the results of weak excitation test of soil deposit (see, Table.3.16). The shear modulus is expressed as

$$G = \rho \cdot V_s^{\,2} = \rho \cdot (4H \cdot \nu)^2 \tag{4.51}$$

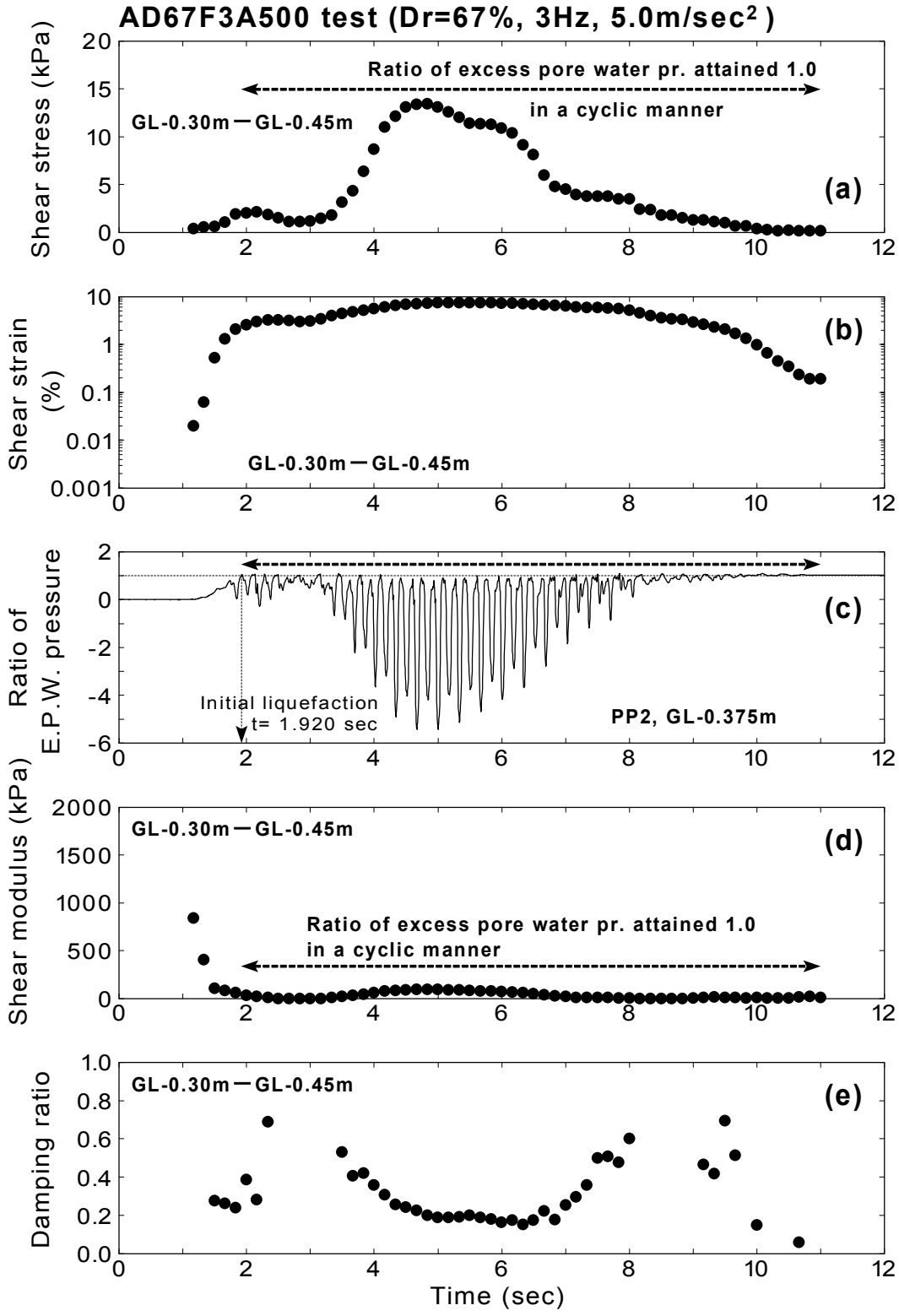

Fig.4.70: Change of shear modulus and damping ratio with respect to time (AD67F3A500 test)

where H is the thickness of soil deposit, ρ is the mass density, Vs is the shear wave velocity, and ν is the natural frequency of soil deposit. In this calculation for the approximate initial shear modulus, ρ =1.9 and H=0.85m were assumed. It was seen that the shear modulus was reduced to 1/500～1/2800 of the initial values during complete liquefaction in a loose backfill and 1/90～1/300 in a dense backfill which behaved in a dilative manner.

Table 4.4: Average shear modulus of backfill during liquefaction

Case No	Average shear modulus during liquefaction (kPa)	Approximate initial shear modulus (kPa)	Approximate ratio (Liquefied / initial)
AD35F3A50	12	8400	1/ 700
AD39F5A50	18	8400	1/ 500
AD41F3A200	3	8400	1/2800
AD61F3A200	4	10600	1/2700
AD67F3A500	32*	10600	1/ 300
AD32F3A500	5	8400	1/1700
BD36F3A500	4	8400	1/2100
BD78F3A500	117*	10600	1/ 90

* the soil behaved in a dilative manner.

Experimental relationships between shear strain and shear modulus, damping ratio

The shear strain dependency of shear modulus and damping ratio of soil is a well known fact in the field of soil dynamics. Hence, the experimental relationship between the reproduced shear modulus and the shear strain amplitude from shaking table tests was drawn in order to observe qualitative feature of strain dependency. For the observation under the same condition of the effective confining stress of soil, the data only before the excess pore pressure generation were selected from the results of shaking table tests. In this procedure, the data, which seemed to be affected by noises at the initiation of shaking (e.g., Fig.4.67, 1.0sec～2.33sec), was removed. The initial shear modulus derived by the weak excitation test was also plotted at the strain level of 10^{-6}. The experimental relationship between the shear modulus, damping ratio and the shear strain amplitude are illustrated in Fig.4.71.

For the comparison with the shaking table tests, the shear modulus and the damping ratio of Toyoura sand derived by triaxial tests are plotted. The triaxial tests were performed under the condition of very low effective confining stresses (2.94ka and 4.9kPa), which was of the same

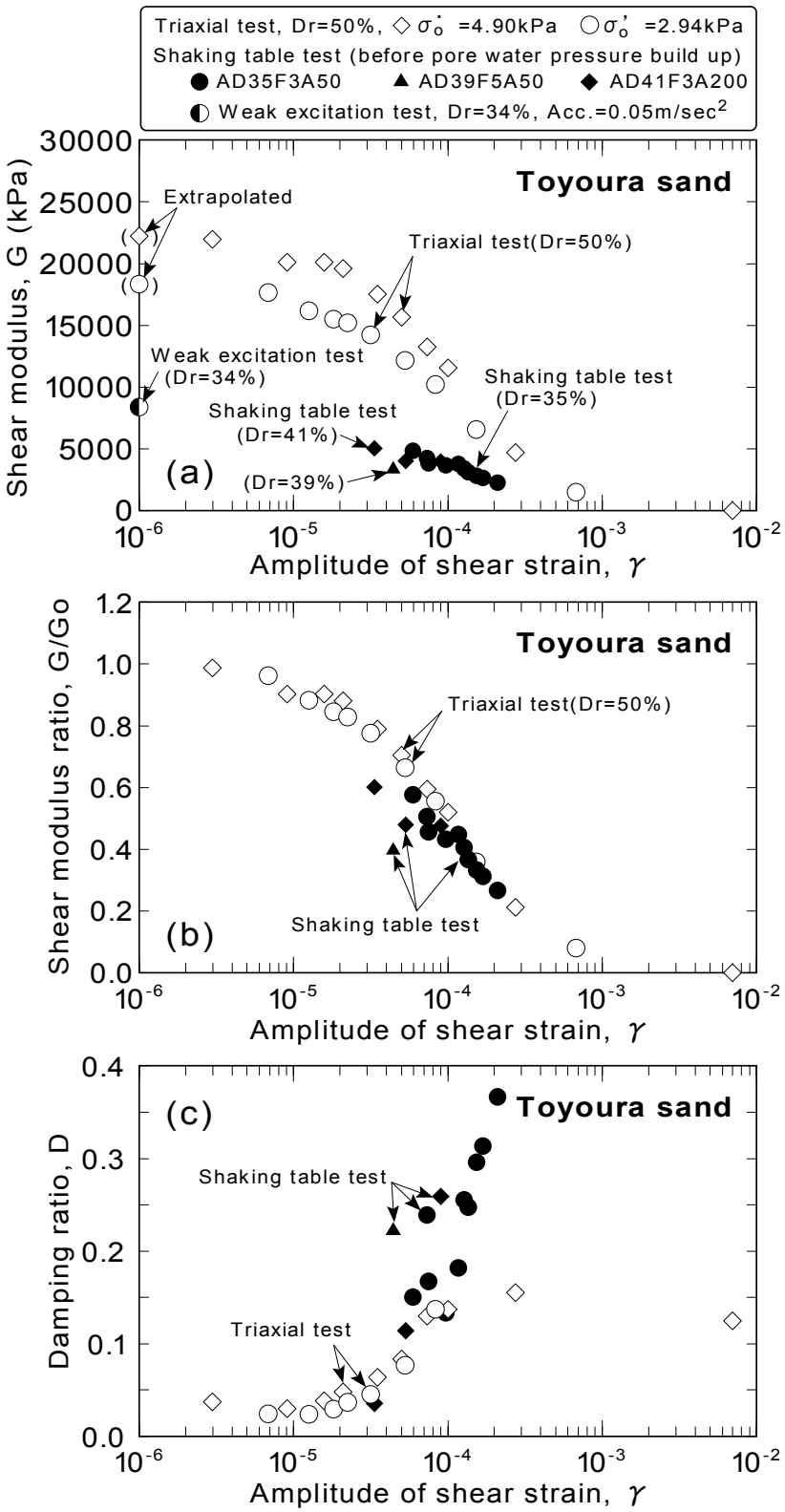

Fig.4.71: Experimental relationships between shear strain and shear modulus, damping ratio

level of effective confining stress in the backfill used in the shaking table test. The relative density of Toyoura sand in the triaxial test was adjusted to 50%.

It is seen in Fig.4.71(a) that the initial shear modulus by weak excitation test of relative density at 34% is about 10000kPa, being smaller than the shear modulus of 20000kPa by the triaxial test of relative density of 50%. It causes the difference of the relative density of soil.

Fig.4.71(b) shows the relationship between the shear modulus ratio, G/G_0, and shear strain amplitude. The shear modulus derived by shaking table tests is normalized by the initial shear modulus due to the weak excitation test. It is seen that the shear modulus ratio due to shaking table tests reasonably agrees with those due to triaxial tests. Fig.4.71(c) illustrates the relationship between the damping ratio and the shear strain amplitude. It is observed that the damping ratio by shaking table tests at the level of strain amplitude more than about 10^{-4} is in the range of about 0.20～0.35, being larger than those about 0.15 by triaxial tests. In contrast, the damping ratios by both tests are in the same range of 0.05～0.15 at the strain amplitude of less than 10^{-4}. It suggests that the strain dependency of the shear modulus and the damping ratio are reasonably reproduced by the shaking table tests.

4.5.3 Change of shear modulus with depth

The share modulus during shaking is calculated referring to reproduced stress-strain relationships at the whole depth of backfill (GL-0.0m to GL-0.70m) in order to observe the material change along the depth. The share modulus during shaking is calculated by the same procedure as presented previously using Eq.(4.47).

Approximate initial shear modulus at each depth

The approximated initial shear modulus at each depth is calculated considering the dependence of initial confining stress. It is known that the initial shear modulus of Toyoura sand is proportional to the square root of confining stress (Kokusho, 1980) as

$$G_{m0} = 8400 \frac{(2.17-e)^2}{1+e} \cdot (\sigma_{m0}{}')^{0.5} \quad kPa \tag{4.52}$$

where G_{m0} is the initial shear modulus, e is the void ratio and σ_{m0}' is the initial confining stress. Assuming that the void ratio is constant in a uniform backfill, the initial shear modulus G_0 at arbitral point where the amount of confining stress is σ_0' is expressed as

$$G_0 = G_{m0} \cdot \left(\frac{\sigma_0'}{\sigma_{m0}'} \right)^{0.5} \tag{4.53}$$

The confining stress σ_0' is calculated as

$$\sigma_0' = \frac{1}{3}\left(\sigma_{v0}' + 2 \cdot \sigma_{h0}' \right) = \frac{1}{3}\left(\sigma_{v0}' + 2K_0 \cdot \sigma_{v0}' \right) = \frac{\sigma_{v0}'}{3} \cdot (1 + 2K_0) \tag{4.54}$$

where σ_{v0}' and σ_{h0}' are the effective vertical and horizontal stress, respectively, and K_o is the coefficient of earth pressure at rest. The effective vertical stress is expressed as

$$\sigma_{v0}' = \gamma' \cdot z \tag{4.55}$$

where γ' is the submerged unit weight, and z is the depth. Assuming that the submerged unit weight, γ', and the coefficient of earth pressure at rest, K_o, does not vary with depth, Eq.(4.53) is reduced taking Eq.(4.55) and Eq.(4.54) into consideration as

$$G_0 = G_{m0} \cdot \left(\frac{z}{z_m} \right)^{0.5} \tag{4.56}$$

where z_m is certain depth where the amount of initial shear modulus is G_{m0}. In the calculation, the approximate initial shear modulus which was derived by the weak excitation test (see Table 4.3) is used for G_{m0} (=8400 kPa or 10600 kPa), and the middle depth of the backfill is referred for z_m (=0.425m) in Eq.(4.56).

Typical results (AD35F3A50 test)

The result from AD35F3A50 test is presented in Fig.4.72. It is observed that the shear modulus before about 2.5 is fluctuating at the all depth. It is considered that the stress-strain relationship before 2.5 seconds is not reproduced correctly (see Fig.4.67, 1^{st} to 4^{th} cycle). As a result of this, the shear modulus was calculated incorrectly only the initial of shaking. In this respect, supposed change at each depth is illustrated between the initial of shaking of 1 second and 2.5 seconds by arrows.

It is seen that the shear modulus at each depth decreases with time relatively rapidly until about 4.5 seconds. From the time history of the pore pressure ratio (PP2, GL-0.375m) in Fig.4.68, the time of 4.5 seconds corresponds to the initiation of generation of pore water pressure. It indicates that decrease of shear modulus before about 4.5 seconds causes the increase of dynamic shear strain. From about 4.5 seconds to 8 seconds, the shear modulus continues to decrease in all depth relatively slowly than before. The decrease of effective confining stress causes the decrease of shear modulus during this time period. It is observed that the all shear modulus becomes zero at one time at about 8 seconds. This is due to the liquefaction of backfill.

It is observed that the shear modulus at deep portion of backfill (GL-0.575m to GL-0.70m) is larger than that at the other depth all the time. In contrast, the shear modulus at shallow portion (GL-0.0m～0.15m) is smallest through the duration. It shows the dependence of confining stress on the shear modulus. From 9 to 10 seconds, the shear modulus at the depth of GL-0.575m to GL-0.70m is increasing up to about 400 kPa. It is because that the effective vertical stress at that depth increased during the time probably due to dissipation of excess pore water pressure (see, Fig.4.34(e)).

Results of the test with intense input motion (AD32F3A500 test)

The change of shear modulus at all depth from AD32F3A500 test is depicted in Fig.4.73. Since the model is shaken by the intense input acceleration of 5.0m/sec^2, the decrease of shear modulus occurs very quickly at all depth. It takes only 0.4 seconds after the initiation of shaking (1 second) to make the shear modulus decrease less than about 3000kPa.

Results of the test with dense backfill (BD78F3A500 test)

The result from BD78F3A500 test is illustrated in Fig.4.74. In order to show the behavior of shear modulus of an extremely dense backfill, BD78F3A500 test is chosen to illustrate instead of AD67F3A500 test. The soil did not liquefy due to high density of backfill in this test, and the dilative behavior of soil was observed. In this respect, it is observed that the soil has still some shear modulus thorough the depth all the time. It is clearly seen that the shear modulus of soil mass during shaking becomes larger as the depth is larger.

These results suggest that the decrease of shear modulus due to shaking occurs at the same time through the depth. The complete loss of shear modulus due to liquefaction also seems to be induced at once. It is recognized experimentally that the shear modulus during shaking has a dependence on the confining stress.

The change of shear modulus with time at all depth from AD39F5A50 test, AD41F3A200 test, AD61F3A200 test, AD67F3A500 test and BD36F3A500 test are shown in Fig.4.117～Fig.4.121 at the end of this chapter.

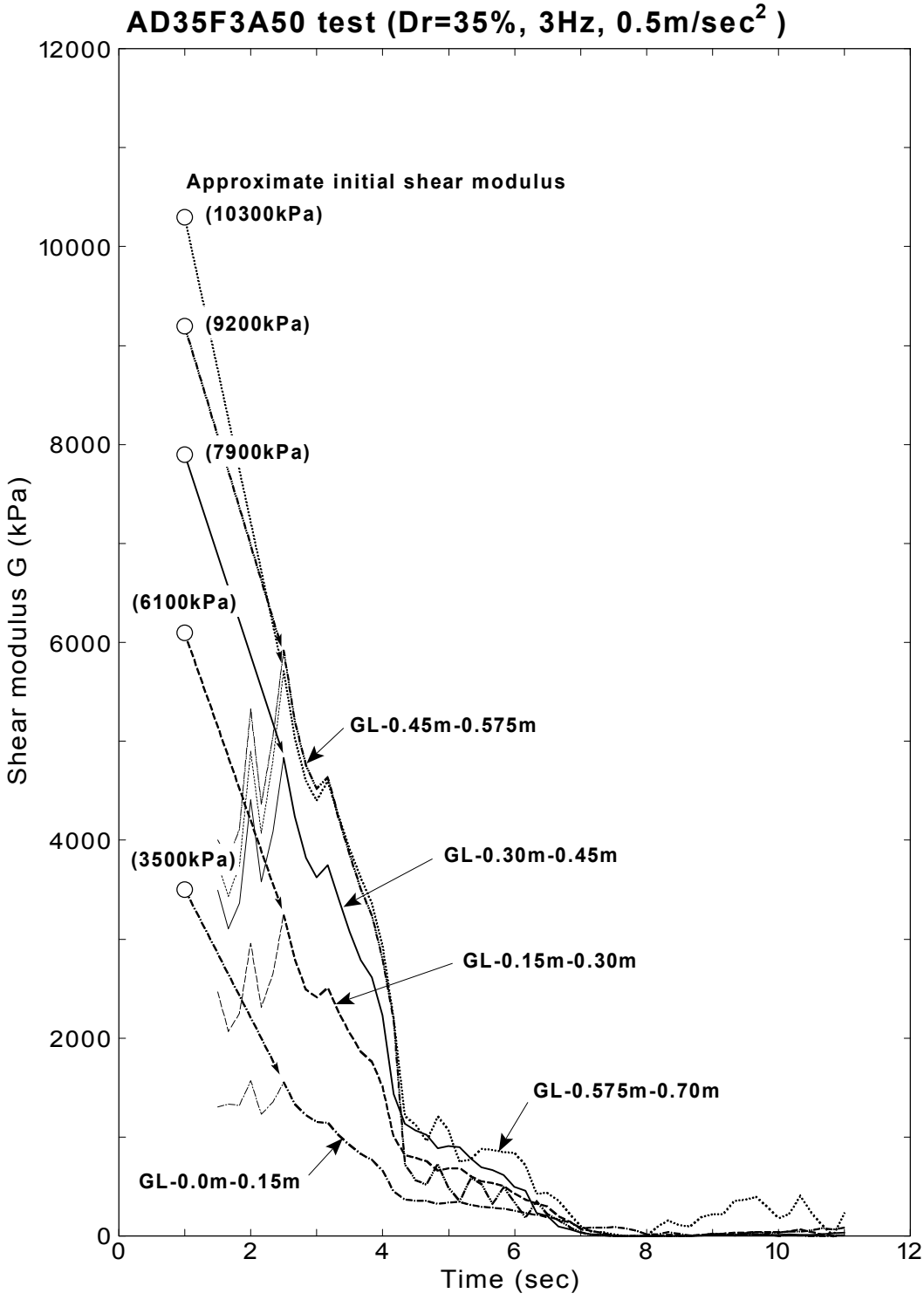

Fig.4.72: Change of shear modulus with time at each depth (AD35F3A50 test)

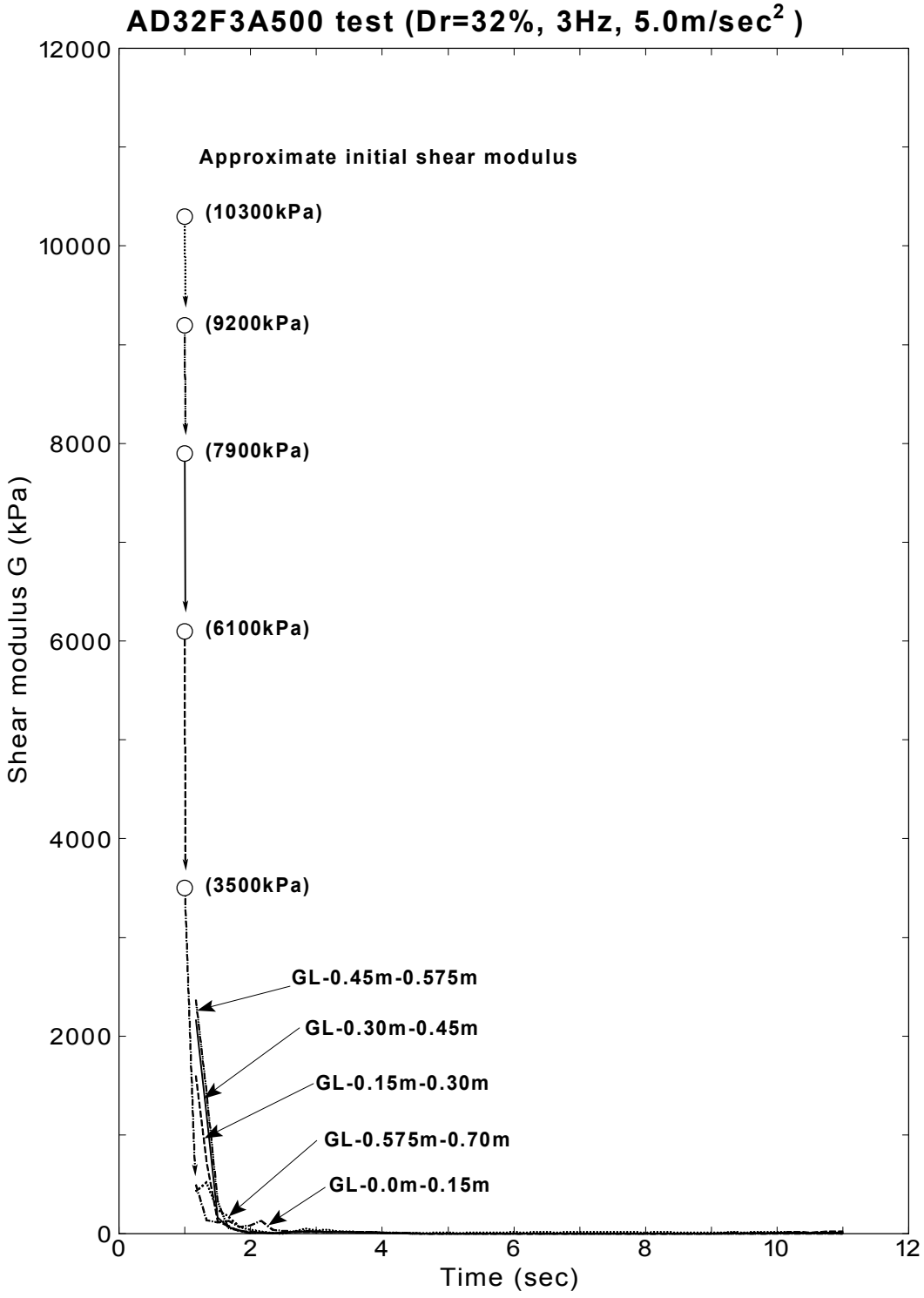

Fig.4.73: Change of shear modulus with time at each depth (intense input motion, AD32F3A500 test)

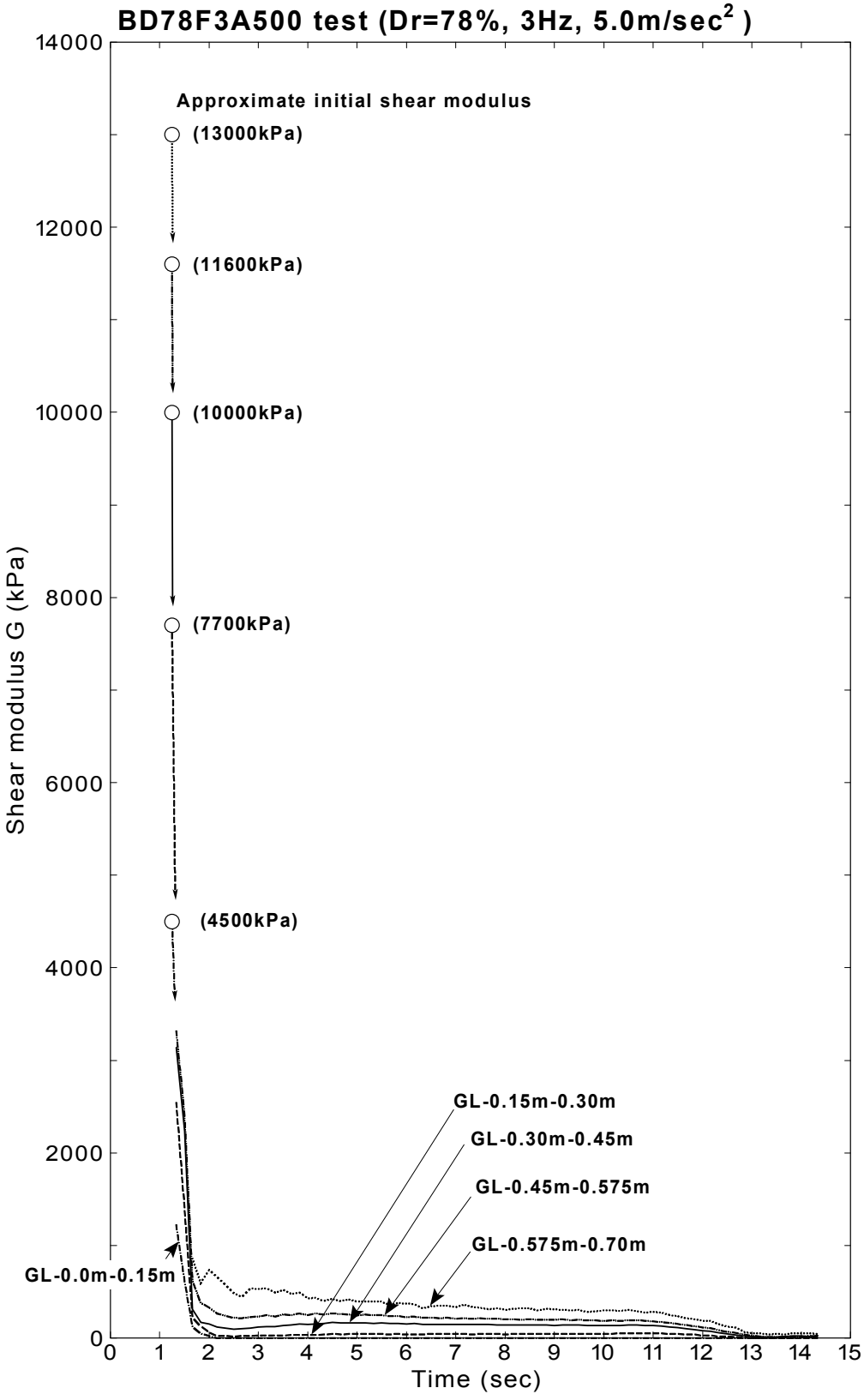

Fig.4.74: Change of shear modulus with time at each depth (dense backfill, BD78F3A500 test)

4.5.4 Natural frequency of backfill

The nature of the seismic response of the embedded structure is investigated in terms of the natural frequency of the backfill. The natural frequency, ν , of a soil column adjacent to the embedded structure can be calculated as

$$\nu = \frac{\sqrt{G/\rho}}{4H} \tag{4.57}$$

where G is the shear modulus of backfill, ρ is the mass density, and H is the depth of the ground adjacent to the embedded structure (=0.7m). The shear modulus of backfill G at each cycle was calculated by Eq.(4.47) refereeing stress-strain relationship at the depth of 0.3m～0.45m.

Typical result (AD35F3A50 test)

Natural frequencies of a soil column adjacent to the structure at each cycle, and the ratio of excess pore water pressure at GL-0.375m (PP2) from AD35F3A50 test are plotted with respect to time in Fig.4.75. The initial natural frequency of 19.5Hz, which was derived by the weak excitation test of soil deposit at 34% relative density, is plotted at the beginning of the shaking of 1.0 second. It was seen that the natural frequency finally decreased to zero crossing the input frequency of 3Hz at about 6.5 seconds with the increasing ratio of excess pore water pressure. It is considered that the amplification of structure could occur around this time.

Results of test with intense input motion (AD41F3A200 and AD32F3A500 test)

The results from AD41F3A200 test are illustrated in Fig.4.123. It was observed that the reduction of the natural frequency occurred more rapid than the AD35F3A50 test by the intense shaking. The curve crossed the input frequency of 3Hz at about 2.2 seconds. Natural frequency of nearly zero was maintained after 4 seconds.

Fig.4.76 shows the results from AD32F3A500 test. It was seen that the natural frequencies became lower than the input frequency at about 1.5 seconds.

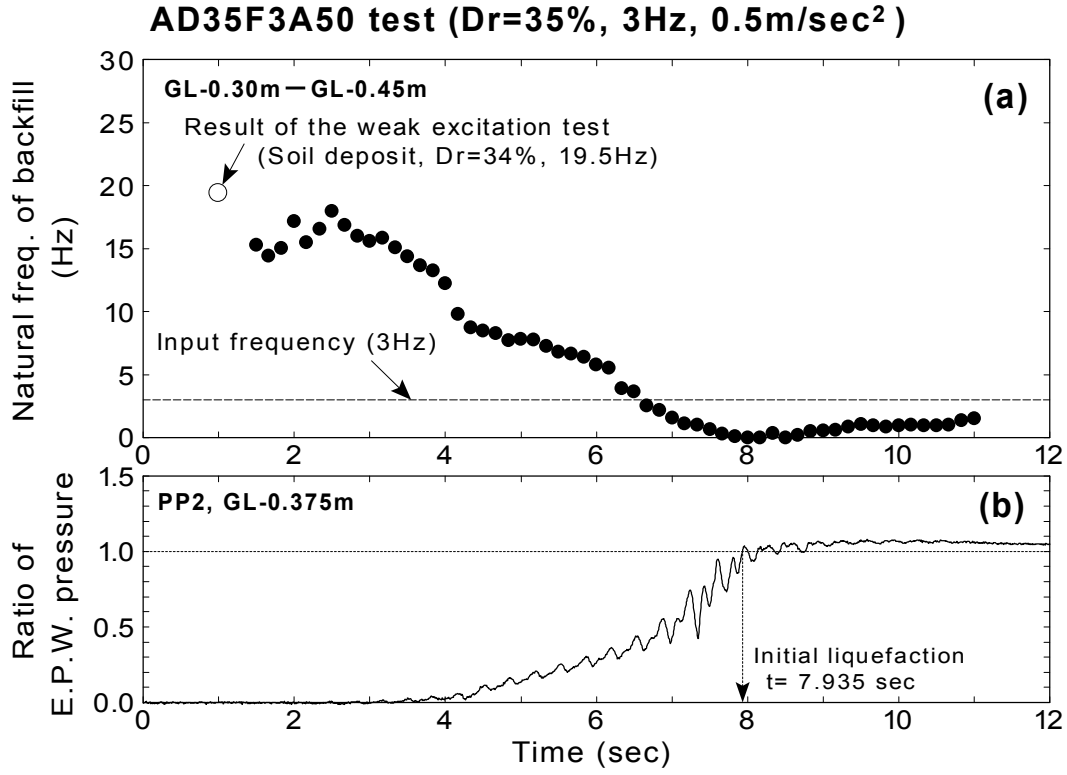

Fig.4.75: Change of natural frequency of backfill (AD35F3A50 test)

Results of test with dense backfill (AD67F3A500 test)

Fig.4.77 shows the results from AD67F3A500 test. It was seen that the natural frequencies became lower than the input frequency at about 1.5 seconds. The natural frequency, which once decreased to zero, was increased after 3 seconds up to about the level of 3Hz. The ratio of the excess pore water pressure oscillated significantly at that time, showing the dilative behavior of soil. No such a phenomenon was observed in previously presented test of AD32F3A500 test in which loose sand was used.

The results from AD39F5A50 test, AD61F3A200 test, BD36F3A500 test and BD78F3A500 test are presented in Fig.4.122～Fig.4.126 at the end of this chapter.

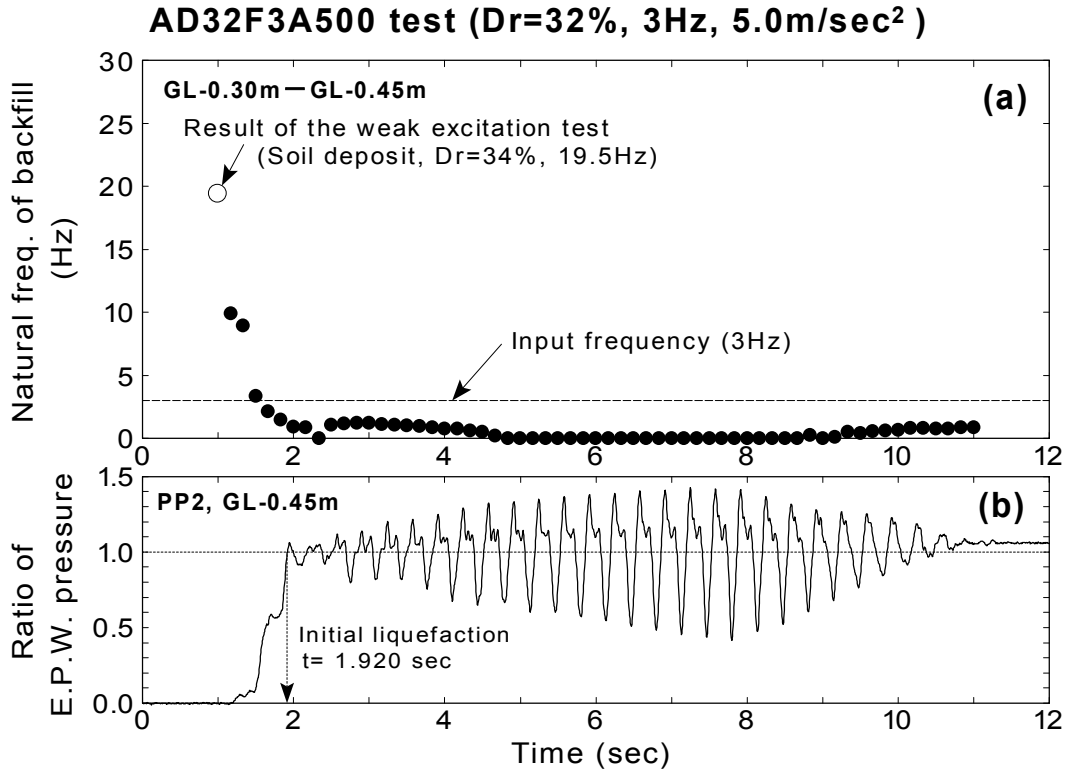

Fig.4.76: Change of natural frequency of backfill (AD32F3A500 test)

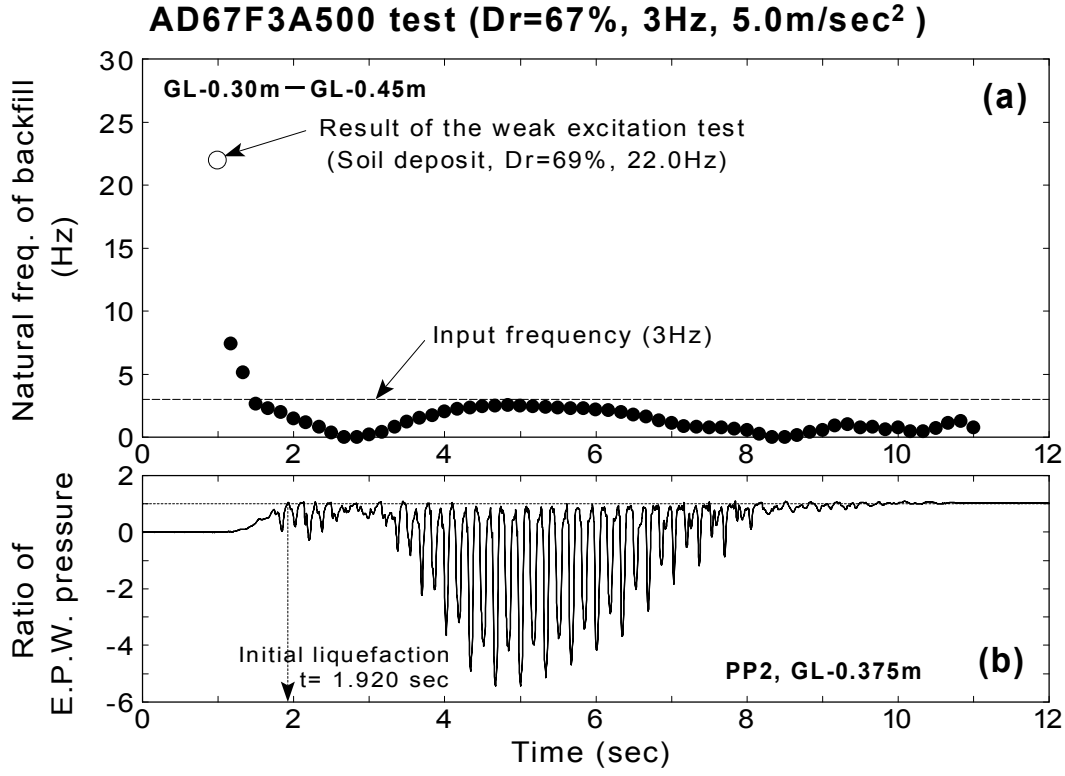

Fig.4.77: Change of natural frequency of backfill (AD67F3A500 test)

Natural frequencies of a soil column at each cycle from all tests are plotted with respect to the ratio of pore water pressure at GL-0.375m (PP2) in Fig.4.78. The plots of data at each test are shown in Fig.4.127(a)～(h) at the end of this chapter. It was seen that the initial natural frequency of approximately 19.5Hz or 22Hz finally decreased to almost zero crossing the input frequency of 5Hz and 3Hz with the increasing ratio of excess pore water pressures. No significant differences are recognized among soil densities. Further discussion about the amplifications and the phase differences of structure during the reduction of natural frequency of backfill will be made in the chapter 5.

The results from AD41F3A200 test are illustrated in Fig.4.123. It was observed that the reduction of the natural frequency occurred more rapid than the AD35F3A50 test by the intense shaking. The curve crossed the input frequency of 3Hz at about 2.2 seconds. Natural frequency of nearly zero was maintained after 4 seconds.

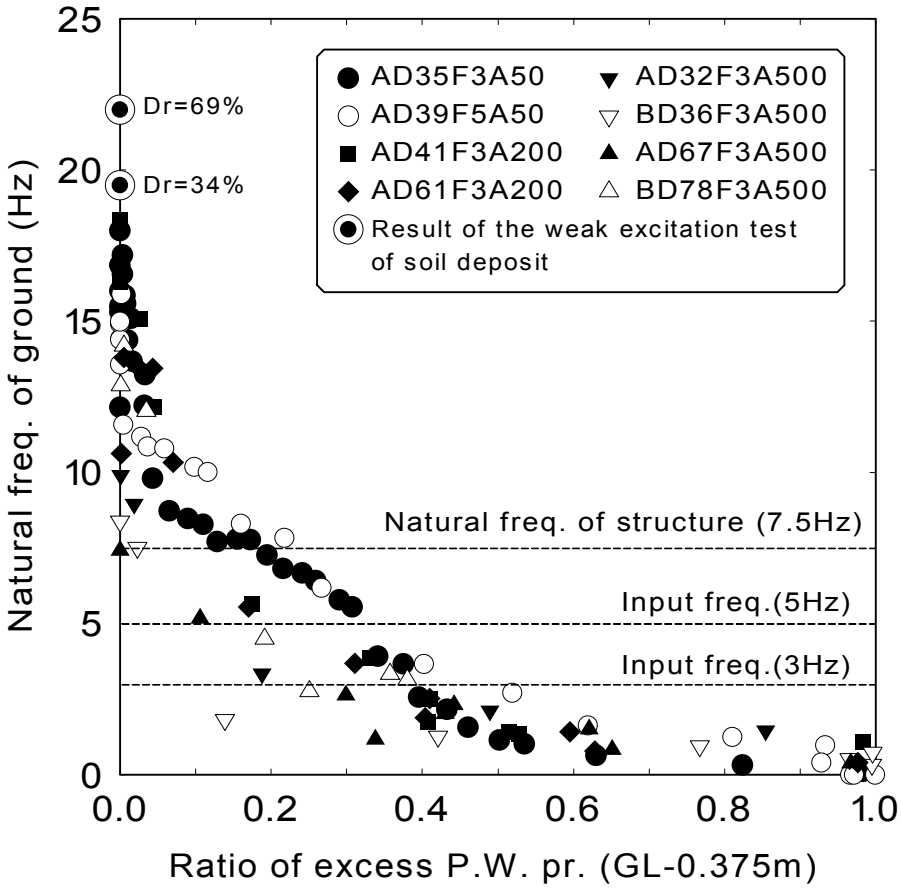

Fig.4.78: Change of natural frequency of backfill with respect to pore pressure ratio

4.6 CONCLUDING REMARKS

The shear stress, shear strain and effective vertical stress during shaking were calculated from the dynamic measurements in order to reproduce the stress-strain relationship and the effective stress path. Not only the inertia force of a soil mass but also the normal stress difference in the horizontal direction were taken into account for the calculation of shear stresses.

It was found that the stress-strain relationship and the effective stress path during shaking were reasonably reproduced. The shape of the curve in a cycle became similar to an ellipse with an inclined axis before the build-up of the excess pore water pressure and the direction of rotation was clockwise. The shape of the stress-strain relationship in the loose backfill changed to be flat accompanied by the rise of the excess pore water pressure. In contrast, the amplitude of the shear stress in the dense backfill increased as the shaking was continued due to the dilative behavior of soil.

The shear modulus and damping ratio at each cycle of shaking was calculated from the reproduced stress-strain relationship. It was found that the average shear modulus during liquefaction in the loose backfill at the relative density of 30～40% reduced to the level of 1/500～1/2800 of the initial shear modulus. And in the dense backfill more than relative density of about 70%, the reduction of shear modulus was more than the level of 1/90～1/300 due to the dilative behavior. It was observed that the decrease of shear modulus due to shaking occurs at the same time through the depth. It is recognized experimentally that the shear modulus during shaking has a dependence on the confining stress.

The damping ratio before liquefaction was calculated to be a extent of 0.1～0.4. On the other hand, it was difficult to evaluate damping ratio during complete liquefaction due to irregularity of shape of hysteresis loop. It was characteristic that the damping ratio was decrease slightly when pore pressure generates.

Study on the stress-strain relationship of the backfill during shaking suggested that the useful information of the property change for backfill near the structure, such as the shear modulus and the natural frequency of backfill, could be obtained experimentally.

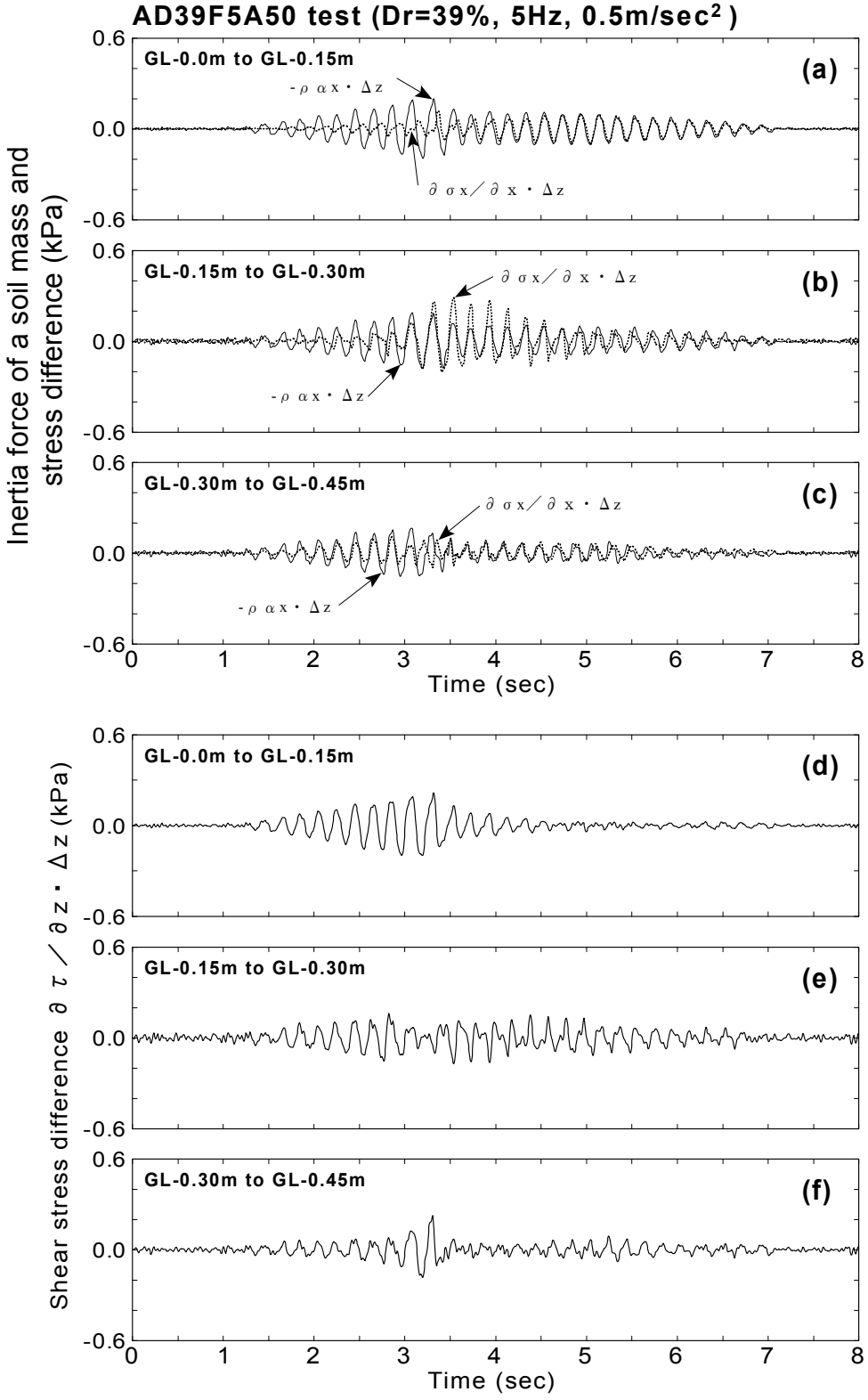

Fig.4.79: Inertia force, normal and shear stress difference (AD39F5A50 test)

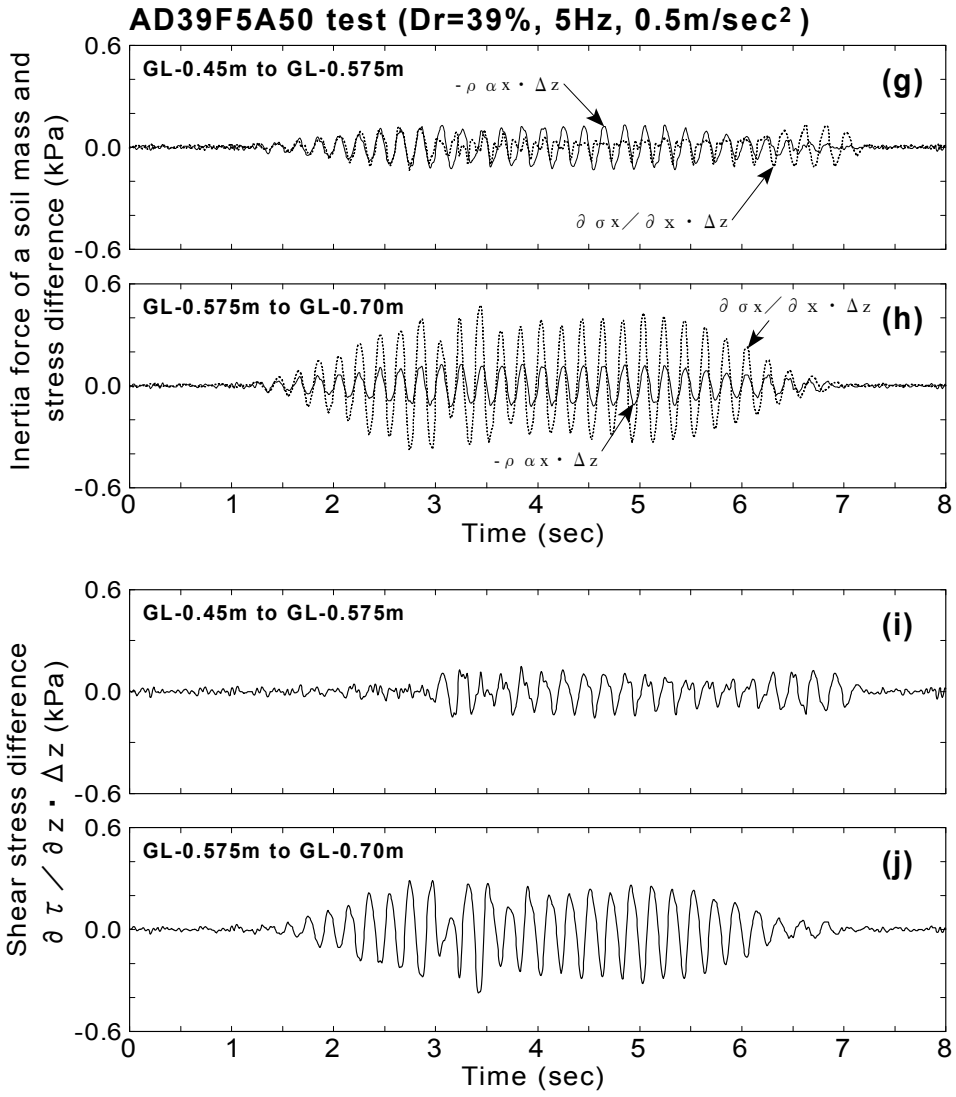

Fig.4.79: Continued

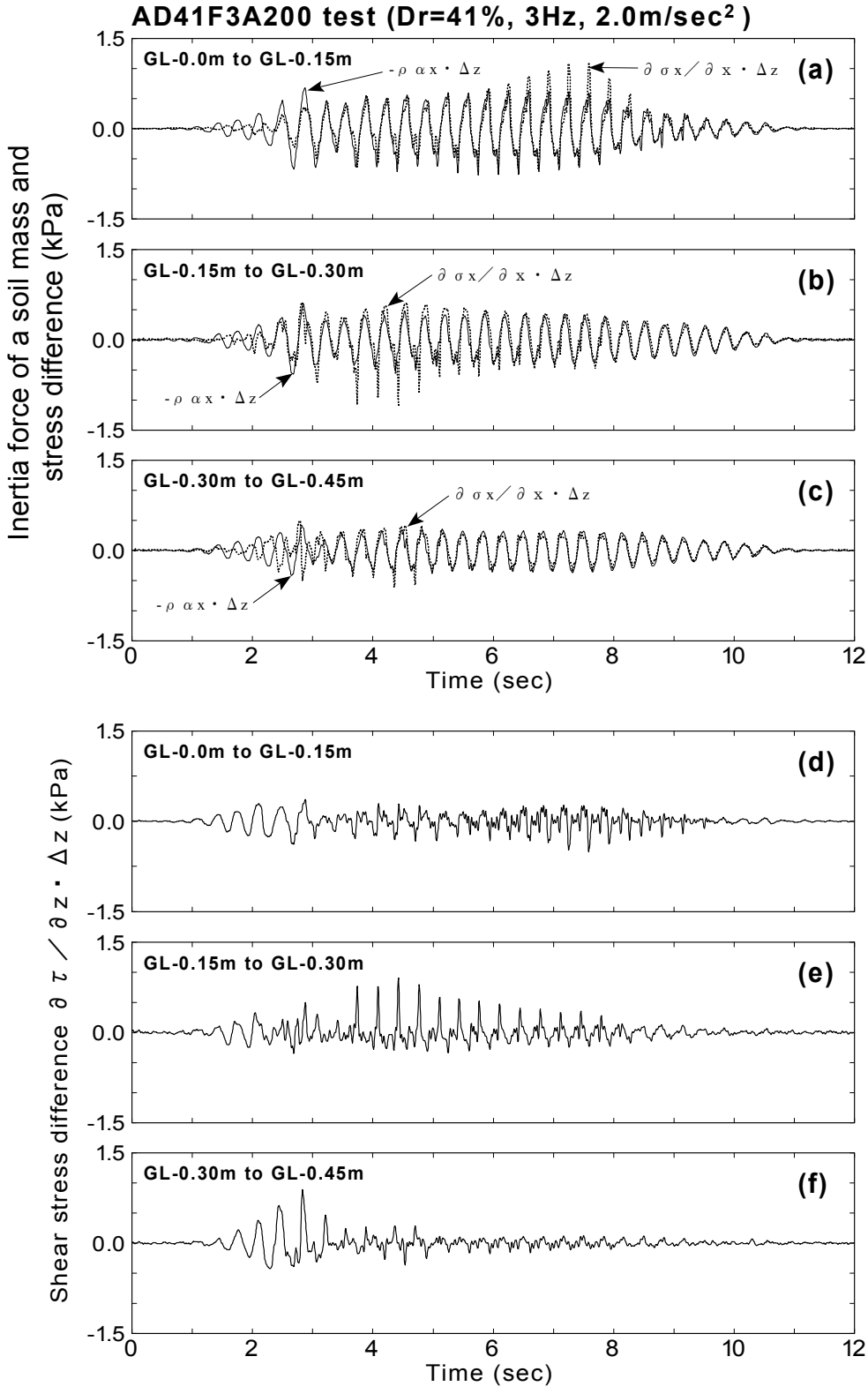

Fig.4.80: Inertia force, normal and shear stress difference (AD41F3A200 test)

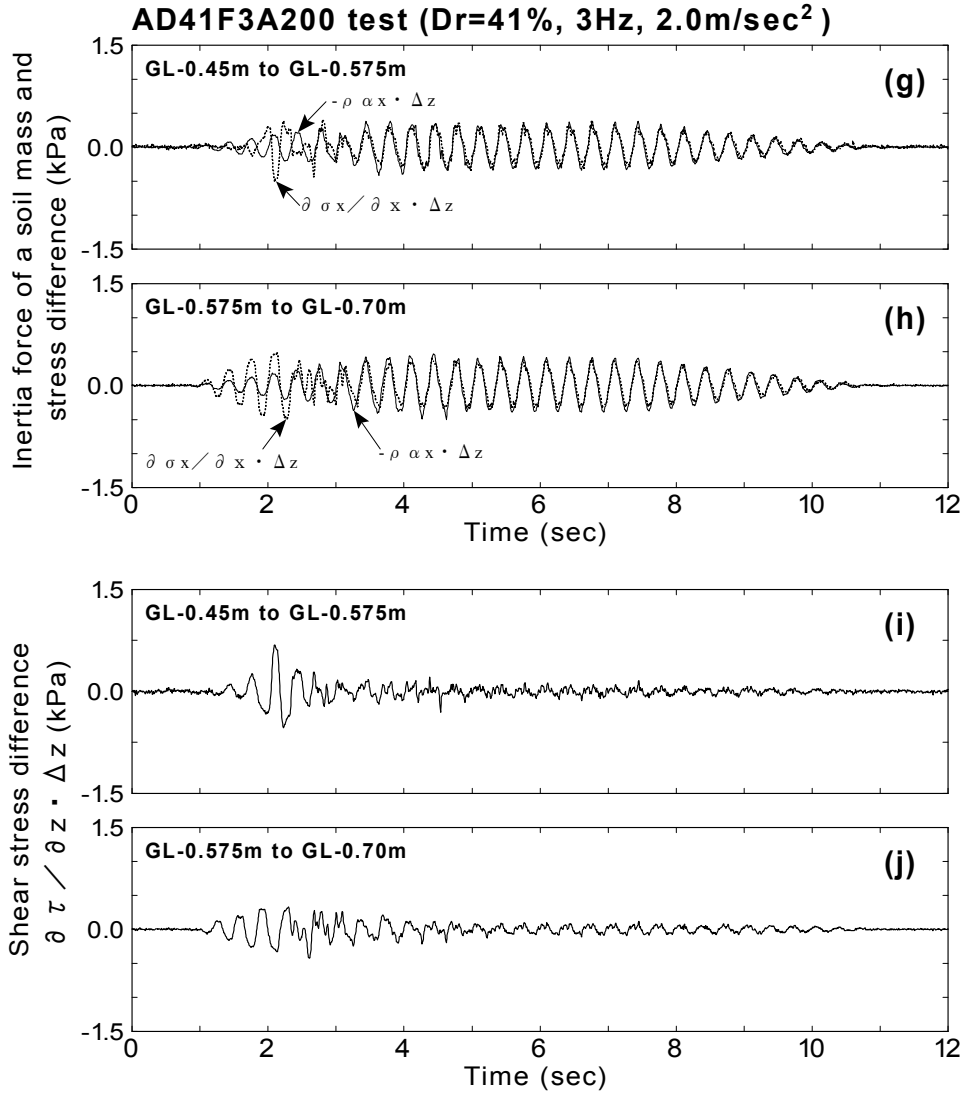

Fig.4.80: Continued

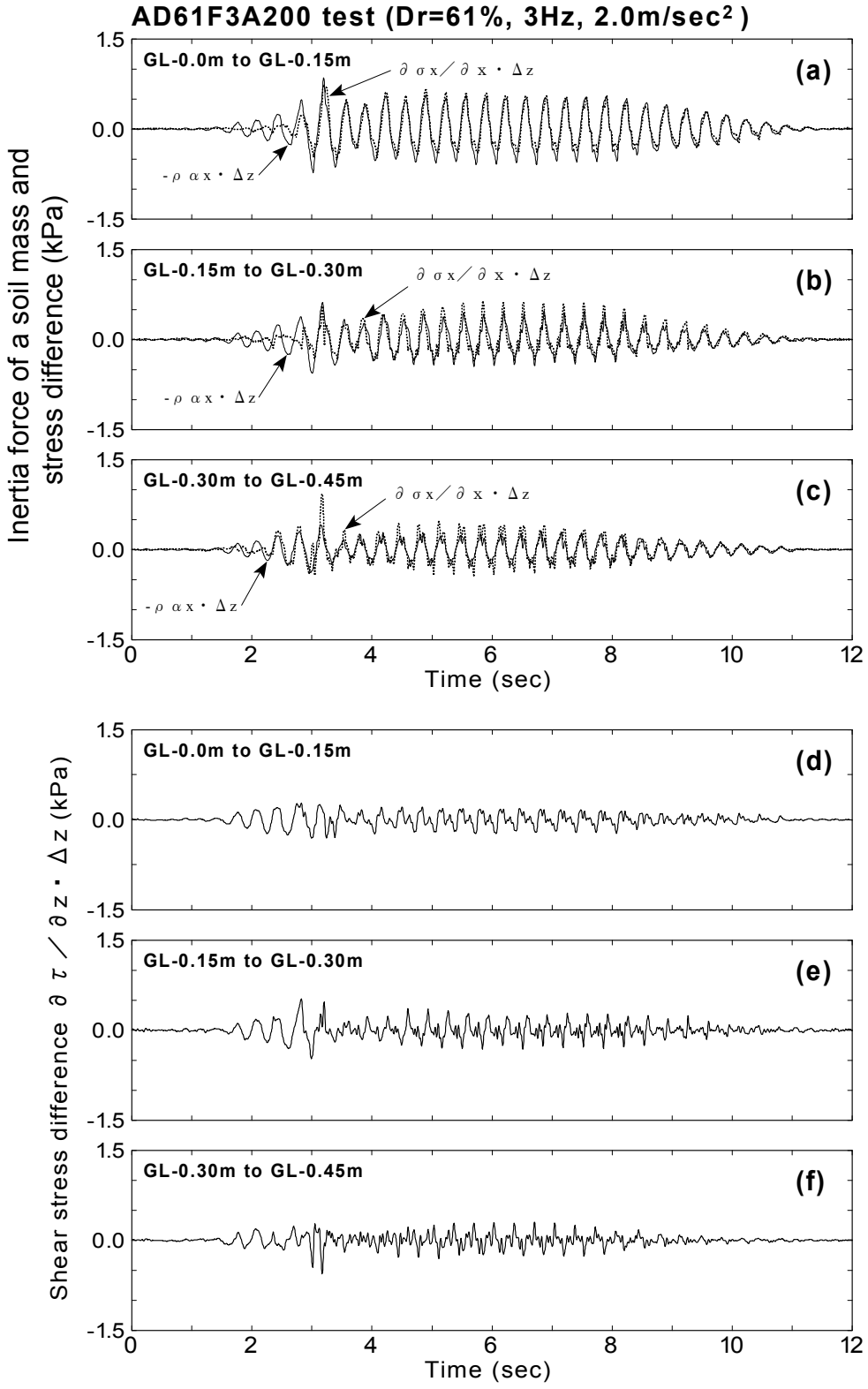

Fig.4.81: Inertia force, normal and shear stress difference (AD61F3A200 test)

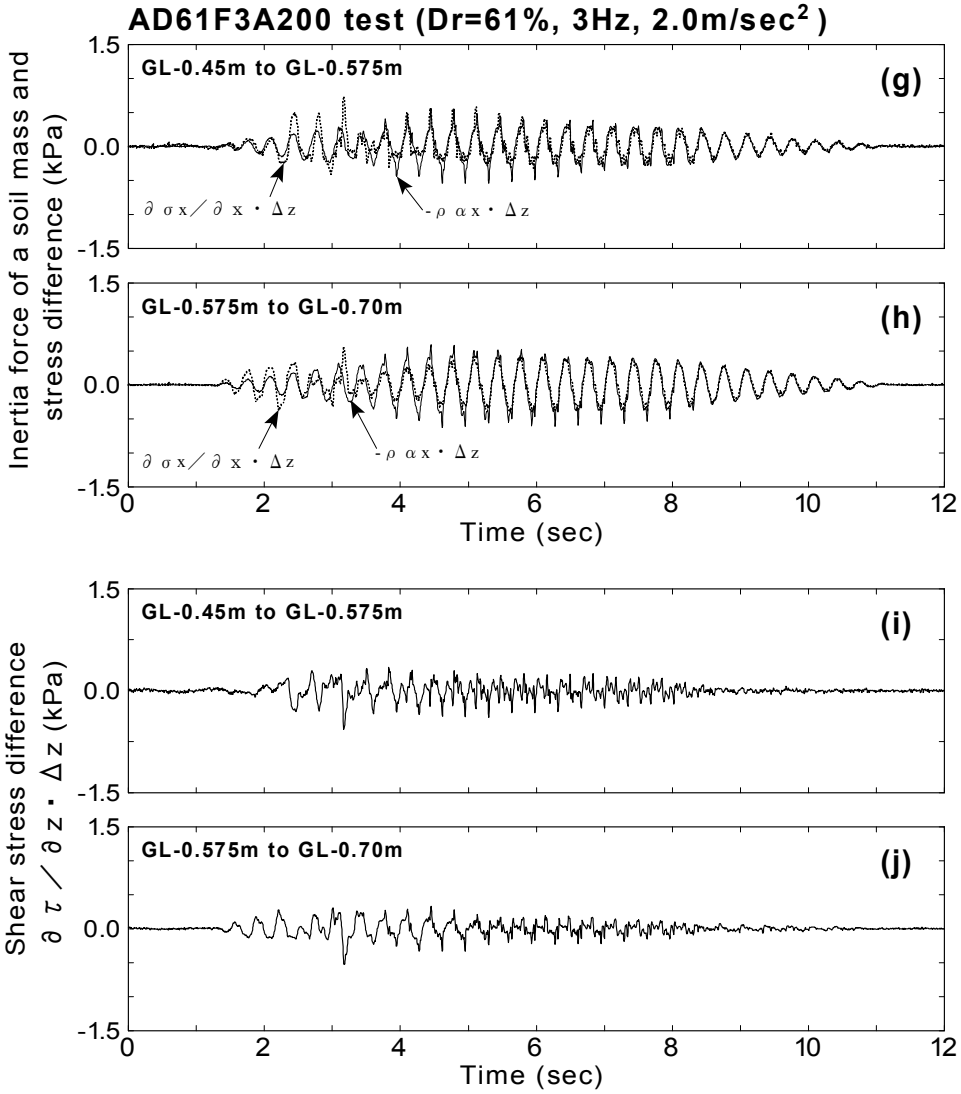

Fig.4.81: Continued

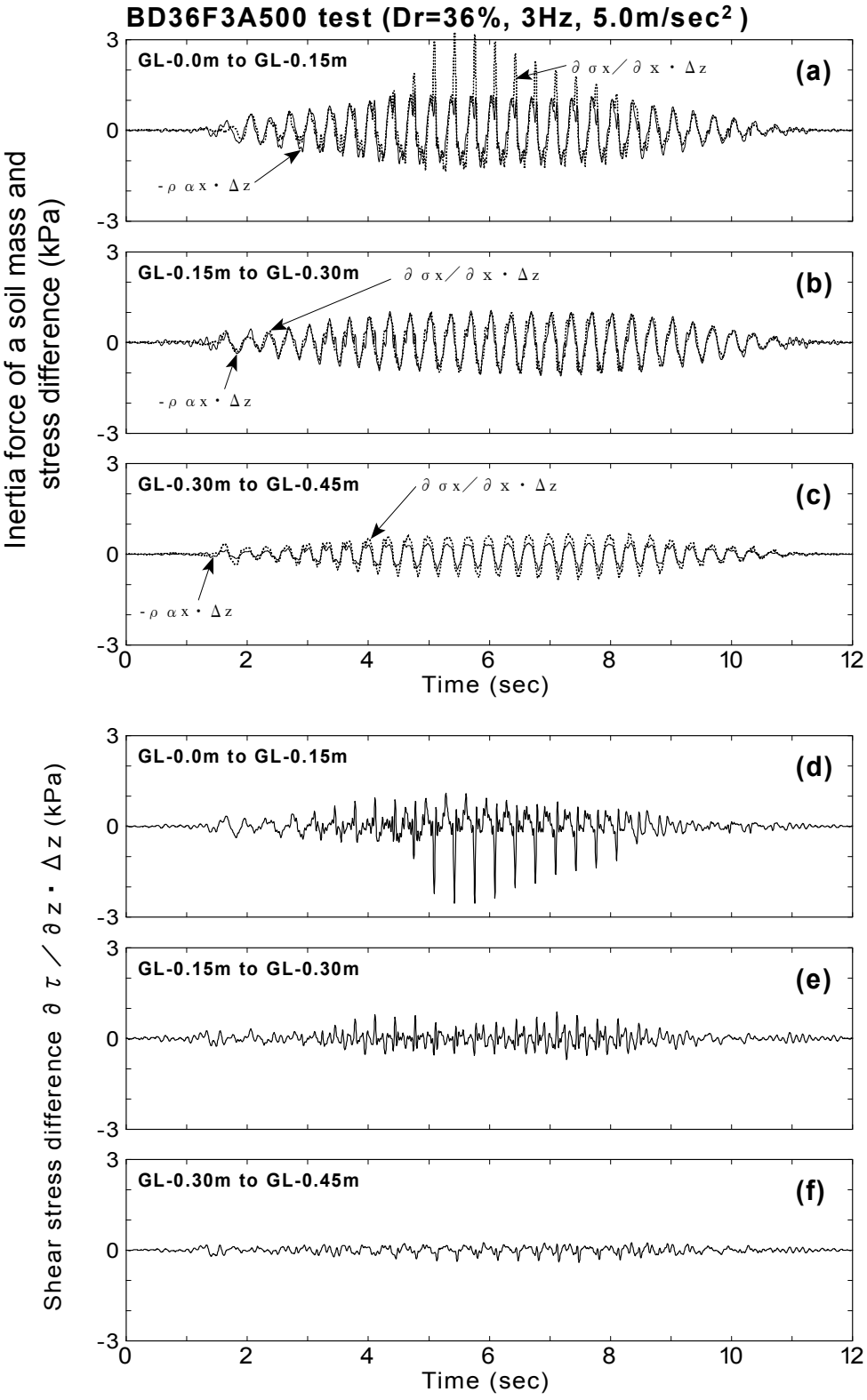

Fig.4.82: Inertia force, normal and shear stress difference (BD36F3A500 test)

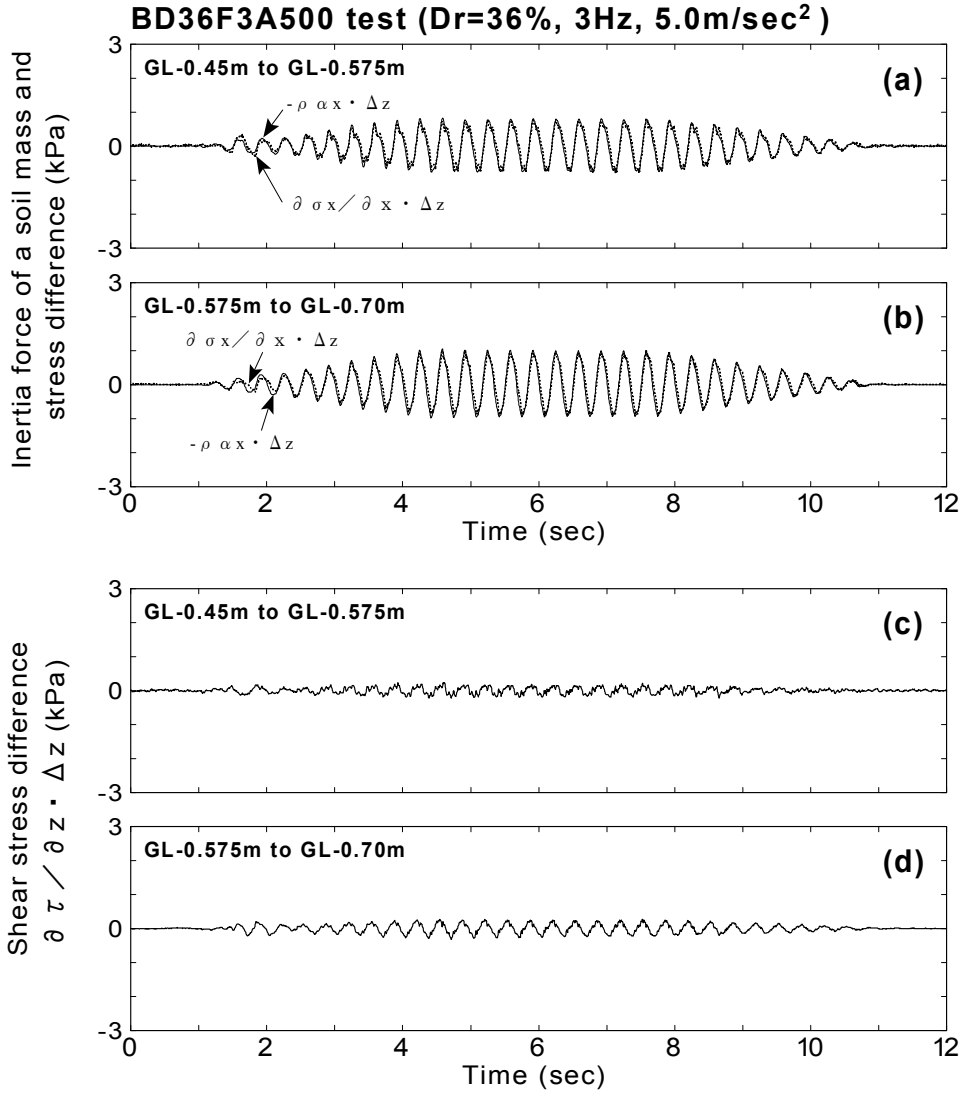

Fig.4.82: Continued

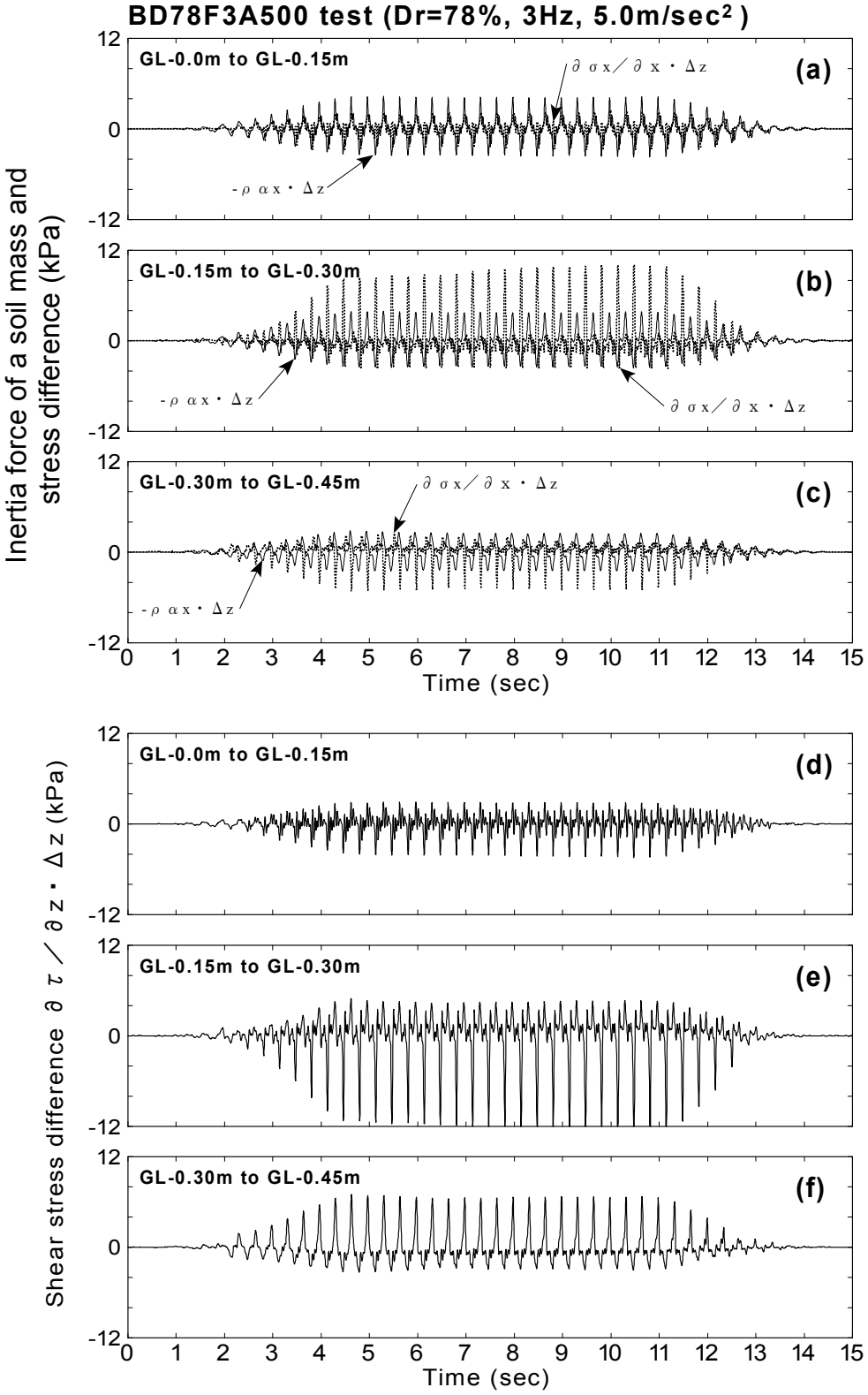

Fig.4.83: Inertia force, normal and shear stress difference (BD78F3A500 test)

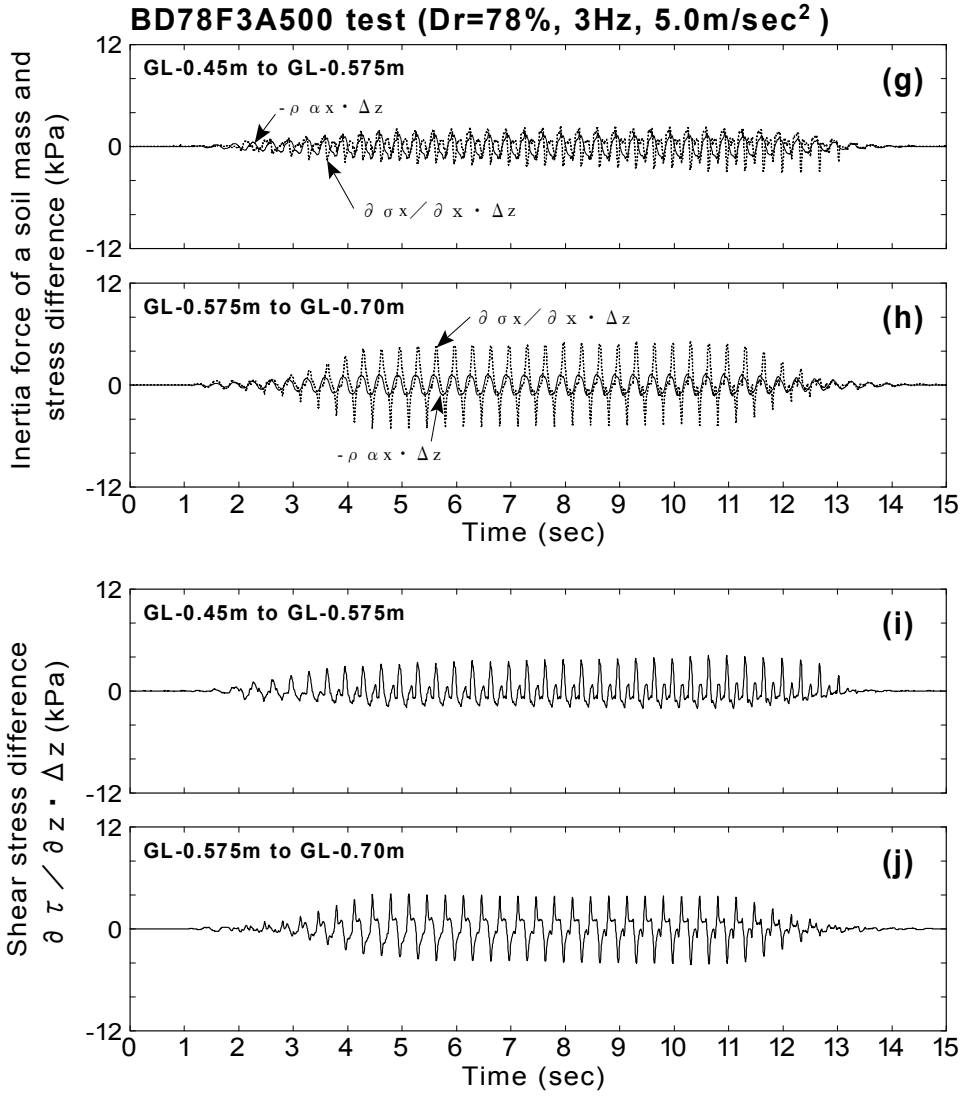

Fig.4.83: Continued

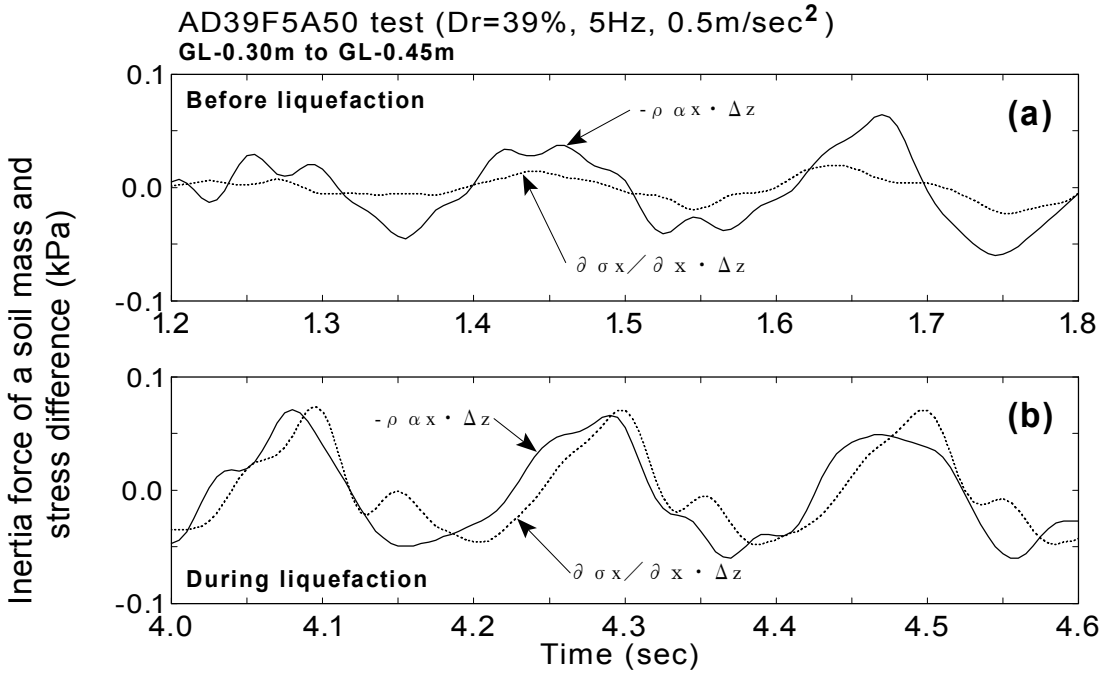

Fig.4.84: Inertia force and normal stress difference (AD39F5A50 test)

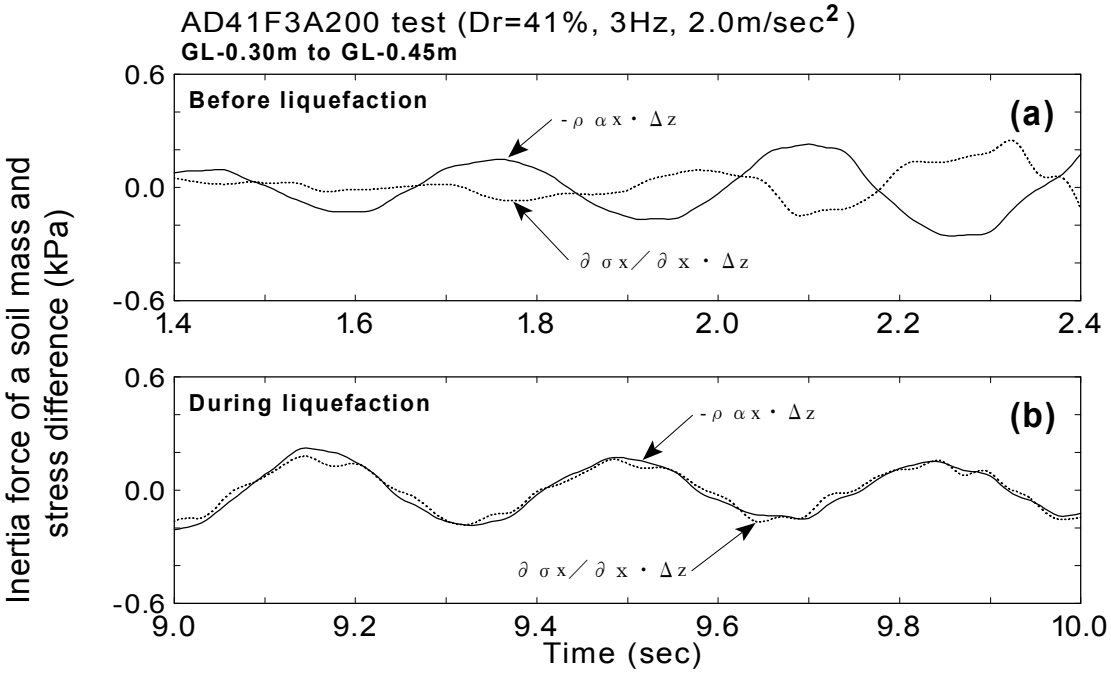

Fig.4.85: Inertia force and normal stress difference (AD41F3A200 test)

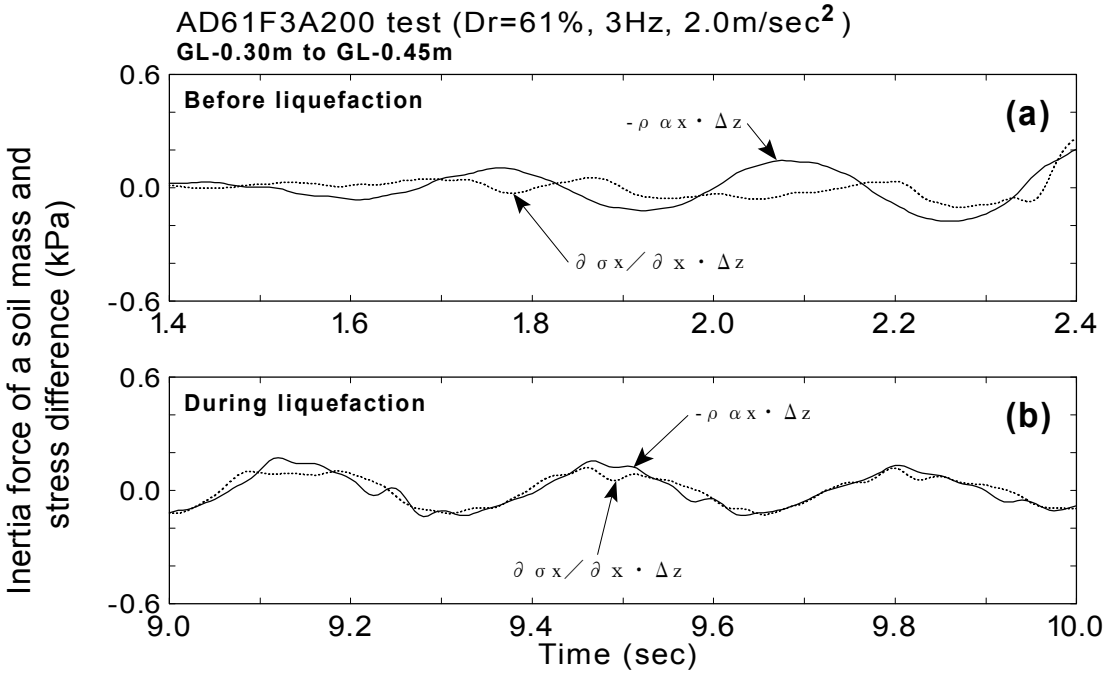

Fig.4.86: Inertia force and normal stress difference (AD61F3A200 test)

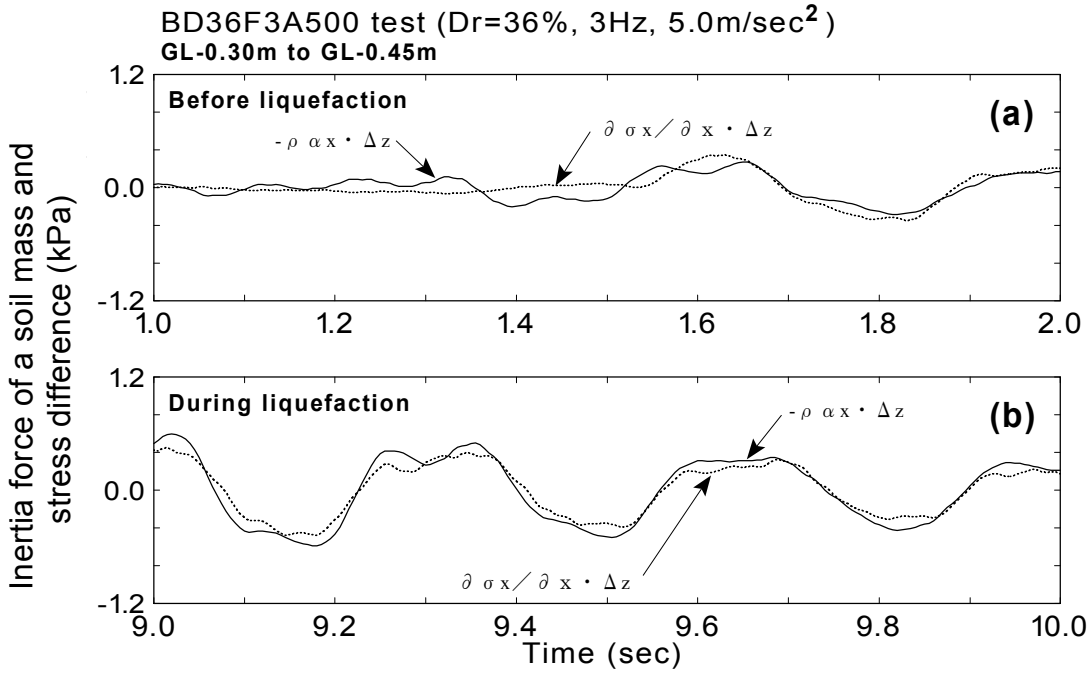

Fig.4.87: Inertia force and normal stress difference (BD36F3A500 test)

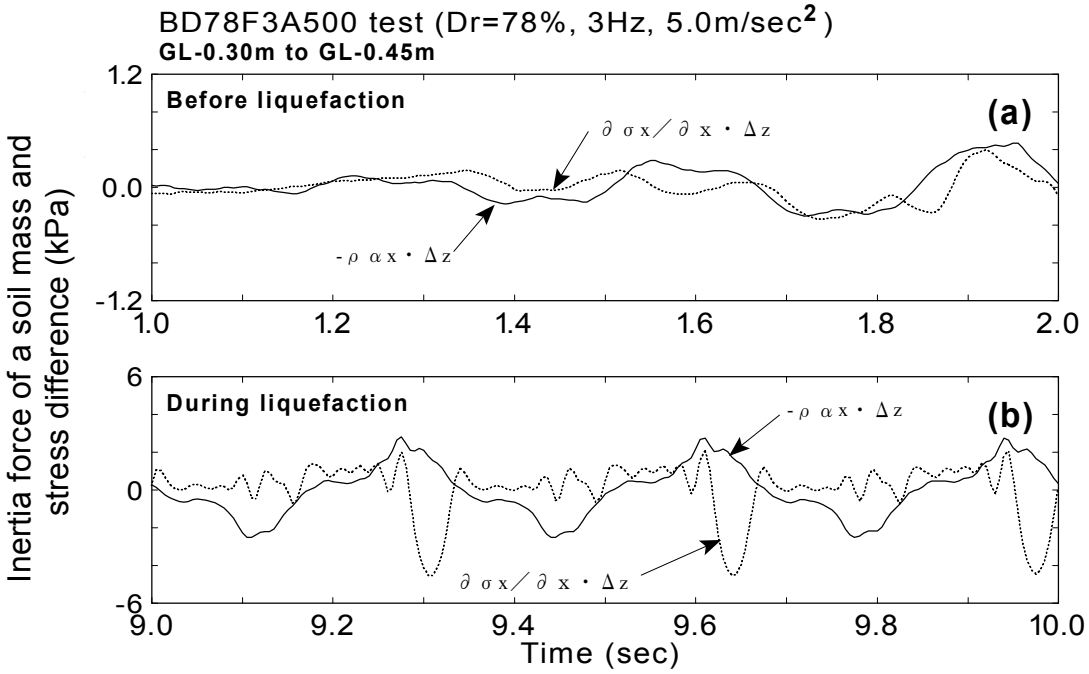

Fig.4.88: Inertia force and normal stress difference (BD78F3A500 test)

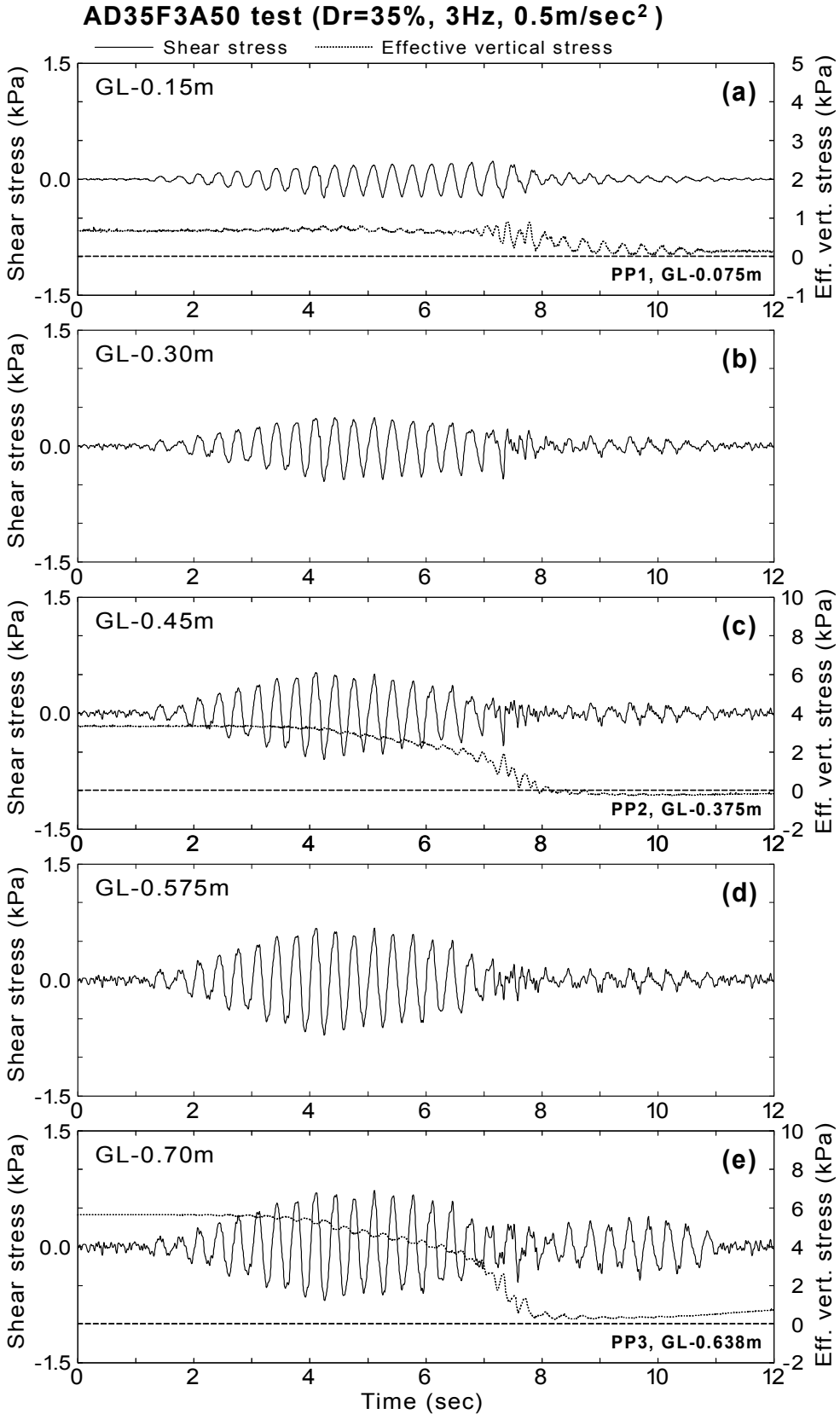

Fig.4.89: Shear stress and effective vertical stress (AD35F3A50 test)

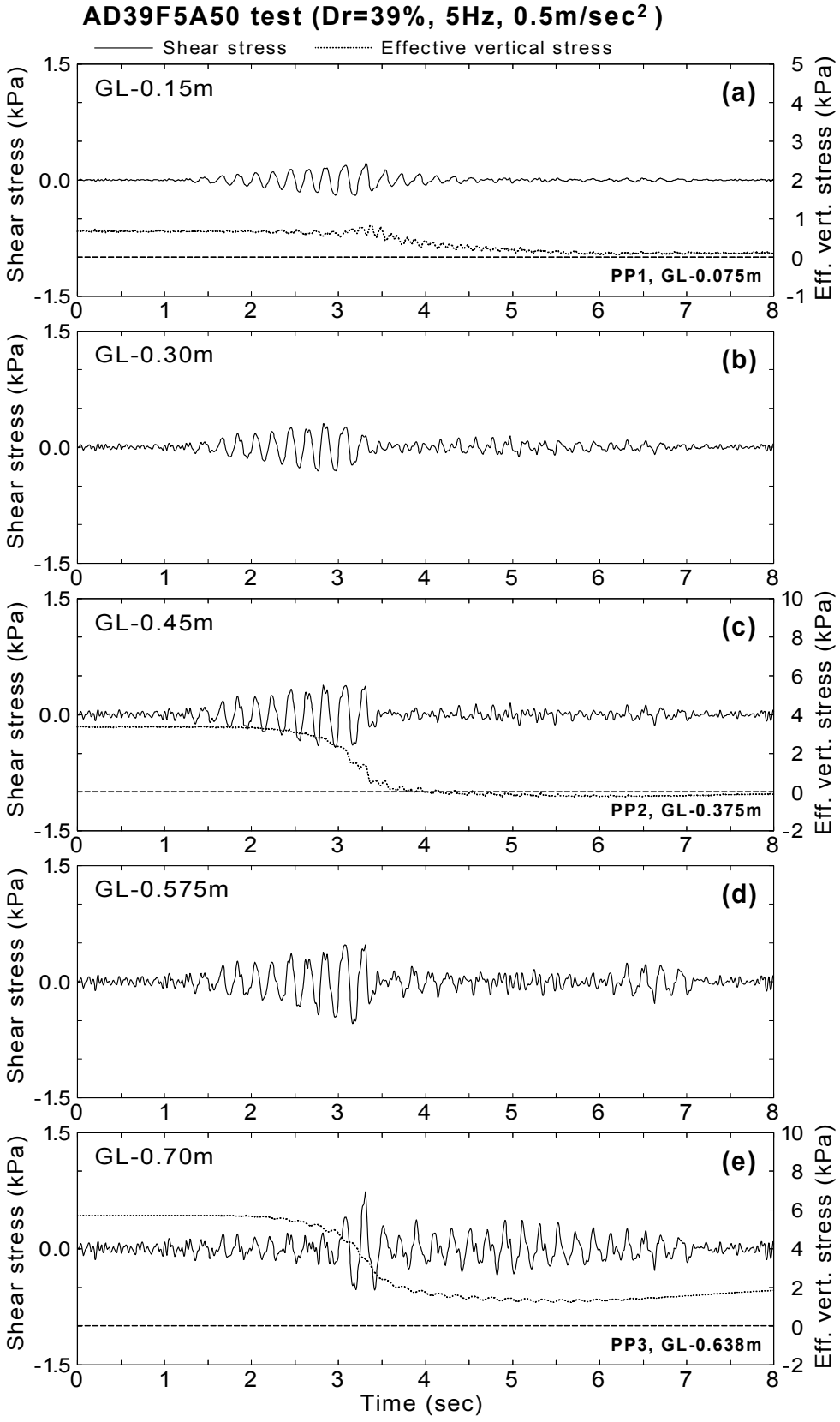

Fig.4.90: Shear stress and effective vertical stress (AD39F5A50 test)

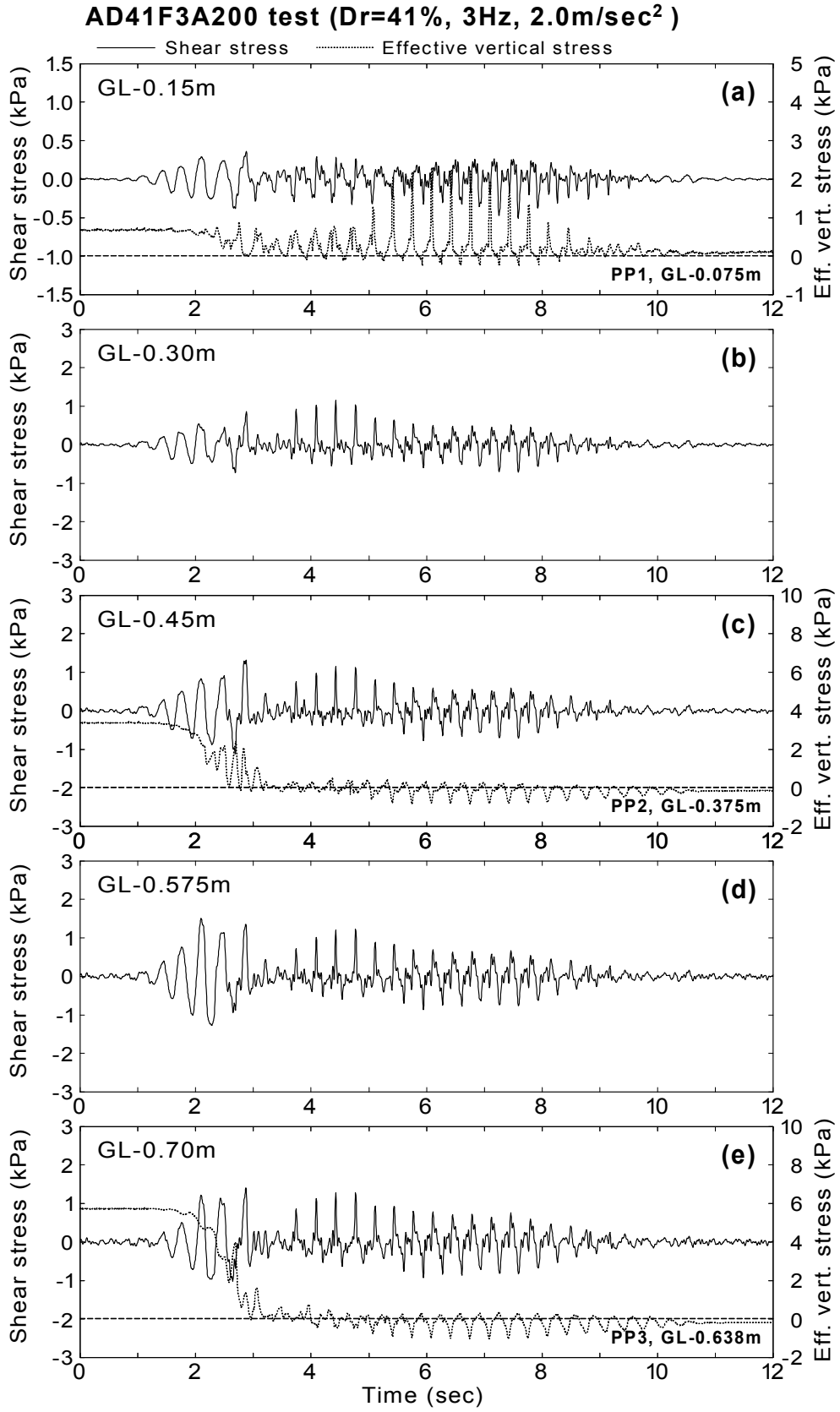

Fig.4.91: Shear stress and effective vertical stress (AD41F3A200 test)

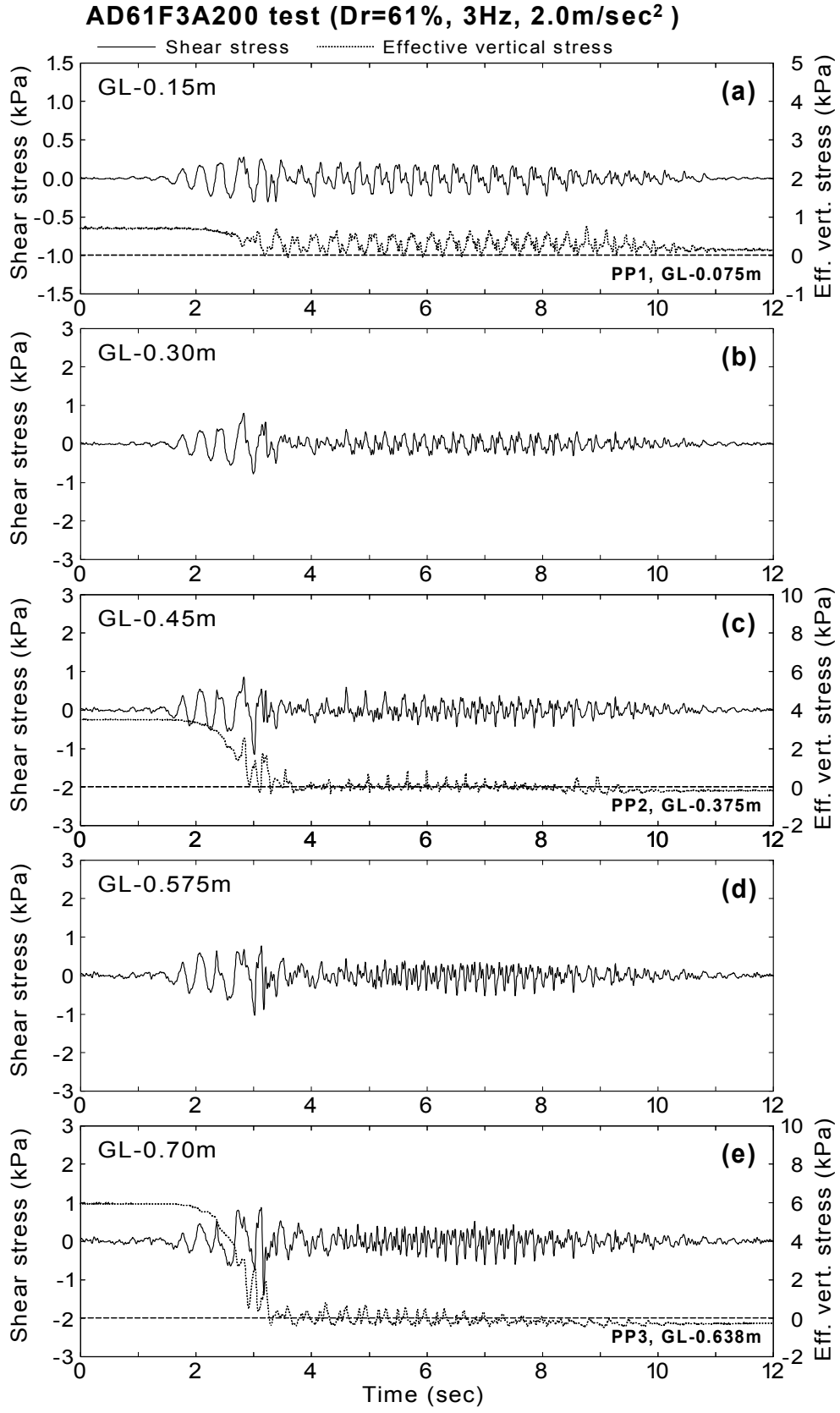

Fig.4.92: Shear stress and effective vertical stress (AD61F3A200 test)

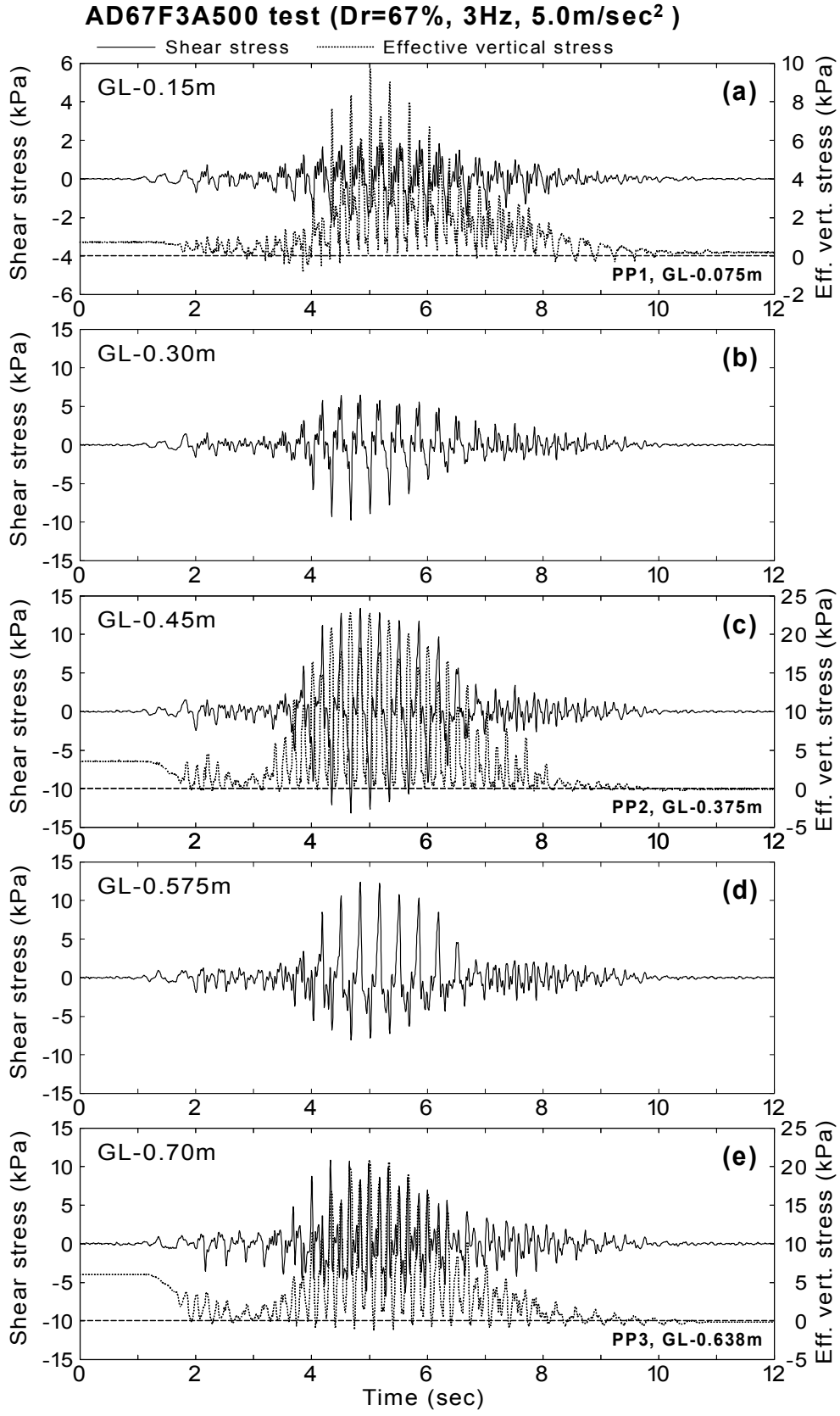

Fig.4.93: Shear stress and effective vertical stress (AD67F3A500 test)

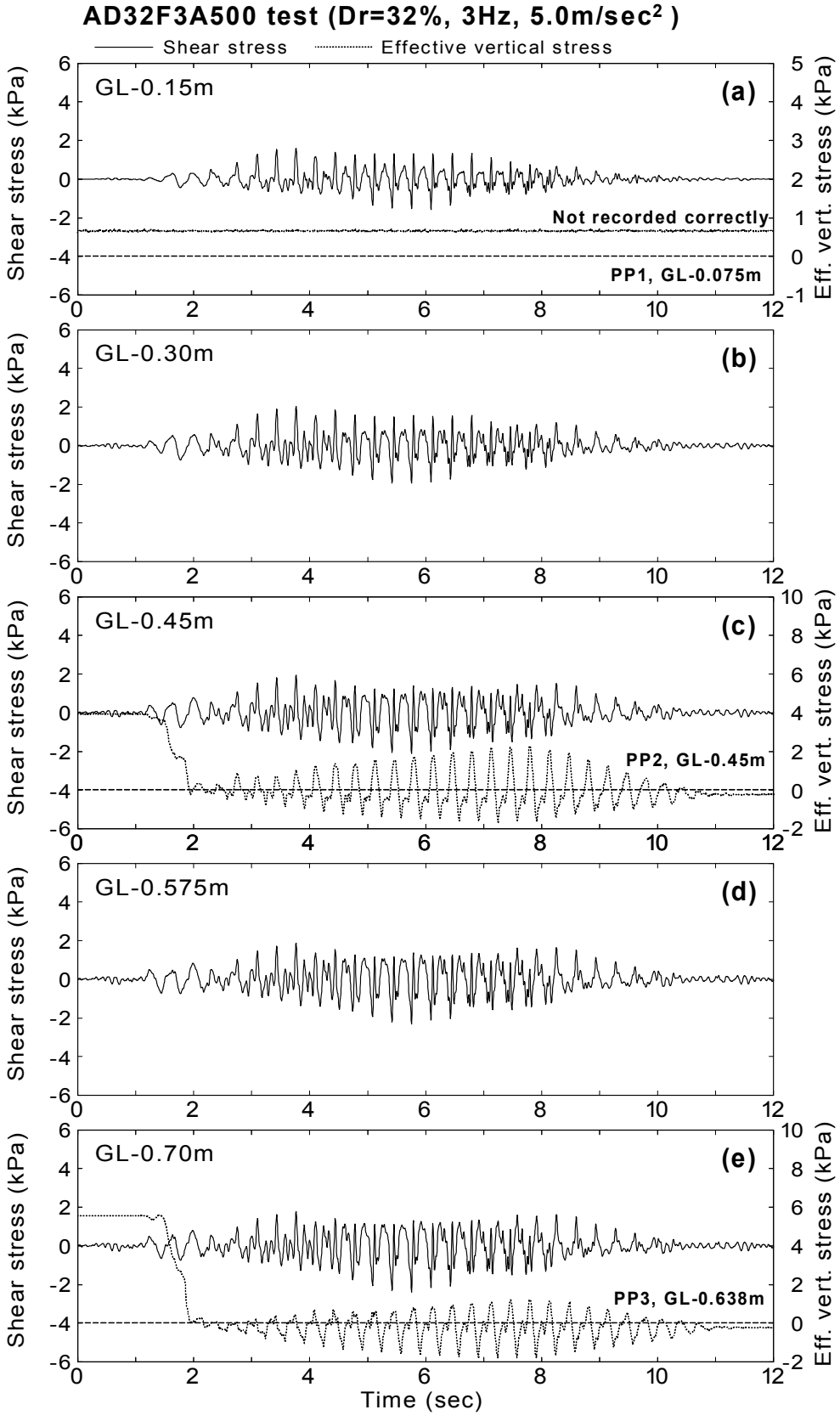

Fig.4.94: Shear stress and effective vertical stress (AD32F3A500 test)

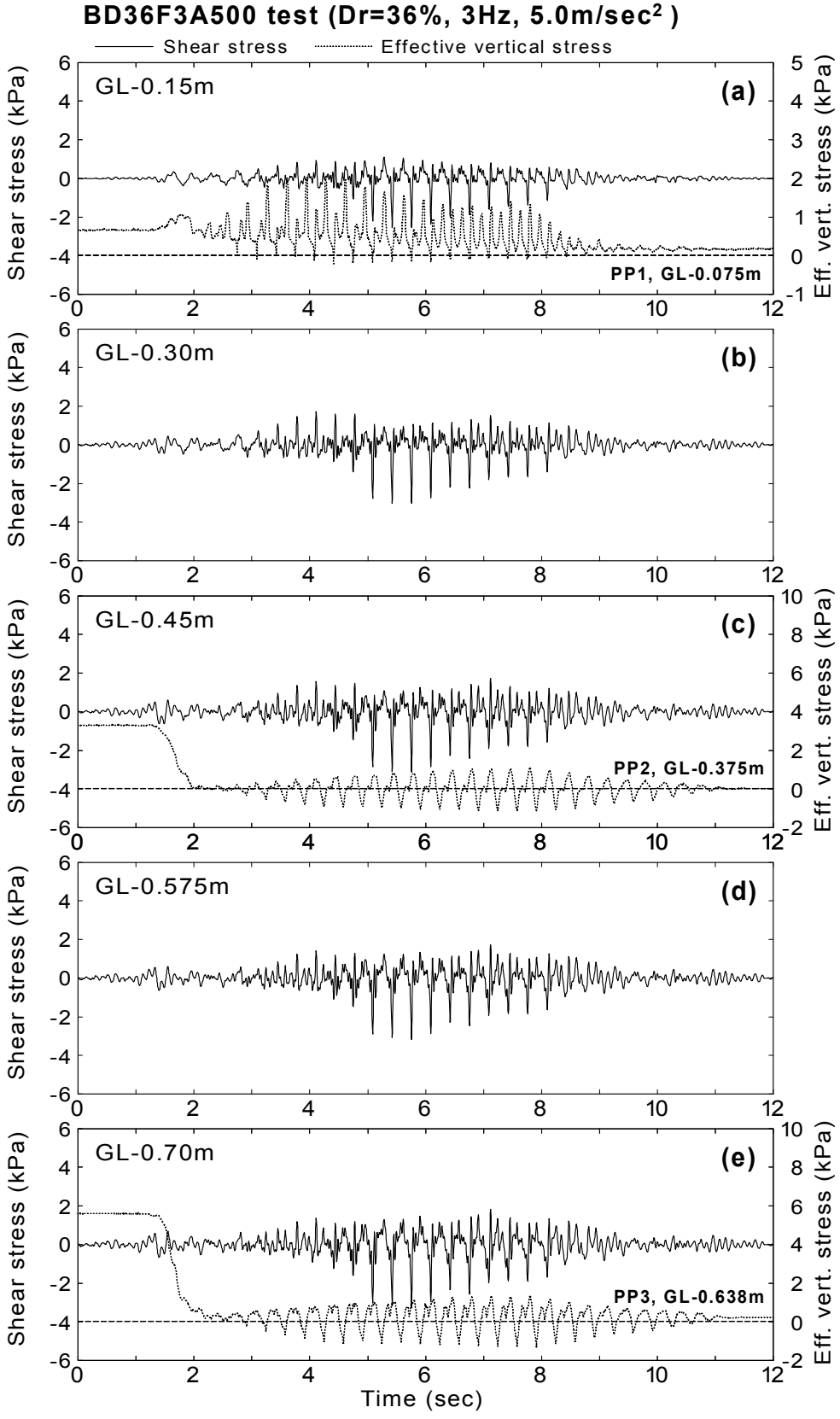

Fig.4.95: Shear stress and effective vertical stress (BD36F3A500 test)

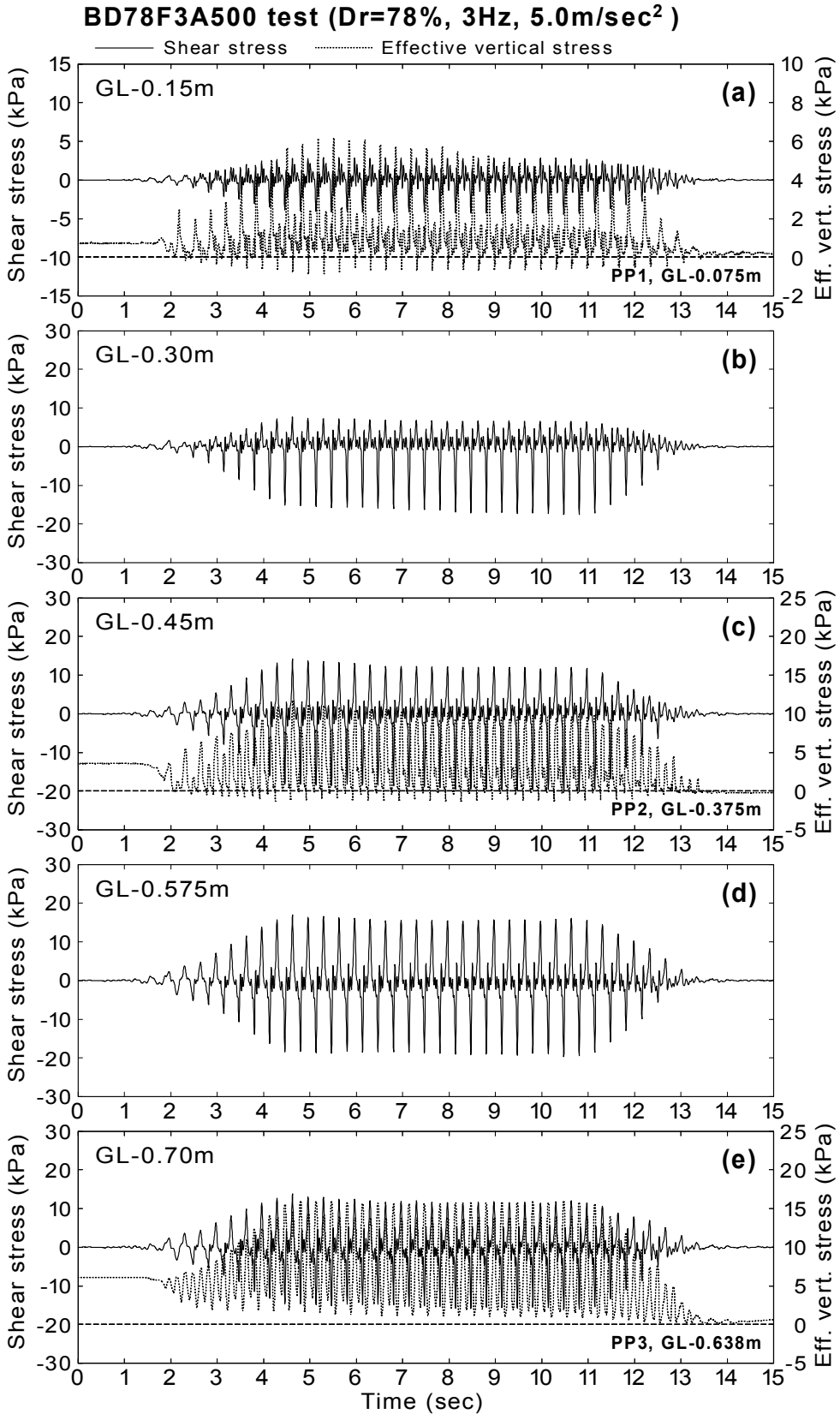

Fig.4.96: Shear stress and effective vertical stress (BD78F3A500 test)

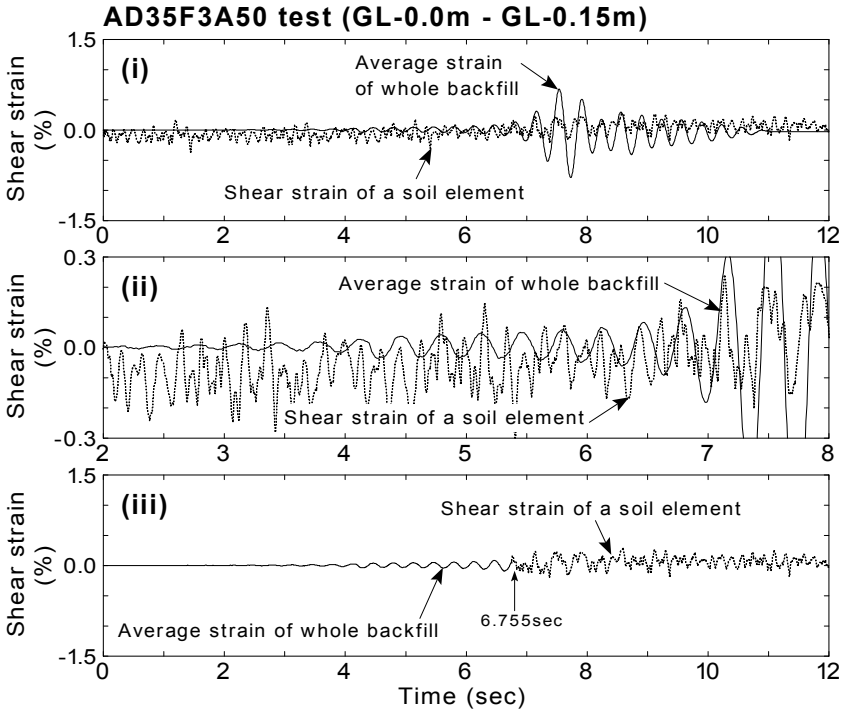

(a) GL-0.0m ～ GL-0.15m

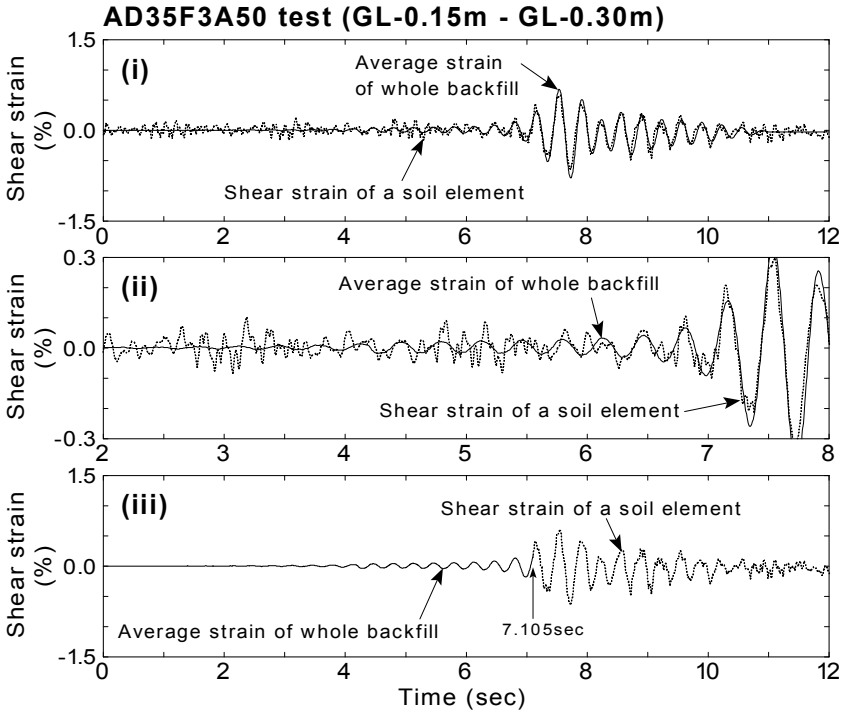

(b) GL-0.15m ～ GL-0.30m

Fig.4.97: Reproduced shear strain at each soil element (AD35F3A50 test)

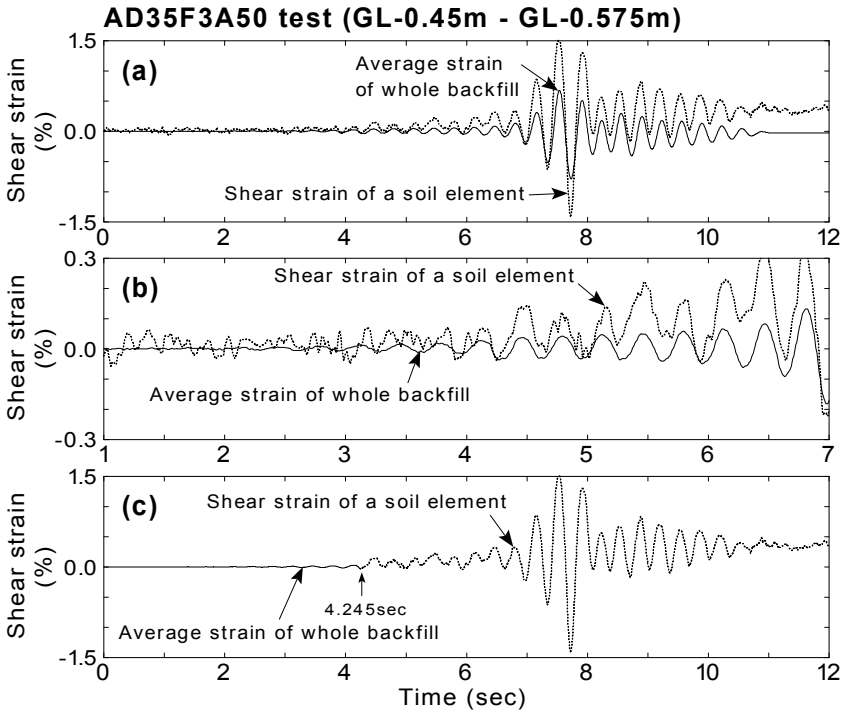

(c) GL-0.45m ～ GL-0.575m

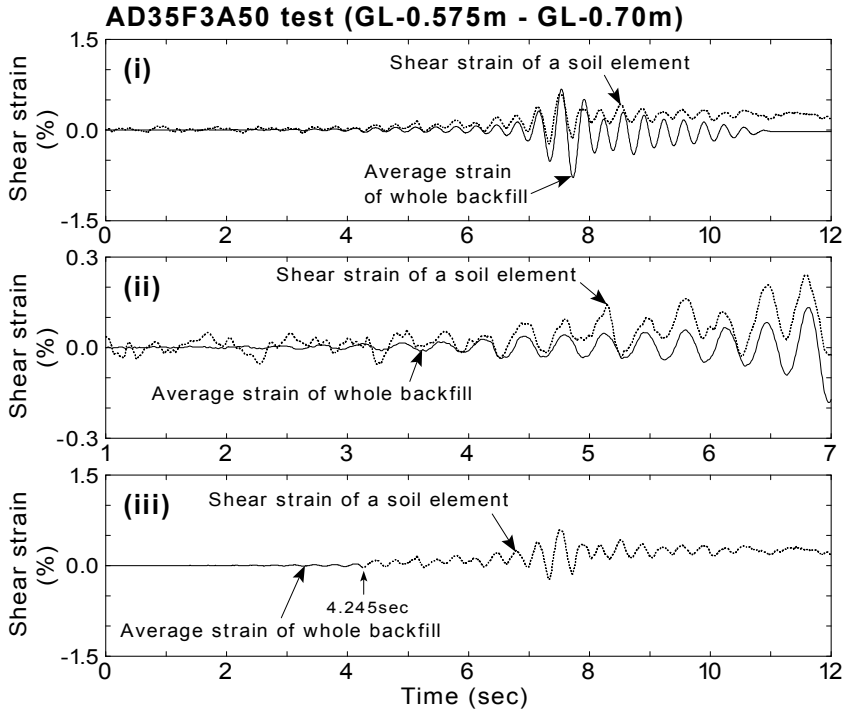

(d) GL-0.575m ～ GL-0.70m

Fig.4.97: Continued

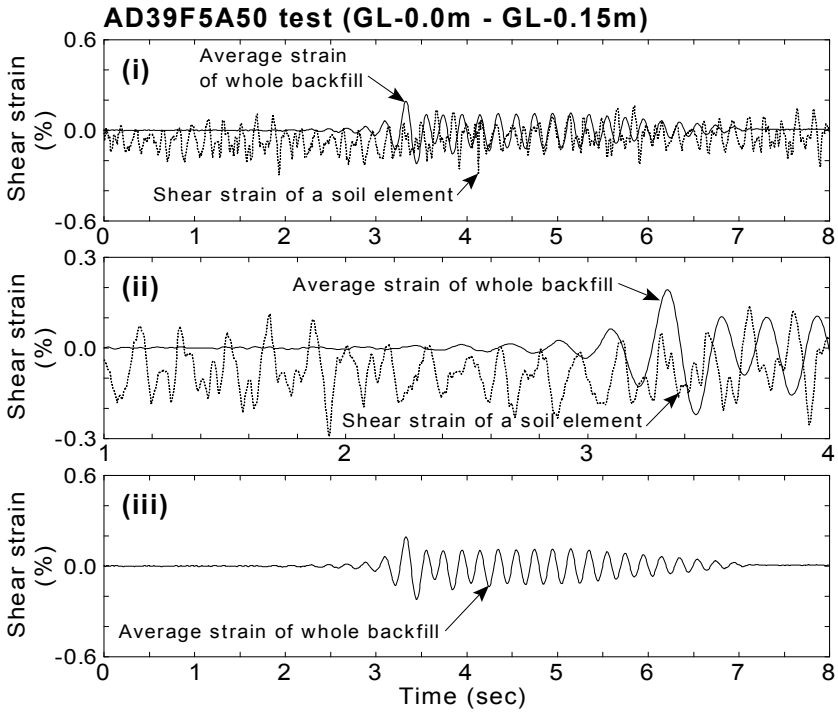

(a) GL-0.0m ～ GL-0.15m

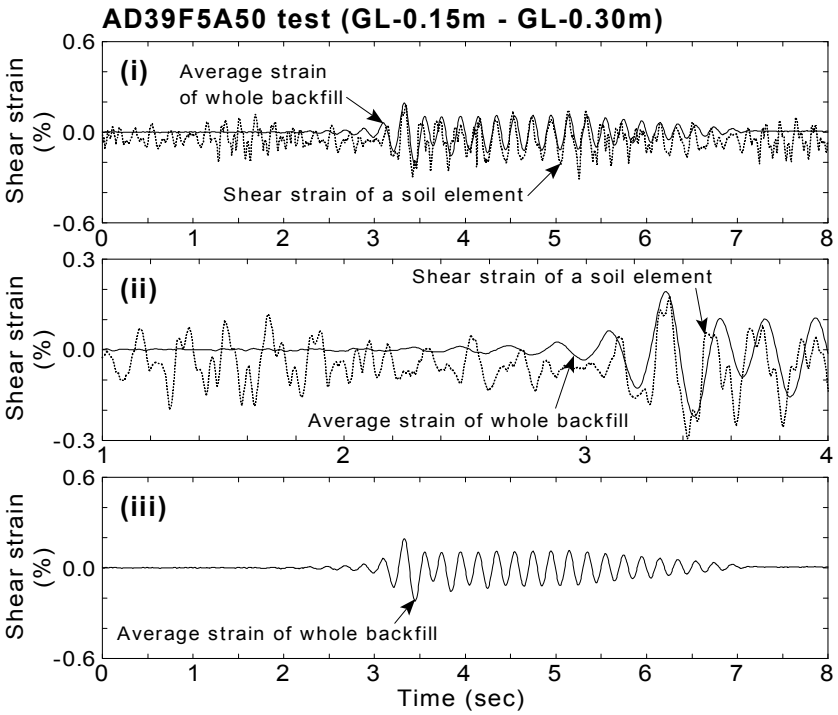

(b) GL-0.15m ～ GL-0.30m

Fig.4.98: Reproduced shear strain at each soil element (AD39F5A50 test)

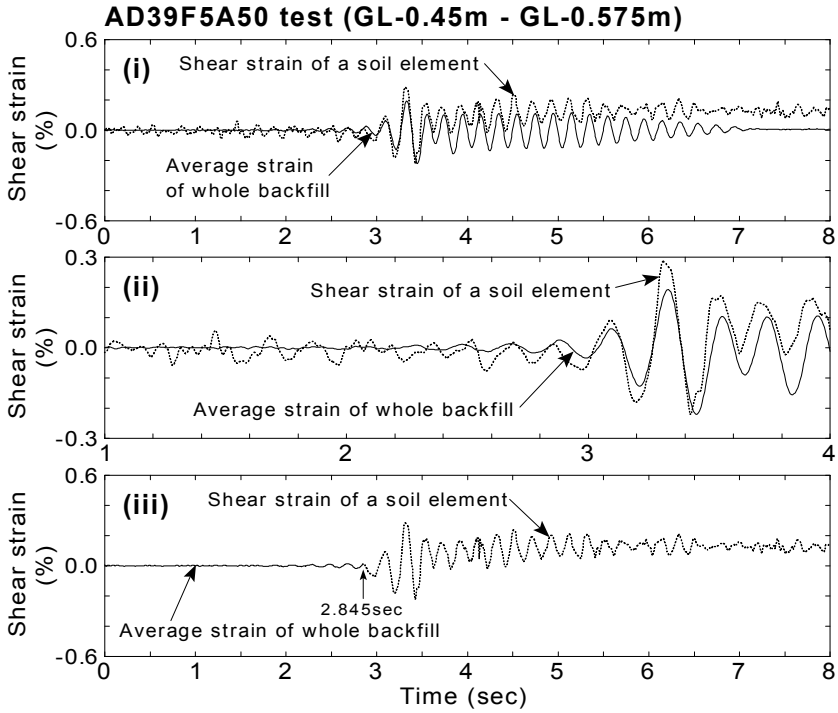

(c) GL-0.45m ～ GL-0.575m

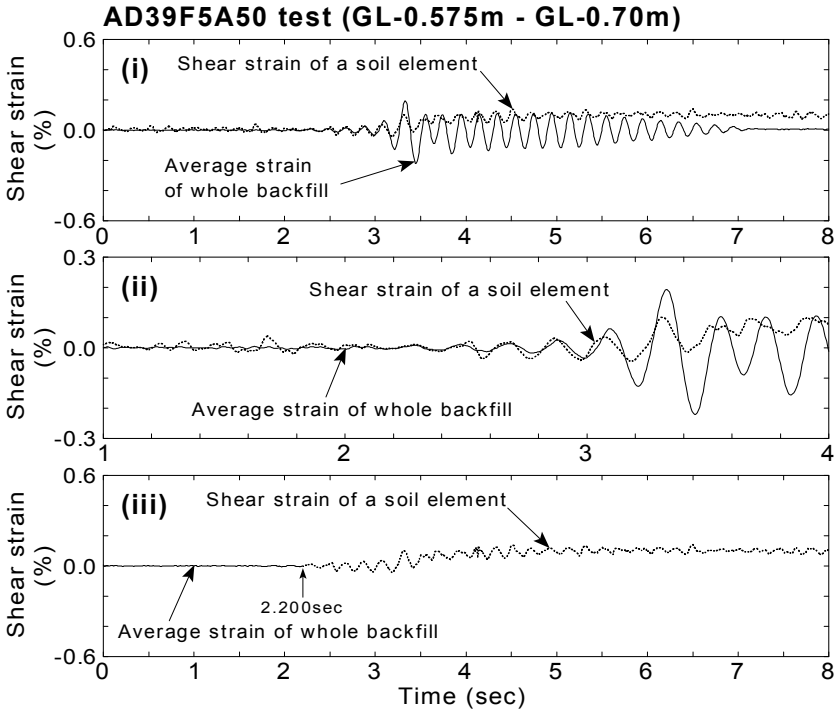

(d) GL-0.575m ～ GL-0.70m

Fig.4.98: Continued

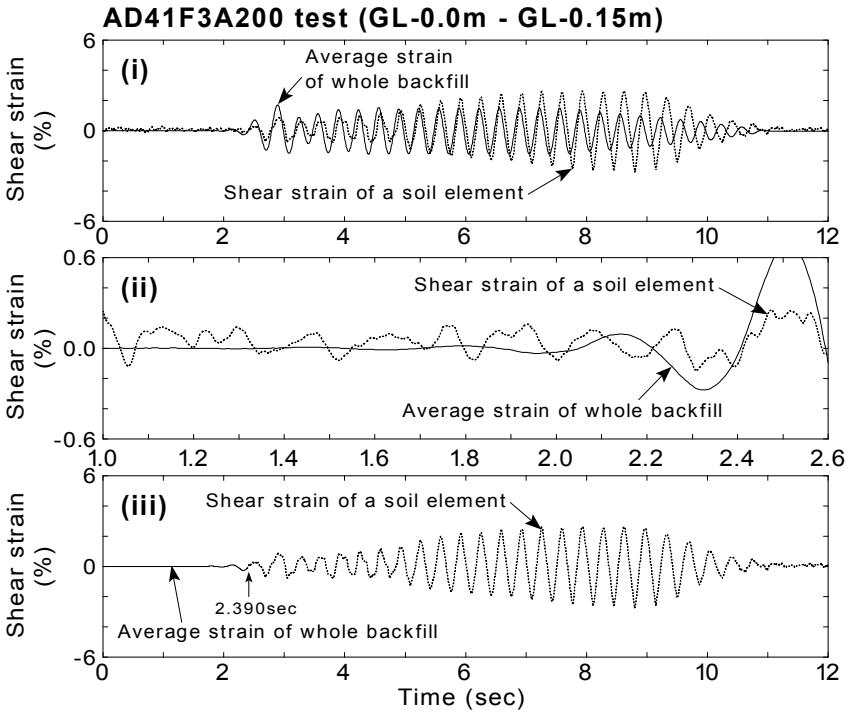

(a) GL-0.0m ～ GL-0.15m

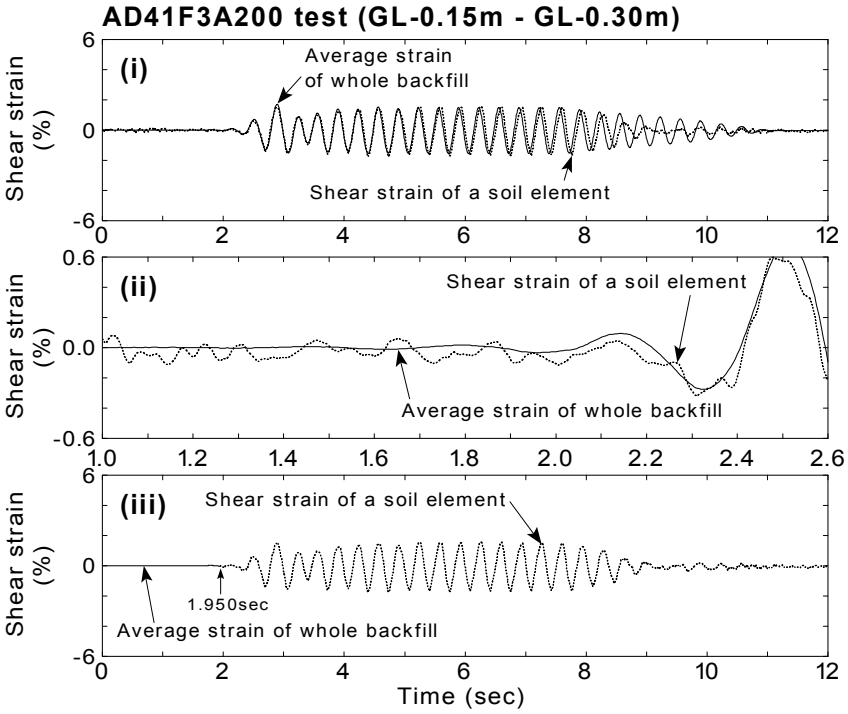

(b) GL-0.15m ～ GL-0.30m

Fig.4.99: Reproduced shear strain at each soil element (AD41F3A200 test)

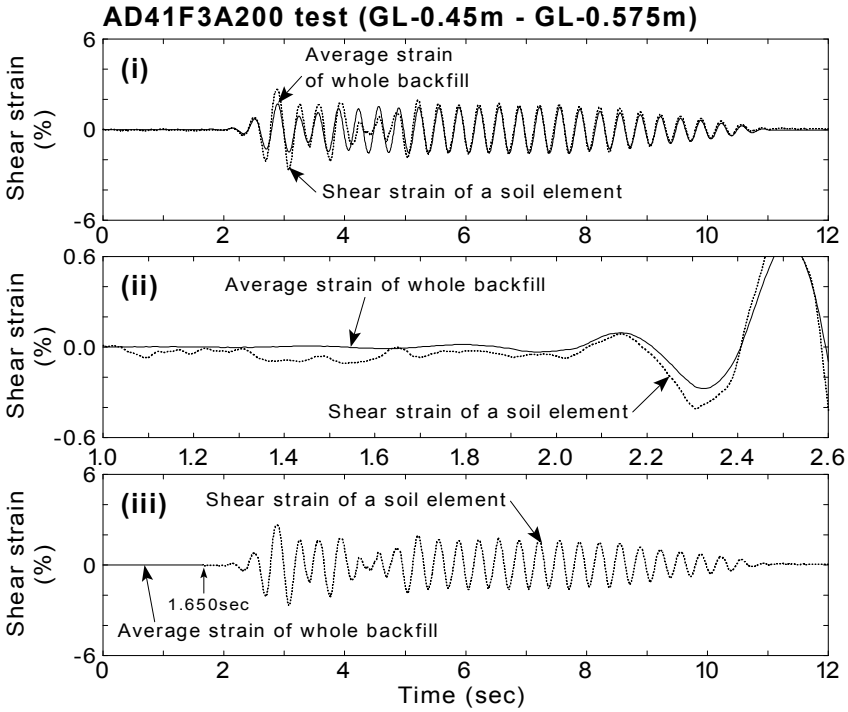

(c) GL-0.45m ～ GL-0.575m

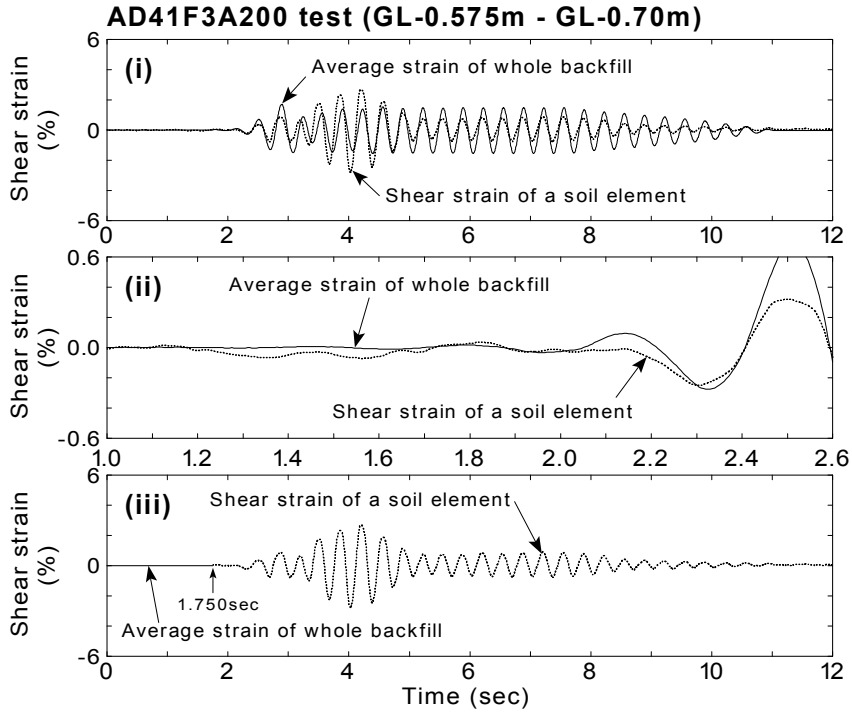

(d) GL-0.575m ～ GL-0.70m

Fig.4.99: Continued

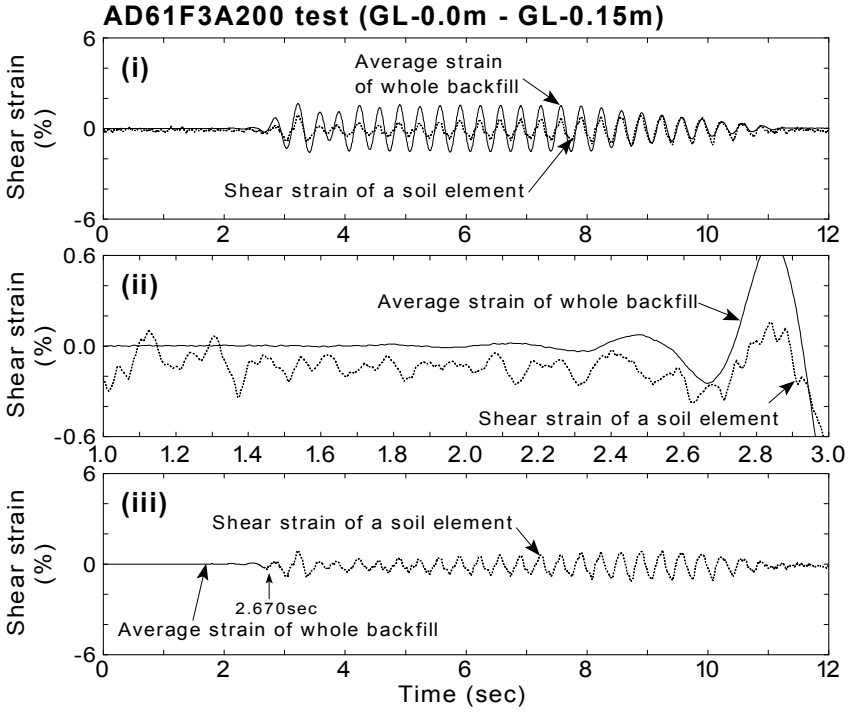

(a) GL-0.0m ～ GL-0.15m

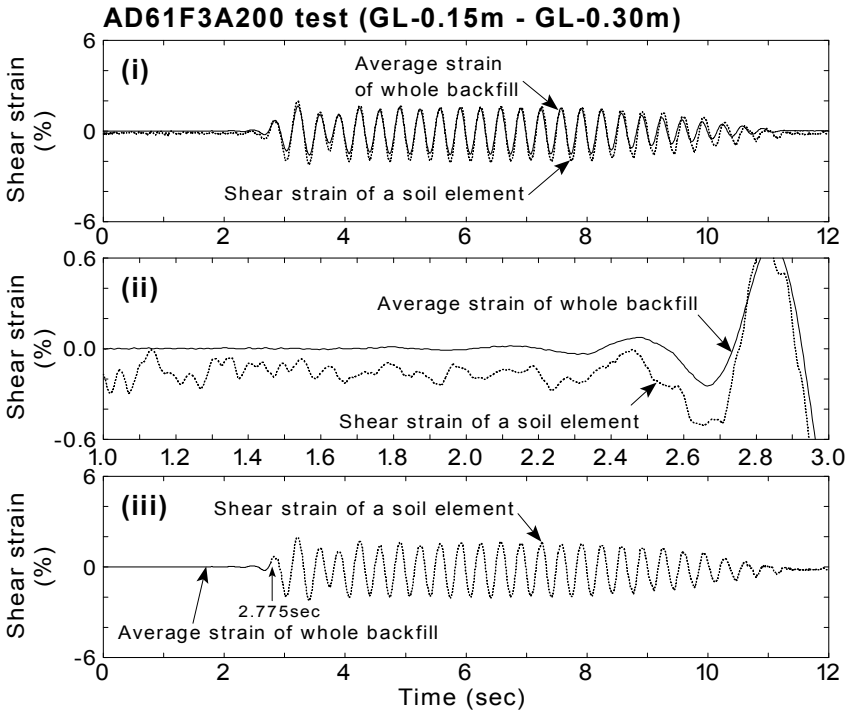

(b) GL-0.15m ～ GL-0.30m

Fig.4.100: Reproduced shear strain at each soil element (AD61F3A200 test)

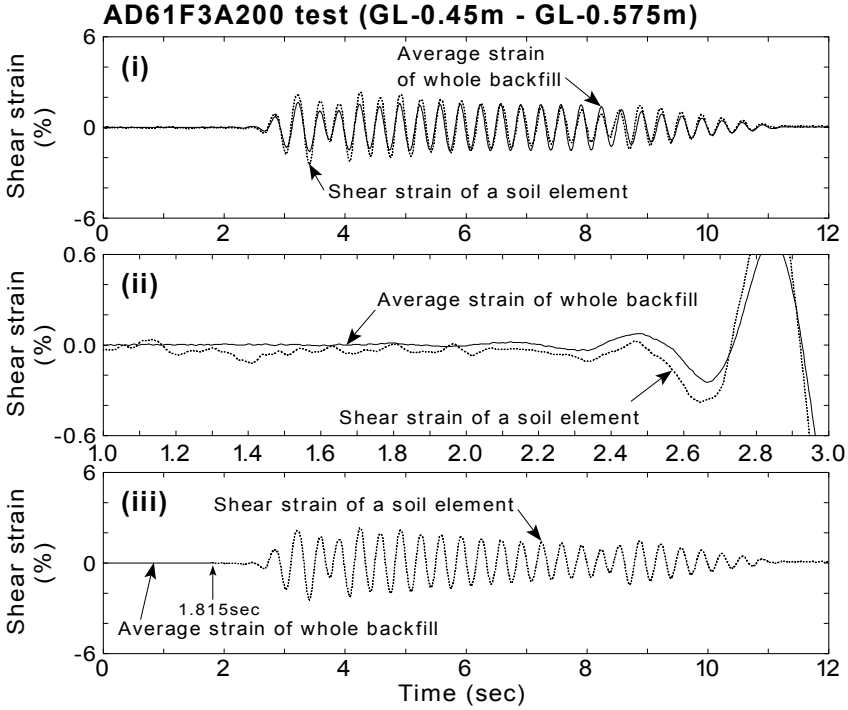

(c) GL-0.45m ～ GL-0.575m

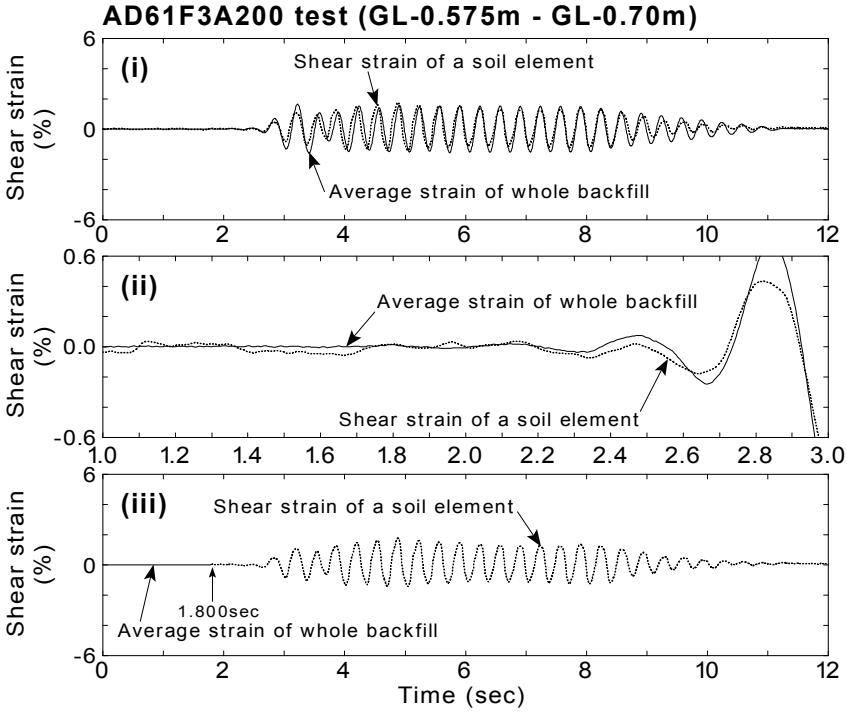

(d) GL-0.575m ～ GL-0.70m

Fig.4.100: Continued

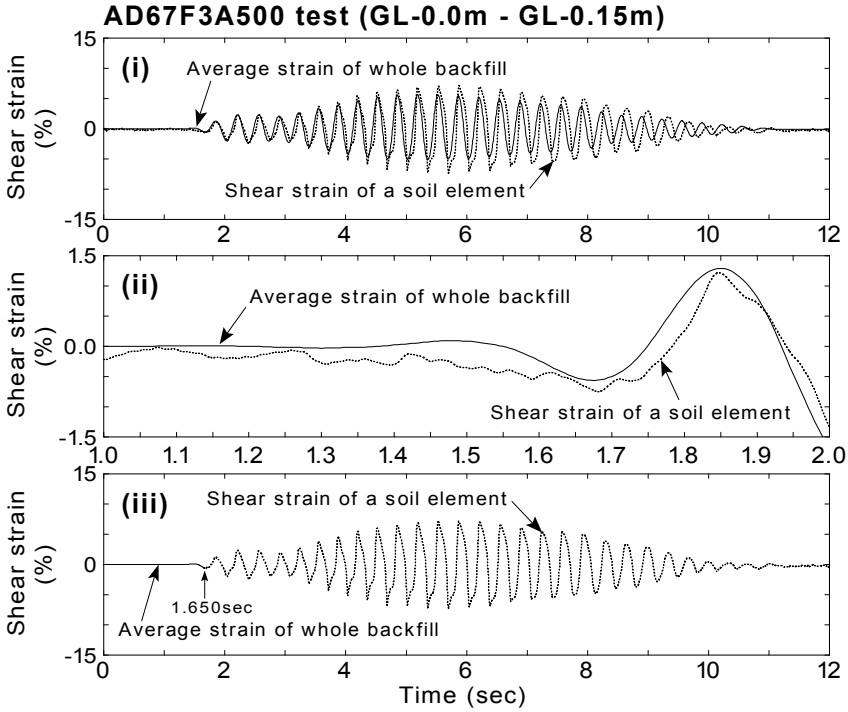

(a) GL-0.0m ～ GL-0.15m

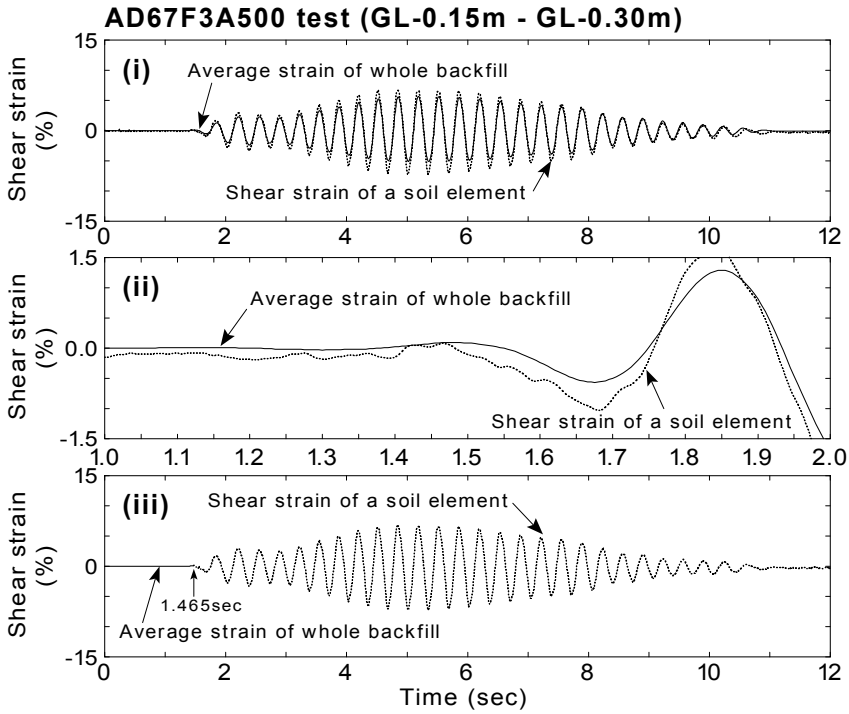

(b) GL-0.15m ～ GL-0.30m

Fig.4.101: Reproduced shear strain at each soil element (AD67F3A500 test)

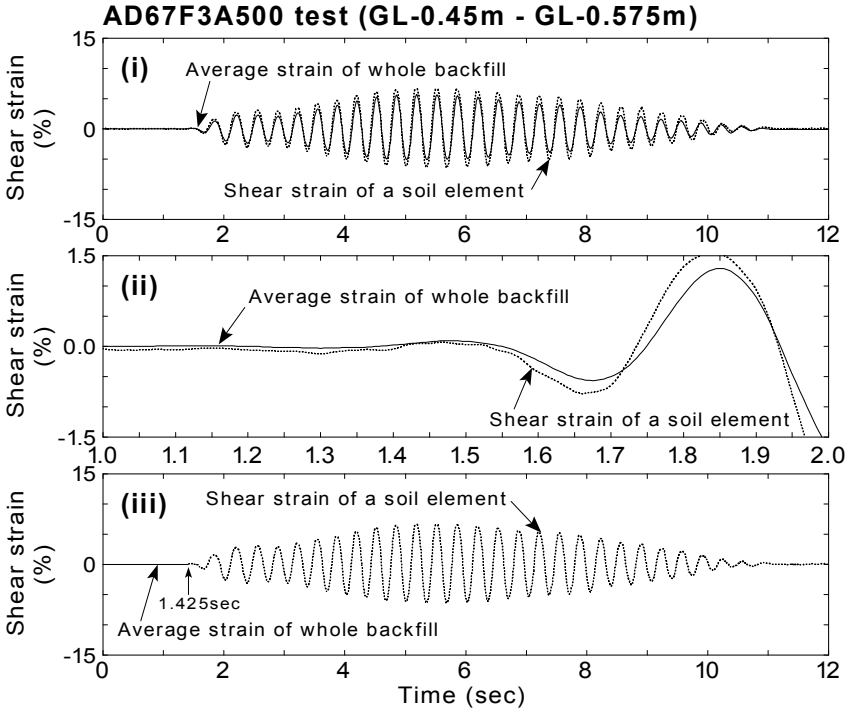

(c) GL-0.45m ～ GL-0.575m

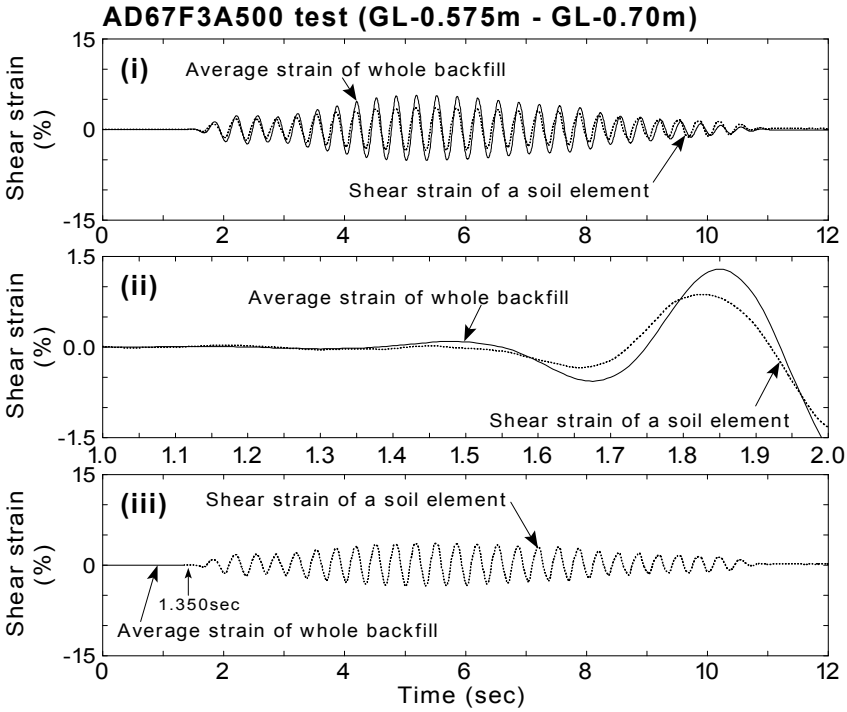

(d) GL-0.575m ～ GL-0.70m

Fig.4.101: Continued

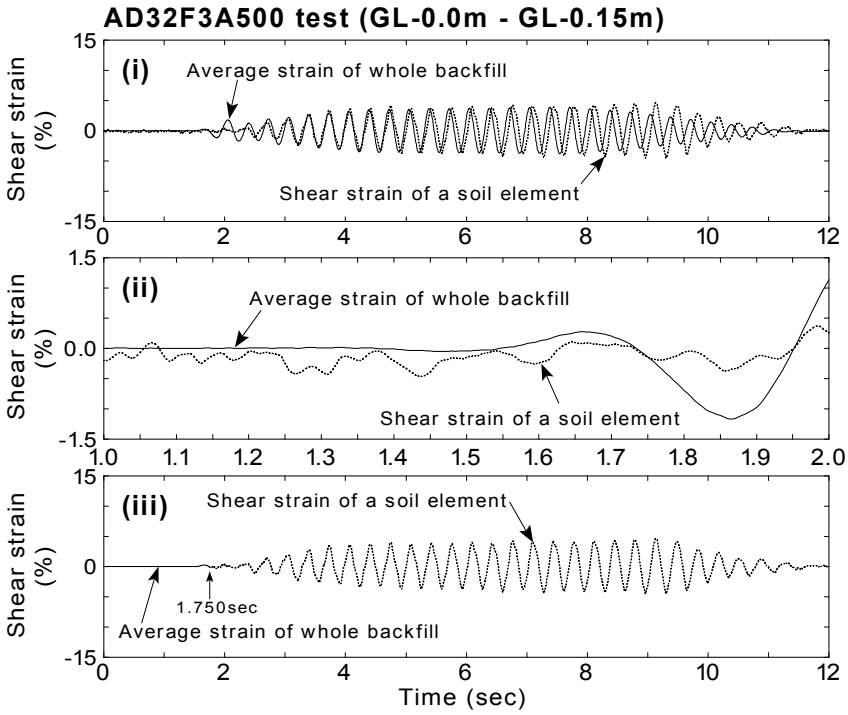

(a) GL-0.0m ～ GL-0.15m

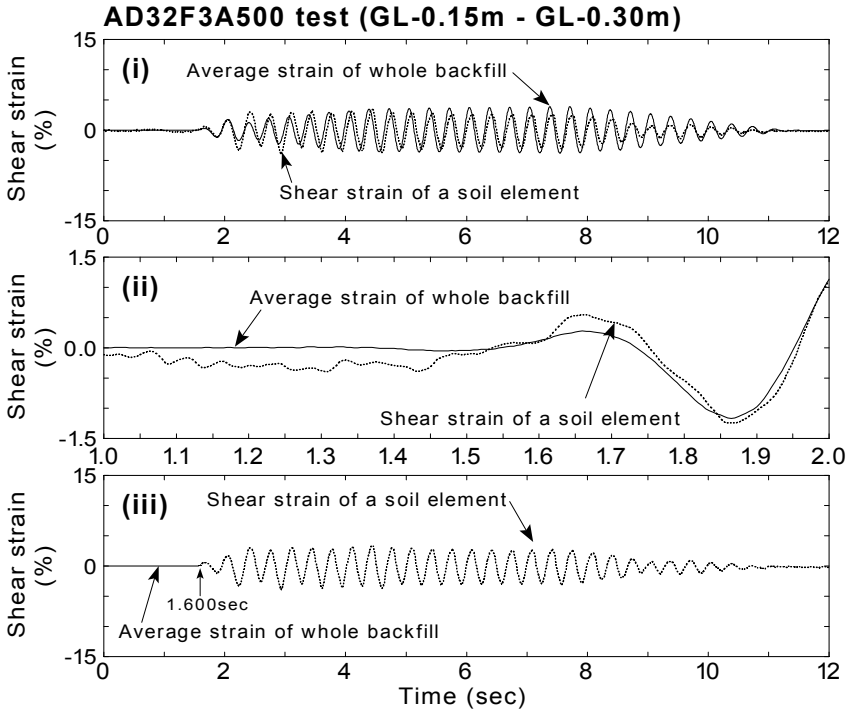

(b) GL-0.15m ～ GL-0.30m

Fig.4.102: Reproduced shear strain at each soil element (AD32F3A500 test)

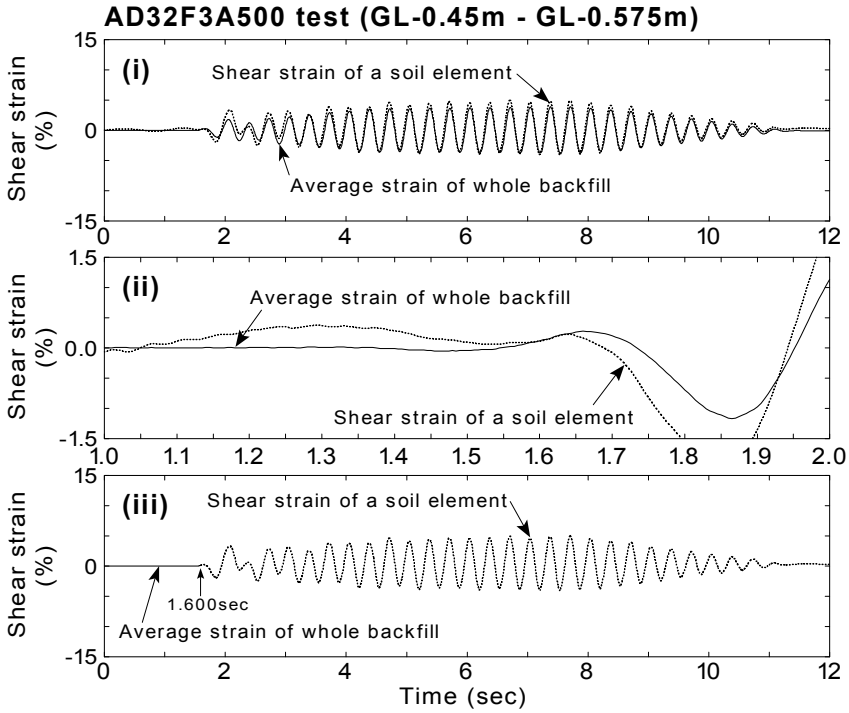

(c) GL-0.45m ～ GL-0.575m

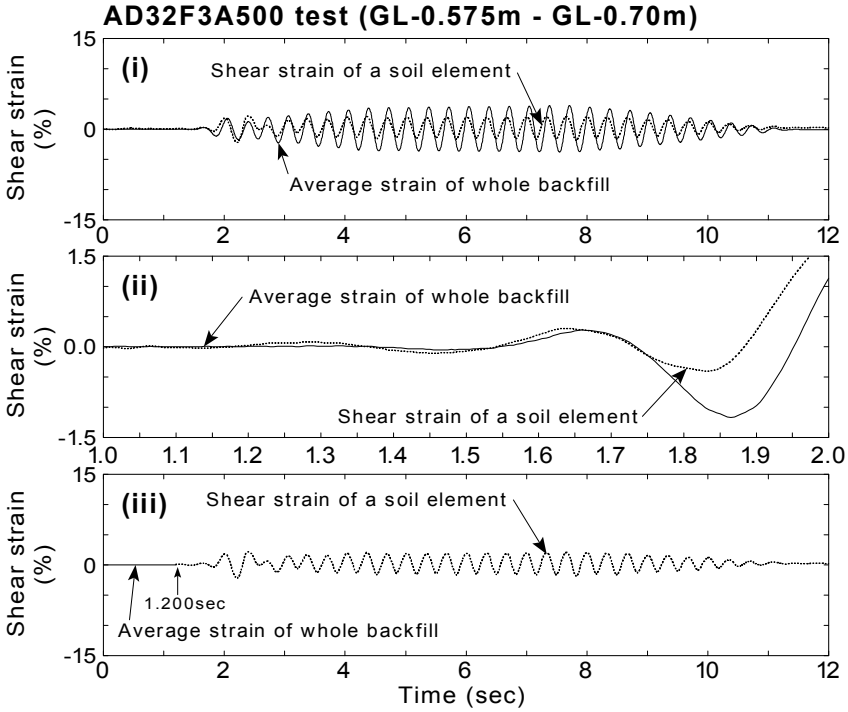

(d) GL-0.575m ～ GL-0.70m

Fig.4.102: Continued

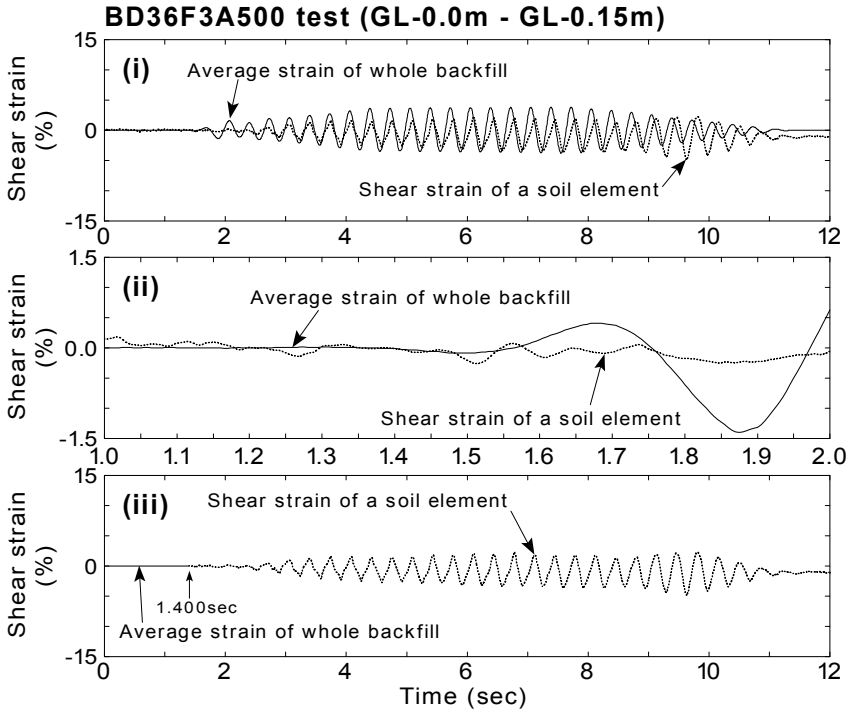

(a) GL-0.0m ～ GL-0.15m

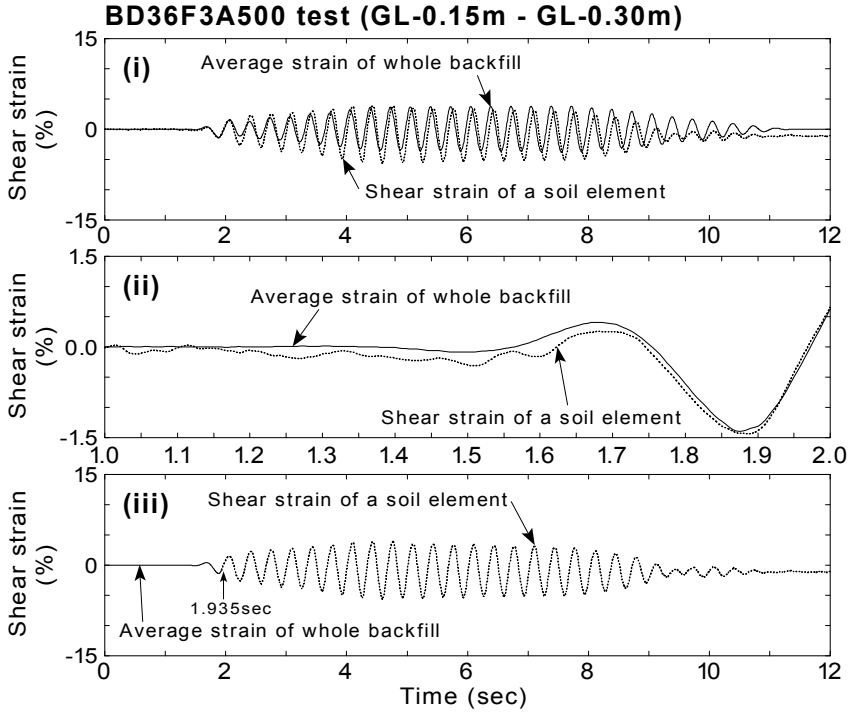

(b) GL-0.15m ～ GL-0.30m

Fig.4.103: Reproduced shear strain at each soil element (BD36F3A500 test)

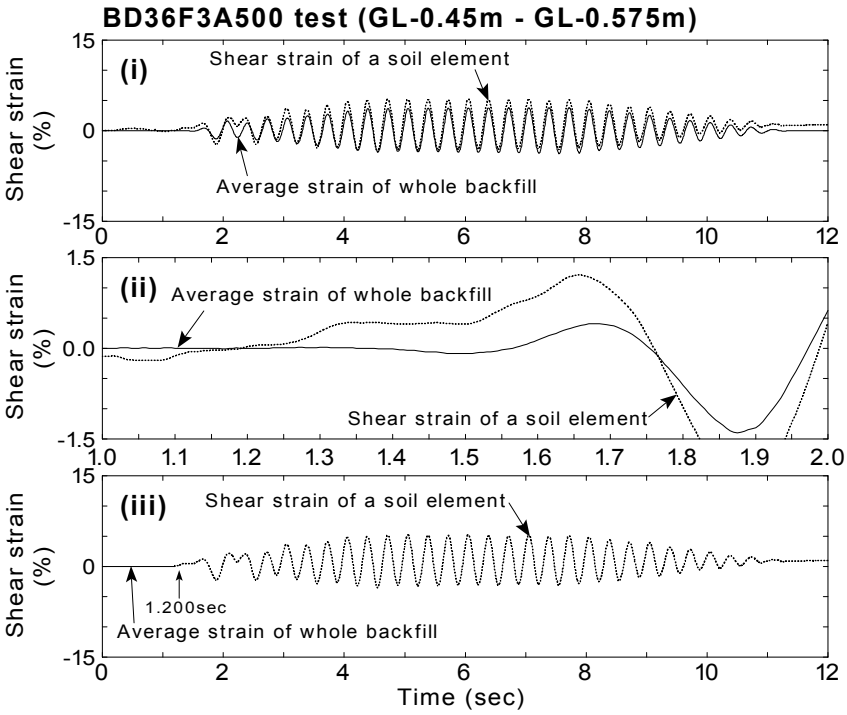

(c) GL-0.45m ～ GL-0.575m

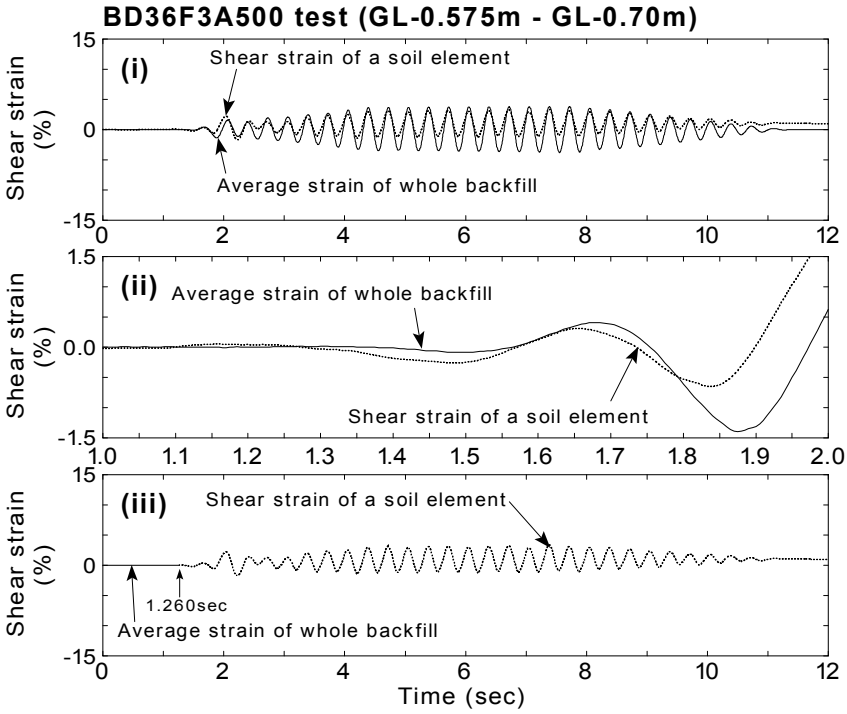

(d) GL-0.575m ～ GL-0.70m

Fig.4.103: Continued

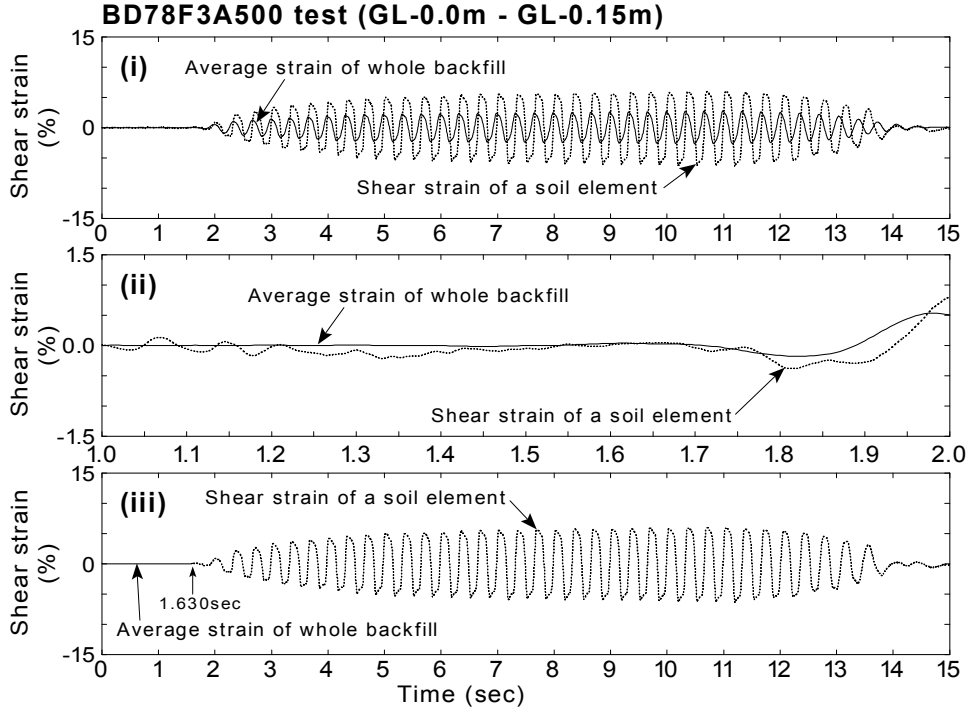

(a) GL-0.0m ～ GL-0.15m

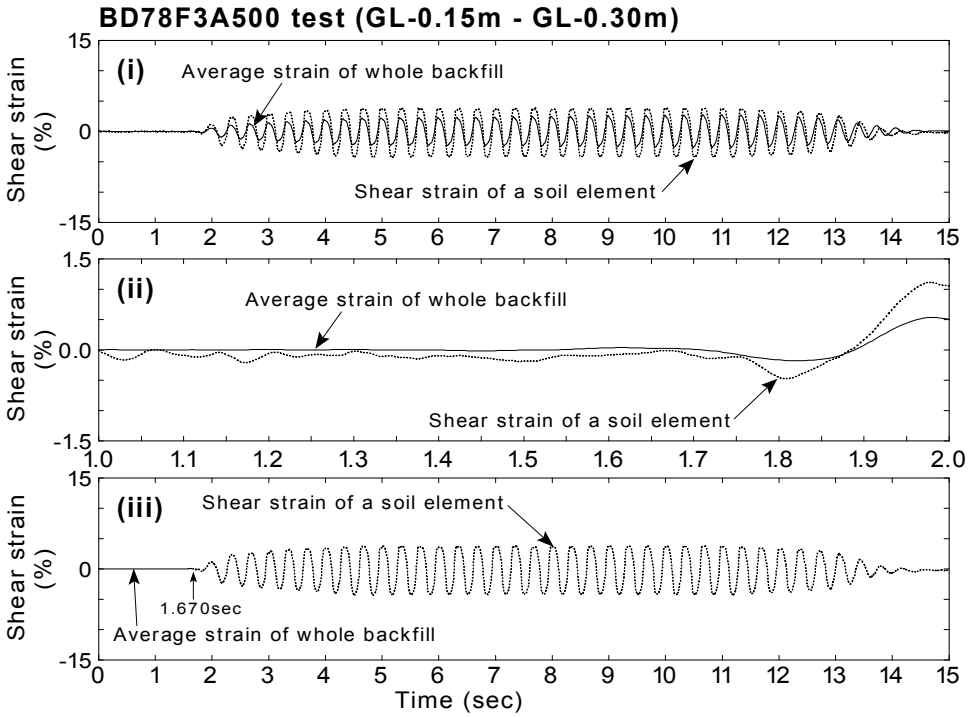

(b) GL-0.15m ～ GL-0.30m

Fig.4.104: Reproduced shear strain at each soil element (BD78F3A500 test)

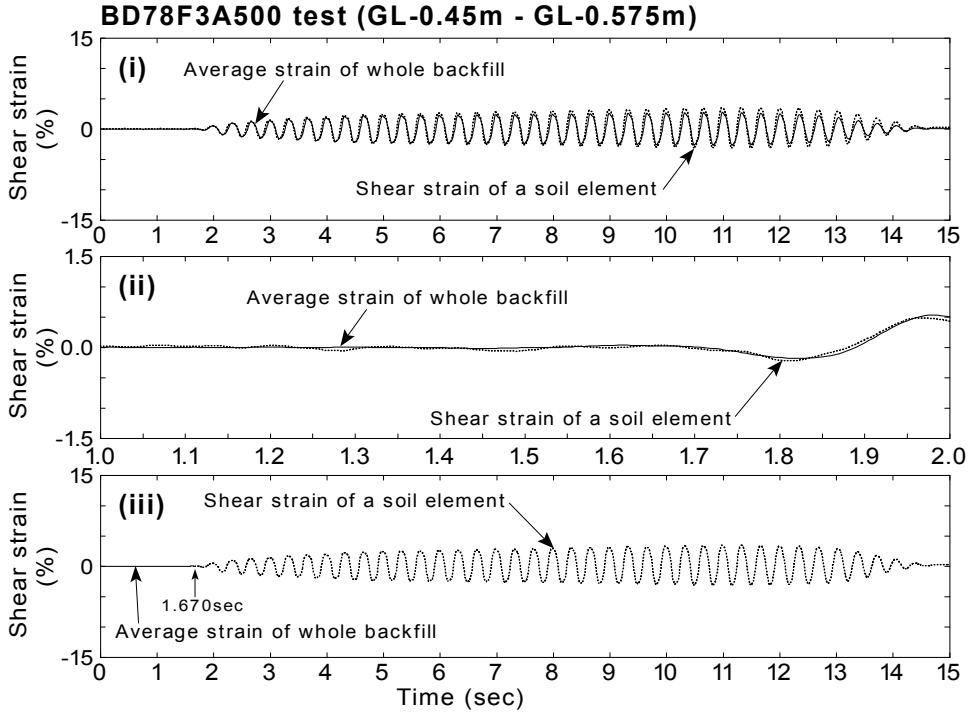

(c) GL-0.45m ～ GL-0.575m

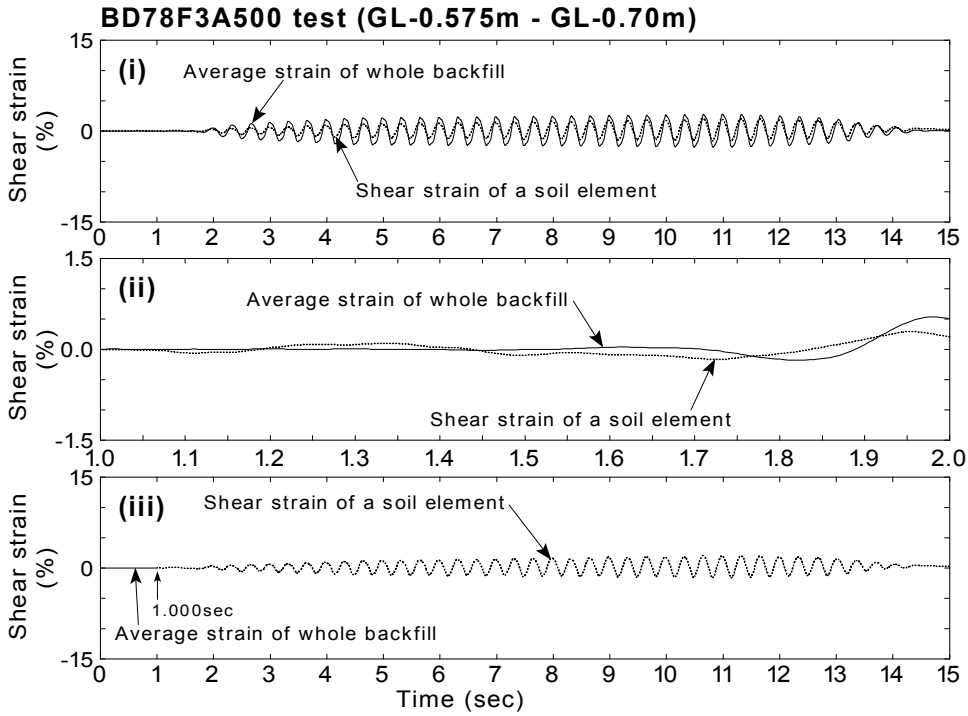

(d) GL-0.575m ～ GL-0.70m

Fig.4.104: Continued

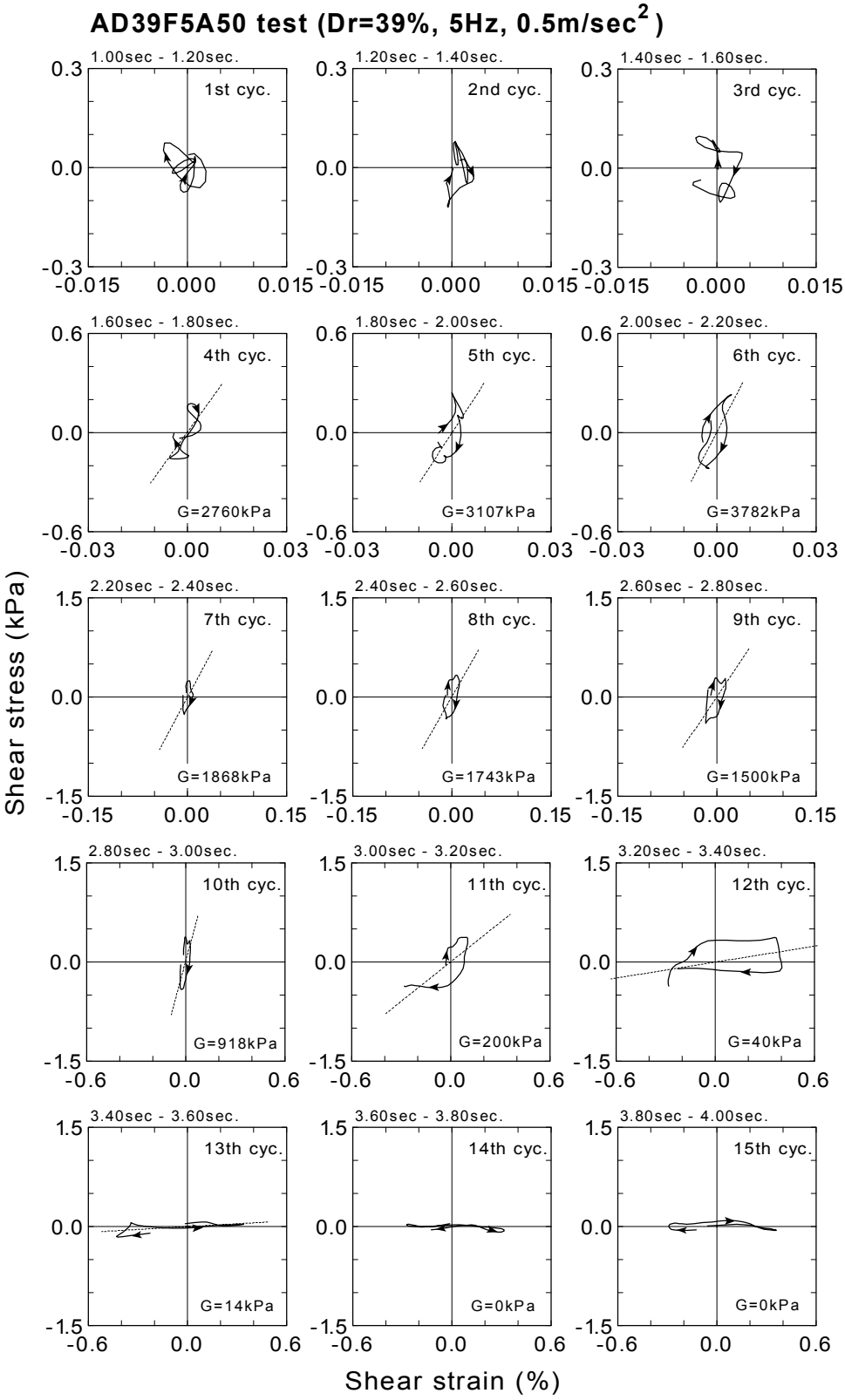

Fig.4.105: Stress-strain relationship of each cycle and calculated shear modulus (AD39F5A50 test, 1～15 cycles)

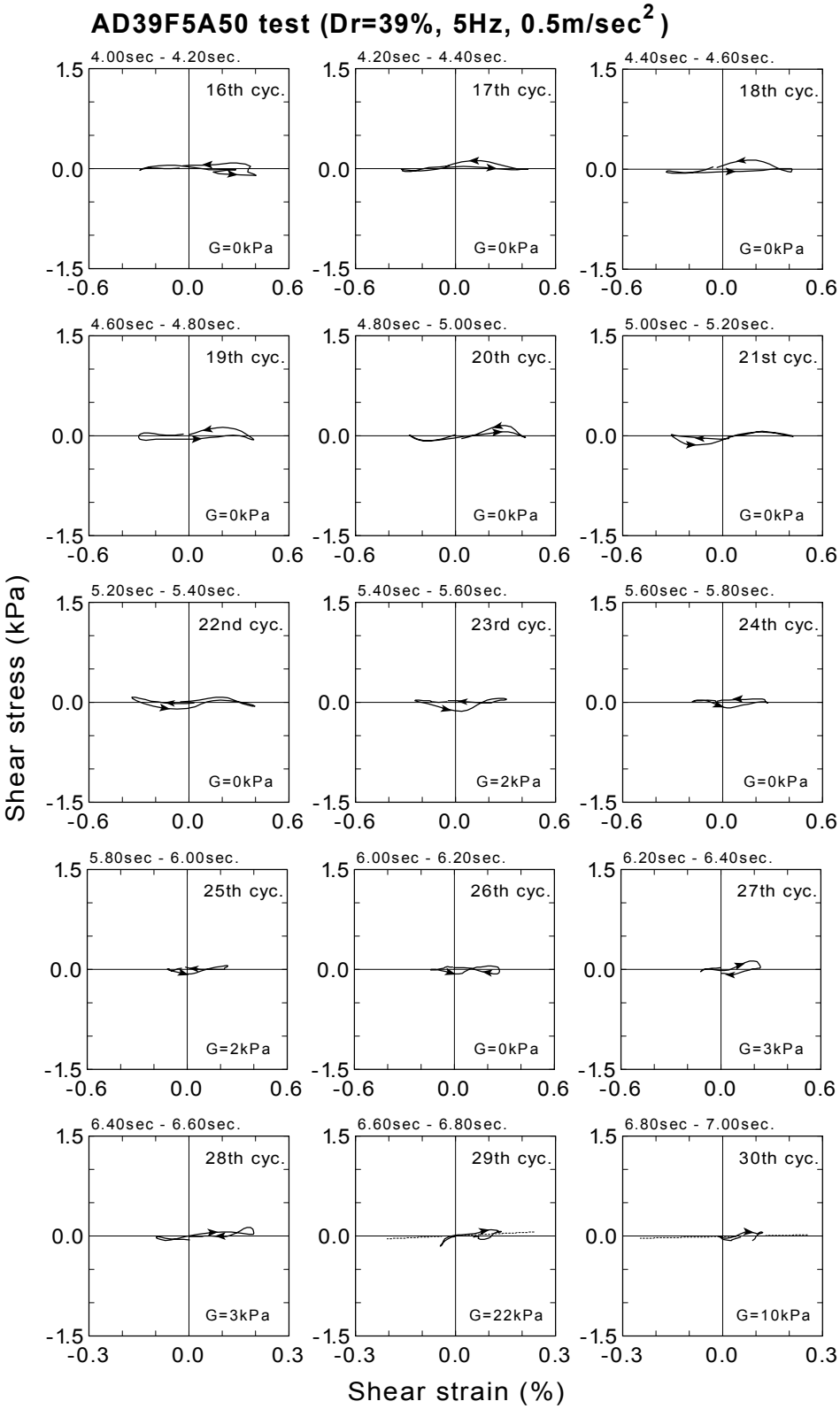

Fig.4.105: Continued (AD39F5A50 test, 16～30 cycles)

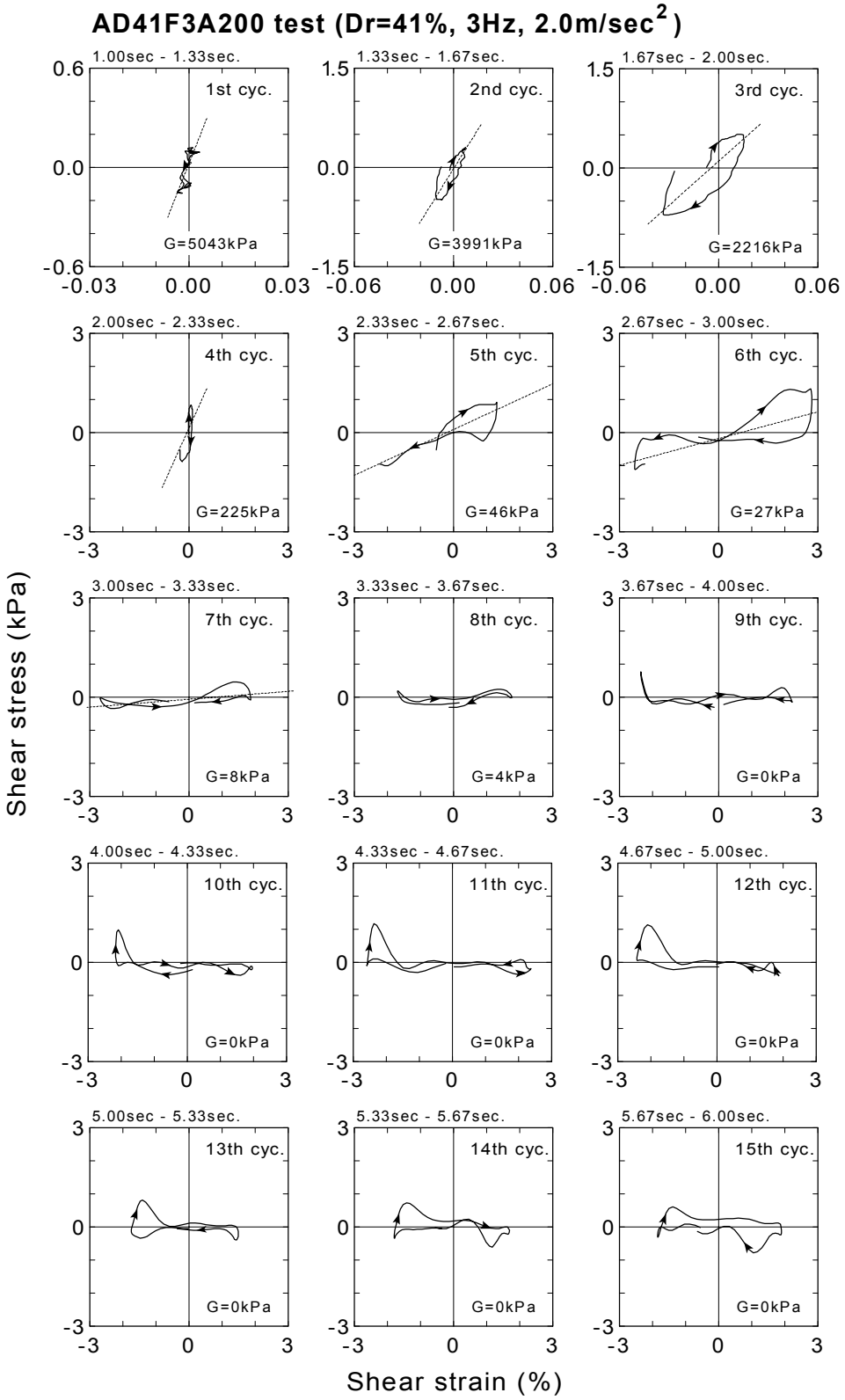

Fig.4.106: Stress-strain relationship of each cycle and calculated shear modulus (AD41F3A200 test, 1～15 cycles)

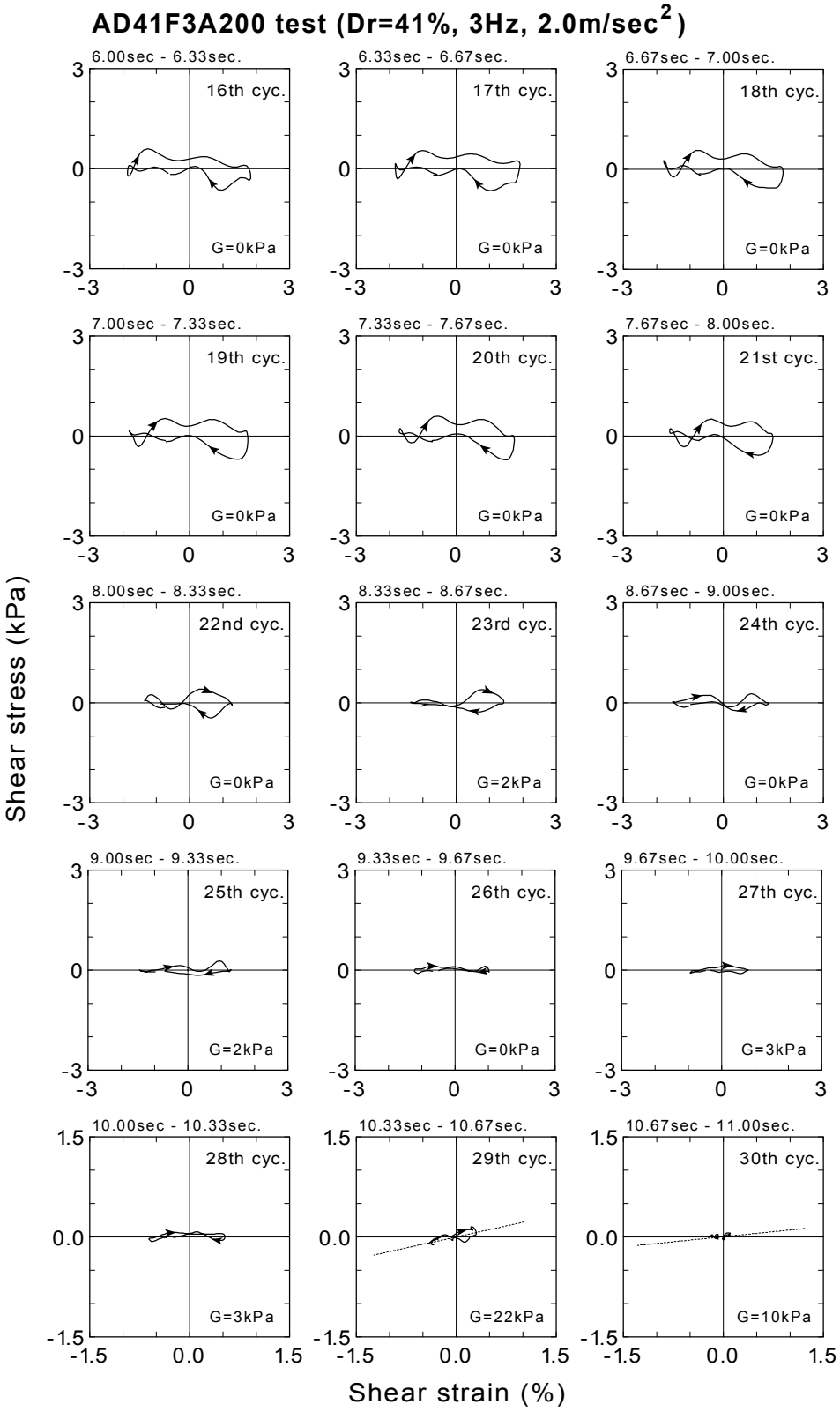

Fig.4.106: Continued (AD41F3A200 test, 16～30 cycles)

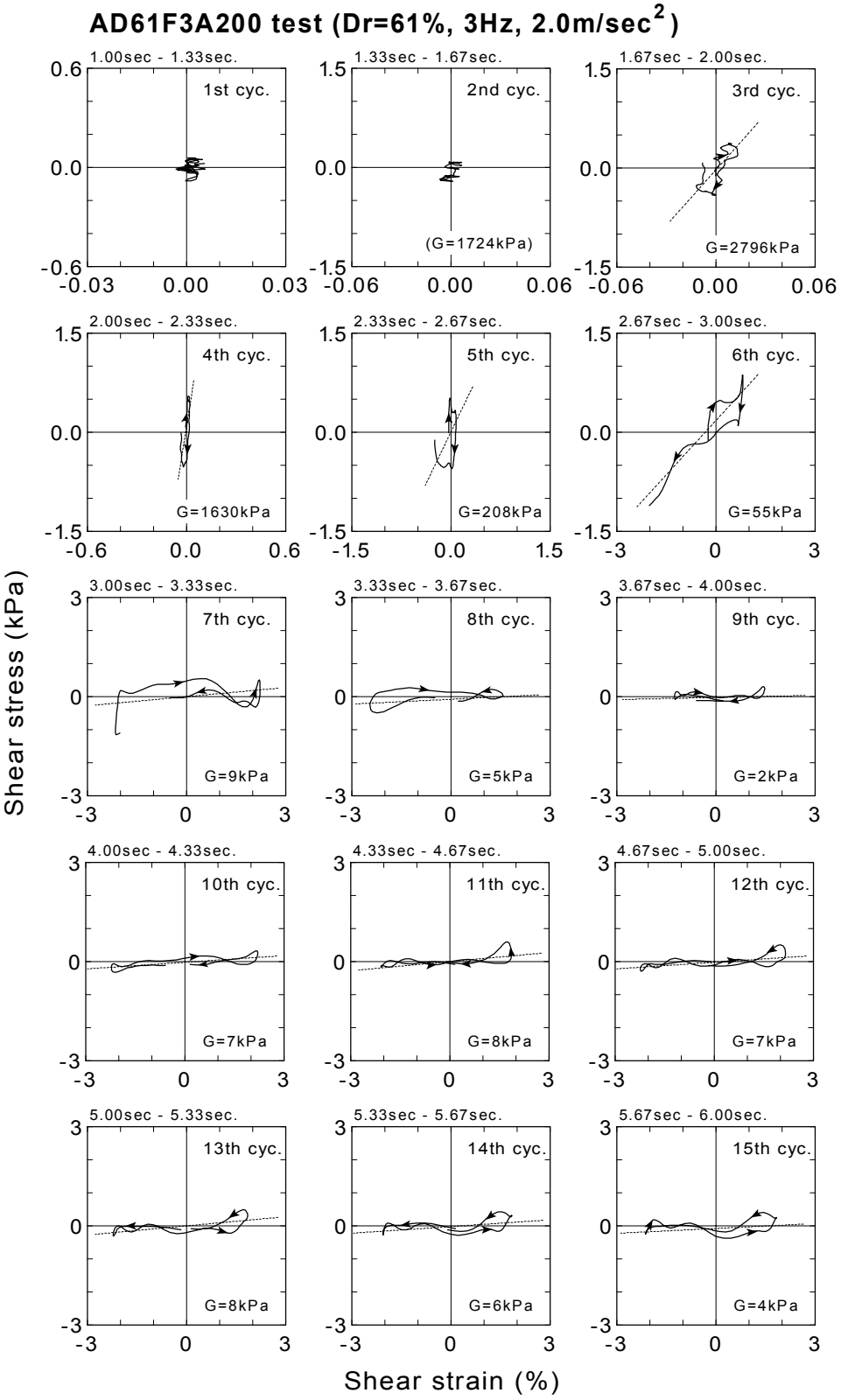

Fig.4.107: Stress-strain relationship of each cycle and calculated shear modulus (AD61F3A200 test, 1～15 cycles)

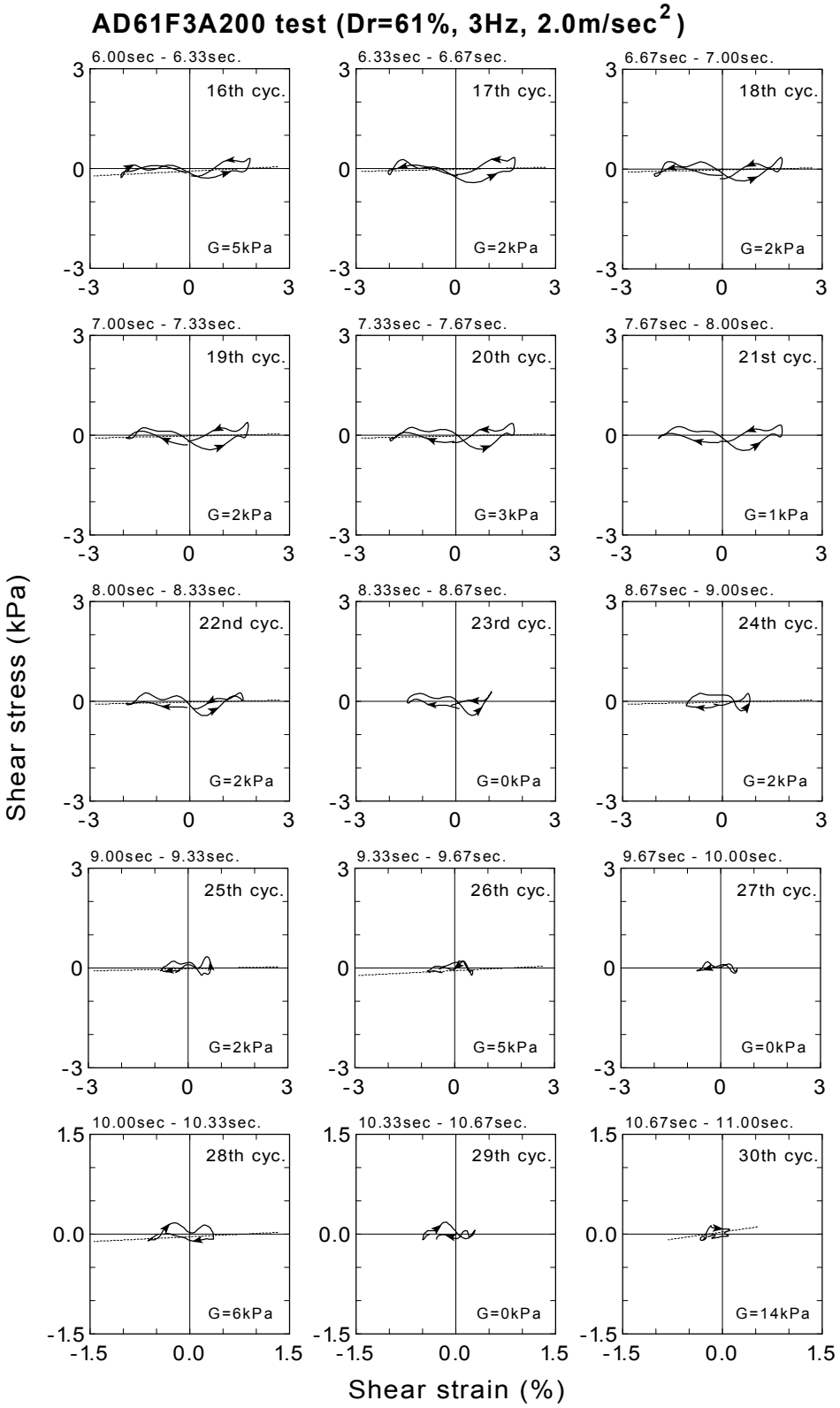

Fig.4.107: Continued (AD61F3A200 test, 16～30 cycles)

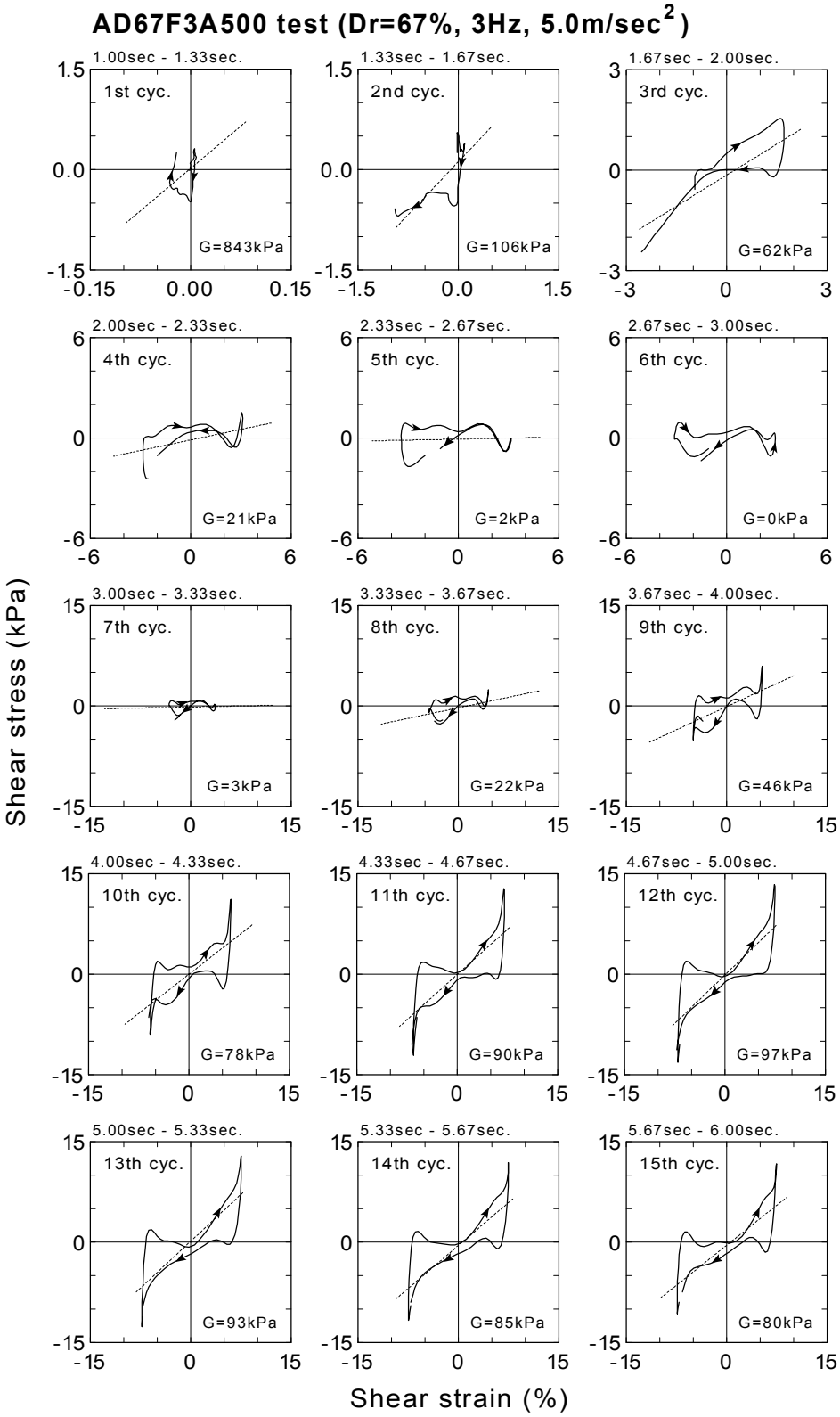

Fig.4.108: Stress-strain relationship of each cycle and calculated shear modulus (AD67F3A500 test, 1～15 cycles)

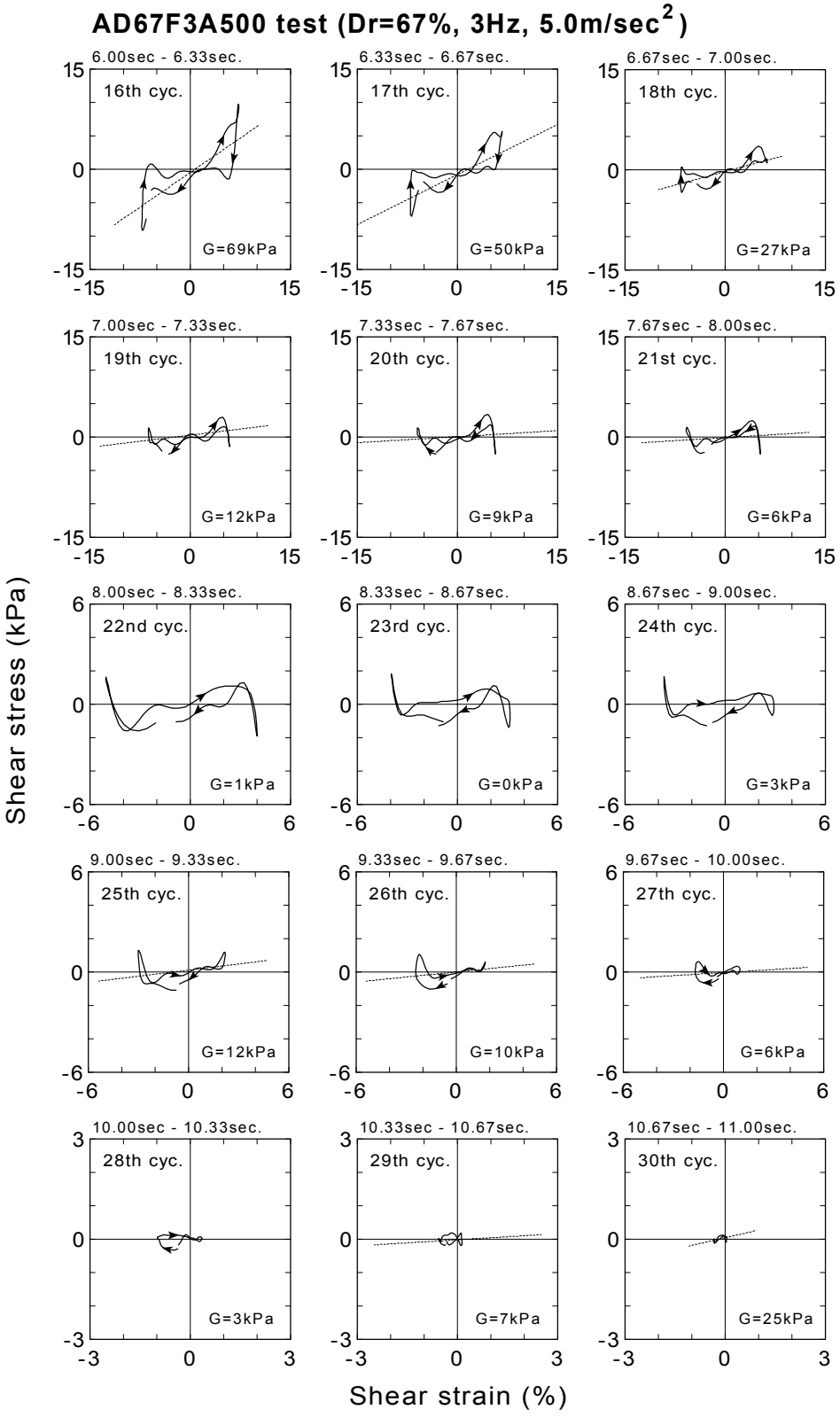

Fig.4.108: Continued (AD35F3A50 test, 16～30 cycles)

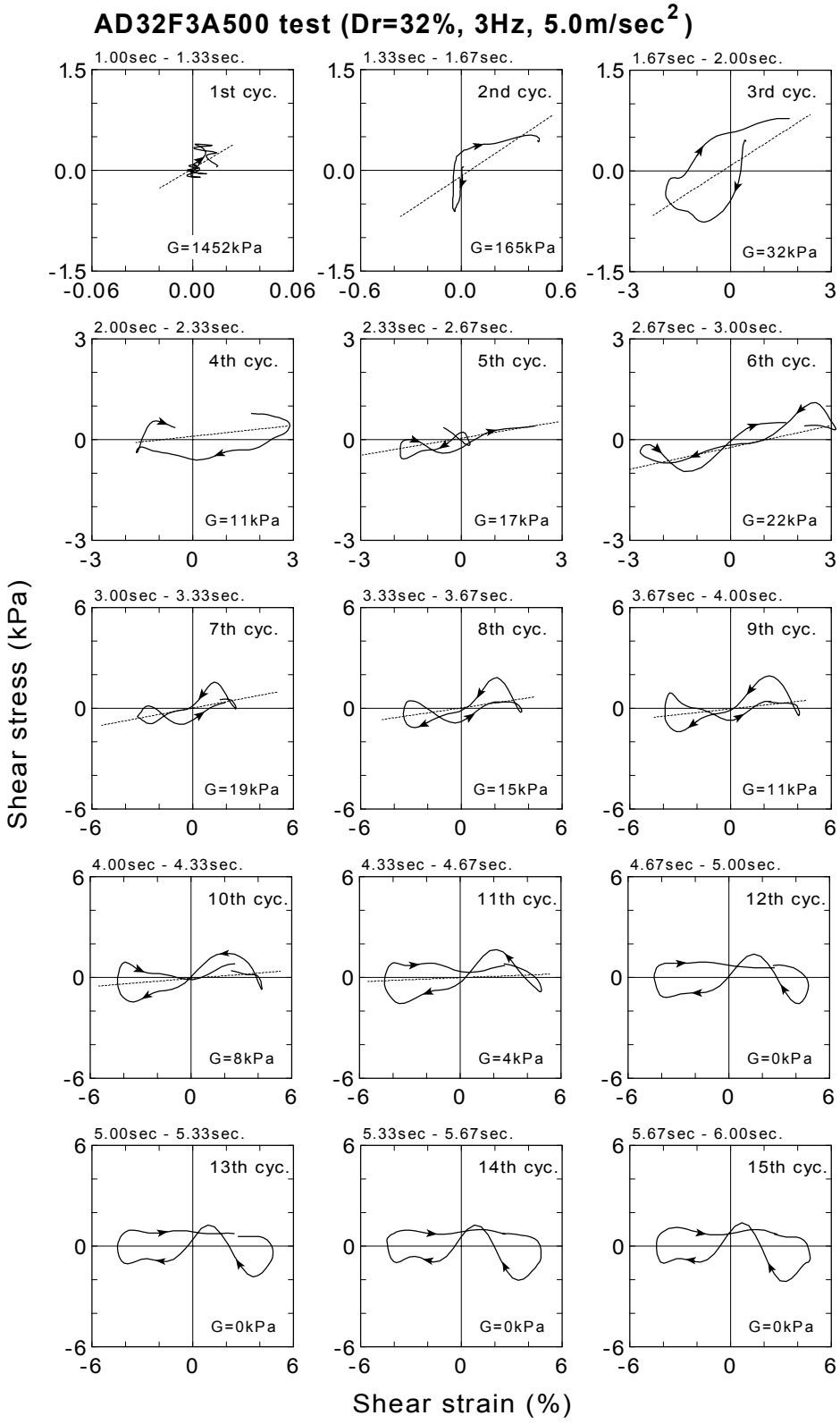

Fig.4.109: Stress-strain relationship of each cycle and calculated shear modulus (AD32F3A500 test, 1～15 cycles)

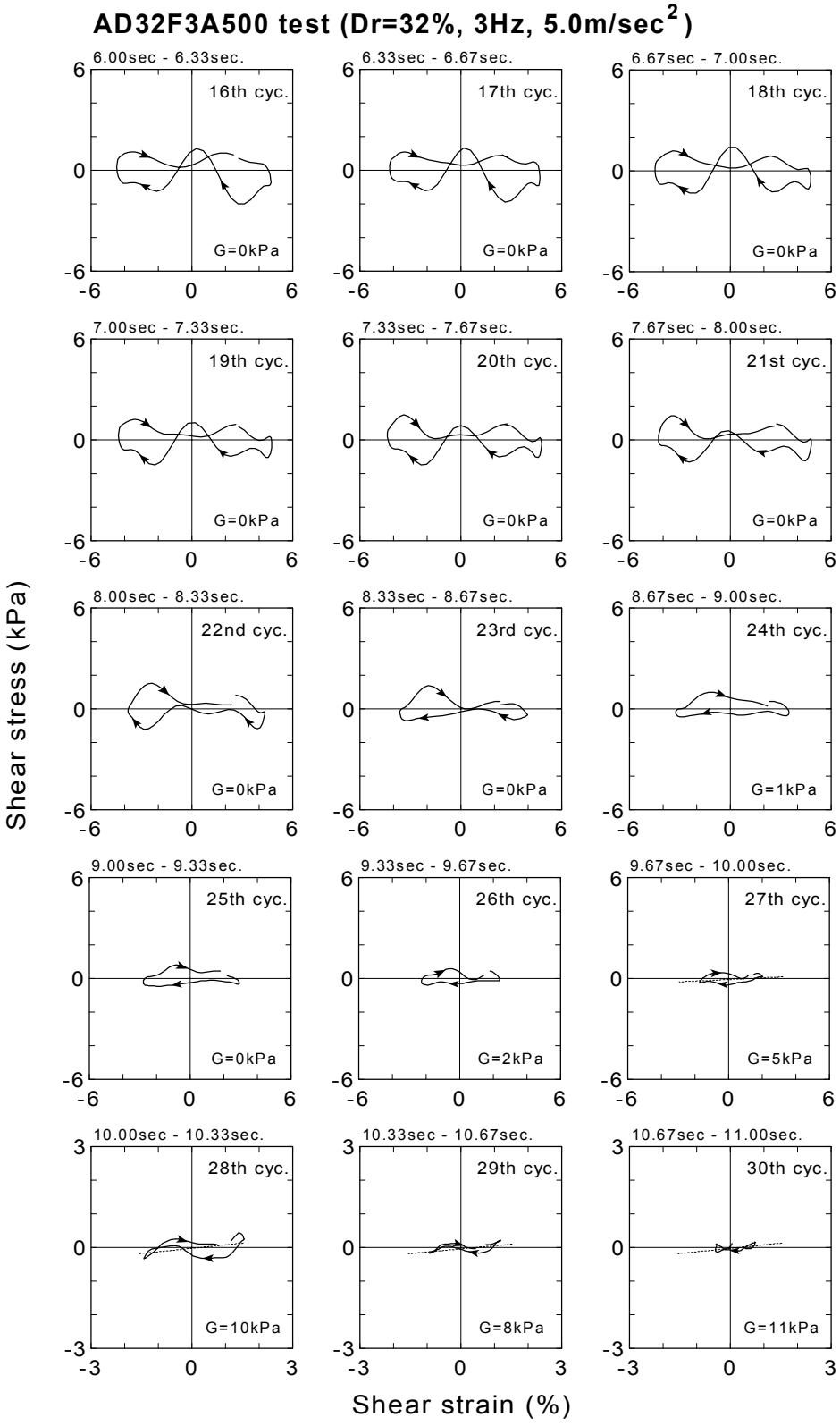

Fig.4.109: Continued (AD32F3A500 test, 16～30 cycles)

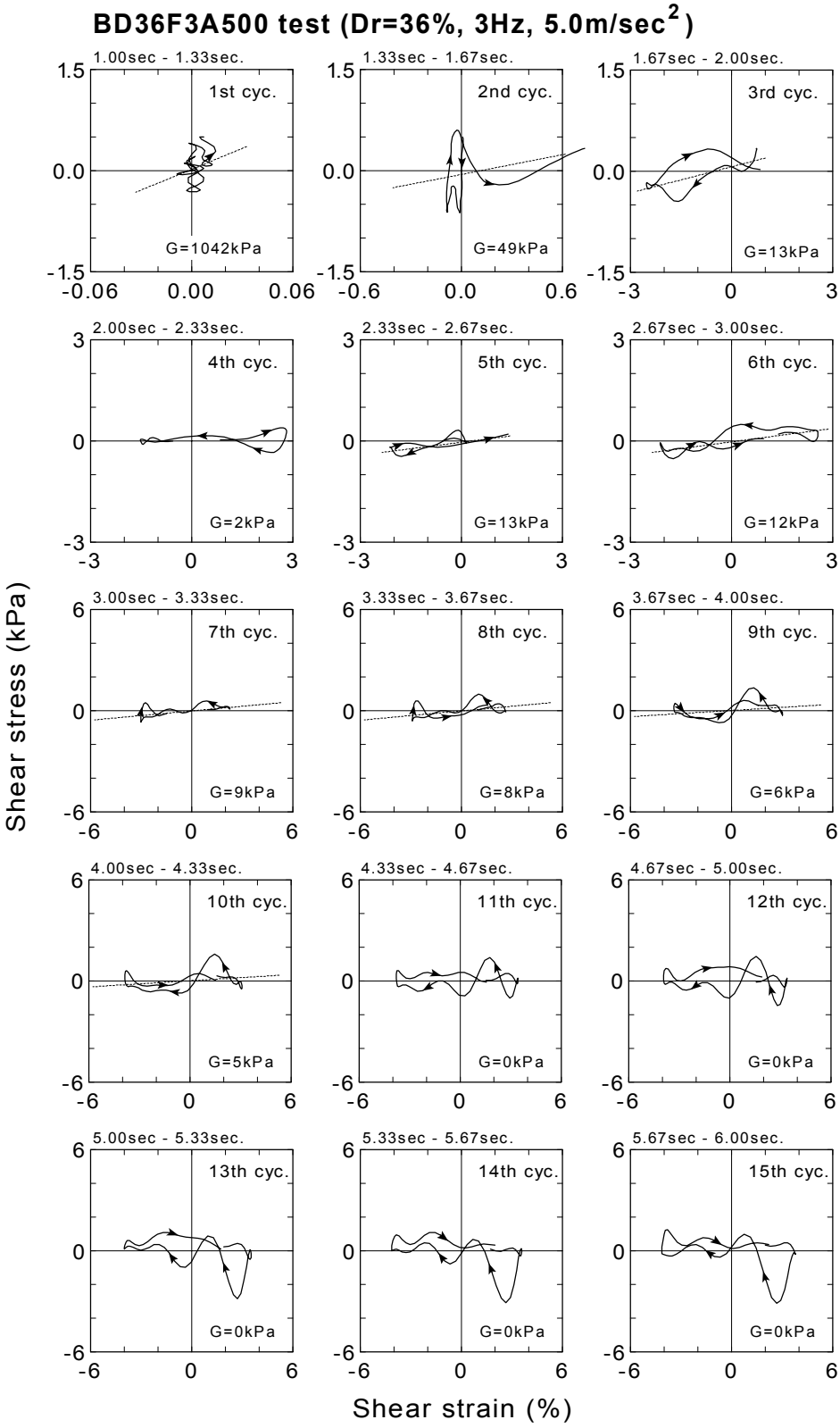

Fig.4.110: Stress-strain relationship of each cycle and calculated shear modulus (BD36F3A500 test, 1～15 cycles)

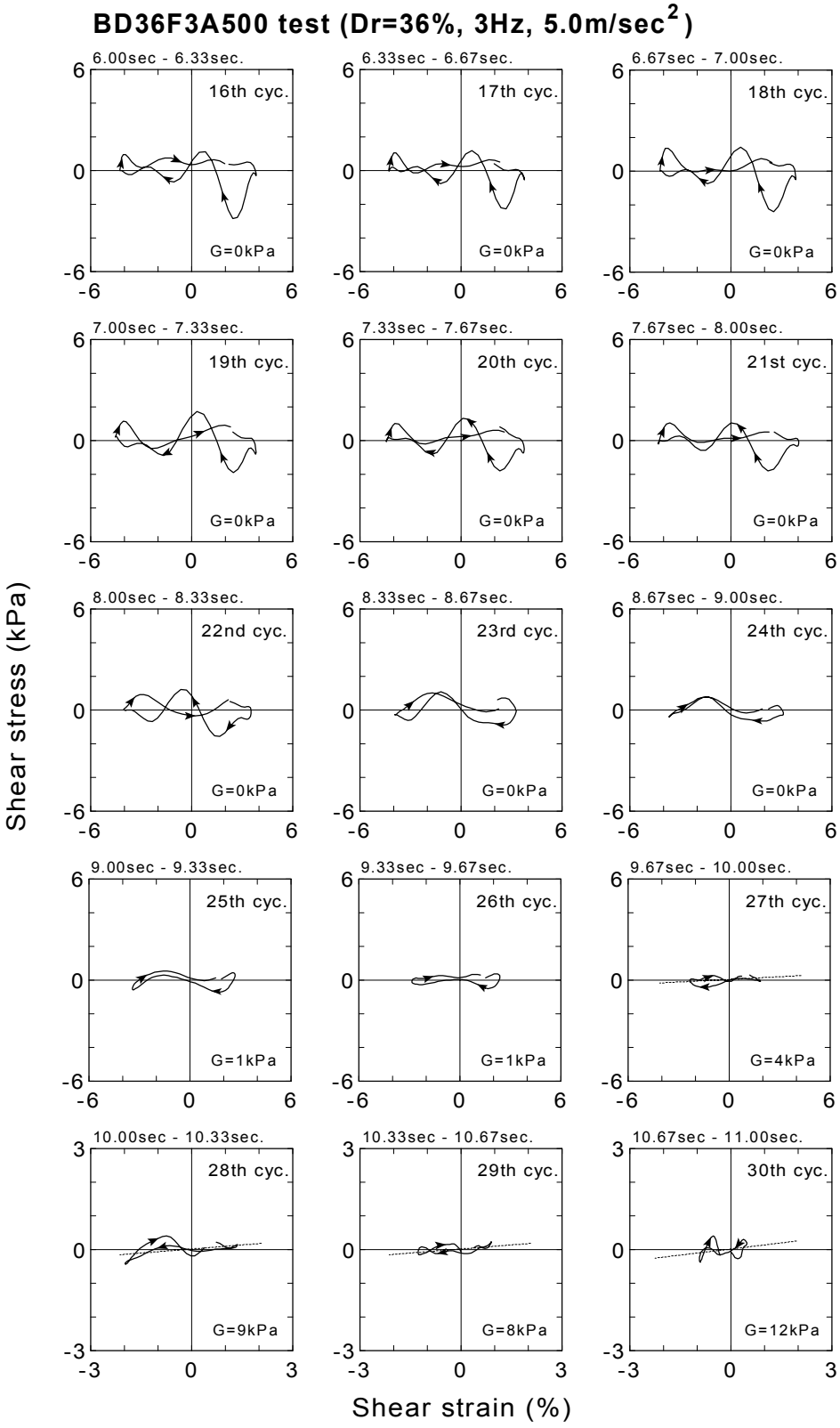

Fig.4.110: Continued (BD36F3A500 test, 16～30 cycles)

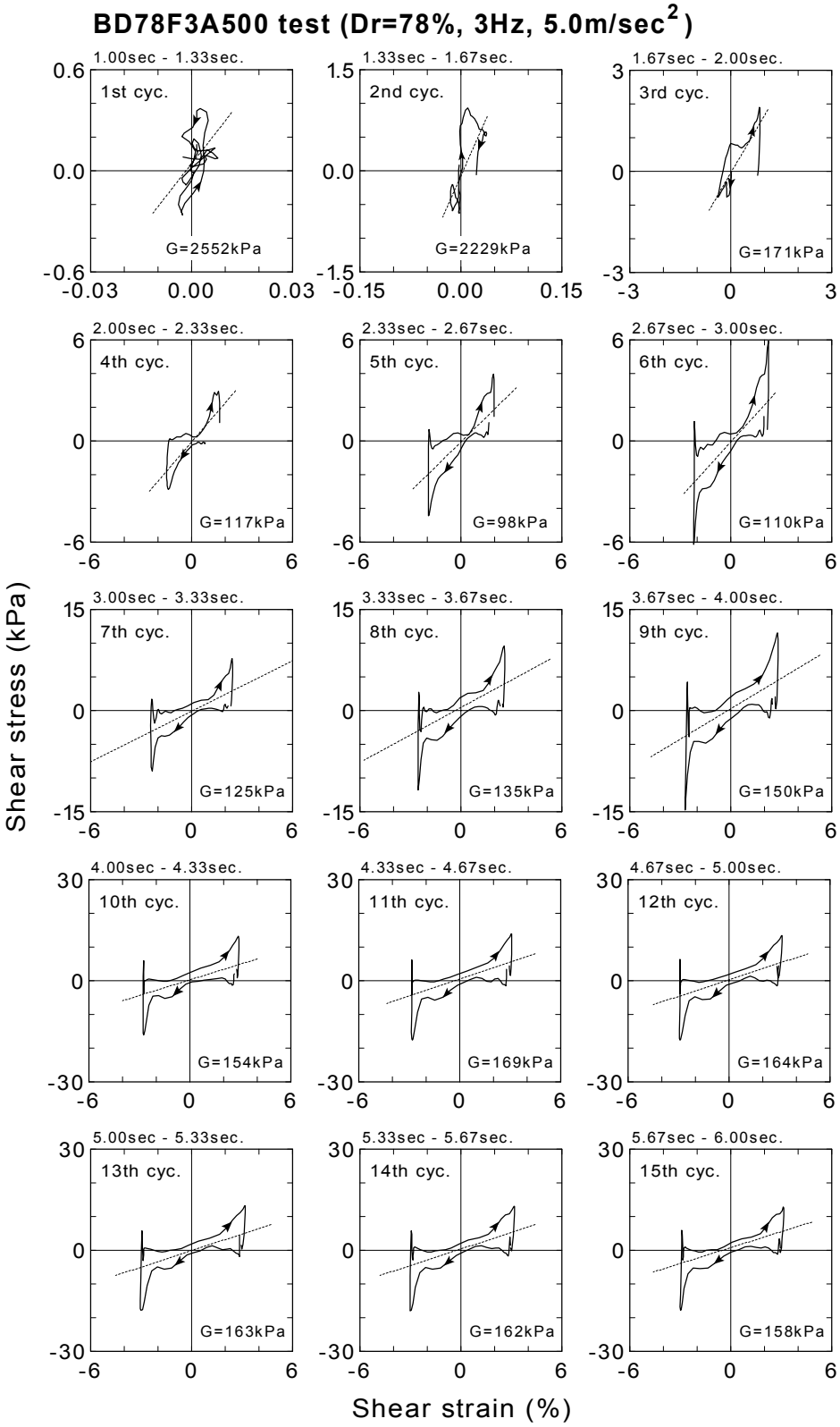

Fig.4.111: Stress-strain relationship of each cycle and calculated shear modulus (BD78F3A500 test, 1～15 cycles)

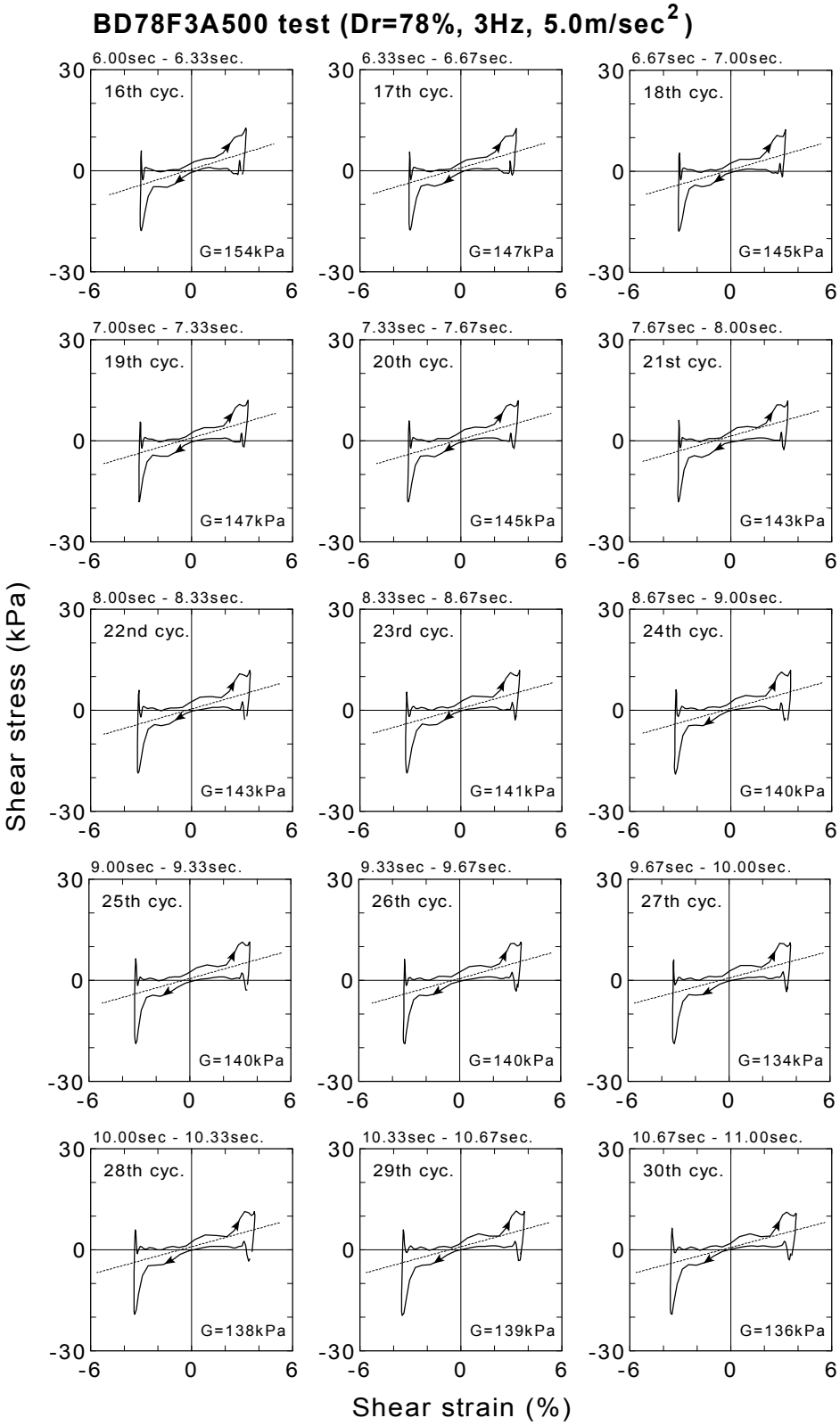

Fig.4.111: Continued (BD78F3A500 test, 16～30 cycles)

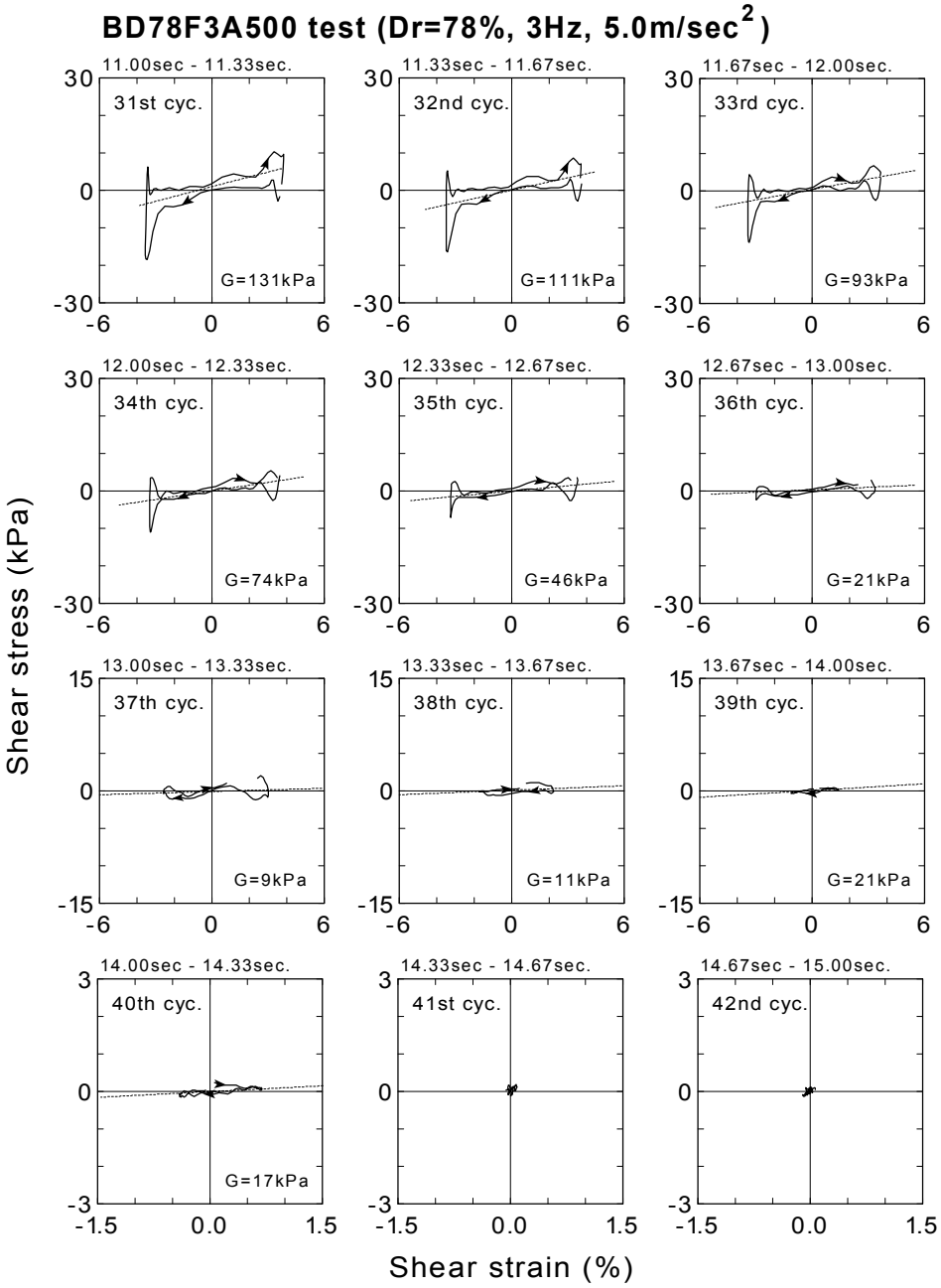

Fig.4.111: Continued (BD78F3A500 test, 31～42 cycles)

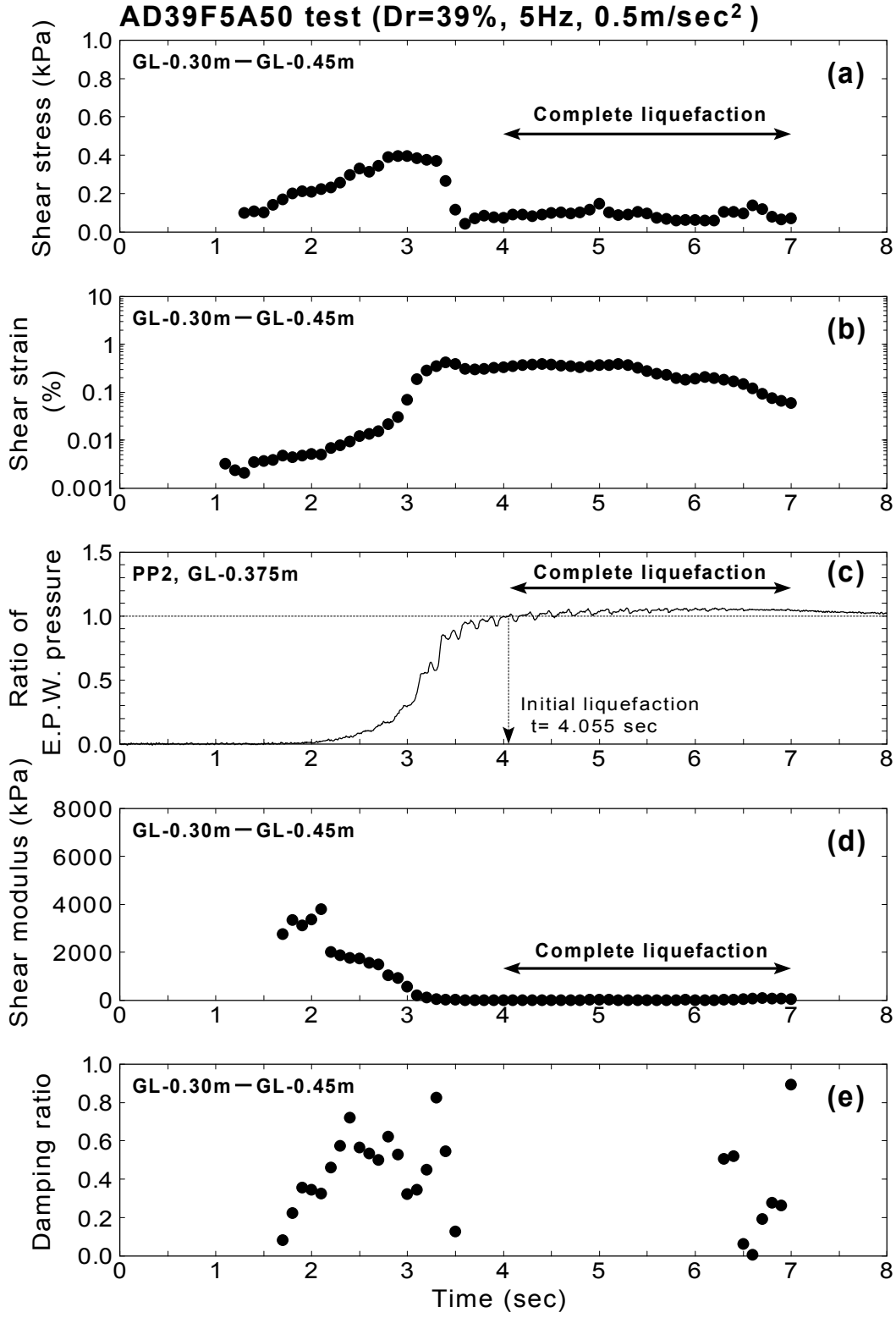

Fig.4.112: Change of shear modulus and damping ratio with respect to time (AD39F5A50 test)

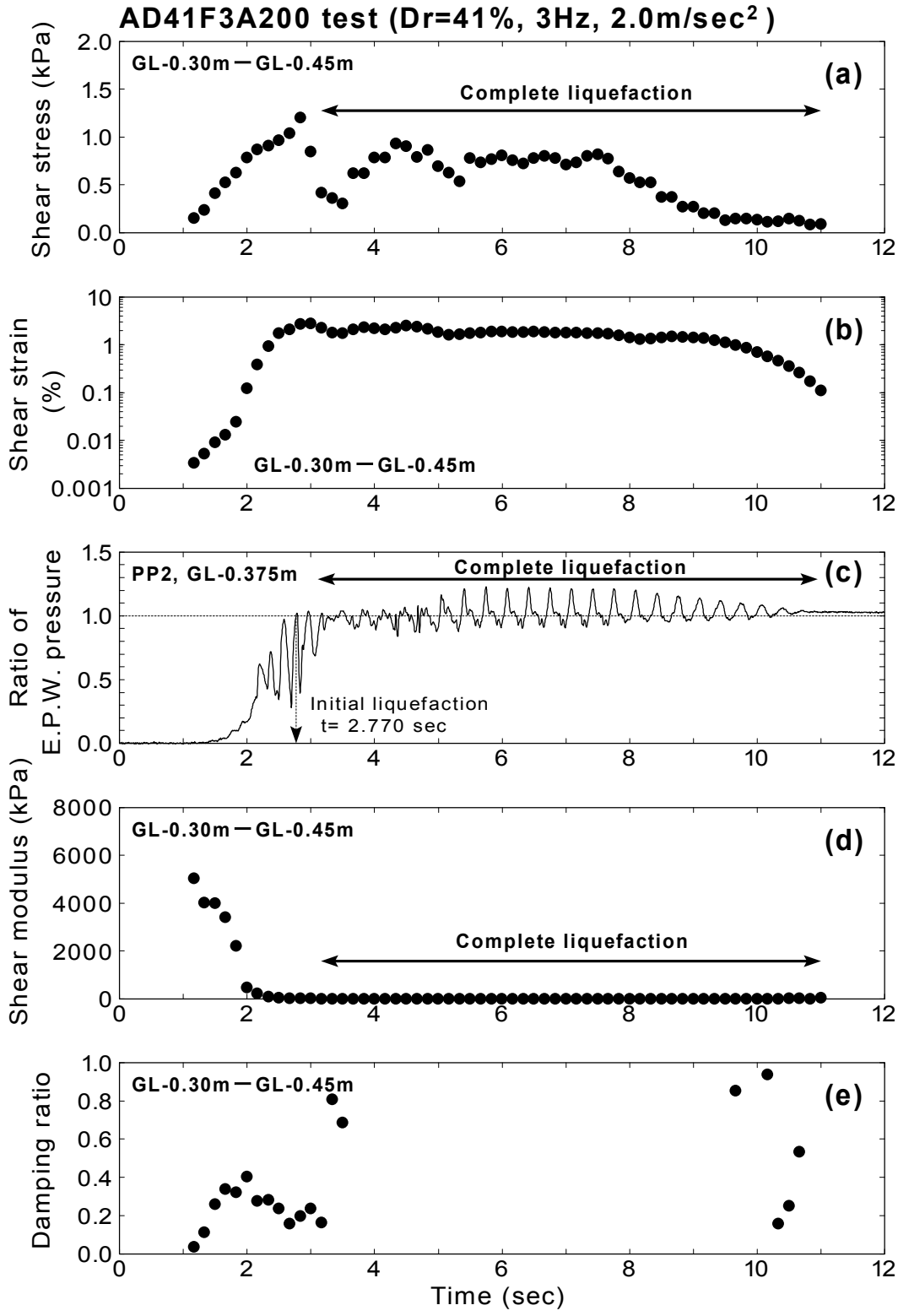

Fig.4.113: Change of shear modulus and damping ratio with respect to time (AD41F3A200 test)

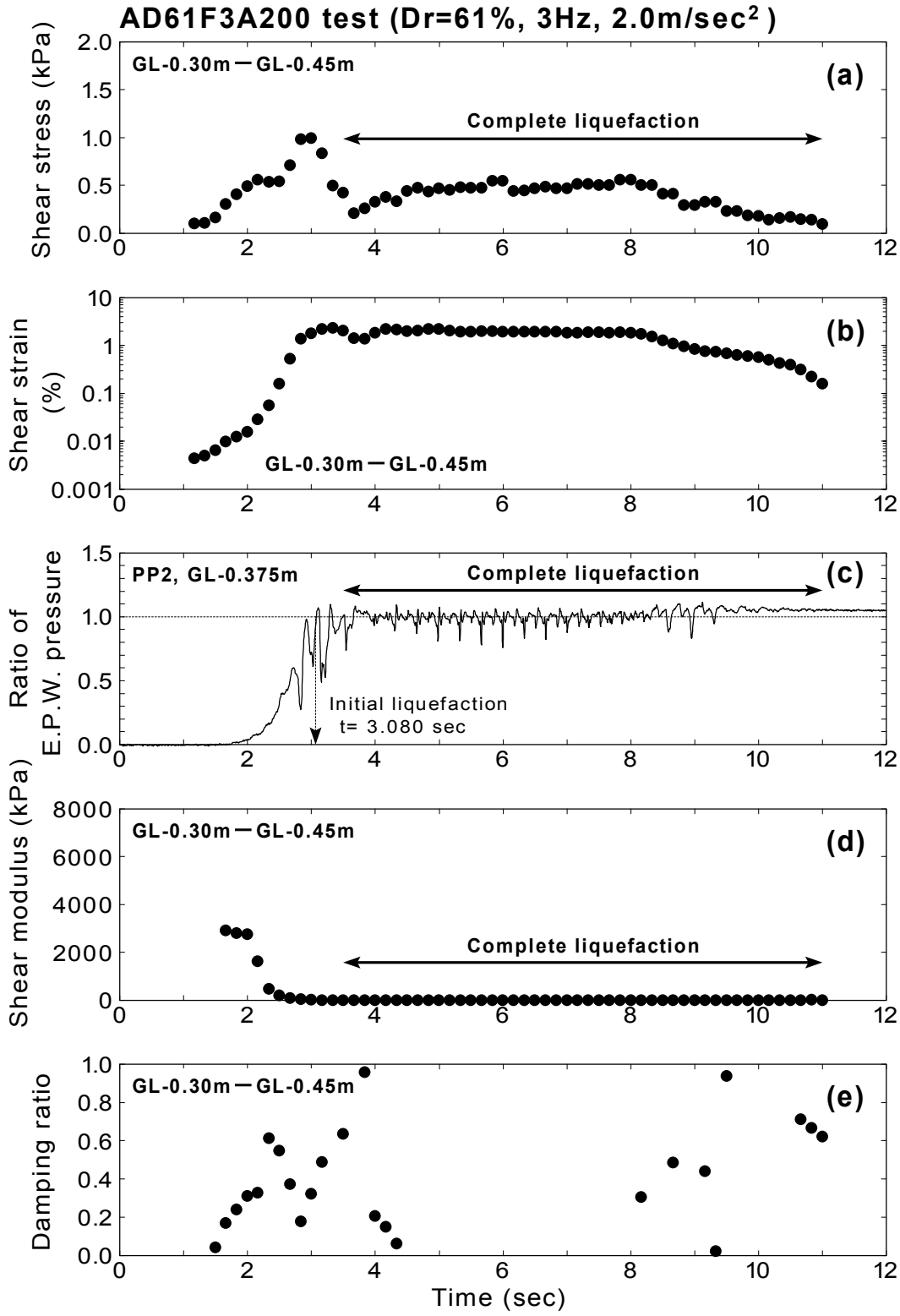

Fig.4.114: Change of shear modulus and damping ratio with respect to time (AD61F3A200 test)

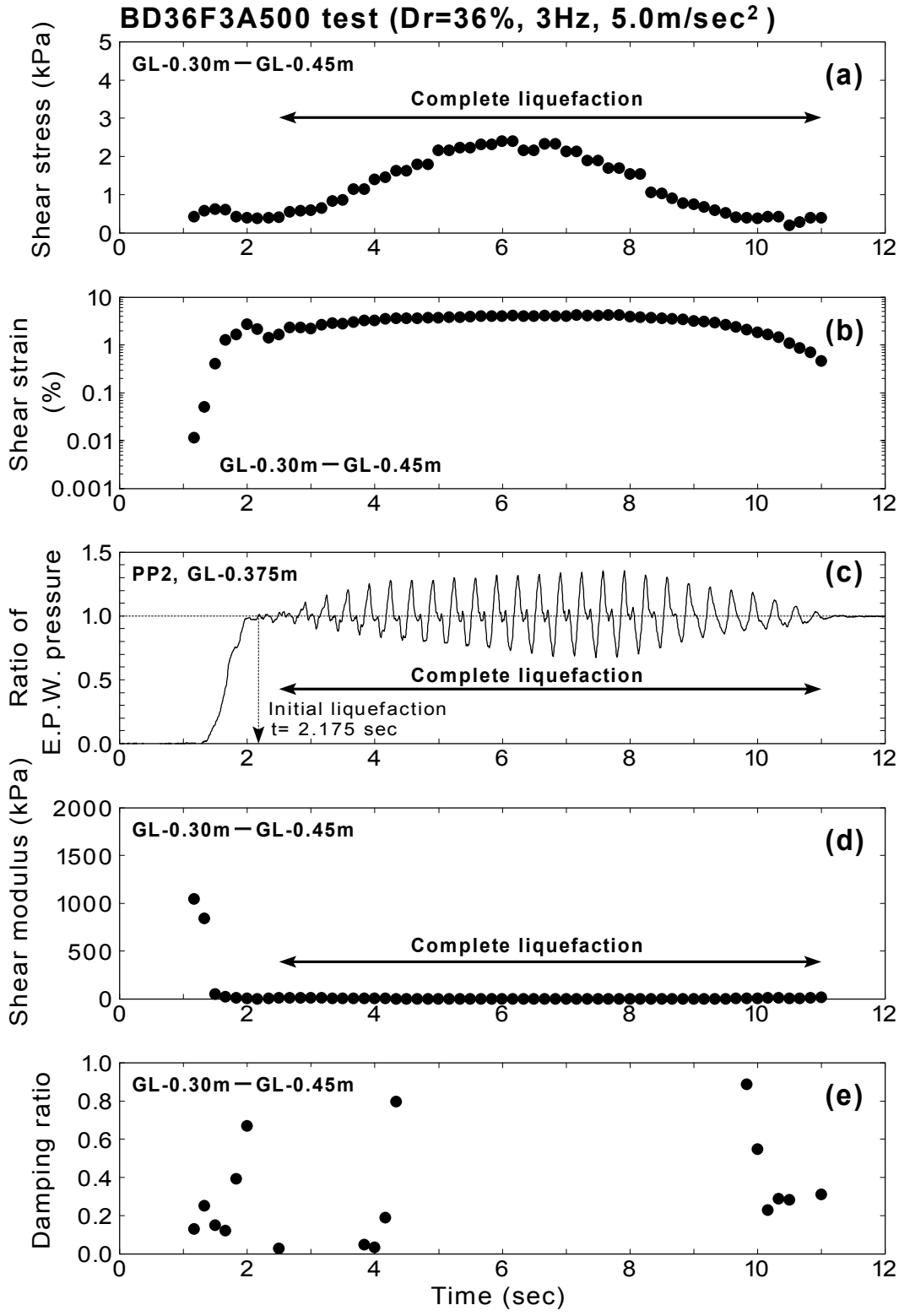

Fig.4.115: Change of shear modulus and damping ratio with respect to time (BD36F3A500 test)

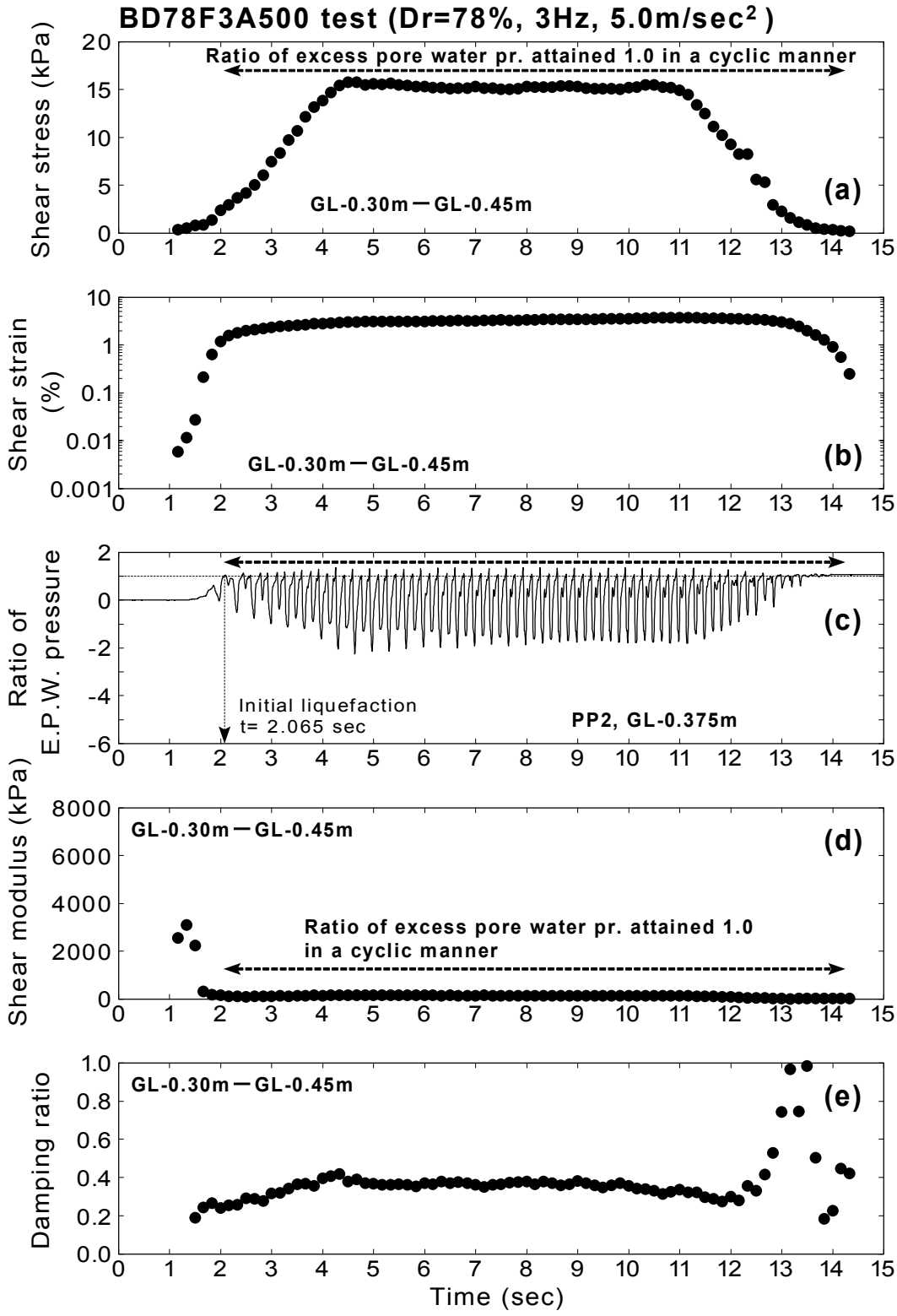

Fig.4.116: Change of shear modulus and damping ratio with respect to time (BD78F3A500 test)

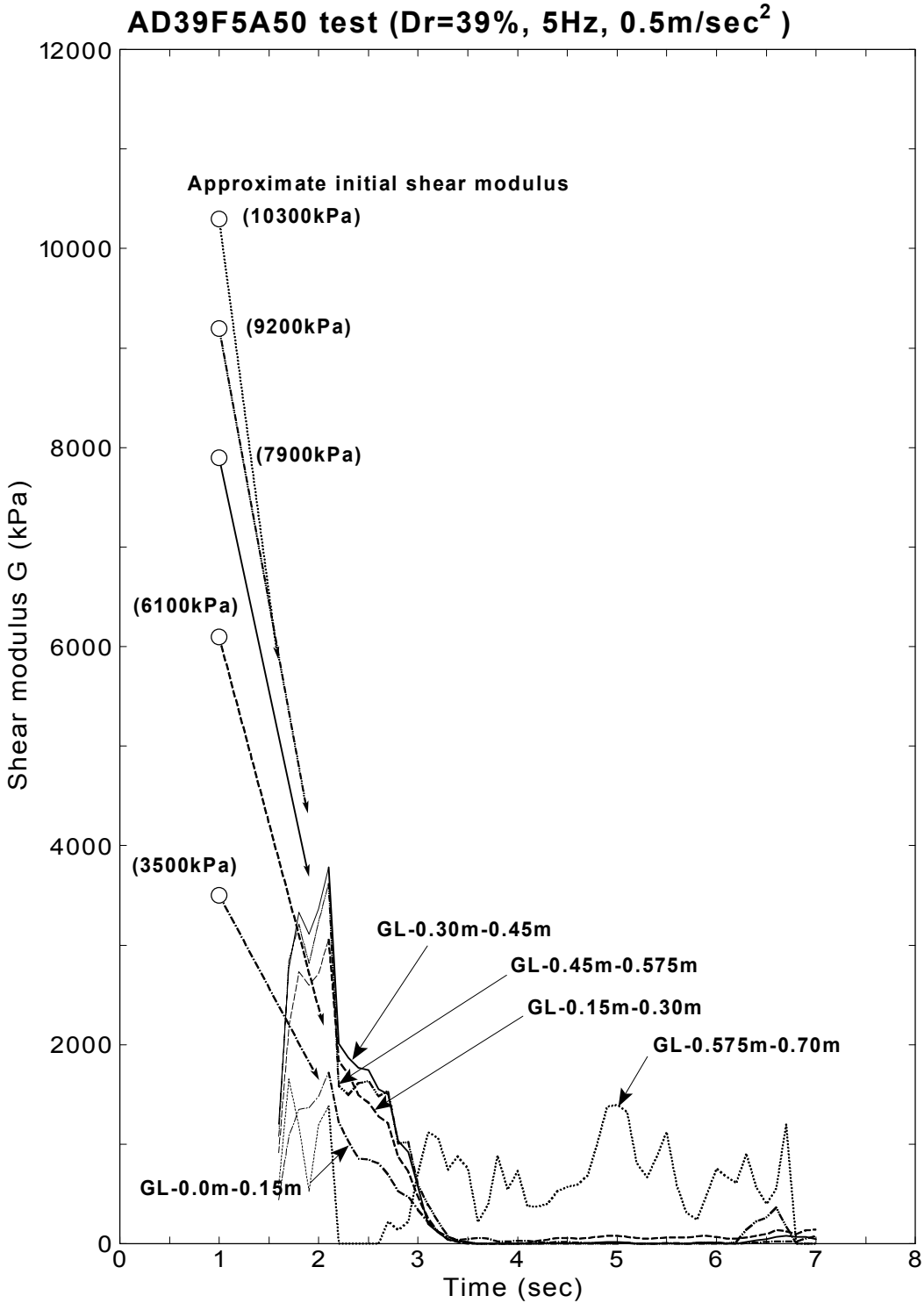

Fig.4.117: Change of shear modulus with time at each depth (AD39F5A50 test)

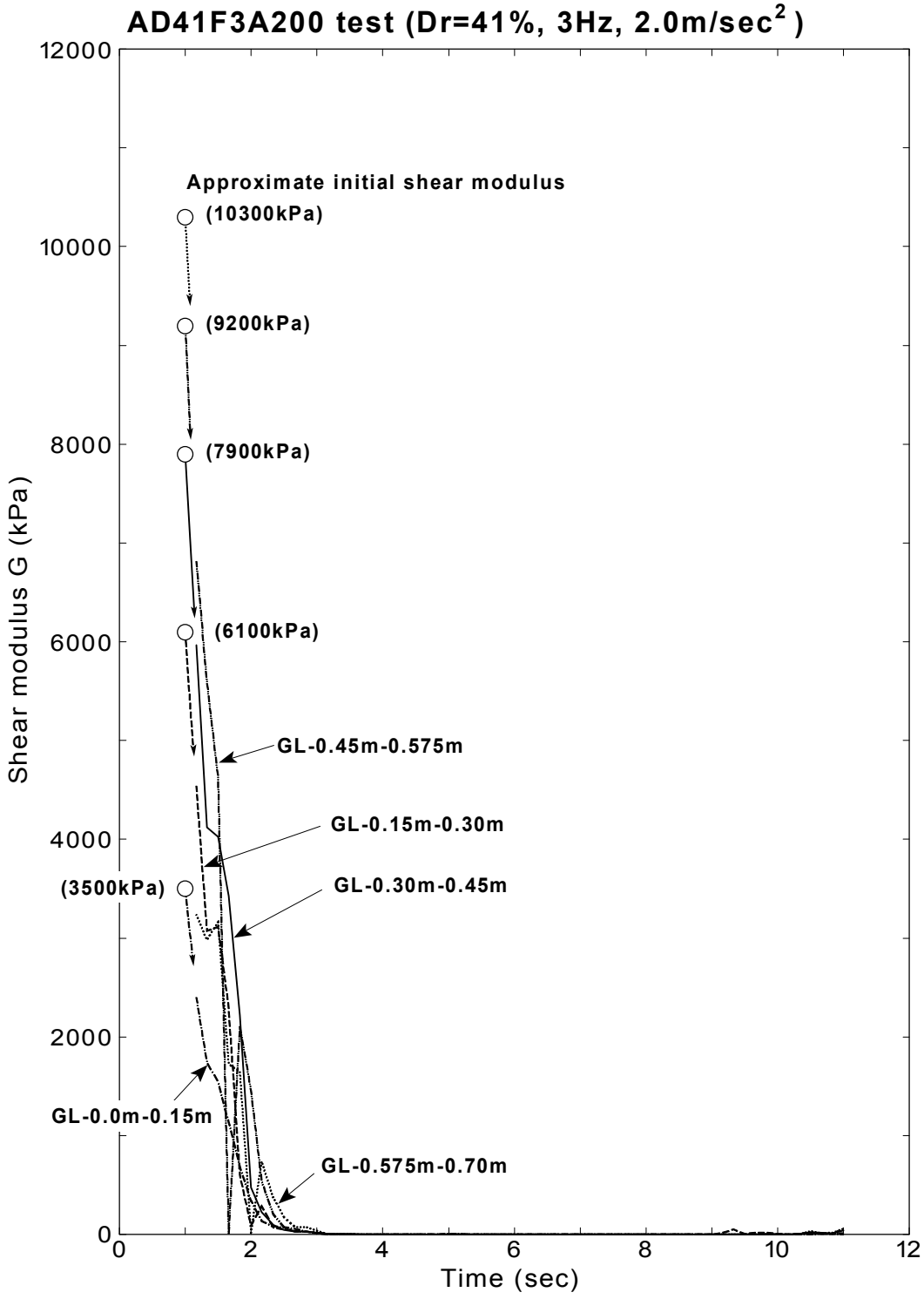

Fig.4.118: Change of shear modulus with time at each depth (AD41F3A200 test)

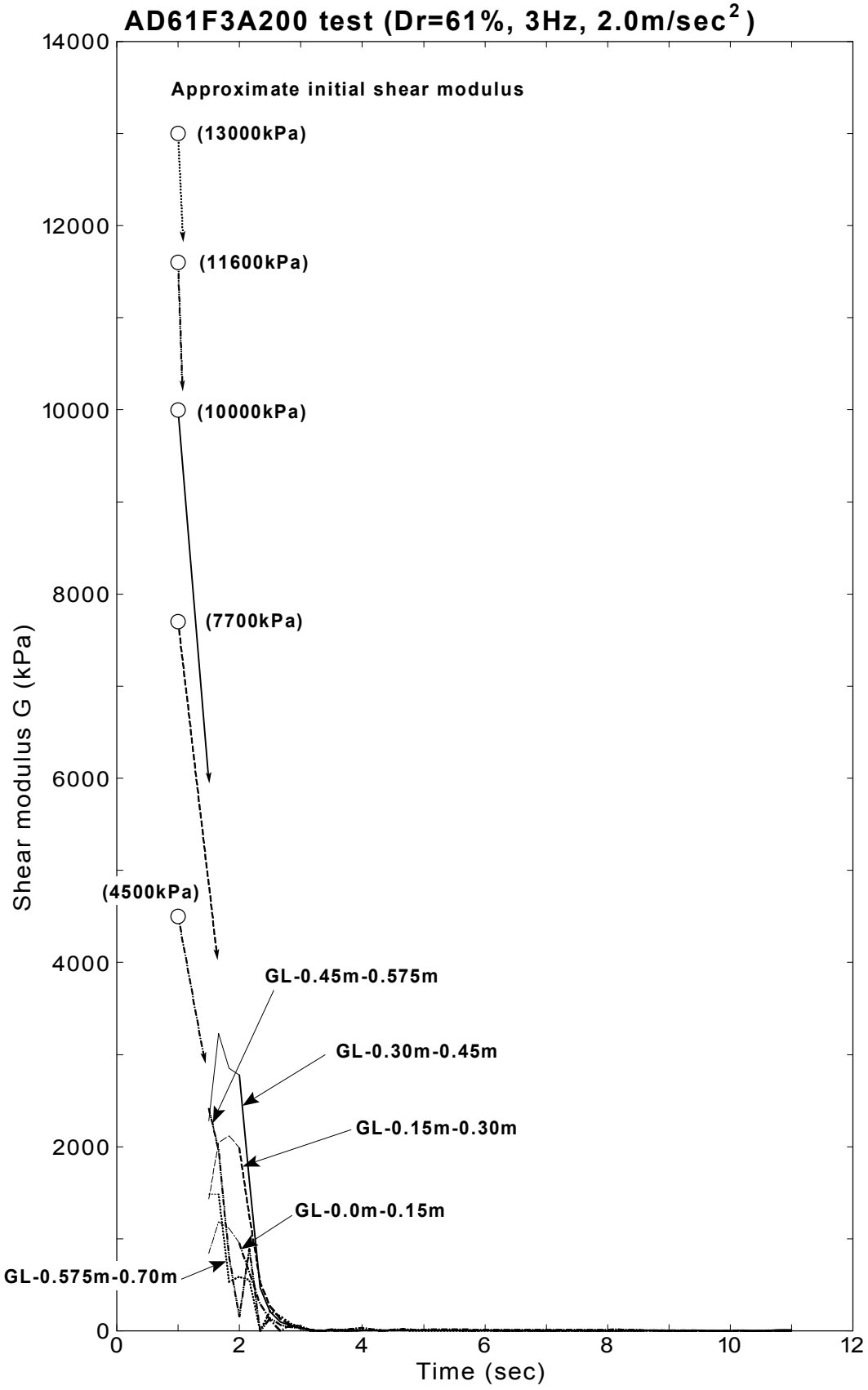

Fig.4.119: Change of shear modulus with time at each depth (AD61F3A200 test)

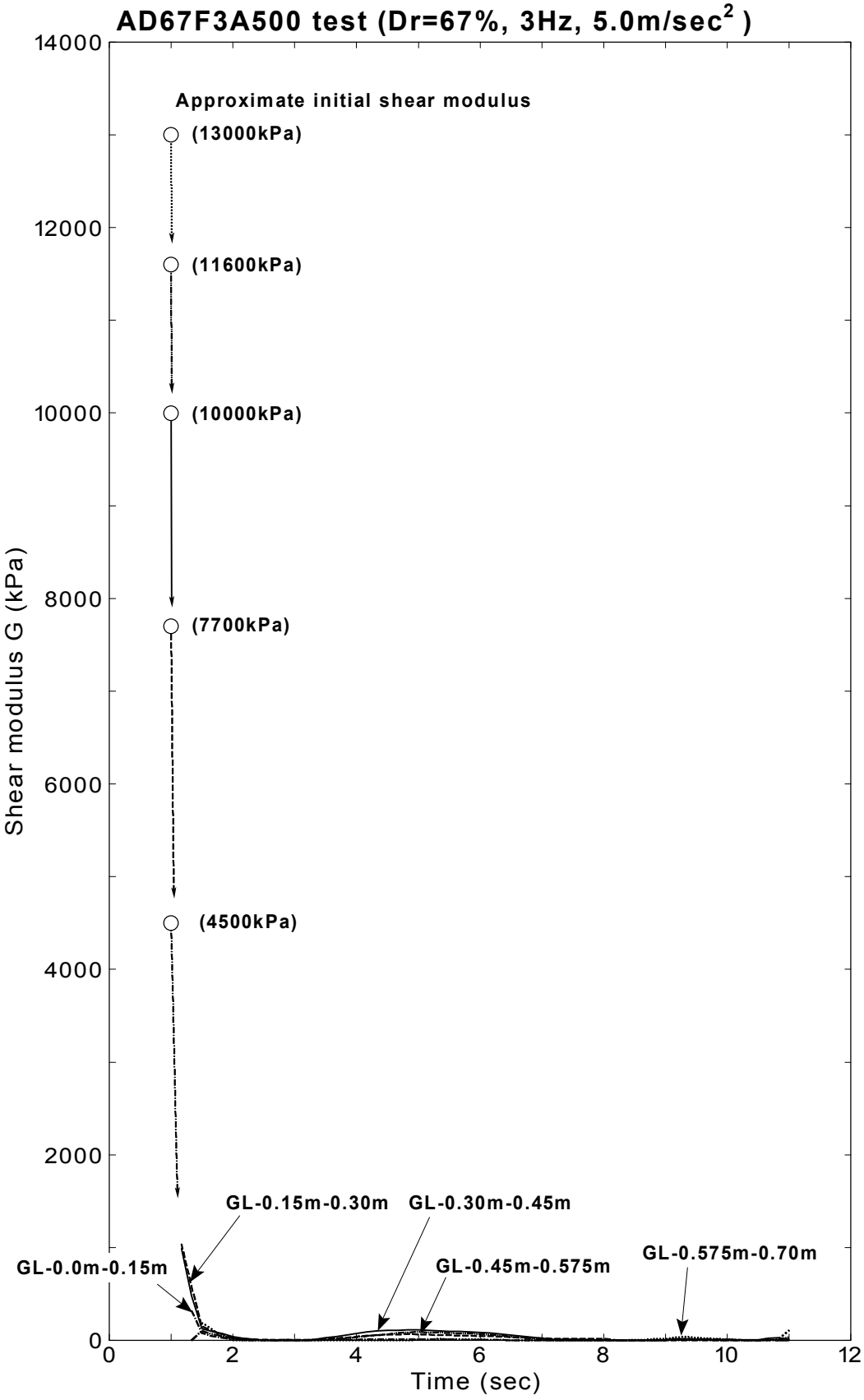

Fig.4.120: Change of shear modulus with time at each depth (AD67F3A500 test)

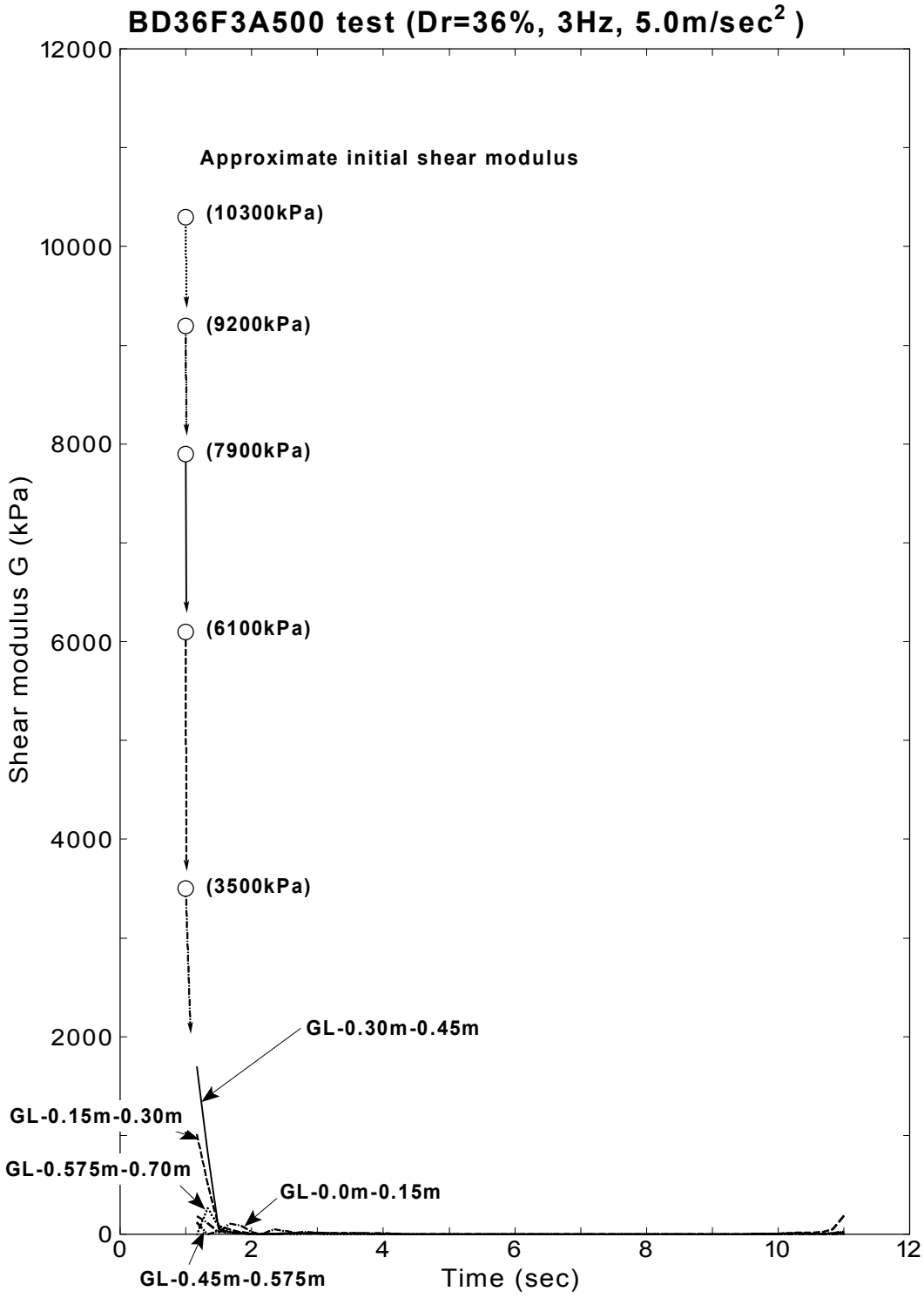

Fig.4.121: Change of shear modulus with time at each depth (BD36F3A500 test)

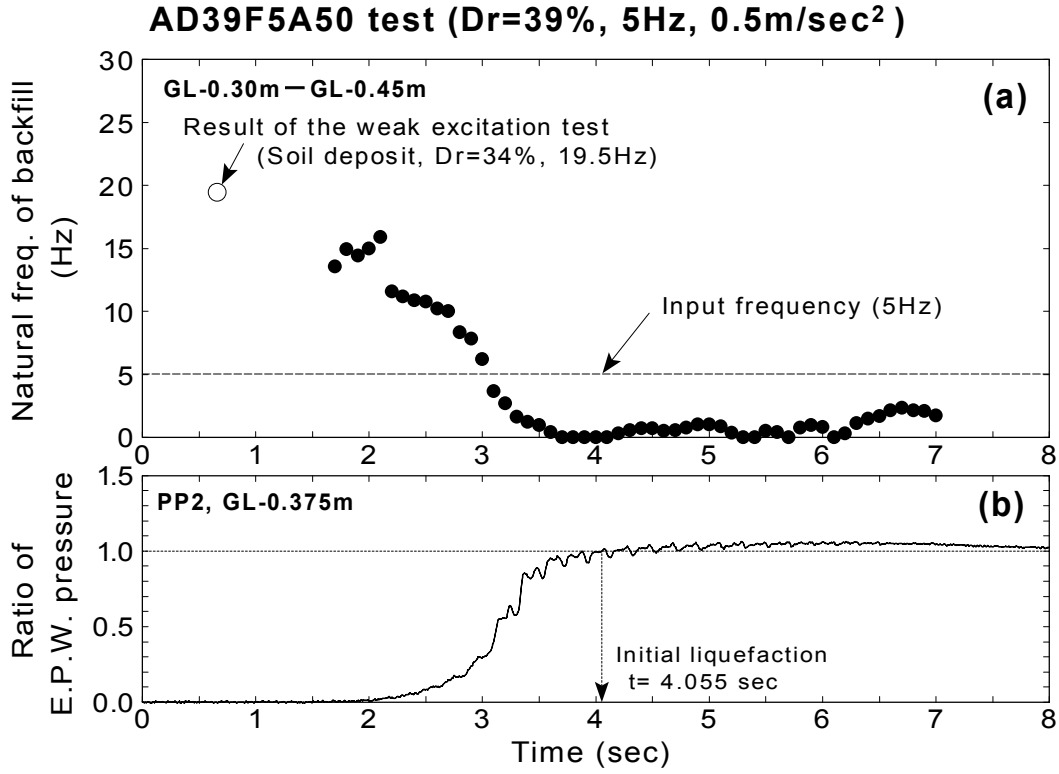

Fig.4.122: Change of natural frequency of backfill (AD39F5A50 test)

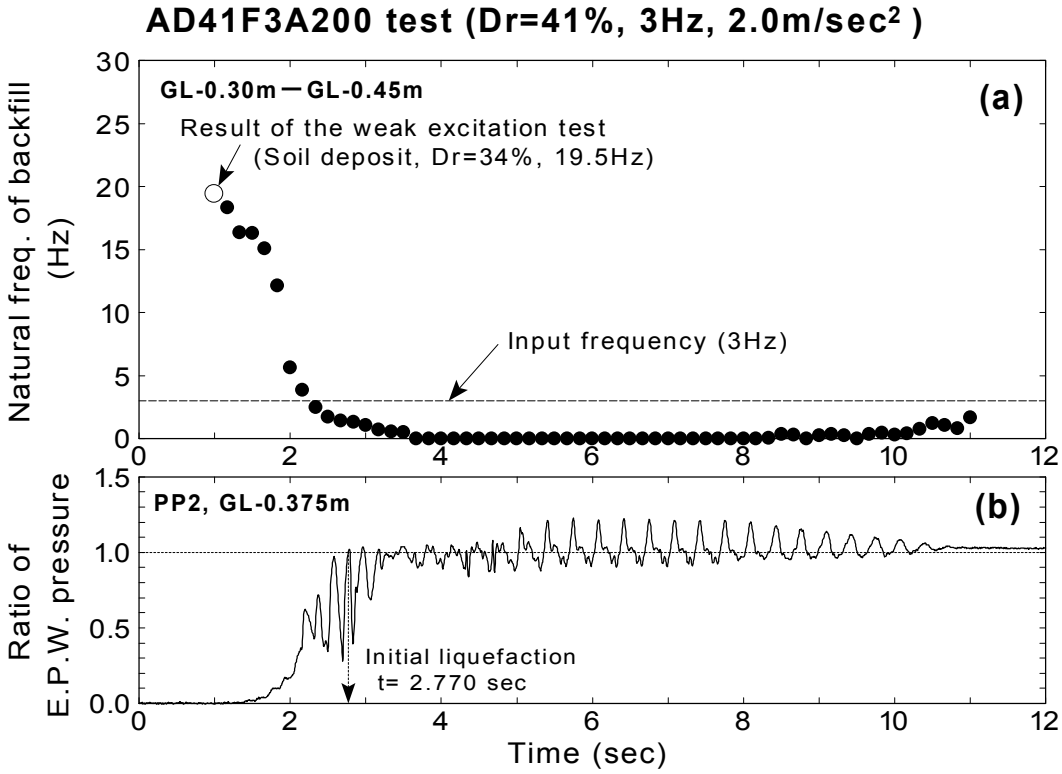

Fig.4.123: Change of natural frequency of backfill (AD41F3A200 test)

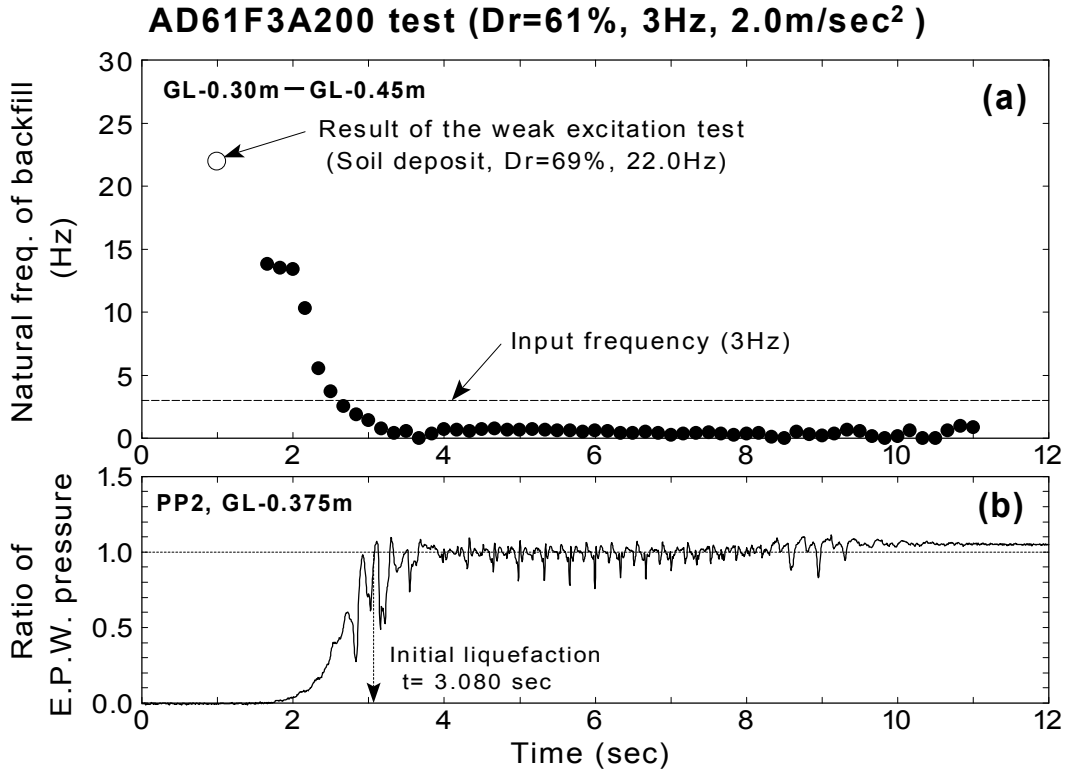

Fig.4.124: Change of natural frequency of backfill (AD61F3A200 test)

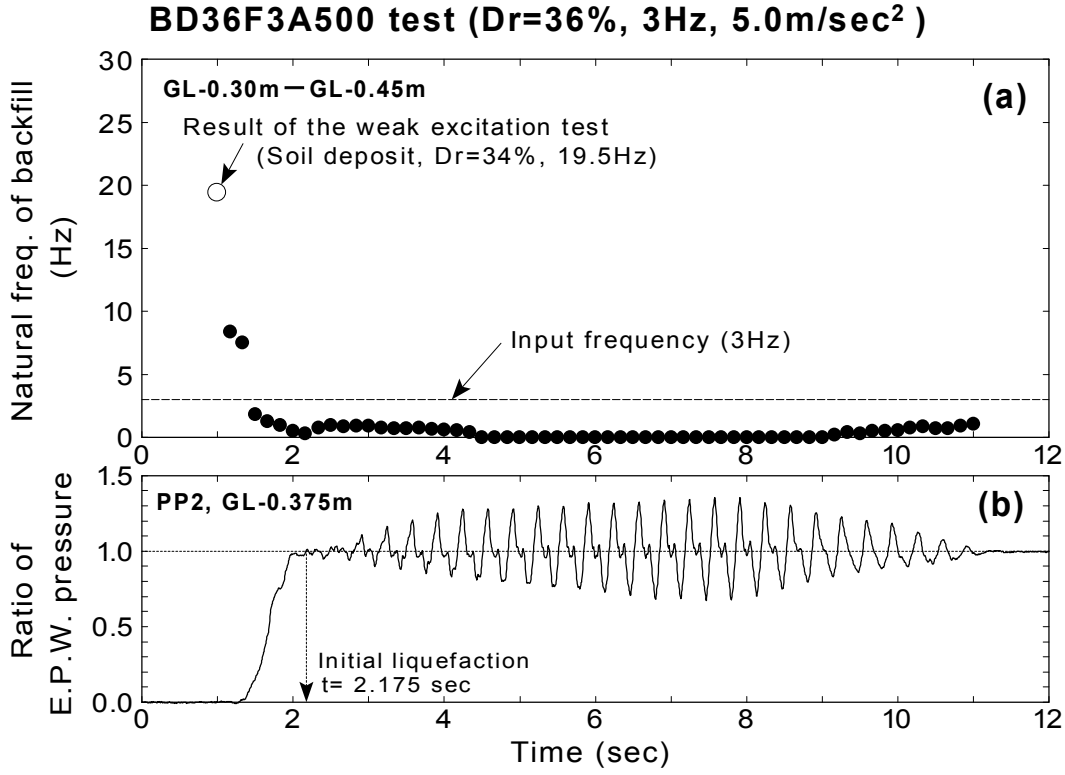

Fig.4.125: Change of natural frequency of backfill (BD36F3A500 test)

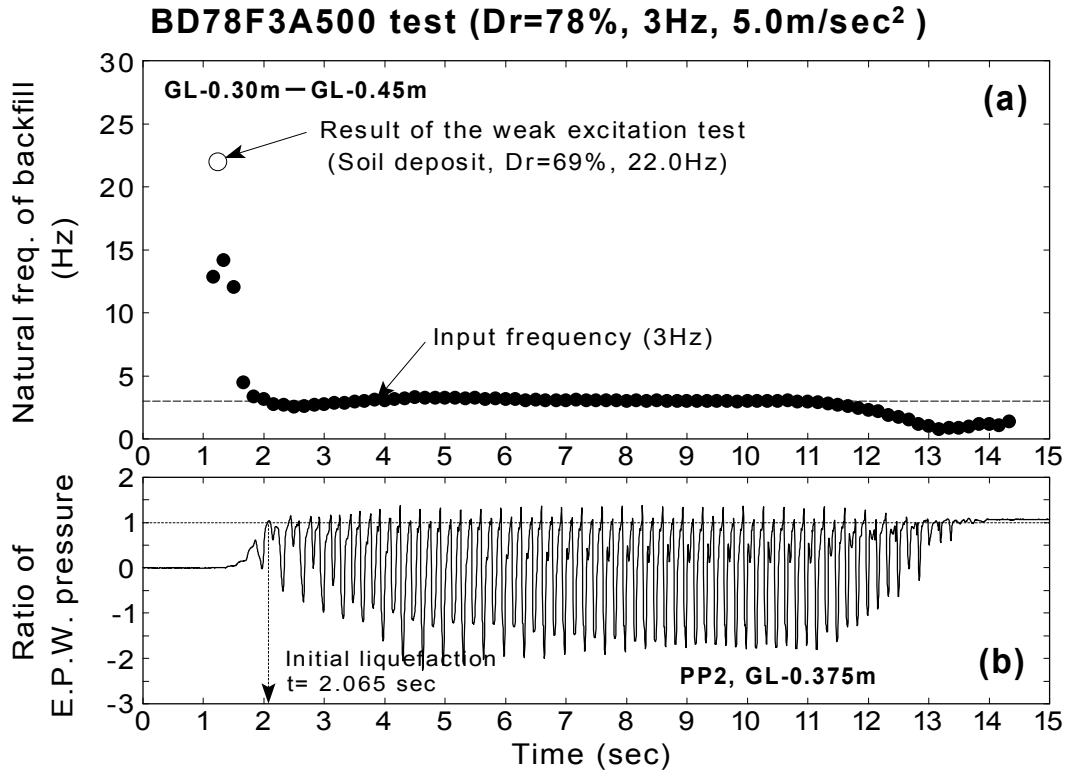

Fig.4.126: Change of natural frequency of backfill (BD78F3A500 test)

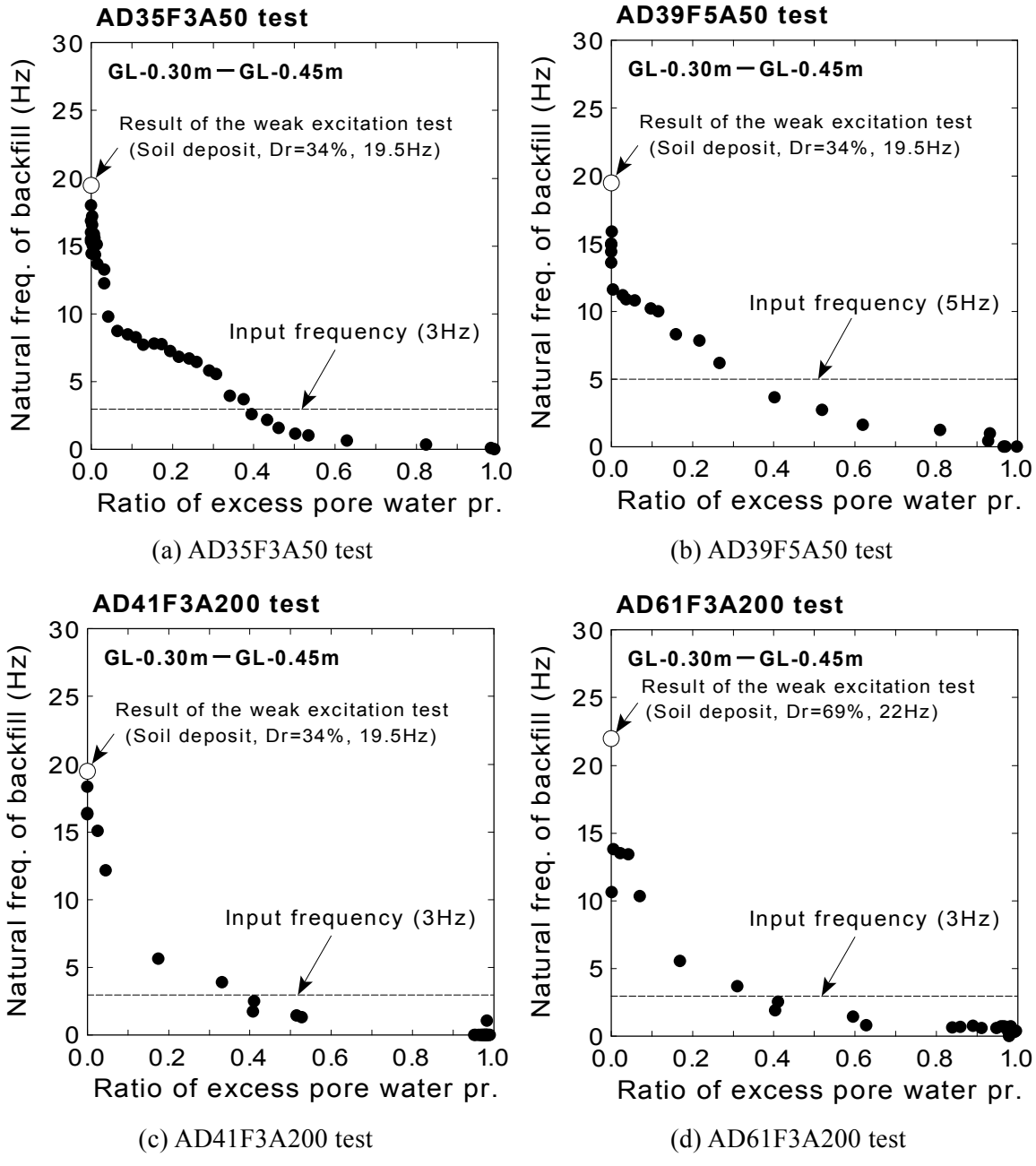

(a) AD35F3A50 test

(b) AD39F5A50 test

(c) AD41F3A200 test

(d) AD61F3A200 test

Fig.4.127: Change of natural frequency of backfill with respect to pore pressure ratio

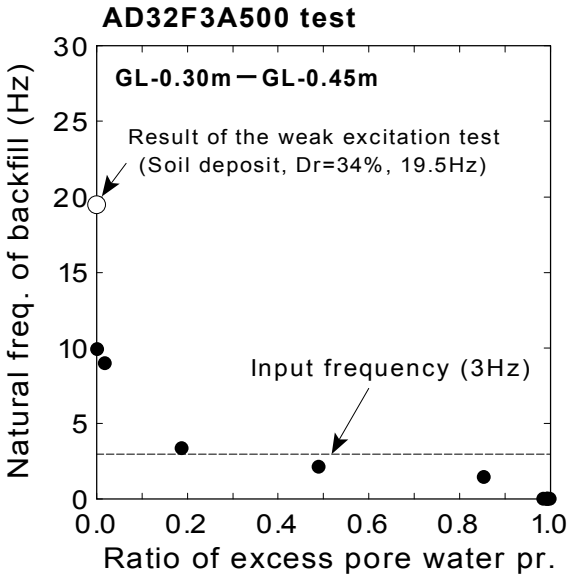

(e) AD32F3A500 test

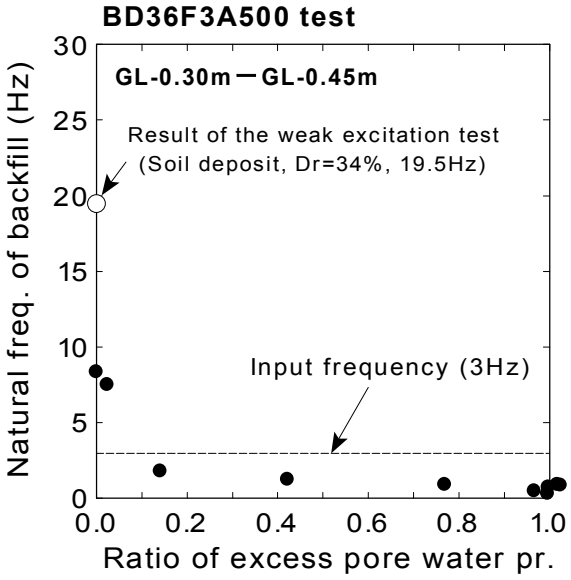

(f) BD36F3A500 test

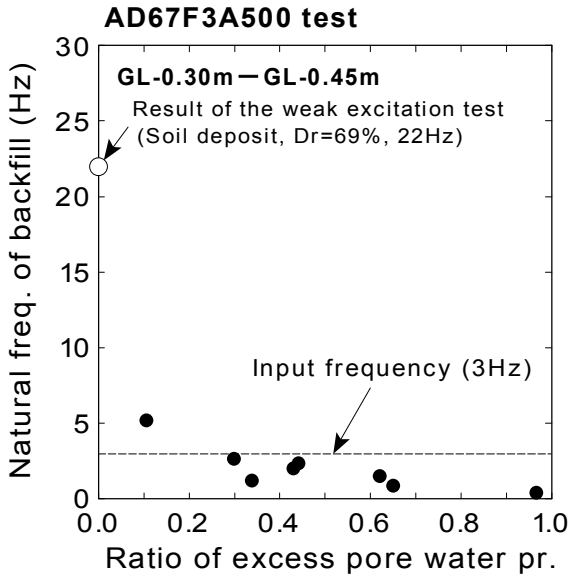

(g) AD67F3A500 test

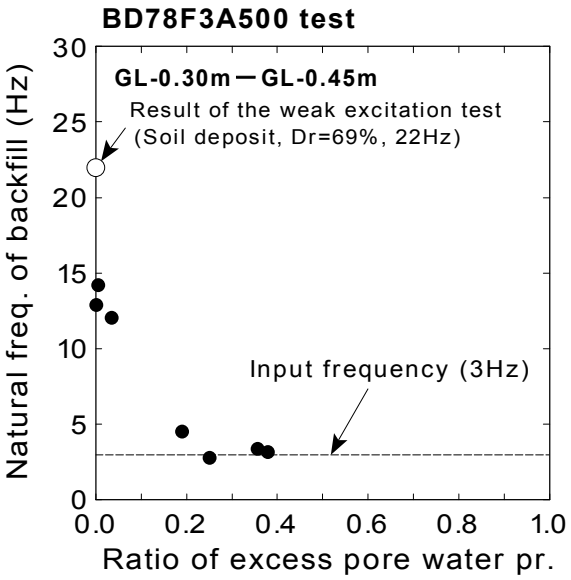

(h) BD78F3A500 test

Fig.4.127: Continued

Chapter 5

RESPONSE CHARACTERISTICS OF UNDERGROUND STRUCTURE

5.1 GENERAL REMARKS

In this chapter, the amplification and the phase difference of acceleration between the top and the bottom of the structure will be analyzed precisely. In this respect, a relationship between the amplification of acceleration at the structure and the natural frequency/period of the backfill during shaking, which were calculated in Chapter 4, will be derived experimentally in order to examine its effect on the response characteristics of an embedded structure in a liquefiable backfill during earthquakes.

The analysis will be focused on the responses before and after the initial liquefaction of backfill. Since it is observed in Chapter 4 that the shear modulus of backfill is reduced significantly before the initial liquefaction, the occurrence of resonance will be examined at the period. An effect of dilative behavior of dense backfill on the response of the structure will be shown in distinction from liquefaction of contractive loose backfill.

5.2 ACCELERATION RESPONSE OF STRUCTURE

5.2.1 Acceleration responses at the top and the bottom of the structure

One of the key studies is analysis of the response of the embedded structure such as amplification and the phase difference of the acceleration between the top and the bottom of the structure during shaking. Fig.5.1 illustrates the measured accelerations at the top (AC2) and the bottom (AC1) of the structure and the ratio of excess pore water pressure in the backfill (PP2) from AD35F3A50 test.

The locations of the transducers are shown in the inset of Fig.5.1. Since the bottom part of the structure that is made of a thick aluminum alloy plate (t= 150 mm) is tightly fixed on the bottom of the container, the acceleration at the stem of the wall of the structure is regarded identical to the acceleration on the shaking table (AC1). Thus, the acceleration on the shaking table (AC1) is referred to as the acceleration at the bottom of the structure.

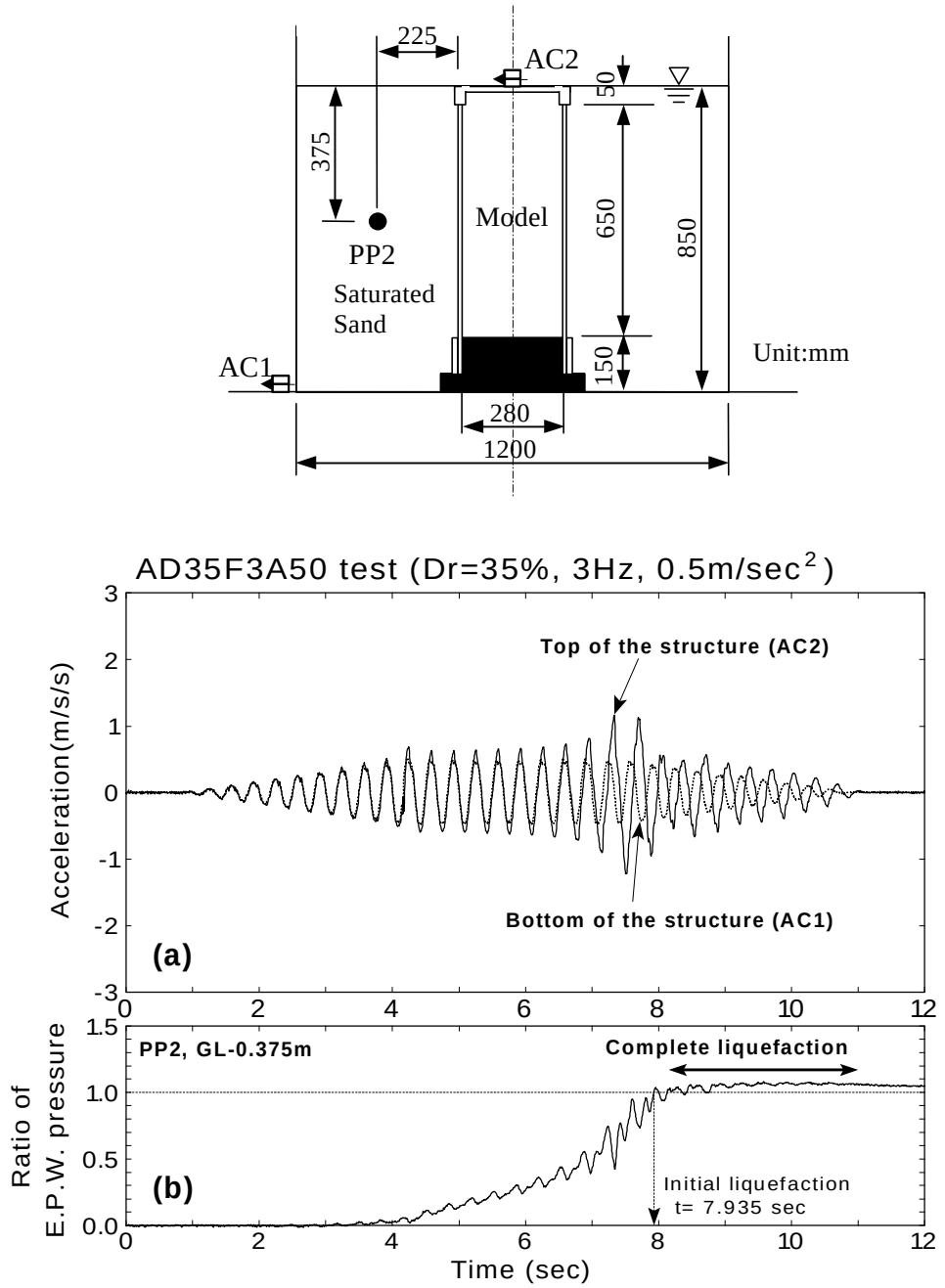

Fig.5.1: Typical results of acceleration of structure and pore pressure ratio in backfill

It was seen in Fig.5.1 that the acceleration at the top of the structure was in-phase with the acceleration at the bottom from 1 to 4 seconds when the excess pore water pressure did not develop yet. It suggests that the structure translated in the horizontal direction with the hard backfill. The ratio of excess pore water pressure rose from 0.05 to about 0.3 between 4 and 6 seconds, and in the mean time, the amplitude of acceleration at the top was slightly amplified while the phase difference between them was not significant.

The time history of accelerations (AC1 and AC2) between 6.2 and 7.2 seconds when the ratio of excess pore water pressure changed from 0.3 to 0.6 are shown in Fig.5.2(a) with an enlarged time axis. The amplifications and the time differences between the peaks are indicated in the figure. It is observed that the amplification, which was 1.47 at the peak of around 6.6 seconds, increased up to 1.65 in the next cycle. The time difference, being 0.02 seconds at around 6.6 seconds, also became as large as 0.04 seconds in the next cycle.

Fig.5.2(b) illustrates the time history of accelerations between 7.0 and 8.0 seconds. The excess pore water pressure increased from 0.6 up to 1.0 during the period. The amplification became as much as 2.42, and the time difference increased up to 0.115 seconds at around 7.25 seconds. Fig.5.2(c) further depicts the accelerations between 8.0 and 9.0 seconds when the pore pressure ratio was maintained at 1.0. It is observed that the amplification dropped about 1.7 at 8.2 seconds and the time difference between two cycles was about 0.13 seconds in both cycles. It is known that time difference of quarter period corresponds to that of the resonance. Considering that the time difference of 0.13 seconds is larger than that of quarter period of 0.083 seconds (=0.33 seconds / 4), the resonance of the structure already had occurred. It suggests that the generation of the excess pore water pressure of backfill causes the change of amplifications and time differences of accelerations between the top and the bottom of the embedded structure.

5.2.2 Amplification and phase difference of accelerations

The amplification and the phase difference of accelerations between the top and the bottom of the structure were calculated at each half cycle of sinusoidal input motion. The amplification was defined as the ratio of the maximum absolute values of accelerations in a half cycle. The amplification in the *i*-th half cycle is expressed as

$$Amp._{,i} = \frac{\left|a_{top,i}\right|_{,\max}}{\left|a_{bottom,i}\right|_{,\max}} \tag{5.1}$$

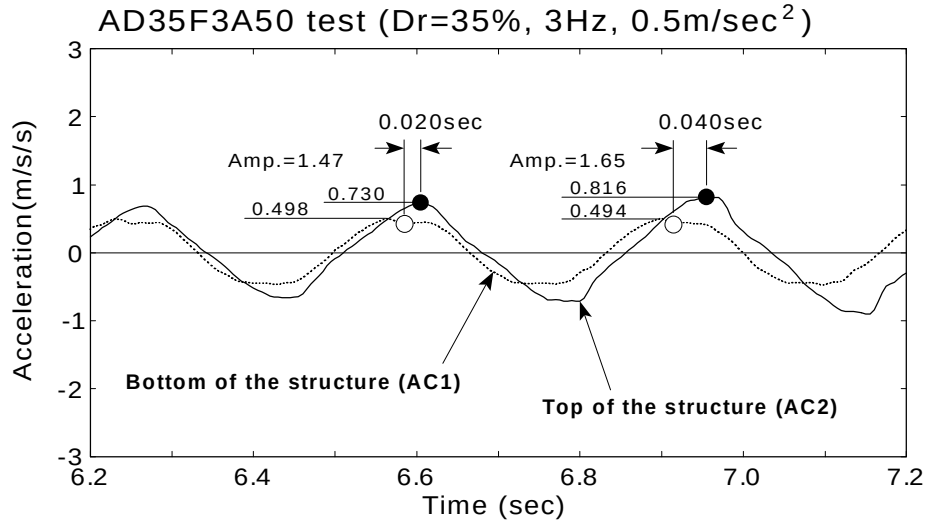

(a) Pore pressure ratio 0.3～0.6 (6.2sec～7.2sec)

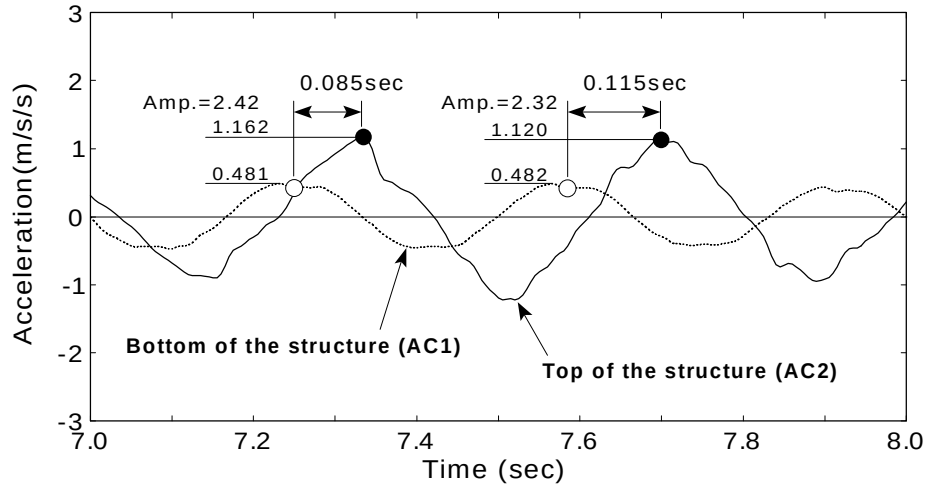

(b) Pore pressure ratio 0.6～1.0 (7.0sec～8.0sec)

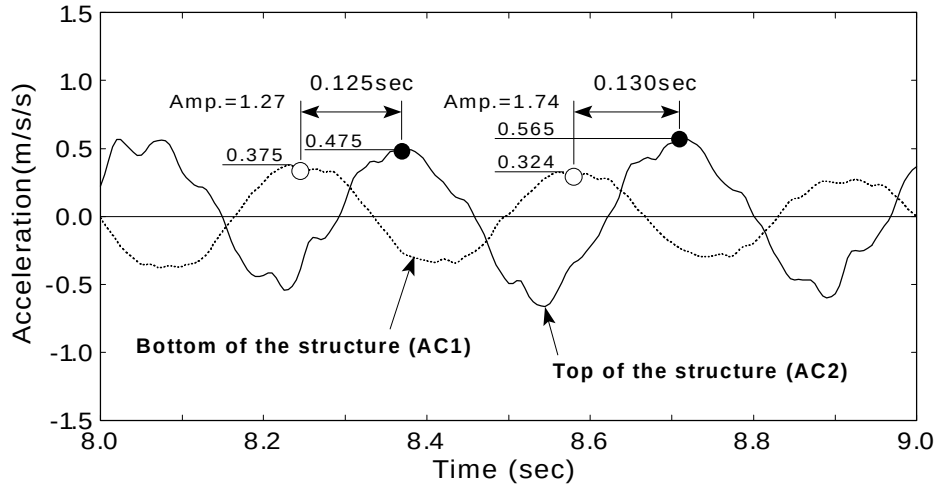

(c) Pore pressure ratio 1.0 (8.0sec～9.0sec)

Fig.5.2: Amplification and phase difference of accelerations at each pore pressure ratio

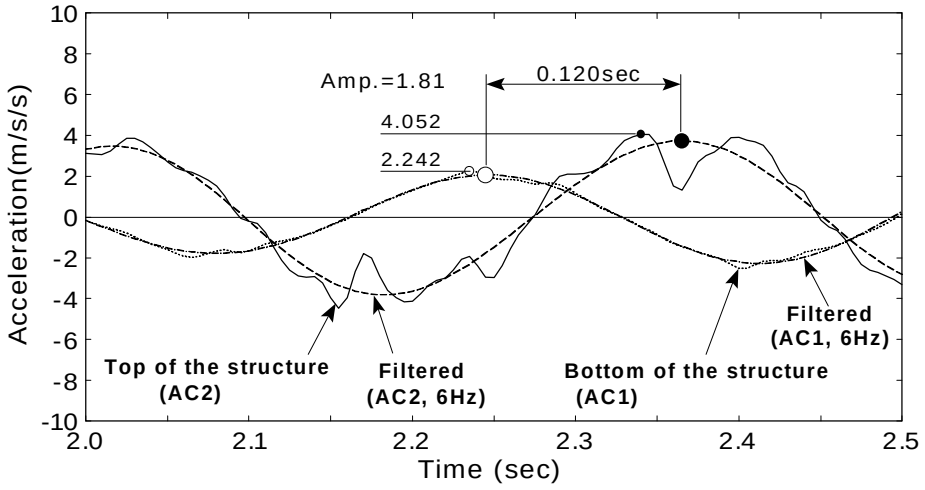

Fig.5.3: Time history of acceleration at the top and the bottom of the structure (AD67F3A500 test)

where $\alpha_{top,i}$ is the acceleration at the top of the structure in the *i*-th half cycle, and $\alpha_{bottom,i}$ at the bottom of the structure. The phase difference is calculated as

$$q_i = \frac{t_{top,peak,i} - t_{bottom,peak,i}}{T} \times 360 \quad (\deg.) \tag{5.2}$$

where $t_{top,peak,i}$ is a time instance of occurrence of the peak acceleration at the top of the structure in the *i*-th half cycle, while $t_{bottom,peak,i}$ in the one at the bottom of the structure, and T is a period of the input excitation.

A shape of a response acceleration time history curve became complicated due to high frequency components in the test involving a dense backfill. An example of the acceleration time history that contains high frequency components from AD67F3A500 test is shown in Fig.5.3 by a solid line (AC2). To avoid difficulties in calculation of phase difference, the high frequency components were removed by a low-pass filter. An example of a filtered acceleration time history curves with a low-pass filter of 6Hz and the obtained time difference between peaks are illustrated in Fig.5.3. The low-pass filtering frequencies in this procedure were determined within 4Hz～10Hz depending on the test.

The acceleration time histories from the other tests are presented in Fig.5.19～Fig.5.32 at the end of this chapter.

5.2.3 Change of amplification and phase difference with time

Changes of amplification and phase difference of acceleration with time are illustrated in Fig.5.4. The positive peaks and the negative peaks are plotted by different symbol for distinction in those figures. The unit of phase difference is defined in degrees.

Fig.5.4(a) shows the results from AD35F3A50 test. The amplification of acceleration, being about one at the beginning of shaking, increased gradually to about 1.3 between 2 to 6 seconds. A rapid increase of amplification was observed after 6 seconds, becoming the maximum amplification of 2.6 at about 7.5 seconds. The amplification decreased suddenly to the level of 1.5 at 8 seconds. It was seen that the phase difference was 0～15 degrees up to 6 seconds and became larger quickly to the maximum of about 150 degrees after that. It maintained more or less the same level during 8.5～11 seconds. It is noted that the phase difference at the time instance of peak acceleration was about 90 degrees, suggesting the occurrence of resonance in the structure.

The results from AD39F5A50 test are shown in Fig.5.4(b). It was observed that the amplification, increasing gradually from the beginning of the shaking, became the maximum of 1.5 at about 3.2 seconds. Then, it decreased the level of less than 1.0 just after the peak. The phase difference of initially zero started to change at 3 seconds and reached about 140 degrees after 3.2 seconds when the amplification became the maximum.

Fig.5.4(c) and (d) depicts the results from AD41F3A200 test and AD61F3A200 test. Only the relative density of backfill was different in the test condition between them. It was observed that the amplification reached the maximum at about 2.6 seconds in AD41F3A200 test, while about 3 seconds in AD61F3A200 test. It was imagined that the denser backfill of 61% relative density took more time to liquefy under the same shaking condition than the backfill of 41% relative density, causing the delay of time when the maximum amplification occurs. The phase difference quickly increased from zero to about 140 degrees when the peak amplification occurred in both tests. It kept the same value during shaking after that.

The results from AD32F3A500 test and BD36F3A500 test are illustrated in Fig.5.4(e) and (f), respectively. Structure-A (natural frequency: 7.8Hz, tensile strength of material: 146MPa) was used in the former test, and Structure-B (Natural frequency: 7.3Hz, Tensile strength of material: 86MPa) in the latter test. The other test conditions were same. It was seen in the former test that the amplification increased as soon as the shaking started at 1 second and achieved the peak at around 1.8 seconds. It decreased once and gradually increased again as the excitation continued.

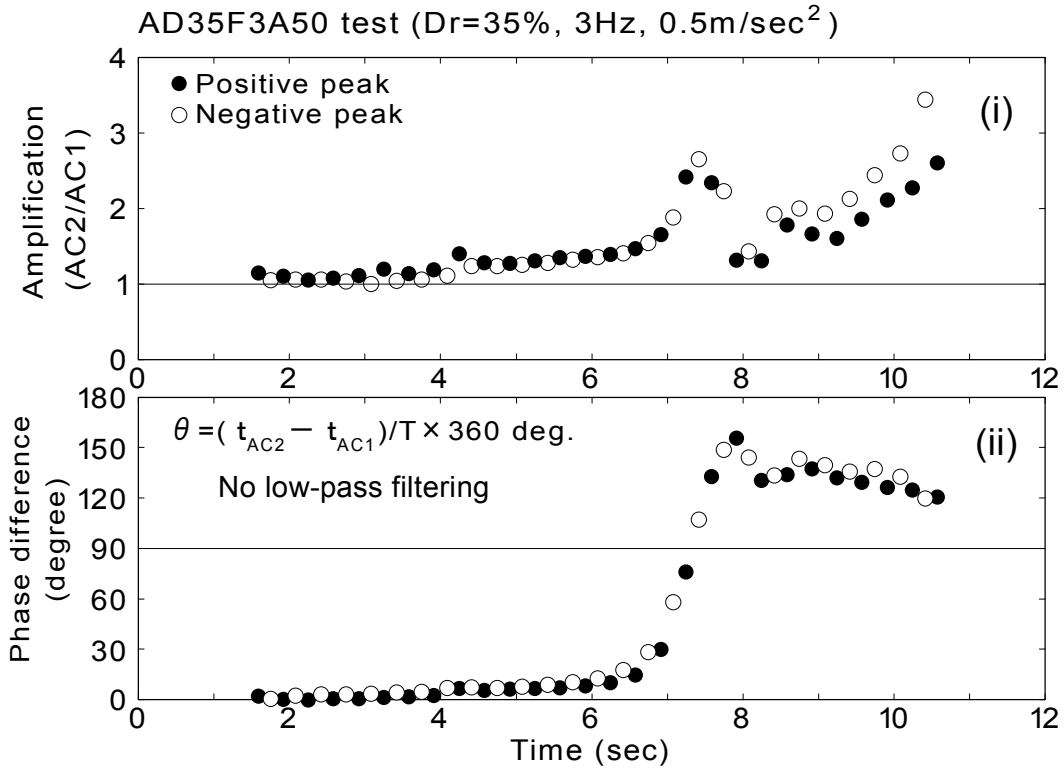

(a) AD35F3A50 test

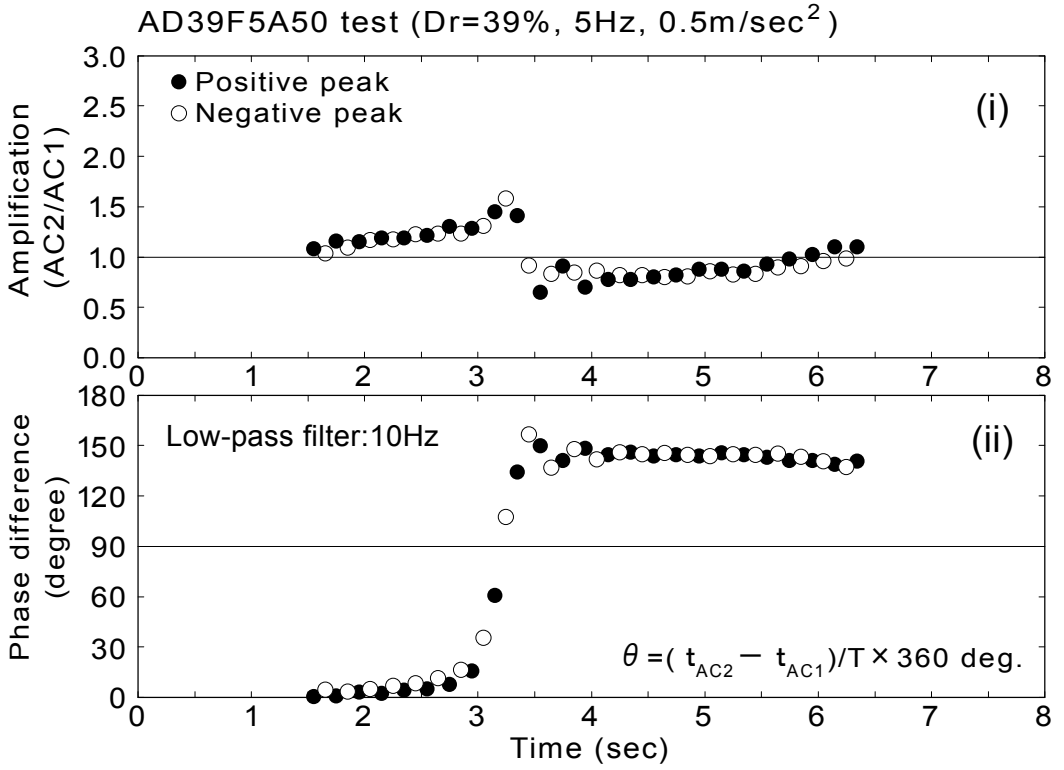

(b) AD39F5A50 test

Fig.5.4: Change of amplification and phase difference with respect to time

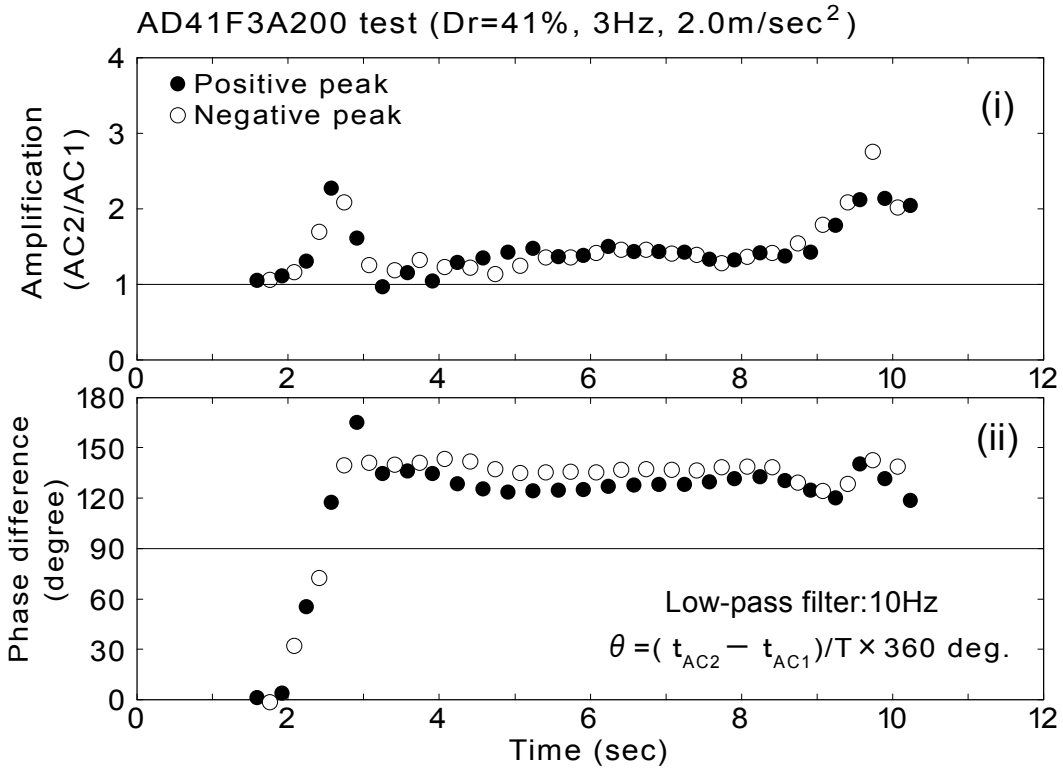

(c) AD41F3A200 test

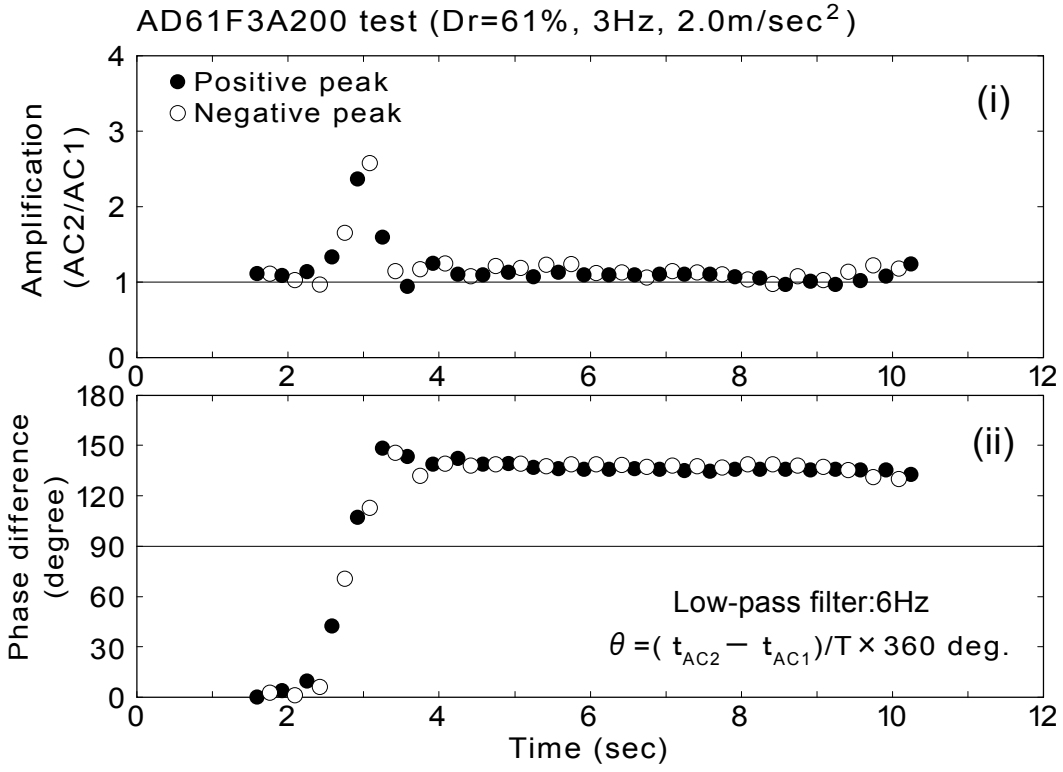

(d) AD61F3A200 test

Fig.5.4: Continued

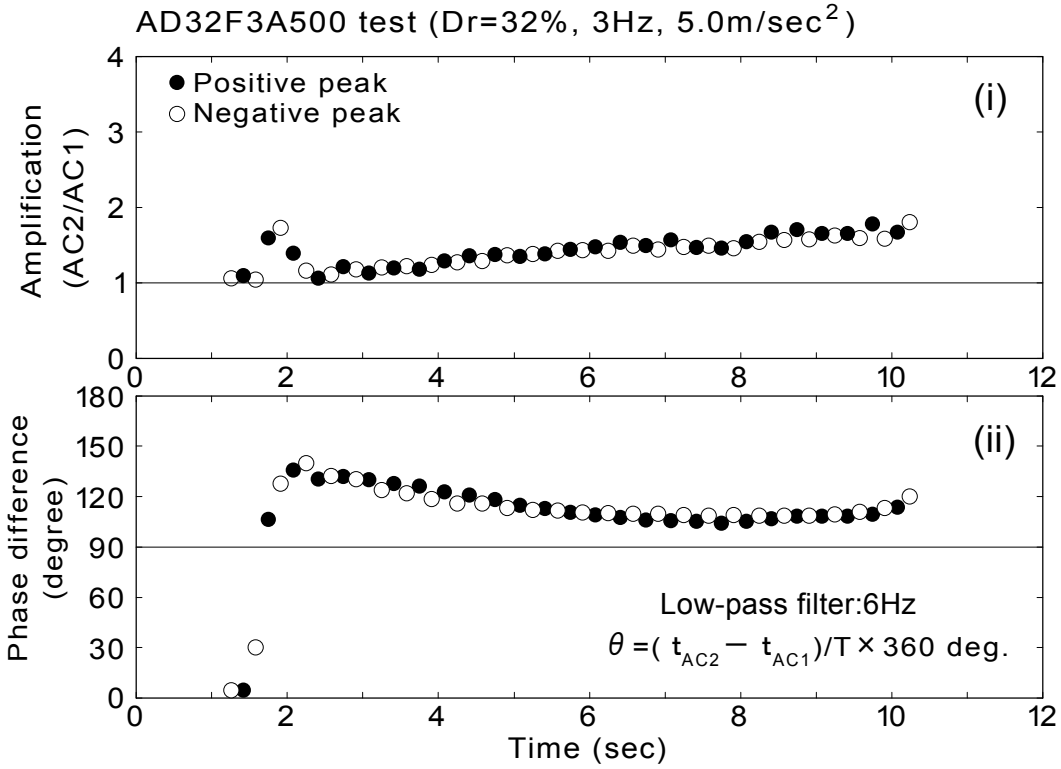

(e) AD32F3A500 test

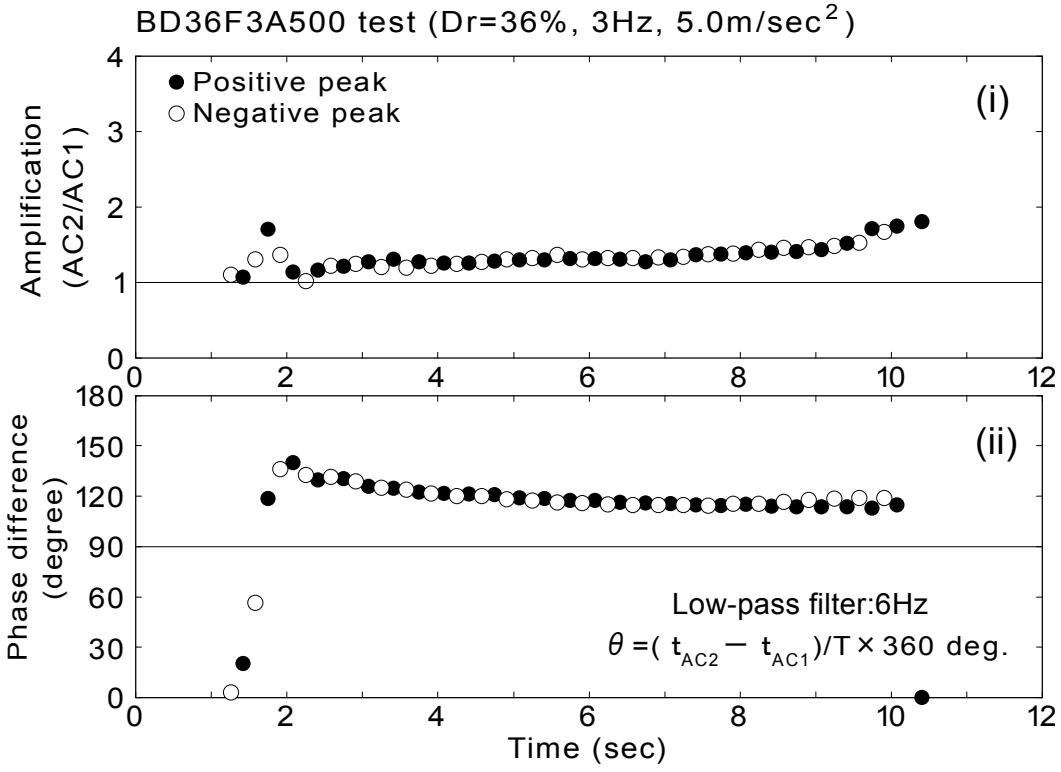

(f) BD36F3A500 test

Fig.5.4: Continued

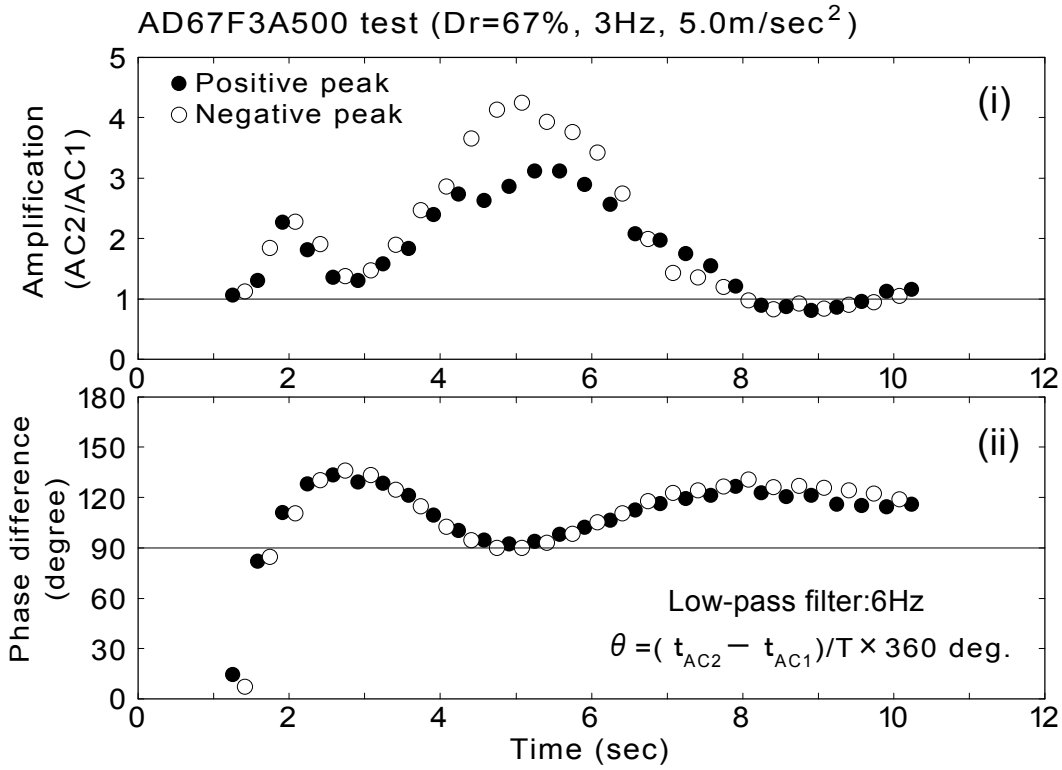

(g) AD67F3A500 test

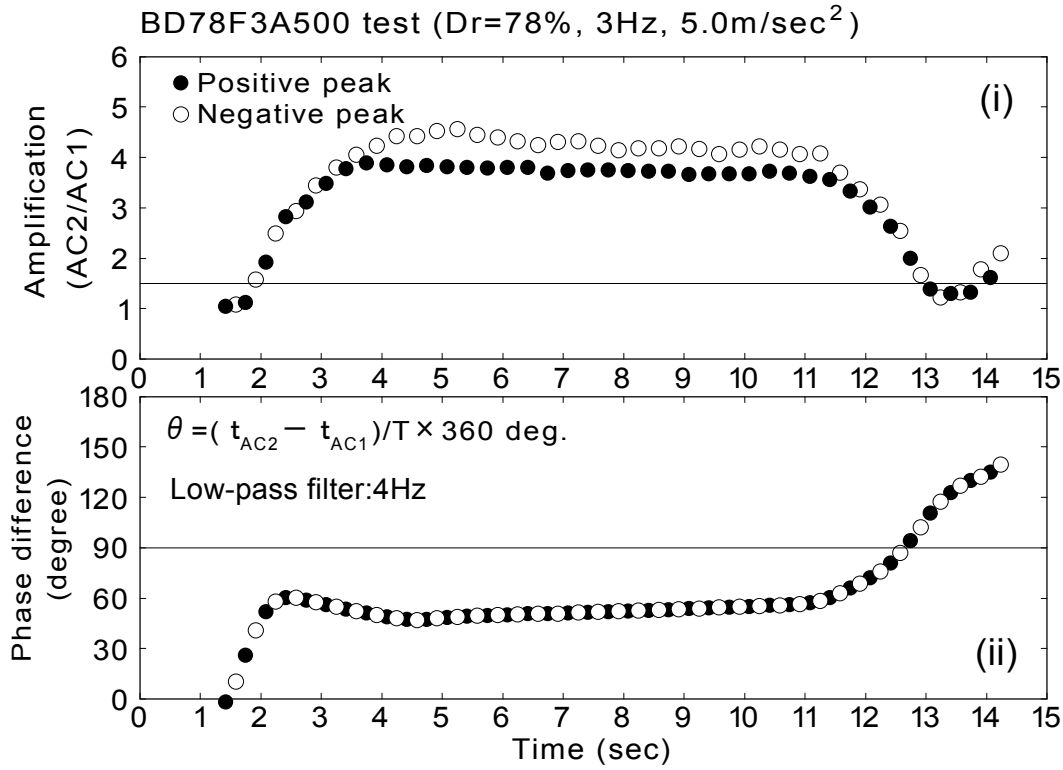

(h) BD78F3A500 test

Fig.5.4: Continued

The phase difference changed from zero to about 140 degrees at about 1.8 seconds when the peak amplification occurred. The feature of response in BD36F3A500 test seemed consistent with the AD32F3A500 test. It was shown that the aluminum yielded in BD36F3A500 test (see, Fig.3.31) but the amplitude of dynamic curvature was almost the same level as AD32F3A500 test (see, Fig.3.34). It seems therefore that the natural frequency of the structure affected the response of the structure more than the strength of material.

Fig.5.4(g) shows the result from AD67F3A500 test. The feature of amplification seemed different from other test results shown above. It was seen that the amplification peaked with the value of 2.4 at about 2 seconds first, and peaked again at about 5 seconds with the maximum value of about 4.4. The phase difference changed from 0 to 130 degrees at 2 seconds. Then, it decreased to 90 degrees at around 5 seconds and increased up to about 120 degrees again. Occurrence of two peaks of amplification is the most interesting feature in this test. It was considered that the dilative behavior of soil due to large shear strain of backfill, which occurred between 3 and 8 seconds (see, Fig.4.70), affected the acceleration response during shaking.

The results from BD78F3A500 test are illustrated in Fig.5.4(h). Dense backfill with relative density of 78% was used in this test. The dilative behavior of soil was observed through the shaking from the measurements of pore water pressure (Fig.4.116(c)). It was seen that the amplification increased up to about 4.8 in 3 seconds from the initiation of excitation, and kept constant until 11 seconds. The phase difference, changing from 0 to 60 degrees at the beginning of excitation, did not exceed 90 degrees during shaking until 12 seconds. It was considered that the dilative behavior of dense backfill constraint the phase difference between the top and the bottom of the structure.

It was shown that the amplification and the phase difference of acceleration varied with time as the shaking continued. This suggests that their significant change occurred in the process of pore pressure build-up, and the dilative behavior of backfill also affected the response of the structure.

Fig.5.5 shows the experimental relationship between the initial amplification and the maximum amplitude of acceleration of base motion. Focusing on the base motion of 3Hz, the amplification becomes smaller as the input motion is intense. In addition, it is also seen that the dense backfill of Dr=61% and Dr=67% produces larger amplification than the loose backfill of Dr=41% and Dr=32% under the same intensity of input motion. Furthermore, the amplification in the test shaken by 5Hz input motion (AD39F5A50) is much smaller than that of 3Hz input motion (AD35F3A50). These observation indicates that the intensity of input motion, density of backfill

and frequency of input motion affect the magnitude of amplification of the structure.

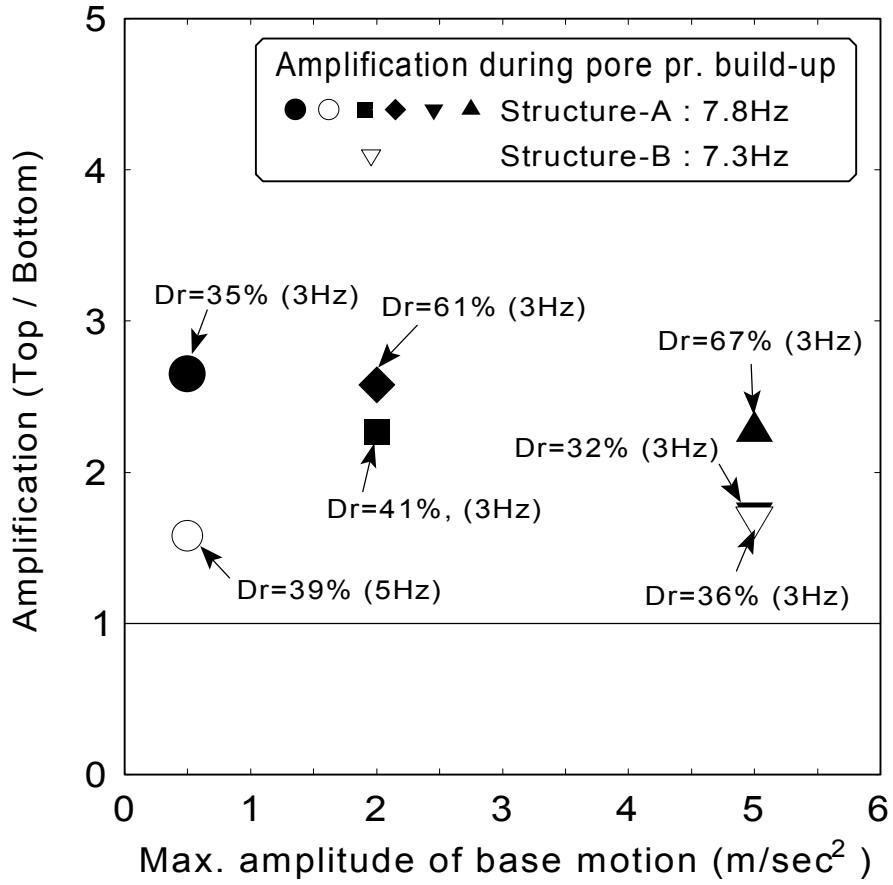

Fig.5.5: Amplification and base acceleration

5.3 RESPONSES IN THE PROCESS OF PORE PRESSURE BUILD-UP

The time period of process of pore pressure build-up will be focused on for the analysis of responses of the embedded structure. Time period of the process of pore pressure build-up and time of initial liquefaction are summarized in Table 5.1. The time of initial liquefaction was defined as the time when the ratio of excess pore water pressure at the middle depth of the backfill (GL-0.375m) reach 1.0 first. Each time history of ratio of excess pore water pressure is illustrated in Fig.4.68～Fig.4.70 and Fig.4.112～Fig.4.116 in the previous chapter. The time period when the soil behaved in a dilative manner, pore pressure fluctuates in the double frequency of input motion, is shown in distinction from a soil behavior in a contractive manner.

Table 5.1: Time period of pore pressure build-up and time of initial liquefaction

Case No	Process of pore pressure build-up (Ratio.E.P.W.Pr.<1.0)	Time of initial lique-faction	After initial liquefaction (After pore pr. ratio once attained 1.0)	
			Contractive manner (Liquefaction)	Dilative manner
AD35F3A50	1.0sec～7.935sec (1～20 cycles)	7.935sec	7.935sec～8.0sec (21 cycles)	—
AD39F5A50	1.0sec～4.055sec (1～16 cycles)	4.055sec	4.055sec～5.0sec (17～20 cycles)	—
AD41F3A200	1.0sec～2.770sec (1～5 cycles)	2.770sec	2.770sec～8.0sec (6～20 cycles)	—
AD61F3A200	1.0sec～3.080sec (1～6 cycles)	3.080sec	3.080sec～8.0sec (7～20 cycles)	—
AD67F3A500	1.0sec～1.920sec (1～3 cycles)	1.920sec	1.920sec～3.0sec (4～6 cycles)	3.0sec～8.0sec (7～20 cycles)
AD32F3A500	1.0sec～1.920sec (1～3 cycles)	1.920sec	1.920sec～8.0sec (4～20 cycles)	—
BD36F3A500	1.0sec～2.175sec (1～3 cycles)	2.175sec	2.175sec～8.0sec (4～20 cycles)	—
BD78F3A500	1.0sec～2.065sec (1～3 cycles)	2.065sec	—	2.065sec～11.0sec (4～30 cycles)

5.3.1 Amplification and excess pore water pressure

The amplifications and the phase differences of accelerations (AC2/AC1) changing with the ratio of excess pore water pressure (PP2, GL-0.375m) for various tests are plotted. Fig.5.4 in the previous section were referred to for the amplifications and the phase differences, and Fig.4.68～Fig.4.70 and Fig.4.112～Fig.4.116 were referred to for the ratio of excess pore water pressure in the backfill. The plots of each test are shown in Fig.5.6. Figs (i) in each test are amplifications and (ii) are phase differences. Values of peak amplification and corresponding phase difference are indicated in each figure. In addition, the directions of paths are illustrated by arrow.

Fig.5.6(a) shows the results from AD35F3A50 and AD39F5A50 test. The input frequencies of those tests were 3Hz and 5Hz, respectively. The other test conditions such as intensity of excitation and a density of backfill were almost identical. It is seen that the pore pressure ratio at the peak amplification were 0.75 in AD35F3A50 test and 0.65 in AD39F5A50 test. A difference was also observed between the curves of phase difference. It suggests that the higher frequency of input motion made the acceleration at the top of the embedded structure amplify in the earlier state of liquefaction.

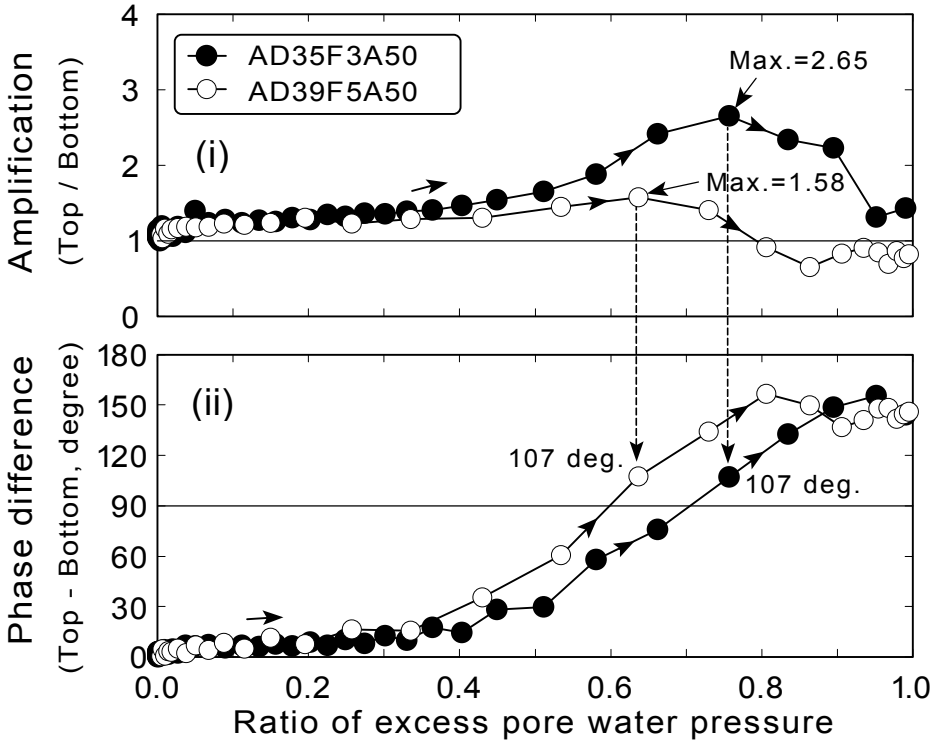

(a) AD35F3A50 and AD39F3A50 test

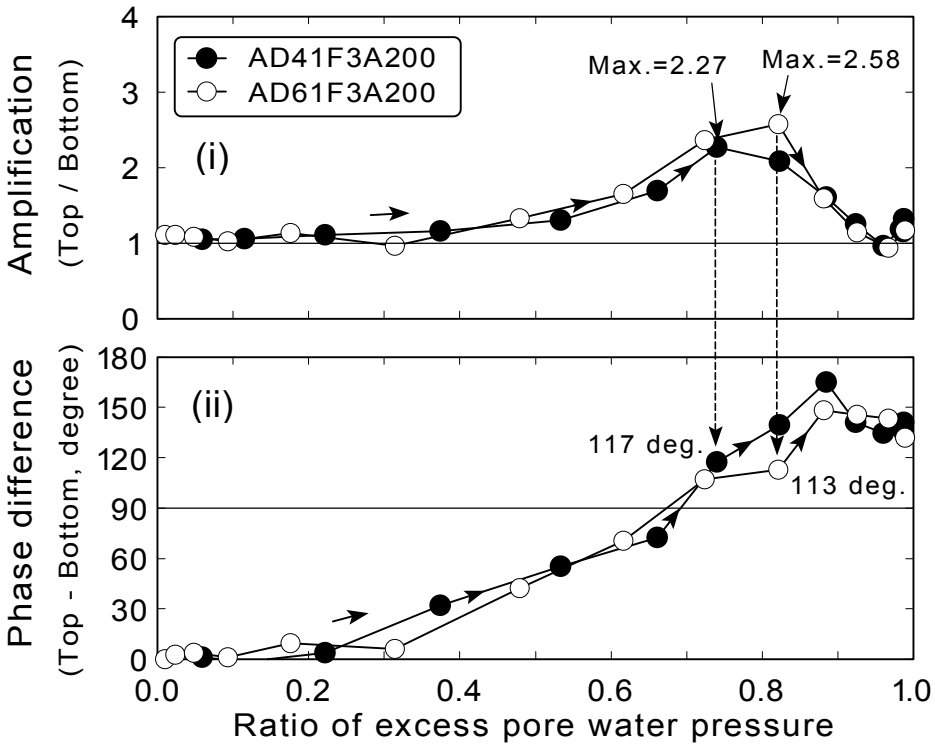

(b) AD41F3A200 and AD61F3A200 test

Fig.5.6: Amplification and phase difference with respect to pore pressure ratio

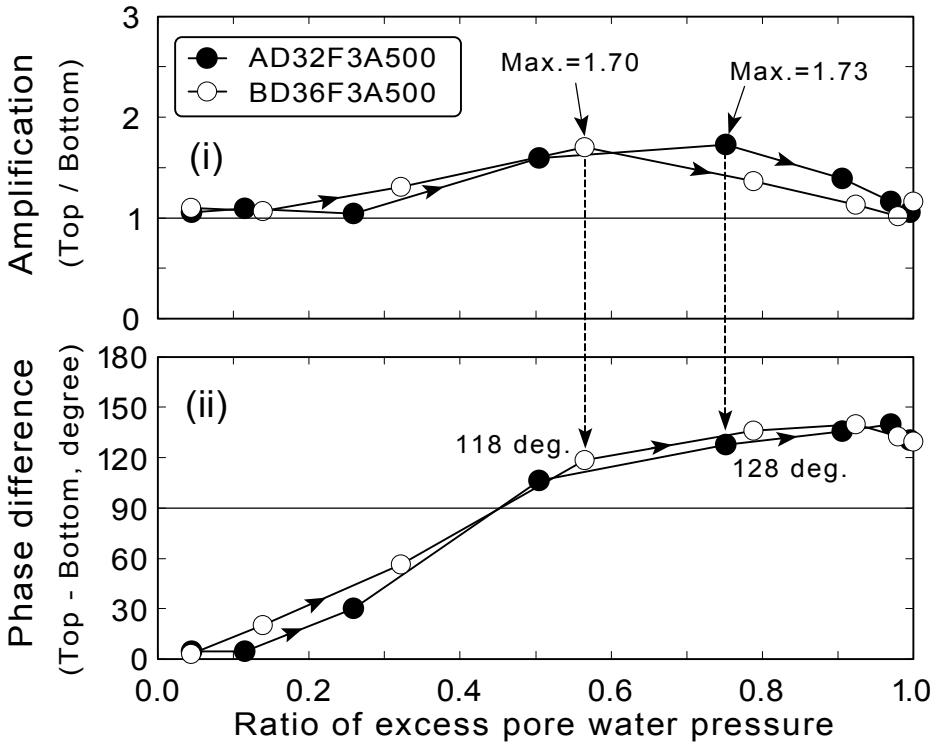

(c) AD32F3A500 and BD36F3A500 test

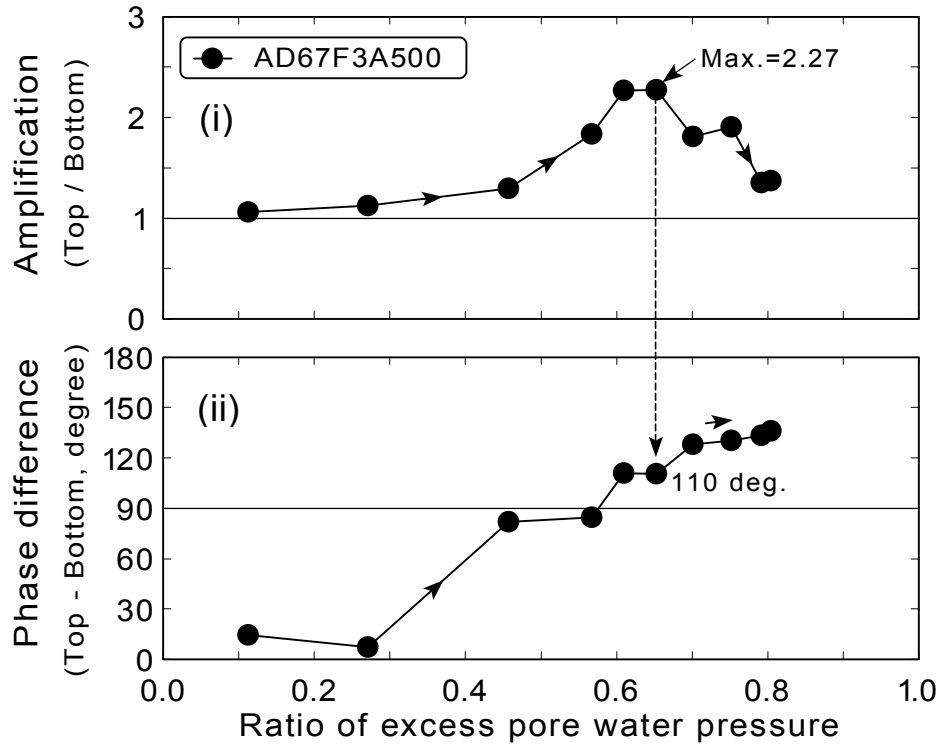

(d) AD67F3A500 test

Fig.5.6: Continued

The results from AD41F3A200 test and AD61F3A200 test are illustrated in Fig.5.6(b). The relative densities of backfill of those tests were 41% and 61%, respectively. Although the pore pressure ratio at the peak amplification of AD61F3A200 test is slightly higher than the one at the peak of AD41F3A200 test, the curves for both amplification and phase difference were consistent on the whole. It was seen that the pore pressure ratio at the peak amplification were 0.72 in AD41F3A200 test and about 0.8 in AD61F3A200 test.

Fig.5.6(c) depicts the results from AD32F3A500 test and BD36F3A500 test. Structure-A (Natural frequency: 7.8Hz, Tensile strength of material: 146MPa) was used in the former test, and Structure-B (Natural frequency: 7.3Hz, Tensile strength of material: 86MPa) in the latter test. Although significant difference is not seen between values of amplifications, the pore pressures ratio at the peak amplification were different between them. They were approximately 0.75 in AD32F3A500 test and 0.58 in BD36F3A500 test, respectively. The peak amplification occurs at lower pore pressure ratio in the test with lower stiffness of structure. It suggests that the stiffness of structure affects the pore pressure ratio at the peak amplification.

Fig.5.6(d) shows the results from AD67F3A500 test. The data at more than 0.8 of pore pressure ratio is not plotted in this figure since the soil behaved in a dilative manner after that. It was seen that the feature of amplification and phase difference was similar to those of other tests of 3Hz shaking. The pore pressure ratio at the peak amplification was 0.65 in this test.

All test results from Fig.5.6(a)～(d) were plotted in Fig.5.7. As seen, response accelerations amplify when the ratio of pore water pressure is at around 0.7 to 0.8 in 3Hz shaking tests on the whole. It was suggested that the reduction of shear modulus of backfill due to pore pressure build-up affected the response of embedded structure such as the amplification and phase difference on acceleration.

Fig.5.8 presents the experimental relationship between the pore pressure ratio when the amplification becomes the maximum and the maximum amplitude of acceleration of base motion. Among the input motion of 3Hz, the pore pressure ratio with large input motion of 5.0 m/sec^2 seems to be slightly smaller than the others. It was considered that the backfill shaken by intense input motion already became soft by the effect of large shear strain and then less pore water pressure was enough to make the structure with soil resonant by the input motion of 3Hz.

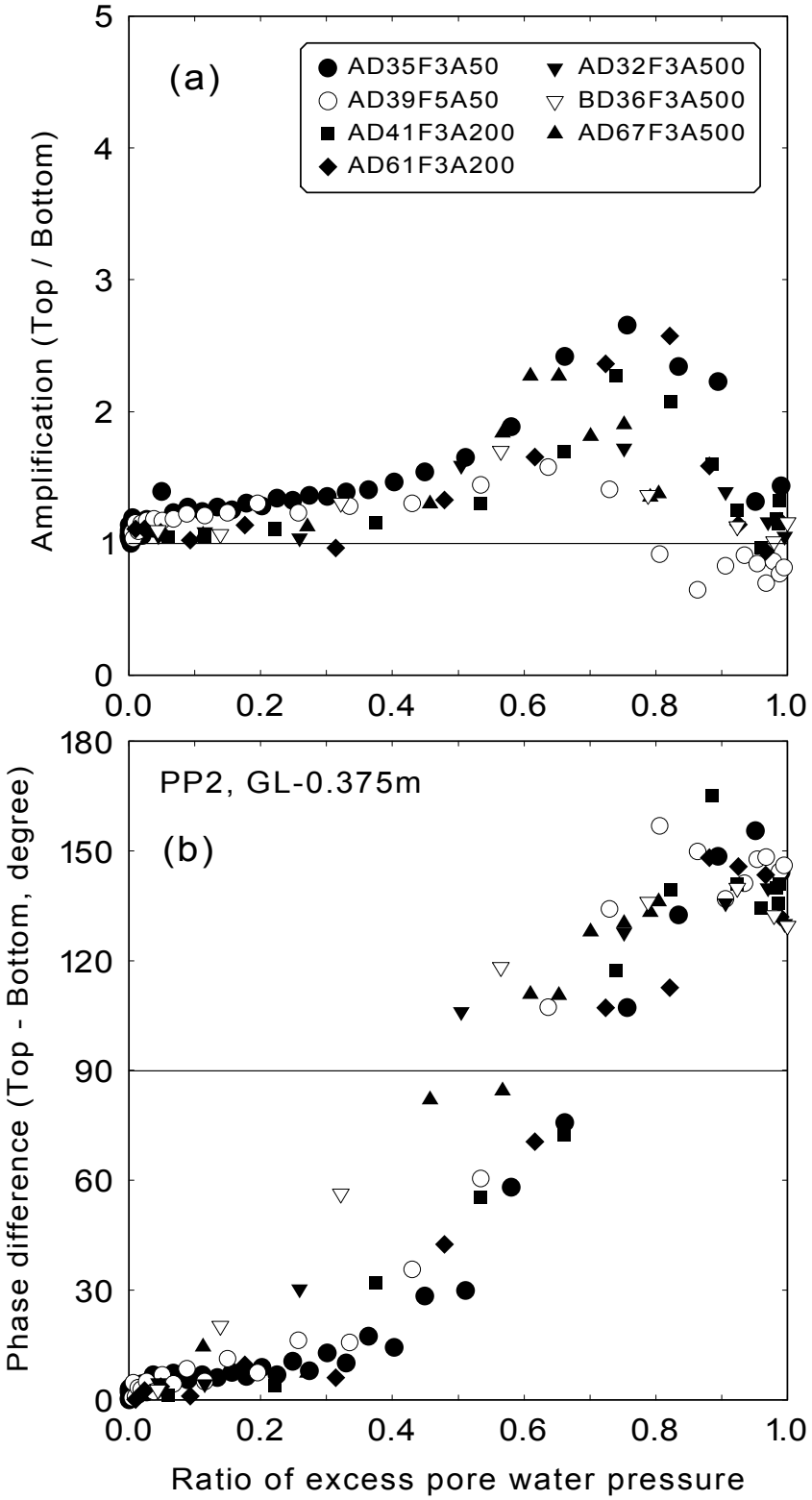

Fig.5.7: Amplification and phase difference with respect to pore pressure ratio (All tests)

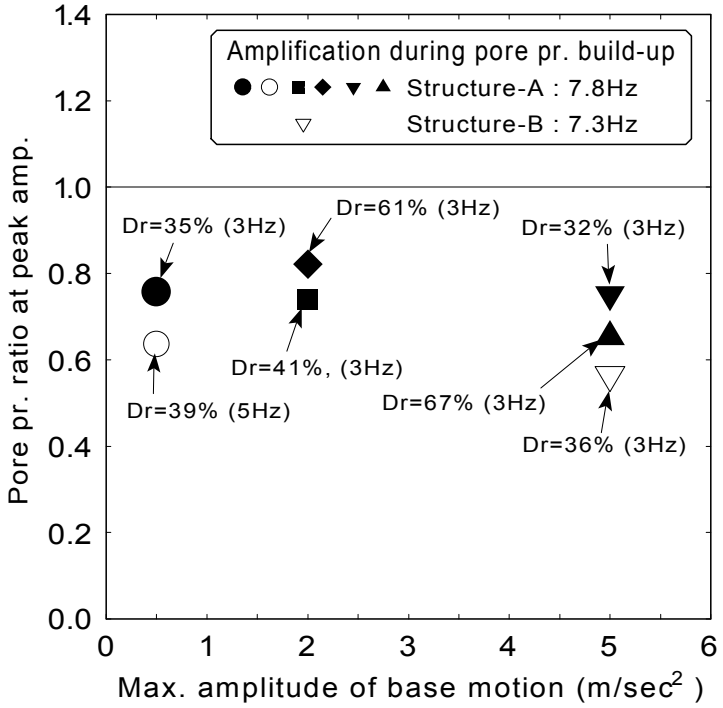

Fig.5.8: Pore pressure ratio at peak amplification with respect to base acceleration

5.3.2 Amplification and natural period of backfill

The amplifications (AC2/AC1) and the phase differences of accelerations with the natural period of backfill for various tests are plotted. The change of amplification and the phase difference with time (see, Fig.5.4) and the natural frequency of backfill with time during shaking (see, Fig.4.75～Fig.4.77 and Fig.4.122～Fig.4.126) were used. Natural frequencies of backfill were converted to natural period by taking reciprocal for convenience of indication.

The plots of each test are shown in Fig.5.9. Figs (i) in Fig.5.9 are amplifications and (ii) are phase differences. Since the natural period of backfill becomes longer with shaking, the path of hysteresis moved from left side to right side in the figure. It should be noted that the natural period of backfill shown is different from the natural period of soil-structure system.

The results from AD35F3A50 test and AD39F5A50 test are illustrated in Fig.5.9(a). It was observed that the natural period of backfill at the peak amplification was about 1.1 seconds in AD35F3A50 test and 0.45 seconds in AD39F5A50 test. Considering that the periods of input sinusoidal wave are 0.33 seconds (3Hz) and 0.20 seconds (5Hz), the model shaken by 5Hz

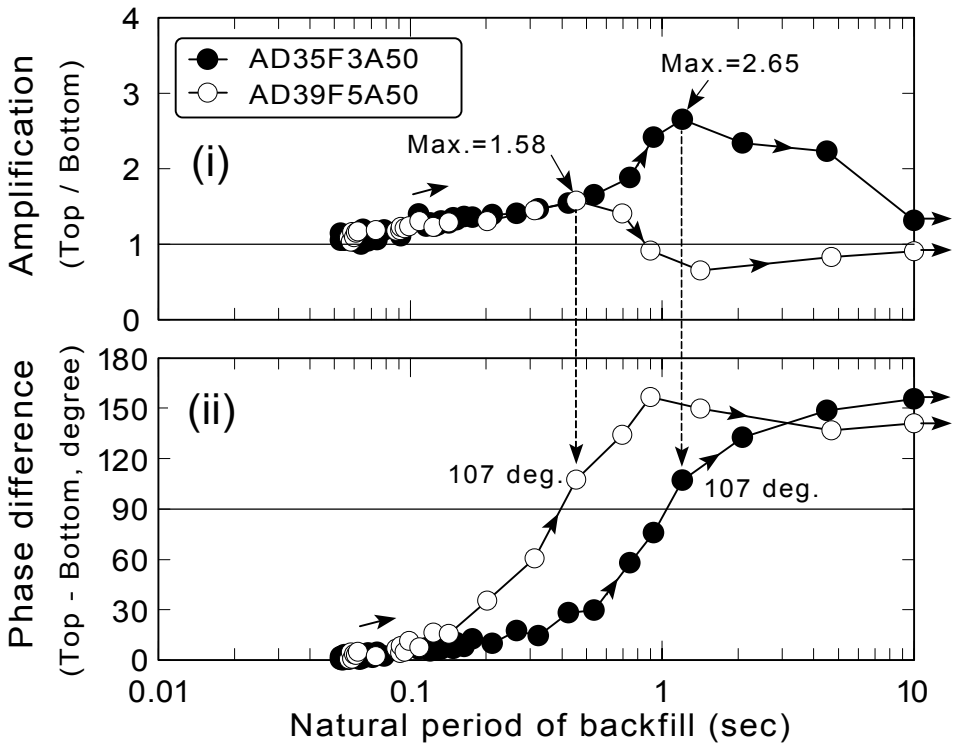

(a) AD35F3A50 and AD39F3A50 test

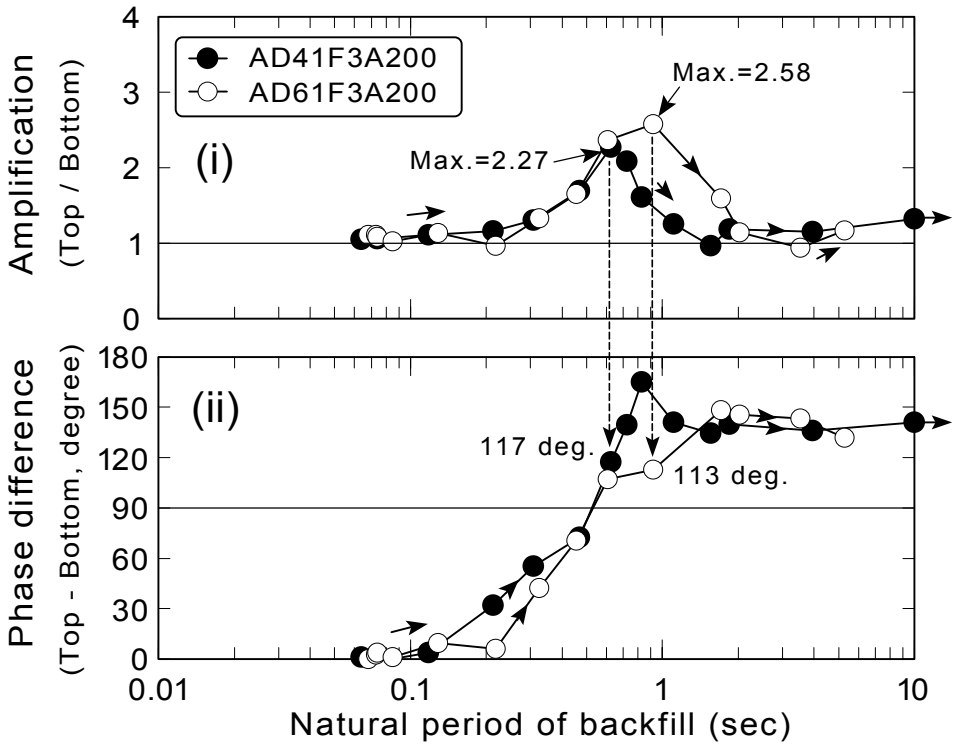

(b) AD41F3A200 and AD61F3A200 test

Fig.5.9: Amplification and phase difference with respect to natural period of backfill

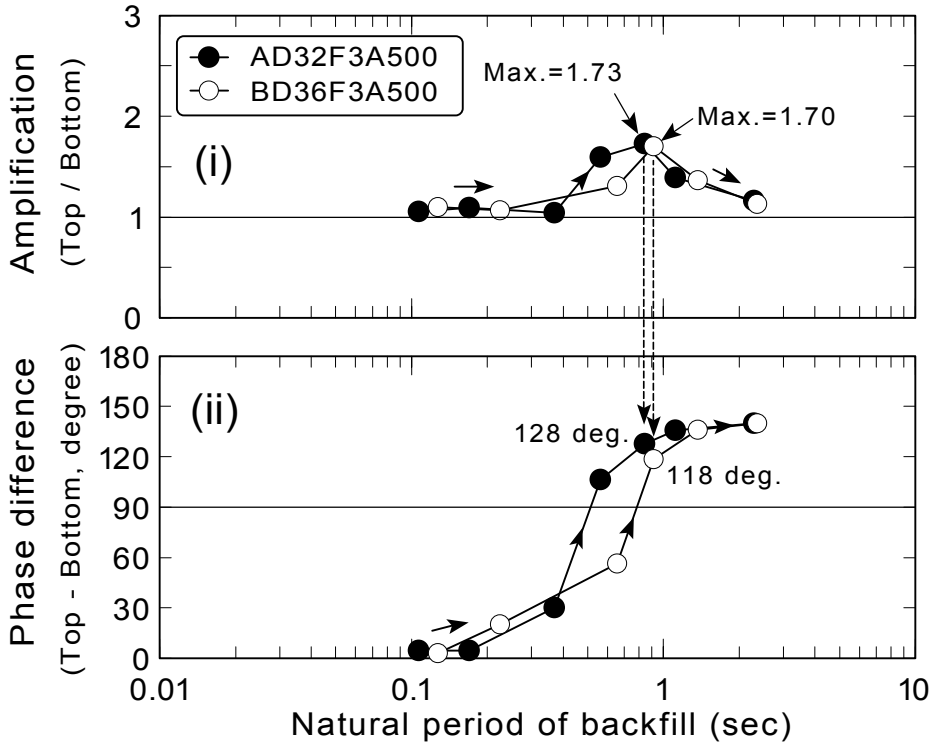

(c) AD32F3A500 and BD36F3A500 test

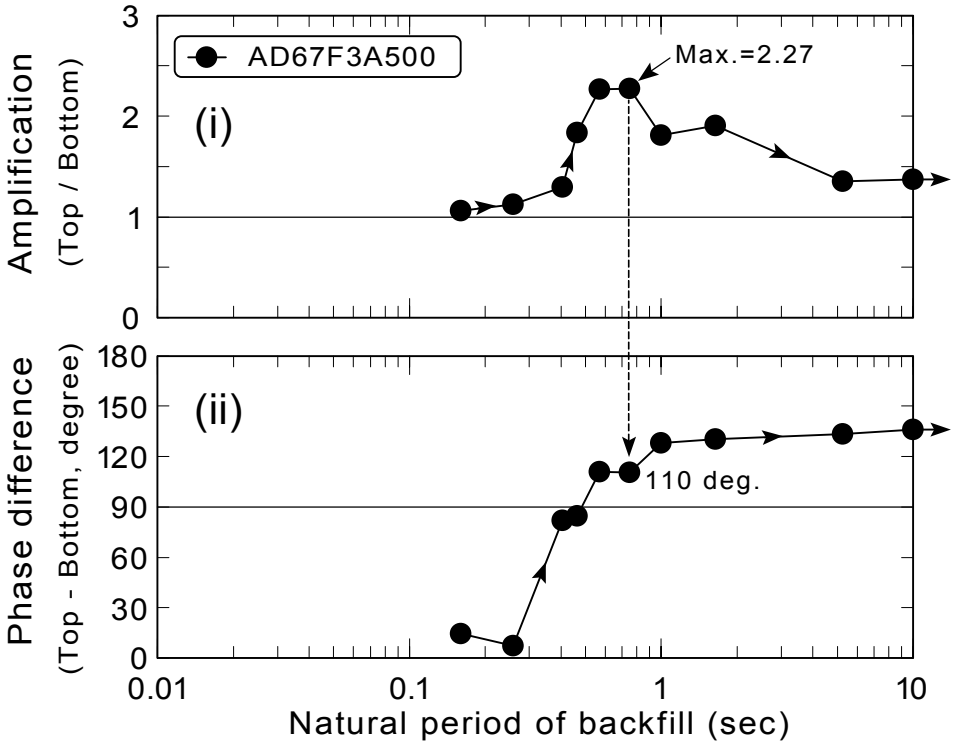

(d) AD67F3A500 test

Fig.5.9: Continued

sinusoidal motion could be amplify in shorter natural period of backfill than the model shaken by 3Hz sinusoidal wave qualitatively. Fig.5.9(b)～(d) show the results from tests which were shaken by 3Hz sinusoidal input motion (period: 0.33 seconds). It was remarkable that the peak amplification occurred in the range of 0.6～0.9 seconds of the natural periods.

All the plots between the amplification, phase difference, and natural period of back fill are summarized in Fig.5.10. The test result by 5Hz input motion is distinguished from those by 3Hz input motion. It was observed that the amplification of the maximum of 2.6 occurred in the process of change of natural period. In addition, the phase difference changed from zero to about up to 150 degrees as well. It suggests that the response of the underground structure is strongly affected by the change of natural period of backfill due to liquefaction.

5.3.3 Examinations on occurrence of resonance at the structure

Although it is difficult to exactly calculate the natural frequency (or natural period) of a soil-structure system at each cycle of excitation by a simplified method, it is possible to determine the natural frequency of the system at a particular time instance. Furthermore, the range of natural frequency of the soil-structure system also can be detected in a particular time period.

First, the initial natural frequency of the soil-structure system is determined by the weak excitation test (see, Table 3.13). The initial natural frequency lies in the range of 18.5Hz～21.5Hz depending on tests.

Second, the natural frequency of soil-structure system must be equal to the natural frequency of the structure itself when the natural frequency of backfill becomes the same as that of structure itself. Considering that the natural frequency of structure itself is 7.8Hz for Structure-A, 7.3Hz for Structure-B (see, Table.2.7), the natural frequency of the soil-structure system should be 7.8Hz or 7.3Hz instantaneously when the natural frequency of backfill became 7.8Hz (or 7.3Hz) by shaking. In this connection, no amplification is observed in Fig.5.10 when the natural period of the backfill becomes 0.13 seconds (7.3Hz～7.8Hz) in any tests. It was considered that the smaller frequency of input motion (3Hz or 5Hz) than the natural frequency of the soil-structure system (7.8Hz or 7.3Hz) did not make the soil-structure system resonant.

A range of natural frequency of the system at a particular time period can be determined by considering the natural frequency of both the structure and the backfill. As observed previously, the natural frequency of the backfill changes from the initial value to zero due to softening.

Suppose the situation in which the natural frequency of backfill decreased in a range of 3Hz to zero as illustrated in Fig.5.11(a). On the other hand, assume that the natural frequency of structure keeps constant (7.8Hz, Structure-A) during shaking as depicted in Fig.5.11(b). Taking that the soft backfill is in contact with the wall of the structure into account, the natural frequency of the soil-structure system in this situation must be in a range of more than 0Hz and less than 7.8Hz as presented in Fig.5.11(c).

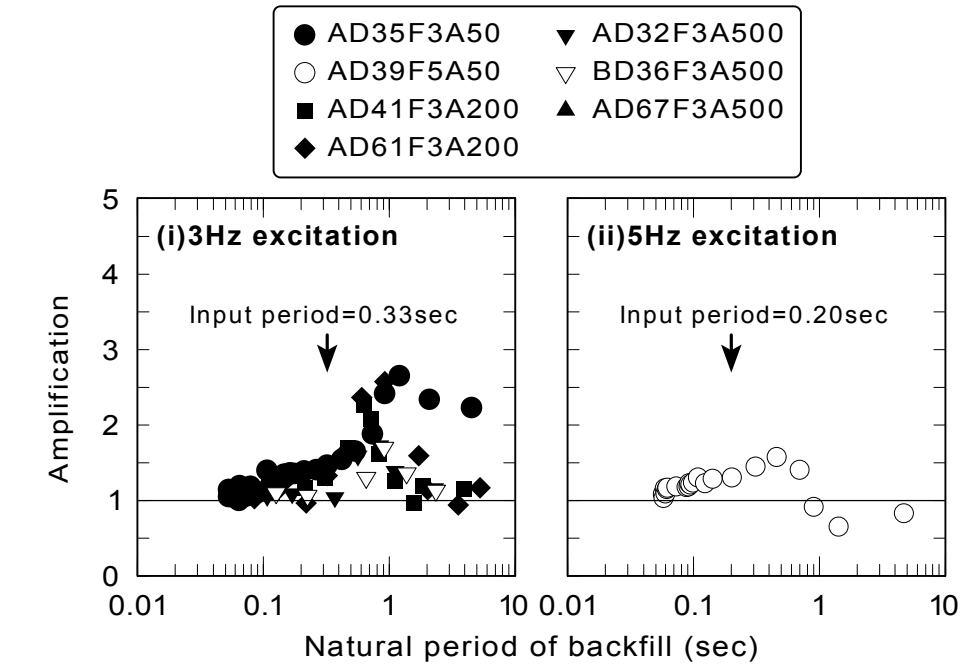

(a) Amplification

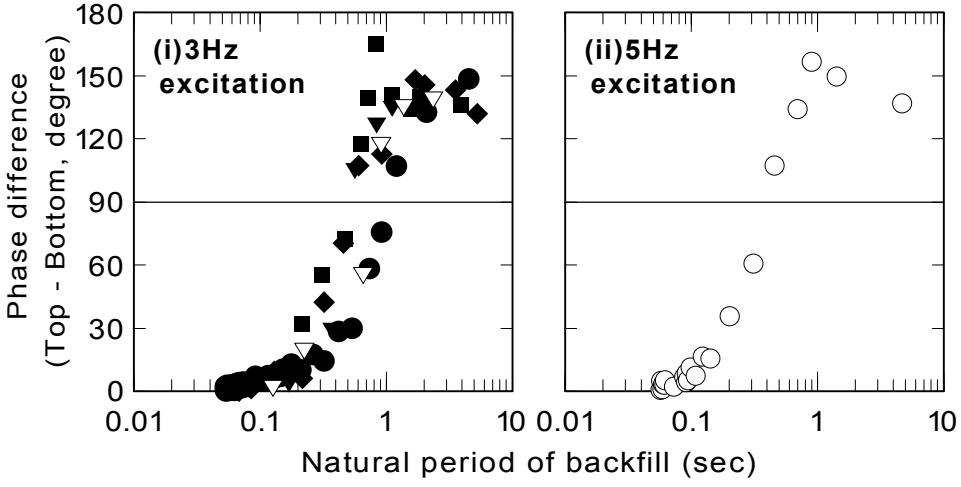

(b) Phase difference

Fig.5.10. Changes of (a)amplification and (b)phase difference with respect to natural period of backfill (All tests)

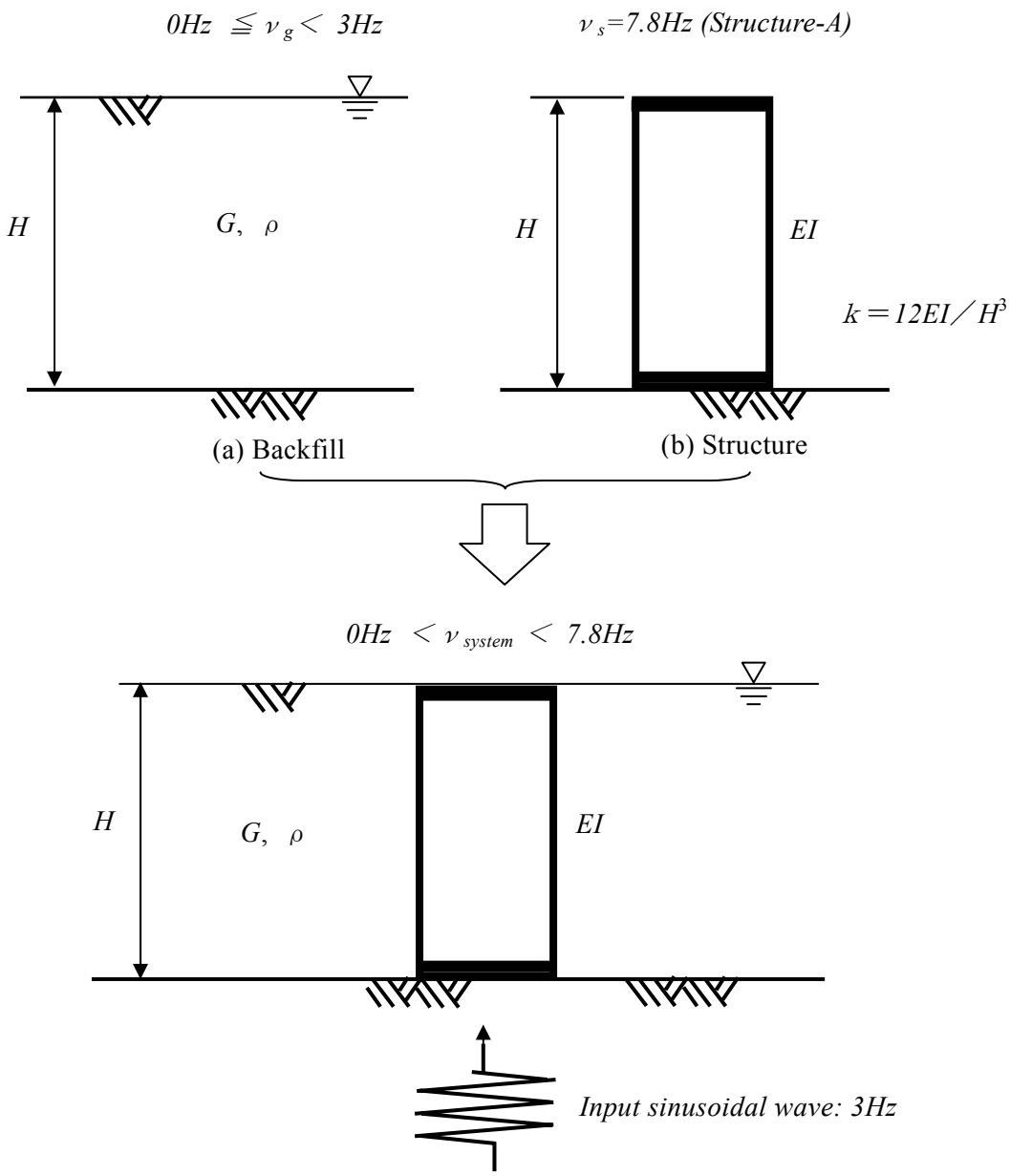

(c) Soil-structure system

Fig.5.11: Possible situation of occurrence of resonance in soil-structure system

The change of natural frequencies with time in AD35F3A50 test is shown in Fig.5.12(a). In case of this test, the natural frequency of backfill changed from 19.5Hz to zero. In contrast, that of the structure kept constant of 7.8Hz during shaking since the structure behaved in an elastic manner in the test. It is seen that the natural frequency of the backfill is 0～3Hz in the time period of 6.7～8 seconds. Based on the previous consideration, the natural frequency of the soil-structure

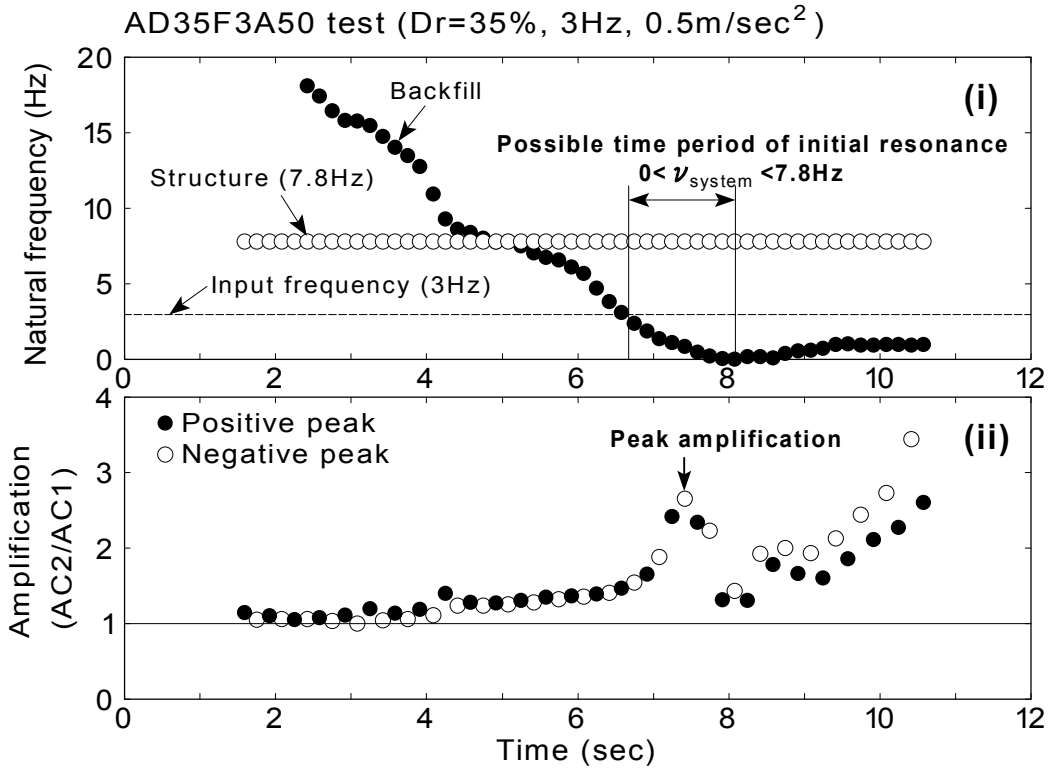

(a) AD35F3A50 test

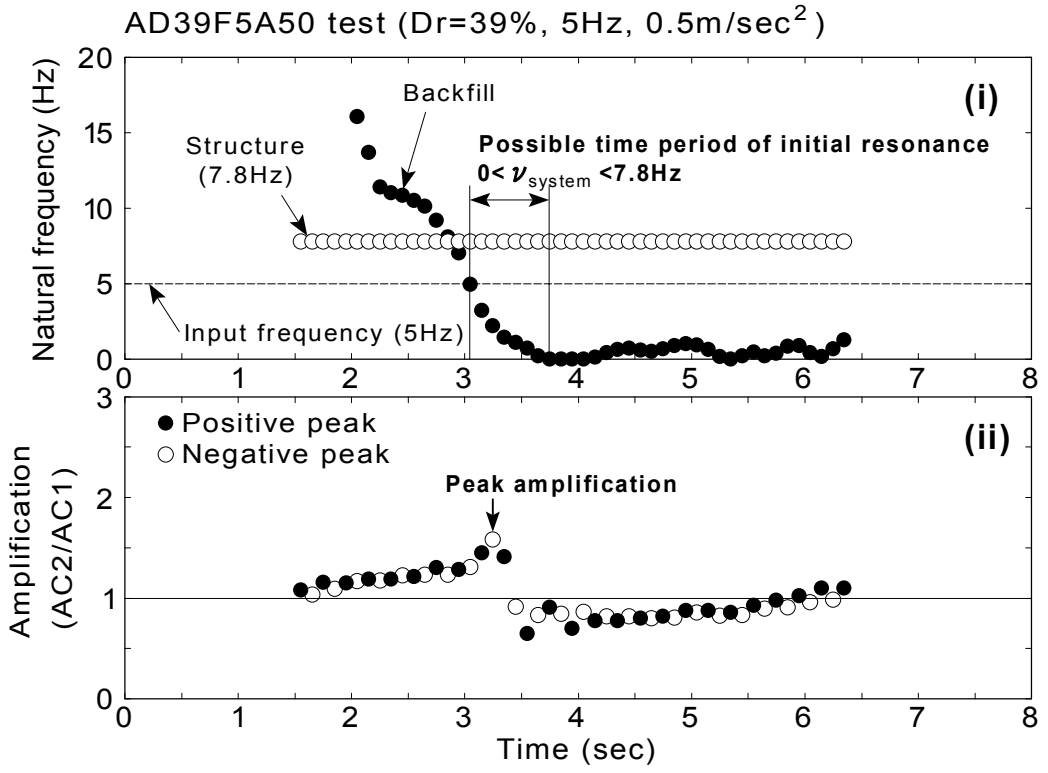

(b) AD39F5A50 test

Fig.5.12: Possible time period of initial resonance and peak amplification

system during this time period is shorter than the 7.8Hz and longer than zero. Considering that the frequency of the input sinusoidal wave is 3Hz in AD35F3A50 test, the possible time period of initial resonance for the soil-structure system is 6.7～8 seconds. This time period is indicated in Fig.5.12(a)(i). On the other hand, the change of amplification with time is depicted in Fig.5.12(a)(ii). It was seen that the peak amplification appeared at about 7.5 seconds which was within the possible time period of initial resonance shown in Fig.5.12(a)(i). As was illustrated in Fig.5.4(a), the phase difference was 90 degrees in this time period of 6.7～8 seconds. Therefore, it was indicated that the phenomenon was the resonance of structure with soil.

Fig.5.12(b)(i) shows the possible time period of initial resonance and change of amplification from AD39F5A50 test in the same way. As was shown in the figure, the possible time period of initial resonance was during 3.1～3.7 seconds considering the input frequency of 5Hz. It was seen that the time for the peak amplification of 3.3 seconds was in the period for the initial resonance of 3.1～3.7 seconds. The structure was thus resonant with the input sinusoidal wave of 5Hz in the process of liquefaction.

Fig.5.12(c) and (d) illustrate the possible time period of initial resonance for AD41F3A200 test and AD61F3A200 test in the same manner, respectively. It was observed that the time when the peak amplification occurred came in the possible time period of initial resonance in each test. The minimum possible natural frequency of soil-structure system is indicated as 0.19Hz in Fig.5.12(d)(ii). It was because the natural frequency of backfill decreased up to 0.19Hz, it did not reduce to zero in AD61F3A200 test.

Fig.5.12(e) and (f) depicts the results from AD32F3A500, BD36F3A500 which are shaken by sinusoidal wave of 3Hz with a peak acceleration of 5.0 m/sec^2. The peak amplifications were observed within the time period of initial resonance in both results. Fig.5.12(g) illustrates the result from AD67F3A500 test. The first peak amplification was seen during the time period. It was remarkable that the amplification, which was once decreased after first amplification, increased again after 3 seconds and the second amplification occurred at about 5 seconds as shown in Fig.5.12(h). Considering the natural period of backfill, the possible time period of second amplification becomes between 3 seconds and 8.5 seconds as illustrated in the figure. The second peak amplification is observed to occur at 5 seconds. As illustrated in the previous section, the phase difference becomes 90 degrees at 5 seconds (see Fig.5.4(g)). It indicates that the second is also due to resonance of structure.

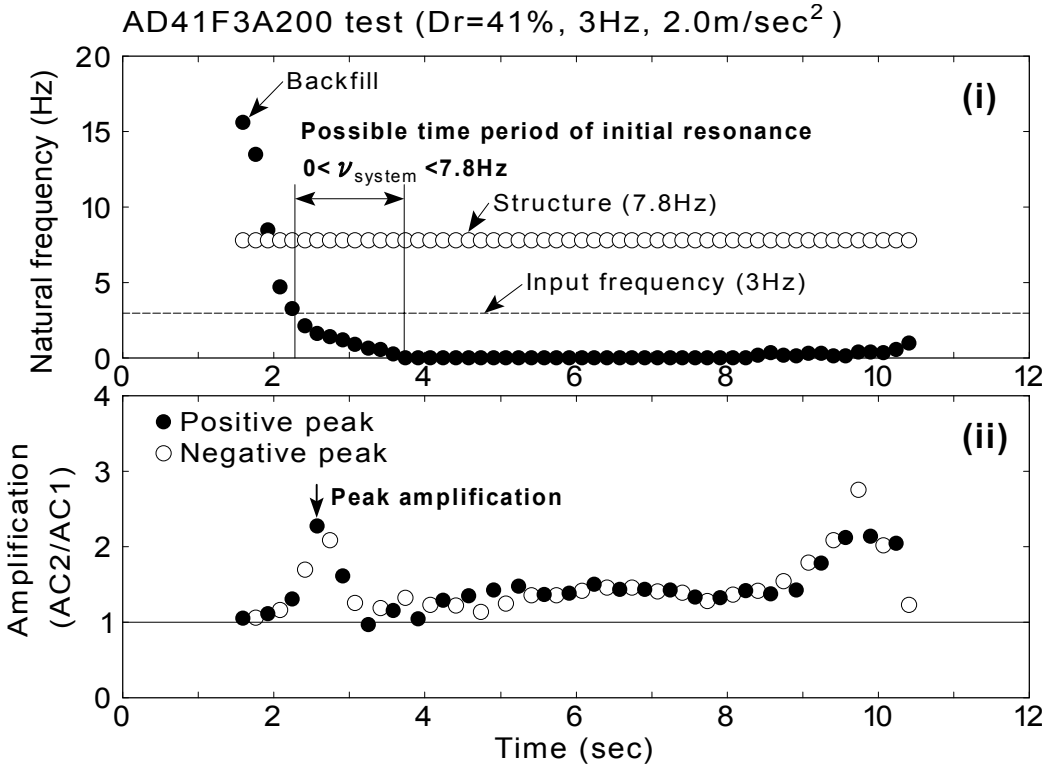

(c) AD41F3A200 test

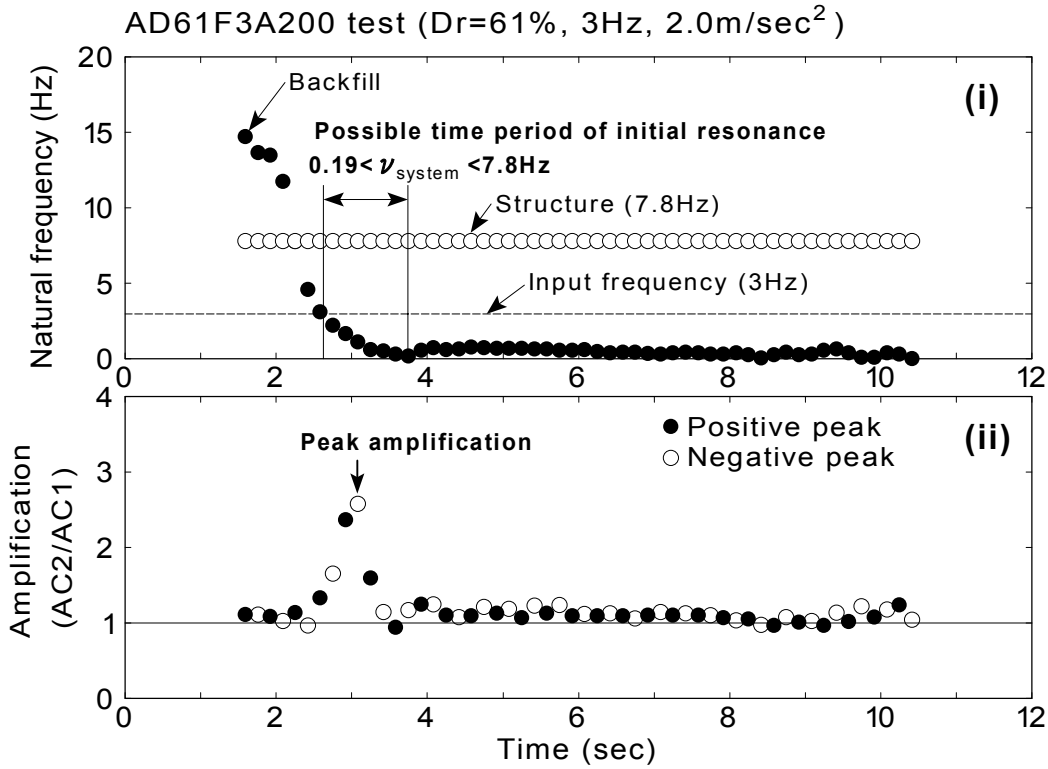

(d) AD61F3A200 test

Fig.5.12: Continued

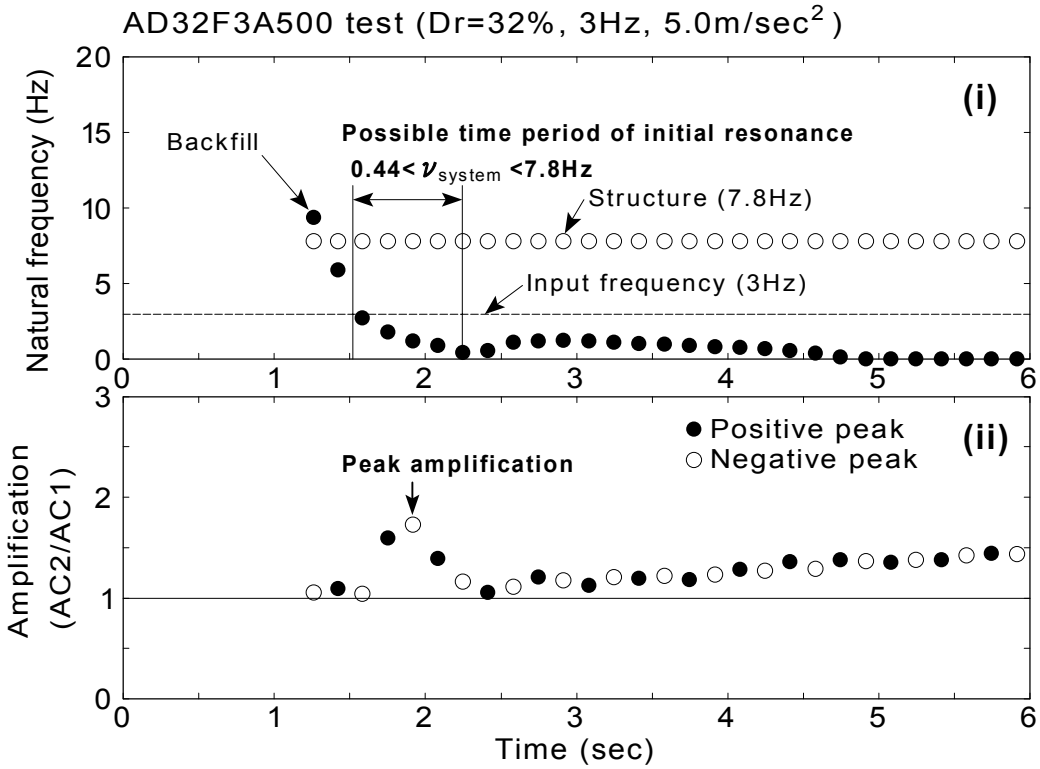

(e) AD32F3A500 test

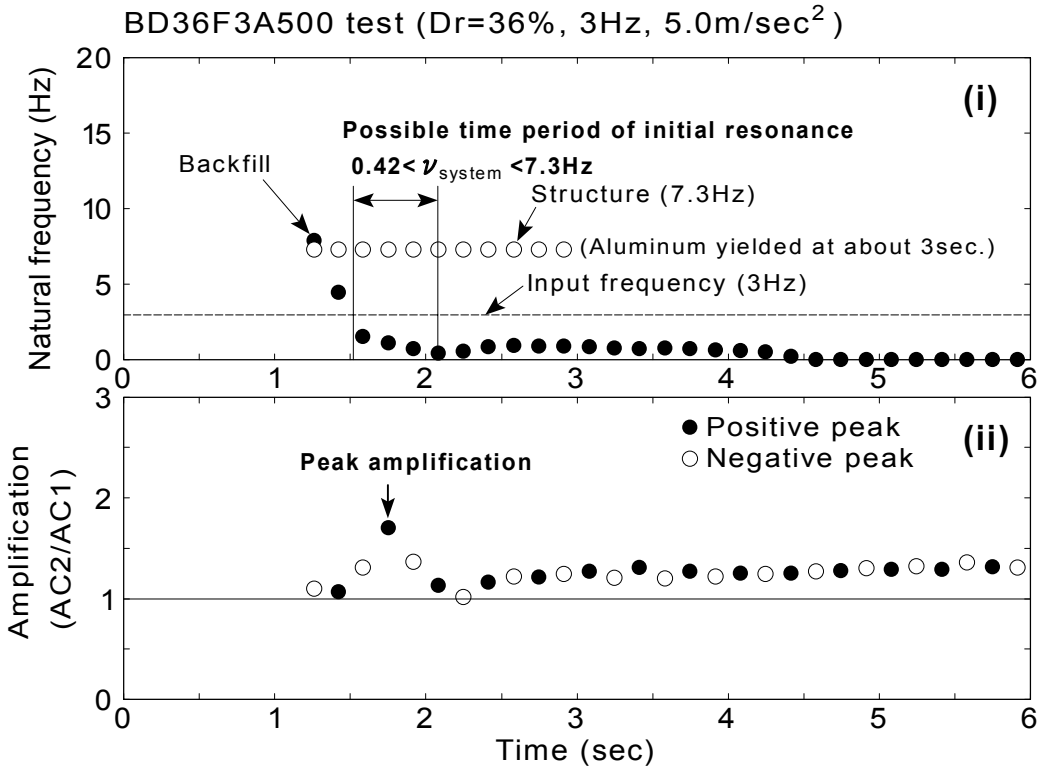

(f) BD36F3A500 test

Fig.5.12: Continued

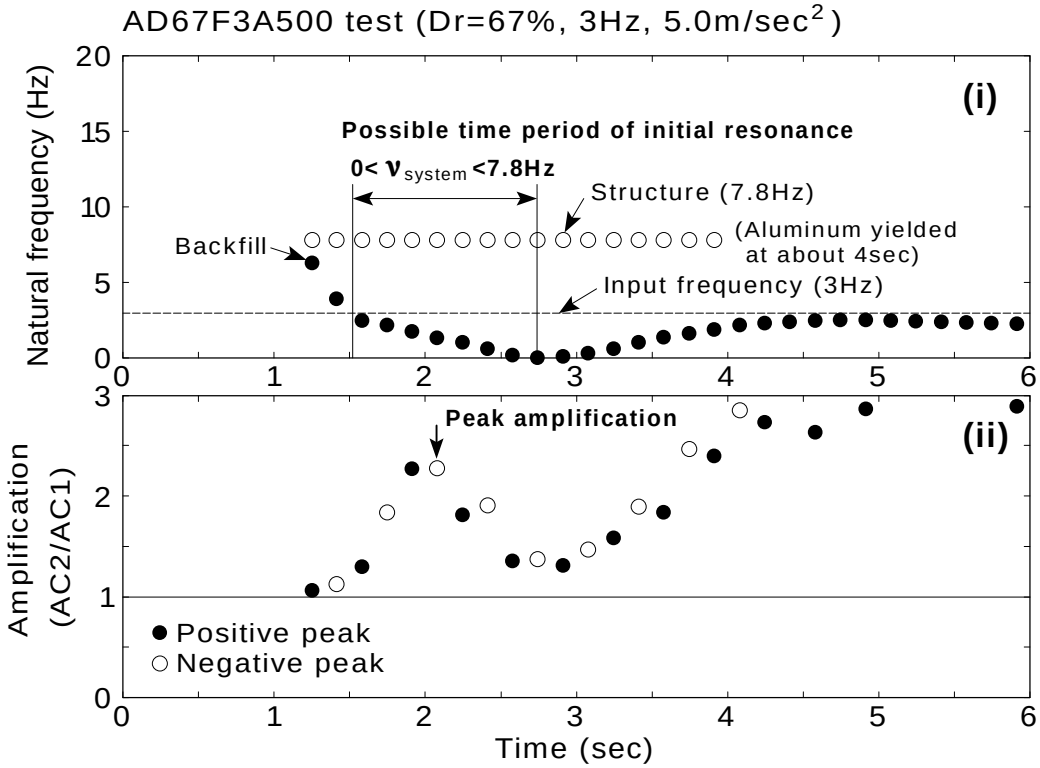

(g) AD67F3A500 test (initial amplification)

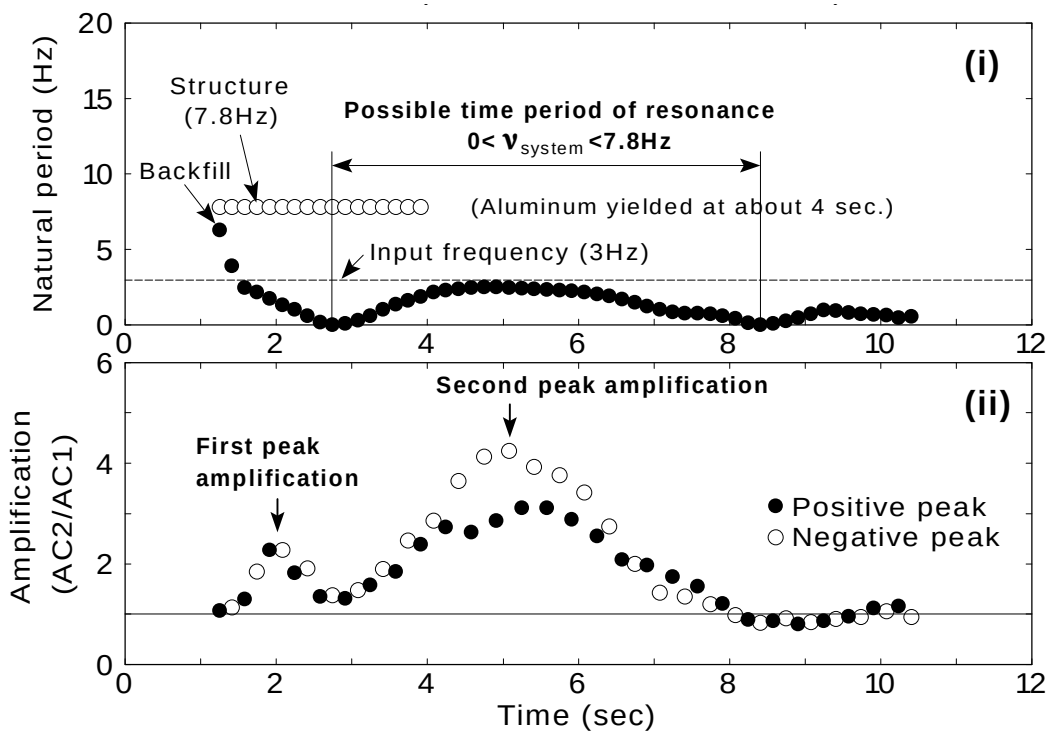

(h) AD67F3A500 test (second amplification)

Fig.5.12: Continued

These observations indicate that the significant reduction of shear modulus of backfill due to liquefaction causes the change of natural frequency of the soil-structure system, and it exerts the resonance of underground structure. In addition, the dilative behavior of soil may cause the change of the natural frequency as well.

5.3.4 Damping ratio of underground structure and soil at resonance

Observed damping ratio of structure model

The amplification at the resonance of a single mass model with a dashpot, which is supposed to produce a velocity proportional to the load, is expressed as

$$\left(\frac{\alpha_{top}}{\alpha_{bottom}}\right)_{\max} = \frac{1}{2D\sqrt{1-D^2}} \tag{5.3}$$

where D is damping ratio. It is noted that the damping ratio D has a velocity dependency. Assuming the structure model used in this study as a single mass model, it is possible to calculate the damping ratio of soil-structure model at resonance by Eq.(5.3). The observed amplification and calculated damping ratio are summarized in Table 5.2. The calculated damping ratio of soil-structure model at resonance is denoted as $D_{soil\text{-}structure}$ in the table.

Table 5.2: Observed amplification and damping ratio at the resonance

	Test case	Observed amplification at the resonance	Time when resonance occurred (Peak time of AC1)	Damping ratio $D_{soil\text{-}structure}$
Weak excitation test	AD35	4.00	-	0.126
	AD32	4.40	-	0.114
	BD36	5.00	-	0.100
	BD78	7.90	-	0.063
Shaking table test	AD35F3A50	2.65	7.415 sec.	0.192
	AD39F5A50	1.58	3.248 sec.	0.336
	AD41F3A200	2.27	2.574 sec.	0.226
	AD61F3A200	2.58	3.085 sec.	0.198
	AD32F3A500	1.73	1.916 sec.	0.303
	BD36F3F500	1.70	1.753 sec.	0.310
	AD67F3A500	2.27	2.080 sec.	0.226
	AD67F3A500	4.24*	5.080 sec.	0.119
	BD78F3A500**	－(4.56)	-	(0.110)

* dilative behavior ** The resonance did not occur

It is seen that the range of calculated damping ratio by the weak excitation test is about between 0.06 and 0.13. In contrast during strong shaking, it lies between 0.19 and 0.34. The amplification at the resonance during dilative behavior of soil is about 0.12. Considering that the damping ratio of the structure itself derived by free vibration test is 0.0054 (see, Table 2.7), the damping of the underground structure becomes larger by existence of the backfill. It becomes much larger when the pore water pressure of backfill builds up and much smaller when the soil behaves in the dilative manner.

Damping ratio of backfill just before the resonance

The damping ratio of backfill just before resonance was calculated from the reproduced stress-strain relationship at the depth of 0.3m to 0.45m using Eq.(4.48). Different from the damping ratio defined in Eq.(5.3), the damping ratio of soil thus derived does not have velocity dependency. Table 5.3 summarizes the time of resonance, the time period when damping ratio is calculated, and the damping ratio in the backfill. The hysteresis loop for the calculation at each test is presented in Fig.5.13. The direction of rotation and time of resonance are drawn in each figure. It is observed that most of the direction of rotation is clockwise. Only the hysteresis loop in BD36F3A500 test is really complicated, indicating the value of damping ratio is invalid.

The calculated damping ratio of soil-structure system (see Table 5.2) is compared with the damping ratio of backfill at resonance (see Table 5.3) in Fig.5.14. It is remarkable that the proportional relation is clearly recognized between them, excluding the result from BD36F3A500

Table 5.3: Damping ratio of backfill at resonance

	Test case	Time when resonance occurred (Peak time of AC1)	Time period when damping ratio is calculated (Second)	Damping ratio at backfill
Shaking table test	AD35F3A50	7.415 sec.	7.00 - 7.42	0.154
	AD39F5A50	3.248 sec.	3.00 - 3.25	0.454
	AD41F3A200	2.574 sec.	2.24 - 2.57	0.391
	AD61F3A200	3.085 sec.	2.70 - 3.09	0.309
	AD32F3A500	1.916 sec.	1.55 - 1.92	0.462
	BD36F3F500	1.753 sec.	1.41 - 1.75	(0.048)
	AD67F3A500	2.080 sec.	1.65 - 2.08	0.292
	AD67F3A500	5.080 sec.	4.74 - 5.08	0.201
	BD78F3A500*	-	-	-

* The resonance did not occur

test. Although this comparison between the damping ratio with velocity dependency and that of soil without velocity dependency is not appropriate, this indicates that the amplification of underground structure due to liquefaction has some relation with the damping ratio of backfill.

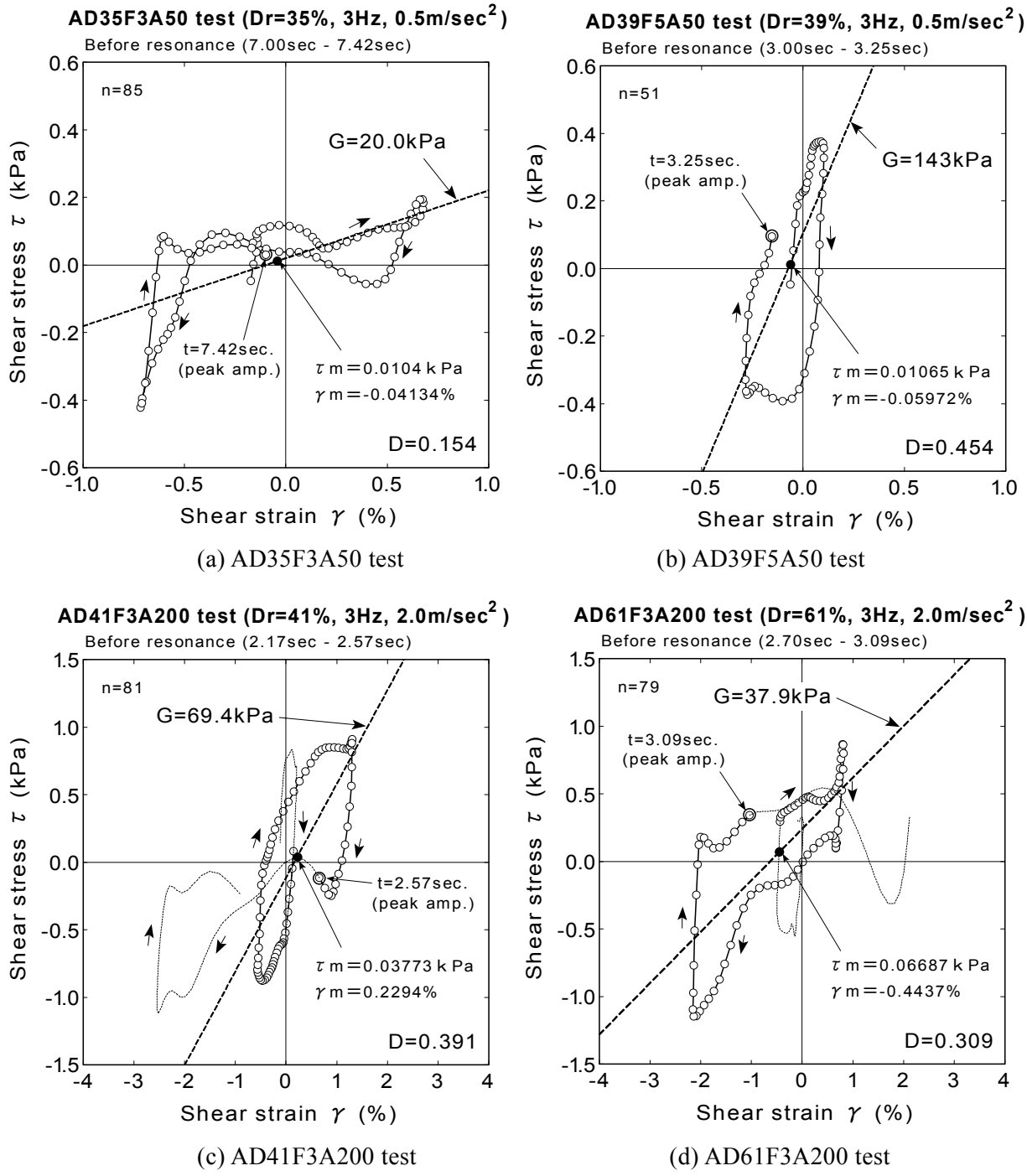

(a) AD35F3A50 test (b) AD39F5A50 test

(c) AD41F3A200 test (d) AD61F3A200 test

Fig.5.13: Hysteresis loop for calculation of damping ratio just before resonance

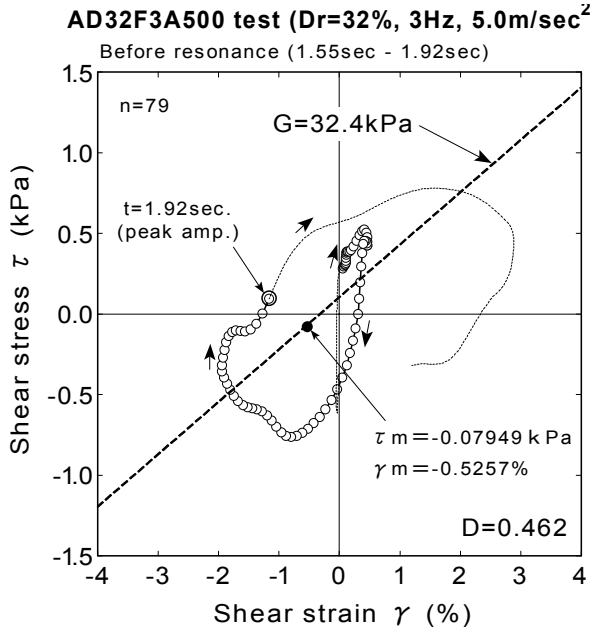

(e) AD32F3A500 test

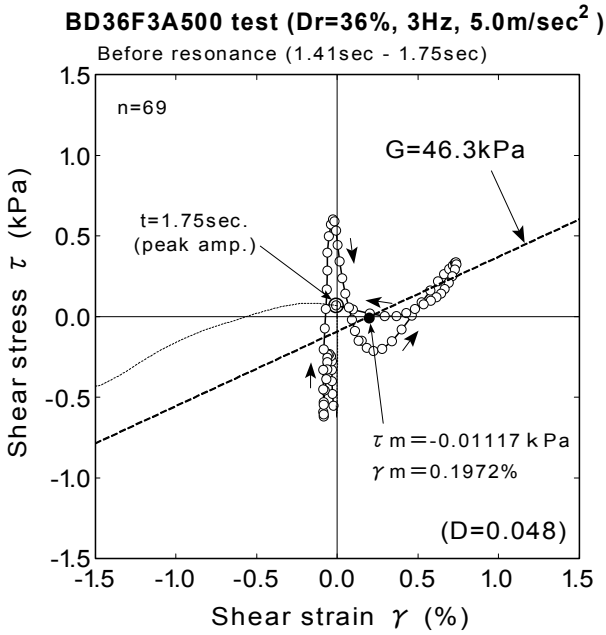

(f) BD36F3A500 test

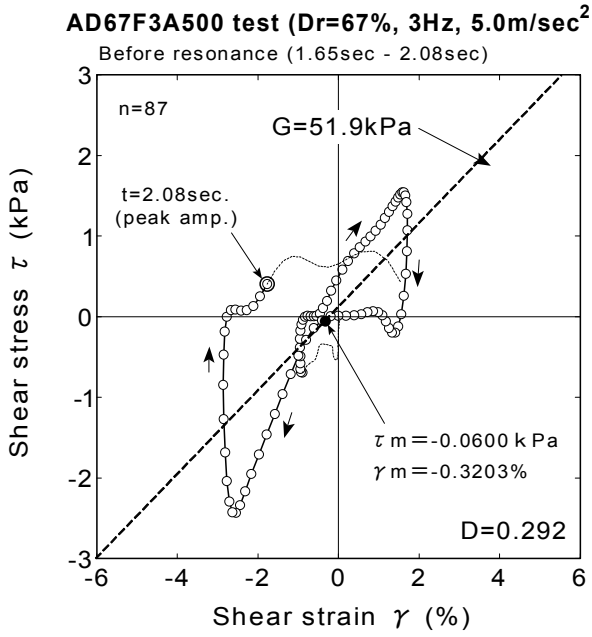

(g) AD67F3A500 test (initial resonance)

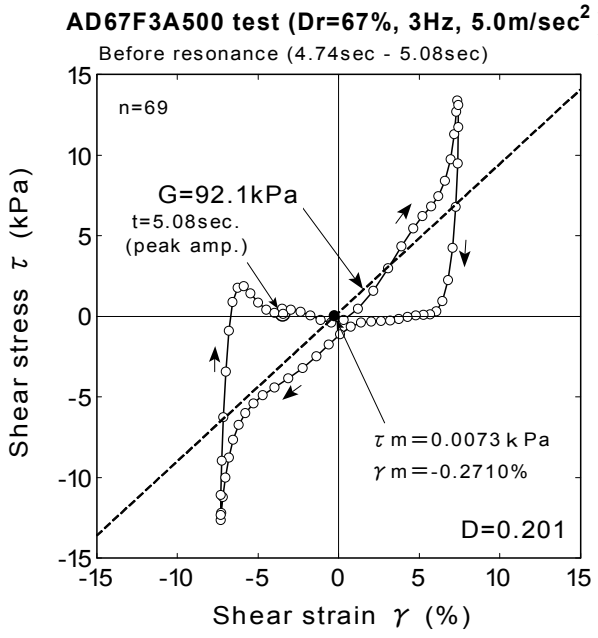

(h) AD67F3A500 test (second resonance)

Fig.5.13: Continued

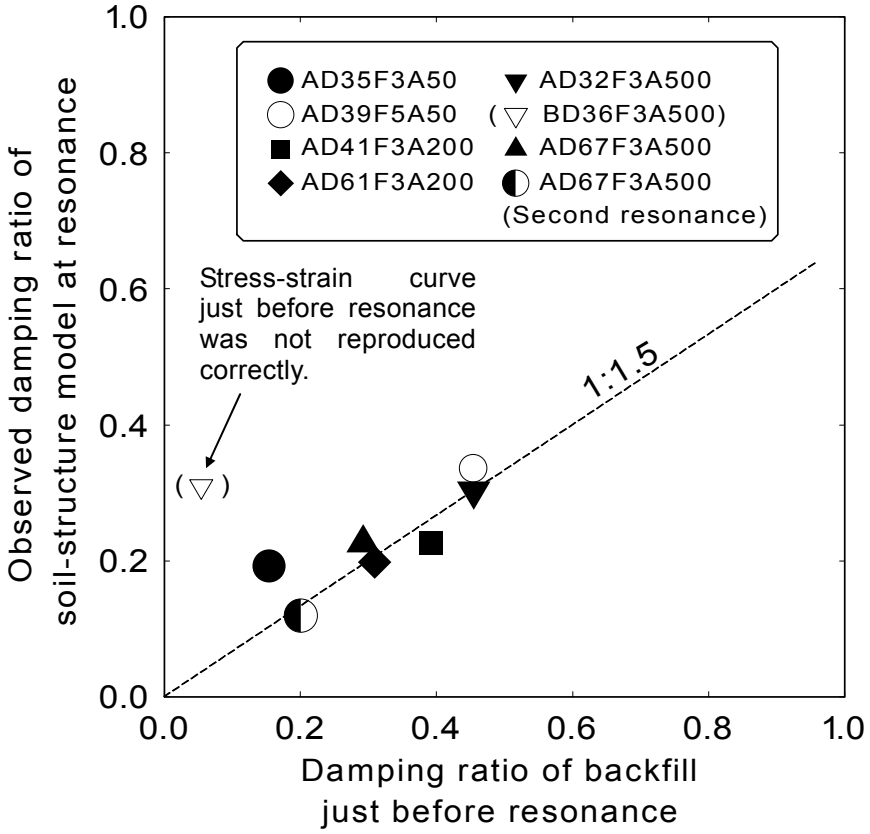

Fig.5.14: Observed damping ratio of soil-structure model at resonance and damping ratio of backfill just before resonance

The damping ratio of soil-structure model at resonance, $D_{soil-structure}$ can be expressed experimentally as

$$D_{soil-structure} = A \cdot D_{backfill} \tag{5.4}$$

where $D_{backfill}$ is the damping ratio of backfill just before resonance and A is a coefficient of proportionality. Substituting Eq.(5.4) into Eq.(5.3), the maximum amplification of underground structure at resonance can be expressed as

$$\left(\frac{\alpha_{top}}{\alpha_{bottom}} \right)_{\max} = \frac{1}{2A \cdot D_{backfill} \sqrt{1-(A \cdot D_{backfill})^2}} \tag{5.5}$$

In this series of shaking table tests, the value of coefficient is determined as

$$A \approx \frac{2}{3} \tag{5.6}$$

5.4 RESPONSES DURING LIQUEFACTION OF BACKFILL

Responses of the structure after the initial liquefaction of backfill will be focused on in this section. The time of initial liquefaction is summarized in Table 5.1. It was observed that the shear modulus of soil reduced almost 1/500～1/2800 of the initial shear modulus after the initial liquefaction due to contractive behavior of soil in the loose backfill (see, Table4.4). In contrast, the behavior of cyclic mobility, which was caused by the dilative behavior of soil, was observed after the initial liquefaction in the dense backfill. Both behaviors of soil after the initial liquefaction will be distinguished from each other in the following discussion.

5.4.1 Loose backfill behaving in a contractive manner

The experimentally derived relationship between the amplification of acceleration and the natural period of backfill is shown in Fig.5.15. For the comparison, the plots after the initial liquefaction (figures (ii)) as well as that before the initial liquefaction (figures (i)) are illustrated in the figure.

It was seen that the natural period of backfill stayed longer than one second after the initial liquefaction and the amplification and phase difference did not change significantly. No resonance was observed to occur after the initial liquefaction since the phase difference was maintained between 120 to 150 degrees. It was considered that the natural period of the structure together with soil was maintained longer than the period of the input sinusoidal shaking and it prevented the resonance; i.e., it worked in the state of seismic isolation. It suggests that the natural period of underground structure with loose backfill stays long after the initial liquefaction and this phenomenon helps avoid the continued resonance of the underground structure due to earthquakes.

The approximate values of amplification and phase difference during liquefaction as well as those before initial liquefaction by the series of shaking table tests are summarized in Table 5.4. These values will be referred to for the calculation of dynamic earth pressures on the flexible wall of the structure in Chapter 8.

Table 5.4: Approximate values of amplification and phase difference

	Amplification	Phase difference
When resonance occur	2.5 to 3	90 deg.
When soil liquefy	1 to 1.5	150 deg.

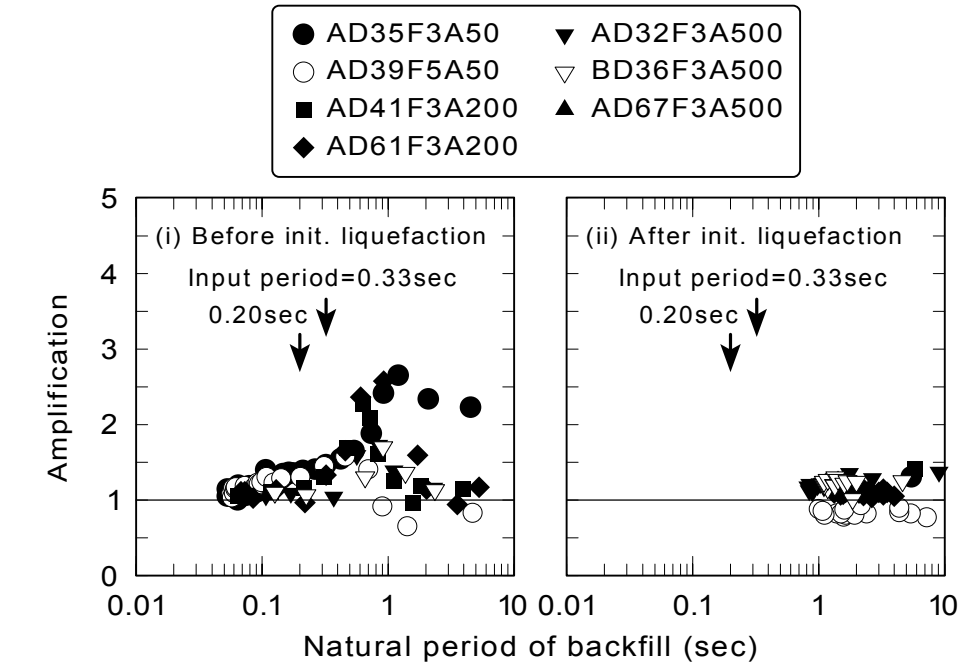

(a) Amplification

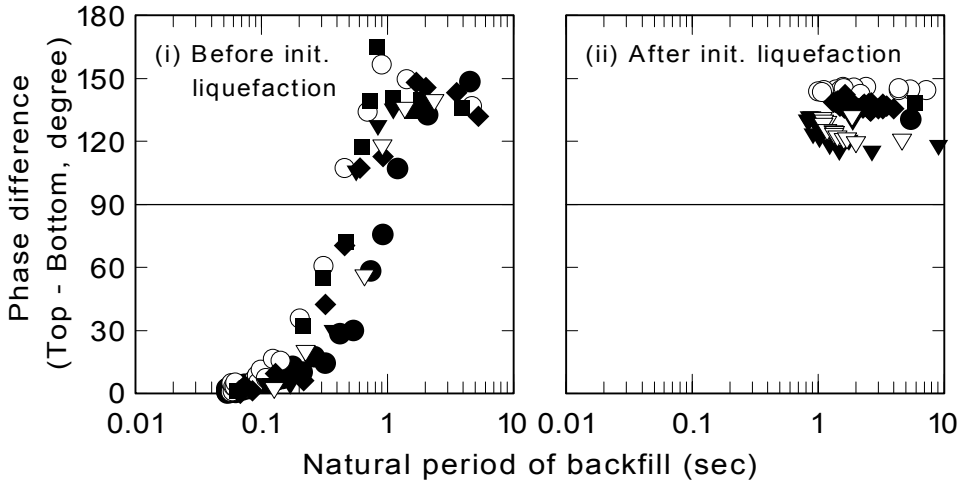

(b) Phase difference

Fig.5.15. Amplification and phase difference with respect to natural period of backfill during liquefaction

5.4.2 Dense backfill behaving in a dilative manner

The dilative behavior of soil was observed after initial liquefaction in AD67F3A500 test. The behavior was seen before the initial liquefaction in BD78F3A500 test. As was summarized in Table 4.4 in Section 4.5.1, the shear modulus does not decrease to zero but 1/90～1/300 of the initial shear modulus during a dilative behavior.

The natural frequencies of backfill calculated by Eq.(4.57) after initial liquefaction are plotted in Fig.5.16 with respect to relative density of backfill. It is seen that the natural frequency of dense backfill at relative density of 67% and 78% became between 0.5Hz～3Hz. In contrast, it is less than 1Hz in the test with loose backfill of less than about 60% relative density. The natural frequency of dense backfill near 3Hz could make the backfill amplify extensively by the 3Hz input motion.

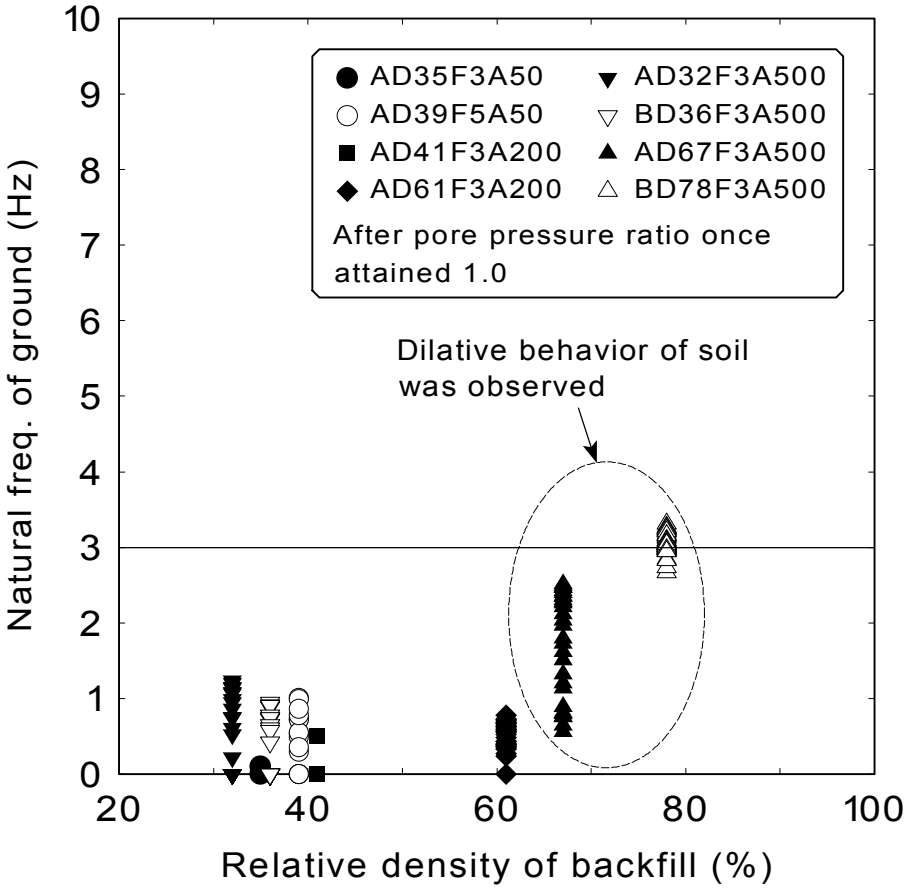

Fig.5.16: Natural frequency of backfill during shaking at each relative density

Fig.5.17 shows the change of amplification and phase difference with respect to the natural period of backfill from AD67F3A500 test and BD78F3A500 test. Figures (i) illustrate the situation before initial liquefaction and figures (ii) after initial liquefaction. The feature of the changes before initial liquefaction in AD67F3A500 test is similar to that of the tests with loose backfill qualitatively (see, figures (i) in Fig.5.15(a)). In contrast, the dilative behavior of soil in BD78F3A500 test did not make the natural period of backfill longer than about 0.4 seconds.

As was presented previously, the amplification of structure in AD67F3A500 test, which once decreased after resonance (A direction in Fig.5.17(a)(i)), increased again (B direction in Fig.5.17(a)(ii)). It was clarified in the previous section that this phenomenon is resonance due to the natural period of backfill changed by dilative behavior of soil. After the significant amplification of acceleration more that 4, the amplification decreased with the change of natural period (C direction in Fig.5.17(a)(ii)).

The phase difference became close to 90 degrees as the natural period changed shorter (see the direction B in Fig.5.17(b)(ii)) indicating the occurrence of resonance. In this respect, the phase difference increased again to about 130 degrees as shown in the direction C in Fig.5.17(b)(ii) after the yield of aluminum of the structure.

The amplification increased up to 4.5 in BD78F3A500 test which is larger than the amplification before initial liquefaction of about 2.5～3.0. The phase difference stayed at about 60 degrees during shaking and did not exceed 90 degrees. It was considered that the amplification of the structure in the dilative dense backfill became as large as the amplification at the initial state derived by weak excitation test (see, Table 5.2).

Fig.5.18 illustrates the typical behavior of both dilative backfill (figure (i)) and contractive backfill (figure (ii)). It is clearly seen that the responses of the structure does not change so much in the structure with contractive backfill. In contrast, they change with dilative backfill. It was shown that the dilative behavior of backfill after initial liquefaction affects the response characteristics of underground structure.

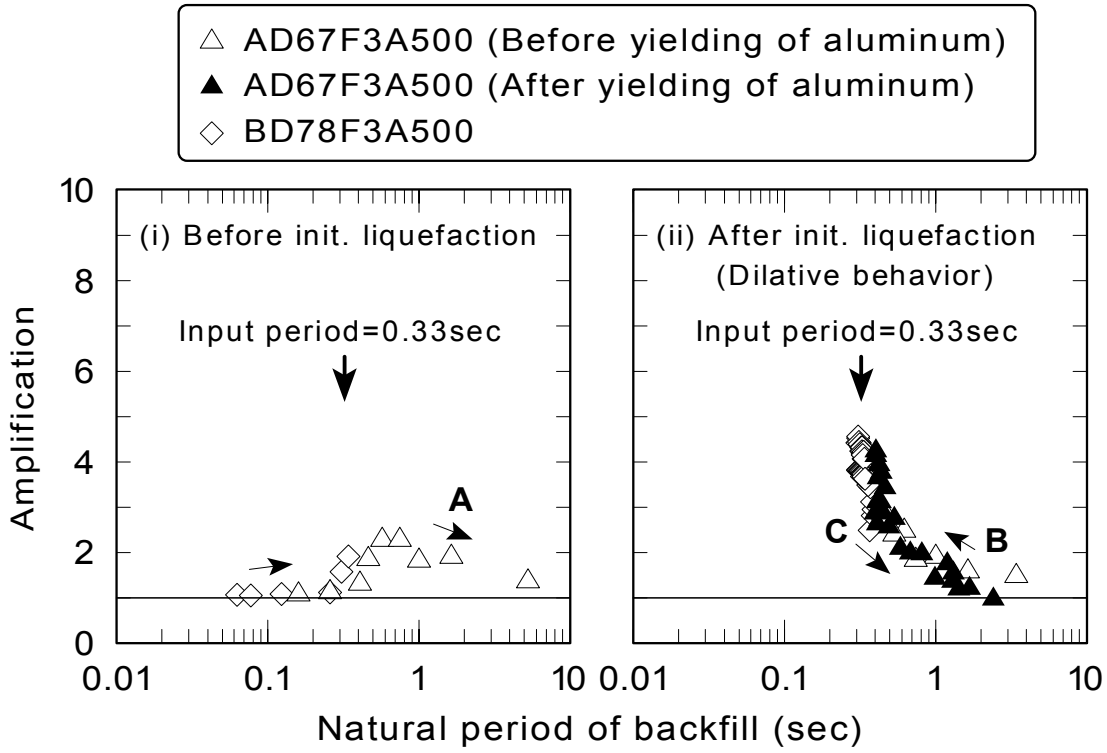

(a) Amplification

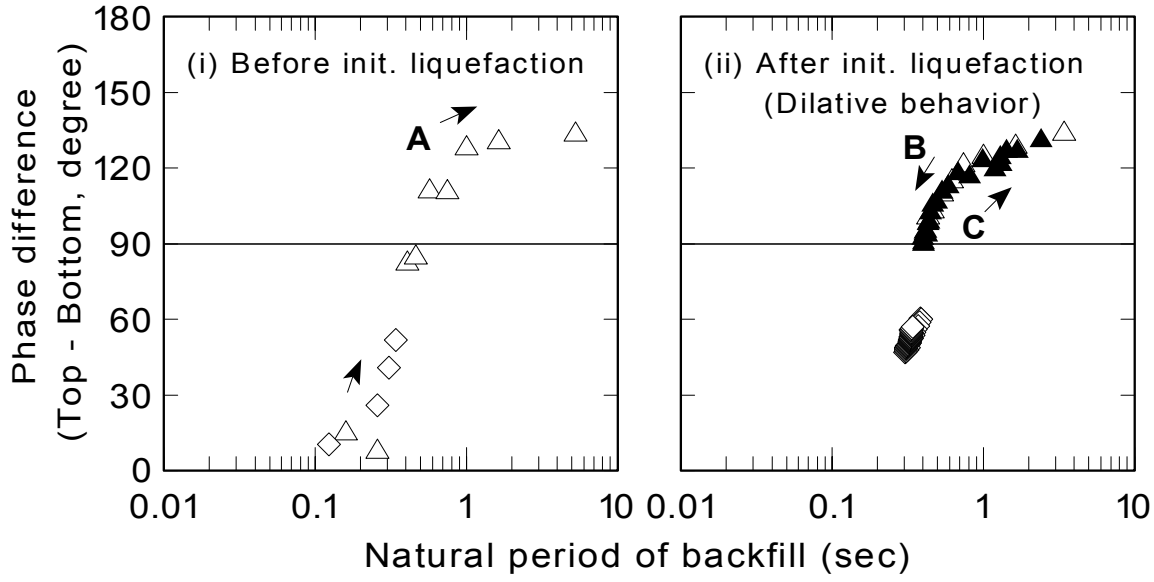

(b) Phase difference

Fig.5.17. Amplification and phase difference with respect to natural period of backfill during dilative behavior of soil

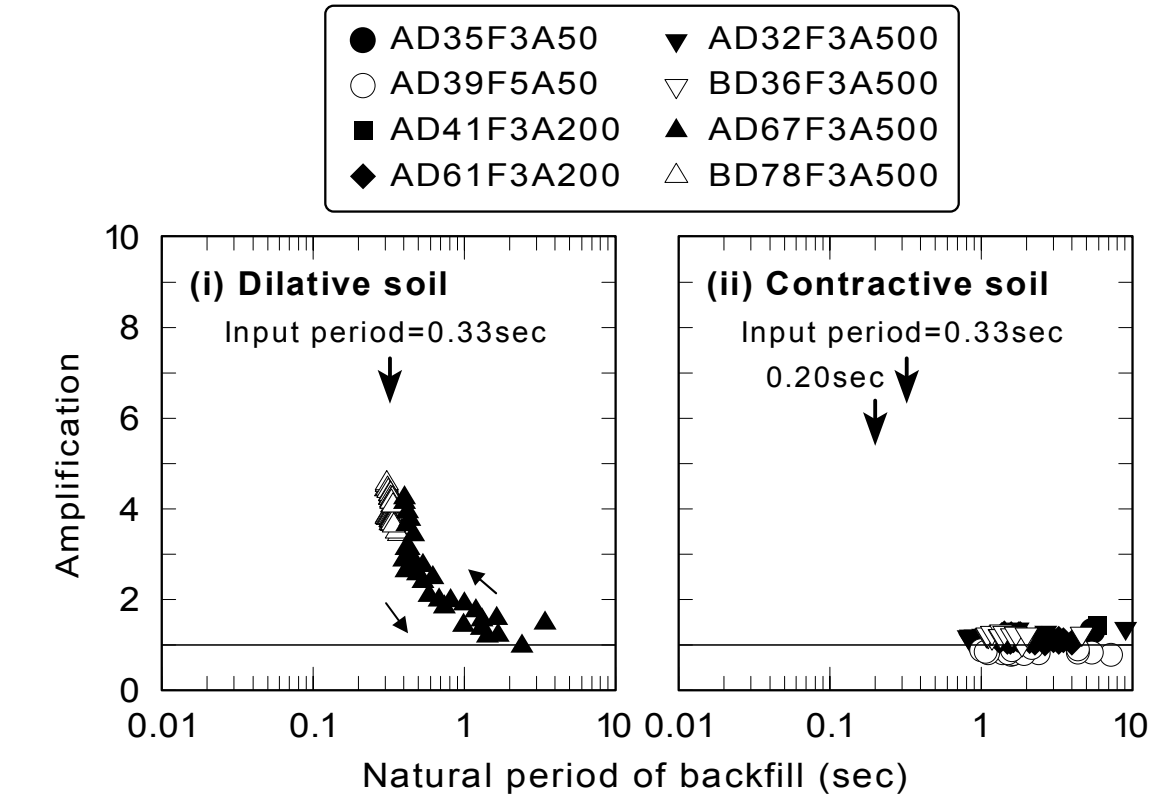

(a) Amplification

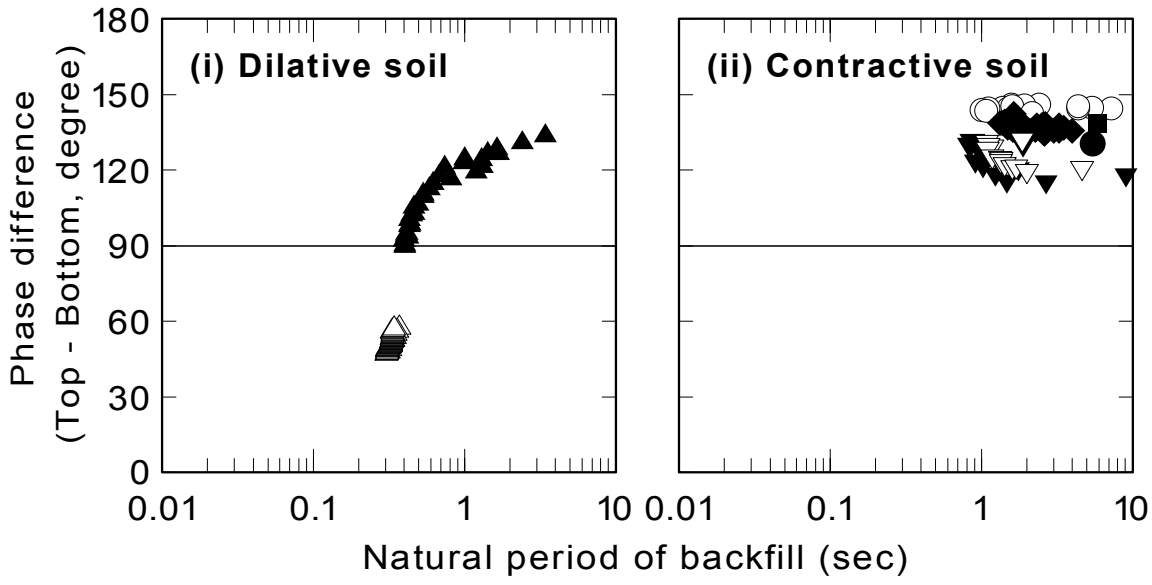

(b) Phase difference

Fig.5.18: Comparisons of responses between (i)dilative soil, (ii)contractive soil

5.5 CONCLUDING REMARKS

A series of shaking table test results was analyzed in order to investigate the response characteristics of underground structure subjected to soil liquefaction. The natural period or natural frequency of backfill, which was derived in Chapter 4, were related to the response characteristics such as the amplification and the phase difference between the top and the bottom of the structure. The following are conclusions based on the study in this chapter:

1. Significant change of amplification and phase difference of underground structure occurs before the initial liquefaction when the shear modulus of backfill decreased rapidly due to pore pressure generation.
2. The backfill with reduced shear modulus makes the natural period of underground structure long, and the process of shear modulus reduction causes the resonance of underground structure.
3. Ratio of excess pore water pressure at resonance depends on the period of base horizontal motion. When the period of base horizontal motion is long, the resonance occurs in the condition of higher pore water pressure ratio. In contrast, the period of base horizontal motion is short, the resonance occurs at lower pore water pressure ratio. The maximum pore pressure ratio at resonance is about 0.8 in tests conducted in this study.
4. The maximum amplification of this type of embedded structure at the resonance are experimentally in the range of 2.5～3.0, corresponding to the damping ratio of 0.2～0.3 when the structure is assumed as a single mass spring model. Phase difference between the top and the bottom of the structure is 90 degrees. In addition, the amplification during complete liquefaction is experimentally in the range of 1.0～1.5, and phase difference between the top and the bottom of the structure is about 150 degrees.
5. The damping ratio of underground structure at resonance has a correlation with the damping ratio of backfill during shaking. Although a theoretical reason is not clarified, the maximum amplification of underground structure at resonance seems have some relation to the damping ratio of liquefied soil.
6. After the initial liquefaction, the backfill behaves either in a contractive manner or in a dilative manner depending on the initial relative density of the backfill. When the backfill behaves in a contractive manner, the acceleration does not amplify by the effect of state of seismic isolation

due to liquefied soil.

7. When the backfill behaves in a dilative manner, the complicated change of amplification could be occurred due to residual shear modulus of backfill.

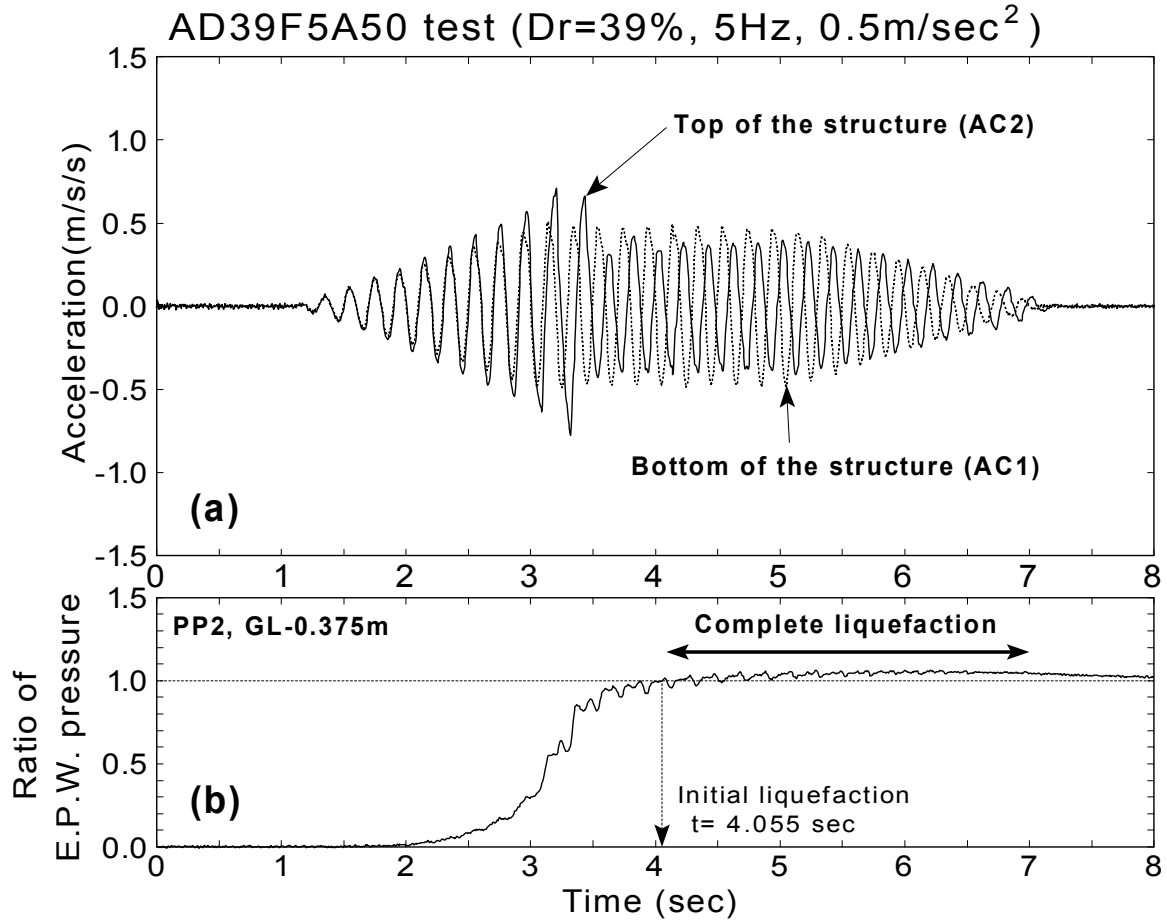

Fig.5.19: Acceleration of structure and pore pressure ratio (AD39F5A50 test)

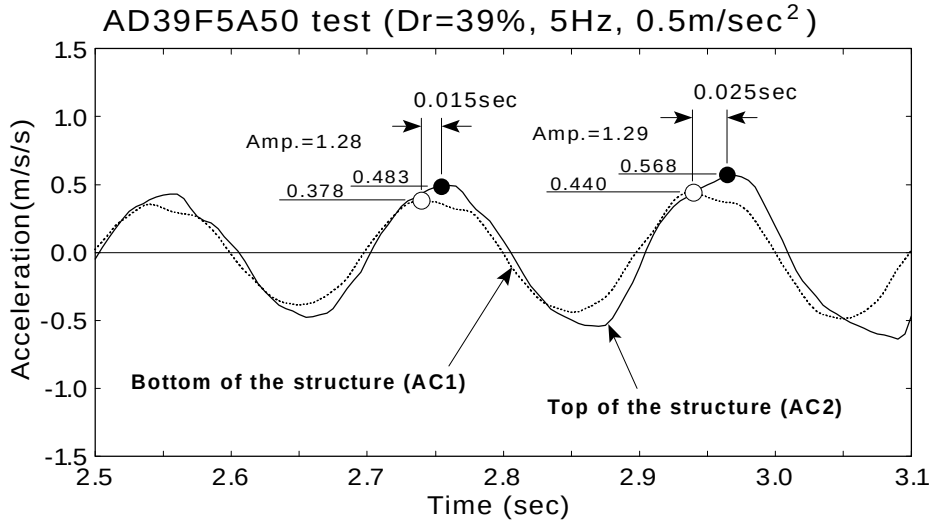

(a) Pore pressure ratio 0.3～0.6 (2.5sec～3.1sec)

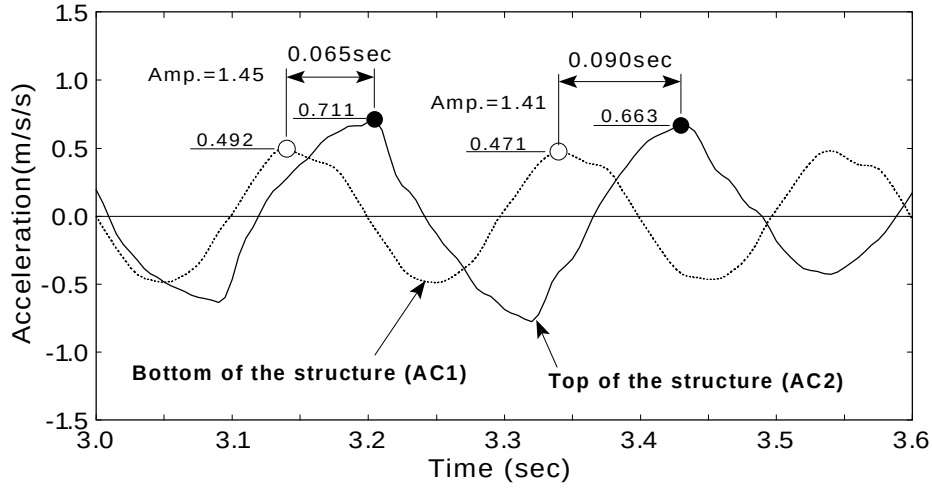

(b) Pore pressure ratio 0.6～1.0 (3.0sec～3.6sec)

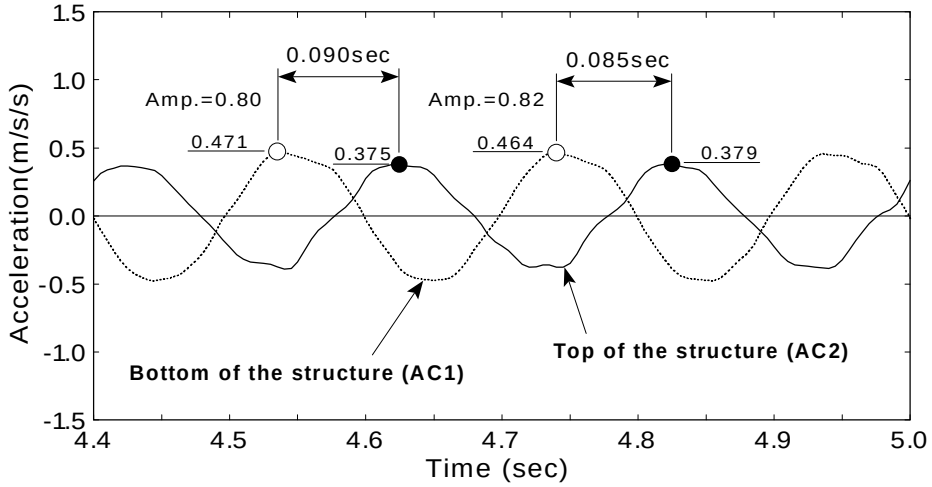

(c) Pore pressure ratio 1.0 (4.4sec～5.0sec)

Fig.5.20: Amplification and phase difference of accelerations (AD39F5A50 test)

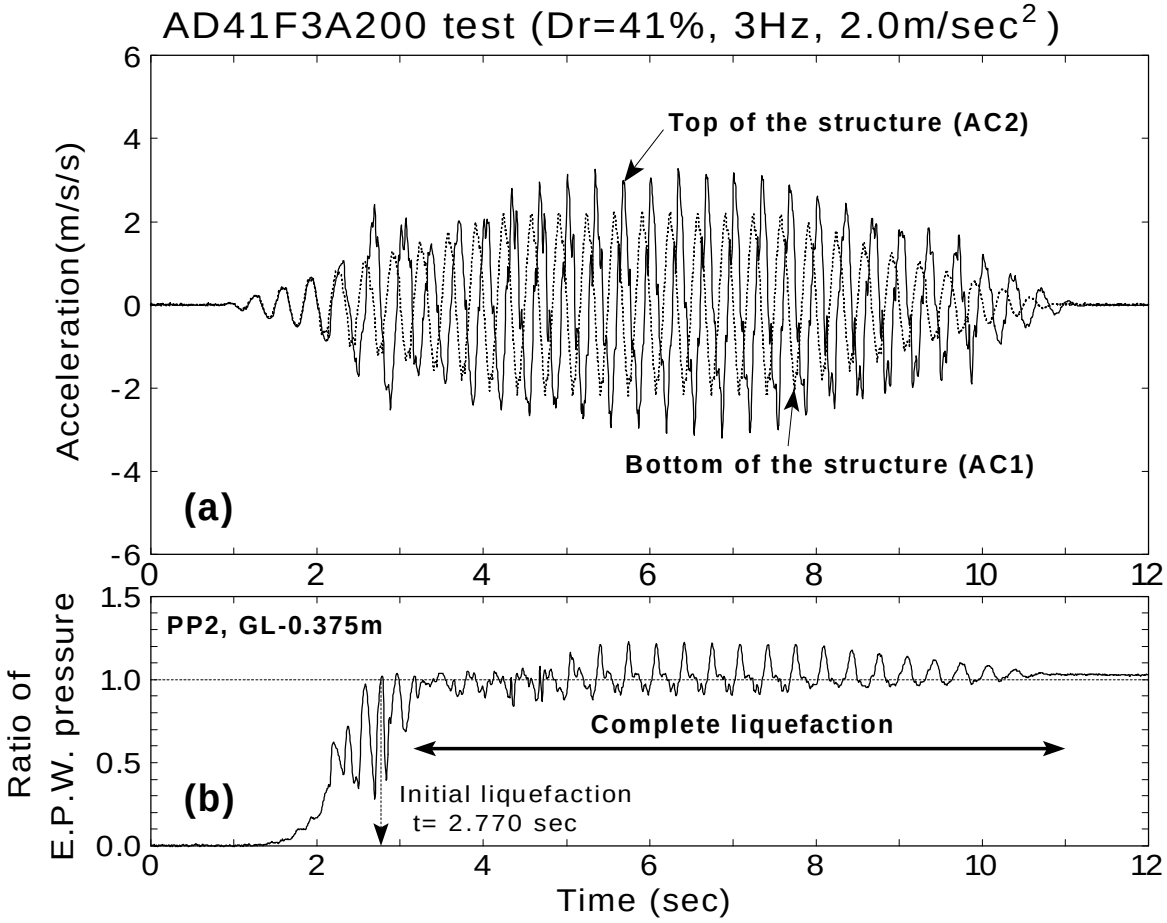

Fig.5.21: Acceleration of structure and pore pressure ratio (AD41F3A200 test)

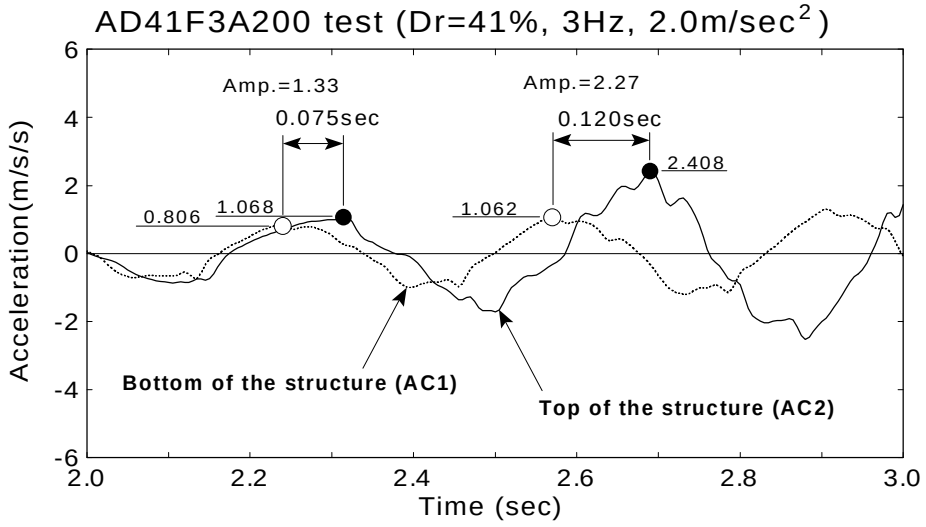

(a) Pore pressure ratio 0.3～0.7 (2.0sec～3.0sec)

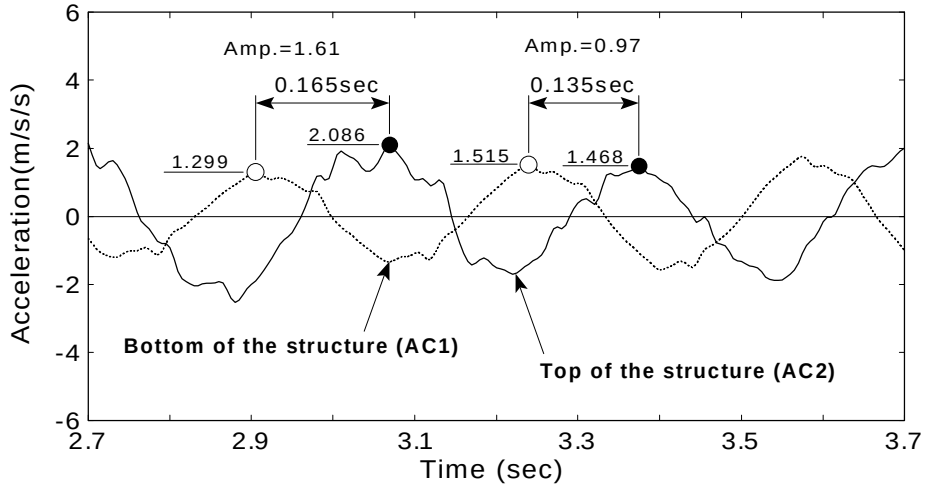

(b) Pore pressure ratio 0.7～1.0 (2.7sec～3.7sec)

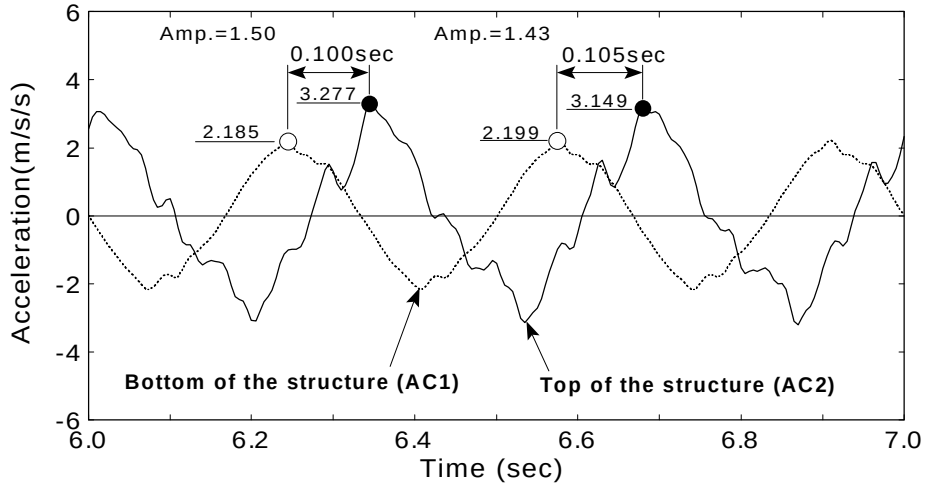

(c) Pore pressure ratio 1.0 (6.0sec～7.0sec)

Fig.5.22: Amplification and phase difference of accelerations (AD41F3A200 test)

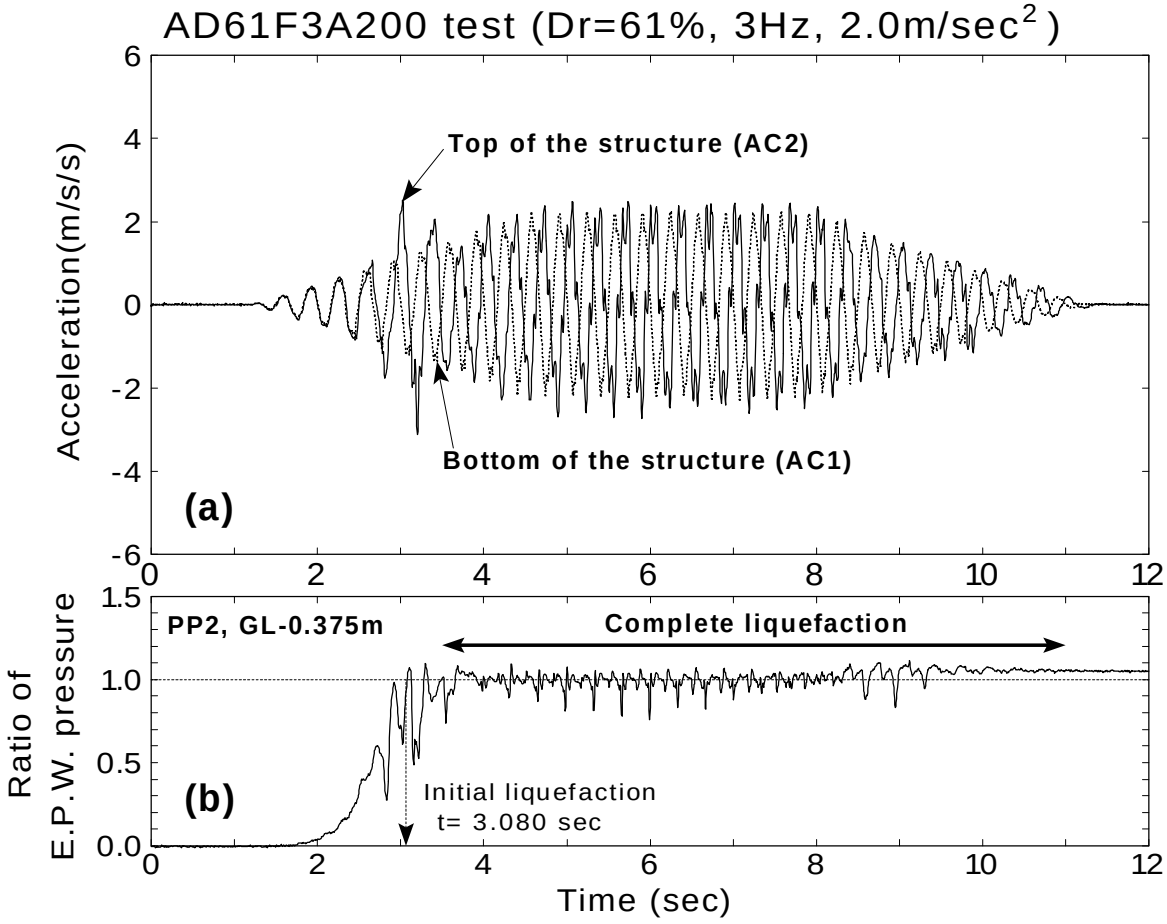

Fig.5.23: Acceleration of structure and pore pressure ratio (AD61F3A200 test)

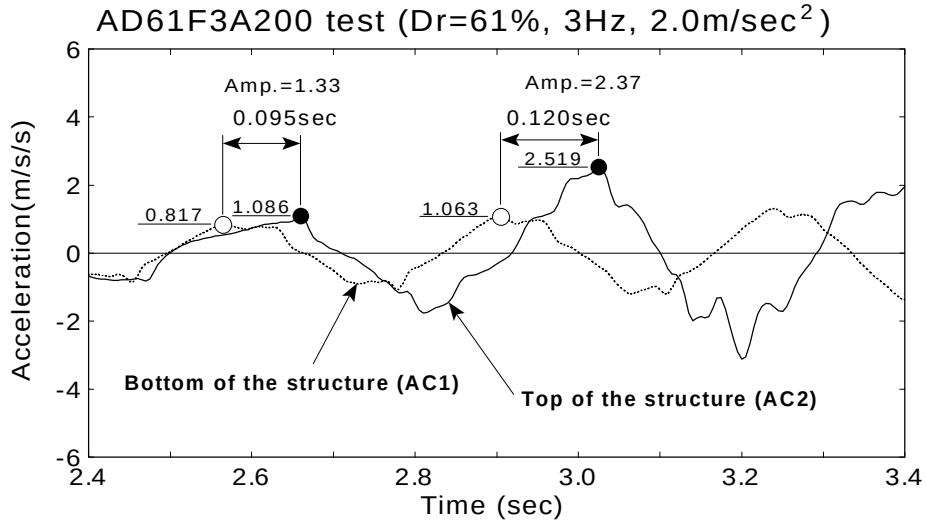

(a) Pore pressure ratio 0.3～0.7 (2.4sec～3.4sec)

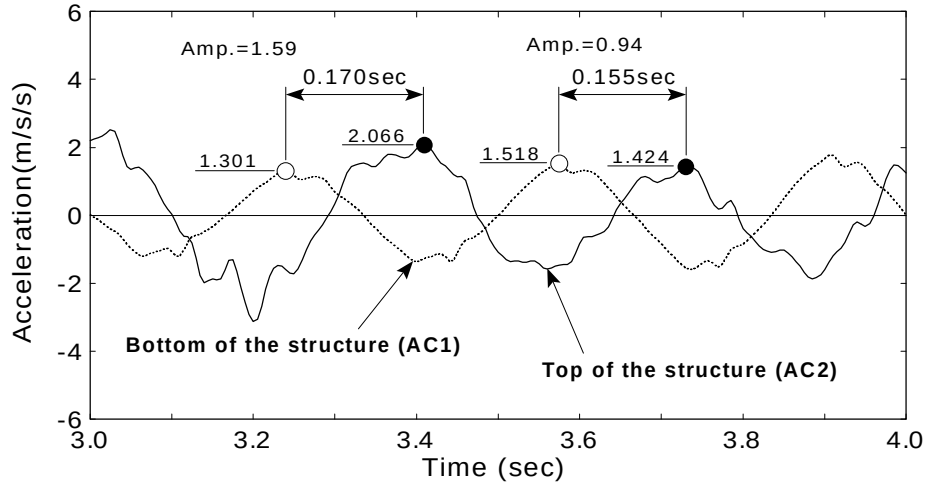

(b) Pore pressure ratio 0.7～1.0 (3.0sec～4.0sec)

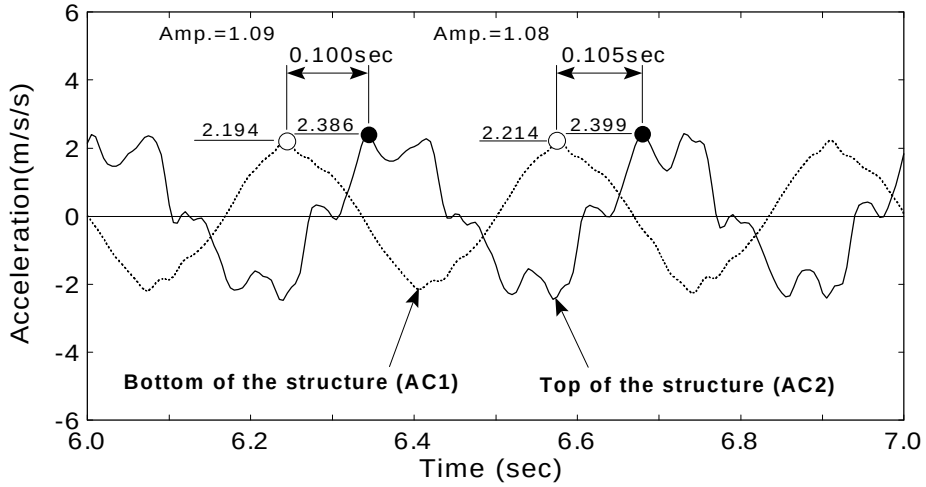

(c) Pore pressure ratio 1.0 (6.0sec～7.0sec)

Fig.5.24: Amplification and phase difference of accelerations (AD61F3A200 test)

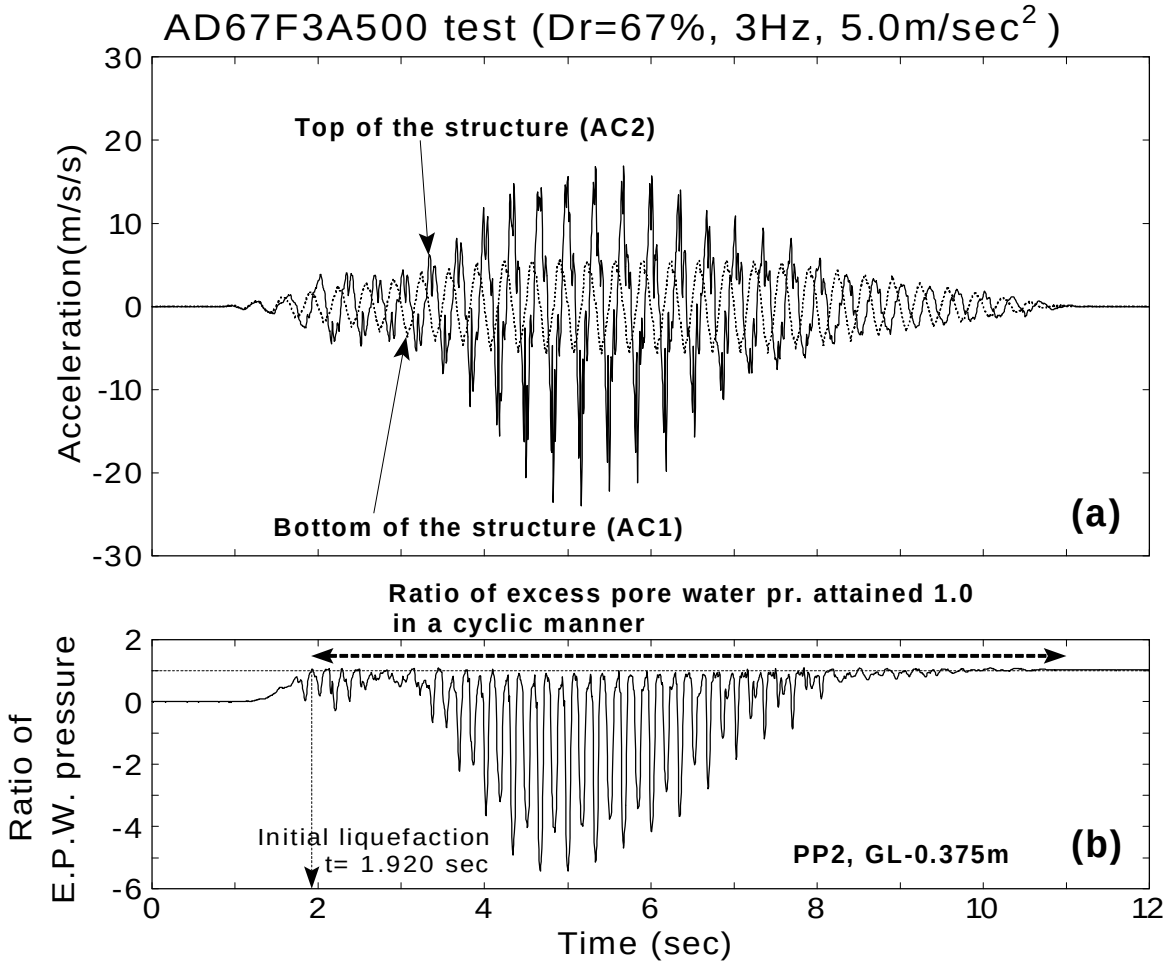

Fig.5.25: Acceleration of structure and pore pressure ratio (AD67F3A500 test)

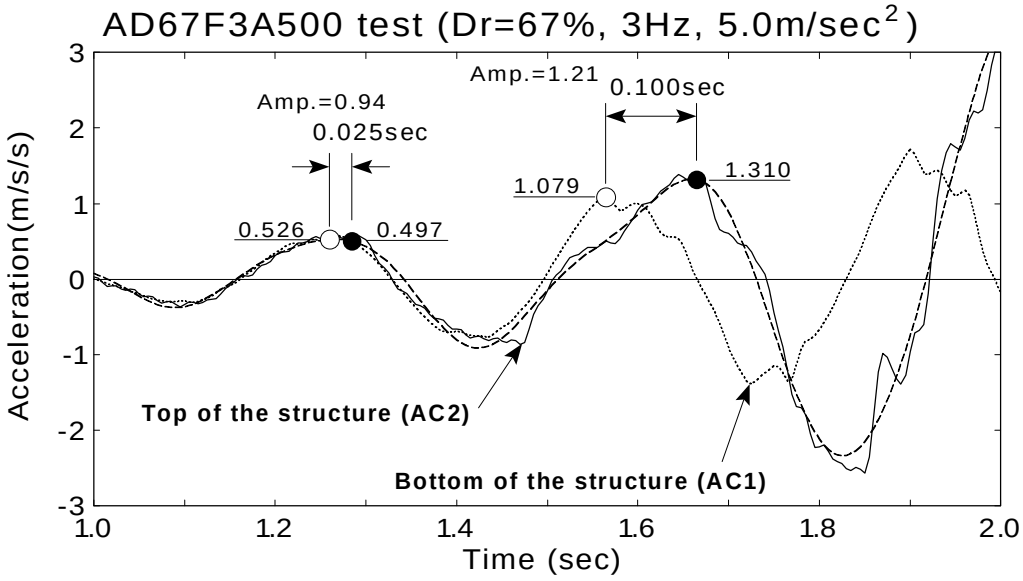

(a) 1.0sec～2.0sec (Pore pressure ratio 0.0～1.0)

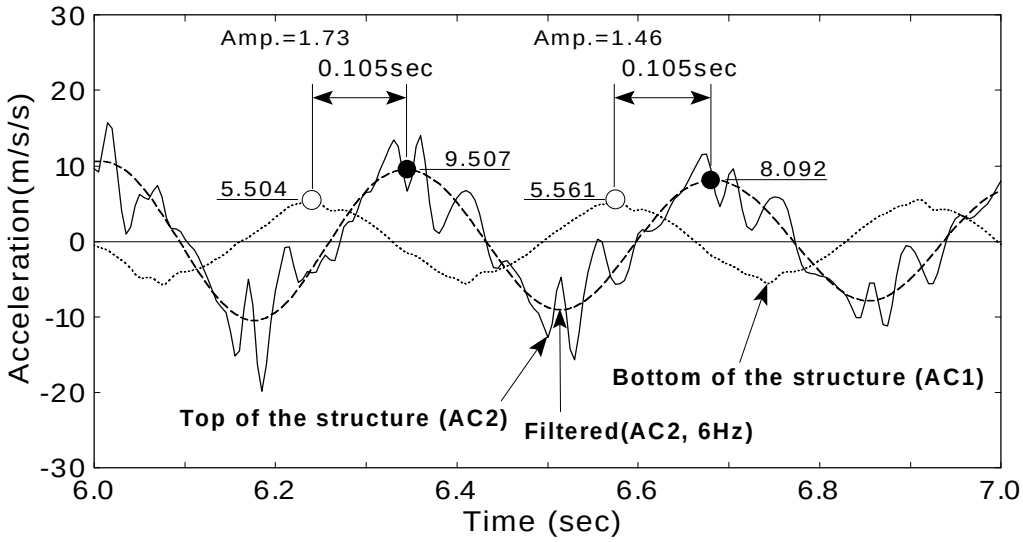

(b) 6.0sec～7.0sec (Pore pressure ratio 1.0)

Fig.5.26: Acceleration time history curves (AD67F3A500 test)

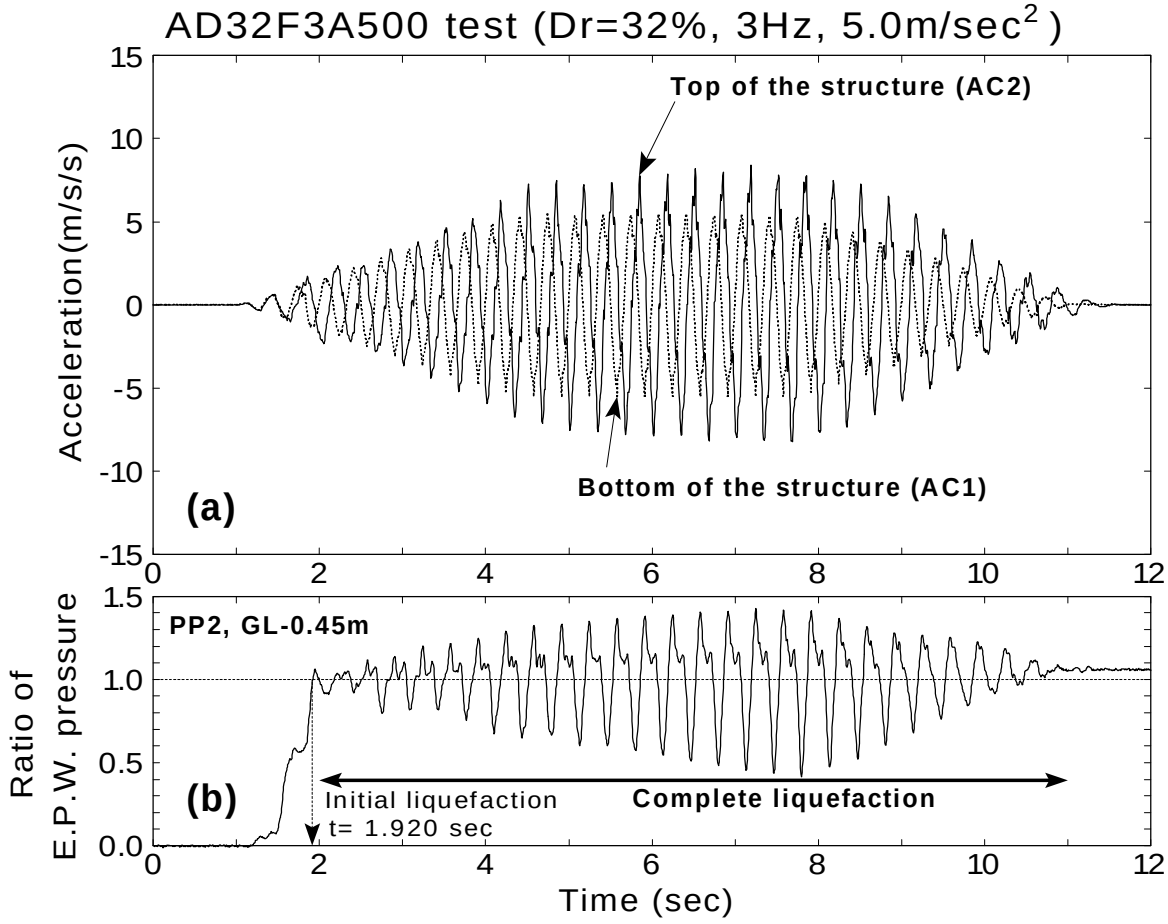

Fig.5.27: Acceleration of structure and pore pressure ratio (AD32F3A500 test)

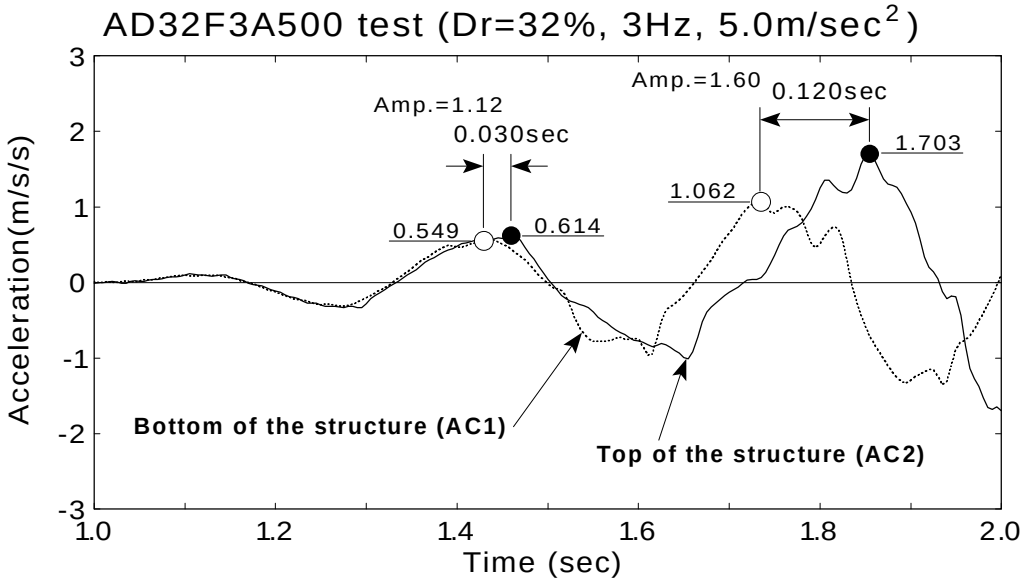

(a) 1.0sec～2.0sec (Pore pressure ratio 0.0～1.0)

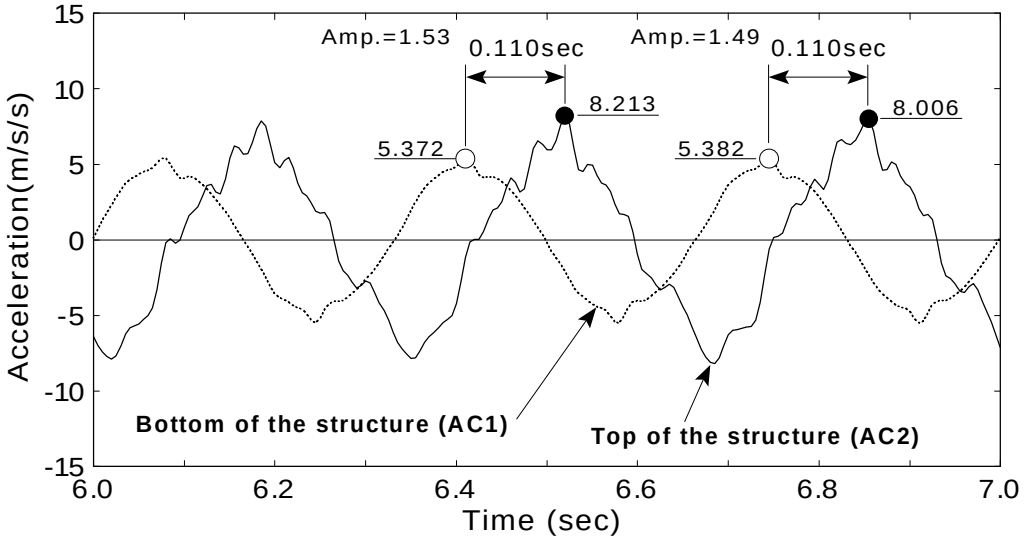

(b) 6.0sec～7.0sec (Pore pressure ratio 1.0)

Fig.5.28: Acceleration time history curves (AD32F3A500 test)

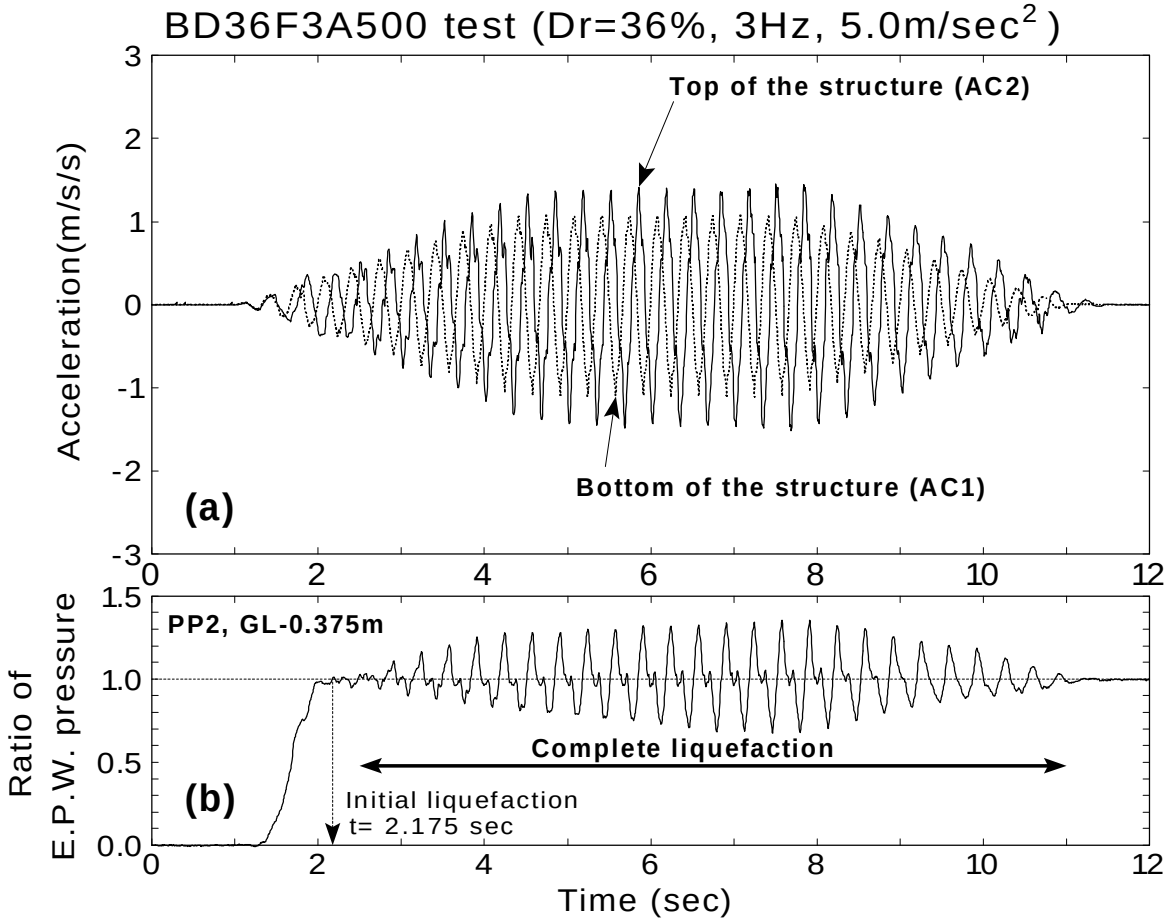

Fig.5.29: Acceleration of structure and pore pressure ratio (BD36F3A500 test)

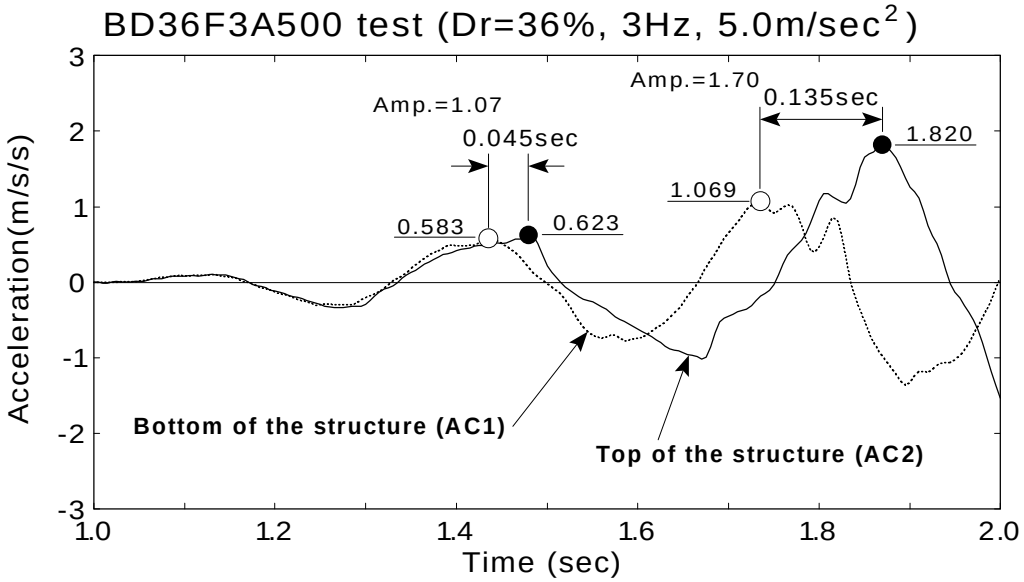

(a) 1.0sec～2.0sec (Pore pressure ratio 0.0～1.0)

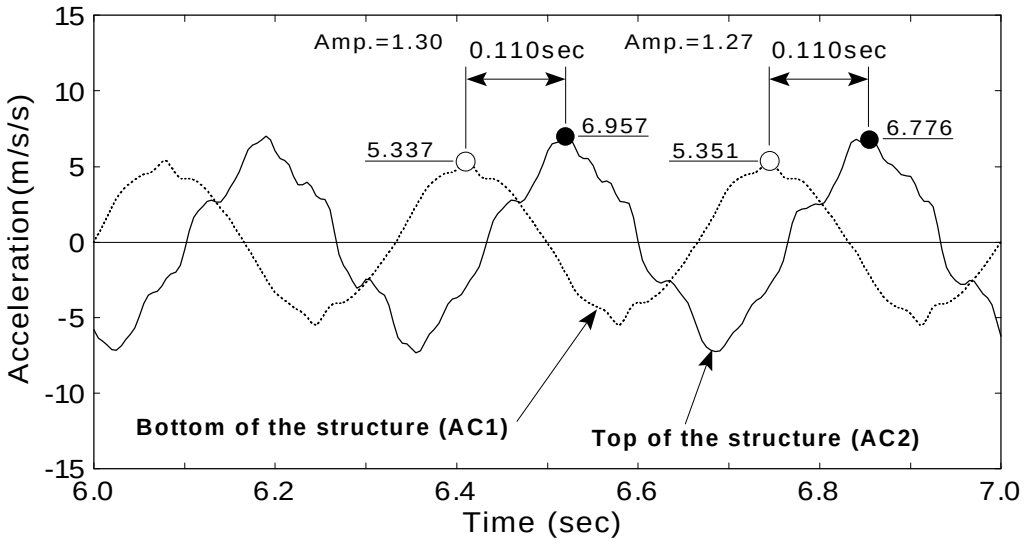

(b) 6.0sec～7.0sec (Pore pressure ratio 1.0)

Fig.5.30: Acceleration time history curves (BD36F3A500 test)

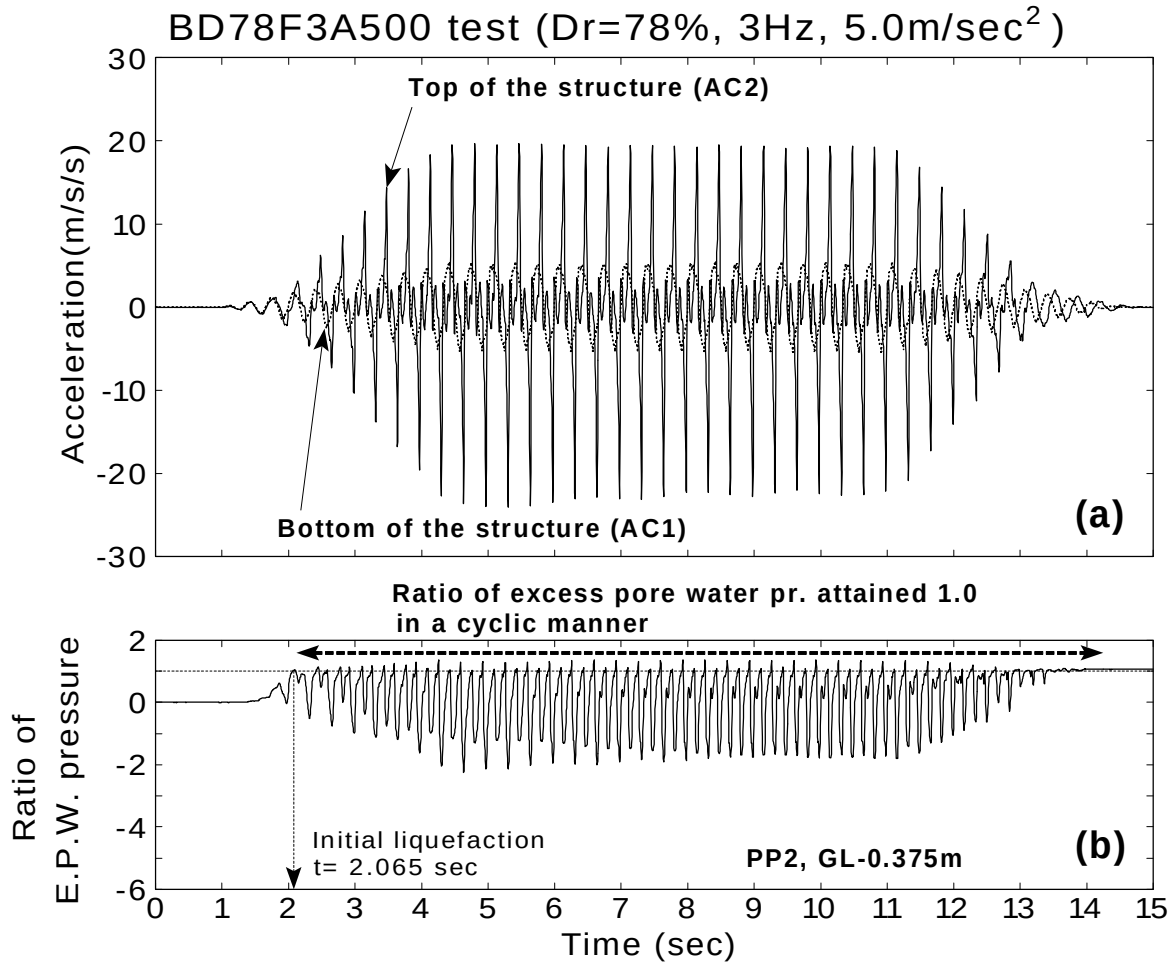

Fig.5.31: Acceleration of structure and pore pressure ratio (BD78F3A500 test)

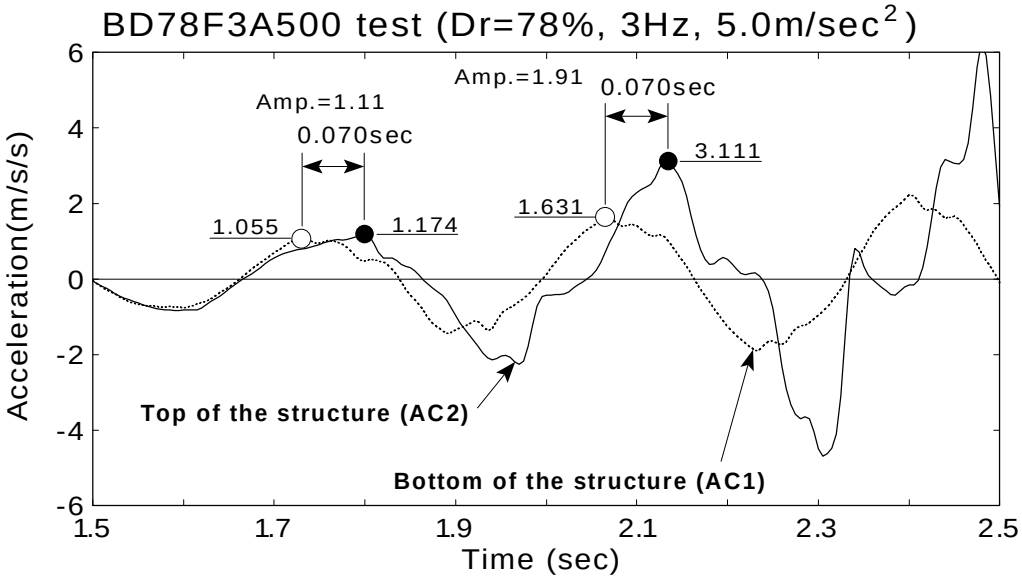

(a) 1.5sec～2.5sec

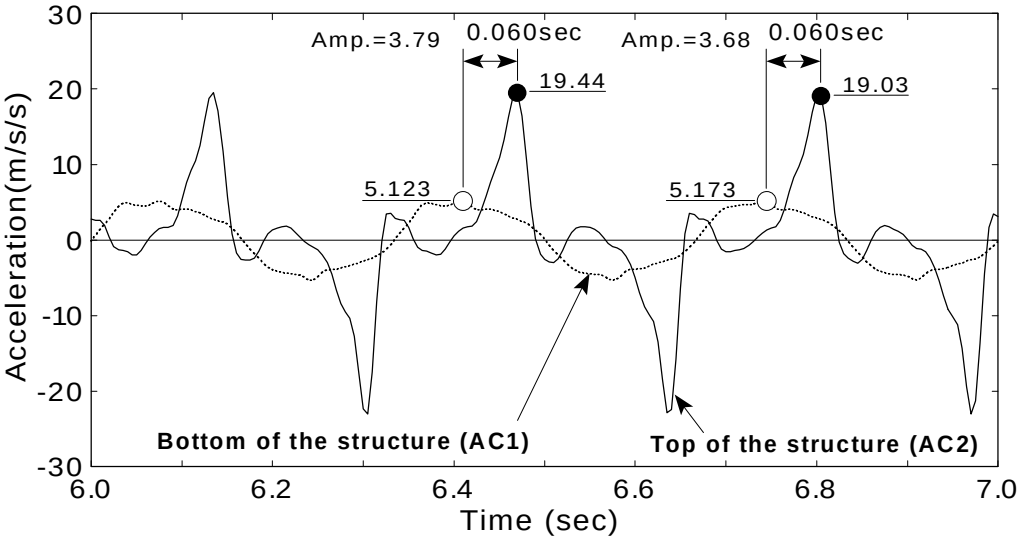

(b) 6.0sec～7.0sec

Fig.5.32: Acceleration time history curves (BD78F3A500 test)